



SORBONNE UNIVERSITÉ  
École doctorale des Sciences de la Terre et de l'environnement et Physique de  
l'Univers, Paris (ED 560)

Laboratoire de Physique Nucléaire et de Hautes Énergies

## Observation du couplage du boson de Higgs aux quarks-b avec le détecteur ATLAS

*Présenté par*

**Ilaria Luise**

THÈSE DE DOCTORAT DE PHYSIQUE

*Dirigée par Dr Gregorio Bernardi  
Co-dirigée par Dr Giovanni Marchiori*

Présentée et soutenue publiquement le 27 Septembre 2019 devant le jury composé de :

M.	Cristophe	BALLAND	Président
M.	Jean-Baptiste	DE VIVIE DE REGIE	Rapporteur
M.	Patrick	JANOT	Rapporteur
M.	Marumi	KADO	Examineur
Ms.	Kerstin	TACKMANN	Examinatrice
M.	Vincent	TISSERAND	Examineur
M.	Gregorio	BERNARDI	Directeur de thèse
M.	Giovanni	MARCHIORI	Co-directeur de thèse







SORBONNE UNIVERSITÉ  
École doctorale des Sciences de la Terre et de l'environnement et Physique de  
l'Univers, Paris (ED 560)

Laboratoire de Physique Nucléaire et de Hautes Énergies

## **Observation of the Higgs boson coupling to b-quarks with the ATLAS detector**

*Presented by*

**Ilaria Luise**

*Submitted in fulfillment of the requirements for the degree of*

DOCTEUR DES SCIENCES SORBONNE UNIVERSITÉ

*Supervised by Dr. Gregorio Bernardi  
Co-supervised by Dr. Giovanni Marchiori*

Defended on the 27th of September 2019 in front of the committee :

Mr.	Christophe	Balland	President
Mr.	Jean-Baptiste	De Vivie De Regie	Referee
Mr.	Patrick	Janot	Referee
Mr.	Marumi	Kado	Examiner
Ms.	Kerstin	Tackmann	Examiner
Mr.	Vincent	Tisserand	Examiner
Mr.	Gregorio	Bernardi	Supervisor
Mr.	Giovanni	Marchiori	Co-Supervisor





# Abstract

This thesis presents the results of the search for the Standard Model Higgs boson decay to a pair of bottom quarks, carried with data at  $\sqrt{s} = 13$  TeV collected with the ATLAS detector at the LHC between 2015 and 2017.

The Standard Model Higgs boson - with a mass of  $m_H = 125$  GeV - is expected to decay to a pair of bottom quarks, also referred to as  $H \rightarrow b\bar{b}$ , more than half of the times (58%). An experimental confirmation of this process is crucial to probe the mechanism of quark mass generation of down type quarks and heavily constrain the possibility of new physics in the Higgs sector.

The search has been carried selecting the Higgs boson produced in association with a vector boson (VH), which ensures high background rejection thanks to the additional leptonic signatures in the final state.

The core of this thesis work is the analysis performed in 2018 with 80 fb<sup>-1</sup> of ATLAS data. The analysis strategy, the event selection and the treatment of the systematic uncertainties affecting the measurement are presented in details in the document. The measured signal strength ( $\sigma \cdot BR / \sigma_{SM} \cdot BR_{SM}$ ) is  $\mu = 1.16^{+0.16}_{-0.16}(\text{stat.})^{+0.21}_{-0.19}(\text{syst.})$ , while the significance of the measurement is 4.9 standard deviations ( $\sigma$ ) compared to an expected significance of 4.3 standard deviations.

The sensitivity of the analysis has been enhanced combining this result with the Run-1 analysis at 7 and 8 TeV, for a total of 105 fb<sup>-1</sup>. A total observed (expected) significance of 4.9 (5.1) standard deviations has been obtained, with a signal strength of  $\mu_{VH}^{bb} = 0.98^{+0.22}_{-0.21} = 0.98 \pm 0.14(\text{stat.})^{+0.17}_{-0.16}(\text{syst.})$ .

The sensitivity to the VH production mode has been increased combining the VH,  $H \rightarrow b\bar{b}$  Run-2 result with other Run-2 analyses sensitive to the VH production mode. Fixing the branching ratios of each final state to its SM value, the overall signal strength of the VH process is  $\mu_{VH} = 1.13^{+0.24}_{-0.23} = 1.13 \pm 0.15(\text{stat.})^{+0.18}_{-0.17}(\text{syst.})$ , with an observed significance of 5.3 standard deviations, and an expected significance of 4.8 standard deviations.

Similarly, the sensitivity to the  $H \rightarrow b\bar{b}$  decay has been enhanced by a combination with other Run-1 and Run-2 analyses sensitive to this decay channel. The signal strength of the  $H \rightarrow b\bar{b}$  decay has been obtained fixing the production modes to their SM predictions. The combined value is  $\mu_{H \rightarrow b\bar{b}} = 1.01 \pm 0.2 = 1.01 \pm 0.12(\text{stat.})^{+0.16}_{-0.15}(\text{syst.})$ , with an expected (observed) significance of 5.4 (5.5) standard deviations.

Both combinations have a significance above the 5 $\sigma$  threshold, meaning that for the first time the VH production mode and the  $H \rightarrow b\bar{b}$  decay have been measured with enough precision to claim their observation.

The thesis summarizes the main aspects of my contribution to the 2018 round of this analysis and the next one, expected to be public for the end of 2019. Furthermore, it also focuses on another aspect of my contribution in ATLAS during the three years of PhD, which is the energy calibration of low energy electrons, used for example in the  $H \rightarrow 4\ell$  analysis, with  $J/\psi \rightarrow e^- e^+$  events.



## Acknowledgements

The work of these three years would not have been possible without the support and the encouragement of many people.

First and foremost, I would like to thank my two supervisors, Giovanni and Gregorio, for assigning me to such a stimulating analysis and for the help during these three years. Nothing of this would have been possible without you.

A big thank you goes at the same time to Valerio, for all the guidance, advice and support given throughout the last two years. Thanks for all the b-tagging coffees at building 13, most of the work presented in this thesis comes from those fruitful discussions. You are a great person and a great teacher, and I am doubtful that I will ever be able to pay the debt that I owe you, in time or patience. I have learned more from those discussions, than from days and days spent on codes, books or twikis. I feel extremely lucky to have met you!

I would also like to thank all the members of the  $H \rightarrow b\bar{b}$  group, past and present, I had the pleasure to work with in the last years. Thank you for the fruitful discussions and for all the emotions we went through together during the incredible experience of the one week rush in July 2018. The beauty of this result really reflects the quality of the group (and the super-powers of some of us). Thank you also to the ATLAS "tracking" group at the LPNHE, especially to Marco, for letting me be involved in the ITk test beams and for cultivating my interests in hardware physics.

I would like to thank all the people I met during these four amazing years of life in Paris. Thanks for letting me taste, imagine and live all these hints of everyday life in your beautiful countries. The list of places I want to visit thanks to your suggestions is almost endless.

A big thank goes to all the PhD students at LPNHE, especially Ahmed, Louis and Emilie in my office and those I know since NPAC, for the friendly environment we have been able to create inside and outside the office. Thank you also to the friends I made at CERN, especially the Milano group (of PhDs), who welcomed me in during my months in Geneva.

And then, obviously, thanks to my family abroad: Lucia, Scarpa and Pino. The Italian corner will keep existing, even if we will be separated by oceans and life choices. You have been fundamental pillars of my life for the last eight years (eight!), and probably this PhD would have never been finished without your support in many many occasions. Thank you for making me feel at home, even at 1000 km distance.

A big thank you goes to my lifelong friends, Otti, Bob, Dodo and all the others, as well as the newcomers like Matilde. Despite the distance and all these years abroad, you really make me feel as I never left. You always find a way to put back a smile on my face, and I have missed the magic atmosphere we are able to create when we are all together. Thank you for coming to Paris, no words will be enough to explain the joy of having all of you with me at the defence, and how grateful I am to have friends like you. I love you, little foxes of my heart.

Finally, thanks to my mum and dad, who have always supported my choices, even if they brought me far from home. Thanks for being able to find the right words to cheer me up in the difficult moments, and for making me feel always loved and supported in any moment of this journey. Thanks for all the encouragement and advice, I will be eternally thankful for suggesting me to go to CERN, it has been a life-changing experience that I would redo thousands of times. Thanks to my grandma, for the dish of home-made *cappellacci* always ready for me when I come back home, and thanks to my grandpa, Claudio, for inspiring me to pursue my studies in this field. If I had to dedicate the thesis to somebody, it would be you.

At last, thanks to Michele for being my safe harbour, especially in this last year of emotional storms. Thank you for reminding me that life is much more than a PhD. Even when separated by 10,000 km, you made it always worthwhile.

# Contents

<b>Abstract</b>	<b>iii</b>
<b>Acknowledgements</b>	<b>v</b>
<b>1 Introduction</b>	<b>1</b>
<b>2 Theoretical framework</b>	<b>5</b>
2.1 The Standard model Lagrangian . . . . .	6
2.1.1 Fundamental particles . . . . .	7
2.1.2 Quantum Chromodynamics . . . . .	8
2.1.3 The Electroweak unification . . . . .	10
2.2 Mass generation and the Higgs mechanism . . . . .	12
2.2.1 The Brout-Englert-Higgs mechanism . . . . .	12
2.2.2 Yukawa coupling to the fermion sector . . . . .	14
2.3 Cross sections and Decay rates . . . . .	15
2.3.1 Definition of cross section . . . . .	15
2.3.2 Definition of decay width . . . . .	17
2.3.3 Measurement of Higgs couplings . . . . .	17
2.4 The need for higher order corrections . . . . .	18
2.4.1 The parton model beyond the Leading Order . . . . .	20
2.5 Searching for the Higgs boson at the LHC . . . . .	22
2.5.1 Higgs production modes at LHC . . . . .	22
2.5.2 Higgs decay channels . . . . .	23
2.6 Experimental verifications . . . . .	24
2.6.1 Limitations of the Standard Model . . . . .	27
2.7 From theory to event simulation . . . . .	30
2.7.1 Available generators . . . . .	33
<b>3 The Large Hadron Collider and the ATLAS detector</b>	<b>35</b>
3.1 The Large Hadron Collider . . . . .	36
3.1.1 Luminosity . . . . .	37
3.1.2 Mean number of interactions per bunch-crossing . . . . .	38
3.1.3 LHC experiments and physics research . . . . .	38
3.2 The ATLAS experiment . . . . .	40
3.2.1 The magnet system . . . . .	41
3.2.2 Inner Detector and Tracking . . . . .	42
Pixel Detector . . . . .	42
SemiConductor Tracker . . . . .	44
Transition Radiation Tracker . . . . .	45
3.2.3 Electromagnetic Calorimeter . . . . .	45

3.2.4	Hadronic Calorimeter . . . . .	46
3.2.5	Muon spectrometer . . . . .	48
3.2.6	Trigger System . . . . .	49
	Luminosity detectors . . . . .	50
<b>4</b>	<b>Reconstruction of physics objects</b>	<b>53</b>
4.1	Tracking and Vertex reconstruction . . . . .	53
4.2	Electrons . . . . .	56
4.2.1	Identification algorithms . . . . .	59
4.2.2	Isolation . . . . .	60
4.3	Muons . . . . .	61
4.3.1	Identification . . . . .	62
4.3.2	Isolation . . . . .	63
4.4	Jets . . . . .	65
4.4.1	Jet calibration . . . . .	66
4.4.2	Jet cleaning . . . . .	68
4.4.3	Truth flavour labelling . . . . .	69
4.5	Overlap removal . . . . .	69
4.6	Taus . . . . .	70
4.7	Missing transverse momentum . . . . .	70
<b>5</b>	<b>Flavour Tagging in ATLAS</b>	<b>73</b>
5.1	Basic flavour tagging algorithms . . . . .	73
5.1.1	Track-jet matching . . . . .	74
5.1.2	The Impact Parameter based Algorithms: IPxD and IP RNN . . . . .	74
	IPxD algorithms . . . . .	75
	IP RNN . . . . .	78
5.1.3	The Secondary Vertex based Algorithms: SV . . . . .	79
5.1.4	The decay chain multi-vertex Algorithm: JetFitter . . . . .	81
5.1.5	Soft Muon Tagger: SMT . . . . .	82
5.2	High-level tagging algorithms . . . . .	84
5.2.1	MV2c10 algorithm . . . . .	87
5.2.2	DL1 algorithm . . . . .	89
5.2.3	Enhanced Multivariate Algorithms . . . . .	89
5.2.4	B-tagging working Points . . . . .	92
5.3	Calibration of the flavour tagging efficiency . . . . .	92
5.3.1	Reduction of the b-tagging variations . . . . .	96
5.4	Statistical tagging . . . . .	97
5.4.1	The efficiency maps . . . . .	99
5.5	Summary . . . . .	99
<b>6</b>	<b>Electron and photon energy calibration</b>	<b>103</b>
6.1	Overview of the calibration procedure . . . . .	104
6.2	Simulation based energy calibration . . . . .	105
6.3	Layer intercalibrations . . . . .	105
6.4	Uniformity corrections . . . . .	110
6.5	In-situ energy scale and resolution corrections . . . . .	110
6.6	Systematic uncertainties . . . . .	113
6.7	Photon calibration with $Z \rightarrow l\bar{l}\gamma$ events . . . . .	115
6.8	Low-momentum electron energy calibration . . . . .	116
6.8.1	Data and simulated samples . . . . .	117

6.8.2	Event selection	118
6.8.3	Kinematic distributions	123
6.8.4	Energy scale measurement	123
6.8.5	Systematic uncertainties	126
6.8.6	Results	128
	Transverse energy dependence	130
6.8.7	Resolution corrections	130
6.9	Summary	134
<b>7</b>	<b>Observation of the Higgs boson decay to <math>b\bar{b}</math> quarks</b>	<b>137</b>
7.1	Data and simulated samples	138
7.1.1	Signal processes	140
7.1.2	Background processes	141
7.1.3	Multi-jet estimation	142
7.2	Object and Event selection	143
7.2.1	Improvements on $m_{bb}$ resolution	146
7.2.2	Di-jet mass analysis additional selection	149
7.2.3	Analysis regions	149
	W+HF control region	150
	Top $e\mu$ control region	151
7.3	Multivariate analysis	151
7.3.1	Boosted Decision Trees	152
	Boosting	154
7.3.2	The MVA training setup	155
7.3.3	BDT transformation	157
7.4	Statistical Treatment	157
7.4.1	Hypothesis Testing	158
7.4.2	Likelihood Ratio	159
7.4.3	Asimov dataset	161
7.4.4	Correlations	162
7.5	Systematic uncertainties	163
7.5.1	Experimental systematic uncertainties	163
7.5.2	Introduction to modelling uncertainties	164
7.5.3	Signal uncertainties	165
7.5.4	Background uncertainties	167
7.5.5	Smoothing of the systematic uncertainties	173
7.5.6	Pruning of the systematic uncertainties	173
7.6	BTagging studies	173
7.6.1	MV2c10 vs DL1 studies	173
7.6.2	Statistical tagging	176
7.6.3	Hybrid tagging	176
7.7	Fit Results	182
7.7.1	Post-fit plots	182
7.7.2	Significances and signal strength	187
7.7.3	Ranking of the systematic uncertainties	189
7.7.4	Focus on the one-lepton channel	190
7.8	Cross-check analyses	190
7.8.1	The di-jet analysis	190
7.8.2	The diboson analysis	196
7.8.3	Signal strength	199
7.9	Combinations	200

7.9.1	Combination with the Run-1 $VH, H \rightarrow b\bar{b}$ search	200
7.9.2	VH combination	201
7.9.3	$H \rightarrow bb$ combination	202
7.10	Summary	203
<b>8</b>	<b>Further improvements towards the full Run-2 analysis</b>	<b>205</b>
8.1	Statistical tagging in $VH, H \rightarrow b\bar{b}$	205
8.1.1	Efficiency maps	207
8.1.2	Results	211
8.1.3	Hybrid tagging and impact on the analysis	211
8.2	Inclusion of the b-tagging score in the final classifier	217
8.2.1	Truth tagging in pseudo-continuous working point	218
	Customized efficiency maps	219
8.2.2	Training of the $BDT_{VH}$	222
8.2.3	Pruning of the systematic uncertainties	223
8.2.4	Impact on the analysis	227
	Impact on the signal strength	234
8.3	Summary	235
<b>9</b>	<b>Conclusions</b>	<b>237</b>
<b>A</b>	<b>Additional material for the <math>J/\psi \rightarrow ee</math> calibration</b>	<b>239</b>
A.0.1	Comparison with Run-1	239
A.0.2	Pile-up dependence	239
A.0.3	Resolution fit	244
<b>B</b>	<b>Additional material for the full Run-2 <math>VH, H \rightarrow b\bar{b}</math> analysis</b>	<b>245</b>
B.1	Compatibility cross-checks for the new customized maps	245
B.2	Zero-lepton validation plots	248
B.3	Yield tables for different tagging regimes	249
B.4	Pruned uncertainties in the pseudo-continuous WP	249



# 1 | Introduction

Our knowledge of the fundamental particles in the Universe and their mutual interactions in space and time is regulated by two main theoretical pillars: quantum mechanics and special relativity. Together with general relativity, they form a comprehensive framework able to explain the fundamental laws of the Universe spanning over 40 orders of magnitude in spatial scale. This remarkable result has been achieved in the last 150 years, with profound impacts on our perception of the laws of nature.

The mathematical formalism used to describe the subnuclear interactions is the Standard Model of particle physics (SM). The main peculiarity of the theory is that the fundamental elements are not described as individual particles in the classical sense, but as *quantum fields*. The fields are defined as operators of the spacetime which allow to compute probability distributions, more than deterministic equations of motions, to reflect the probabilistic nature of quantum mechanics. The SM particles are classified in bosons, which act as mediators of the interacting fields, and fermions, divided into quarks and leptons, which represent the fundamental building blocks of the known matter in the Universe.

The definition of *fundamental* particle evolved with time. Today quarks and leptons are commonly recognized as the main constituents of matter, but only 150 years ago such particles were not even theorized, and the atoms (literally 'uncuttable') were considered as fundamental. The discoveries of the last 150 years completely changed our idea of *fundamental*, lowering by 8 orders of magnitude what today is referred to as constituent (atom:  $10^{-10}$  m  $\rightarrow$  quark:  $< 10^{-18}$  m).

The first breakthrough opening the era of subatomic physics has been the discovery of the electron by J.J. Thomson in 1897 [1]. Then, the structure of the atom has been first investigated by Rutherford [2], and later by several fixed target experiments [3] [4]. Higher and higher energy and complexity have been achieved in the last 50 years, thanks to the remarkable developments in accelerator physics. A series of increasingly complex machines at SLAC, FermiLab and later at CERN allowed to study the subatomic scale in great detail, leading to the discovery of all the spectrum of particles predicted by the SM.

The latest missing piece has been discovered in July 2012 by ATLAS and CMS [5] [6], the two general-purpose experiments of the Large Hadron Collider (LHC) at CERN, in Geneva. They claimed the observation of a scalar particle of mass around 125 GeV, compatible with the so-called Higgs boson and with the predictions from electroweak precision measurements in the SM context. This particle plays a crucial role in describing the mechanism of mass generation of all the particles in the SM (including the Higgs boson itself), without breaking the gauge invariance of the theory. In a nutshell, the fermions are expected to acquire mass thanks to their interaction with the *Higgs field*, a scalar field carried by the Higgs boson, while the massive bosons acquire their mass during the electroweak spontaneous symmetry

breaking. Two mechanisms are thus at play: the Brout-Englert-Higgs mechanism [7] [8] to explain the mass generation of the weak interaction massive carriers and the Yukawa mechanism for quarks and leptons.

The discovery of July 2012 has been done using mostly the bosonic decay modes of the Higgs boson ( $H \rightarrow \gamma\gamma$ ,  $H \rightarrow ZZ$  and  $H \rightarrow WW$ ). The observed results are in remarkable agreement with the expectations of the Brout-Englert-Higgs mechanism. The same dataset collected during the first Run (Run-1) of LHC - between 2010 and 2012 - allowed for the measurement of the coupling with  $\tau$  leptons from  $H \rightarrow \tau\tau$  decays, made combining ATLAS and CMS analyses [9], which has been the first and sole significant test of the Yukawa mechanism in Run-1.

One of the main goals of the second Run of LHC (Run-2) is thus to study the Higgs boson coupling to the other particles of the fermion sector, to verify the predictions or to identify possible deviations from the Yukawa theory. In this spirit, the first significant test with Run-2 data came from the observation of the  $t\bar{t}H$  production mode by both ATLAS and CMS [10] [11], which for the first time probed the coupling of the Higgs boson to top quarks with significant results.

After the top quark, the second heaviest quark of the Standard Model is the bottom-quark (or beauty), with a mass around 5 GeV. The  $H \rightarrow b\bar{b}$  decay is kinematically allowed in the SM, and it represents the most direct way to access the coupling between the Higgs boson and the down type quarks. The  $H \rightarrow b\bar{b}$  decay mode is predicted to have the highest branching ratio (58%) for  $m_H = 125$  GeV. However, large backgrounds from multi-jet production make this search very challenging at hadron colliders. The most sensitive production modes for detecting  $H \rightarrow b\bar{b}$  decays are the associate production of a Higgs boson and a W or Z boson (VH), since the leptonic decay of the vector boson ensures an efficient triggering and a significant reduction of the multi-jet background. This combination of production and decay mode, in this work referred to as  $VH, H \rightarrow b\bar{b}$ , has the double advantage of probing both the dominant decay of the Higgs boson, while providing the best sensitivity to the ZH and WH production modes, which are important elements in the interpretation of the Higgs boson properties.

This thesis represents a non-comprehensive summary of my three years of PhD, from October 2016 to July 2019, mainly focused on this analysis. As a member of the ATLAS collaboration at the LHC, I had the possibility to work on a variety of different aspects covering hardware, performance and analysis. My direct contributions are briefly listed below. More details will be given in the dedicated Chapters.

**Analysis:** My main contribution has been in the context of the  $VH, H \rightarrow b\bar{b}$  analysis, in which I have been actively involved since 2017. In total, I participated to two rounds: the first iteration in 2018, which led to the observation of both the VH and the  $H \rightarrow b\bar{b}$  processes and the second in 2019 (still not public) which aims at interpreting the results in terms of a more precise formalism (Simplified Template Cross Sections, "STXS" [12]). My interests spanned many aspects of the analysis. Regarding the multivariate analysis (MVA), I performed the retraining of the 1-lepton BDT in both iterations, making optimization studies related to the tagging strategy and the number of variables. Then, I have been an active member of the fitting team which performed the statistical analysis for the publication. Among other tasks, I have been directly responsible for the fit in the 1-lepton channel and the diboson cross-check (all channels).

Furthermore, during these years I have always tried to make liaisons between the developments in performance and the analysis. In this context, since the first round of the analysis, I have been involved in the implementation and optimization

of the *statistical tagging*, an alternative b-tagging technique which allows for a better treatment of c- and light-jet dominated backgrounds. I had an active role in the implementation of the statistical tagging used for the 2018 publication, and at the same time I contributed to the development of the so-called *hybrid tagging*, which allows the features of statistical tagging to be better exploited in the analysis. In preparation for the next publication, I developed new "efficiency maps" for hybrid tagging. These "efficiency maps" are two-dimensional maps representing the building blocks of statistical tagging.

Since 2018, I also started some studies to enhance the overall sensitivity of the MVA by better exploiting the b-tagging information (+15% in expected significance for a fit to the 1-lepton channel). To do that, I implemented a new version of the MVA discriminant with additional variables related to b-tagging, and I contributed to the implementation of the pseudo-continuous b-tagging working point in the analysis.

**Flavour-tagging:** As said before, my contributions to the flavour tagging working group have been transversal between analysis and performance. My active contributions in flavour-tagging are mainly related to the statistical tagging, where I actively contributed to the development and maintenance of the tool and I made detailed studies to understand and solve the problems with the official efficiency maps. Furthermore, I have been interested in linking pseudo-continuous working point and statistical tagging, so I actively contributed to the development of a working version of the statistical tagging in the pseudo-continuous working point, which had never been implemented in the official ATLAS framework before.

**Electrons:** I made my Qualification Task in the electron-photon working group, where I performed the energy scale and resolution calibration of low energy electrons using  $J/\psi \rightarrow ee$  events. This independent check has been used to validate the full ATLAS electron energy calibration chain, and it has been particularly useful in the context of the  $H \rightarrow 4\ell$  analysis, which makes use of such low energy electrons. This expertise has been useful also in the  $VH, H \rightarrow b\bar{b}$  working group, where I became the Electron "Combined Performance" contact for 2 years.

**Detector:** I have been involved in two campaigns of shifts in the ATLAS control room. The first in 2016-2017 being responsible for the Calorimeters Desk for a total of 200 allocated hours. The second in 2018, being responsible for the Inner Detector Desk for a total of 230 allocated hours.

**Hardware and upgrades:** I have been involved in test beams aiming at testing the radiation hardness of the next generation of silicon detectors for the upgrade of the ATLAS Inner Tracker. I participated at test beams at DESY and at CERN, where I contributed in setting the test-beam setup, tuning sensors and reconstructing tracks from test beam data.

This report is structured as follows: the theoretical framework is presented in Chapter 2. The ATLAS detector is briefly described in Chapter 3, while the techniques used to reconstruct and identify the object used in the analysis are described in Chapter 4. Chapter 5 focuses on the flavour tagging algorithms, giving an overview of the current methods used to perform jet tagging in ATLAS. The work performed during my qualification task is presented in Chapter 6. The  $VH, H \rightarrow b\bar{b}$  analysis and the combinations which allowed to claim the observation of the two processes are presented in Chapter 7. And finally, Chapter 8 summarizes some improvements

on the b-tagging side, developed for the future round of the analysis, expected at the end of 2019.

## 2 | Theoretical framework

The Standard Model (SM) of particle physics is the theory describing our knowledge of the Universe at the subnuclear scales in terms of physics of the fundamental interactions. It provides a unified description of the fundamental constituents of matter and their interactions, mathematically formalizing the strong, weak, and electromagnetic forces in a single joint theory. Additionally, it incorporates a scalar term, the so-called Higgs field, able to explain the mechanisms of particle mass-generation for all the constituents included in the theory.

The SM has been extensively studied during the last 50 years, showing a remarkable capability to predict the experimental observations at colliders with a high level of precision. The discoveries of the Z and W bosons at the SPS [13, 14, 15] or the top quark at the Tevatron by the CDF and DØ experiments [16] [17] are just a few examples of particles which have been first theoretically predicted by the SM and only later confirmed by an experimental evidence, which for the first time established their existence and the values of their masses. The latest result giving further confirmation to the theory has been the observation of the Higgs boson at LHC in 2012 by the ATLAS and CMS experiments [5, 6].

Despite the remarkable prediction power showed so far, several experimental indications - from the subnuclear to the astrophysical scale - suggest that the standard model could be just a limited part of a more fundamental theory. For example, the baryon asymmetry in the universe, the smallness of the neutrino masses or the origin of the dark matter observed in the universe can only be explained adding extra terms to the SM formalism. A large number of such extensions - also referred to as Beyond the Standard Model (BSM) theories - has been developed in the last years, like extra-dimensions or supersymmetric models but no experimental evidence has yet confirmed one particular scenario.

The Higgs sector can be a powerful portal to answer some of these questions. The dark matter candidates, for example, are expected to be massive, thus they could interact with the Higgs field leaving both direct and indirect signatures detectable by the experiments. A precise understanding of the mechanism of particle mass generation, and its precise confirmation through experimental measurements, are thus important phenomenological tools to probe the SM theory and constrain these possible BSM scenarios.

The scope of this Chapter is to briefly discuss the theoretical framework used in this thesis work, with particular attention to the Higgs sector. The second part of the Chapter will be devoted to the Higgs searches at LHC, with some details about the physics of proton-proton collisions, used to produce the data analyzed in this work.

## 2.1 The Standard model Lagrangian

The mathematical formulation of the SM [18, 19, 20] is based on a renormalizable quantum field theory<sup>1</sup>. The dynamic of a quantum field system can be written in terms of a Lagrangian density  $\mathcal{L}(x)$  (or simply *Lagrangian*) having dimension 4 in momentum-energy and a dependence on the space-time coordinate  $x$ . The form of such Lagrangian is required to be invariant under a continuous group of local transformations, called gauge transformations or gauge symmetries. The gauge invariance means that the physics of the system and the equation of motion remain the same under the application of such transformations.

Most of the physics theories are described by lagrangians which remain invariant only under transformations of the coordinate system applied identically to every point of the space-time (global symmetries). The gauge symmetries generalize this concept, requiring that the form of the Lagrangian remains invariant also under transformations having a dependence on the space-time coordinate (*local* transformations). Intuitively, the concept of local symmetry allows for transformations in limited regions of the space-time, without impacting the rest of the universe. This is fundamental to satisfy the requirements of special relativity, for which no signal can travel faster than the speed of light.

Fields are seen as operators that can create and destroy particles. The dynamic of the constituents of matter in relativistic quantum field theory is represented by four-component spinors  $\psi(x)$ , obeying the Dirac equation:

$$(i\gamma_\mu\partial^\mu - m)\psi(x) = 0 \quad (2.1)$$

with  $\gamma_\mu$  the Dirac matrices and  $m$  the fermion mass. The equation of motion of these particles can be derived from the Lagrangian, which can be written as:

$$\mathcal{L} = \bar{\psi}(i\gamma_\mu\partial^\mu - m)\psi, \quad (2.2)$$

and interpreted as the Lagrangian describing the dynamic of a free non-interacting fermion of mass  $m$ . A slightly more complicated - but also more physical - example occurs when trying to write down the Lagrangian of the electromagnetic (EM) interaction, which involves fermions and electromagnetic fields. In its simplest version, this Lagrangian should be able to describe at least the dynamic of free charged particles and free fields in space. Such Lagrangian can be written as the sum of a Dirac term and an EM field, taken from the Maxwell equations [21]:

$$\mathcal{L} = \bar{\psi}(i\gamma_\mu\partial^\mu - m)\psi - \frac{1}{4}F_{\mu\nu}F^{\mu\nu} \quad (2.3)$$

with  $F_{\mu\nu} = \partial_\mu A_\nu - \partial_\nu A_\mu$  the EM field strength tensor. The  $\psi$  term describes non-interacting spin 1/2 charged fermions, such as the electron and the positron, while  $A_\mu$  represents the spin 1 EM carrier, identified as the photon. The Lagrangian is invariant under the global continuous symmetry:

$$\psi(x) \rightarrow e^{i\alpha}\psi(x) \quad (2.4)$$

with  $\alpha$  constant. This symmetry can be promoted to a local symmetry:

$$\psi(x) \rightarrow e^{i\alpha(x)}\psi(x). \quad (2.5)$$

---

1. A quantum field theory is a theory where particles are associated to quantum fields depending on the space-time coordinates.

The gauge invariance of the Lagrangian under this transformation is obtained introducing additional terms to the derivative of the free field equation in order to cancel the non vanishing terms introduced by the transformation. In particular, the derivative of the Dirac field must be changed into a *covariant* derivative as follows:

$$D_\mu \psi = (\partial_\mu + ieA_\mu)\psi \quad (2.6)$$

with  $e$  the fermion electric charge and  $A_\mu$  a vector field transforming as:

$$A_\mu \rightarrow A_\mu - \frac{1}{e} \partial_\mu \alpha(x) \quad (2.7)$$

Substituting the derivative in equation 2.3 and expanding, the Lagrangian becomes:

$$\mathcal{L}_{\mathcal{QED}} = \bar{\psi}(i\gamma_\mu \partial^\mu - m)\psi - \frac{1}{4}F_{\mu\nu}F^{\mu\nu} - eA_\mu \bar{\psi}\gamma^\mu \psi \quad (2.8)$$

This interacting Lagrangian contains again the free Lagrangians but with an additional term from the covariant derivative representing the interaction between two Dirac spinors and the photon field. This is the mathematical expression of the EM interaction vertex. This vertex and the other propagators can be visualized in terms of Feynman diagrams [22] and used, for example, to build the electromagnetic interaction of two particles through the exchange of a photon, like in the case of Compton scattering. This formulation of the EM interaction has been introduced by Feynman in the first half of the 20th century and it is also known as Quantum Electrodynamics (QED) [23].

Following Noether's theorem [24], each symmetry of the Lagrangian is expected to translate in a conserved physical quantity of the system. In QED, the gauge invariance leads to the conservation of electric charge, which is a well known experimental observation.

More generally, the Standard Model is based on the following symmetry group:

$$SU(3)_C \times SU(2)_L \times U(1)_Y. \quad (2.9)$$

The group can be divided into two main sub-groups:  $SU(3)_C$ , which is the group of three-dimensional rotations in the *colour* space describing the colour symmetry of strong interactions, and  $SU(2)_L \times U(1)_Y$  which are the gauge symmetries related to the conservation of the *weak isospin* and *hypercharge* in the electro-weak interaction. The full Lagrangian is the sum of the following pieces:

$$\mathcal{L}_{SM} = \mathcal{L}_{QCD} + \mathcal{L}_{EW} + \mathcal{L}_{Higgs} + \mathcal{L}_{Yukawa} \quad (2.10)$$

with  $\mathcal{L}_{QCD}$  describing the strong interaction, also called Quantum Chromodynamics,  $\mathcal{L}_{EW}$  describing the electro-weak interactions and  $\mathcal{L}_{Higgs} + \mathcal{L}_{Yukawa}$  for the Higgs sector. All these building blocks will be briefly discussed in the next Sections.

### 2.1.1 Fundamental particles

In the Standard Model, matter consists of three families of spin 1/2 fundamental particles, called fermions, whereas the interactions are mediated by the exchange of spin-1 carriers, called bosons. Additionally, the scalar Higgs boson interactions with the elementary particles generate their masses. A scheme of this classification is shown in Figure 2.1. Each family of fermions contains an up- and a down-type quark, a charged lepton and a neutral lepton (neutrino). For every fermion, there



is an anti-fermion with opposite charge. The three families are distinguished by the mass of the particles, described in increasing order. Such mass difference between fermion families spans several orders of magnitude and this hierarchy is still an open question of particle physics.

Quarks are colour-charged particles divided in up- and down-types depending on the carried electric charge:  $+2/3$  for the up-type and  $-1/3$  for the down-type. The up-type quarks take their name from the up ( $u$ ), the first generation quark of this type; the other two up-type quarks are the charm ( $c$ ) and the top ( $t$ ). In the same way, the down-type quarks take their name from the down ( $d$ ) quark, the first generation quark with charge  $-1/3$ ; the other two down-type quarks are the strange ( $s$ ) and the bottom ( $b$ ). Quarks are the only particles that can interact through all the three forces. The quark flavor is conserved in strong and electromagnetic interactions but not in the weak ones. The matrix describing the transition between mass eigenstates and the weak interaction eigenstates is the Cabibbo–Kobayashi–Maskawa (CKM) matrix [25, 26]. The CKM matrix is a unitary complex matrix that describes the transition probability between the quark  $q$  and  $q'$ . This probability is proportional to  $|V_{qq'}|^2$ . The highest  $V_{qq'}$  values are for quark-mixing within the same family (i.e.  $|V_{tb}| \sim 1$ ) and they rapidly decrease when considering quark-mixing between different families, with the lowest values occurring for mixing between the first and the third family (i.e.  $|V_{td}| \sim 0.0087$ ) [20].

Leptons are fundamental particles interacting via the electroweak force. As said before, leptons are divided in two categories depending on the electric charge: three charged leptons - electron ( $e$ ), muon ( $\mu$ ) and tau ( $\tau$ ) - carrying one unit of electric charge, and three corresponding neutrinos ( $\nu_e$ ,  $\nu_\mu$ ,  $\nu_\tau$ ), which are electrically neutral. Both the  $\mu$  and the  $\tau$  leptons decay into lighter particles with decay times of the order of  $2.2 \mu\text{s}$  and  $2.9 \times 10^{-13} \text{ s}$  respectively. The decay time of the  $\tau$  is so short that at LHC it can only be detected through its decay products. Leptons do not carry colour-charge so they do not interact via the strong interaction; neutrinos are also electrically neutral, so they can interact only via the weak force. The mass values of the three neutrino eigenstates are not yet known, but the observation of the neutrino oscillations proves that these particles must be massive [27]. In particular, from studies of the tritium  $\beta$  decay spectrum [28], their masses are expected to be below  $\mathcal{O}(1\text{eV})$ , so much lower compared to the charged leptons. The relation between neutrino flavour eigenstates and mass eigenstates is given by the Pontecorvo-Maki-Nagakawa-Sakata (PMNS) matrix [29, 30].

In the SM each force has its own set of vector bosons to mediate the interactions. The electromagnetic interaction between charged particles is mediated by the photon, which is massless and neutral. The massive  $W^+$ ,  $W^-$  and  $Z$  bosons are the mediators of the weak interaction:  $W^+$  and  $W^-$  carry  $+1$  and  $-1$  electric charge respectively while the  $Z$  is neutral. The strong interaction is carried by eight massless gluons; gluons themselves have colour charge and participate in the strong interaction. Finally, the Higgs field is carried by the Higgs boson, which is a neutral massive particle.

## 2.1.2 Quantum Chromodynamics

The Quantum Chromodynamics (QCD) is a non-abelian<sup>2</sup> gauge theory describing the strong interaction. It was developed after the quark model, to explain the experimentally observed spectrum of hadrons. The charge of QCD is referred to as

2. A non-abelian gauge symmetry group is a gauge set of gauge transformations which do not obey the commutative law.



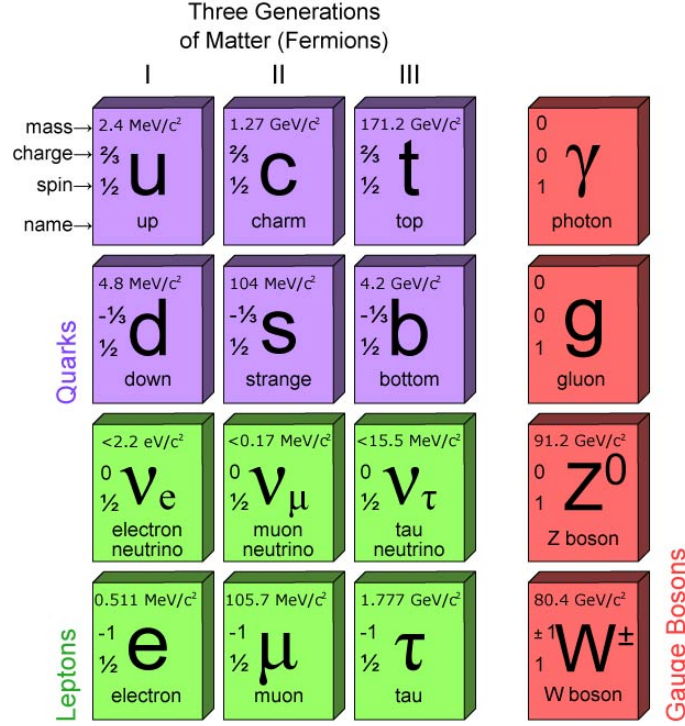


FIGURE 2.1 – Fermions and bosons in the Standard Model. For the fermions: the three families increase from left to right depending on the mass. Each family contains two quarks and two leptons classified by the electric charge. The Higgs boson is not shown (see Section 2.2.1).

colour (either red, green, or blue) and reflects an internal symmetry with a  $SU(3)$  gauge group. The strong force is mediated by 8 gluons, massless colour-charged particles interacting also among themselves due to the non-abelian structure of the  $SU(3)_c$  group.

Two regimes can be distinguished depending on the energy scale. The perturbative regime, which occurs at short distances (or high energies,  $E \gg \Lambda_{QCD} \sim 200$  MeV), when the interaction between quarks and gluons (partons) is small and the particles are considered as *asymptotically free*. In this case the Feynman vertices of the quark-gluon interaction are obtained using a method similar to the one described for the QED case. As before, the free QCD Lagrangian is required to respect the local gauge invariance:

$$q_A(x) \rightarrow e^{i\vec{\alpha}(x) \cdot \vec{\lambda}} q_A(x) \quad (2.11)$$

where  $q_A$  is the Dirac spinor describing a quark carrying colour  $A$  and  $\vec{\lambda} = \lambda_1 \dots \lambda_8$  are the so-called Gell-Mann matrices, eight  $3 \times 3$  traceless, hermitian matrices generalizing the  $SU(2)$  Pauli matrices to an  $SU(3)$  theory. The QCD Lagrangian is therefore:

$$\mathcal{L}_{QCD} = -\frac{1}{4} G_{\alpha\beta}^A G_A^{\alpha\beta} + \sum_{flavours} \bar{q}_A (i\gamma^\mu D_\mu - m)_{AB} q_B \quad (2.12)$$

where  $G_{\alpha\beta}^A$  is the field strength tensor which is found from the gluon field  $A_\alpha^A$ ,

$$G_{\alpha\beta}^A = \partial_\alpha A_\beta^A - \partial_\beta A_\alpha^A - g_S f^{ABC} A_\alpha^B A_\beta^C \quad (2.13)$$

The indices  $A, B, C$  run over the colour degrees of freedom of the gluon fields. The third term in Equation 2.13 is a non-Abelian term leading to the gluon tri-linear and

quartic self-interactions, which distinguishes QCD from QED. The coupling constant,  $g_s$ , determines the strength of the interaction between coloured partons, and  $f^{ABC}$  are the structure constants of the  $SU(3)_c$  colour group.

At lower energies the strength of the partonic interaction increases and the particles can not be considered as asymptotically free. In this case, the low energy QCD regime takes place and a property called *confinement* appears, reflecting the fact that in nature quarks are only observed as *confined* in colourless combinations called hadrons. The potential energy between quarks at these energies is dominated by  $V(r) \propto r$ , so increasing the separation between quarks (which is equivalent to extract one quark from a hadron) becomes so energetically unfavorable that new quark anti-quark pairs (and gluons) come from the vacuum to form new hadrons with the original quarks. This process is called *hadronization* and explains why at high energy colliders the quarks and gluons are only observed as hadronic jets instead of single strongly interacting final state particles. Hadrons are divided into two sub-categories depending on the number of quarks in the bound state: the *mesons* are hadrons made out of a quark-antiquark pair, while *baryons* are composed of three quarks.

### 2.1.3 The Electroweak unification

Sheldon Glashow [31], Steven Weinberg [32] and Abdus Salam [33] formulated a unified theory capable to describe both the electromagnetic and the weak interaction. The formalism of the electroweak interaction is based on local  $SU(2) \times U(1)$  gauge symmetry transformations.

Two types of weak interactions are observed in nature: the first ones to be discovered were the *charged current* interactions, responsible for example for the  $\beta$  decays. A pioneering mathematical description of these processes was already published in 1934 by Fermi in terms of a non renormalisable contact interaction [34]. These interactions involve only left-handed particles and are mediated by a charged  $W^\pm$  boson. The second type of weak interaction involves the so-called *neutral currents*, which have been a puzzle of particle physics until the Glashow, Weinberg and Salam (GWS) model published in the 1960's. In these processes the flavour of the reacting particles is conserved at the vertex, so the interaction must be mediated by a neutral particle, predicted to be the Z boson.

Experimental observations from charged pion, muon and neutron decays proved that the weak interaction is strongly related to the so-called *chirality*. The chirality can be left-handed or right-handed, and it is related to an abstract concept determined by whether the particle transforms in a left- or right-handed representation of the Poincaré group<sup>3</sup> [35]. The chirality projections are mathematically described in the Lagrangian by the  $\gamma^5$  Dirac matrix, which has eigenvalues  $\pm 1$ . In particular, it has been proved that the weak interaction allows only for couplings between left-handed particles and right-handed antiparticles. To mathematically formalize this property, left handed and right handed particles are treated differently. The left handed fermions are grouped in isospin 1/2 doublets, for example:

$$\begin{pmatrix} e \\ \nu_e \end{pmatrix}_L \quad \begin{pmatrix} u \\ d \end{pmatrix}_L \quad (2.14)$$

3. The chirality is related to the concept of helicity, which is calculated as the sign of the projection of the spin vector on the momentum vector. Left helicity is negative, right helicity is positive. For massless particles the two concepts coincide.

while right handed particles form singlets.

Experimentally, the weak interaction preserves two quantities at the vertex: the weak isospin ( $T$ ) and the weak hypercharge ( $Y$ ). The hypercharge is related to the fermion electric charge ( $Q$ ) and the weak isospin ( $T$ ), and in particular to its third component  $T_3$ , following the *Gell-Mann-Nishijima* relation:

$$Y = 2(Q - T_3). \quad (2.15)$$

For the Noether's theorem the two conserved quantities -  $Y$  and  $T$  - are related to symmetries in the SM Lagrangian. In particular, the weak isospin rotation of the left handed part can be parametrized by a non-abelian  $SU(2)$  transformation:

$$\psi_L = \begin{pmatrix} \psi_1 \\ \psi_2 \end{pmatrix}_L \rightarrow e^{i\vec{\alpha}(x) \cdot \frac{\vec{\sigma}}{2}} \psi_L \quad (2.16)$$

with  $\vec{\alpha}(x)$  a vector of three real parameters and  $\vec{\sigma}$  the Pauli matrices.

The hypercharge transformation is just a local change of phase, which is represented by the  $U(1)$  group:

$$\psi_{L,R} \rightarrow e^{i\beta(x)Y_{L,R}} \psi_{L,R} \quad (2.17)$$

with  $\beta(x)$  a real parameter. In order to preserve this  $SU(2) \times U(1)$  local gauge invariance, four new vector fields must be introduced: one ( $B_\mu$ ) for the  $U(1)$ , and three ( $W_\mu^a$   $a=1,2,3$  - two charged and one neutral) for the  $SU(2)$  group. In this way the covariant derivative becomes:

$$D_\mu = (\partial_\mu - igW_\mu^a T^a - \frac{i}{2}g'B_\mu Y) \quad (2.18)$$

with  $T^a$  the three components of the weak isospin and  $Y$  the operator of the weak hypercharge.

The couplings between fermions and these new gauge bosons are obtained substituting this covariant derivative in the Dirac part of the free Lagrangian. The coupling constants are denoted by  $g$  for the couplings with the  $W_\mu^a$  fields and  $g'$  for the couplings to  $B_\mu$ .

Considering only massless particles, the full electroweak Lagrangian becomes:

$$\mathcal{L}_{EW} = \bar{\psi}(i\gamma_\mu D^\mu)\psi - \frac{1}{4}W_{\mu\nu}^a W_a^{\mu\nu} - \frac{1}{4}B_{\mu\nu}B^{\mu\nu} \quad (2.19)$$

where:

$$W_{\mu\nu}^a = \partial_\mu W_\nu^a - \partial_\nu W_\mu^a - gf^{ab}W_\mu^a W_\nu^b \quad (2.20)$$

$$B_{\mu\nu}^a = \partial_\mu B_\nu - \partial_\nu B_\mu \quad (2.21)$$

are the two tensor field strengths describing the three  $SU(2)$  vector fields  $W_\mu^a$  ( $a = 1, 2, 3$ ) and the single vector field  $B_\mu$  from the  $U(1)$  gauge invariance. The electroweak unification is valid at high energies, where the  $B_\mu$  and  $W_\mu^a$  can be considered as massless particles. At low energies, the electroweak symmetry is spontaneously broken and the electromagnetic and weak forces are decoupled. The weak bosons ( $W^\pm, Z$ ) are observed to be massive, while the electromagnetic carrier (photon) is massless. This can be obtained through the so-called *Brout-Englert-Higgs mechanism*, explained in the next Section.

## 2.2 Mass generation and the Higgs mechanism

As said before, the Lagrangian reported in Equation 2.19 describes massless particles, since adding mass terms would destroy the gauge invariance. However, this scenario is highly in contradiction with the experimental observations, since both fermions and weak bosons are observed to be massive. The mass problem has been solved for both bosons and fermions. The weak bosons acquire mass thanks to the *Brout-Englert-Higgs mechanism*, where the spontaneous symmetry breaking of the  $SU(3)_C \times SU(2)_L \times U(1)$  to  $SU(3)_C \times U(1)_Q$  provides masses to the weak bosons, while the photon remains massless, since it is associated to the residual  $U(1)_Q$  symmetry. Fermion masses are generated by Yukawa interaction terms with the Higgs field.

### 2.2.1 The Brout-Englert-Higgs mechanism

The Brout-Englert-Higgs mechanism [7, 8], starts with the introduction of a new complex scalar doublet field  $\Phi$  to the SM Lagrangian:

$$\mathcal{L}_{Higgs} = (D^\mu \Phi)^\dagger (D_\mu \Phi) - V(\Phi) \quad (2.22)$$

with a kinetic term invariant under  $SU(2) \times U(1)$  symmetry (the covariant derivative has the same form as Equation 2.18) and  $V(\Phi)$  the potential of the Higgs scalar field, which can be written as:

$$V(\Phi) = -\mu^2 \Phi^\dagger \Phi + \frac{\lambda}{2} (\Phi^\dagger \Phi)^2 \quad \text{with} \quad \Phi = \begin{pmatrix} \phi^+ \\ \phi^- \end{pmatrix} \quad (2.23)$$

It contains a mass-type term with constant  $\mu^2$  and a 4- $\Phi$  interaction term with coupling constant  $\lambda > 0$ . This second requirement is necessary to have a *renormalizable* theory. Depending on the values of  $\mu$  and  $\lambda$ , the  $V(\Phi)$  potential assumes different shapes. If  $\mu^2 > 0$  there is only one minimum corresponding to  $\Phi_0 = 0$ , while if  $\mu^2 < 0$  there are multiple ground states, which can be obtained minimizing the potential:

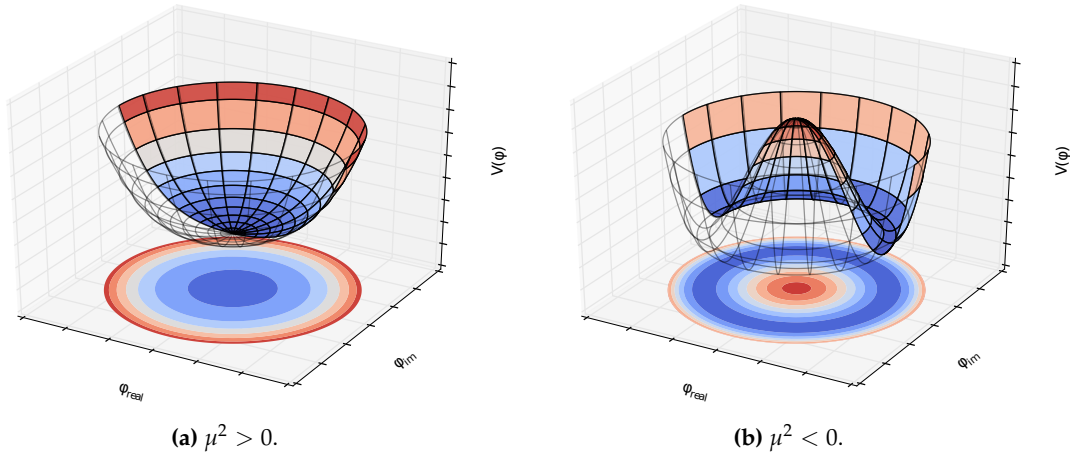
$$\frac{\partial V(\Phi)}{\partial \Phi} = 0 \quad \Rightarrow \quad |\Phi_0| = v = \sqrt{\frac{\mu^2}{\lambda}} \quad (2.24)$$

where  $v$  is the vacuum expectation value, determined thanks to its relation with the mass of the W boson (see later) to be  $v = 246.22$  GeV [20]. In this case the potential assumes a so-called Mexican hat shape, as shown in Figure 2.2. In this case the  $SU(2) \times U(1)$  symmetry is spontaneously broken choosing the system to fall into one of the multiple ground states, for example:

$$\Phi_0 = \frac{1}{\sqrt{2}} \begin{pmatrix} 0 \\ v \end{pmatrix}. \quad (2.25)$$

Expanding around the ground state, and working in the *unitary gauge* ( $\text{Im}\Phi = 0$  and  $\text{Re}\Phi^\dagger = 0$ ), the field can be written as:

$$\Phi(x) = \frac{1}{\sqrt{2}} \begin{pmatrix} 0 \\ v + h(x) \end{pmatrix} \quad (2.26)$$

FIGURE 2.2 – Effective potential of the Higgs field for different values of  $\mu$ . [36].

with  $h(x)$  a real scalar field. Evaluating the kinetic term  $(D^\mu \Phi)^\dagger (D_\mu \Phi)$  in  $\Phi_0$ :

$$(D^\mu \Phi)^\dagger (D_\mu \Phi) \ni \frac{1}{8} v^2 g^2 [(W_1^\mu)^2 - (W_2^\mu)^2] + \frac{1}{8} v^2 [g W_3^\mu - g' B_\mu]^2 \quad (2.27)$$

$$= \frac{1}{2} m_W^2 W_\mu^+ W^{\mu-} + \frac{1}{2} m_Z^2 Z_\mu Z^\mu + \dots \quad (2.28)$$

with  $W_\mu^\pm$  and  $Z_\mu$  the observable gauge bosons, related to  $W_\mu^a$  and  $B_\mu$  as:

$$W_\mu^\pm = \frac{1}{\sqrt{2}} (W_\mu^1 \mp W_\mu^2) \quad (2.29)$$

$$\begin{pmatrix} Z_\mu \\ A_\mu \end{pmatrix} = \begin{pmatrix} \cos \theta_W & -\sin \theta_W \\ \sin \theta_W & \cos \theta_W \end{pmatrix} \begin{pmatrix} W_\mu^3 \\ B_\mu \end{pmatrix} \quad (2.30)$$

where  $\theta_W$  is known as the Weinberg mixing angle experimentally measured to be  $\sim 30^\circ$ . It can be expressed in terms of  $g$  and  $g'$  as:

$$\sin \theta_W = \frac{g'}{\sqrt{g^2 + g'^2}} \quad (2.31)$$

$$\cos \theta_W = \frac{g}{\sqrt{g^2 + g'^2}} \quad (2.32)$$

The masses of the physical gauge bosons are related to the vacuum expectation value and to the couplings  $g$  and  $g'$  as follows:

$$m_W = \frac{v}{2} g \quad \text{and} \quad m_Z = \frac{v}{2} \sqrt{g^2 + g'^2} \quad \text{with} \quad \frac{m_W^2}{m_Z^2 \cos^2 \theta_W} = 1 \quad (2.33)$$

As expected, there is no mass term for the  $A^\mu$  field, so the photon remains massless. The other terms in the expansion of the covariant derivative define the interaction vertices between the Higgs scalar field  $h(x)$  and the observable gauge bosons:

$$\mathcal{L}_{V\Phi H} = \frac{2m_W^2}{v} W_\mu^+ W^{\mu-} h(x) + \frac{m_Z^2}{v} Z_\mu Z^\mu h(x) \quad (2.34)$$

and

$$\mathcal{L}_{VVHH} = \frac{m_W^2}{v^2} W_\mu^+ W^{-\mu} h(x) h(x) + \frac{m_Z^2}{v^2} Z^\mu Z_\mu h(x) h(x). \quad (2.35)$$

The vertices are composed by one (or two in  $\mathcal{L}_{VVHH}$ ) Higgs bosons and a couple of massive gauge bosons. In both cases the coupling strength is proportional to the squared mass of the gauge boson.

Redoing this expansion with the terms of the potential in Equation 2.23, the Higgs Lagrangian becomes:

$$\mathcal{L}_H = -\mu^2 h^2 - \lambda v h^3 - \frac{1}{4} \lambda h^4 = -\frac{1}{2} m_h^2 h^2 - \sqrt{\frac{\lambda}{2}} m_h h^3 - \frac{1}{4} \lambda h^4 \quad (2.36)$$

with:

$$m_h = \sqrt{2}|\mu| = \sqrt{2\lambda}v \quad (2.37)$$

which is the mass of a scalar massive particle, the Higgs boson, identified as the carrier of the Higgs field  $h(x)$ . The Higgs boson itself interacts with the Higgs field acquiring a mass related to the vacuum expectation value  $v$ . The Higgs boson mass is not predicted by the SM and needs to be determined experimentally. The different types of Higgs interaction vertices, including the self-coupling terms, are summarized in Figure 2.3.

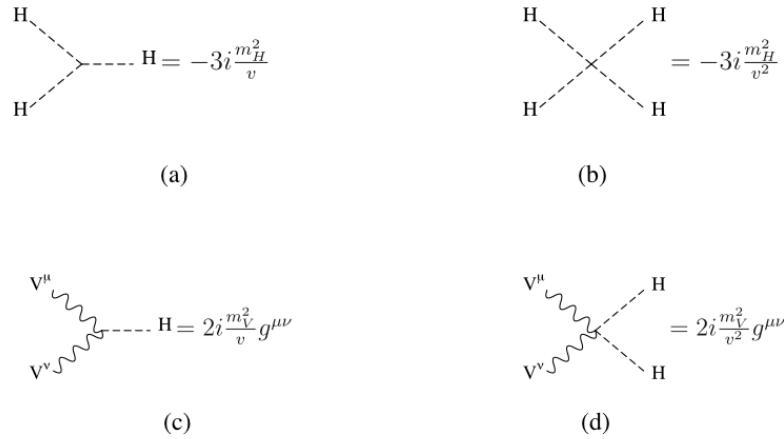


FIGURE 2.3 – Tree level interaction vertices of the Higgs boson arising from the Higgs mechanism. a) and b) are the self couplings of the Higgs boson, described by the  $h^3$  and  $h^4$  terms in  $\mathcal{L}_H$ , while c) and d) describe the interaction terms with the gauge bosons  $W$  and  $Z$  in  $\mathcal{L}_{VVH}$  and  $\mathcal{L}_{VVHH}$ .

### 2.2.2 Yukawa coupling to the fermion sector

The mechanism used to explain how fermions acquire mass is based on the same principles of the vector boson masses, but the formalism is slightly different. The coupling between the fermion fields  $\psi$  and the scalar field  $\Phi$  is expressed by a Yukawa interaction Lagrangian. For leptons it is expressed as:

$$\mathcal{L}_{Yukawa} = -\lambda \bar{L}_L \Phi e_R + h.c. \quad (2.38)$$

expanding around the Higgs field vacuum it is possible to obtain the fermion masses and their coupling with the Higgs:

$$m_e = -\frac{v}{\sqrt{2}}\lambda_e \quad g_{eeH} = -\frac{m_e}{v} \quad (2.39)$$

In this way, the Yukawa coupling of the fermions to the Higgs boson is proportional to their mass. The mechanism is analogous for quarks. The Yukawa theory allows for one possible vertex at lowest perturbation order, as illustrated in Figure 2.4.

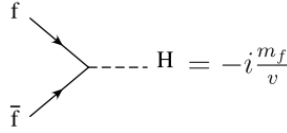


FIGURE 2.4 – The allowed tree level Higgs-to-fermion interaction vertex of the Yukawa theory.

## 2.3 Cross sections and Decay rates

The mathematical descriptions showed in the previous Sections can be combined to perform quantitative formulations of the dynamics of elementary particles. In practice, this translates in the calculation of decay rates ( $\Gamma$ ) and cross sections ( $\sigma$ ). In both cases, the procedure involves two ingredients: the so-called *amplitude* of the process, containing the dynamical information and the *phase space* available, which is purely kinematic. The calculation of all reaction rates, so both decay fractions and cross sections, follows the Fermi's *golden rule* [37, 38], stating that the differential reaction rate is proportional to the product of the phase space and the absolute square of the amplitude terms, as will be shown later. The computation of the production cross sections has an additional complication in case of hadron colliders. In fact, the momentum of the colliding partons is not known a priori, and the calculation of the exact kinematic phase space is not possible. To overcome this problem, the cross sections are reweighted by functions describing the distribution of momenta of the partons and integrated. More details are given in the next Sections.

### 2.3.1 Definition of cross section

The cross section of a process ( $\sigma$ ), for example  $ij \rightarrow k$ , represents the probability for the initial particles to interact with each other to produce a final state  $k$ . From the Fermi's golden rule the calculation of the total cross section of the two particles  $i$  and  $j$  annihilating to produce the particle  $k$  can be written as:

$$\hat{\sigma}_{ij \rightarrow k} \propto \int d\Phi_k |\mathcal{M}_{ij \rightarrow k}|^2(\Phi_k) \quad (2.40)$$

with  $|\mathcal{M}_{ij \rightarrow k}|^2(\Phi_k)$  the *transition amplitude* squared proportional to the so-called matrix element (squared), and  $d\Phi_k$  the phase space element. The matrix element ( $\mathcal{M}$ ) includes the information of the particle propagators and the interaction vertices computed from the Lagrangian. The matrix element is often calculated perturbatively using Feynman diagrams.

In hadron colliders such as the LHC, the cross section calculation is complicated by the composite nature of the colliding particles. Protons are composite objects



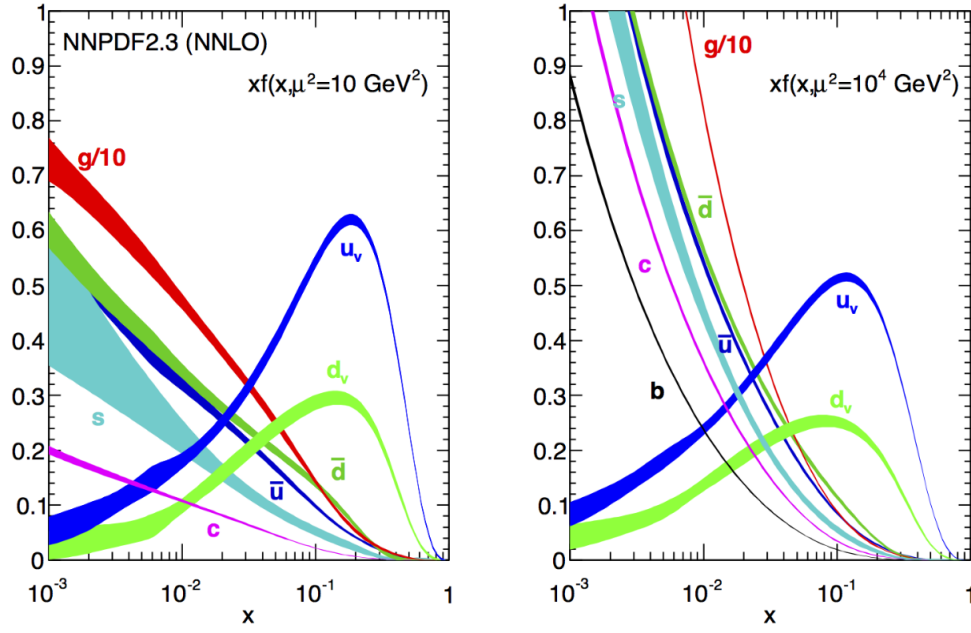


FIGURE 2.5 – Parton distribution functions for a low energy scale of  $\sim 3$  GeV (left) and a higher one of 100 GeV (right) [42].

made of three valence quarks ( $uud$ ) and a sea of quarks and gluons. The energy is so high that the real collisions happen directly between these sub-components, which carry just a fraction of the total proton momentum. In particular, two types of parton interactions occur simultaneously when two protons collide: the hard process, in which two partons interact with large momentum transfer, and multiple low energy interactions of the other partons. These soft processes can be a source of QCD background.

The fraction of longitudinal momentum of the partons taking part in the hard interaction is unknown. This quantity is defined in a probabilistic way using the so-called Parton Distribution Functions (PDFs): functions describing the distribution  $xf_i^A(x, Q^2)$  of the fraction  $x$  of the momentum of a parton  $i$  with respect to the mother hadron  $A$  calculated at a certain  $Q^2$  defined as the momentum transfer squared, see Figure 2.5. Since the mathematical description of the confinement in the low energy limit of QCD is not well understood, a full mathematical derivation of hadron parton distributions does not yet exist; the PDFs are determined experimentally, for example from Deep Inelastic Scatterings (DIS), at some energy scale (depending on the process) and extrapolated at any other scale using the DGLAP evolution equations [39, 40, 41].

Hadronic interaction cross sections can be calculated with the help of the QCD factorization theorem. The QCD factorization theorem states that the hadronic cross section  $\sigma_{AB \rightarrow k}$  (hadron  $A$  and hadron  $B$  collide to produce the final state  $k$ ) is a convolution of the partonic cross section  $\hat{\sigma}_{ij \rightarrow k}$  with the parton distribution functions  $f_i^A(x_1)$  and  $f_j^B(x_2)$ :

$$\sigma_{AB \rightarrow k} = \int dx_1 \int dx_2 f_i^A(x_1, Q^2) f_j^B(x_2, Q^2) \hat{\sigma}_{ij \rightarrow k} \quad (2.41)$$

Valence quarks have on average a higher momentum than sea quarks or gluons.



With increasing momentum of the proton, the fraction of sea quarks and gluons increases more than for the valence quarks. This has consequences for the production of massive resonances at the LHC. For the Higgs boson for example, predictions and observations confirm that the cross section for gluon fusion increases more than the other channels when the center of mass energy increases (see Figure 2.9, right), because the probability to have sea gluons carrying the right fraction of momentum increases.

### 2.3.2 Definition of decay width

The decay width of a process ( $\Gamma$ ) is the probability per unit time that a given particle will decay. It has an inverse relation with the lifetime of the particle ( $\tau = 1/\Gamma_{tot}$ ). The decay widths are calculated in the same way as the cross sections, following the Fermi's golden rule, but with substantial differences in the matrix element and phase space calculations since initial and final states are reversed.

Usually, particles can decay into many possible final states. The calculations are performed separately for each case and summed together to obtain the total decay width of the particle. The probability for a particle to decay into a *specific* final state  $X$  is related to the so-called Branching Ratio (BR). The BR is defined as the ratio of the partial decay width of the specific final state over the total decay width of the particle:

$$BR(H \rightarrow X) = \frac{\Gamma(H \rightarrow X)}{\sum_i \Gamma(H \rightarrow X_i)} \quad (2.42)$$

### 2.3.3 Measurement of Higgs couplings

Experimentally, at hadron colliders isolating the decay width of the process from the production cross section of the decaying particle is difficult, and it can be achieved only making additional theoretical assumptions on one of the two processes. The observed number of Higgs signal events for a certain production and decay mode at LHC has a linear dependence with the corresponding  $\sigma \cdot BR$ , with a proportionality term depending on the integrated luminosity (see Section 3.1.1) and the signal acceptance<sup>4</sup>. This quantity is strictly related to the Higgs coupling constants, since:

$$\sigma \times BR(ii \rightarrow H \rightarrow ff) \propto \frac{\sigma_{ii} \cdot \Gamma_{ff}}{\Gamma_H} \quad (2.43)$$

with  $\sigma_{ii}$  the production cross section of the  $ii \rightarrow H$  process,  $\Gamma_{ff}$  the partial decay width of the  $H \rightarrow ff$  process, and  $\Gamma_H$  the total decay width.

In order to provide an easy comparison with the theoretical prediction, most of the experimental measurements quote directly the ratio of the production cross section and the decay BR over the SM prediction:

$$\mu = \frac{\sigma \cdot BR}{\sigma_{SM} \cdot BR_{SM}} \quad (2.44)$$

this is called *signal strength* and it is usually referred to as  $\mu$ . This quantity will be extensively used later in this work to quote the experimental results of the  $VH, H \rightarrow b\bar{b}$  analysis.

4. This is true in case of *narrow* resonances like the Higgs boson. The broader the resonance, the less Equation 2.43 is valid [20]

## 2.4 The need for higher order corrections

The beauty of the SM consists in the fact that, thanks to the gauge invariance, the dynamic of fermions and the related gauge field Lagrangians can be completely determined by just a few parameters: the gauge couplings ( $g_s, g, g'$ ) the Higgs vacuum ( $v$ ), the Higgs self-coupling  $\lambda$  and the mass of the fermions. In particular, as showed in Equation 2.33, the properties of the weak bosons - in terms of mass, self-couplings and interactions to other particles - are fully determined by just  $g, g'$  and  $v$ <sup>5</sup>.

One powerful measurement performed to constrain these parameters is the precise estimation of the Weinberg mixing angle  $\theta_W$  which, from the relation explicated in Equation 2.33, is also expected to be related with the  $m_W^2/m_Z^2$  ratio. The electroweak mixing angle is either expressed by the W and Z boson masses or by the ratio of the vector and axial-vector couplings of the fermions, as described in Ref. [43]. This second way of expressing the  $\sin \theta_W$  gives access to the *effective* weak mixing angle,  $s_{\text{eff},f}^2$  since it is sensitive to the effective weak couplings of the fermion  $f$ . This difference must be explicated as  $s_{\text{eff},f}^2 = k_f \sin^2 \theta_W$ , with  $k_f$  a form-factor to be measured.

The most precise measurement of  $s_{\text{eff},f}^2$  for leptons comes from LEP/SLD [44]:

$$s_{\text{eff},\ell}^2 = 0.23153 \pm 0.00016. \quad (2.45)$$

with a precision of 0.08%. From Ref. [20], the most precise measurements of the Z and W masses are  $M_Z = 91.1876 \pm 0.0021$  GeV and  $M_W = 80.379 \pm 0.012$  GeV, which inserted in Equation 2.33 leads to a value of  $\sin^2 \theta_W$ :

$$s_M^2 = 0.22301 \pm 0.00027. \quad (2.46)$$

The value extracted from the  $m_W^2/m_Z^2$  is several standard deviations away from the first result which assessed the effective angle. This suggests that the simple relation expressed in Equation 2.33, is not sufficient to explain the observed LEP results, and the approximation necessitates the inclusion of additional corrections, as briefly discussed here. Such discrepancy is explained by the fact that the quoted relation holds only in case of simple Feynman diagrams, also called *tree level* diagrams, which do not account for the quantum fluctuations in the vacuum. The theoretical SM predictions are remarkably improved when including the treatment of such fluctuations, which manifest as additional radiative corrections to the tree-level process. In practice, they enter in the Feynman diagrams as additional loops, or as emission of additional soft particles (radiative case), like the ones shown in Figure 2.6. The  $s_{\text{eff},\ell}^2$  variable has been chosen as example because it is particularly sensitive to these corrections, which modify the vector and axial-vector couplings (as explained later) and so the effective form factor  $k_f$  when including the higher orders.

The computation of such additional corrections is not straightforward since it leads to divergences in the calculation of the total reaction rates. Mathematically, the loops enter as additional terms in the matrix element, which must be integrated over all the possible momenta and particle-types, to account for all possible states and all possible energies of the propagator. This can lead to infinite values of these integrals at low or high energy values (named infrared or ultraviolet divergences respectively), depending on the loop structure. Several different techniques have

5. Experimentally this is achieved by precisely measuring the following three parameters:  $\alpha_0$ , the electromagnetic fine structure constant,  $G_F$ , the Fermi constant and  $m_Z$ , the Z boson mass, which are strictly related to these quantities.

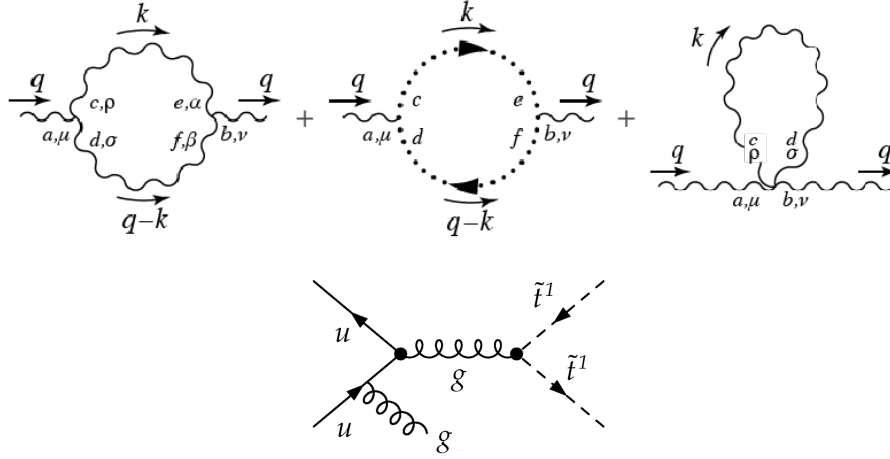


FIGURE 2.6 – Examples of NLO corrections in (top) loops and (bottom) as additional radiation.

been developed to reabsorb the infinities in the redefinition of masses, fields, and couplings for each level of divergence. The procedure is more generically named *renormalization*, and more details can be found in Refs. [45] [46]. The additional terms added during the renormalization to counterbalance the divergences have the advantage to help in improving the tree-level approximations and the natural relations such as Equation 2.33, which are altered by these corrections.

The propagators inside the loop corrections are integrated over all the possible existing particles (in the limits of the SM coupling rules), no matter their mass. This implies that these loop corrections can give indirect access to the couplings to particles that are too heavy to be produced directly in the collider. This was largely exploited at LEP and then at the Tevatron to infer indirect constraints on the Higgs boson and top-quark masses before their discoveries [47].

Given the computational complexity of the loop corrections, the reaction rates are never computed exactly, but just as perturbation expansions in the coupling constants. In practice, the result comes as an asymptotic series of terms depending on the coupling constant. At LHC usually the higher order corrections are computed as a function of the strong coupling, since  $\alpha_s \gg \alpha_{EW}$ . For example, a generic cross section calculation can be written as:

$$\sigma = \alpha_s^\gamma \sum_{i=0}^{N_{QCD}} \alpha_s^i A_i, \quad (2.47)$$

where  $\gamma$  is the lowest possible order of the strong coupling allowing the process, while the terms in the sum with  $i > 0$  are the higher order corrections, with  $A_i$  the factorized amplitude containing the physics of the process. The  $i = 0$  term is the Leading Order (LO) term, and usually it represents the tree-level process, the term with  $i = 1$  is the Next-To-Leading-Order (NLO) term, the  $i = 2$  is the Next-To-Next-to-Leading-Order (NNLO) and so on. The calculations beyond NLO are rapidly growing in complexity, thus usually the processes are calculated at NLO or NNLO. For some specific processes also the calculations at N3LO are available. The impact of the  $\alpha_{EW}$  higher order corrections represents a minor correction and is evaluated

process by process.

The so-called "k-factor" (NLO/LO, NNLO/NLO, etc..) quantifies the changes between two consecutive orders of calculation. For example, the addition of the NLO corrections can change the value of the reaction rate by 10-20% or even more depending on the process. The changes then asymptotically go to zero at higher orders.

### 2.4.1 The parton model beyond the Leading Order

The computation of the reaction rates beyond the leading order is sensitive to three main types of divergences: *ultraviolet*, when the divergence comes from the integration region associated to high momenta circulating in the loop, *infrared*, when the divergence is associated to the integration region of the momenta circulating in the loop that tend to zero, and *collinear* divergences, which are associated to collinear parton radiation. The infrared divergences cancel in virtual and real diagrams in the inclusive cross section, so there is in principle no need to cure such infinities, but the UV and collinear divergences need to be treated with renormalization techniques. This introduces a dependence on two energy parameters, called renormalization scale ( $\mu_R$ ) and factorization scale ( $\mu_F$ ).

**Renormalization scale:** The main idea of the renormalization procedure, introduced in the previous Section, is to add a series of counterterms to the Lagrangian to exactly cancel the ultraviolet divergences introduced in the loops. In case of renormalizable theories (i.e. EW, QCD, QED) these counterterms can be obtained modifying the constant parameters of the Lagrangian (i.e. electric charges, masses and couplings:  $e_0, m_0, g_0$ ), which then assume a non trivial dependence on the energy scale of the process. This energy scale is also called renormalization scale or simply  $\mu_R$ .

In practice, the quantities appearing in the Lagrangian formulation, also called *bare* quantities of the theory, do *not* correspond to the *physical quantities* measured by the experiments because they do not take into account the contributions of the vacuum fluctuations. These constants are thus rewritten in terms of *renormalized quantities* ( $e_0 \rightarrow e, m_0 \rightarrow m$  or  $g_0 \rightarrow g$ ), which are the real measurable quantities of the theory. This procedure adds an energy dependence to these quantities, which become *running constants* since their value varies with the energy of the process. For example, considering only one-loop corrections, a generic renormalized coupling  $\alpha_{\text{ren}}$  can be written as:

$$\alpha_{\text{ren}}(\mu^2) = \frac{1}{b_0 \log(\mu^2 / \Lambda^2)} \quad (2.48)$$

with  $b_0$  a constant depending on the theory,  $\mu$  the energy scale of the process (a.k.a. the renormalization scale), and  $\Lambda$  a constant defining a momentum cutoff beyond which the theory is not defined anymore (because  $\alpha \rightarrow \infty$ ).

Intuitively, this parameter  $\Lambda$  sets an energy separation from what can be considered perturbation theory (and solved analytically) and what is not a case of interest, because considered a long distance behaviour. In the case of QCD,  $\Lambda$  is an infrared cutoff corresponding to  $\sim 200$  MeV. This separation divides the two physical regimes of QCD: for  $\mu \gg \Lambda$  the coupling constant  $g \ll 1$  and the perturbation theory holds (asymptotic freedom), while for  $\mu \ll \Lambda$  the coupling constant  $g \sim 1$  and the confinement regime dominates. On the contrary, for QED  $\Lambda$  is an ultraviolet cutoff, such that  $g \ll 1$  for  $\mu \ll \Lambda$ . The evolution of the inverse of the three running couplings is shown in Figure 2.7: the electromagnetic constant increases with

energy<sup>6</sup>, while both weak and strong coupling constants are expected to decrease.

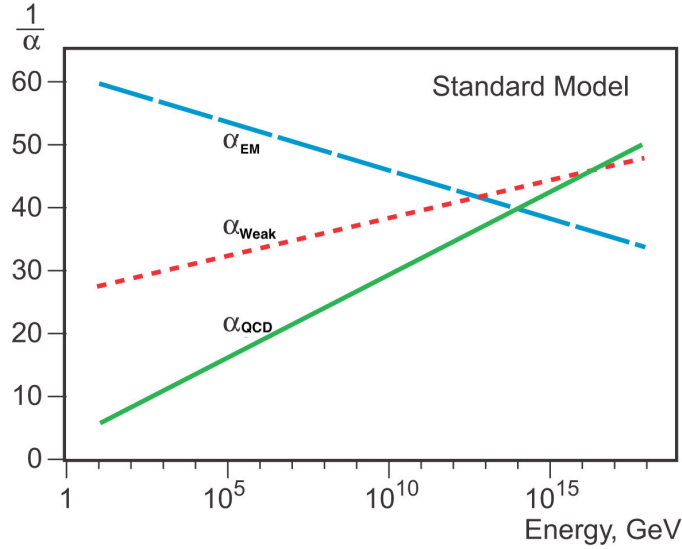


FIGURE 2.7 – Running coupling constants in the Standard Model. The three lines represents the inverse value of the coupling constant for the three fundamental forces as a function of the energy of the process. Blue: electromagnetic force, dashed red: weak interaction and green: strong force. Source: Nobel prize 2004.

**Factorization scale:** As described in Section 2.3.1, the calculation of cross sections in hadron colliders can be factorized in *hard scattering* cross section and the contribution of the *parton distribution functions*. This factorization is mainly introduced to handle the higher order corrections. In fact, the hard scattering part isolates the part remaining infrared finite, while the PDF part is characterized by non vanishing infrared logarithmic divergences, arising from the possible collinear emission of partons by the initial quarks. These contribution could be cancelled when summing all possible real and virtual diagrams of the process (this is true for example for the final states, or for specific regions of the phase space, like in jets<sup>7</sup>), but for the initial state this can not be true since the radiative case is clearly distinguishable from the non-radiative case by the different momentum of the parton entering in the hard scattering process. Such non-vanishing divergences are then reabsorbed in the parton density functions, which are non-perturbative objects determined experimentally.

In practice, this factorization scheme has the role to distinguish between which partons are absorbed in the parton density functions and which are assigned to the hard scattering. The division is made applying a cutoff at a certain energy, called factorization scale ( $\mu_F$ ), to divide long term from short term physics. Intuitively, a parton with transverse momentum lower than  $\mu_F$  is considered in the hadron structure and absorbed in the PDF part, while partons with larger momenta are considered as asymptotically free and included in the hard scattering process. Once the two contributions are factorized, the collinear divergences are regulated using techniques similar to the UV renormalization. The factorization theorem is however just an approximation since there is always soft gluon interaction between two hadrons.

6. This phenomenon is explained by QED: when increasing the energy, the *bare* charge is less and less screened from the vacuum fluctuations, so the strength of the coupling increases.

7. In case of jets the divergent contributions from the radiation around the hard parton are perfectly canceled by the virtual contributions to have, in the end, a finite object probability.

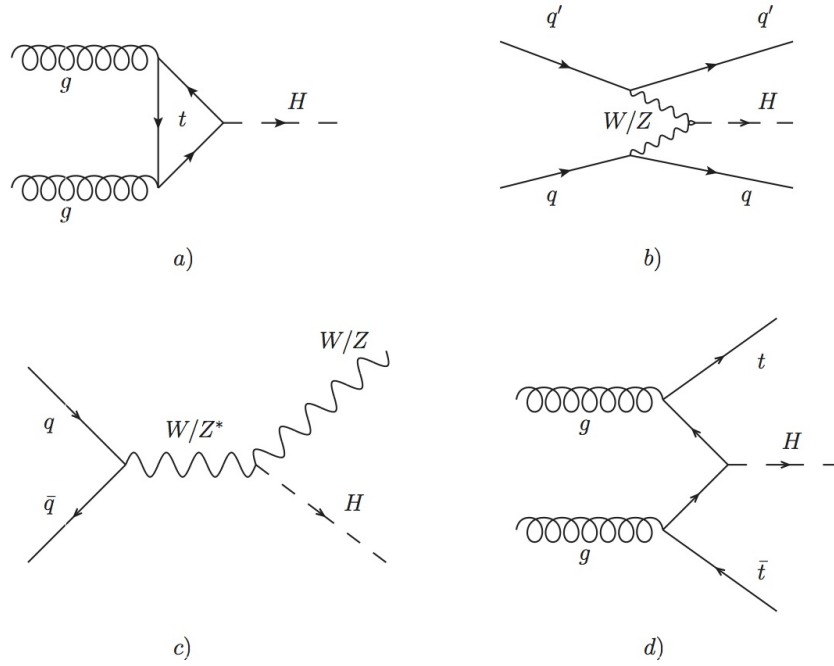


FIGURE 2.8 – Feynman diagrams for the four leading order Higgs production modes at LHC.

## 2.5 Searching for the Higgs boson at the LHC

In July 2012, the discovery of a new boson by both ATLAS [5] and CMS [6] was a crucial step in probing the mechanism of the electroweak symmetry breaking as the last building block of the SM. This section introduces a more phenomenological approach to study the Higgs boson physics at LHC, focusing on the detectable production and decay modes. More detailed references about the Higgs boson production modes and decay channels are given in Refs. [48, 49].

### 2.5.1 Higgs production modes at LHC

In proton-proton collisions at the LHC there are several possible Higgs boson production modes, as summarized in Figure 2.9. They come from quark and gluon initial collisions, and their Feynman diagrams are shown in Figure 2.8. The Higgs boson can be also produced by lepton or photon initial states, exploited for example in lepton colliders, but they will not be discussed here as their cross section is much smaller.

Thanks to the large density of low momentum gluons inside the proton, the main production mode at LHC is the gluon fusion ( $gg \rightarrow H$  or shortly  $ggH$ , Figure 2.8a). Since the Higgs boson coupling is proportional to the mass of the other particles, the production is mainly mediated by a loop of heavy quarks (or vector bosons). The  $ggH$  mode represents  $\sim 90\%$  of the total Higgs production cross section.

The cross section for the second largest production mode, vector boson fusion (VBF, Figure 2.8b and Figure 2.9), is about one order of magnitude smaller. This production mode has a peculiar signature in the detector, since two jets in the forward region (with opposite directions) are produced in addition to the Higgs boson decay products. This feature helps in increasing the signal to background ratio in the search for Higgs bosons.



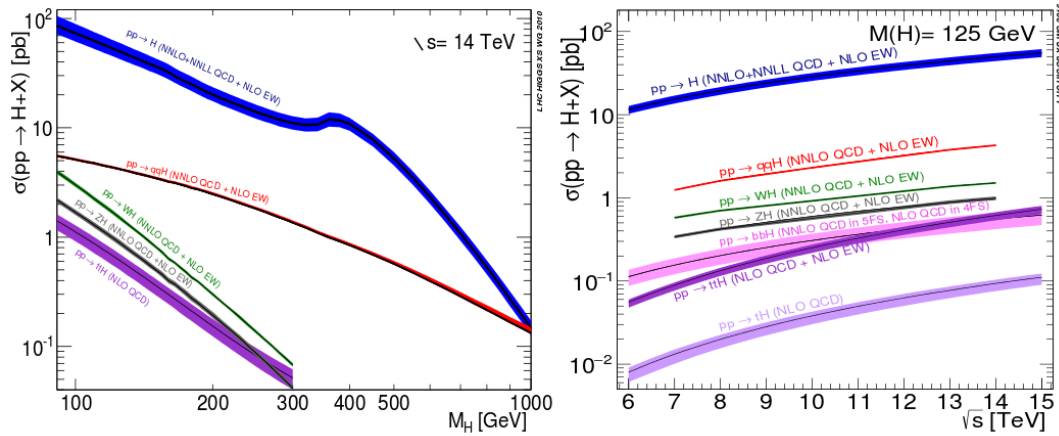


FIGURE 2.9 – Cross section of the Higgs production modes in  $pp$  colliders as a function of the Higgs boson mass value (left) and the center of mass energy (right).

Two other processes contribute to Higgs boson production: the Higgsstrahlung (Figure 2.8c) together with a W or Z boson and the associate production (figure 2.8d) together with two heavy quarks (top or bottom quarks). Leptonic vector boson decays and b-tagged jets from the top quark decays are helpful to identify these processes although their cross sections are about two orders of magnitude smaller than the one of the gluon fusion process. At the LHC Higgsstrahlung is suppressed, since at a proton-proton collider the antiquark has to be a sea quark.

### 2.5.2 Higgs decay channels

The Higgs boson is an unstable particle decaying into other particles almost instantly after it is produced. The only way to detect it is therefore through its decay products. The Higgs boson can decay directly to pairs of fermions or vector bosons or, through loop diagrams, to gluon pairs, photon pairs, or to a photon and Z boson. As a general rule, the Higgs boson is more likely to decay into heavy fermions than light fermions, since the strength of its interaction with particles is proportional to the mass of the considered particle. The top mass is too large for a direct decay in a  $t\bar{t}$  pair ( $m_H = 125 \text{ GeV}$  and  $m_t = 172.5 \text{ GeV}$ ), so the dominating fermionic channels are pairs of b-quarks and  $\tau$  leptons. The highest branching fraction, expected to be  $\sim 58\%$ , is for a Higgs decay to a pair of bottom quarks, which is the decay channel targeted in this thesis work. More details are given in Chapter 7. The Higgs to charm quark pair decay has a low branching ratio ( $\sim 3\%$ ) and it suffers from large contamination from QCD SM processes, like  $g \rightarrow c\bar{c}$  production. For these reasons, this decay channel has not been experimentally observed yet. The decays to leptons are also allowed, the highest branching ratio is expected to be in a pair of  $\tau$  leptons ( $\sim 6.3\%$ ), while the decays to lighter leptons, like muons ( $BR \sim 0.02\%$ ) are extremely suppressed due to the very small mass of the leptons.

The bosonic decay channels, on the contrary, have in general smaller branching fractions but cleaner signal. The highest decay rate is expected for the Higgs decay into a pair of W bosons, which represents the second highest branching ratio after  $H \rightarrow b\bar{b}$  ( $BR \sim 22\%$ ). The W bosons can subsequently decay either into a quark and an antiquark or into a charged lepton and a neutrino. The decays of W bosons into quarks are difficult to distinguish from the QCD background, and the decays into leptons must account for the neutrino missing energy. A cleaner signal - at

the price of a smaller rate - is given by decays into a pair of Z-bosons, with the bosons subsequently decaying into pairs of charged leptons (electrons or muons),  $H \rightarrow ZZ \rightarrow 4\ell$ , with  $\ell = \mu, e$ , expected to have a  $BR \sim 0.02\%$ .

Decay into massless gauge bosons (i.e., gluons or photons) are also possible, but they require intermediate loops of virtual heavy quarks (top or bottom) or massive gauge bosons. The most common process is the decay into a pair of gluons through a loop of virtual heavy quarks. This process, which is the reverse of the gluon fusion process mentioned above, is undistinguishable from the background. On the contrary, the decay into a pair of photons is much more relevant for experimental searches. The di-photon decay is mediated by a loop of W bosons or heavy quarks and it occurs approximately twice for every thousand decays. The energy and direction of the photons can be measured very precisely, giving an accurate reconstruction of the mass of the decaying particle. Thanks to its clear signature, the  $H \rightarrow \gamma\gamma$  channel was used, complementary to  $H \rightarrow ZZ \rightarrow 4\ell$ , as 'golden channel' to claim the observation in 2012. A similar decay is  $H \rightarrow Z\gamma$ , expected to have comparable BR, but a much more challenging signal to background ratio due to the higher contamination from radiative Z processes. A summary of the BR of all the possible Higgs decay channels is presented in Table 2.1.

Decay mode	BR
$b\bar{b}$	58.24%
$c\bar{c}$	2.89%
$\tau^-\tau^+$	6.27%
$\mu^-\mu^+$	0.02%
$gg$	8.19%
$\gamma\gamma$	0.23%
$Z\gamma$	0.15%
$WW$	21.37%
$ZZ$	2.62%
Total width	4.1 MeV

TABLE 2.1 – Summary of the branching fractions of the possible final states of the Higgs boson decay and the total expected width of the Higgs boson (with a mass of 125 GeV).

## 2.6 Experimental verifications

The experimental Higgs boson searches are split in direct and indirect analyses. The indirect analyses are based on precision measurements of the properties of some other SM particles, such as the W boson, to infer constraints on the Higgs boson properties. For example, the W boson mass can be expressed as

$$m_W^2 \left( 1 - \frac{m_W^2}{m_Z^2} \right) = \frac{\pi\alpha}{\sqrt{2}G_\mu} (1 + \Delta r) \quad (2.49)$$

where  $\Delta r$  includes the higher-order corrections beyond tree-level, and is sensitive to the top-quark and the Higgs boson masses [50]. Even if the Higgs-boson contribution is less important than the component associated to the top quark, the Z, W and  $t$  masses are measured with enough precision to infer limits on the Higgs boson



mass parameter. Other pseudo-observables are listed in Ref. [51]. Combining the constraints from all these pseudo-observables sensitive to the SM Higgs boson mass, the LEP electroweak Working Group has obtained a preferred value of  $m_H = 94^{+25}_{-22}$  GeV [52], which is consistent with the current best value from direct searches (see later) within  $1.3\sigma$ .

Direct analyses include the search of the Higgs boson decays to predicted decay channels. Before LHC started in 2010, direct searches for a light Higgs boson (below 200 GeV) had already been carried out at LEP and at the Tevatron. The best LEP limit have been set in the early 2000's [53], for a preferred fit value of  $m_H = 114.4 \pm 1$  GeV. In early 2012 a combined CDF and DØ measurement with all available data claimed an excess in the region  $115 < m_H < 135$  GeV with global significance of  $2.2\sigma$ , led by the  $H \rightarrow b\bar{b}$  channel [54].

As already mentioned, the first direct observation of a new boson compatible with the Higgs boson was published in July 2012 by both the two general purpose LHC detectors, ATLAS and CMS. The excess was found for a mass around 126 GeV, based on a combination of all analyses available at that time, where mainly the channels  $H \rightarrow \gamma\gamma$ ,  $H \rightarrow WW$  and  $H \rightarrow ZZ \rightarrow 4\ell$  contributed [5, 6]. Both channels profit from a very precise mass resolution and from relatively low and well understood background contributions. Figure 2.10 shows the diphoton and  $4\ell$  invariant mass distribution for the complete Run-1 ATLAS data set, taken in 2011 and 2012. A significant excess over the background is visible at the same mass value in both channels. In addition, Figure 2.11 shows the so-called  $p$ -value of the ATLAS and CMS measurements, which quantifies the probability that the observed excess could be due to a fluctuation of the background. In both cases, this probability is lower than  $3 \times 10^{-7}$ , which is considered sufficient to exclude the background-only hypothesis and confirm the discovery of a new resonance by both the experiments.

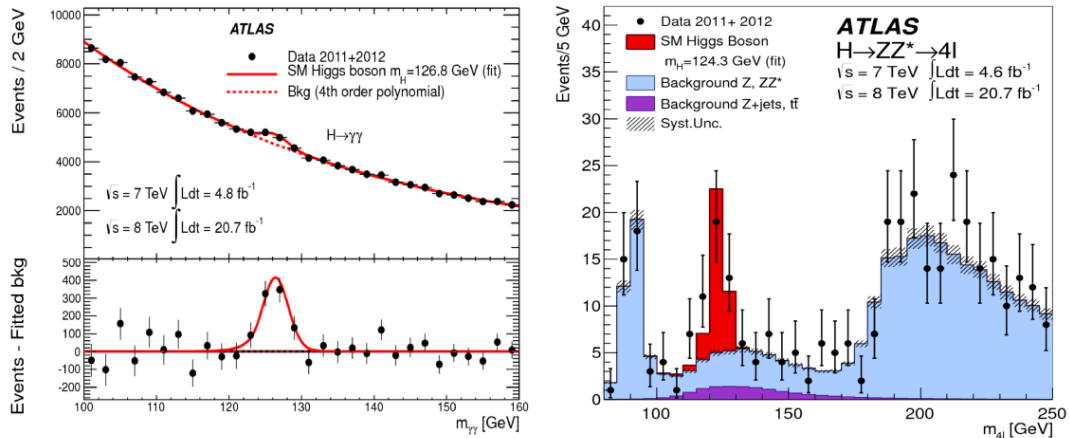


FIGURE 2.10 – Di-photon (left) and four-lepton (right) invariant mass distributions for  $20 \text{ fb}^{-1}$  of data at 7 and 8 TeV recorded with the ATLAS detector [5, 6].

The same bosonic 'golden' channels have been also used to characterize this new particle in terms of mass, spin and parity. The Run-1 combination of ATLAS and CMS analyses in the high precision channels  $H \rightarrow \gamma\gamma$  and  $H \rightarrow ZZ \rightarrow 4\ell$ , yielded

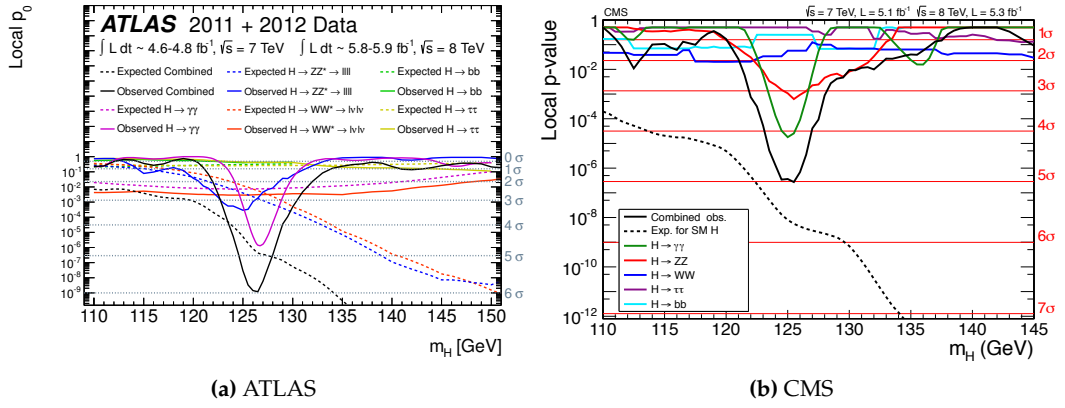


FIGURE 2.11 – Local p-value and corresponding significance (see Section 7.4.2) for the background only hypothesis as a function of the Higgs boson mass hypothesis for ATLAS [5] (a) and CMS [6] (b). The solid lines represent the observed p-value in data, while the dashed lines are the expected p-value.

to a Higgs boson mass value of:

$$m_H = 125.09 \pm 0.24 \text{ (0.21 stat } \pm 0.11 \text{ syst) GeV.}$$

The analysis has been repeated with  $36 \text{ fb}^{-1}$  of Run-2 data by the two experiments. The CMS experiment quoted a value of  $125.20 \pm 0.20 \pm 0.11 \text{ GeV}$  using the four-lepton channel [55], while ATLAS measured a value of  $124.86 \pm 0.27 \text{ GeV}$  including both di-photon and four-lepton channels [56]. The spin and parity have been tested in Run-1 looking at the angular distributions and correlations of the final stated decay products. Various hypotheses have been tested, but at 99.9% confidence level all spin and parity hypotheses are disfavored with respect to the  $J^P = 0^+$  prediction of the SM [57].

The first measurement of the couplings to the fermion sector was obtained in Run-1, with the observation of the  $H \rightarrow \tau\tau$  decay at  $5.5\sigma$  from a combination of the ATLAS and CMS analyses [9]. The result have been confirmed separately by both experiments using  $36 \text{ fb}^{-1}$  of 13 TeV data [58] [59].

The other leptonic decay channel with active searches at LHC is  $H \rightarrow \mu\mu$ . Due to the large irreducible Drell-Yann background ( $pp \rightarrow Z + X, Z \rightarrow \mu\mu$ ) and the very small branching ratio, no significant excess has been observed so far by both experiments even with datasets between  $36 \text{ fb}^{-1}$  and  $139 \text{ fb}^{-1}$  [60] [61]. Upper limits on the signal strength between 2.9 (CMS) and 2.2 (ATLAS) times the SM predictions have been set at 95% confidence level.

The other analyses probing the Higgs-to-fermion couplings are targeting the  $H \rightarrow b\bar{b}$ ,  $H \rightarrow c\bar{c}$  decays, and the  $t\bar{t}H$  production mode. As mentioned before the  $H \rightarrow b\bar{b}$  has the highest decay rate but suffers for the huge background contamination from QCD multi-jets. Since it represents the main core of this work, the analysis strategy and the existing public results will be discussed in more details in Chapter 7. Regarding the  $H \rightarrow c\bar{c}$  channel, it is expected to be heavily contaminated by the same QCD backgrounds of  $H \rightarrow b\bar{b}$  but with an additional drawback added by the much lower BR. Searches from ATLAS with a dataset of  $36 \text{ fb}^{-1}$  at a center of mass energy of 13 TeV showed no significant excess over the background, so upper limits on the  $\sigma(pp \rightarrow ZH) \times BR(H \rightarrow c\bar{c})$  of 2.7 pb were set at 95% CL, while the SM value

is expected to be 26 fb [62]. A more updated measurement with 36 fb<sup>-1</sup> has been recently presented by CMS in Ref. [63].

The  $t\bar{t}H$  production mode is the most direct probe of the Higgs coupling to top-quarks. In Run-1, a combination of the ATLAS and CMS analyses allowed to claim evidence for the  $t\bar{t}H$  production mode with  $4.4\sigma$  significance [9]. The increase in the center of mass energy in Run-2 enhanced by a factor four the  $t\bar{t}H$  production cross section, so the two experiments could independently claim the observation with significances larger than  $5\sigma$  using 80 fb<sup>-1</sup> of 13 TeV  $pp$  collisions each [11] [10]. The signature of this process is characterized by two b-quarks and two W bosons (decaying hadronically or leptonically), coming from the  $t \rightarrow Wb$  decay, in addition to the Higgs decay products. The observation has been performed combining different decay channels of the Higgs boson, leading to very different final states and background compositions. The leading channel in sensitivity is the *multi-lepton channel* which includes the  $H \rightarrow WW$ ,  $H \rightarrow \tau\tau$  and  $H \rightarrow ZZ \rightarrow qq\ell\ell$  of the Higgs bosons, excluding the  $t\bar{t}H, H \rightarrow ZZ \rightarrow 4\ell$  contribution, which is treated separately as an event category of the  $H \rightarrow 4\ell$  analysis. Also the  $t\bar{t}H, H \rightarrow \gamma\gamma$  has a clean signal and contributed non-negligibly to the final sensitivity. The  $t\bar{t}H, H \rightarrow b\bar{b}$  and  $t\bar{t}H, H \rightarrow ZZ$  were also included in the combination, but with much lower separation power due to the higher QCD background contamination. The  $t\bar{t}H, H \rightarrow b\bar{b}$  analysis will be later used in combination with the  $VH, H \rightarrow b\bar{b}$  analysis to increase the sensitivity to  $H \rightarrow b\bar{b}$  decays.

The search for the other expected Higgs production modes is also very active at LHC. All the modes described in Section 2.5.1 have been probed by both experiments in the last years. The gluon gluon fusion is the one giving less distinctive signatures, but thanks to its large cross section, it was the first to be observed in Run-1 by both ATLAS and CMS [9]. The VBF mode is characterized by two additional jets in the forward region, coming from the scattering quarks. This mode has been observed in Run-1 combining ATLAS and CMS analyses [9], and the result was reconfirmed in Run-2 separately for the two experiments.

The VH production mode is characterized by two additional particles coming from the decay of the vector boson. The best sensitivity to this production mode is achieved considering only leptonic decays of the vector bosons ( $W \rightarrow \ell\nu$ ,  $Z \rightarrow \ell\ell$  and  $Z \rightarrow \nu\nu$ ). In Run-1, a combination of ATLAS and CMS analyses allowed to claim evidence at  $3.5\sigma$  level [9]. The observation of the VH production mode was claimed by both experiments in Run-2, combining several decay channels led by  $H \rightarrow b\bar{b}$ , which has the best sensitivity to this production mode. More details about this combination will be given in Chapter 7.

The overall picture of the latest available Run-1 and Run-2 ATLAS Higgs-related measurements is given in Figure 2.12. The values are found to be generally in agreement with the SM predictions within the uncertainties.

### 2.6.1 Limitations of the Standard Model

As said in the introduction, despite the robustness and the remarkable prediction capabilities showed so far, there are motivations to suspect that the current formulation of the SM is just a limited part of a broader theory. This Section contains a brief summary of the experimental indications suggesting such hypothesis.

**The hierarchy problem:** The range of physics scales, from the strong force scale to the Planck scale<sup>8</sup>, is extremely broad. There are 19 orders of magnitude between

8. The energy scale at which gravity starts to play a role in quantum field theory.

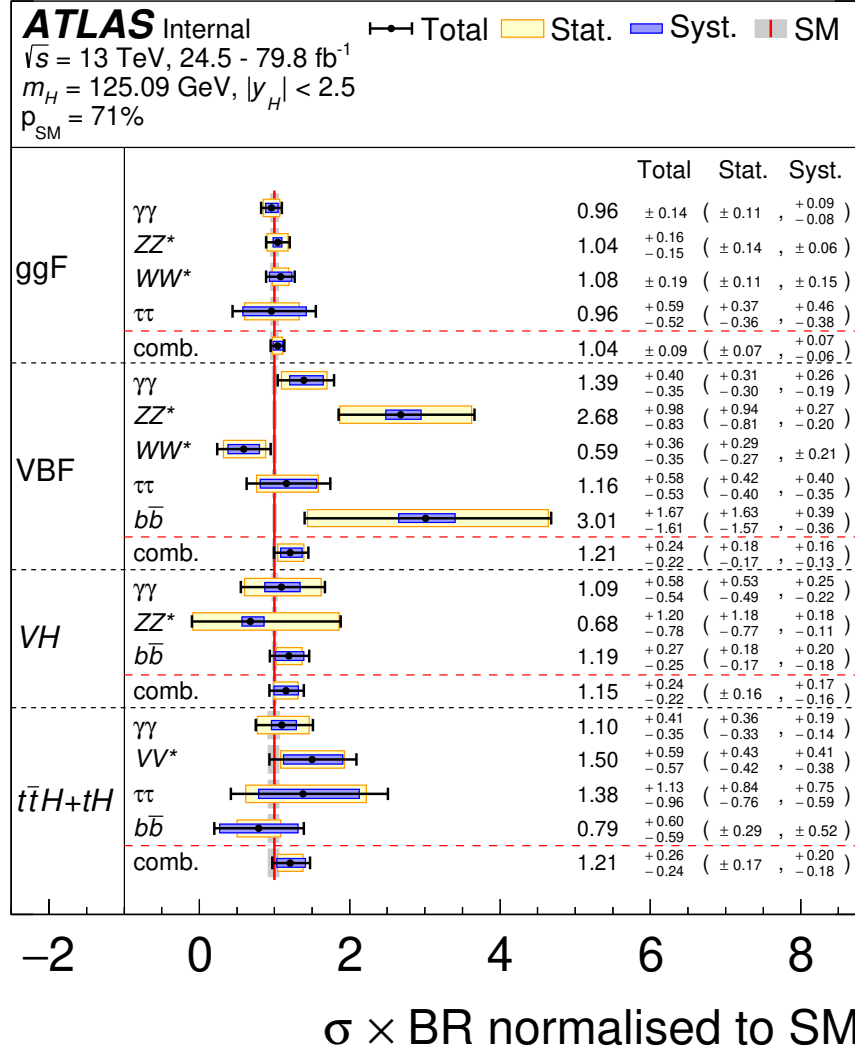


FIGURE 2.12 – The  $\sigma \times \text{BR}$  normalized to the SM predictions for the various decay channels using Run-1 and Run-2 ATLAS data. The values are found to be in agreement with the SM predictions within the uncertainties [64].

the proton mass and the Planck energy scale and the weak force is roughly  $10^{24}$  times stronger than gravity. Such a huge gap does not seem natural, and it requires a precise cancellation between bare values and quantum corrections to obtain the known values of the coupling constants (see description of the *naturalness problem*).

**Higgs mass and naturalness problem:** The tree-level predicted Higgs mass is expected to receive large radiative loop corrections when including higher orders in perturbation. As introduced in Section 2.4.1, in renormalized theories the physical quantities are modified by the inclusion of higher order corrections (coming from contributions of fermions, bosons and self interactions in loops), transforming the bare quantities in physical observables.

For the Higgs mass this can be written as [65]:

$$m_H^2 = (m_H^2)_0 + \frac{y_t^2}{16\pi^2} \Lambda^2 + \mathcal{O}(m_{\text{weak}}^2) \quad (2.50)$$

with  $y_t$  the top quark Yukawa coupling with a value close to 1,  $\mathcal{O}(m_{\text{weak}}^2)$  all other quantum corrections, and  $\Lambda$  the scale until which the SM is valid. Up to now, the next known energy scale after the electroweak scale is the Planck scale ( $\sim 10^{18}$  GeV). Supposing that the SM remains valid up to this scale, the bare mass of the Higgs boson should be very large in order to cancel the large contribution of the  $\Lambda^2$  term, implying that the Higgs mass and the Planck mass<sup>9</sup> should be similar. The measured value of the Higgs boson mass,  $M_H \sim 125$  GeV, is however extremely small compared to the Planck mass, which requires very fine tuning of the parameters to be reproduced. This is also known as *the naturalness problem*, since such fine cancellation is possible, but seems very unlikely. A cutoff at lower energies  $\sim$  TeV would be a more natural solution to explain the observed value of the Higgs mass. This is one of the strongest arguments in favour of the presence of new physics beyond the SM at higher energy scales. This would make the SM just the low energy limit of this new larger theory.

**Dark matter and dark energy:** Astrophysics observations, as for example Ref. [66], probing the composition of the Universe showed that the ordinary known matter represents just 4% of the total content of the universe. The rest is divided between dark matter (22%), known from its gravitational effect, and dark energy (74%), necessary to explain the acceleration in the expansion of the universe. The SM formalism can only explain the dynamic of the 4% of known matter, and it would require some extensions, such as Supersymmetry, to include some dark matter candidates. Many models lead to stable supersymmetric particles which might act as dark matter candidates, but no one has been experimentally observed yet.

**CP violation and matter/anti-matter asymmetry:** In the early universe, the Big Bang should have produced the same amount of matter and antimatter. However, many cosmological observations [67] show that the universe is entirely dominated by matter over anti-matter. The SM indeed allows for CP violation, described as additional phases in the CKM and PMNS matrices. Such asymmetry between decays can explain an excess of particles over anti-particles in the universe, but it is however insufficient to explain why matter dominates. The baryon - anti-baryon asymmetry of the universe is quantified as the ratio of the difference between the number of baryons and anti-baryons over their initial sum. The baryon anti-baryon

9. The Planck mass is the mass of a particle having Compton wavelength equal to the Planck length.

interaction occurs via annihilation, which produces photons, thus the initial sum can be inferred by the number of photons in the early universe, which is a measurable quantity. Since there are no anti-baryons observed, the asymmetry can be inferred by the baryon-to-photon ratio, which has been estimated to be  $\eta \sim 10^{-10}$  [68]. This asymmetry can be obtained as described in Ref. [69] only if three necessary conditions are fulfilled: the baryon number violation, the P and CP symmetries are broken in the SM and there is a deviation from the thermal equilibrium (expansion of the universe). All these conditions are fulfilled, however, the values of the CP violation in the SM are too small to explain this number correctly.

**Inclusion of Gravity:** In its current formulation the Standard Model is not able to include gravity, which is the last fundamental force still not included in the theory. The main limitation comes from the quantization of general relativity, which so far has not been achieved. Super-string and loop gravity theories are the first attempts able to unify quantum field theory and general relativity, but their experimental verification remains very challenging.

**Grand unification:** As described in Section 2.4.1, the SM couplings are *running* coupling constants depending on the energy of the process. In particular, focusing on the three fundamental couplings ( $\alpha_s, \alpha_{EW}$  and  $\alpha_{EM}$ ), and scanning a large interval of energies, it seems that these couplings tend to converge at high energies, as shown in Figure 2.7. The interaction point does not coincide for all the couplings, but the peculiarity is that they are all crossing in the range  $10^{12} - 10^{15}$  GeV. In these unified scenarios, the couplings of the known fundamental forces are seen as the manifestation of a single unified force, decoupled at low energies. The theory of SuperSymmetry represents an elegant way to explain the force unification in terms of spontaneous symmetry breaking, as in the case of the electro-weak unification.

**Hierarchy of fermionic families:** Figure 2.1, summarizes the mass values of all the constituents of matter. Focusing on the quark sector, the range of masses spans from the few MeV ( $u$ ) to the 172.5 GeV of the top-quark. These striking differences between families are one of the main puzzles of the SM. Many models tried to answer this question [70, 71], but so far no one gave detailed predictions.

**Neutrino masses:** Neutrinos are fundamental objects described as massless left handed particles in the SM. However, the observation of the neutrino oscillations [27], implies that the neutrinos are not massless. Mass terms for the neutrinos could be introduced in the SM without breaking the gauge invariance, but the open question is if the mass term should be of type Dirac (like the other fermions) or Majorana (so the neutrino is its own antiparticle). The latter would be confirmed by the observation of neutrinoless double beta decay. In addition, since neutrinos have mass-eigenstates differing from the detectable flavour-eigenstates it is difficult to understand the structure of such term in the Lagrangian.

## 2.7 From theory to event simulation

The Lagrangian formalism of the SM allows to simulate the full dynamic of the interaction between particles with a high level of precision. Typically, LHC analyses consist in comparing the outcome of such generated samples representing our theoretical expectation, with the real recorded data from the detector, looking for



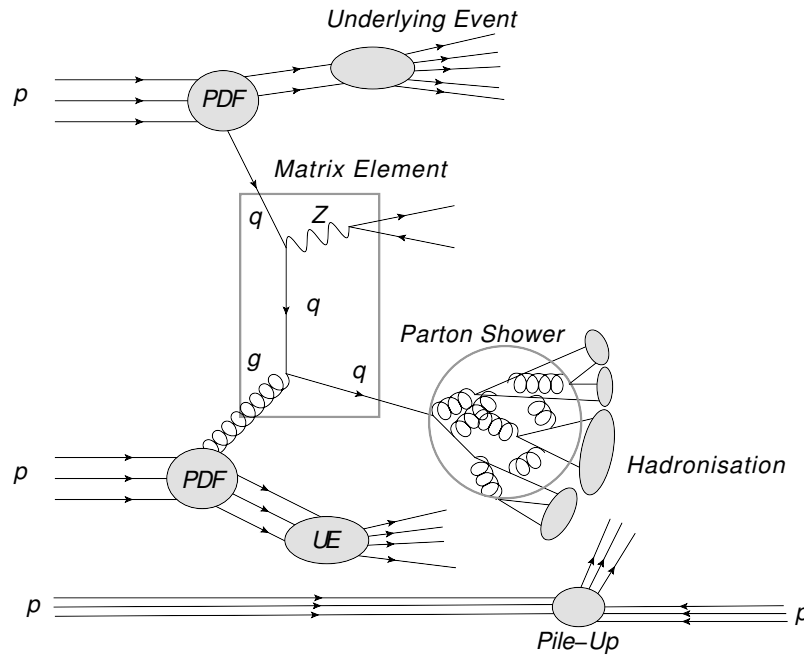


FIGURE 2.13 – Schematic picture of a proton-proton collision. Shown are the incoming protons and their parton content described by the PDFs, the partonic interaction given by the matrix element (ME), the parton shower (PS) and hadronisation of the quarks and gluons in the event and additional activity in the event originating from the underlying event and pile-up [72].

significant deviations from the SM hypothesis or to precisely measure the SM expectation.

The simulations are relying on several available programs based on Monte Carlo methods [73], which can simulate all the different phases of the parton scattering. As shown in Figure 2.13, the  $pp \rightarrow X$  interactions are complex to simulate, thus the full process is divided into steps: the underlying event, the hard scattering part (matrix element), the evolution of the parton showers and the hadronisation.

**Parton distribution functions (PDF):** As described in Section 2.3.1, the PDFs are used to describe the probability to find a parton carrying a fraction  $x$  of the total momentum. The results are extracted from deep-inelastic scatterings and fixed-target experiments or the LHC, to cover different energies, and combined in a global fit to extrapolate the PDF over a broad range of scales. There is a non-negligible space for arbitrary choices in the fit, like in the choice of input datasets, the order in perturbation theory or the input parametrization, which can lead to differences in the results. Several collaborations, characterized by different choices in the global fit procedure, are regularly releasing updated PDF sets (i.e. CT14, NNPDF3.0 or MMHT14, PDF4LHC), in particular when new data become available. The associated PDF uncertainties are typically covering the spread between the fitting groups in the region 50-500 GeV, but beyond that, differences begin to emerge and the uncertainties are around  $\mathcal{O}(10\%)$ .

**Matrix Element (ME):** The matrix element represents the hard scattering part of the process, calculated applying the Feynman rules. In the case of NLO simulations, the matrix element accounts also for the additional Feynman diagrams coming from

the higher order corrections. In this way the number of Feynman diagrams rapidly increases and so the computation time to calculate all the possibilities, making the simulation process quite slow.

In addition to the hard scattering process, the ME simulation of many available generators also includes the simulation of the decay process of the short lived particles, such as  $H \rightarrow b\bar{b}$  or  $W \rightarrow \ell\nu$ . The ME simulations are calculated at a fixed renormalization scale  $\mu$ . Thus, changing the choice of  $\mu$  can change the outcome of the simulation.

**Parton Shower (PS):** The parton shower represents the connection between the ME partons and the final state hadrons. Partons produced at ME do not immediately form hadrons, since they are still in the asymptotic freedom regime, but they lose energy through several stages of radiation, until their energy is low enough to break perturbation theory and build complex states. The PS aims at modelling this extra radiation before hadronization and it is extremely important in the description of the jet structure. The radiation stages are encoded in the so-called Sudakov form factors [74], which define the probability for a parton  $q$  *not to* emit radiation in the interval  $\Delta t$ . The Sudakov factors are defined as a function of a certain evolution variable  $t$ , which sets the time for the shower evolution. In final state showers it should gradually decrease, while for the initial state radiation it should gradually increase towards the hard scattering. The choice of the evolution variable is different across the generators: opening angle (HERWIG) or transverse momentum (PYTHIA 8) are some examples used by the currently available algorithms.

For the final-state radiation, the parton shower modelling follows the so-called *forward evolution*, which starts with a given number of hard partons and assigns further emission according to the Sudakov weights. On the contrary, for initial state radiation the PS model follows the so-called *backward evolution*, since it fixes the hard scattering and it works backwards to establish the incoming hadrons. The main complication arises from the fact that the DGLAP equations must be satisfied at all steps.

In case the ME and PS are simulated with different generators, the two have to be carefully matched in order to remove the overlapping diagrams. For example, ME generators at NLO already count for the radiation of one extra parton, so these diagrams should be removed from the PS, otherwise the final probability of the process is biased.

**Hadronization:** Perturbation theory breaks down at the end of the shower (scale  $\sim 1$  GeV) and partons begin to bound together into hadrons. This step happens at energies which are in the transition zone between the two QCD regimes, where physics is not well known, and it is usually modelled by the parton shower generators. To overcome this problem, the parton shower event generators use *phenomenological models* involving a dozen of parameters (that must be tuned to existing data from LEP collisions), to translate the final partons into hadrons. Well tested examples are the *Lund string model* used in PYTHIA and the *cluster model* used in HERWIG and SHERPA. Many of the hadrons produced by these models are unstable and further decay into lighter hadrons, according to known branching ratios.

**Underlying Event (UE):** The underlying event simulation contains all the events not coming from the primary hard scattering. The UE involves contributions from initial and final state radiation, beam-beam remnants or multiple parton interactions. The energy scale of the underlying processes is expected to be smaller than



the energy of the hard scattering event. For this reason, the UE is not expected to create additional jets, but a uniform underlying activity represented by low energy hadrons ( $E \sim 3$  GeV at LHC). The underlying event is divided from the PS by an energy cutoff: interactions above this value will be treated in the PS, while all the activity below this value is included in the underlying event. The choice of the cutoff depends on the PDF set, the collision energy and the impact parameter of the protons. The UE activity is simulated by tunable parametric tools based on minimum bias data collected with very loose triggers [75, 76].

**Pile-up:** As described later in Section 3.1.2, at LHC there is high chance that multiple inelastic  $pp$  collisions happen simultaneously at the collision points (for each bunch, see later). This phenomenon is called *pile-up*, and it has a dedicated simulation step, different from the hard scattering event.

### 2.7.1 Available generators

Several programs are available to simulate the events [77]. The programs able to simulate the full event - from ME to the hadronization - are also called multi-purpose generators (like SHERPA, PYTHIA and HERWIG), while there are also some specialized programs able to generate only part of the event - i.e. only the hard scattering, like MADGRAPH or POWHEG- so they need to be interfaced with other specialized programs for the simulation of the PS. This is convenient because the simulation is faster and can be parallelized, but then ME and PS simulations need to be carefully matched to remove the double-counting of emissions [72].

**Pythia** [78]: This is a multi-purpose generator providing PS, UE and ME calculations. The ME calculations are given at LO and both PS and UE models are tuned on existing measurements. The hadronization step is based on the Lund model. Several sets of such tunes are provided for testing. The most common sets are the so-called AZNLO and A14 [79], which will be later used to study the impact of UE and PS on the MC modelling. This generator has a "hybrid" version, meaning that it can simulate just certain parts of the event. This feature is useful since the default accuracy of the ME is just at LO, and therefore it is often substituted by POWHEG event generation.

**Sherpa** [80]: This generator is a multi-purpose generator providing both ME and PS simulations at once. It is the preferred generator for processes with additional radiated jets, which are directly included in the ME calculation. No "hybrid" version of this generator is available to generate just part of the event.

**Herwig** [81]: This is another multi-purpose generator. Contrary to PYTHIA, its hadronization model is based on the cluster fragmentation model. This generator will be later used in combination with POWHEG to quantify the systematic uncertainties related to the fragmentation/hadronisation modelling.

**Powheg** [82]: This is an NLO generator able to simulate the matrix elements of a broad variety of processes. It has to be coupled with other generators for the PS, and undergo the ME-PS matching. In this work, it will be usually interfaced to PYTHIA or HERWIG.

**Madgraph** [83]: Similar to POWHEG, this generator provides only ME calculations at NLO (and LO). In this work it will never be used as the default generator, but just as an alternative sample to study the modelling uncertainties. The PS generators which are interfaced with MADGRAPH are PYTHIA or HERWIG.

### 3 | The Large Hadron Collider and the ATLAS detector

The ability to probe nature at the scale of its constituents requires huge experimental devices, able to accelerate particles at the highest energies ever reached in controlled environments on Earth. Such high energies are useful to exploit two fundamental properties of nature:

- **The De Broglie relation** [84]: thanks to the De Broglie relation  $\lambda = h/p$  the energy scale ( $p$ ) of an object is inversely related to its De Broglie wavelength  $\lambda$ . From this relation follows that one of the ways to reach the resolution power necessary to probe infinitesimally small objects - such as the constituents of the nucleon - can be obtained with very high momentum probe particles, having De Broglie wavelengths compatible to the quark length scale ( $10^{-20}$  m) <sup>1</sup>.
- **The mass-energy relation** [86]: the Einstein's mass-energy relation  $E = mc^2$  states that in case of relativistic kinematics, mass can be converted to energy and vice-versa. In particular, new particles with mass  $m_0$  higher than the initial mass of the mother particles can be created if their equivalent in energy is concentrated in a point. The higher the energy of the initial particles, the higher is the limit on  $m_0$ . The main advantage of creating real particles is that their kinematic can be directly assessed by reconstructing their decay products, allowing for direct searches of new resonances. Particles can also be created, for a very short time and out of mass shell <sup>2</sup>, with vacuum polarization in virtual loops. However, in this case their signature can be assessed only indirectly.

These two fundamental aspects were highly considered while designing the experimental apparatus. The highest performance is reached when high energy particles travelling in opposite directions collide to create new particles out of the collision. The largest example of such device is the Large Hadron Collider (LHC) built at the European Centre for Nuclear Research (CERN). The LHC is a 27 km circumference proton-proton collider reaching center of mass energies up to 14 TeV.

These newly produced particles are then captured by experiments surrounding the interaction points in which the proton beams intersect and collide. The whole system can be seen as a high precision microscope, with a resolution power up to

---

1. Complementary results can be achieved with smaller energies but higher intensities and ultra-high precision measurements, which can compensate for the lack of energy and reach similar scales, like in b-factories [85].

2. Virtual particles that do not satisfy the energy-momentum relation.

the quark scale. This Chapter will mainly focus on the ATLAS experiment, used to collect the data analyzed in the next Chapters.

### 3.1 The Large Hadron Collider

The Large Hadron Collider [87] is currently the largest particle accelerator in the world. It is also the most powerful hadron collider ever built, with an achievable center of mass energy seven times higher than the previous record detained by the Tevatron [88], allowing access to very rare phenomena and precision measurements.

These high center of mass energies can be efficiently reached only accelerating relatively heavy particles, such as protons, for which the energy loss in curved trajectories due to synchrotron radiation is considerably reduced for a machine of fixed radius, with respect to lighter particles such as electrons. Furthermore, the momentum distribution of partons inside the protons allows to probe multiple energy ranges simultaneously. The possibility of a proton-antiproton collider was rejected due to difficulties in maintaining high-intensity antiproton beams for long periods, which would have affected the final instantaneous luminosity, without a considerable gain in the production rates, since at these energies the dominant contribution comes from  $gg$  collisions.

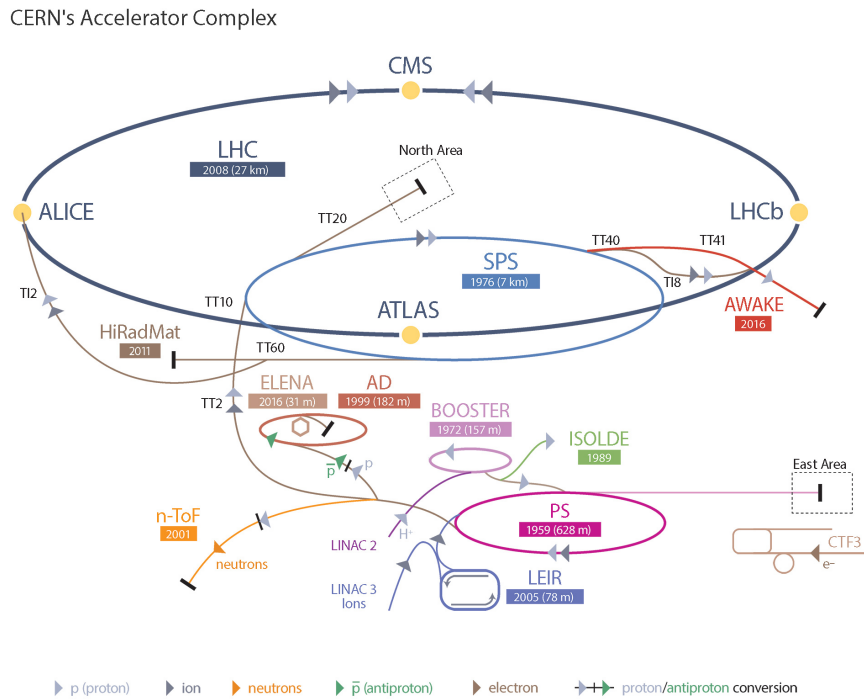


FIGURE 3.1 – Scheme of LHC beamlines and experiments. The current LHC injection chain (from Linac2 to PSB to PS to SPS and finally to LHC) is visible.

Inside the accelerator, two high energy proton beams travel in opposite directions in separate beam pipes kept at ultrahigh vacuum ( $10^{-10}$  Torr). The LHC was designed to accelerate protons up to an energy of 7 TeV producing collisions at a center of mass energy of 14 TeV at a maximum instantaneous peak luminosity of  $L = 10^{34} \text{ cm}^{-2}\text{s}^{-1}$ . The LHC started operations in 2008 and during the period 2010-2011 it provided a center of mass energy of 7 TeV and a peak luminosity of  $L = 4 \times 10^{33} \text{ cm}^{-2}\text{s}^{-1}$ . The center of mass energy has been increased to 8 TeV during 2012. After

a shut down of two years, the accelerator has been upgraded and from 2015 to 2018 it was operated at a center of mass energy of 13 TeV. The peak instantaneous luminosity was increased in 2017 to  $2 \times 10^{34} \text{ cm}^{-2}\text{s}^{-1}$ , corresponding to twice the design value, thanks to new techniques able to reduce the size of the beams [89].

The acceleration is only possible through several steps that take place in different ever-increasing accelerators before the beam injection at the LHC. Protons are first injected from Linac 2 (a linear accelerator) into the Proton Synchrotron Booster (PSB) with an energy of 50 MeV. The PSB accelerates protons to 1.4 GeV and injects them into the Proton Synchrotron (PS). The PS accelerates the protons to 26 GeV before injecting them into the Super Proton Synchrotron (SPS). The SPS accelerates the protons to 450 GeV before injecting them into the LHC. This injection chain is sketched in Figure 3.1.

The LHC accelerator has many parts which have important and necessary roles in accelerating protons. The acceleration is performed by radio-frequency (RF) cavities. Eight superconducting cavities, operating at 400 MHz, increase the beam energy by 485 keV at each turn until it reaches 6.5 TeV. Furthermore, there are 1232 superconducting dipole magnets made of Nb-Ti used to bend the protons' trajectories. Superfluid helium is used to cool the Nb-Ti to 1.9 K in the dipole magnets. The limiting factor for the LHC is not the acceleration itself but the bending power of these dipole magnets, which are designed to operate at 8.3 T, with possible operations up to 9 T [90]. There are also 78 superconducting quadrupole insertion magnets which are also made of Nb-Ti. These magnets are used to focus the bunches of protons. In most of the quadrupole magnets a weaker target for magnetic field strength allows for a slightly higher temperature of 4.5 K. In addition there are approximately 3800 single aperture and 1000 twin aperture corrector magnets that are used for orbital corrections. The standard LHC filling scheme foresees two beams each with 2808 bunches, separated by 25 ns, with  $1.15 \times 10^{11}$  protons per bunch in a beam size of  $3.5 \mu\text{m}$ . However, since 2016 the filling scheme has been changed to achieve higher brightness. The Batch Compression Merging and Splitting (BCMS) [91] allows to reduce the beam size to around  $2.5 \mu\text{m}$ , while keeping the same number of protons per bunch. The higher the beam density, the higher the collision rate and hence the luminosity. This new configuration implies also a higher energy density of the beam, which can potentially cause more damage if it is lost. For this reason, the maximum number of bunches is limited to 144 bunches in the SPS. This, combined with the limitations in the technical gaps between batches (225 ns), results in a maximum number of bunches per ring of 2556 bunches. The lifetime of the beams inside the LHC is about  $\sim 15$  h, mainly limited by the decrease in instantaneous luminosity due to collisions at the interaction points.

### 3.1.1 Luminosity

Collecting high statistics during each run is fundamental when studying rare phenomena. The number of events per second generated by a given process in the collisions is given by:

$$N_{\text{events}} = L \times \sigma_{\text{process}} \quad (3.1)$$

with  $\sigma_{\text{process}}$  is the cross section of the process and  $L$  is the instantaneous luminosity, a proportionality constant depending on multiple factors related to the beam properties:

$$L = \frac{N_b^2 n_b f_r \gamma_r}{4\pi\epsilon_n \beta} F \quad (3.2)$$

where the definitions and the design values for an LHC run are summarized in Table 3.1. The instantaneous luminosity is expressed in units of  $\text{cm}^{-2}\text{s}^{-1}$  or  $b^{-1}\text{s}^{-1}$ , with

Variable	Value	Description
$N_b$	$10^{10}\text{-}10^{11}$	Number of particles per bunch
$n_b$	2808	Number of bunches per beam
$f_r$	11 245 Hz	Revolution frequency
$\gamma_r$	$\sim 7000$	Relativistic gamma factor
$\epsilon_n$	$3.75 \mu\text{m}$	Normalized transverse beam emittance, related to its size
$\beta$	0.55 m	Beta function at the collision point, related to its focusing
$F$	0.84	Geometric luminosity reduction factor if the beams do not collide head-on. A crossing angle of $285 \mu\text{rad}$ is introduced to prevent collisions outside the nominal interaction points.

TABLE 3.1 – Summary of the nominal design LHC parameters and their definitions.

$b^{-1}$  being the *inverse barn* ( $1b = 10^{-24}\text{cm}^2$ ).

The *integrated* luminosity in time  $\int L dt$  quantifies the total amount of produced data. For a given process  $pp \rightarrow X$ , the number of predicted events collected in a specific amount of time is given by  $\int L \sigma_{pp \rightarrow X} dt$ , for  $\sigma_{pp \rightarrow X}$  calculated in barns.

### 3.1.2 Mean number of interactions per bunch-crossing

Since each bunch contains around  $\sim 10^{11}$  particles and given that the inclusive cross section of  $pp$  inelastic scattering  $\sigma_{inel}$  is  $\sim 80 \text{ mb}$  at 13 TeV, there is high chance to have multiple  $pp$  collisions during a single bunch crossing, such effect is called in-time pile-up. The mean number of interactions per bunch crossing is calculated as the mean of the Poissonian distribution of the number of collisions for each bunch:

$$\mu = \frac{L_{bunch} \cdot \sigma_{inel}}{n_b \cdot f_r} \quad (3.3)$$

with  $L_{bunch}$  the luminosity per bunch and  $f_r \cdot n_b$  the collision rate at the LHC, calculated as the product of the number of bunches per beam ( $n_b$ ) and the revolution frequency ( $f_r$ ). The value of  $\langle \mu \rangle$  tends to decrease with the life time of the beams inside the LHC due to the lower number of particles in the colliding bunches. High  $\langle \mu \rangle$  values imply more difficulties in disentangling simultaneous  $pp$  collisions. As shown in Figure 3.2, each data-taking period has its specific  $\langle \mu \rangle$  profile, for an average value of 33.3 interactions per bunch crossing summing all Run-2 data taking periods.

### 3.1.3 LHC experiments and physics research

In the LHC ring the beams collide in four points, in correspondence of four detectors dedicated to different purposes:

**ALICE (A Large Ion Collider Experiment)** [92] uses heavy ion collisions to study the quark-gluon plasma, a particular state of matter supposed to be the closest reproduction of the universe some milliseconds after the Big Bang. A single ion-ion

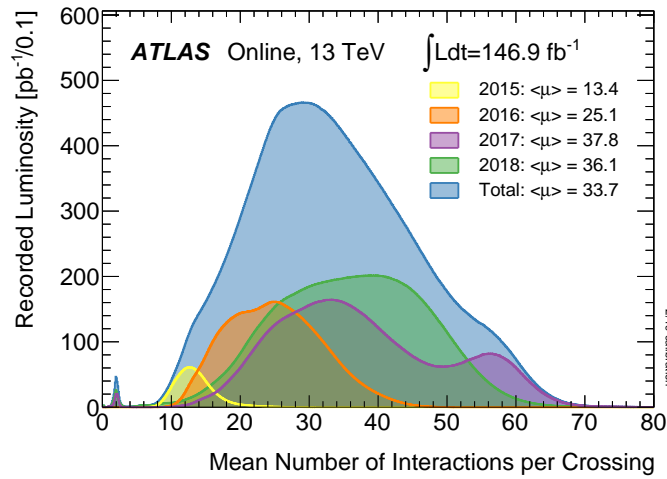


FIGURE 3.2 – Shown is the luminosity-weighted distribution of the mean number of interactions per crossing for the 2015-2018 pp collision data at 13 TeV center of mass energy. All data recorded by ATLAS during stable beams is shown, and the integrated luminosity and the mean  $\mu$  values are given in the figure. The mean number of interactions per crossing corresponds to the mean of the poisson distribution of the number of interactions per crossing calculated for each bunch. It is calculated from the instantaneous luminosity per bunch as  $(L_{\text{bunch}} \cdot \sigma_{\text{inel}}) / (f_r \cdot n_b)$  as explained in Equation 3.3.

collision produces a huge number of particles in the final state, which can be up to three orders of magnitude larger than a typical proton-proton interaction. This makes the environment very challenging in terms of event reconstruction and radiation resistance.

**ATLAS (A Toroidal LHC ApparatuS)** [93] is one of the two general purpose detectors at LHC. Its name is given by the big toroidal magnetic system, consisting of three large superconducting air-core toroid magnets placed in the outer part of the detector. This experiment has a wide spectrum of research, with a particular focus on precision SM measurements, the Higgs boson physics and on searches for physics Beyond the Standard Model (BSM), as predicted for instance by SUSY and extra-dimensions theories. More details are given in the next Section.

**CMS (Compact Muon Solenoid)** [94] is the other LHC general-purpose detector, with a physics program very similar to ATLAS: Higgs boson physics and the searches of new particles in the context of BSM models are the main domains. The main difference from ATLAS is the design, in fact all the detectors are placed around a unique superconducting solenoid of 3.8 T, generating an axial magnetic field both for the tracker and the muon system.

**LHCb (Large Hadron Collider beauty)** [95] is a forward detector focused on flavour physics, performing precise measurements of CP violation and rare decays of bottom and charm hadrons. The structure of this experiment is completely different with respect to the other experiments, in fact it is developed only on one side of the interaction point, to catch particles in the forward region.



### 3.2 The ATLAS experiment

The ATLAS detector [93] is one of the two general purpose detectors set up along the LHC ring. With a total length of 42 m, a radius of 11 m and a weight of 7000 tons, it is the largest LHC experiment (See Figure 3.3). The detector has an overall cylindrical symmetry and it is composed by the inner detector (ID), the calorimetric system and the muon spectrometer (MS). The combination of all these different instruments allows for the reconstruction of the trajectory and momentum of the outgoing particles.

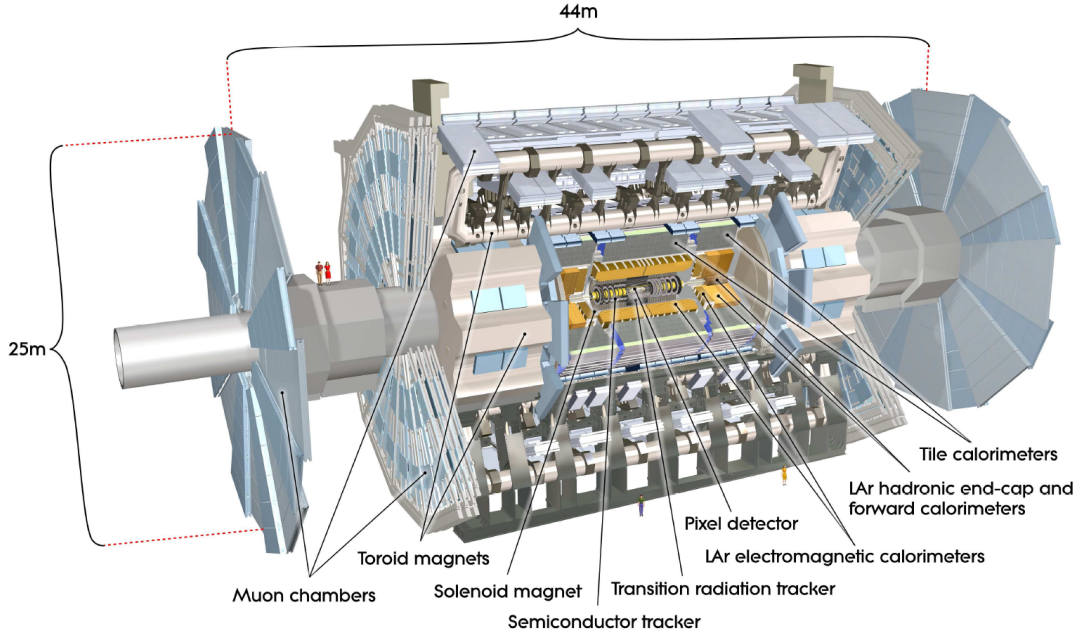


FIGURE 3.3 – Picture of the ATLAS experiment. All the sub-detectors described the section are shown.

In the ATLAS standard coordinate system the beam direction corresponds to the  $z$ -axis while the  $x$ - $y$  plane corresponds to the plane transverse to the beam pipe, in particular the  $x$ -axis points radially towards the center of the LHC ring and the  $y$ -axis points upwards to the surface. The nominal collision or interaction point defines the origin of the coordinate system, placed at the center of the detector. A polar coordinate system is also largely used: the azimuth angle ( $\phi$ ) is measured in the  $(x, y)$  plane with respect to the  $x$  axis, and the polar angle ( $\theta$ ) is the angle that a particle forms with the beam axis. The  $\theta$  coordinate is usually substituted with the pseudorapidity:

$$\eta = -\log\left(\tan\frac{\theta}{2}\right) \quad (3.4)$$

For ultra-relativistic particles this is an approximation of the rapidity:

$$y = -\frac{1}{2}\ln\left[\frac{E + p_z}{E - p_z}\right] \quad (3.5)$$

which transforms additively under boosts in the  $z$ -direction. Since boosts along the beam axis do not affect the  $\phi$  angle, a useful quantity to measure is the angular distance in the  $\eta - \phi$  plane, such as:

$$\Delta R = \sqrt{(\Delta\eta)^2 + (\Delta\phi)^2} \quad (3.6)$$



Since the initial momentum of the colliding partons is not known, the longitudinal coordinate can not be determined a priori. Some quantities are therefore expressed directly in the transverse plane, such as the transverse momentum ( $p_T$ ) and the transverse energy ( $E_T$ ), defined as:

$$p_T = p \sin \theta \text{ or } E_T = E \sin \theta. \quad (3.7)$$

### 3.2.1 The magnet system

Exploiting the properties the Lorentz force, charged particles momenta are measured by the particle deflection in magnetic fields. The detector is therefore immersed in a non-homogeneous magnetic field produced by four large superconducting magnets placed in different parts of the detector. The system is composed of a central solenoid for the inner tracker and three open-air toroids for the muon spectrometer [96]. This design has been chosen to reduce the influence of the magnetic field on the sampling calorimeters, which would translate in a degradation of the overall energy response<sup>3</sup> [97]. Starting from the beam pipe, the first magnet is the central solenoid of 2 T, placed immediately after the inner detector, providing a magnetic field parallel to the beam axis. The solenoid has a radius of 2.5 m and a length of 5.3 m. The toroid system is located around the calorimeters and it can be divided

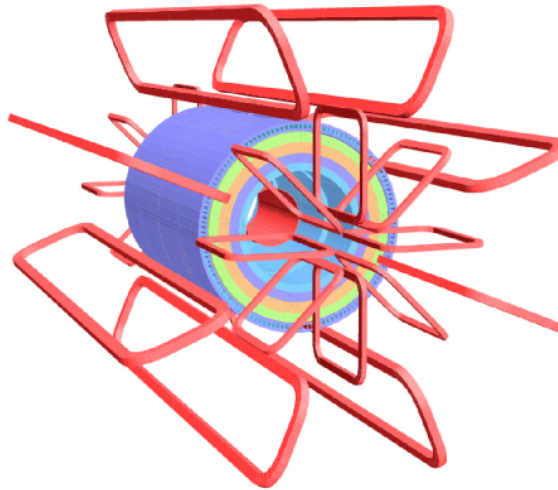


FIGURE 3.4 – Schematic view of the ATLAS solenoidal (inner cylinder) and toroidal magnets (outer coils) [96].

in two *end-cap toroids* and one *barrel toroid*, as shown in Figure 3.4. Each toroid is composed of eight independent coils arranged in the radial direction following the ATLAS coordinate system. The end-cap toroids are rotated of  $22.5^\circ$  with respect to the barrel toroid, to improve the overlap across the magnetic fields and increase the uniformity. The two end-cap toroids produce a field of 4.1 T, while the barrel toroid generates a field of 3.9 T. In both cases a helium cooling system is used to maintain the magnets at a temperature of 4.5 K.

3. The magnetic field has effects on the shower profile, for example the lateral development of the shower can be broadened or the soft EM component can be bend within the inactive areas of the calorimeter and get lost. In copper-based calorimeters more than half of the EM shower is deposited by soft electrons of  $\sim 4$  MeV, and already for a 2 T field perpendicular to their direction the radius of curvature is only  $\Sigma 6$  mm.

### 3.2.2 Inner Detector and Tracking

The inner part of ATLAS is the tracking detector [98]. The tracker is surrounded by the superconducting solenoid of 2 T magnetic field as described in the previous section, and it is designed to achieve good momentum resolution and pattern recognition for charged particle tracks in the range  $|\eta| < 2.5$ . A schematic view of the detector design is presented in Figure 3.5. To ensure a good intrinsic spatial resolution and mitigate the occupancy problems due to the high pile-up environment, the tracking system has been designed using highly segmented sub-detectors.

The final design has been chosen as a trade-off between high performance and considerations about the amount of material in the tracker. In fact, large amounts of material in the innermost layers of the detector are highly influencing both the intrinsic momentum resolution due to multiple scattering, and the performance of the calorimeters. The overall thickness of the inner detector varies from 0.4 radiation lengths<sup>4</sup> ( $X_0$ ), to a maximum of  $2.5X_0$  in the forward region. A sketch of the amount of material in the area before the calorimeter as a function of  $\eta$ , including the supporting staves and the cryogenic system, is presented in Figure 3.6.

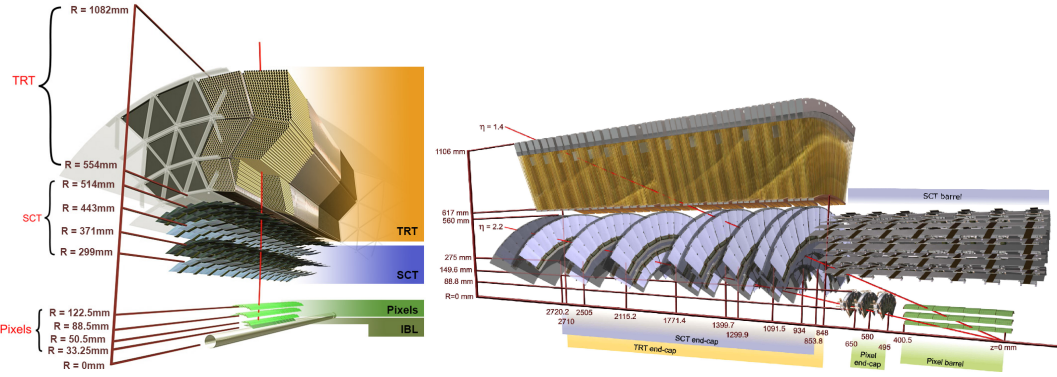


FIGURE 3.5 – Schematic view of (a) the front and (b) the longitudinal designs of the ATLAS Inner Detector. The new Insertable B-Layer (IBL) is visible only in the front view. [98].

The inner detector is contained within a cylinder of length  $\pm 3.5$  m and 1.15 m of radius around the beam pipe, starting at a few cm from the collision axis. Three main technologies are used, with decreasing granularity at higher radial distances from the beam-pipe. The innermost part of the tracker consists of a silicon pixel detector, which is surrounded by a Semi Conductor Tracker (SCT) consisting of modules with two layers of silicon micro-strip sensors. The outermost region is covered by a Transition Radiation Tracker (TRT) consisting of straw drift tubes filled with a gas mixture dominated by Xenon, interleaved with polypropylene/polyethylene transition radiators. The designed track momentum resolution of the ID is [98]:

$$\sigma_{p_T}/p_T = 3.8 \times 10^{-4} \cdot p_T(\text{GeV}) \oplus 0.015. \quad (3.8)$$

#### Pixel Detector

The pixel detector [100] is the closest detector to the beam-pipe. This sub-detector is crucial for a good vertex reconstruction and a precise measurement of the track

4. The *radiation length* of a material is defined as the mean length (in cm) needed to reduce the energy of a relativistic electron by a factor  $1/e$ .

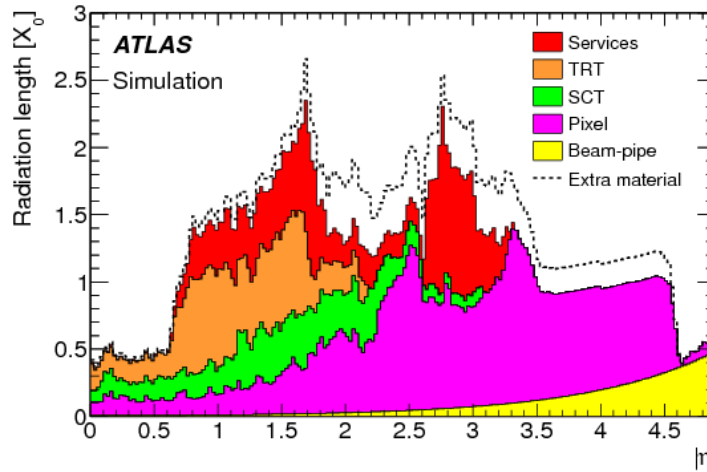


FIGURE 3.6 – Amount of material traversed by a particle,  $X/X_0$ , as a function of  $|\eta|$ , in the improved simulation, up to the ID boundaries (left), and up to the PS and the EM calorimeter (right). The contributions of the different detector elements, including the services and thermal enclosures are shown separately by filled colour areas [99].

impact parameters, defined as the minimum distance between the track and the primary vertex. These are key ingredients in many aspects of the analysis, i.e. a good object and event reconstruction (see Chapter 4) or for the so-called *b*-tagging as described in Chapter 5.

The pixel detector has different designs for barrel and end-caps. The end-caps are composed of three disks of 34 cm radius placed at  $|z| = 49.5, 58.0$  cm and 65.0 cm from the nominal interaction point. The barrel is composed of four cylinders of 80 cm length and radii of 3.33 cm, 5.05 cm, 8.85 cm and 12.25 cm, conventionally referred to as Insertable B Layer (IBL), b-layer, layer 1 and layer 2 respectively. The IBL has been added in 2014 [101] to help in the reconstruction of displaced vertices and increase the discrimination power between b-jets and jets from gluons and light quarks.

Each layer of the detector is made of silicon sensors segmented in  $\phi$  and  $z$ . The outer layers and 75% of the IBL are equipped with planar pixel sensors [100], while the remaining parts are instrumented with pixel modules using the 3D technology [102]. The minimum pixel size in  $\phi \times z$  is  $250 \mu\text{m} \times 50 \mu\text{m}$  for the IBL modules and  $50 \times 400 \mu\text{m}^2$  for the other layers, resulting in an overall accuracy in the barrel region of  $10 \mu\text{m}$  in the  $\phi$  direction and  $115 \mu\text{m}$  in the  $z$  direction. The IBL alone has a hit spatial resolution of  $10 \mu\text{m}$  in the  $\phi$  direction and  $66 \mu\text{m}$  in the  $z$  direction [103]. The accuracy in the end-caps is  $10 \mu\text{m}$  in the  $\phi$  direction and  $115 \mu\text{m}$  in the  $R$  direction. The radiation hardness of all sensors has been extensively studied in beam tests [101] [104] for fluences up to  $5 \times 10^{15} \text{ n}_{\text{eq}}/\text{cm}^2$ <sup>5</sup>.

The proximity to the collision point makes the innermost layers particularly exposed to the received radiation damage. By the end of the 2017 *pp* collision period the IBL and the b-layer received integrated fluences of  $6 \times 10^{14}$  and  $3 \times 10^{14} \text{ n}_{\text{eq}}/\text{cm}^2$  respectively [105]. The other two layers received less than half the fluence of the two b-layers. Figure 3.7 shows the 1 MeV neutron-equivalent fluence as a function of time for the four ID layers. At the end of Run-2 the integrated fluence received by the IBL is about  $1 \times 10^{15} \text{ n}_{\text{eq}}/\text{cm}^2$ . Thus, the expected integrated fluence on the IBL

5. The  $\text{n}_{\text{eq}}/\text{cm}^2$  is the unit of "neutron equivalent fluence". The fluence of an arbitrary type of particle is expressed in fluence of 1 MeV neutrons, which are taken as reference particles.

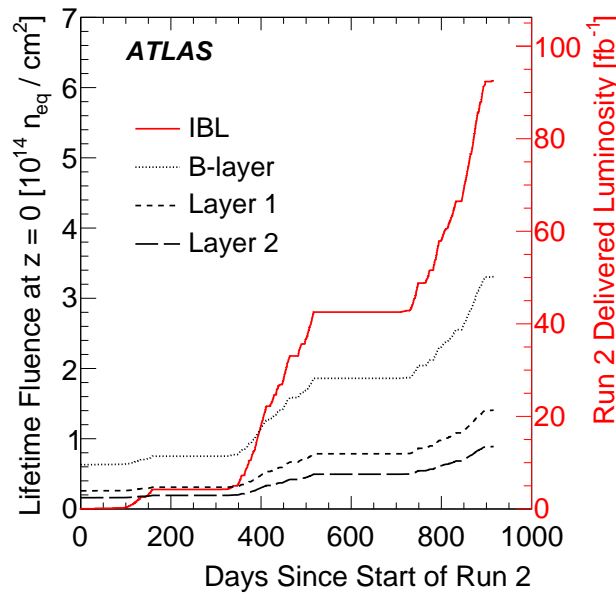


FIGURE 3.7 – Predictions for the lifetime fluence experienced by the four layers of the current ATLAS pixel detector as a function of time since the start of Run-2 (June 3, 2015) at  $z \sim 0$  up to the end of 2017. For the IBL, the lifetime fluence is only due to Run-2 and for the other layers, the fluence includes all of Run-1. The IBL curve represents both the fluence on the IBL (left axis) as well as the delivered integrated luminosity in Run-2 (right axis) [105].

at the end of Run 3, considering a total of  $300 \text{ fb}^{-1}$ , will be around  $2 \times 10^{15} \text{ n}_{\text{eq}}/\text{cm}^2$ , considering an expected fluency per unit of luminosity of  $6.1 \times 10^{12} \text{ n}_{\text{eq}}/\text{cm}^2/\text{fb}^{-1}$ , with uncertainties of the order of 10% [105].

The pixel detector is providing ideally four measurement points for charged particle. According to the Bethe-Bloch formula [20], the charged particles interact with the silicon losing energy in the pixel and electron-hole pairs are created by ionization along its path. The electron-hole pair is created when an electron moves from the valence band to the conduction band. The amount of energy needed to create an electron-hole pair in silicon is about 3.6 eV. Once the free electron and holes are created, they drift in the sensor towards the collecting electrodes, following the applied electric field. Finally, they are collected and converted in an electrical signal.

### SemiConductor Tracker

The Semi Conductor Tracker (SCT) is a silicon micro strip detector [106]. The SCT barrel is composed of eight strip layers, mounted on four cylinders equipped on both sides, and placed at a radial distance from the beam of 30.0, 37.3, 44.7 and 52.0 cm. The SCT end-caps are composed of 9 disks with modules arranged in the radial direction. One module consists of two single-side layers of microstrips mounted back to back. The microstrips have  $80 \mu\text{m}$  width and a length of 6.4 cm in the  $z$  direction. In the barrel, the  $z$  component is measured exploiting the stereoscopic effect: the front layers of each module are mounted parallel to the beam direction (orthogonal for the end-caps), while the back module is rotated by a small angle of 40 mrad. The crossing point of the strips in the two modules is used to determine the space position. The same effect is exploited in the barrel to measure the  $R$  position.

The overall spatial resolution is  $17\ \mu\text{m}$  in the  $\phi$  direction and  $580\ \mu\text{m}$  in  $z$  ( $R$  in the end-cap), the latter determined with the strip crossing method.

### Transition Radiation Tracker

The Transition Radiation Tracker (TRT) [107] represents the outermost part of the ATLAS tracker. The TRT is divided into a barrel ( $|\eta| < 0.7$ ) and two end-caps ( $0.7 < |\eta| < 2.0$ ). The TRT barrel extends from a radius of 56 cm to 108 cm, just before the edge of the cryostat serving both the magnet and the ID, while the end-caps are placed in the range between 61-110 cm in  $R$  and 82-274 cm in  $z$ .

Both barrel and end-caps are instrumented with straw drift tubes with a diameter of 4 mm filled with a Xenon mixture, interleaved with polypropylene/polyethylene transition radiators. In the barrel the straws are parallel to the beam axis and are 144 cm long, while the end-caps are instrumented with 37 straws arranged radially in wheels.

The gas mixture is composed of 70% Xe, 27% CO<sub>2</sub> and 3% O<sub>2</sub>. The gas is ionized by the interaction with the charged particles crossing the detector, the free electrons generated by the ionization drift thanks to the high voltage applied, and the induced signal is collected by  $31\ \mu\text{m}$  tungsten anode wires placed at the center of each tube. The spatial resolution of the TRT is  $130\ \mu\text{m}$  per straw, with information only on the transverse plane. For charged particles with transverse momentum  $p_T > 0.5\ \text{GeV}$ , the TRT typically provides 35 hits per track. The detector offers also additional electron identification capability thanks to the transition radiation produced by high-energy electrons.

### 3.2.3 Electromagnetic Calorimeter

The electromagnetic calorimeter (ECAL) [108] is an hermetic lead/liquid-Argon (LAr) sampling calorimeter which measures energy, starting point and direction of electromagnetic showers within  $|\eta| < 3.2$ . The calorimeter is divided in a barrel section ( $|\eta| < 1.475$ ) and two end-cap regions ( $1.375 < |\eta| < 3.2$ ). The transition region between the barrel and the end-caps ( $1.37 < |\eta| < 1.52$ ) has a large amount of material upstream of the first active calorimeter layer, as visible in Figure 3.6. The total thickness of the EM calorimeter is higher than 22 radiation lengths in the barrel and 24 in the end-caps, counting both active and inactive layers. The *active* layers of the sampling calorimeter occupy  $\sim 9.7$  radiation lengths in the barrel (10 in the end-caps) out of the 22 (24) total radiation lengths quoted above. The geometry of the electrodes follows an accordion shape in  $\phi$ , to reduce the inactive regions seen by the particle. In the region  $|\eta| < 2.5$  the calorimeter is divided in three different sections in depth, as displayed in Figure 3.8. The first sampling (strips) has a fine segmentation in  $\eta$  (in the region  $|\eta| < 1.4$  and  $1.5 < |\eta| < 2.4$ ) which allows isolated photons and neutral pions to be differentiated for transverse momenta up to 100-200 GeV. The second sampling (middle) collects most of the energy measured and is the thickest, while the third one is thinner and is mainly used to estimate the amount of energy leaking beyond the ECAL. In front of the accordion calorimeter, a thin presampler (PS) layer (in the region  $|\eta| < 1.8$ ) is used to correct for energy loss upstream of the calorimeter. This longitudinal segmentation is useful to reconstruct the direction of the incident particle. High voltage is applied in the active layers (between the absorbers) to collect the drifting electrons generated by the ionization of the liquid argon interacting with the charged particle.

The energy resolution of the accordion calorimeter is parametrized as the quadratic



sum of three terms:

$$\frac{\sigma}{E} = \frac{a}{\sqrt{E}} \oplus \frac{b}{E} \oplus c \quad (3.9)$$

where  $a$ ,  $b$  and  $c$  are  $\eta$ -dependent parameters. The  $a$  term is the *sampling term*, reflecting the stochastic behaviour of the shower development;  $b$  is the *noise term*, accounting for electronic and pile-up noise and  $c$  is the *constant term*, including contributions which do not depend on the energy of the particle, such as non-uniformities in the geometry, ageing and radiation damage. The relative importance of the various terms depends on the energy of the incident particle. The sampling term dominates at relatively low energies (few GeV), while for lower energies the major contribution comes from the noise term. The constant term is asymptotically dominating at high energies, where the energy dependence suppresses the other two terms. The design value for  $a$  is 10%, while for  $c$  is 0.7%; the noise term  $b$  was estimated to be  $350 \times \cosh \eta$  MeV for a  $3 \times 7$  cluster in the  $\eta \times \phi$  space in the barrel and for a mean number of interaction per bunch crossing equal to 25 [109]. At high  $\eta$  the noise term is dominated by the pile-up noise. Different methods are used to have direct measurements of both the noise term and the constant term:  $b$  (accounting for the electronic and pile-up contributions) is accessed comparing pile-up only events in data and simulation [109], while  $c$  is extracted comparing the width of the  $Z \rightarrow ee$  invariant mass peak in data and simulation as described in Chapter 6, to obtain measurements with a precision around  $10^{-3}$  [111]. Regarding the sampling term, it has been determined from beam tests [112] before the ATLAS commissioning (2006). More details about an alternative data-driven method to cross-check the sampling term value are presented in Section 6.8.7.

Overall, the accordion calorimeter in the barrel region allows for a  $\sim 1\%$  invariant mass resolution in  $H \rightarrow \gamma\gamma$  and  $H \rightarrow 4e$  channels for a Higgs mass between 100 and 200 GeV.

### 3.2.4 Hadronic Calorimeter

The description of the hadronic shower development is rather complicated. It comes as the sum of an electromagnetic component (i.e.  $\pi \rightarrow \gamma\gamma$ ) and a strong component due to the interactions between the hadron and the atomic nuclei.

The hadronic calorimeter (HCAL) [113] is placed directly behind the EM calorimeter covering a range  $|\eta| < 4.9$ , and it is designed to measure the hadronic showers. The particle interacts with the atomic nuclei of the calorimeter generating additional particles out of the strong interaction, or due to a partial disintegration of the nuclei (leading to spallation of neutron and protons). If these secondary particles are energetic enough, they can undergo further inelastic collisions and this can trigger a shower. The shower grows until the energy of the secondary particles reaches the pion production threshold.

The HCAL is divided in three main parts: the Tile Calorimeter (TileCal) in the region  $|\eta| < 1.7$ , the Hadronic End-cap Calorimeter (HEC) extending to  $1.5 < |\eta| < 3.2$  and the LAr hadronic forward Calorimeter (FCal) from  $3.1 < |\eta| < 4.9$ . The Tile calorimeter is a sampling calorimeter using steel as absorber and scintillating tiles as active material. The TileCal has one fixed central barrel and two moveable extended barrels, all of them composed of 64 modules covering an azimuthal  $\phi$  angle of  $2\pi/64 = 0.1$  rad. The scintillating tiles are placed perpendicularly to the colliding beams and staggered along the  $R$  axis. Each cell has a segmentation of  $\Delta\eta \times \Delta\phi = 0.1 \times 0.1$  rad. A schematic view of one TileCal module is presented in

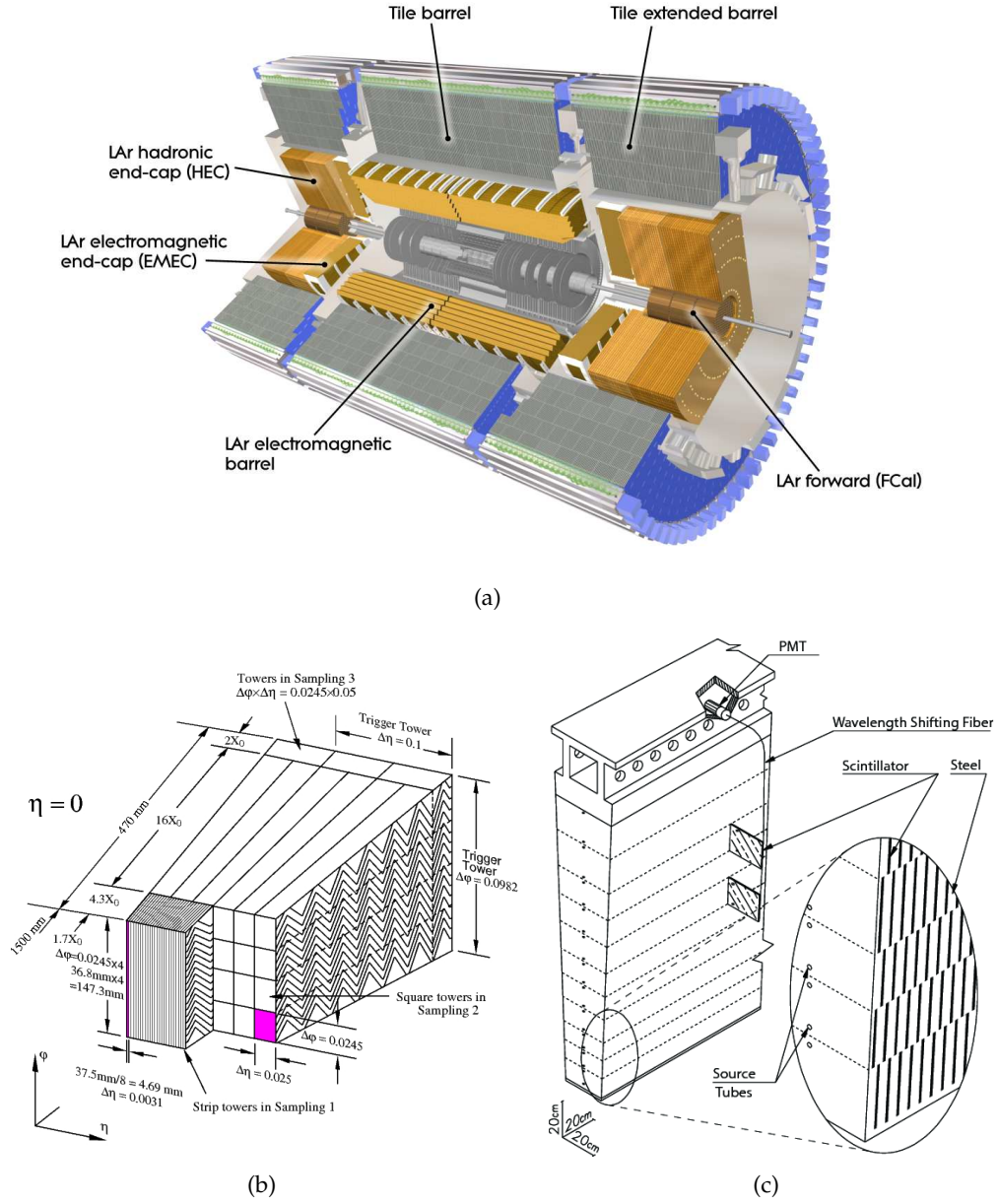


FIGURE 3.8 – (a) Layout of the ATLAS calorimetry system, (b) detailed view of the accordion structure [108] and (c) detailed view of the TileCal module [110].

Figure 3.8(c). Gap/crack scintillators have been installed [110] to improve the performance in the transition region between barrel and end-caps, which are occupied by many staves and electronics from the inner tracker.

The Hadronic Endcap Calorimeter (HEC) is located directly behind the EM calorimeter end-caps and has the same structure, consisting of two independent wheels per end-cap and it is designed to overlap with the forward calorimeter. The HEC is a sampling calorimeter alternating flat copper absorbers and liquid argon as active material to ensure good radiation resistance. Each wheel has an outer diameter of 4 m and is made out of 32 identical modules.

The LAr hadronic forward calorimeter (FCal) [114] is integrated into the end-cap nearby the beam axis with the front face recessed by about 1.2 m with respect to the EM calorimeter and it has two main purposes: increase the uniformity of the coverage of the calorimetric system and reduce radiation background in the muon spectrometer. The FCal consists of three modules in each end-cap: the first one uses copper as absorber, being optimised for electromagnetic measurements, while the other two use tungsten-based absorbers, mainly to measure the energy of hadronic interactions.

Together with the EM calorimeter, the TileCal and HEC provide a design energy resolution for jets of [113]:

$$\sigma/E \sim \frac{50\%}{\sqrt{E(\text{GeV})}} \oplus 3\% \quad (3.10)$$

and response linearity within 1-2% up to few TeV. The design resolution of the FCal is [114]:

$$\sigma/E \sim \frac{100\%}{\sqrt{E(\text{GeV})}} \oplus 10\% \quad (3.11)$$

### 3.2.5 Muon spectrometer

Muons are the only particles having a dedicated sub-detector able, thanks to the dedicated toroidal magnets, to perform precise measurements of the momenta without requiring information from the inner detector. This is crucial for a fast event triggering (more details about trigger in Section 3.2.6). The muon spectrometer [115] is placed outside the calorimeters and consists of a system of precision tracking gas chambers and fast-tracking chambers for triggering. A schematic overview of the muon spectrometer is given in Figure 3.9. As said before, this part of the detector works within a dedicated magnetic field generated by three large superconducting air-core toroid magnets, each with eight coils. The magnetic field of 4T is mostly orthogonal to the muon trajectories to minimize the multiple scattering that would imply a degradation of resolution. This means that, contrary to what happens in the inner detector, muons are bent in the  $R - z$  plane. In the barrel region, tracks are measured in chambers arranged in three cylindrical layers around the beam axis; in the transition and end-cap regions, the chambers are installed in planes perpendicular to the beam, also in three layers. The chambers are divided in *tracking chambers*, with high granularity to allow for precise measurements of the momenta, and *triggering chambers* with coarser granularity but faster response used for the online triggering of the muon events and their association to a specific bunch crossing. The momenta are measured by the Monitored Drift Tubes (MDT's) and the Cathode Strip Chambers (CSC's). The MDT's are installed on most of the  $\eta$  range and provide a precision



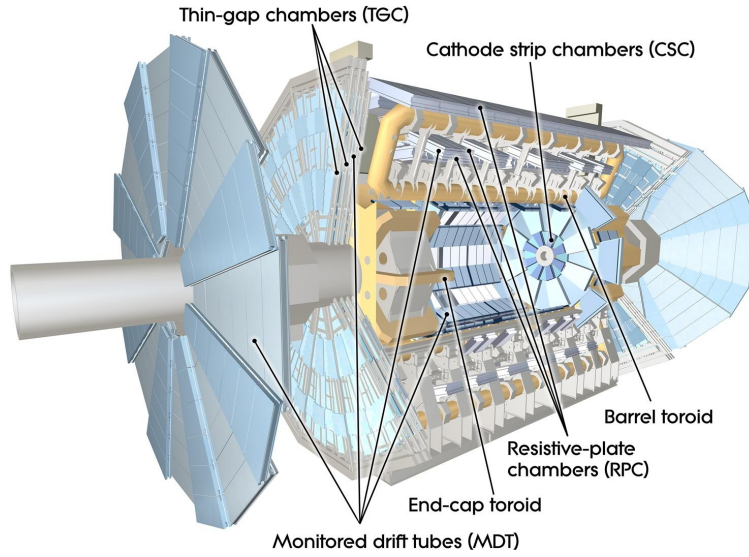


FIGURE 3.9 – Overview of the ATLAS muon spectrometer.

measurement of the track coordinates in the principal bending direction of the magnetic field ( $z$ ), with a precision of  $35 \mu\text{m}$ . The chambers consist of two groups of tubes separated by a mechanical support covering the pseudo-rapidity region up to  $|\eta| = 2.7$ . On the contrary, the CSC's are located only in the innermost end-cap layer, at large pseudorapidities ( $2 < |\eta| = 2.7$ ), and they consist of multiwire proportional chambers with cathodes segmented into strips with high granularity to fulfill rate and background rejection requests. They can provide both  $R$  and  $\phi$  direction measurements with a precision of  $40 \mu\text{m}$  and  $10 \text{ mm}$  respectively. The performance of the muon spectrometer in terms of transverse momentum resolution varies between 3% and 12%, for  $p_T$  values between 10 GeV and 1000 GeV. The spectrometer can measure muon momenta with adequate momentum resolution and excellent charge identification in the range between  $\sim 3 \text{ GeV}$  and  $\sim 3 \text{ TeV}$ . At lower energies the resolution is improved adding the information of the tracks reconstructed in the inner detector.

The trigger system is made by the Resistive Plate Chambers (RPC's), used in the barrel region, and Thin Gap Chambers (TGC's), in the end-cap regions. The RPC's are made of parallel electrode plates and gas-filled gaps covering the region  $|\eta| = 1.05$ . A spatial resolution of  $\sim 10 \text{ mm}$  is achieved in both  $z$  and  $\phi$  directions. The TGC's are multi-wire proportional chambers placed in the end-cap wheels ( $1.05 < |\eta| = 2.7$ ). Their main feature is that the wire-to-cathode distance is smaller than the wire-to-wire distance, to ensure a fast collecting time. The intrinsic time resolution of the trigger components is  $1.5 \text{ ns}$  for the RPC's and  $4 \text{ ns}$  for the TGC's. The identification of the correct bunch crossing is performed with an accuracy of 99% [115].

### 3.2.6 Trigger System

With the current LHC filling scheme, the number of proton-proton collisions observed by the ATLAS detector can be up to 1.7 billion collisions per second, potentially leading to a volume of more than 60 million megabytes per second. However, only a few of these events will contain interesting characteristics for physics analyses. A complex triggering system that stores only those events of interest is therefore vital for the manageability of the final recorded volume of data.

The ATLAS experiment uses a complex Trigger and Data Acquisition (collectively

TDAQ) [116] system to manage the selections of events, needed to reduce the information rate from 40 MHz to  $\sim 1$  kHz for permanent storage. The trigger system was originally designed to have three distinct levels: LVL1, LVL2, and the event filter. Each trigger level refines the decisions made at the previous level and, where necessary, applies additional selection criteria. The level-1 (LVL1) [117] trigger is based on custom-built electronics, and it makes an initial selection based on reduced-granularity information from just a subset of detectors. In particular, muons are identified using the muon trigger chambers, while the other particle selections are based on reduced-granularity information from the calorimeters (EM and hadronic; barrel, endcap and forward).

The LVL1 trigger decision is based on combinations of objects required in coincidence or veto. The system takes around  $2 \mu\text{s}$  to take a decision, so the information about the next events must be stored in memory pipelines between the detectors and the LVL1 trigger. The frequency of the LVL1 is defined by the frequency at which the front-end systems can accept LVL1 triggers (limited to 100 kHz). An essential requirement on the LVL1 trigger is that it should uniquely identify the bunch-crossing of interest. The level-2 (LVL2) analyses the information of the subset of detectors only in the Regions of Interest (RoI) identified by the first level trigger, but using the full granularity of each detector. This level of trigger takes  $\sim 10$  ms to take a decision. The events passing also the LVL2 selection are fully analysed in the third level trigger (Event Filter), which uses the same offline algorithms and methods, calibration and alignment information (including the magnetic field map), just adapted to the offline environment. The EF makes the final selection of physics events, so the events passing this selection are written on mass storage for subsequent full offline analysis. The output rate from LVL2 should then be reduced by an order of magnitude, giving a final output frequency of  $\sim 1$  kHz. In Run-2 the trigger system has been modified to just two levels, the LVL1 and a High Level Trigger (HLT), which unifies LVL2 and EF in one level. Contrary to the LVL1, the HLT is entirely based on software algorithms running on commercial farms of PCs [118].

### Luminosity detectors

A series of online and offline luminosity monitors are constantly providing information on the luminosity delivered by LHC. The *Beam Condition Monitors* (BCM's) [119] are  $1 \text{ cm}^2$  diamond detectors located at  $z = \pm 184 \text{ cm}$  around the beam pipe. They have a fast time response of  $0.7 \text{ ps}$  to provide online luminosity information for each bunch crossing. They are also used to detect the beam losses. An automatic beam dump based on the BCM's measurements is induced in case of extensive beam losses, to protect the inner detector from uncontrolled beams. A complementary luminosity detector is *LUCID* [93], a Cherenkov detector of 16 aluminium tubes surrounding the beam at  $17 \text{ m}$  from the interaction point. The tubes are filled with  $\text{C}_4\text{F}_{10}$  and coupled to photomultipliers.

In addition, off-line cross-checks are performed using information from other sub-detectors. For example, by counting the number of reconstructed primary vertices in the ID or by measuring the integrated signal from the Tile and the FCal. Overall, the final uncertainty on the integrated luminosity is of the order a 1-2% per cent, depending on the data taking period [120].

The integrated luminosity for the full Run-2 data taking period is shown in Figure 3.10. The small difference between the luminosity delivered by LHC and that collected by ATLAS is mainly due to the slow ramping up of the voltages at the

beginning of the stable beam conditions, or to the dead time<sup>6</sup> of the detector data acquisition system. In addition, the data are retained for physics analysis only when they are flagged as 'good quality data', meaning that they were recorded when all the subdetectors were fully functional, leading to an additional inefficiency. Table 3.2 summarizes these three integrated luminosities for each year of the Run-2 data-taking period.

year	LHC delivered	ATLAS recorded	ATLAS 'good' quality
2015	4.2 fb <sup>-1</sup>	3.9 fb <sup>-1</sup>	3.2 fb <sup>-1</sup>
2016	38.5 fb <sup>-1</sup>	35.6 fb <sup>-1</sup>	33.6 fb <sup>-1</sup>
2017	50.2 fb <sup>-1</sup>	46.9 fb <sup>-1</sup>	43.6 fb <sup>-1</sup>
2018	63.3 fb <sup>-1</sup>	60.6 fb <sup>-1</sup>	58.5 fb <sup>-1</sup>
Total	156.2 fb <sup>-1</sup>	147.0 fb <sup>-1</sup>	138.9 fb <sup>-1</sup>

TABLE 3.2 – Integrated luminosity for each year of data-taking.

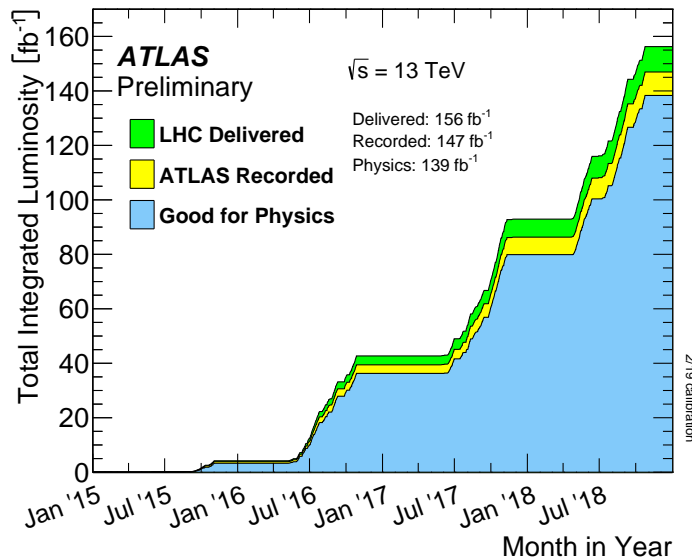


FIGURE 3.10 – Cumulative luminosity versus time delivered to ATLAS (green), recorded by ATLAS (yellow), and certified to be good quality data (blue) during stable beams for  $pp$  collisions at 13 TeV center of mass energy in 2015-2018. The complete  $pp$  data sample in 2018 is shown. The All Good Data Quality criteria require all reconstructed physics objects to be of good data quality.

6. In case of unexpectedly high rates of events, the trigger and DAQ system are not able to process the data correctly and some data are lost.



## 4 | Reconstruction of physics objects

In order to ensure a good reconstruction of the event, the detector must be able to identify and measure the kinematic properties of a large spectrum of particles produced in the collisions over a wide energy range (from few GeV to TeV). This includes charged leptons, photons and particles in jets produced by the hadronisation of quarks and gluons as well as neutral particles, like neutrinos, measurable only through indirect detection. All these particles are reconstructed starting from the recorded electronic signal in the different sub-detectors (or from the energy imbalance for the neutral particles). The procedure to convert these electronic signatures in the detector in fully reconstructed particles is complex and undergoes different steps.

The first step aims at reconstructing the signatures in the different sub-detectors, also defined *detector objects*, mainly tracks, energy clusters or in some cases combined objects (particle-flow). Then, these simple detector objects are used as inputs to a series of algorithms and techniques which combine them to obtain the *reconstructed physics objects*, such as muon, electron, jet candidates, missing transverse momentum and so on. At this stage, many physics quantities, such as momentum, position and charge of the physics object are fully determined, but ambiguities in the particle-type still arise. For this reason, once the object candidates are reconstructed, their properties are combined in *particle identification schemes* to uniquely assign them to a specific particle-type. The efficiency of this reconstruction and identification chain is crucial to minimize the misclassification and achieve a reliable event reconstruction.

Usually, the event reconstruction involves different types of physics objects. For example, the  $VH, H \rightarrow b\bar{b}$  analysis uses electrons, muons, jets and missing transverse energy, but not photons. This Chapter summarizes the techniques used to reconstruct and identify these objects, with a brief description of the systematic uncertainties associated with their use in the analysis.

### 4.1 Tracking and Vertex reconstruction

Reconstructed charged-particle tracks are key ingredients for all physics analyses. They are extensively used in many aspects, like the primary and secondary vertex reconstruction, object reconstruction (i.e. electrons, muons, jets) or the suppression of pile-up jets. Tracks are built assembling collections of hits in the inner detector, using different pattern recognition algorithms [121]. The procedure starts from track *seeds* in the silicon part of the tracker, which are then extrapolated outwards to the full tracker. At least 7 hits in the silicon detectors (so the sum of the

pixel detector and the SCT) are required to build a *track seed*. This requirement ensures good discrimination between true and fake tracks, as well as good spatial and momentum resolution. The track seed is then extended outwards to the TRT hits to complete the track candidate.

The track building is based on the combinatorial Kalman Filter (KF) method [122]. Starting from a particle seed, a vector of 5 track parameters is built to describe the track. The variables of the track state vector are:

**The transverse impact parameter  $d_0$ :** the projection of the point of closest approach to the beam axis in the transverse plane. The transverse impact parameter resolution of the Inner Detector (ID) is approximately [123] :

$$\sigma(d_0) = \frac{90\mu\text{m}(\text{GeV}/c)}{p} \oplus 12.5\mu\text{m}. \quad (4.1)$$

The addition of the IBL to the ID between Run-1 and Run-2 improved the resolution by roughly a factor of two at low  $p_T$  ( $< 1$  GeV) in the full  $\eta$  range [124], as shown in Figure 4.1.

**The longitudinal impact parameter  $z_0$ :** the distance between the projection of the point of closest approach to the beam axis and the nominal interaction point on the  $z$  axis. As shown in Figure 4.1, the addition of the IBL improved by roughly a factor two the resolution of this parameter in the full  $p_T$  and  $\eta$  range.

**The transverse momentum ( $q/p_T$ ):**  $p_T$  is the transverse momentum expressed in GeV, while  $q$  is the charge of the particle. As said in Section 3.2.1, the ID is immersed in a 2T magnetic field, therefore charged particles are bent in the transverse plane, so the overall trajectory follows a helicoidal path. The  $q/p_T$  quantifies the curvature of the particle tracks in the transverse plane ( $p_T \propto qBr$  with  $r$  the radius of curvature, for relativistic particles in a magnetic field  $\mathbf{B}$  perpendicular to  $\mathbf{p}_T$ ), crucial for the TRT extrapolation. It is invariant under Lorentz boosts along the  $z$  direction.

**The track azimuthal angle  $\phi$ :** the direction of the track in the  $R - \phi$  plane at the point of closest approach.

**The track polar angle  $\theta$ :** the direction of the track in the  $R - z$  plane at the point of closest approach.

An illustration of the track helix parameters is given in Figure 4.2. The KF algorithm proceeds iteratively updating the estimated track position and direction adding information from each successive layer of the ID. The best estimation of the state vector variables for each specific layer is the weighted (on the uncertainty) average between prediction and measured hit.

This generic algorithm works well for hadron tracks reconstruction, but is not suitable for electrons, due to bremsstrahlung effects. For all the tracks corresponding to an electron candidate another algorithm called Gaussian Sum Filter (GSF) [125] is used to perform the electron track reconstruction. In ATLAS, the KF algorithm is first applied to all the tracks and then the tracks loosely matched to an ECAL seed cluster are re-fitted with the GSF algorithm for a better estimation of the track parameters. The GSF is a way to adapt the Kalman filter to non Gaussian noise. The energy loss distribution is reproduced using a convolution of  $n$  different Gaussians

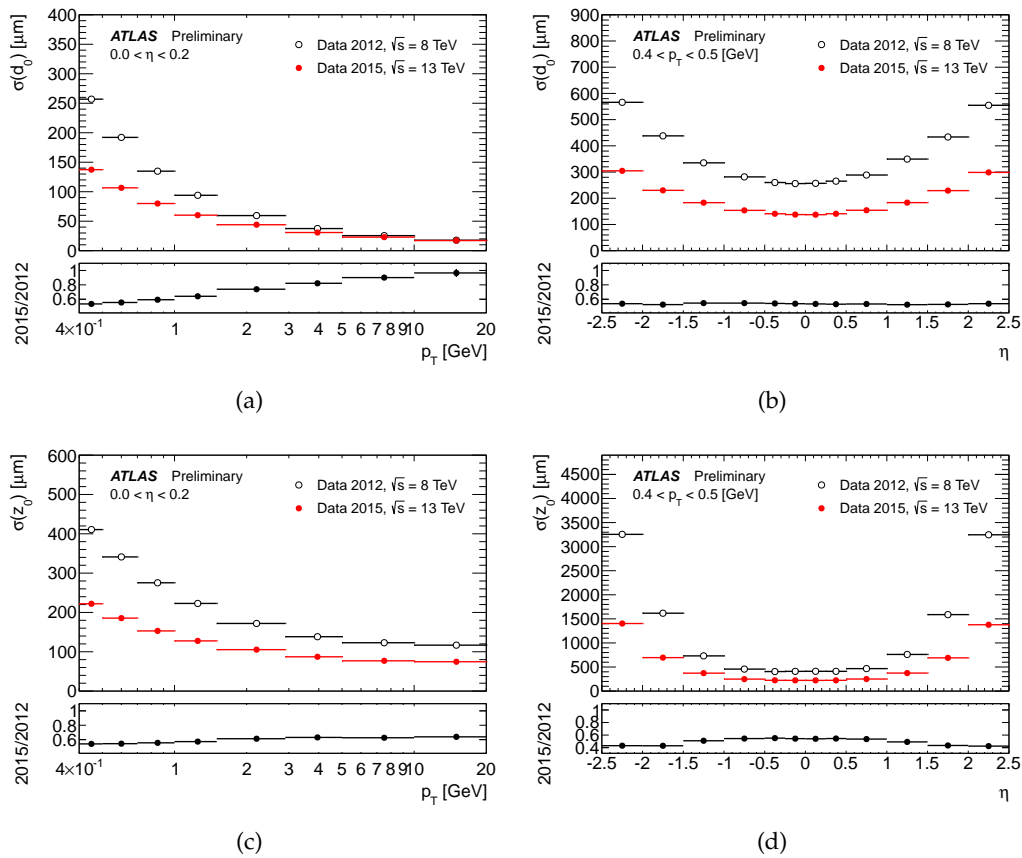


FIGURE 4.1 – In Red, (top) transverse and (bottom) longitudinal impact parameter resolution measured from data in 2015 at  $\sqrt{s} = 13$  TeV, with the Inner Detector including the IBL, (a)-(c) as a function of  $p_T$ , for values of  $0.0 < \eta < 0.2$ , and (b)-(d)  $\eta$  for values of  $0.4 < p_T < 0.5$  GeV, compared to that measured from data in 2012 at  $\sqrt{s} = 8$  TeV without the IBL (black) [124].



(5 in ATLAS) and then the KF algorithm is applied to each Gaussian. The final output is a set of  $n$  probability distribution functions, one set for each of the parameters in the vector state. The parameters can be estimated either as the global weighted mean ("weight") or as the value of the highest weight Gaussian ("mode").

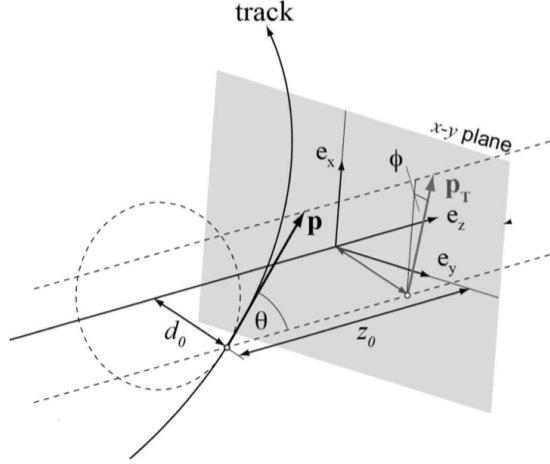


FIGURE 4.2 – Illustration of the track helix parameters defined in the perigee representation in the ATLAS detector.

The primary vertex is defined as the initial colliding point between two partons from individual proton-proton collisions. In the case of high pile-up, multiple interaction vertices occur at the same time leading to increased complexity in the track-vertex matching procedure. A new approach has been introduced in Run-2, inspired by medical imaging. The primary vertices are reconstructed using a *3D imaging algorithm* [126], which simultaneously attempts to identify all possible vertex locations along the bunch crossing considering all tracks as input. These locations are then used as *vertex seeds* for the vertex fitting processes. Tracks are assigned to the seed which is closer to their trajectory, and an iterative procedure is applied to remove the tracks not compatible with that vertex position. The primary vertex is determined as the one with the highest sum of the transverse momenta squared ( $p_T^2$ ) of all associated tracks. The efficiency of the vertex matching algorithm has been measured on  $t\bar{t}$  events at  $\mu = \langle 30 \rangle$  to be  $\sim 99\%$  [126]. Other vertex fitting algorithms are used to identify secondary and tertiary vertices, which are mainly coming from heavy hadron decays. More details on how to determine the secondary vertices are given in Section 5.1.3.

## 4.2 Electrons

Electrons are reconstructed matching a cluster of neighbouring cells of the EM calorimeter with reconstructed tracks in the inner tracker [127]. The electron energy reconstruction is complicated by the possibility of bremsstrahlung emission when the electron interacts with service material, like the beam pipe or the supporting material of the tracking system. In Run-1 and beginning of Run-2 electrons were reconstructed using a sliding-window algorithm with a  $0.075 \times 0.175 = \Delta\eta \times \Delta\phi$  fixed size tower matrix, corresponding to  $3 \times 7$  cells of the middle layer in the barrel. The cluster window was larger in  $\phi$  than in  $\eta$  because the magnetic field bends the charged particles in the  $R - \phi$  plane, so the resulting shower spreads more in that



direction. This spread is enhanced for low energy particles, which are bent more by the magnetic field. For low energy electrons the spread is so large that a separation of the shower in different sub-clusters can be observed.

In the endcaps the sliding-window algorithm has a fixed size matrix of  $5 \times 5$  cells. The number of cells is higher in  $\eta$  because the value of  $\Delta\eta = 0.025$  converts in a smaller physical size of the cells than in the barrel, while in  $\phi$  the number of cells is reduced because the effect of the magnetic field is smaller than in the barrel.

The cluster energy was then corrected via software algorithms to account for leakages and fluctuations in the energy deposit. The position of the incoming particle was estimated as the weighted average of all the cells in the cluster<sup>1</sup>, using the deposited energy per cell as weight. The sliding window algorithm was the nominal electron reconstruction algorithm used for the study in Chapter 6.

An alternative method based on varying size *topological clusters* (topo-clusters) [128] has been recently introduced to substitute the sliding-window algorithm. The main advantages of this method are an improved treatment of the bremsstrahlung induced sub-clusters, which lowers the limit to reconstruct showers down to the  $O(100 \text{ MeV})$  range in energy, and an improved capability to reconstruct the actual shower shape development of the EM showers even in the longitudinal direction, both leading to an overall improvement in the energy resolution.

The primary clusters, containing the highest fraction of energy, and the bremsstrahlung induced sub-clusters, are all reconstructed from so-called topo-cluster seeds. The seeding of topo-clusters is based on the so-called *cell significance*  $\zeta_{\text{cell}}^{\text{EM}}$ , computed as:

$$\zeta_{\text{cell}}^{\text{EM}} = \left| \frac{E_{\text{cell}}^{\text{EM}}}{\sigma_{\text{noise,cell}}^{\text{EM}}} \right|, \quad (4.2)$$

with  $|E_{\text{cell}}^{\text{EM}}|$  the absolute cell energy and  $\sigma_{\text{noise,cell}}^{\text{EM}}$  the expected noise in the cell. The topo-cluster seed candidates (*proto-clusters*) are selected requiring  $\zeta_{\text{cell}}^{\text{EM}} \geq 4$ , using only cells from the second and third layers of the EM calorimeter to suppress pure-noise clusters. The neighbouring cells with significance  $\zeta_{\text{cell}}^{\text{EM}} \geq 2$  are iteratively added to the proto-cluster proceeding outward from the seeding initial cell. Once all the cells with cell significance above 2 are added, an additional layer of neighbouring cells with  $\zeta_{\text{cell}}^{\text{EM}} \geq 0$  is added to the cluster to better control the activity at the edges. The topo-clusters are merged if they share a common cell with  $\zeta_{\text{cell}}^{\text{EM}} \geq 2$ , but they can also be split into separate clusters if they contain two or more local maxima with  $E_{\text{cell}}^{\text{EM}} > 500 \text{ MeV}$ <sup>2</sup>. This split happens only if the maximum cells are left with at least 4 neighbours and none of the neighbours have larger signal.

The capability to select clusters originating from true electromagnetic showers can be enhanced by tightening the requirements on the fraction of cluster energy in the EM calorimeter. The variable used for this purpose is the electromagnetic fraction  $f_{\text{EM}}$ , defined as the ratio of the energy deposited in the electromagnetic layers, over the total cluster energy  $E_{\text{total}}$  which includes also the hadronic component:

$$f_{\text{EM}} = \frac{E_{\text{L1}} + E_{\text{L2}} + E_{\text{L3}} + w \cdot (E_{\text{E4}} + E_{\text{PS}})}{E_{\text{total}}}, \quad (4.3)$$

1. Plus additional corrections, such as "s-shape" or  $\phi$  corrections. More details are given in Ref. [108].

2. A fractional weight proportional to the total energies of the two clusters and the distance of the cell from the center of gravity of the two clusters is assigned to the cells that are shared across the two topo-clusters after the split.

with  $E_{Lx}$  the energy deposited in the layer  $x$  of the EM calorimeter, and  $w$  a binary parameter equal to 1 in the region  $1.37 < |\eta| < 1.63$  and 0 elsewhere, to recover the non-negligible losses in the pre-sampler and in the  $E_4$  scintillators placed in the barrel-endcaps transition region. The electromagnetic fraction is expected to be close to 1 for electrons and lower for hadrons (i.e. pions). Furthermore, topo-clusters are accepted only if their total transverse energy fulfills the requirement  $E_T > 400$  MeV, to reduce the contamination from pile-up and  $\pi^0 \rightarrow \gamma\gamma$  decays. This threshold was set from studies presented in Ref. [129] and Ref. [130]. An optimal threshold for the EM fraction of  $f_{EM} > 0.5$  has been chosen as the best trade-off between high pile-up suppression ( $\sim 60\%$ ) and high topo-cluster selection efficiency [128]. Overall, the varying size clusters collect more energy than the sliding window clusters, so fewer corrections from energy losses before and inside the calorimeter are required.

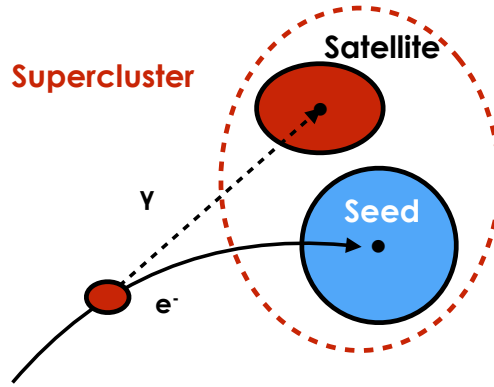


FIGURE 4.3 – Diagram of an example supercluster showing a seed electron cluster and a satellite photon cluster [128].

Once tracks and clusters are reconstructed, they are matched together by dedicated algorithms to build the final electron candidates. Both the sliding-window clusters and the superclusters are treated in the same way by the track-cluster matching algorithm. A series of geometric requirements are imposed to perform the matching. In particular:

- The distance in  $\eta$  between the ECAL reconstructed position and the extrapolated position from the track parameters must be lower than 0.05 for silicon tracks.
- The distance in  $\phi$  must be lower than 0.2 in the bending direction and 0.05 in the opposite side.
- TRT-only tracks, i.e. tracks with less than four hits in the silicon detectors, are retained with stricter requirements in the  $\eta - \phi$  minimum distance, and later used just to reconstruct converted photons.

In this procedure, more than one track can be associated with a cluster. Priorities based on track quality are imposed to solve these ambiguities [131]. In case multiple clusters are associated with a single track, the cluster with the highest energy is selected since the others might come from bremsstrahlung. An electron candidate is considered to be reconstructed if at least one track is matched to the seed cluster. In the absence of a matching track, the cluster is classified as an unconverted photon candidate. Converted photons behave like electron candidates, but they are recovered in the previous step imposing conditions on the tracks [131].

In the topo-cluster method, the bremsstrahlung losses are recovered by the formation of *superclusters* after the track-cluster matching. The topo-clusters are divided into possible *supercluster seeds* and *satellite clusters*, formed in the bremsstrahlung

process. A cluster becomes an electron supercluster seed if it has a minimum of 1 GeV and a track with at least 4 hits in the silicon detector. All the remaining clusters are considered as possible satellite clusters. If a satellite cluster falls within a window of  $\Delta\eta \times \Delta\phi = 0.075 \times 0.125$  from a seed cluster barycenter<sup>3</sup>, it is considered as a secondary EM shower originated by the same electron candidate and the two clusters are merged in one single super-cluster. The procedure is repeated iteratively sorting the clusters in  $p_T$  until all the available clusters are considered.

### 4.2.1 Identification algorithms

Once the electron candidates are built by the reconstruction algorithm, the second step is the identification of these candidates. This is achieved by applying selection criteria based on a set of discriminating variables having different distributions for signal and background [127]. The variables providing discriminating power are grouped into three main categories:

- *Calorimetric variables*, to separate real electrons and photons from misidentified jets. They are based on the transverse and longitudinal shape of the shower in the ECAL and the energy fraction in the HCAL.
- *Tracking variables*, are fundamental to recover the converted photons and to improve the rejection power of charged hadrons for electrons.
- *Track-cluster variables*, which compare measurements of the ECAL and the Tracker, such as track-cluster matching or energy-momentum matching.

Three sets of reference selection criteria, labelled *loose*, *medium* and *tight* identification are defined. These criteria are designed in a hierarchical way so as to provide increasing background-rejection power at some cost in identification efficiency: the tighter the criteria, the purer in signal is the sample, but the smaller the efficiency. The operating points are inclusive, such that the loose is a subset of the medium, which in turn is a subset of the tight.

The nominal ATLAS electron identification algorithm is based on a multivariate approach. The idea is to combine different shower shape and tracking variables to best discriminate isolated electrons, considered as signal, from background electrons originating from photon conversion, heavy flavour decays or from misidentified hadrons. In particular, a Likelihood method (LH) is used to combine multiple probability density functions (PDF), one for each discriminating variable, simultaneously. Based on these PDFs, an overall probability is calculated for the object to be signal or background. The signal and background probabilities for a given electron are then combined in a unique output discriminant  $d_L$ . A series of tightening thresholds on the  $d_L$  likelihood is then applied to identify the candidate as a loose-LH, medium-LH or tight-LH electron.

The identification efficiencies for electrons at 40 GeV are 75% for the tightest operating point to 90% for the loosest, as visible in Figure 4.4. The difference in efficiency between barrel and end-caps is between 3% and  $\sim 10\%$ . The electron identification efficiencies in simulation are matched to the ones in data using MC correction scale factors computed on pure samples of  $Z \rightarrow ee$  events with the Tag-and-Probe method [127]. The scale factors are typically close to unity, with uncertainties calculated at the per-mil level.

---

3. Electrons undergo an additional search with an enlarged window of  $\Delta\phi = 0.125 \times 0.3$  around the seed cluster barycenter, since the bremsstrahlung can occur earlier.

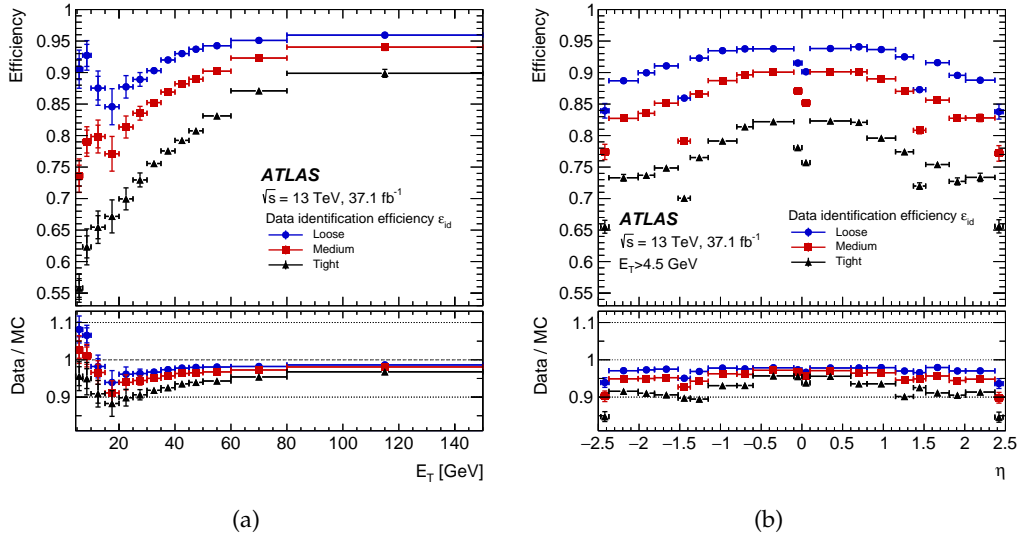


FIGURE 4.4 – Measured LH electron-identification efficiencies in  $Z \rightarrow ee$  events for the Loose (blue circle), Medium (red square), and Tight (black triangle) operating points as a function of  $E_T$  (a) and  $\eta$  (b). The vertical uncertainty bars (barely visible because they are small) represent the statistical (inner bars) and total (outer bars) uncertainties. The data efficiencies are obtained by applying data-to-simulation efficiency ratios that are measured in  $J/\psi \rightarrow ee$  and  $Z \rightarrow ee$  events to the  $Z \rightarrow ee$  simulation. For both plots, the bottom panel shows the data-to-simulation ratios. [127]

#### 4.2.2 Isolation

One of the main sources of background for prompt electrons at LHC comes from real electrons in jets, produced by in-flight hadron decays. Many of these events are not rejected with identification algorithms, because they are real electrons. This source of background can be suppressed requiring the electron candidate to be isolated from nearby hadronic activity. Two types of isolation requirements are defined: the calorimeter-isolation and the track-isolation, depending on the detector involved. The calorimeter isolation, also called cluster isolation, is performed summing all the transverse energy contributions from the HCAL and the ECAL in a small cone around the particle candidate of radius  $\Delta R$ , requiring that the total energy ( $E^{\text{iso}}$ ) does not exceed a certain threshold. The contribution from the particle candidate itself is subtracted before the calculation. This procedure is sensitive to pile-up effects and underlying events so corrections must be applied to maintain the same isolation efficiency even in the regions of higher pile-up. The correction is evaluated multiplying the effective area of the isolation cone  $A_{eff}$  by a correction term  $\rho_{UE}(\eta)$ , defined as the ambient transverse energy density. This term takes into account the average energy from underlying events and pile-up, evaluated from jet-finding algorithms [132]. This algorithm reconstructs all the jets (see Section 4.4) without any transverse momentum threshold in the region  $|\eta| < 1.5$  and  $1.5 < |\eta| < 3.0$ , starting from seed clusters in the calorimeters. The  $\rho_{UE}(\eta)$  is evaluated as the median of the transverse energies  $p_T^{\text{jet}} / A_{\text{jet}}$ . The typical correction is 2 GeV in the central region and 1.5 GeV in the forward region. The track-based isolation consists in the scalar sum of the  $p_T$  of all the tracks in a cone of variable size around the particle candidate trajectory, considering only tracks from the primary vertex. The three isolation working points relevant for the electron energy calibration and the  $VH, H \rightarrow b\bar{b}$  analysis are:

**The Loose-Track isolation**, based on variable track isolation requirements depending on  $p_T$  and  $\eta$ , optimised to keep the efficiency equal to 99% for real electrons across the full  $p_T$  range.

**The HighPt-Calo isolation**, optimised on fixed radius isolation requirements, meaning that the sum of the energy in the calorimeter within a cone of radius  $\Delta R = 0.2$ , excluded the energy associated with the electron candidate, must not exceed the 3.5 GeV or  $0.015p_T$ . This gives an efficiency around 95% for  $p_T$  values from 50 GeV to 1 TeV [127].

**The Fixed-Cut Loose isolation**, optimised on fixed radius isolation requirements. The ratio between the sum of the energy in the calorimeter within a cone of radius  $\Delta R = 0.2$ , excluded the energy associated with the electron candidate, and the  $p_T$  of the electron must not exceed 0.2. This is combined with a requirement on track isolation: the ratio between the sum of the  $p_T$  associated with tracks within a cone of radius  $\Delta R = 0.2$ , excluded the one associated with the electron candidate, and the  $p_T$  of the electron must not exceed 0.15.

The isolation efficiencies have been measured for all the isolation working points using  $Z \rightarrow ee$  events [127] in the momentum range 4.5 - 500 GeV. Isolation scale factors are applied to the simulation in order to match the efficiency of the isolation requirements in data. The corrections are computed using a tag and probe techniques with large statistics sample of  $Z \rightarrow ee$  decays. The scale factors are close to unity with uncertainties mostly at the per-mil level for  $p_T > 10$  GeV, while in the low part of the spectrum (5 – 10 GeV) the uncertainties increase with values up to 5-8%.

### 4.3 Muons

Muons are reconstructed from signatures in the muon spectrometer and tracks in the inner detector [133]. Four main strategies are adopted to reconstruct and identify muons. The first one is a direct approach where muons are reconstructed as *standalone* muons using mainly the information of the muon spectrometer, while the second one *combines* the tracks measured in the muon spectrometer and in the inner detector to extract a single candidate from the two independent measurements. The *combined* muon strategy significantly reduces the rate of non-prompt muons originating from  $\pi$  and  $K$  decays. The drawback is that it can only be applied to a reduced region of the acceptance ( $|\eta| < 2.5$ ), due to the limited coverage of the ID. A  $\chi^2_{match}$  fit is used to match hits in the muon spectrometer with hits in the ID. The  $\chi^2$  reflects the probability for the track parameters of the ID and MS to be compatible with each other within their experimental uncertainties.

A third strategy is adopted for low  $p_T$  muons or muons crossing regions of the MS with reduced acceptance, such that just a few layers of the MS are crossed. In these cases, a variant of the combined muon algorithm, mainly based on ID tracks, is defined to recover these muons. These are referred to as *segment-tagged* muons and they are built matching a high-quality ID track to at least one local track in the MDT or CSC chambers.

Due to the supporting structure of the ATLAS detector and services for the ID, the MS has a gap in the acceptance for  $|\eta| < 0.1$ . Thus, a fourth strategy is used to

recover efficiency in this region: muons are reconstructed matching tracks in the ID with energies in the calorimeters compatible with minimum ionizing particles (MIP), so very localized deposits of two or three cells. These are also referred to as *calorimeter-tagged* (CaloTag) muons.

The overall reconstruction efficiency summing all these methods is above 99% for  $|\eta| < 2.7$  in the range  $5 \leq p_T \leq 100$  GeV [133]. The reconstruction efficiency is measured from  $Z \rightarrow \mu\mu$  and  $J/\psi \rightarrow \mu\mu$  events at the per-mil precision and, as for electrons, reconstruction efficiency scale factors are computed to match the efficiency measured in data and simulation.

The calibration of the muon momentum resolution and scale is obtained from a large sample of  $Z \rightarrow \mu\mu$  and  $J/\psi \rightarrow \mu\mu$  events with a simultaneous template fit in different  $p_T$  and  $\eta$  bins similar to what will be described in Chapter 6 [133]. Figure 4.5 shows the  $Z \rightarrow \mu\mu$  mass peak in data and MC after the energy scale and resolution corrections have been applied.

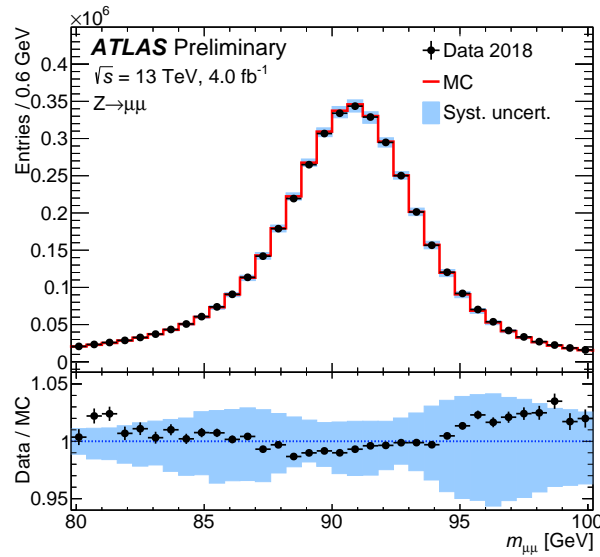


FIGURE 4.5 – Dimuon invariant mass distribution of  $Z \rightarrow \mu\mu$  candidate events reconstructed with *combined* muons out of  $4.0 \text{ fb}^{-1}$  of proton-proton collision data collected in 2018. The upper panels show the invariant mass distribution for data and for the signal simulation plus the background estimate. The points show the data. The continuous line corresponds to the simulation with the momentum corrections (derived from the 2016 dataset) applied. The band represents the effect of the systematic uncertainties on the momentum corrections. The lower panels show the data to simulation ratios. The simulation distributions are normalised to the data[134].

### 4.3.1 Identification

The identification algorithms aim at efficiently disentangling "prompt" muons coming from boson decays or semi-leptonic decays of heavy flavour hadrons, from non-prompt muons produced by in-flight pion and kaon decays or fake muons, such as charged hadrons *punching through* the HCAL. The muon identification makes no difference between muons produced in the hard scattering and muons produced in semi-leptonic decays, this is done at analysis level adding isolation requirements (see next Section) and cuts on  $d_0$  and  $z_0$ .



The following criteria are applied to suppress pion and kaon decays or the fake component:

- Muon candidates need to have high-quality ID tracks, with at least one hit in the pixel detector and at least 5 hits in the SCT detector, with less than 3 holes. This is useful to reduce the fake component.
- Non-prompt muons from late pion and kaon decays are usually originated in-flight, with consequent degradation of the track-matching quality  $\chi_{match}^2$  in case of combined muons. In addition to the  $\chi_{match}^2$  value, the quality of the fit is estimated computing the significance of the  $q/p$  balance<sup>4</sup>, defined as the significance of the absolute difference between the charge-over-momentum measurements performed in the ID and the MS. Real muons are expected to have  $\sigma_{q/p}$  values around zero, while in case of  $\pi$  or  $K$  decays  $q/p$  can be different in the MS and ID.
- Additionally, the ratio of the absolute momentum balance, defined as the difference  $p_T^{ID} - p_T^{MS}$ , to the transverse momentum of the combined track ( $p_T^{CB}$ ) provides good discrimination against fake muons. This is again valid only for combined muons.

Four muon identification selections are defined as *medium-ID*, *loose-ID*, *tight-ID* and *High- $p_T$* . Loose, medium, and tight IDs are defined as inclusive categories so, as for electrons, the tighter requirement is a sub-set of the looser categories. The *loose* ID criterion is designed to maximize the reconstruction efficiency, combining all the four muon definitions in the highest acceptance region  $|\eta| < 2.7$ . The *medium* ID criterion on the contrary considers only combined muons and standalone muons. The *tight* ID considers only combined muons passing the medium ID, furthermore the requirement on  $\chi_{match}^2$  and the  $q/p$  significance are tightened to minimize the number of fake muons. At last, the *high- $p_T$*  working point is optimised to improve the momentum resolution for muons above 100 GeV. It is based on combined muons passing the medium ID requirement, but in addition the MS tracks must have hits in at least three different MDT or CSC layers and the regions of poor alignment of the chambers are vetoed for precaution.

The identification efficiency of a muon in the  $20 < p_T < 100$  GeV range and  $|\eta| < 2.7$  is 98%, 96% and 92% for the loose, medium and tight ID requirements respectively, as can be seen in Figure 4.6. The drop in acceptance around  $\eta < 0.1$  described before has a 15-20% impact on the identification efficiency of the medium and tight ID working points. For the high- $p_T$  working point ( $> 100$  GeV) the identification efficiency is 80% [133], with minimal  $\eta$  dependence. The measurement has been performed with a tag and probe method on  $Z \rightarrow \mu\mu$  events with uncertainties below 0.1% over a large momentum range, and reaching up to  $\sim 1\%$  for low muon momenta.

#### 4.3.2 Isolation

As in the case of electrons, additional rejection power against non-prompt muons inside jets is achieved using isolation criteria. Seven isolation criteria are defined, mainly based on the following three isolation variables:

---

4. This variable is calculated as:  $\sigma_{q/p} = \frac{(q/p)^{MS} - (q/p)^{ID}}{\sqrt{[\sigma(q/p)^{MS}]^2 + [\sigma(q/p)^{ID}]^2}}$

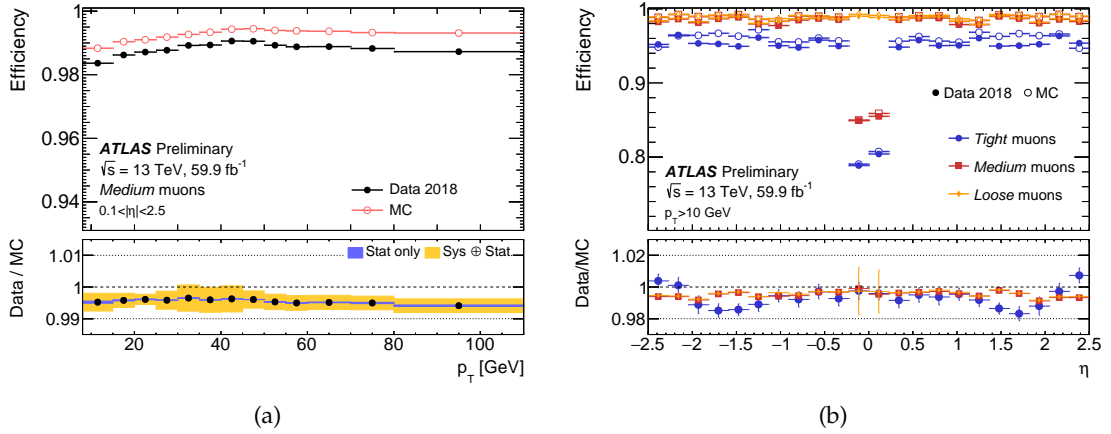


FIGURE 4.6 – (a) Muon reconstruction efficiency for the Medium identification algorithm measured as a function of the  $p_T$  of the muon in the region  $0.1 < |\eta| < 2.5$  and (b) Muon reconstruction efficiencies for the Loose/Medium/Tight identification algorithms as a function of the muon pseudorapidity for muons with  $p_T > 10$  GeV. The results are measured in  $Z \rightarrow \mu\mu$  event, using the full  $pp$  collision dataset collected in 2018 at 13 TeV. Open circles: prediction by the detector simulation. Filled dots: the observation in collision data with statistical uncertainties. The bottom panel shows the ratio between expected and observed efficiencies, while the errors show the quadratic sum of statistical and systematic uncertainties. [135].

- *Calorimeter isolation*: defined as the sum of the transverse momenta of all the topological clusters within a cone of radius  $\Delta R$  around the muon axis, typically fixed to 0.2.
- *Variable radius track isolation*: defined as the sum of the transverse momenta of all the tracks within a cone of radius  $\Delta R = \min(x, 10\text{GeV}/p_T)$  around the muon track, with  $p_T$  the transverse momentum of the muon candidate and  $x$  a chosen value of the radius, typically 0.3 or 0.2.
- *Fixed radius track isolation*: defined as the sum of the transverse momenta of all the tracks within a cone of radius  $\Delta R = 0.2$  around the muon track.

The two isolation working points relevant for the  $VH, H \rightarrow b\bar{b}$  analysis are:

**The Loose-Track isolation**, based on variable track isolation requirements depending on  $p_T$ , optimised to keep the efficiency equal to 99% for prompt muons across the full  $p_T$  range.

**The HighPt-Track isolation**, optimised on fixed radius isolation requirements, which gives a prompt muon efficiency of around 95%, depending on  $\eta$  and  $p_T$ .

The isolation efficiency of all the isolation working points has been measured in the momentum range 10-120 GeV using  $Z \rightarrow \mu\mu$  events [133]. At the same time, scale factors have been derived to correct the muon isolation efficiency in simulation to match the measured values in data for each working point. The scale factors are compatible with unity with uncertainties varying between 2% and 0.5%.



## 4.4 Jets

Jets are collimated sprays of particles produced in the hadronization of quarks. Jets are reconstructed from the energy deposits in both the EM and hadronic calorimeters. The energy deposits are first merged into clusters to define the contributions of the single hadrons and then the full jet structure is reconstructed using the anti- $k_t$  algorithm [132].

The calorimeter clusters are reconstructed using the same formalism of *topological-clusters* [136] described in Section 4.2 for the electron cluster reconstruction. In fact, at sub-detector level the quantities are computed without distinguishing between particle-type candidates, therefore the topo-cluster seeds are shared between jets and electrons. To summarize, they are formed summing together cells with a significant amount of signal above the noise, based on the *cell significance* variable defined in Equation 4.2. The lower thresholds on the cell significance are set to 4, 2 and 0 for the seed cell, the neighbouring cells and the additional contouring cells respectively. This kind of jets are also identified as *topo-cluster* jets. However, the topo-clustering is not the only algorithm used to define the inputs for the jet clustering algorithm. An alternative possibility is to build the jets from the reconstructed tracks in the detector. These jets are usually referred to as *track jets* [137] and they can be complementary used to extract information on the event, especially in boosted topologies. The main feature of the track-based approach is the higher robustness to pile-up, thanks to the better precision of the ID in measuring the longitudinal impact parameter  $z_0$ . However, relying only on tracks completely ignores the treatment of the neutral-hadron and photon component, which on the contrary is well accounted in the calorimeter-based definition.

As said before, the algorithm used to combine the topo-clusters into jets is the anti- $k_t$  jet clustering algorithm. Topo-clusters are clustered sequentially one at a time, based on the following distance variables:

$$d_{ij} = \min\left(\frac{1}{k_{T,i}^2}, \frac{1}{k_{T,j}^2}\right) \frac{\Delta R_{ij}^2}{R}, \quad (4.4)$$

$$d_{iB} = \frac{1}{k_{T,i}^2}, \quad (4.5)$$

with  $k_{T,i(j)}$  the transverse momentum of the cluster  $i$  ( $j$ ),  $\Delta R_{ij} = \sqrt{(y_i - y_j)^2 + (\phi_i - \phi_j)^2}$  the geometrical distance between two clusters, and  $R$  a fixed parameter of the algorithm, related to the radius of the jet. The typical value used to reconstruct the jets used for the  $VH, H \rightarrow b\bar{b}$  analysis is  $R = 0.4$ . Intuitively, the  $d_{ij}$  variable defines the distance between two clusters  $i, j$ , while  $d_{iB}$  is the distance between a cluster  $i$  and the beam. The clustering procedure is performed iteratively following these steps:

- Compute  $\min(d_{ij}, d_{iB})$ .
- If  $d_{ij}$  is the smallest, the  $i$  and  $j$  four momenta are combined.
- Else if  $d_{iB}$  is the smallest,  $i$  is removed from the list of available topo-clusters and it is denoted as "jet" in the event.
- The procedure is repeated until all the available clusters are merged or marked as jets.

A nice feature of the anti- $k_t$  algorithm is that the outcoming harder jets have a circular shape in the  $\eta - \phi$  plane, as visible in Figure 4.7.

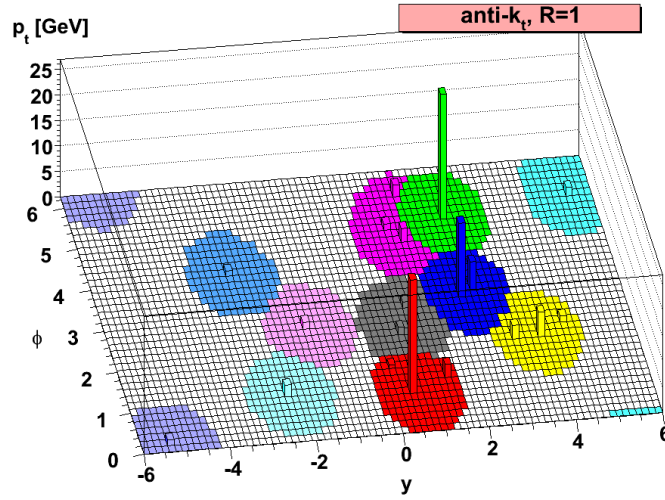


FIGURE 4.7 – A sample parton-level event (generated with Herwig [138]) clustered with the anti- $k_t$  algorithm, illustrating the "active" catchment areas of the resulting hard jets [132].

#### 4.4.1 Jet calibration

The jet energy calibration aims at recovering the real energy of the jet, starting from the recorded energy in the detectors. These energy calibration corrections account for the non-homogeneous response of the detector, pile-up contaminations, limiting factors in the jet reconstruction algorithm (i.e. out-of-cone corrections) or the so-called "punch-through" jets<sup>5</sup>. In addition, in-situ corrections are applied to jets in data to account for the difference in jet response between data and MC simulation. The overall corrections are divided into Jet Energy Scale (JES) [139] and Jet Energy Resolution (JER) [140] corrections. The final calibrated jet energy is obtained after several sequential steps [141]:

**Origin correction:** The direction of topoclusters initially points back to the center of the detector. The resolution in  $\eta$  can be improved by modifying the topocluster four-momentum to point back to the primary vertex of the hard scattering. No changes in energy are applied at this stage.

**Pile-up effects:** The pile-up subtraction is performed in two steps. First, the average pile-up contribution is subtracted from the total jet energy. This contribution is determined as a function of the active area of the jet ( $A$ ), as  $\rho A$  with  $\rho$  the median  $p_T$  density ( $p_T/A$ ) of the reconstructed jets. The second correction aims at subtracting the residual pile-up dependence. This extra correction depends on the exact number of primary vertices ( $N_{PV}$ ) and the average number of interaction per bunch crossing  $\langle\mu\rangle$ .

**Absolute JES correction:** The energy scale corrections are derived from MC simulation as  $E_{\text{reco}}/E_{\text{truth}}$  [139]. The truth and the reconstructed jets are geometrically matched within a cone of  $\Delta R = 0.3$ . Isolation requirements are added to avoid ambiguities during the truth matching. The  $E_{\text{reco}}/E_{\text{truth}}$  distribution is supposed to be Gaussian, so the best value of the scale is defined as the mean of the Gaussian fit to

5. Energetic jets extending beyond the hadronic calorimeter.

the  $E_{\text{reco}}/E_{\text{truth}}$  distribution. The scales are extracted in bins of  $E_{\text{truth}}$  and  $\eta$ .

**Absolute eta-intercalibration:** The energy response differs across  $\eta$ , especially at boundaries between different calorimeter technologies and granularities. The forward jets ( $0.8 < |\eta| < 4.5$ ) are calibrated with respect to the central part of the detector by balancing their energy against the central jets ( $|\eta| < 0.8$ ).

**Global Sequential Calibration (GSC):** The GSC is a residual correction to compensate for the different response of the calorimeters to quark-initiated and gluon-initiated showers or to recover the energy from punch-through jets. The corrections are derived matching the reco and truth distribution of five variables related to the energy deposit in calorimeters, track information and muon segments.

**In-situ calibration:** This is the last step of the calibration chain. It corrects for potential differences between data and simulation. The corrections are applied only to data. The in-situ methods are extracted from well understood processes, like  $\gamma/Z$ +jets or multijet events, where the energy of the well-calibrated reference objects ( $\gamma$  or  $Z$ ) are used to constrain the  $p_T$  of the recoiling jet, using the conservation of energy. The  $Z$ +jet *balance* technique is used to calibrate jets in the range  $20 < p_T < 500$  GeV, while the  $\gamma$ +jet *balance* calibration is used for jets in the range  $36 < p_T < 950$  GeV. The *multijet balance* method, extends the calibration to the range  $95 \text{ GeV} < p_T < 2 \text{ TeV}$  by balancing the jet energy against a system of lower  $p_T$  jets, previously calibrated with the  $\gamma/Z$ +jet balance. The jet energy scales and the jet energy resolution extracted with the three methods are shown in Figure 4.8.

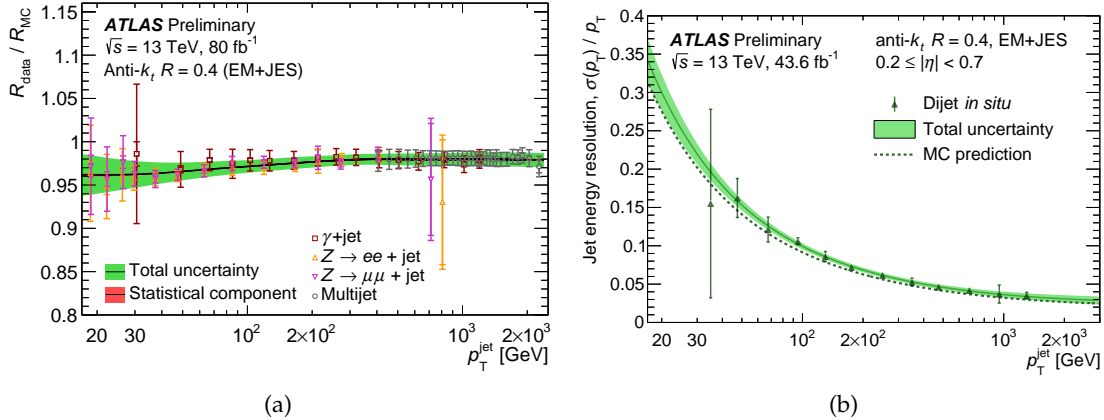


FIGURE 4.8 – (a) Data-to-simulation ratio of the average jet  $p_T$  response as a function of jet  $p_T$ . The combined result is based on three in situ techniques: the  $Z$ +jet balance method (downward-pointing triangles),  $\gamma$ +jet balance method (open squares) and the multijet balance (open circles). The errors represent the statistical (inner error bars and small inner band) and the total uncertainty (statistical and systematic uncertainties added in quadrature, outer error bars and outer band). (b) The relative jet energy resolution  $\sigma(p_T)/p_T$  as a function of jet  $p_T$ . The result is a combination of two in situ techniques: the momentum balance of dijet events (triangles) or the random cone method (not shown), which measures the noise term at low  $p_T$ . These results apply to anti-kt jets with  $R=0.4$ , reconstructed from electromagnetic-scale topo-clusters. The calibration curve and its uncertainty are smoothed using a sliding Gaussian kernel [142, 143].

The systematic uncertainties associated with the jet calibration are mainly coming from the in-situ calibration methods. The in-situ uncertainties are derived by varying different parameters, like the event selection, the MC generators or the identification criteria. These systematic uncertainties are evaluated separately for each in-situ method ( $\gamma$ ,  $Z$  and multijet balance). Another important source of uncertainty comes from the flavour dependence, both in terms of differences in the jet composition between quarks and gluons and in the jet response between quark- and gluon-initiated jets. The remaining uncertainties come from pile-up, punch through or  $\eta$ -intercalibration uncertainties. All these uncertainties result in variations of the final jet energy scale, therefore they are also referred to as JES uncertainties. An additional systematic uncertainty is added to account for the uncertainty on the jet energy resolution (JER). This uncertainty is derived using the *dijet balance* technique [140]. The main sources of uncertainty affecting JES and JER are shown in Figure 4.9 as a function of jet- $p_T$ .

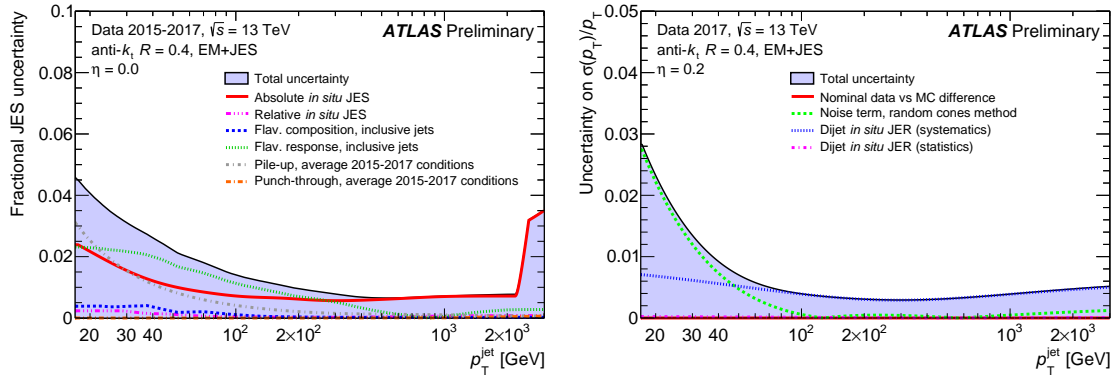


FIGURE 4.9 – (a) Fractional jet energy scale systematic uncertainty components as a function of jet  $p_T$  at  $\eta = 0.0$  and (b) the uncertainty on the relative jet energy resolution, defined as the uncertainty on  $\sigma(p_T)/p_T$ , shown for  $\eta = 0.2$  as a function of  $p_T$ . The jets are reconstructed from electromagnetic-scale topo-clusters with the anti- $k_t$  algorithm with a radius parameter of  $R=0.4$ . The total uncertainty (all components summed in quadrature) is shown as a filled region topped by a solid black line [142, 143].

#### 4.4.2 Jet cleaning

The signal in the calorimeter is contaminated by *in-time* and *out-of-time* pileup. The *in-time* pileup comes from additional  $pp$  interactions in the same bunch-crossing, while the *out-of-time* pileup arises from energy deposits from previous and following bunch crossings. On average, the pile-up contribution is subtracted from the total transverse energy flow, however local fluctuations due to the sum of in-time and out-of-time pileup may generate spurious jets. These jets have typically a lower  $p_T$  and a lower fraction of associated tracks from the primary vertex with respect to hard scatter jets. A jet cleaning procedure is therefore applied to remove these spurious jets from the event. The selection is based on a multivariate combination of jet variables, referred to as Jet Vertex Tagger (JVT) [144]. The input variables are defined in such a way that the JVT output is stable as a function of the number of reconstructed primary vertices in the event ( $N_{vtx}$ ). In practice, the JVT algorithm combines different track variables in a single Likelihood discriminant, which defines the probability for a jet to come from pile-up or from the hard scattering with an output between 0 and 1. Based on studies presented in Ref. [144], a requirement at 0.59 was set as the

default threshold for the jet cleaning selection in ATLAS. This JVT selection is 92% efficient for hard scatter jets, with a 2% fake rate from pile-up jets.

#### 4.4.3 Truth flavour labelling

The jets coming from simulation can be also defined by the flavour of the quark from which they were initiated. In particular there is a distinction between:

- *b-jets*, containing at least one b-hadron,
- *c-jets*, containing at least one c-hadron and no b-hadrons,
- *light-jets*, containing no b- or c-hadrons. This category includes all the so-called light contributions, so gluon,  $u$ ,  $d$  and  $s$  initiated jets.

The labelling scheme is performed at truth level, using an exclusive  $\Delta R$  matching. The final state hadrons with  $p_T > 5$  GeV are matched to the closest jet in  $\Delta R$  space, scanning within a cone of  $\Delta R < 0.3$  from the jet axis. The truth label is determined by counting the number and the type of heavy flavoured hadrons assigned to the jet, looking at their truth particle ID.

### 4.5 Overlap removal

As mentioned in the previous Section, the offline reconstruction process is not exclusive. In fact, the same sub-detector response can be assigned to different physics objects at the same time, i.e. an energy deposit in the calorimeter can be shared by both an electron and a jet candidate at the same time. Thus, a procedure called *overlap removal* (OR) must be used to solve these ambiguities. The algorithm is applied to the object collections selected with the loosest identification requirements, fully reconstructed and calibrated [145]. The following sequential procedure to remove single object-types is applied:

**Electron-muon:** In the - rather rare - cases where a muon and an electron share a track in the ID, the electron is removed, as it is considered as generated from a converted photon radiated by the muon.

**Jet-electron:** jets being at angular distances  $\Delta R < 0.2$  from an electron are removed. This arises from the fact that the energy deposits in the EM calorimeter are always used as inputs for the jet reconstruction, regardless of the electron reconstruction result. Without this step, almost all the electrons would be double-counted as jets.

**Electron-jet:** After the previous step, electrons within a cone of  $\Delta R < 0.4$  from a jet axis are removed, since in this case the electron is considered as coming from semi-leptonic decays of heavy-flavoured hadrons.

**Jet-muon:** If a muon and a jet are found to be closer than  $\Delta R < 0.2$ , the jet is removed only if it has less than three tracks, because such a low track multiplicity can be compatible with radiation effects from the muon.

**Muon-jet:** After the previous removal, if the remaining jet-muon pairs are found to be closer than  $\Delta R < 0.2$ , the muon is considered as a product of a semi-leptonic heavy-flavour hadron decay, so it is removed and its energy is summed to the final jet energy.

## 4.6 Taus

Tau leptons ( $\tau$ ) have a mean life time of  $2.9 \cdot 10^{-13}$  s [20], so they typically decay before reaching the ATLAS active area. The taus can decay leptonically ( $\tau \rightarrow \ell \nu_\ell \nu_\tau$ ) or hadronically ( $\tau \rightarrow \text{hadrons} \nu_\tau$ ). The leptonic decays are not explicitly recognized, since they are detected as prompt muons or electrons in the detector. On the contrary, the hadronic decays - which occur with a BR of 65% - can be used to explicitly reconstruct  $\tau$  objects. The signature in the detector is reconstructed as a spray of particles, also called  $\tau$ -jets, with high probability to contain one charged pion (75%) or three charged pions (22%). The  $\tau$ -jets are reconstructed with the anti- $k_t$  algorithm with a size parameter of  $R = 0.4$ . In addition, the  $\tau$ -candidates are selected in the kinematic region with  $p_T > 20$  GeV and  $|\eta| < 2.5$ , and requiring one or three charged tracks within a cone of  $R = 0.2$  around the jet axis. A BDT-based  $\tau$  identification is used to reject the background from quark- and gluon-initiated jets [146].

## 4.7 Missing transverse momentum

Neutral weakly-interacting particles like neutrinos or dark matter particle candidates are expected to leave no direct signature in the detector. Their presence can be only detected indirectly looking at the apparent imbalance of momentum in the transverse plane. Following the conservation of momentum, the total transverse momentum of all particles in the event should sum to zero, therefore the total momentum associated with these non-interacting particles can be computed as the negative vector sum of the momenta of the other detected particles. This quantity is referred to as missing transverse momentum,  $E_T^{\text{miss}}$ . The same statement should be true for the  $z$  component, but the longitudinal momenta of the colliding partons are not known a priori, so the missing longitudinal momentum can not be computed. The  $E_T^{\text{miss}}$  is computed combining the information from the calorimeters and the muon spectrometer for all the *hard objects*, such as leptons, jets, photons and hadronic  $\tau$  jets [147]. The calculation is sensitive to acceptance effects, object miscalibrations and momentum mismeasurements, as well as pile-up contamination effects, which can fake a missing transverse energy imbalance. The overall calculation is the sum of the following terms:

$$E_{x(y)}^{\text{miss}} = E_{x(y)}^{\text{miss},e} + E_{x(y)}^{\text{miss},\gamma} + E_{x(y)}^{\text{miss},\tau} + E_{x(y)}^{\text{miss},\text{jets}} + E_{x(y)}^{\text{miss},\mu} + E_{x(y)}^{\text{miss},\text{soft}}, \quad (4.6)$$

with  $E_{x(y)}^{\text{miss},\text{obj.}}$  the (minus)  $x$  ( $y$ ) components of the reconstructed and calibrated physics objects (electrons and photons, taus, jets and muons). The  $E_{x(y)}^{\text{miss},\text{soft}}$  component accounts for the so-called *soft-terms*, defined as all the additional signals not associated with a reconstructed physics object. The double counting of the various clusters is avoided by considering physics objects in the following specific order: muons, electrons, photons, hadronic taus and finally jets [148]. The soft terms are reconstructed as *track-based* soft terms (TST) or *calorimeter-based* soft terms (CST). The track-based terms are reconstructed from ID tracks not associated with physics objects, mainly coming from low momentum tracks. Additional criteria on the track-to-vertex matching are required for these soft tracks to ensure a precise determination of their primary vertex. The calorimeter-based soft terms, on the contrary, are computed from energy deposits in calorimeter cells. This method has the advantage to account for both the charged and the neutral components of the soft terms, at the price of a much higher pile-up contamination dependence. In fact, there is



no way to uniquely associate the energy clusters to a specific primary vertex, due to the very limited angular accuracy of the clusters, and therefore all the soft deposits are summed in the calculation, including the pile-up clusters. Since TST are proved to be more pile-up robust and with a much higher angular resolution than the CST, they are used as the nominal way to compute the soft terms in ATLAS.

The overall missing transverse momentum is given by:

$$E_T^{\text{miss}} = \sqrt{(E_x^{\text{miss}})^2 + (E_y^{\text{miss}})^2}. \quad (4.7)$$

The systematic uncertainties on the  $E_T^{\text{miss}}$  come from the propagation of the energy scale and resolution uncertainties of the reconstructed objects and the soft terms in Equation 4.6. In particular, the first come from the single object computations, while the latter have been evaluated on events with no real expected  $E_T^{\text{miss}}$ , such as  $Z \rightarrow ee$  or  $Z \rightarrow \mu\mu$  events with no additional jets with  $p_T > 20$  GeV as shown in Figure 4.10(a). More details are given in Ref. [149]. Overall, the resolution smearing of the soft terms results in a variation of roughly 2% at low  $E_T^{\text{miss}}$  and increasing up to 10% at high  $E_T^{\text{miss}}$  [147]. Three  $E_T^{\text{miss}}$  working points are provided: Loose, Medium and Tight, corresponding to different requirements in the selection of jets used to calculate the  $E_T^{\text{miss}}$ , as described in Ref. [150]. Overall, the resolution of  $E_T^{\text{miss}}$  depends on the resolution of the single objects, with a dominating contribution coming from the JER. As shown in Figure 4.10(b), the RMS width of the  $E_{x(y)}^{\text{miss}}$  distributions roughly increases as  $\text{RMS}_{x(y)}^{\text{miss}} (\sum E_T) \propto \sqrt{\sum E_T}$ . More details are discussed in Ref. [149].



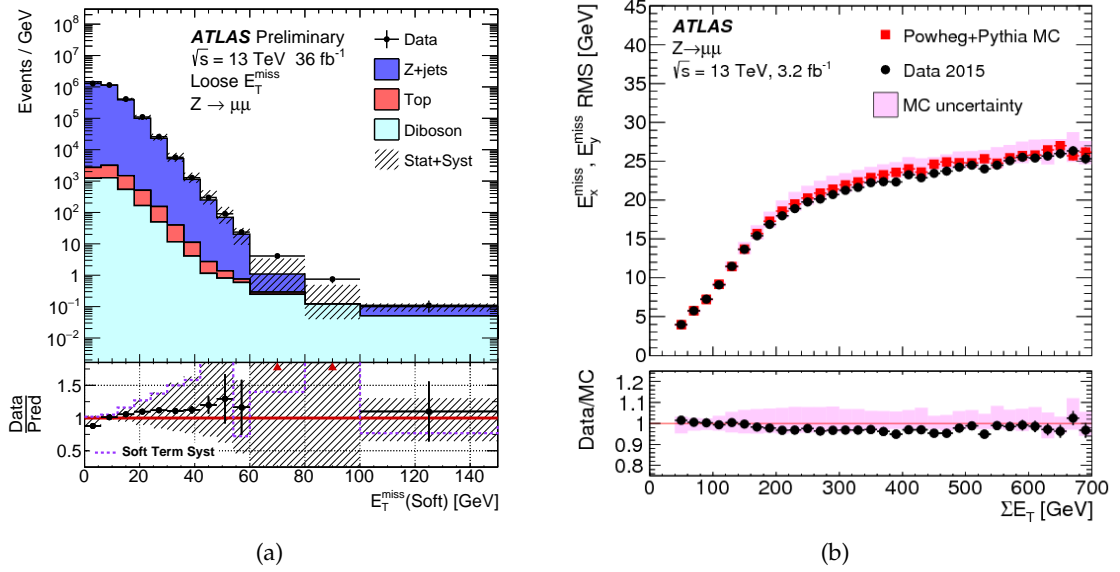


FIGURE 4.10 – (a) Distributions of the  $E_T^{\text{miss}}$  using the Loose  $E_T^{\text{miss}}$  operating point, which includes all jets with  $p_T > 20$  GeV that also pass the JVT criteria when the jet has  $|\eta| < 2.4$  and  $p_T < 60$  GeV. The soft term are shown in data and MC simulation for  $Z \rightarrow \mu\mu$  events. The lower panel of the figure shows the ratio of data to MC simulation, and the band corresponds to the combined systematic and MC statistical uncertainties. The largest contribution to the systematic uncertainty band comes from the soft term systematic uncertainty, and it is shown in a dotted line. The far right bin includes the integral of all events with soft  $E_T^{\text{miss}}$  above 100 GeV [150]. (b) The RMS width of the  $E_{x(y)}^{\text{miss}}$  distributions in bins of  $\Sigma E_T$  in an inclusive sample of  $Z \rightarrow \mu\mu$  events. Predictions from MC simulations are overlaid on the data points, and the ratios are shown below the respective plot. The shaded bands indicate the combined statistical and systematic uncertainties of the resolution measurements [149].

## 5 | Flavour Tagging in ATLAS

As described in Section 4.4 the b-jets are defined as composite objects containing b-hadrons. The capability to identify b-jets, c-jets and light-jets (and in fewer cases also  $\tau$ -jets) is crucial to perform an effective event reconstruction and to reduce contamination from fake background events in many physics analyses. The sequence of algorithms used to identify jets originating from b-quarks against c- or light-flavoured jets is also known as *b-tagging* or *flavour tagging*. It exploits specific kinematic properties of the b-hadrons (i.e. long lifetime, high mass, high decay multiplicity), to quantify the probability for a given jet to contain one or more of them. The main property of b-hadrons is their relatively long lifetime, of the order of  $\sim 1.5$  ps, allowing the hadron to travel inside the detector for about 4.5 mm before decaying to other particles. For example, a b-hadron with momentum of 50 GeV is expected to have a mean flight path length of about 3 mm, and therefore its decay products will be detected in the inner detector as coming from a displaced vertex with respect to the primary vertex.

Furthermore, since the decay point of the b-hadron must lie along its flight path, the child particles related to the displaced decays tend to have higher impact parameters with respect to the tracks originating from the primary vertex. This property can also be used to further discriminate the contribution of the tracks from a b-hadron decay with respect to tracks originating in the hard scattering. Finally, the relatively high mass of the b-hadrons, around 5 GeV, and their distinctive decay chain, which often contains c-hadrons and/or soft leptons, can be used to enhance the fake rejection power of the b-tagging algorithms.

This chapter contains an overview of the flavour tagging techniques currently used in ATLAS, with particular emphasis on how to treat the tagger outputs in physics analyses. Moreover, the last part of the chapter focuses on the so-called *Tag Rate Function* method, which is an efficient statistical approach to emulate flavour tagging for samples with many c- and light-jets.

### 5.1 Basic flavour tagging algorithms

The identification of b-jets in ATLAS is based on a two-stage approach. First, a set of four basic b-tagging algorithms - exploiting different properties of b-hadrons and b-quark fragmentation - aim at building a set of discriminating variables for the b-jets. Then, these variables are used as inputs for higher-level multivariate discriminants (see Section 5.2), to provide the best separation among the different flavour hypotheses.

The first basic tagger is an impact parameter-based algorithm, which uses the individual properties of the tracks associated with the jet to build a single track-based

likelihood discriminant for b-, c- and light-jets. The second algorithm aims at explicitly reconstructing the displaced secondary vertices combining the jet tracks. The algorithm does not only build the secondary vertices, but it also provides a set of eight vertex-related variables to be used as input of the high-level taggers. Similarly, the third algorithm aims at directly reconstructing the entire multi-vertex decay chain of the b-hadron starting from the single tracks in the event. The output of this basic tagger is a set of eight discriminating variables related to the reconstructed multi-vertices. The last basic tagger is a BDT-based soft muon tagger algorithm, which exploits the semi-leptonic decays of the b-hadrons to enhance the light-jet rejection. These four basic algorithms will be briefly described here.

### 5.1.1 Track-jet matching

In case of calorimeter-based jets, the first step of a b-tagging algorithm is to correctly associate the tracks reconstructed in the Inner Detector with the jet candidates obtained from the jet reconstruction (with the anti- $k_t$ ). This association is crucial since the track information will be largely exploited by the b-tagging algorithms. The association is based on the angular separation  $\Delta R(track, jet)$  between the track and the jet, considering the direction of the three-momenta of the track and the jet:

$$\Delta R(\vec{p}_{trk}, \vec{p}_{jet}) < \Delta R_{cut} \quad (5.1)$$

where  $\Delta R_{cut}$  is a threshold varying as a function of  $p_T$ , because the decay products of high- $p_T$  b-hadrons are more boosted and thus collimated than the low- $p_T$  case. The thresholds are

- wider at low- $p_T$ : 0.45 for jet- $p_T = 20$  GeV,
- narrower at high- $p_T$ : 0.26 for jet- $p_T = 150$  GeV.

If the track is assigned to more than one jet, the jet with the smallest  $\Delta R$  is chosen. A single track can be associated with at most one jet.

### 5.1.2 The Impact Parameter based Algorithms: IPxD and IP RNN

The impact parameter (IP) of a track is defined as the distance of closest approach to the primary vertex. The transverse impact parameter,  $d_0$ , is the impact parameter in the  $r - \phi$  projection. The longitudinal impact parameter is calculated in the  $x - z$  plane, and it can be obtained approximating the track by a straight line (starting from the point of closest approach) and multiplying  $z_0$  by  $\sin \theta$ , as can be more easily seen looking at Figure 4.2. The transverse and longitudinal impact parameter significance are defined as  $d_0/\sigma_{d_0}$  and  $z_0 \sin \theta/\sigma_{z_0 \sin \theta}$  respectively, where  $\sigma_{d_0}$  is the uncertainty on  $d_0$ , and  $\sigma_{z_0 \sin \theta}$  is the uncertainty on  $z_0 \sin \theta$ . The resolution of the two impact parameters depends on the track momentum: at larger momenta it is limited by the resolution of the detector sensors and their alignment, while at low  $p_T$  the multiple scattering effects dominate. A more detailed description of how  $\sigma_{d_0}$  and  $\sigma_{z_0 \sin \theta}$  are calculated is reported in Ref. [151]. The impact parameter relative to each plane is conventionally defined as positive if the trajectory of the track crosses the calorimeter-based jet direction in front of the primary vertex (in the considered plane), and negative if it crosses behind the primary vertex. Assuming that the b-hadron decays along its flight path, true secondary vertices must be reconstructed from tracks crossing the jet axis in front of the primary vertex, therefore negative IP tracks are normally due to background or resolution. A schematic view of the sign convention is shown in Figure 5.1.

Two types of impact parameter algorithms are currently used in ATLAS: IPxD [152],

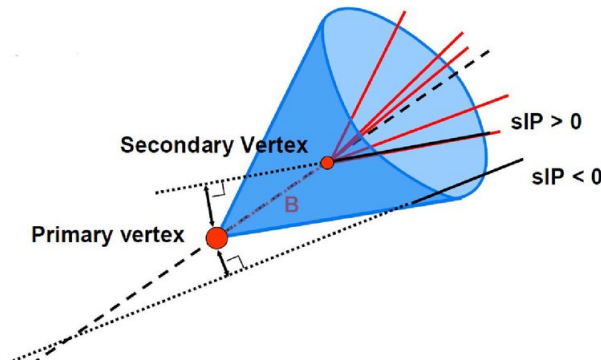


FIGURE 5.1 – Schematic view of a b-hadron decay inside a jet. The secondary vertex is significantly displaced from the primary vertex, thus the decay length is measurable. The track impact parameter is shown for a secondary vertex track and an external track from pile-up. The latter is crossing the jet projection behind the primary vertex, thus its impact parameter significance (sIP) is assigned as negative. The secondary vertex track is crossing along the direction of propagation of the jet, thus a positive sign is assigned.

also used in Run-1, and IP RNN [153], newly introduced in Run-2. The loosest track selection for all the impact parameter algorithms requires:

- At least seven hits in the silicon tracking detector, with less than two missing hits in total in the different layers, and at most one of them in the pixel detector [124], to reject fake tracks with hits not originating from a single charged particle.
- $|d_0| < 1 \text{ mm}$  and  $|z_0 \sin \theta| < 1.5 \text{ mm}$ , to reduce the tracks from long-lived particles (like kaons) or from material interaction (photon conversion or hadronic interactions), which can have impact parameters significantly higher than the tracks from heavy flavour decays<sup>1</sup>. Following a study reported in Ref. [154], these cuts are reducing of  $\sim 70\%$  the tracks from  $K_s$  and of  $\sim 40\%$  the tracks from conversion, while keeping  $\sim 91\%$  of tracks from weakly decaying b- and c-hadrons. The study was conducted in a sample of  $pp \rightarrow WH, H \rightarrow b\bar{b}, u\bar{u}, c\bar{c}$ .
- $p_T$  of the track above 1 GeV.

### IPxD algorithms

The IPxD taggers are based on a likelihood ratio of the smoothed impact parameter significance distributions ( $d_0/\sigma_{d_0}$  and  $z_0 \sin \theta/\sigma_{z_0 \sin \theta}$ ). The distributions of these two variables for a simulated  $t\bar{t}$  event sample are shown in Figure 5.2. The IP3D algorithm uses both the transverse and longitudinal impact parameter significance, while IP2D only uses the transverse IP significance.

In order to increase the discriminating power of the algorithm, the tracks are firstly separated in exclusive categories depending on hit pattern and track quality. A detailed summary of the categories is described in Ref. [155]. Different probability density functions (PDF) for the impact parameter significance of these tracks are obtained from  $t\bar{t}$  simulated samples for each category and jet flavour (b, c and light). They represent the probability for a track to originate from a jet of a given flavour. These probabilities are then used to define ratios of the b- over light-jet hypotheses,

1. The IP largely depends on the lifetime of the decaying particle as discussed in Ref. [154].

and combined in a single log likelihood ratio discriminant (LLR) as follows:

$$\log (P_b/P_u) = \log \left( \frac{\prod_{m=1}^N PDF_b(IP_m)}{\prod_{m=1}^N PDF_u(IP_m)} \right) \quad (5.2)$$

where  $IP_m$  is the impact parameter significance of track  $m$ , and  $N$  is the number of tracks associated with the jet. Alternative LLR discriminants can be constructed based on ratios of the b- and c-jet, or c- and light-flavour jet hypotheses. The  $PDF_i(IP_m)$  can be a 1D or 2D probability density function defined as follows:

$$PDF_i(IP_m) = \begin{cases} PDF_i(d_0/\sigma_{d_0}, z_0 \sin \theta / \sigma_{z_0 \sin \theta}) & \text{(IP3D)} \\ PDF_i(d_0/\sigma_{d_0}) & \text{(IP2D)} \end{cases} \quad (5.3)$$

Figure 5.3 illustrates the final discriminants for both the IP2D and IP3D algorithms.

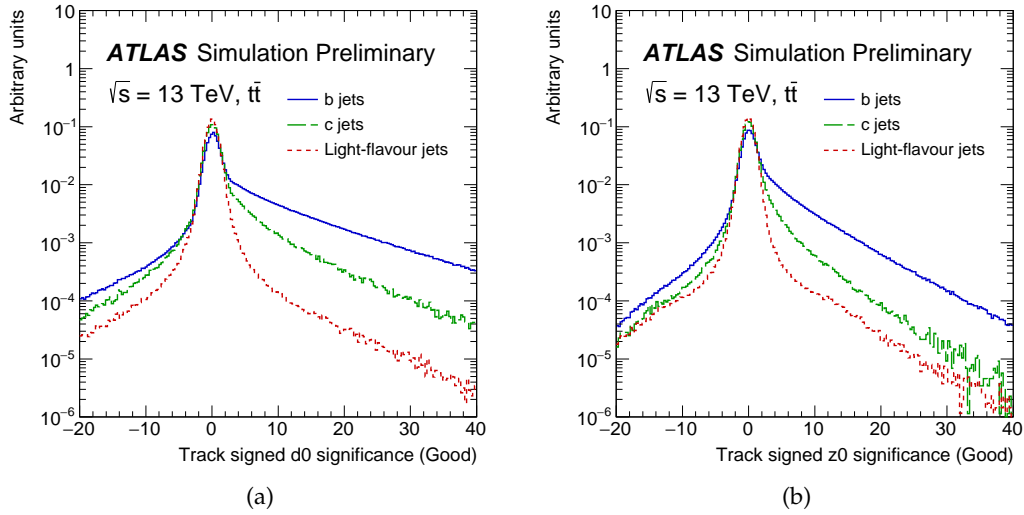


FIGURE 5.2 – Track signed  $d_0$  significance (a),  $z_0$  significance (b) for b-(solid green), c-(dashed blue) and light-flavour (dotted red) jets in the "Good" category for a  $t\bar{t}$  sample at  $\sqrt{s} = 13$  TeV [155]. The "Good" category is the category including all the tracks not fulfilling the requirements of the other categories. This is the most populated of the selection, with more than 80% of fractional contribution.

Two main processes reduce the rejection power of this kind of algorithms: tracks originating from  $\Lambda$  and  $K_s$  decays, and the noise from fragmentation tracks (see below). A solution to the first problem is to use another basic algorithm (SV) to identify and ignore these tracks, see Section 5.1.3. This solution has been introduced in Ref. [155] and allowed for an increase of 15% of the light-flavour rejection for IP3D at 77% fixed efficiency (see working point definition in Section 5.2.4).

The fragmentation tracks are defined as all the tracks in the parton shower not associated with the b-hadron decay. As shown in Figure 5.4, the contribution of these tracks inside the b-jet is observed to be dominant for jet  $p_T > 200$  GeV, representing an important source of background in the medium and high  $p_T$  regime.

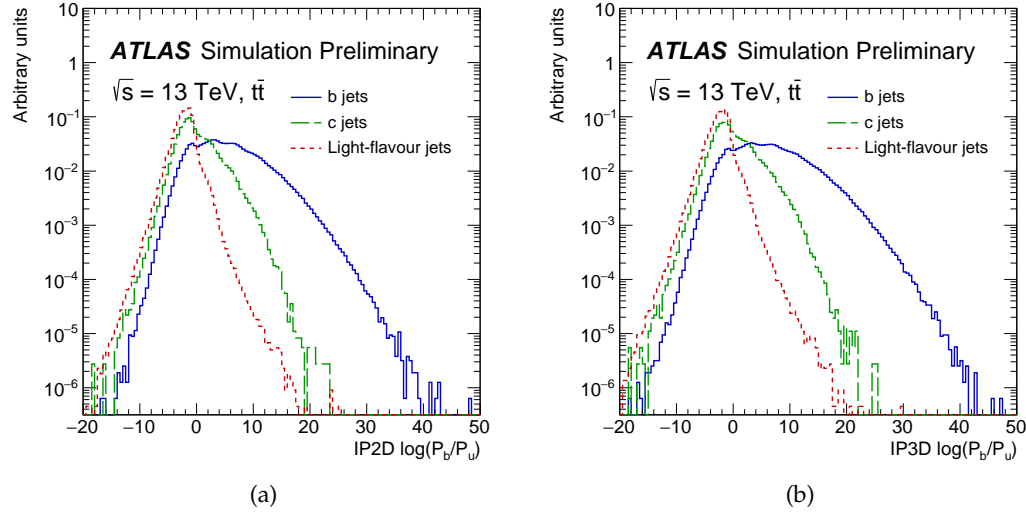


FIGURE 5.3 – IP2D log-likelihood ratio (a) and IP3D log-likelihood ratio (b) for b-(solid green), c-(dashed blue) and light-(dotted red) jets in a  $t\bar{t}$  sample at  $\sqrt{s} = 13$  TeV [155].

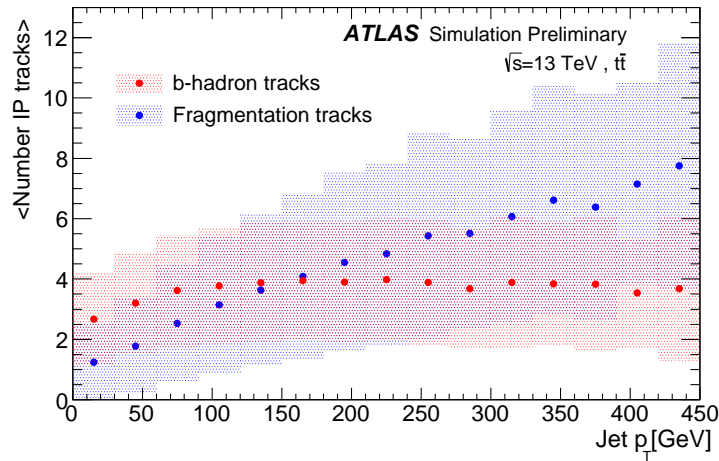


FIGURE 5.4 – Average number of b-hadron and jet fragmentation tracks selected for the IP algorithm as a function of the jet  $p_T$ . The shaded band around the two contributions represents the RMS for each  $p_T$  bin [155].

## IP RNN

One of the main assumptions of the IPxD algorithms is that the per-track flavour probability can be computed independently of the other tracks in the jet. This simplification ignores any interdependency between track parameters of different tracks in a given jet. This assumption maintains a manageable dimension of the likelihood function, but it does not account for the spatial and kinematic correlations between tracks initiated from the same b-hadron. As shown in Figure 5.5, the impact parameters of the tracks within the decay of a b-hadron are intrinsically correlated: if one track is found with a large impact parameter, then finding a second track with large impact parameter is more likely. If no displaced decay is present, as in light-flavour jets, then such a correlation should not exist.

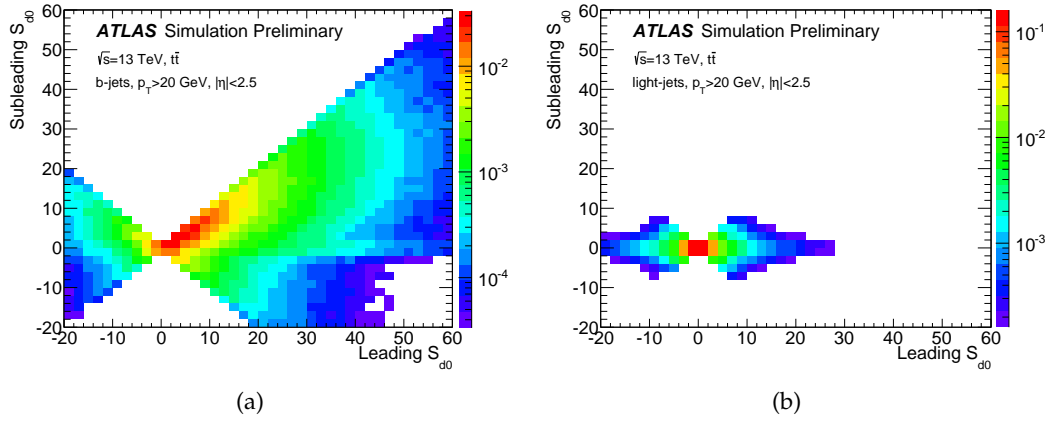


FIGURE 5.5 – The distribution of the  $d_0$  significance for the leading  $d_0$  significance track and subleading  $d_0$  significance track in b-jets (left) and light jets (right). The plots were produced with 700k b-jets and 1M light jets. Each distribution is normalized to unity.

To better exploit these correlations, a new algorithm called IP RNN, based on a recurrent neural network (RNN) [156], was recently introduced in ATLAS [153].

The track quality criteria of IP RNN are the same as the one listed above for IPxD. The input variables of IP RNN are four variables for each track, including  $d_0/\sigma_{d_0}$  and  $z_0 \sin \theta / \sigma_{z_0 \sin \theta}$  significance plus two new variables:

- The fraction of transverse momentum carried by the track relative to the jet,  $p_T^{frac} = \frac{p_T^{track}}{p_T^{jet}}$ , to enhance the difference between fragmentation tracks and tracks from the heavy hadrons.
- The angular distance between the track and the jet axis  $\Delta R(\text{track}, \text{jet})$ , to quantify the goodness of the track-jet matching.

The IP RNN output is a four-class output corresponding to the b-jet, c-jet, light-jet, and  $\tau$ -jet probabilities ( $p_b$ ,  $p_c$ ,  $p_u$ ,  $p_\tau$ ), which can be combined in a single-class output as follows to separate b-jets from others:

$$D_{\text{RNN}}(f_c, f_\tau) = \log \frac{p_b}{f_c p_c + f_\tau p_\tau + (1 - f_c - f_\tau) p_u} \quad (5.4)$$

with  $f_c$  and  $f_\tau$  the fraction of c- and  $\tau$ -jets in the background for the training sample. Similar outputs can be built to separate the other flavours from the rest. A comparison between the c- and light-jet rejection in IP3D and IP RNN is shown in Figure 5.6. For a b-tagging efficiency of 70% the RNN algorithm has  $\sim 2.5$  times the light-jet rejection and  $\sim 1.2$  times the c-jet rejection of IP3D.



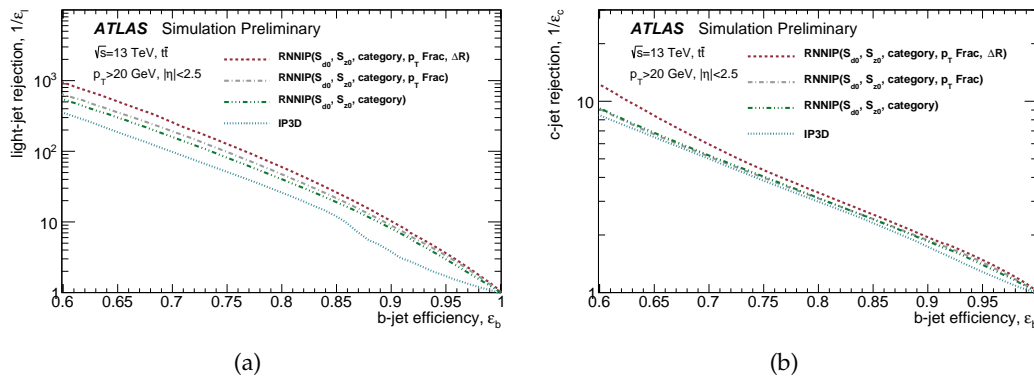


FIGURE 5.6 – The light-jet (a) and c-jet (b) rejection versus b-tagging efficiency for jets with  $p_T > 20$  GeV and  $|\eta| < 2.5$ , for RNNs trained using various sets of input variables, and for IP3D. The RNN without  $p_T^{frac}$  and  $\Delta R(\text{track}, \text{jet})$  uses only the inputs available to IP3D [153].

### 5.1.3 The Secondary Vertex based Algorithms: SV

The secondary vertex finding algorithm (SV) aims at reconstructing the inclusive displaced secondary vertex within the jet, while rejecting vertices compatible with  $K$  or  $\Lambda$ , photon conversions or hadronic interactions. The main Secondary Vertex algorithm in ATLAS is called SV [157].

The SV algorithm uses the tracks with 3D impact parameter significance<sup>2</sup>:

$$d_{3D}/\sigma_{d_{3D}} > 2 \quad (5.5)$$

as input for the fit. First, the valid tracks are combined in pairs, to build as many two-track vertices as possible. A two-track vertex is considered valid only if the fit has  $\chi^2 < 4.5$ . In order to further increase the rejection power of the final tagger, all the vertices compatible with long-lived light-flavoured particle decays such as  $K_S$ ,  $\Lambda$  or detector interactions are rejected.  $K_S$ ,  $\Lambda$  decays are identified by looking at the invariant mass of the charged particle system, while the interactions with the detector material are rejected requiring no hits in the inner detector in a radius smaller than the reconstructed vertex radius<sup>3</sup>.

The remaining pairs are grouped in independent sets of multi-tracks with similar initial vertex position estimate. Each set is then processed by the vertex fitting tool, which finds one single vertex for each independent set. An iterative procedure is applied to remove the least compatible tracks from the vertex. After the vertex fit is attempted, all the tracks not passing a certain  $\chi^2$  threshold are removed and the fit is repeated iteratively, until no such low-compatibility track is present anymore. As a default this  $\chi^2$  threshold is set to 7, corresponding to a 5% probability for the track to be associated with that vertex [158].

Once the secondary vertex has been reconstructed, eight discriminating variables are computed by the SV algorithm to be used as input to the high-level taggers. The full list of these properties is summarized in Table 5.1. Some of their distributions based on jets from simulated  $t\bar{t}$  events are shown in Figure 5.7.

2. This is the 3D distance between the primary vertex and the point of closest approach of the track.

3. No hits between the beamline and the secondary vertex, since secondary vertex tracks can not have hits with  $r\text{-}\phi$  radius smaller than their production vertex radius.

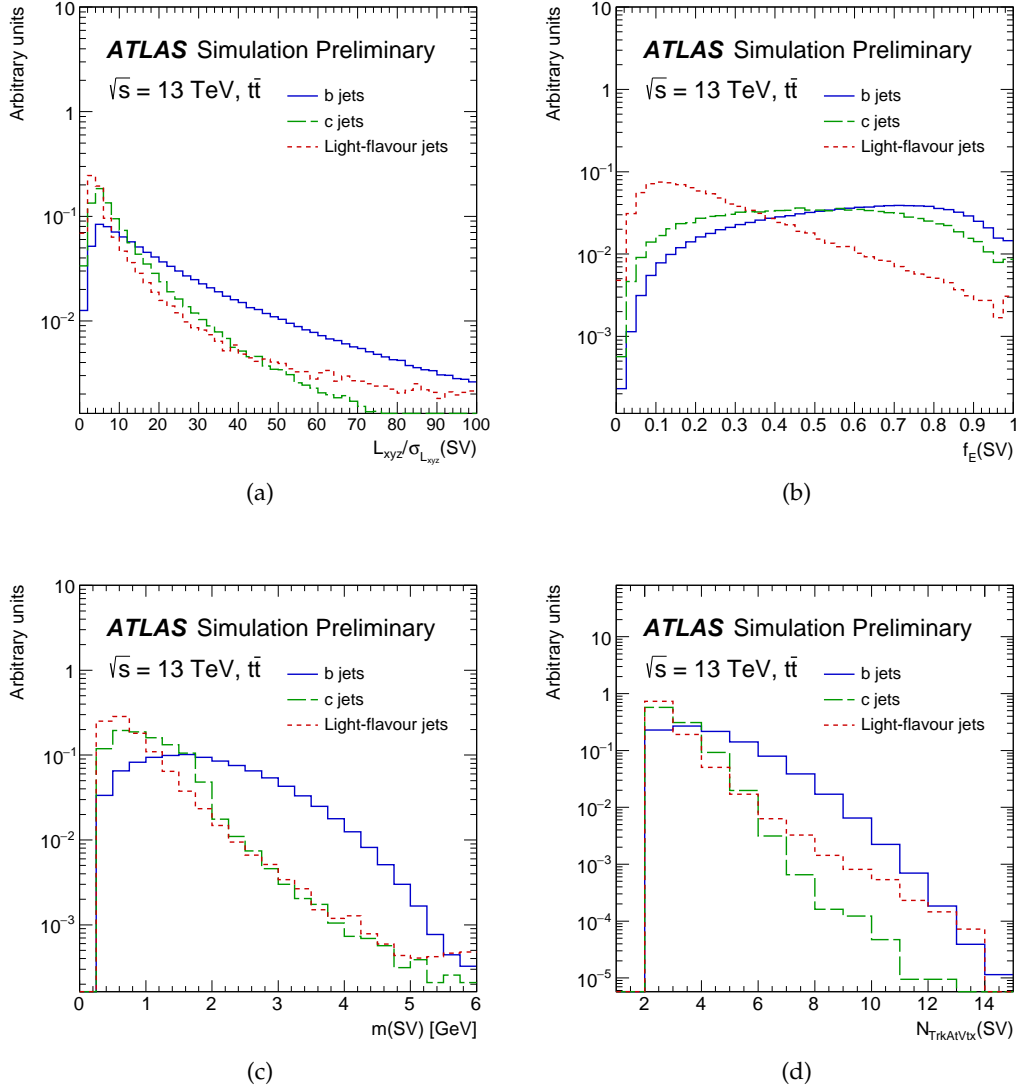


FIGURE 5.7 – Properties of secondary vertices reconstructed by the SV algorithm for b- (solid blue), c- (dashed green) and light-flavour (dotted red) jets in  $t\bar{t}$  events: (a) the 3D decay length significance, (b) the energy fraction, defined as the energy of the tracks in the displaced vertex relative to the energy of all tracks reconstructed within the jet, (c) the invariant mass and (d) the number of tracks associated with the vertex. The increased rate of light-flavour jets at high transverse decay length values is due to residual material interactions.

Variable	Description
$m(\text{SV})$	Invariant mass of all tracks associated with the secondary vertex
$f_E(\text{SV})$	Fraction of the charged jet energy in the secondary vertex defined as the energy from the tracks in the displaced vertex relative to all tracks reconstructed within the jet.
$N_{\text{TrkAtVtx}}(\text{SV})$	Number of tracks associated with the secondary vertex
$N_{2\text{TrkVtx}}(\text{SV})$	Number of two track vertex candidates
$L_{xy}(\text{SV})$	Distance between the primary and secondary vertex in the transverse plane
$L_{xyz}(\text{SV})$	Distance between the primary and secondary vertex
$S_{xyz}(\text{SV})$	$L_{xyz} / \sigma_{L_{xyz}}$ decay length significance
$\Delta R(\text{jet}, \text{SV})$	$\Delta R$ between the jet axis and the secondary vertex

TABLE 5.1 – Discriminating variables computed by the Secondary Vertex finder (SV1).

The SV performance has been evaluated building a log-likelihood ratio discriminant (LLR) based on PDFs built from three of the SV output variables (vertex mass, the energy fraction and the number of two-track vertices). The results will be discussed in Section 5.2. As for the impact parameter based algorithms, the main responsible for performance degradation are the fragmentation tracks in the medium-high  $p_T$  region. Another limitation comes from the relatively low vertex-finding efficiency which is around 80%.

#### 5.1.4 The decay chain multi-vertex Algorithm: JetFitter

The JetFitter algorithm is a decay chain multi-vertex reconstruction algorithm, which tries to reconstruct the full b-hadron decay chain exploiting the topological structure of b- and c-hadron decays inside the jet. As  $|V_{cb}|^2 \gg |V_{ub}|^2$  (see Section 2.1.1), a b-hadron will preferentially decay to a c-hadron, providing a distinct signature of a secondary and tertiary decay chain. The probability to have both the secondary and tertiary vertex with at least two associated tracks is limited by the track reconstruction efficiency of the detector, and second because the resolution of the track parameters is in some cases not sufficient to separate the two vertices. To recover a high multi-vertex reconstruction efficiency, the algorithm adds a constraint to the vertex position of the decay chain: the b- and c-hadron decay vertices must lie on the same axis, defined by the flight path of the b-hadron. The validity of this assumption is discussed in Ref. [159].

A Kalman filter [160] is used to find a common line on which the primary vertex and the bottom and charm vertices lie, approximating the b-hadron flight path, as well as their positions. After the primary vertex and the b-hadron flight axis have been initialised, each track crossing this axis is considered as a potential single vertex. The algorithm proceeds iteratively trying to group the single tracks and create multi-track vertices and then arrange these vertices in single vertices compatible with the rest of the decay chain (looking at the distance from the b-hadron axis). The procedure stops when the remaining vertices have compatibilities below a certain threshold. In this way, the algorithm can recover also the incomplete topologies and identify b- and c-hadron vertices with single tracks associated with them.

The loosest selection requirements used by the JetFitter algorithm are:  $p_T > 500$  MeV,  $|d_0| < 7$  mm and  $|z_0| \sin \theta < 10$  mm.

Variable	Description
$m(\text{JF})$	Invariant mass of the tracks from the displaced vertices, assuming pion masses
$f_E(\text{JF})$	Fraction of the charged jet energy in the secondary vertices
$N_{\text{TrkAtVtx}}(\text{JF})$	Number of tracks from displaced vertices with at least two tracks
$N_{2\text{TrkVtx}}(\text{JF})$	Number of two track vertex candidates
$N_{1\text{-trk vertices}}(\text{JF})$	Number of displaced vertices with one track
$N_{\geq 2\text{-trk vertices}}(\text{JF})$	Number of displaced vertices with more than one track
$S_{xyz}(\text{JF})$	Significance of the average distance between the primary and displaced vertices
$\Delta R(\mathbf{p}_{\text{jet}}, \mathbf{p}_{\text{vtx}})$	Angular distance between the jet axis and the vectorial sum of the momenta of all tracks attached to displaced vertices

TABLE 5.2 – Discriminating variables computed by the JetFitter algorithm.

Once these single and multi-track displaced vertices are reconstructed, a set of eight discriminating variables is computed to be used as input for the high-level taggers. The list of variables is summarized in Table 5.2. Some of the variables described above are presented in Figure 5.8. The b-tagging performance of the JetFitter algorithm is evaluated using a log-likelihood ratio discriminant based on PDFs of three JetFitter output variables (vertex mass, energy fraction and decay length significance). The results will be discussed in Section 5.2. The vertex reconstruction efficiency of the JetFitter algorithm in a  $t\bar{t}$  ( $e\mu$ ) sample is 95% for b-jets 70% for c-jets and between 10% and 50% for light-jets [152].

### 5.1.5 Soft Muon Tagger: SMT

The fourth class of basic algorithms exploits the semileptonic decays of the b-hadrons to enhance the rejection power of the algorithms described above. The b-quarks are expected to decay semileptonically with a BR  $\sim 42\%$ ,  $\sim 22\%$  directly leptonically ( $b \rightarrow l\nu X$ ) and  $\sim 20\%$  indirectly leptonically through the  $b \rightarrow c \rightarrow l\nu X$  chain,  $l$  being  $\mu$  or  $e$ . Therefore looking for soft muons related to the secondary vertex can help to discriminate against light-jets. Using electrons in the same  $p_T$  range is not efficient since it would introduce large background contaminations coming from misidentified electrons. The muons entering in the Soft Muon Tagger (SMT) algorithm are required to fulfill the following selection:

- $\Delta R$  between the muon and the jet axis less than 0.4.
- $p_T > 5$  GeV and  $|\eta| < 2.5$ .
- $|d_0| < 4$  mm.

These muons are expected to have smaller transverse momentum than the typical  $p_T$  of leptons from the hard scattering (hence "Soft" muons) and a large transverse momentum relative to the jet axis ( $p_T^{\text{rel}}$ ). The expected fraction of  $t\bar{t}$  events with muons passing this selection is 12%. A contamination of about  $\sim 1\%$  is expected from prompt muons from closeby W bosons wrongly associated with a jet, another  $\sim 1\%$  from muons from light-hadrons decays (Ks and pions) and finally a small

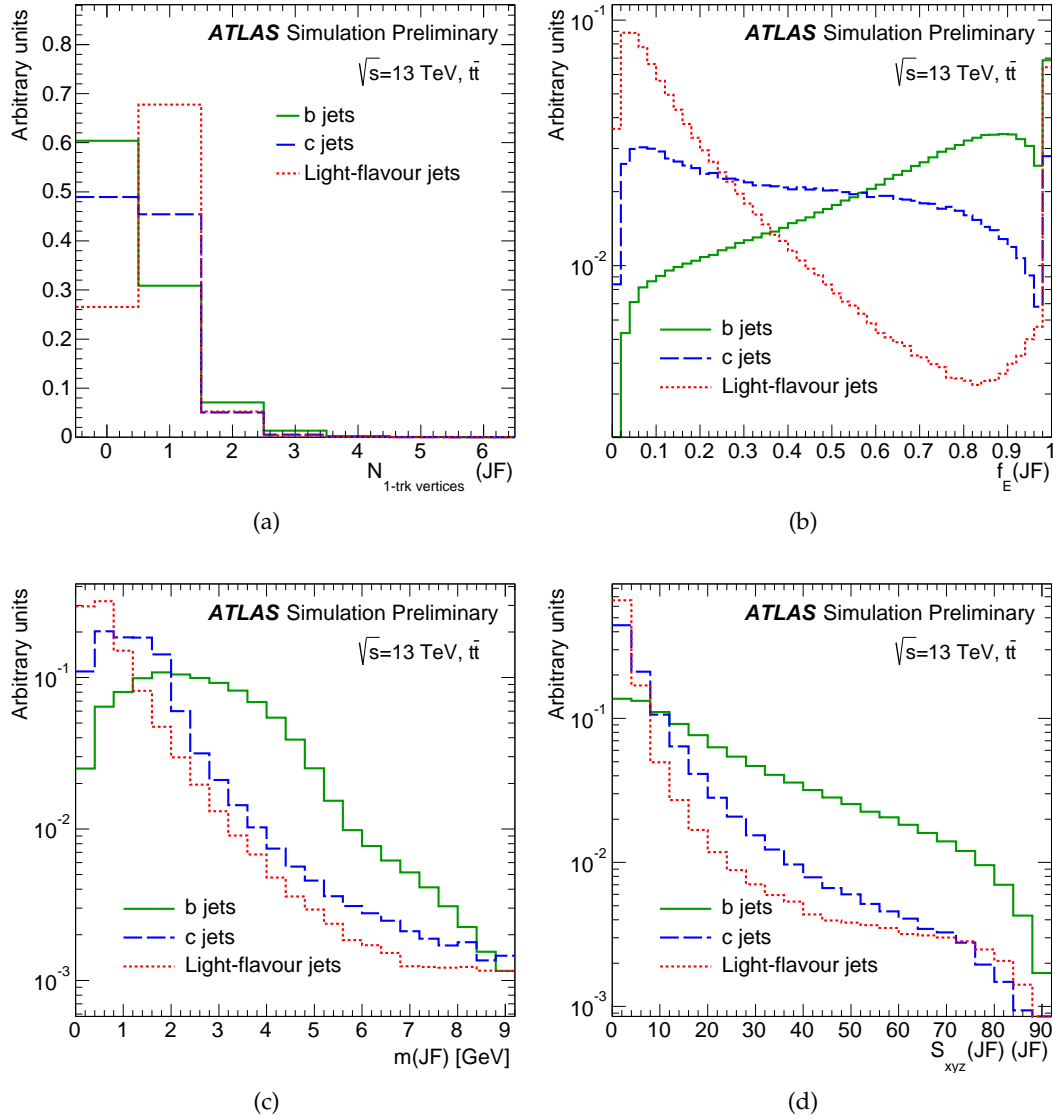


FIGURE 5.8 – Properties of the decay topology and secondary vertices reconstructed by JetFitter for  $b$  (solid green),  $c$  (dashed blue) and light-flavour (dotted red) jets in  $t\bar{t}$  events: (a) the number of 1-track vertices, (b) and the energy fraction, defined as the energy from the tracks in the displaced vertex relative to all tracks reconstructed within the jet, (c) the invariant mass of tracks fitted to one or more displaced vertices and (d) the average flight length significance of the reconstructed vertices.

Variable	Description
$\Delta R(\mu, jet)$	Angular distance between the muon and the associated jet
$p_T^{rel}$	$p_T$ of the muon with respect to the jet + muon axis
$d_0^\mu$	The muon transverse impact parameter
$\mathcal{S}$	Scattering neighbour significance
$\mathcal{M}$	Momentum imbalance significance
$\mathcal{R}$	Double charge-to-momentum-ratio in the Inner Detector and in the Muon Spectrometer

TABLE 5.3 – Discriminating variables used by the Soft Muon tagger algorithm.

(< 0.1%) contamination is expected from "punch-trough" jets leaving a signal in the muon detector.

The SMT is a Boosted Decision Tree (BDT) algorithm based on the discriminating variables listed in Table 5.3. The three muon quality related variables  $\mathcal{S}$ ,  $\mathcal{M}$  and  $\mathcal{R}$  are mainly used to reject muons from  $K$  and  $\pi$  decays. The less intuitive variables are  $\mathcal{S}$  and  $\mathcal{M}$ : the first is defined as the sum of the significance of the angular difference  $\Delta\phi$  between the two half tracks computed by considering pairs of adjacent hits along the track<sup>4</sup>, while the latter is the difference between the momentum in the Inner Detector and in the MS divided by the uncertainty on the energy loss measured by the calorimeters. More details about their definition can be found in Ref. [161]. The efficiency to reconstruct a muon inside jets is  $\sim 65\%$  for b-jets with a semi-leptonic decay to a muon in  $t\bar{t}$  events, with a light-jet mistag of  $\sim 1.8\%$ . The efficiency for accepting a jet having a soft muon candidate with the SMT algorithm is 85% for b-jets and 15% for light-jets in  $t\bar{t}$  events [162].

## 5.2 High-level tagging algorithms

To achieve better discrimination than any of the basic algorithms can individually achieve, the variables of the basic taggers described in the previous Sections are combined into "high-level" algorithms using Multivariate Analysis techniques. Two high-level taggers are currently available in ATLAS: the MV2 algorithm, based on Boosted Decisions Trees, and DL1, based on Recurrent Neural Networks. These high-level taggers combine the information of the input variables of the low-level taggers described in the previous Sections into just one output score, which can be conveniently used by physics analyses to perform the event selection.

Until 2016 the training of the multivariate classifiers was performed only on simulated  $t\bar{t}$  events, but the steeply falling  $p_T$  spectrum of this process was making the training sub-optimal already at 250 GeV, with a consequent degradation in performance at higher  $p_T$ . To overcome this problem, since the 2017 retraining campaign, a  $Z' \rightarrow t\bar{t}$  sample has been added to the  $t\bar{t}$  sample for a total of 8 million events, 5M events from  $t\bar{t}$  and 3M from  $Z'$ . These events have been used to train both the DL1 and MV2 algorithms. Figure 5.10 shows the different jet- $p_T$  distribution in  $t\bar{t}$  and  $Z'$  events, as well as the jet- $p_T$  of the total sample, referred to as the *hybrid* sample, obtained using  $t\bar{t}$  jets for  $p_T < 250$  GeV and  $Z'$  jets for  $p_T > 250$  GeV.

4. This variable quantifies the significance of a change in trajectory, expected in presence of a pion or kaon decay to muon. It measures how many hits in the tracker are out of the reconstructed track. A higher significance is more likely to correspond to a  $\pi$  or  $K$  decay in flight.

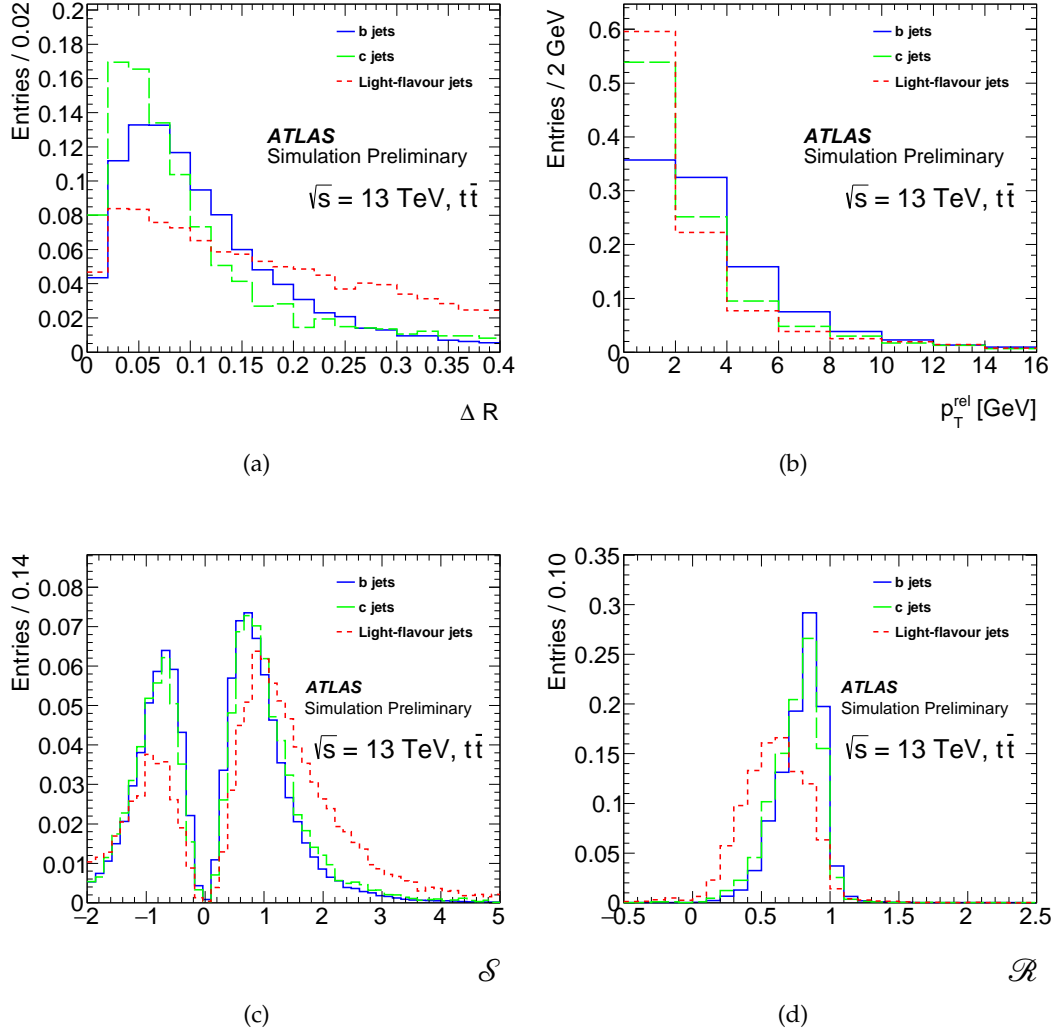


FIGURE 5.9 – Properties of the soft muon candidates in jets used in the SMT algorithm for  $b$  (solid green),  $c$  (dashed blue) and light-flavour (dotted red) jets in  $t\bar{t}$  events: (a)  $\Delta R$ , (b)  $p_T^{\text{rel}}$ , (c) scattering neighbour significance  $\mathcal{S}$  and (d) charge-to-momentum in ID and MS double ratio  $\mathcal{R}$ . The long tails in  $\mathcal{S}$  and the low values in  $\mathcal{R}$  for muons associated with light-jets are mostly due to in-flight decays.



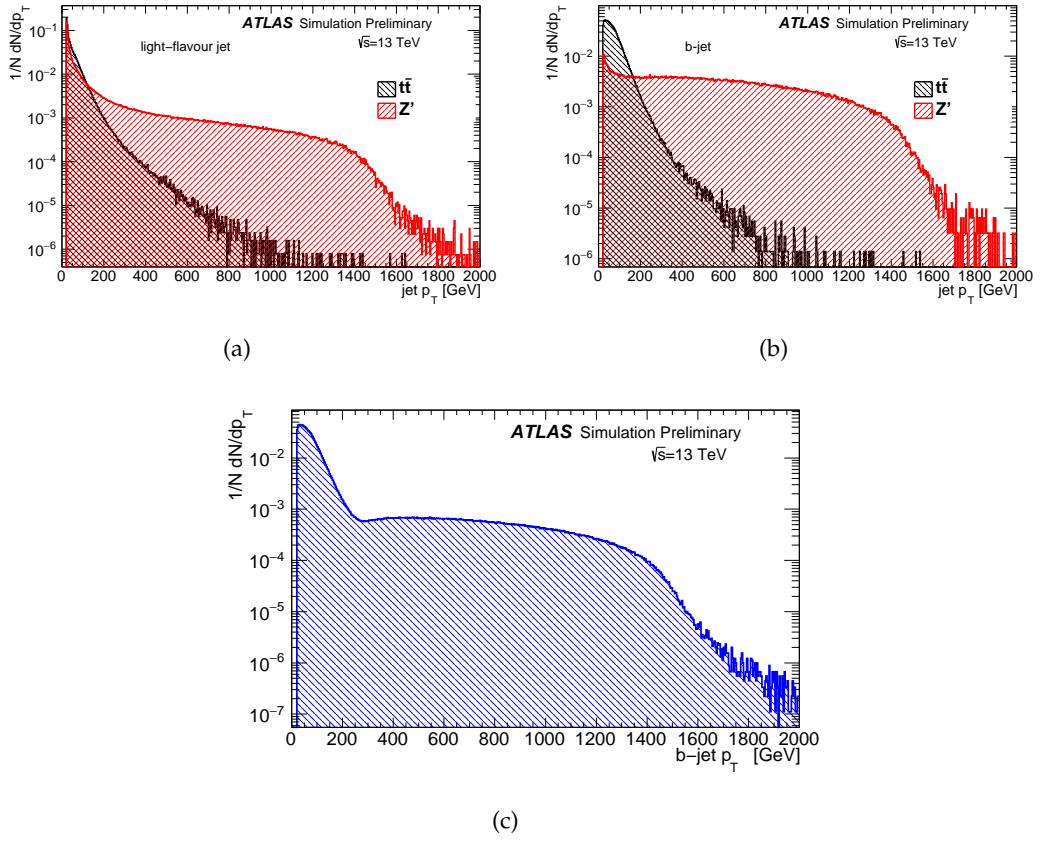


FIGURE 5.10 – Distribution of the jet transverse momentum of the  $Z'$  sample (red) compared to that of  $t\bar{t}$  events (black) for (a) light-flavour (b) and b-jets. (c) b-jet  $p_T$  distribution of the hybrid sample used for the training of the multivariate-based taggers [161].

### 5.2.1 MV2c10 algorithm

This algorithm has been developed in Run-1 and optimised in Run-2 to provide good b-jet identification against the c- and light-jet background. A boosted decision tree is trained on the hybrid sample described above, with b-jets being considered as signal and c- and light-flavour jets considered as background. The performance is evaluated separately on  $t\bar{t}$  and  $Z'$  events. The BDT makes use of all the IPxD, SV1 and JetFitter input variables described in Section 5.1.2, 5.1.3 and 5.1.4 with in addition the jet  $p_T$  and  $\eta$ , for a total of 24 discriminating variables, as shown in Figure 5.4.

Many physics analyses observe a stronger contamination from events with jets originating from c-quarks, rather than from light-quarks. For this reason the c-jet background fraction in the training sample is tuned to enhance the c-jets rejection, at the cost of slightly worse light-jet rejection. The naming convention of the MV2 algorithms is chosen to specify the fraction of c-jets used in the training: the "MV2cXX" version of MV2 corresponds to a training with a sample containing approximately XX% of c-jet background and 100-XX% of light-jet background. Many configurations have been tested and MV2c10, with a 7% c-jet fraction in the training<sup>5</sup>, has been found to have the best balance between light- and c-jet rejection. Figure 5.11 shows the MV2c10 output score for b-, c- and light-jets. The b-jets, confined to the higher BDT output score region, are well separated from c- and light-flavour jets. The nominal b-tagging efficiency of the algorithm is defined a priori by setting different thresholds, also called working points, on this output score. A more accurate definition of the different working points is given in Section 5.2.4.

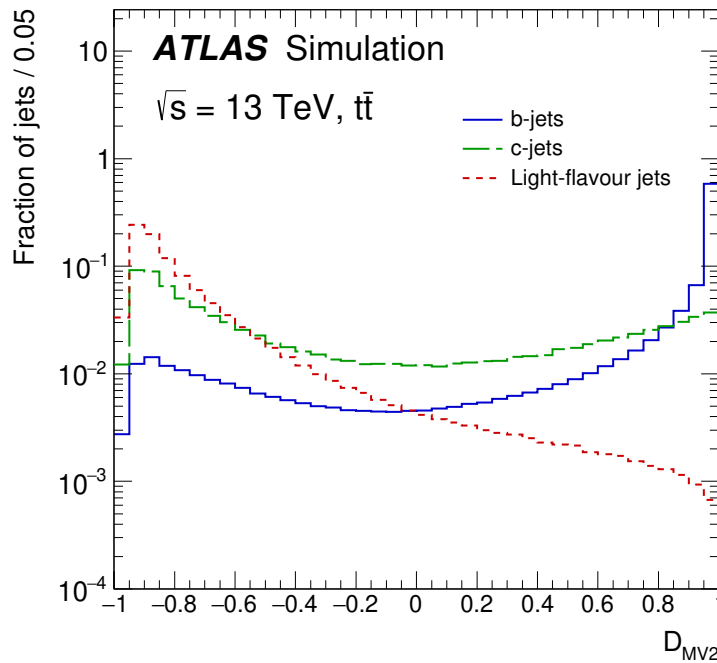


FIGURE 5.11 – MV2c10 BDT output for b- (solid blue), c- (dashed green) and light-flavour (dotted red) jets evaluated with  $t\bar{t}$  events [163].

5. The algorithm is not called MV2c07 for historical reasons. It was decided to maintain the Run-1 naming which was obtained with 10% c-jet fraction, so MV2c10.

Input	Variable	Description
Kinematics	$p_T$	Jet $p_T$
	$\eta$	Jet $ \eta $
IP2D/IP3D	$\log(P_b/P_{\text{light}})$	Likelihood ratio between the $b$ -jet and light-flavour jet hypotheses
	$\log(P_b/P_c)$	Likelihood ratio between the $b$ - and $c$ -jet hypotheses
	$\log(P_c/P_{\text{light}})$	Likelihood ratio between the $c$ -jet and light-flavour jet hypotheses
SV1	$m(\text{SV})$	Invariant mass of tracks at the secondary vertex assuming pion mass
	$f_E(\text{SV})$	Energy fraction of the tracks associated with the secondary vertex
	$N_{\text{TrkAtVtx}}(\text{SV})$	Number of tracks used in the secondary vertex
	$N_{2\text{TrkVtx}}(\text{SV})$	Number of two-track vertex candidates
	$L_{xy}(\text{SV})$	Transverse distance between the primary and secondary vertex
	$L_{xyz}(\text{SV})$	Distance between the primary and the secondary vertex
	$S_{xyz}(\text{SV})$	Distance between the primary and the secondary vertex divided by its uncertainty
	$\Delta R(\vec{p}_{\text{jet}}, \vec{p}_{\text{vtx}})(\text{SV})$	$\Delta R$ between the jet axis and the direction of the secondary vertex relative to the primary vertex.
JETFITTER	$m(\text{JF})$	Invariant mass of tracks from displaced vertices
	$f_E(\text{JF})$	Energy fraction of the tracks associated with the displaced vertices
	$\Delta R(\vec{p}_{\text{jet}}, \vec{p}_{\text{vtx}})(\text{JF})$	$\Delta R$ between jet axis and vectorial sum of momenta of all tracks attached to displaced vertices
	$S_{xyz}(\text{JF})$	Significance of average distance between PV and displaced vertices
	$N_{\text{TrkAtVtx}}(\text{JF})$	Number of tracks from multi-prong displaced vertices
	$N_{2\text{TrkVtx}}(\text{JF})$	Number of two-track vertex candidates (prior to decay chain fit)
	$N_{1\text{-trk vertices}}(\text{JF})$	Number of single-prong displaced vertices
	$N_{\geq 2\text{-trk vertices}}(\text{JF})$	Number of multi-prong displaced vertices
JETFITTER $c$ -tagging	$L_{xyz}(2^{\text{nd}}/3^{\text{rd}}\text{vtx})(\text{JF})$	Distance of $2^{\text{nd}}$ or $3^{\text{rd}}$ vertex from PV
	$L_{xy}(2^{\text{nd}}/3^{\text{rd}}\text{vtx})(\text{JF})$	Transverse displacement of the $2^{\text{nd}}$ or $3^{\text{rd}}$ vertex
	$m_{\text{Trk}}(2^{\text{nd}}/3^{\text{rd}}\text{vtx})(\text{JF})$	Invariant mass of tracks associated with $2^{\text{nd}}$ or $3^{\text{rd}}$ vertex
	$E_{\text{Trk}}(2^{\text{nd}}/3^{\text{rd}}\text{vtx})(\text{JF})$	Energy fraction of the tracks associated with $2^{\text{nd}}$ or $3^{\text{rd}}$ vertex
	$f_E(2^{\text{nd}}/3^{\text{rd}}\text{vtx})(\text{JF})$	Fraction of charged jet energy in $2^{\text{nd}}$ or $3^{\text{rd}}$ vertex
	$N_{\text{TrkAtVtx}}(2^{\text{nd}}/3^{\text{rd}}\text{vtx})(\text{JF})$	Number of tracks associated with $2^{\text{nd}}$ or $3^{\text{rd}}$ vertex
	$Y_{\text{trk}}^{\text{min}}, Y_{\text{trk}}^{\text{max}}, Y_{\text{trk}}^{\text{avg}}(2^{\text{nd}}/3^{\text{rd}}\text{vtx})(\text{JF})$	Min., max. and avg. track rapidity of tracks at $2^{\text{nd}}$ or $3^{\text{rd}}$ vertex

TABLE 5.4 – Input variables used by the MV2 and the DL1 algorithms. The JetFitter  $c$ -tagging variables are only used by the DL1 algorithm [163].

Studies presented in Ref. [152] and confirmed in Ref. [155] showed a dependence of the MV2c performance on the jet  $p_T$ . In particular, the b-tagging efficiency is observed to decrease at both low and high jet  $p_T$ . For jets with lower  $p_T$ , the multiple scattering with the ID material deteriorates the IP resolution and in addition the lower  $p_T$  cuts (1 GeV) reduces the reconstruction efficiency. At significantly higher jet  $p_T$ , the b-hadron will travel further from the primary vertex reducing the tracking impact parameter resolution. The track reconstruction efficiency is also limited in this regime because the tracks become more collimated and more fragmentation tracks are produced.

### 5.2.2 DL1 algorithm

DL1 is a neural-network-based high-level tagger with a three-class output, corresponding to the probabilities for a jet to be a b-, c- or a light-flavour jet ( $p_b$ ,  $p_c$  and  $p_u$ ). In the basic configuration, DL1 combines the inputs of the same basic taggers as the MV2 algorithm: the standard IP2D and IP3D, the SV1 and JetFitter algorithms along with jet  $p_T$  and  $\eta$ . In order to enhance the c-jet rejection power of the algorithm, the JetFitter c-jet tagging variables are added as additional input variables as shown in Table 5.4. Furthermore, the c-jet fraction in the training sample is tuned as in the case of MV2. To facilitate the comparison between DL1 and MV2c10, the default c-jet fraction in the training is set to 7%. The flavours are treated equally in the training, so the algorithm can be used both for b- and c-jet tagging. A final discriminant for b-tagging is obtained by combining the three outputs into one single discriminant:

$$\text{DL1}(f_c) = \log \frac{p_b}{f_c p_c + (1 - f_c) p_u} \quad (5.6)$$

as a function of the fraction of c-jets in the background training sample,  $f_c$ . A similar equation can be derived for c-tagging, by swapping the b and c labels. Figure 5.12 shows the three DL1 output probabilities for a jet to be tagged as b-, c- or light-jet.

The performance of the DL1 and MV2 discriminants is shown in Figure 5.13 in terms of c- and light-jet rejection as a function of the b-jet efficiency [163]. The performance of the LLR built from the single basic taggers are also shown. The combined high-level taggers have significantly better light- and c-jet rejection than the single basic tagger algorithms (these discriminants were described in Section 5.1). The additional JetFitter c-tagging variables used by DL1 bring a  $\sim 30\%$  improvement in the light-flavour jet rejection and a  $\sim 10\%$  improvement in c-jet rejection for a 70% b-tagging efficiency compared to MV2.

Despite the expected improved rejection power of DL1, the two algorithms have shown similar performance for the  $VH, H \rightarrow b\bar{b}$  analysis, as will be discussed in Section 7.6.1. However, the DL1 algorithm seems more promising in terms of future R&D, since it shows improved flexibility to new training techniques (i.e. Adversarial Neural Networks [165]), which might reduce the effects of modelling systematic uncertainties and training time. It grants also the possibility for future combined trainings in conjunction with IP RNN.

### 5.2.3 Enhanced Multivariate Algorithms

Both the SMT and IP RNN basic algorithms are not part of the current definition of MV2 or DL1, but variations are provided for testing. The first variation contains the Soft Muon Tagger in addition to the nominal basic algorithms, the taggers are defined as MV2c10\_mu (DL1\_mu). On top of this variation, there is the so-called MV2c10[mu]\_rnn (DL1[mu]\_rnn) variation, where the IP3D tagger has been

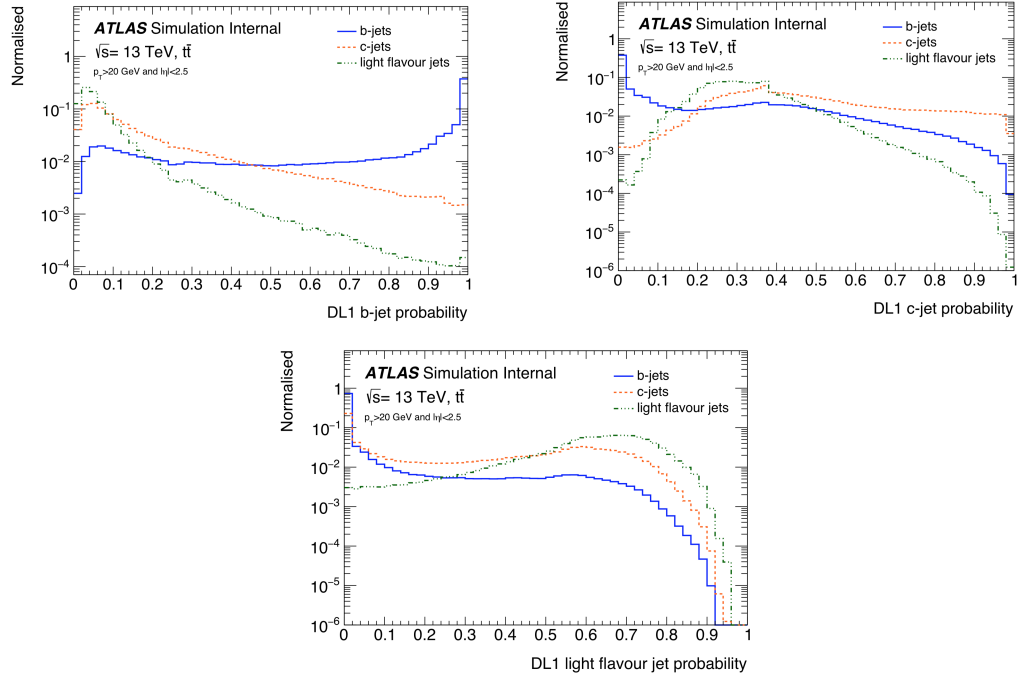


FIGURE 5.12 – DL1 Neural network b-, c- and light-jet probability output distribution for jets with  $p_T > 20$  GeV and  $|\eta| < 2.5$  in  $t\bar{t}$  events with at least one leptonically-decaying W boson. The b-jets are shown in blue, c-jets in orange, and light flavour jets in green. Each histogram is normalised to unity [164].

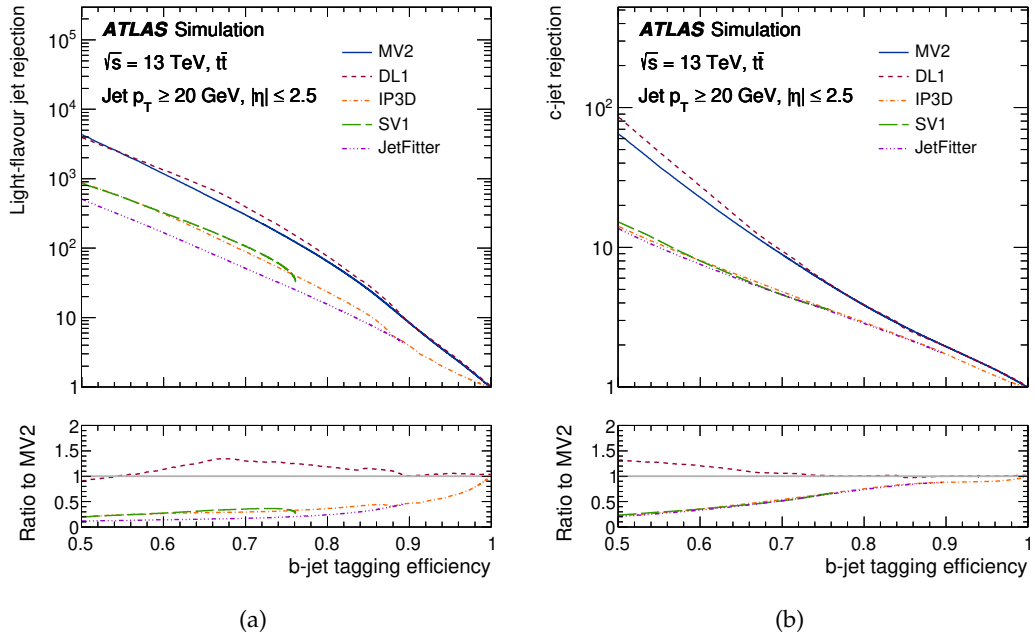


FIGURE 5.13 – The (a) light-flavour jet and (b) c-jet rejections versus the b-jet tagging efficiency for the IP3D, SV1, JetFitter, MV2 and DL1 b-tagging algorithms evaluated on the baseline  $t\bar{t}$  events.

replaced by the IP RNN.

As shown in Figure 5.14, the inclusion of the SMT is expected to provide a 20% improvement in light-jet rejection at low-medium  $p_T$  for  $t\bar{t}$  events, while the c-jet rejection does not profit from the muon-in-jet information since the muons are produced both in b- and c-hadron decays.

Both the c- and light-jet rejections are expected to be considerably improved by the MV2c10[mu]\_rnn variation, which is profiting of the better performance of IP RNN as described in Section 5.1.2. Some studies on the expected performance of these taggers in the context of the  $VH, H \rightarrow b\bar{b}$  analysis are presented in Section 7.6.

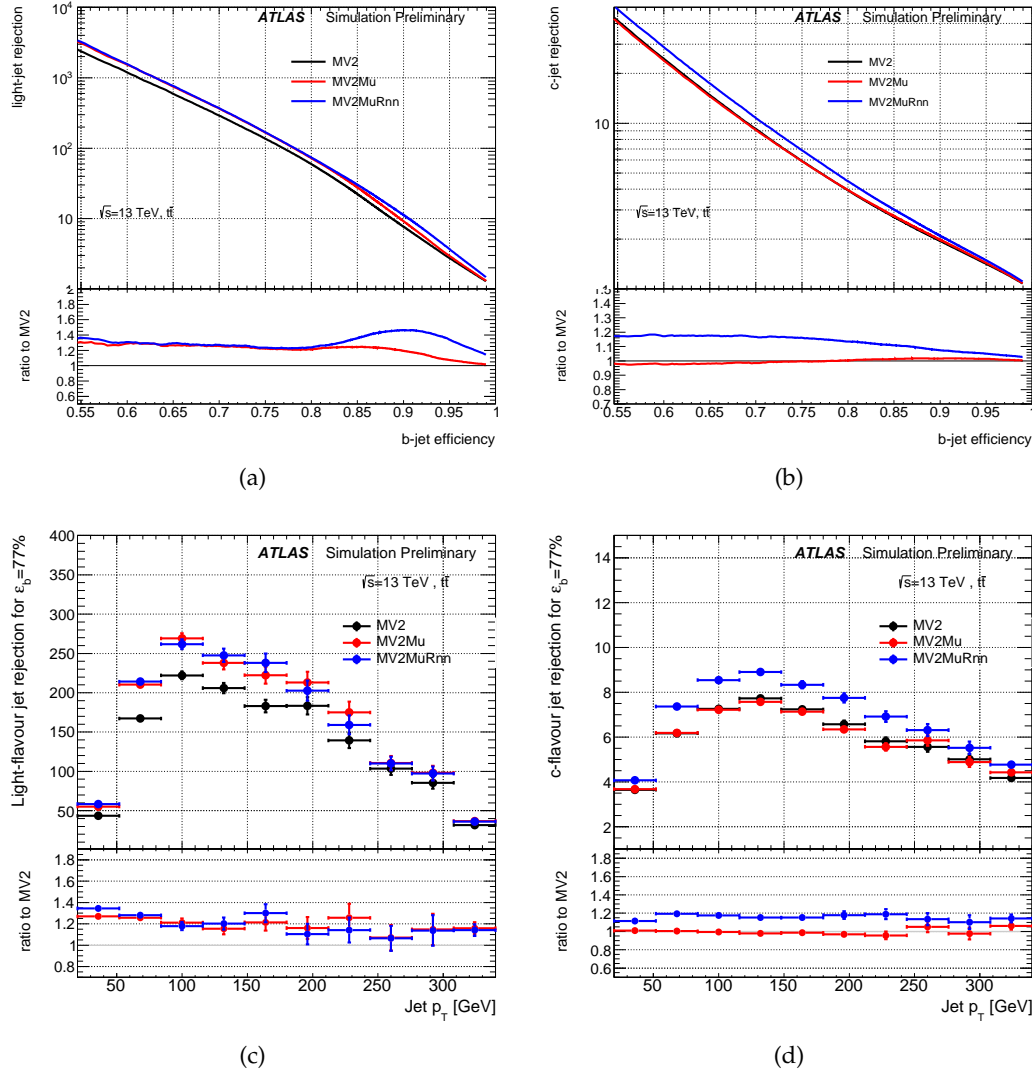


FIGURE 5.14 – (a) Light-flavour and (b) c-jet rejection as a function of b-jet efficiency or (c) and (d) as a function of the jet  $p_T$  for MV2 (black line), MV2Mu (red line), MV2MuRnn (blue line). The algorithm evaluation is performed on  $t\bar{t}$  events. The ratio reported on the bottom of the figure is calculated for each MV2 variant (MV2Mu, MV2MuRnn) with respect to MV2. For (c) and (d) the evaluation has been done for a flat b-jet efficiency of 77% for each  $p_T$  bin [161].

### 5.2.4 B-tagging working Points

The performance of a b-tagging algorithm is quantified by the efficiency ( $\epsilon$ ) to select jets of a certain flavour  $j$ :

$$\epsilon_j = \frac{\text{Number of jets of flavour } j \text{ passing cut}}{\text{Number of jets of flavour } j} \quad (5.7)$$

with the rejection defined as  $1/\epsilon_j$ .

Operating points (or "Working Points") are defined as thresholds on the discriminant output, designed to provide a determined efficiency for identifying b-jets. A lower b-tag efficiency leads to higher light-quark jet rejection. The performance of two or more b-tagging algorithms can be compared at a chosen working point by comparing the corresponding c- and light-flavour jet rejection. Several such Working Points (WP) are designed to provide a well-defined average efficiency when applied to b-jets from a sample of inclusive  $t\bar{t}$  events. Table 5.5 summarises the four supported working points for the Run-2 configuration of the MV2c10 and DL1 algorithms, for AntiKtEMTopo jets (defined in Section 4.4). Taking the 70% b-jet tagging efficiency working point for MV2c10 as an example, the light-flavour jet rejection rate is approximately 300, while the c-jet rejection rate is approximately 9.

$\epsilon_b$	MV2				DL1			
	Selection	Rejection			Selection	Rejection		
		c-jet	$\tau$ -jet	Light-flavour jet		c-jet	$\tau$ -jet	Light-flavour jet
60%	> 0.94	23	140	1200	> 2.74	27	220	1300
70%	> 0.83	8.9	36	300	> 2.02	9.4	43	390
77%	> 0.64	4.9	15	110	> 1.45	4.9	14	130
85%	> 0.11	2.7	6.1	25	> 0.46	2.6	3.9	29

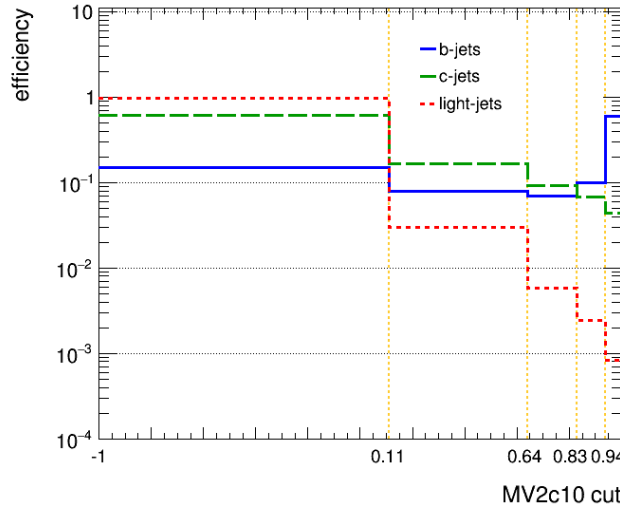
TABLE 5.5 – Operating points for the MV2c10 and DL1 b-tagging algorithms, including benchmark numbers for the efficiency and rejections rates. These values have been extracted from simulated  $t\bar{t}$  events, the main requirement being jet  $p_T > 20$  GeV [163].

The four working points can also be combined in one single binned distribution, called ‘pseudo-continuous’ b-tagging or ‘pseudo-continuous’ operating point. The default binning is defined by edges corresponding to the efficiency working points listed in Table 5.5. This ‘pseudo-continuous’ distribution is easier to calibrate with respect to the full continuous output, and it can be used by physics analyses as a powerful discriminating variable to enhance the sensitivity (see Chapter 8). Figure 5.15 shows a simplified model of the pseudo-continuous distribution for MV2c10.

## 5.3 Calibration of the flavour tagging efficiency

The efficiencies are measured on simulated  $t\bar{t}$  events and corrected with data-driven techniques to match the performance in data. Different methods are used to calibrate the b-, c- and light-flavours [166]. The corrections are extracted as scale factors (SF), to be applied to the event weight in simulation. The SFs are extracted from the data-to-MC comparison for each exclusive region between operating points and as a function of the jet kinematic ( $p_T$  and - for light-jets -  $|\eta|$ ). The b-tagging





(a)

FIGURE 5.15 – Schematic view of the pseudo-continuous approach. In the cumulative case just one cut at a specific value is applied to obtain the efficiencies listed in Table 5.5. On the contrary, the pseudo continuous case uses a binned distribution of the output (here MV2c10). the bins are obtained exploiting the values listed in Table 5.5 as bin edges.

efficiency scale factors are defined as:

$$\kappa_j = \frac{\epsilon_j^{\text{data}}}{\epsilon_j^{\text{MC}}} \quad (5.8)$$

where  $\kappa_j$  is the scale factor for a b-tagged jet of flavour  $j$  and  $\epsilon_j^{\text{data}}$  ( $\epsilon_j^{\text{MC}}$ ) are the efficiencies measured in data (simulation) at a specific working point. If in the events there are jets failing the b-tagging requirement (untagged jets), the event weight is corrected with an inefficiency SF for each untagged jet, defined as:

$$\omega_j = \frac{1 - \epsilon_j^{\text{data}}}{1 - \epsilon_j^{\text{MC}}} = \frac{1 - \kappa_j \epsilon_j^{\text{MC}}}{1 - \epsilon_j^{\text{MC}}} \quad (5.9)$$

applied to preserve the total number of events. Furthermore, it has been observed that differences in the showering and in the hadron decay models are leading to different efficiencies among the MC generators. To reduce these differences, a set of MC-to-MC scale factors is provided as an additional multiplicative correction. The total correction becomes:

$$\omega_j = \frac{\epsilon_j^{\text{data}}}{\epsilon_{j,\text{ref}}^{\text{MC}}} \frac{\epsilon_{j,\text{ref}}^{\text{MC}}}{\epsilon_{j,\text{alt}}^{\text{MC}}} \quad (5.10)$$

where  $\epsilon_{j,\text{ref}}^{\text{MC}}$  is the efficiency of the reference MC (POWHEG +PYTHIA 8+EVTGEN) and  $\epsilon_{j,\text{alt}}^{\text{MC}}$  the efficiency of the alternative generator.

The flavour tagging efficiency of b-jets is measured and calibrated using a sample enriched in dileptonic  $t\bar{t}$  events [163]. The selection is made requiring exactly

two tight-ID leptons with opposite charge and two jets. The MC events are further categorized per truth-flavour ( $bb$ ,  $bl$ ,  $lb$ ,  $ll$ ) following the order in  $p_T$  of leading and sub-leading jets. Three control regions enriched in  $bl$ ,  $lb$  and  $ll$  are built applying cuts on the pseudo-top reconstructed invariant mass  $m_{j,l}$  of each pair. The lepton-jet pairing is performed choosing the combination that minimizes the quantity  $(m_{j1,l1}^2 + m_{j2,l2}^2)$ <sup>6</sup>. In case of true  $t\bar{t}(bb)$  events, the two invariant masses can not exceed the top mass value  $m_t = 172.5$  GeV and the final reconstructed value is actually expected to be much smaller than this threshold, due to the undetected neutrino. No such constraint is expected from the backgrounds, which populate the  $bl$ ,  $lb$  and  $ll$  categories. The four regions are defined as follows:

- Signal Region (SR): with high  $bb$  purity, selected requiring  $m_{j1,l1}$  and  $m_{j2,l2}$  to be *below* 175 GeV.
- Control Region  $bl$  ( $CR_{bl}$ ): with high  $bl$  purity, selected with  $m_{j1,l1} < 175$  GeV and  $m_{j2,l2} > 175$  GeV.
- Control Region  $lb$  ( $CR_{lb}$ ): with high  $lb$  purity, selected with  $m_{j1,l1} > 175$  GeV and  $m_{j2,l2} < 175$  GeV.
- Control Region  $ll$  ( $CR_{ll}$ ): with high  $ll$  purity, selected requiring  $m_{j1,l1}$  and  $m_{j2,l2}$  to be *above* 175 GeV.

The control regions are used to constrain the non- $bb$  fractions in the signal region. A simultaneous fit to a binned log-likelihood function is performed to extract the b-jet tagging probabilities  $\mathcal{P}_b$  as a function of 9  $p_T$  bins from 20 to 600 GeV. The  $\mathcal{P}_b$  are defined as the conditional probabilities for a jet to fall in one specific  $p_T$  bin, while having a b-tagging discriminant  $w$  in one specific bin of the pseudo-continuous distribution. In this scenario, the measurement extracts directly the pseudo-continuous calibration, since all the tag-weight bins are fitted at the same time. The efficiency of the cumulative working points is related to the different  $\mathcal{P}_b$  as:

$$\varepsilon_b(X|T^m) = \sum_{O^k \subset X} \mathcal{P}_b(O^k|T^m). \quad (5.11)$$

with  $X$  the WP of interest,  $(T^m)_{m=1..9}$  the  $p_T$  bins and  $(O^k)_{k=1..5}$  the pseudo-continuous bins.

The main systematic uncertainties affecting the measurement are related to the  $t\bar{t}$  and *single-top* modelling, the jet energy scales and the statistical uncertainties (both in data and simulation). The efficiencies measured for the MV2c10 at 70% working point as a function of  $p_T$  are shown in Figure 5.16, together with the flavour-tagging scale factors, defined as the ratio between the measured b-tagging efficiency in data and simulation.

The correction factors are in general close to unity, with maximum deviations of  $\sim 5\%$  at low  $p_T$ . The uncertainties vary between 1% in the  $40\text{GeV} \leq p_T < 250$  GeV region and 8% in the low  $p_T$  regions with higher jet energy scale uncertainties. In the last bin above 250 GeV the uncertainty increases up to 3% due to the limited statistics in data. Figure 5.17, shows the efficiencies and the correction factors for the pseudo-continuous working point in one  $p_T$  bin ( $110 \leq p_T < 140$  GeV). The total uncertainty here varies between 9% and 1% depending on the tag-weight bin.

The c-jet b-tagging efficiency calibration uses semi-leptonic  $t\bar{t}$  events [167], i.e. one of the  $W$ -bosons decays leptonically (with  $l = e, \mu$ ) and the other hadronically. This is because the decay of the  $W$  boson is expected to produce a c-jet ( $W \rightarrow cX$ )

6. This minimization disfavors asymmetric pairings and high invariant masses, which are unlikely for  $t \rightarrow Wb, W \rightarrow \nu\ell$  decays.

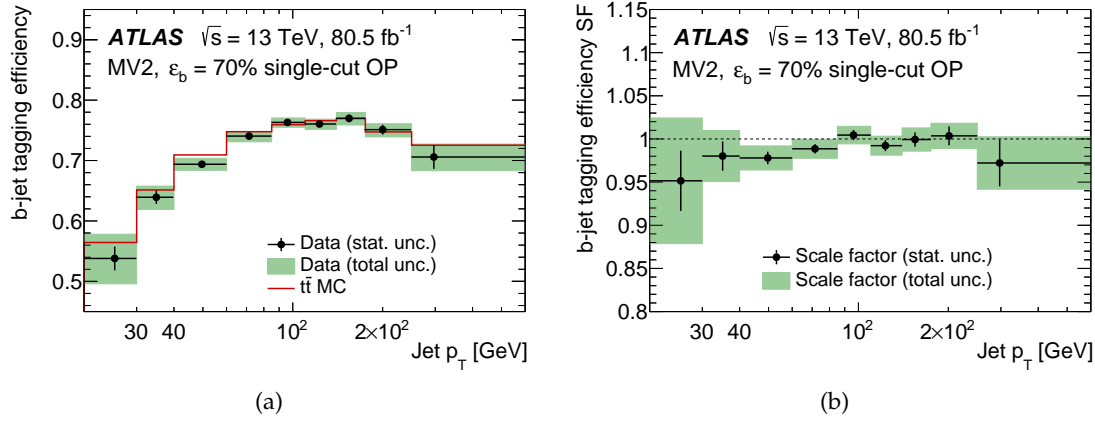


FIGURE 5.16 – The (a) b-jet tagging efficiency and (b) b-jet tagging efficiency simulation-to-data scale factors for the  $\varepsilon_b = 70\%$  single-cut WP of the MV2 tagger as a function of jet  $p_T$ . The efficiency measurement is shown together with the efficiency derived from  $t\bar{t}$  simulated events passing the signal region selection. Vertical error bars include data statistical uncertainties only while the green bands correspond to the sum in quadrature of statistical and systematic uncertainties. The dots are located at the mean of the b-jet  $p_T$  distribution in each  $p_T$  bin [163].

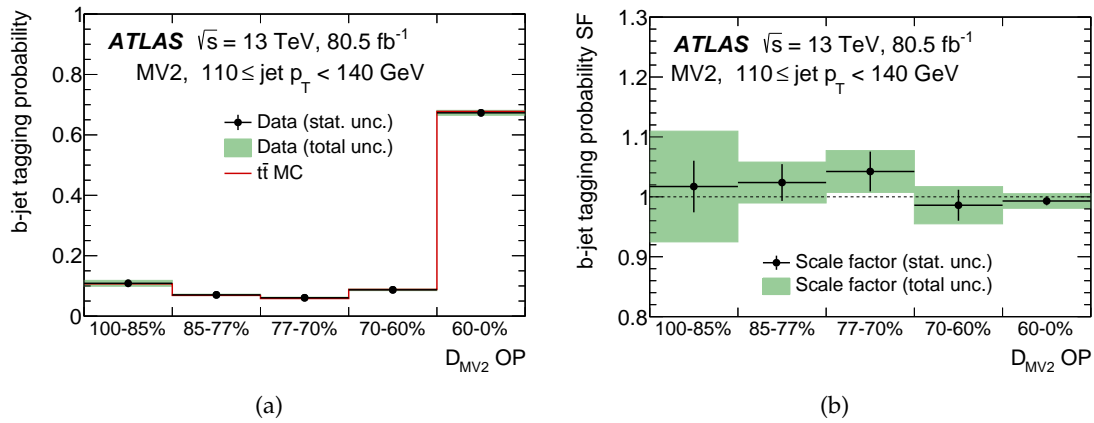


FIGURE 5.17 – The (a) b-jet tagging probability and (b) b-jet tagging probability simulation-to-data scale factors for the MV2 tagger for jets with  $110 \leq p_T < 140$  GeV in the various pseudo-continuous bins. The probability measurement is shown together with the probabilities derived from  $t\bar{t}$  simulated events passing the signal region selection. Vertical error bars include data statistical uncertainties only while the green bands correspond to the sum in quadrature of statistical and systematic uncertainties. The dots are located at the bin centres [163].

with a BR of  $\sim 33\%$ , which represents half of the hadronic decay fraction of the W ( $\Lambda_{cX}/\Lambda_{hadrons} \sim 50\%$ ) [20]. A likelihood fit is used to simultaneously extract the c-jet b-tagging efficiency from the pair of jets associated with the W-boson decaying hadronically in several jet  $p_T$  bins. Monte Carlo templates are used to predict the flavour composition of the jets in the sample. The SFs for the c-jet mistag rate are calculated between 25 GeV and 140 GeV, being between 1.1 for the 85% WP and 1.6 for the 60% WP with statistical (systematic) uncertainties ranging from 1% (7%) to 4% (20%) from the loosest to the tightest operating point.

The light-jets mistag efficiencies are calibrated using the *negative tag method* [168]. The negative-tag method relies on the assumption that light-jets are mistagged as b-jets mainly because of resolution effects of the inner detector. For prompt tracks, the distributions of the lifetime-signed impact parameter are expected to be symmetrically distributed around zero, with smearing due to the finite resolution of the detector. As shown in Figure 5.2, the negative side of the IP distribution is insensitive to the long tails of the b- and c-jets, which are due to the long lifetime, and therefore it represents a good approximation of the impact of the detector resolution on the different flavours.

Jets containing a significant amount of tracks with negative impact parameters and secondary vertices with negative lifetime are selected reverting some of the requirements used in the nominal IP and SV identification algorithms. The rate to tag these events with the modified algorithm (negative tag rate) is therefore a good approximation of the mistag rate in the positive side of the distribution. The measured negative tag rate is converted in the mistag rate applying corrections to account for heavy flavour hadrons contaminations and the asymmetry between positive and negative light-flavour tags, mainly due to particle tracks from long-lived particles ( $K_S$ ,  $\Lambda$  etc.) or interactions with the tracker material. The mistag rate ranges between 0.4% to 16% for the 85% operating point and 0.1% to 0.4% for the 60% operating point. The scale factors are obtained comparing the mistag rates in data and simulation. The measured values are in the range of about 1.5 to 3 with uncertainties up to 50%.

### 5.3.1 Reduction of the b-tagging variations

In order to simplify the treatment of the scale factor uncertainties in physics analyses, a principal component analysis has been developed to reduce the number of variations associated with b-tagging, while preserving the correlation scheme [169]. The method uses an eigenvalue decomposition of the total covariance matrix, built considering all the individual sources of uncertainty (including the statistical variations) in each  $p_T$  bin. Taking for example the b-jet calibration, each source of uncertainty has its own  $9 \times 9$  correlation matrix which considers the bin-by-bin correlations across the different  $p_T$  bins ( $T^m$ ) $_{m=1..9}$ . The total correlation matrix is the sum of the  $9 \times 9$  matrices of all the sources.

Being symmetric and positive-definite, the total covariant matrix can be diagonalized, so to provide orthogonal variations. The total uncertainty of each  $p_T$  bin can be computed as the sum in quadrature of the diagonalized eigenvalues relative to that bin. In the end, the eigenvalues used for physics analyses are one for each  $p_T$  bin used in the calibration, so 9 variations for b-, 4 for c- and 4 for light-jets for the cumulative working points.

After this orthogonalization, most of the eigenvalues are very small, so a further reduction scheme is introduced to remove the values below a certain threshold. The

*loose* reduction scheme provides a complete description of the total uncertainty, the *medium* reduction scheme has a  $\sim 3\%$  relative loss in the total uncertainty (or in correlation) and the *tight* reduction scheme has the maximum reduction in the number of variations, but also a loss in the total uncertainty or correlation of the order of 10-50%.

In the context of the pseudo-continuous calibration, the number of bins to be considered when building the correlation matrix is 5 times larger, since the calibration is performed in 2-D  $p_T \times w$  ( $9 \times 5$ ). The diagonalization is performed in the same way as for the cumulative working points, but the number of quoted variations is 45 for b-jets, 20 for c-jets and 20 for light-jets. Work is in progress to provide reduction schemes for the pseudo-continuous calibration, but up to now no official prescriptions have been released.

## 5.4 Statistical tagging

Due to the high rejection power against c- and light-jets achieved by the current b-tagging algorithms, many physics analyses suffer from a lack in the number of simulated background events after the b-tagging requirements, especially in case of background processes with only c- or light-jets in the final state. This creates issues if the analysis makes use of such samples to model the distributions of one or more variables used in the final fit to data. One way to overcome this issue and reduce the statistical fluctuations in these samples is to avoid removing events failing the b-tagging requirements, and instead apply a reweighting procedure to each MC event, based on the probability to have  $n$  tagged jets in the event. The event weight must be defined in a way to preserve the overall shape and normalization of the underlying distributions.

In practice, this is done by giving events with real b-jets in MC a much higher weight than events having only c- or light-jets. This procedure is referred to as "Truth Tagging" or "Tag-Rate Function" since it makes use of the truth flavour label of the jet to determine the event weight (or "truth tag weight").

The flavour identification efficiency defined in equation 5.7 can be thought as the likelihood for a jet of a given flavour to be b-tagged by a specific algorithm. Hence, b-jets have a much higher b-tagging efficiency than c-jets, which have a higher b-tagging efficiency than light jets.

The truth tag weight is defined as the product of the b-tagging efficiency for each b-tagged jet, times the complement of the b-tagging efficiency for each non b-tagged jet. A combinatorial approach is used in case the number of jets ( $m$ ) in the event exceeds the number of required tagged jets in the analysis ( $n$ ): all possible combinations of b-tagged and non b-tagged jets satisfying the analysis selection are considered, and the total truth tag weight is defined as the sum of the truth tag weights of each single combination. Taking for example an event with three jets, if exactly 2 b-tagged jets are required<sup>7</sup>, and each jet  $i$  has a b-tagging efficiency  $\varepsilon_i$ , then the total truth tagging weight is:

$$w_{tot} = \varepsilon_1 \varepsilon_2 (1 - \varepsilon_3) + \varepsilon_1 (1 - \varepsilon_2) \varepsilon_3 + (1 - \varepsilon_1) \varepsilon_2 \varepsilon_3. \quad (5.12)$$

In some cases, it is required to define precisely which are the b-tagged jets among the selected ones, for instance to apply specific analysis selections on top of the b-tagging requirements. When this is necessary, a particular combination is chosen

7. Here "b-tagged jet" is intended with respect to a specific working point, typically the working point of the physics analysis, which needs to be set a priori in order to compute the efficiencies.

randomly among all the possible ones, with a probability to be chosen being proportional to its truth tag weight. In the three jet example, the probability to choose the combination in which the first two jets are tagged is:

$$P_{12}^{tagged} = \frac{\varepsilon_1 \varepsilon_2 (1 - \varepsilon_3)}{w_{tot}}. \quad (5.13)$$

The higher the weight of the single permutation, the higher the “rate” at which the random choice falls on that particular permutation, and this explains the name “Tag Rate Function”.

Generalizing to the case of an event with  $m$  jets and  $n$  tagged jets required, the possible combinations are  $\binom{m}{n}$ . For a given tagged configuration, referred to as the  $i^{th}$  combination and denoted as  $\binom{m}{n}_i$ , the total number of remaining configurations is  $\overline{\binom{m}{n}} = \binom{m}{n} - \binom{m}{n}_i$ . the efficiency and inefficiency products are:

$$\varepsilon \left( \binom{m}{n}_i, x, f \right) = \prod_{j \in n} \varepsilon_x^f(j) \quad (5.14)$$

$$\varepsilon_{in} \left( \overline{\binom{m}{n}}_i, x, f \right) = \prod_{j \in m-n} (1 - \varepsilon_x^f(j)) \quad (5.15)$$

with  $\varepsilon_x^f(j)$  the tagging efficiency of jet  $j$  of flavour  $f$  at an efficiency working point  $x$ . the  $j \in m - n$  refers to the pool of non tagged jets. Therefore the total event weight:

$$w_{tot}(x) = \sum_i \varepsilon \left( \binom{m}{n}_i, x \right) \cdot \varepsilon_{in} \left( \overline{\binom{m}{n}}_i, x \right) \quad (5.16)$$

with a probability to choose a specific combination equal to:

$$P_i = \frac{\varepsilon \left( \binom{m}{n}_i, x \right) \cdot \varepsilon_{in} \left( \overline{\binom{m}{n}}_i, x \right)}{w_{tot}}. \quad (5.17)$$

This implies that in statistical tagging, the choice of defining a jet as tagged or non-tagged is done *a priori*, choosing randomly among all possible combinations. This decision is completely independent of the *real* b-tagging score of the jets. Thus, in many cases the *real* b-tagging score of the jet is in contrast with the statistical tagging choice (i.e. the jet has been defined as tagged by the randomly picked combination, but it has a very low real MV2c10 score). This represents a serious limitation in case the specific value of the b-tagging discriminant needs to be used in physics analyses, for example when introducing the MV2c10 score as discriminating variable in the BDT (see Chapter 8). To solve these inconsistencies, the b-tagging scores of all the jets in the event are re-assigned accordingly to the choice of the combination. A new b-tagging weight is generated for each jet in the event:

- The jets defined as the *tagged jets* of the combination will have b-tagging scores *above* the b-tagging requirement used in the analysis,
- The jets defined as the *non-tagged jets* of the combination will have b-tagging scores *below* the b-tagging requirement used in the analysis.

These new weights are chosen randomly from the distribution of the output weights (i.e. Figure 5.11), keeping into account its non-flat shape. The procedure of generating the new MV2c10 scores can be better explained with the three jet example. Assuming the three jets to have b-tagging scores equal to  $MV2c10_{j1} = 0.17$ ,



$MV2c10_{j_2} = 0.73$  and  $MV2c10_{j_3} = 0.99$ , then if the chosen combination requires the first two jets as tagged and the third jet untagged at 70% operating point, the real  $MV2c10$  scores are not reflecting this choice (because the 70% operating point threshold is set at 0.83 according to Table 5.5). Therefore, new  $MV2c10$  scores are needed. The  $j_1$  and  $j_2$  should have scores above the 70% WP requirement, with probability to be in the 70%-60% bin or in the  $> 60\%$  one proportional to the relative efficiency between the two bins. A first random choice between these two bins, taking into account their relative difference in the efficiency, is made to set the edges of the new  $MV2c10$  score (i.e. 0.83-0.94 or 0.94-1. according to Table 5.5) and then a flat random number is generated between these edges. The  $MV2c10$  score of the untagged jet is obtained in the same way but considering the efficiency bins below the 70% operating point requirement.

### 5.4.1 The efficiency maps

The b-tagging efficiencies  $\epsilon_x^f(j)$  used to determine the truth tag weight of each jet in the permutation are taken from 2-dimensional maps computed as a function of the jet kinematic ( $p_T$  and  $\eta$ ) and the jet truth flavour label. The 2-dimensional maps are assumed independent of the production process and therefore determined just on  $t\bar{t}$  samples. Figure 5.18 shows the official maps for the nominal  $t\bar{t}$  MC generator configuration (POWHEG +PYTHIA 8+EVTGEN)<sup>8</sup> released by the ATLAS flavour-tagging working group in October 2018. Alternative efficiency maps are computed for the other generators and parton showers models (i.e. SHERPA, HERWIG) and MC-to-MC scale factors are used to match the efficiencies of the nominal sample to correct for differences introduced by the different hadronization and fragmentation models. The jets used to compute the official efficiency maps were required to pass the following criteria:

- $p_T > 20$  GeV
- $|\eta| < 2.4$  GeV
- $JVT > 0.59$  for jets with  $p_T < 60$  GeV
- remove the overlapping electrons and muons in a cone of  $\Delta R = 0.3$  around the jet axis.

Besides its technical complexity, one disadvantage of the truth-tagging method comes from ignoring possible correlations between the b-tagging efficiency of different jets in an event or the dependence with respect to other kinematic variables (for example  $\Delta R$ ). As shown in Chapter 8, one possible solution to this problem is to recompute the efficiency maps for each specific process of the analysis, to reduce as much as possible the topological biases.

## 5.5 Summary

This Chapter described the design and the performance of all the basic and high-level b-tagging algorithms used for the identification of b-jets in Run-2. Improvements in the Run-1 taggers have been implemented, resulting in more performant flavour-tagging algorithms available for the 2017 ATLAS analyses campaign. Overall the new training procedure for  $MV2$  leads to a gain of approximately 40% in c-jet rejection at 77% b-jet efficiency with respect to the previous algorithm used for 2015 analyses [155].

8. POWHEG for the matrix element, interfaced with PYTHIA for the parton shower hadronisation and underlying events model and EVTGEN for heavy flavour decays



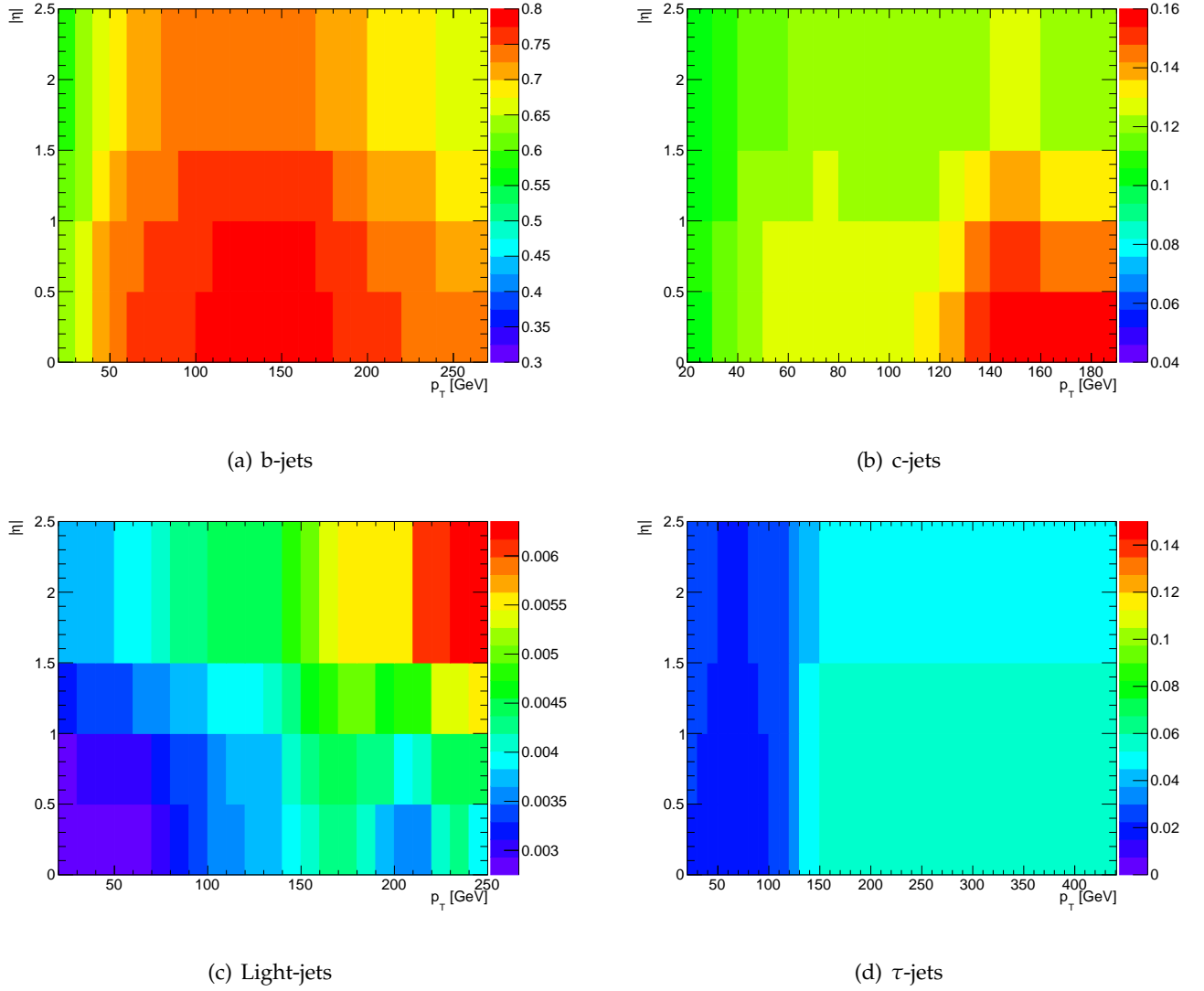


FIGURE 5.18 – Efficiency maps for b-, c-, light- and  $\tau$ - jets as a function of jet  $p_T$  and  $|\eta|$  for MV2c10 at 70% working point computed using  $t\bar{t}$  events generated by POWHEG+PYTHIA 8+EVTGEN. These maps were released in October 2018 by the ATLAS flavour tagging group.

Promising results are coming from alternative neural-network-based algorithms, such as IP RNN, being able to account for correlations among the different tracks. Different enhanced options containing a dedicated soft muon tagger algorithm are also available for testing, with an expected increase in light-jet rejection power.

The second part of the Chapter focused on the definition of efficiency for a b-tagging algorithm. At first order, and for isolated jets, the efficiencies are assumed to be independent of the physics process and therefore they can also be used to implement an alternative statistical method referred to as the *tag rate function* or *truth tagging*, to perform b-tagging on light- and c-jet dominated processes. The theoretical basis of this method has been described in this Chapter, while more details about the performance are given in Chapter 7 and Chapter 8. The data-driven techniques to extract the b-tagging efficiency calibration for b-, c- and light-jets were also described. These data-driven calibration techniques are leading to efficiency SF of the order of 1 for b-jets, 1.2 for c-jets and between 1.5 and 3 for light-jets, depending on the considered working point.



## 6 | Electron and photon energy calibration

Despite the smaller branching ratios, final states involving electrons and photons are often preferred to fully hadronic signatures at hadron colliders, because of their cleaner signal in the detector. An accurate energy determination of electrons (and photons) is therefore mandatory for many precision measurements at LHC, such as the measurement of the Higgs and W boson masses. Electron and photons are reconstructed from showers generated in the electromagnetic calorimeter (Figure 6.1). Their energy is defined as the sum of the energy deposits in the EM calorimeter cells by the shower, as described in Section 4.2. Due to finite dimensions of the cells or material interactions before the calorimeter, part of the initial object energy is lost when computing the energy sum, so a dedicated recovery procedure needs to be applied.

In ATLAS, the nominal electron and photon energy calibration is obtained mainly by the combination of Multi Variate Analyses (MVA) based on Monte Carlo and data-driven techniques exploiting  $Z \rightarrow ee$  decays. Further extrapolations of the systematic uncertainties are performed to account for differences in particle type (electrons/photons) and in the transverse momentum interval (low/high  $p_T$ ).

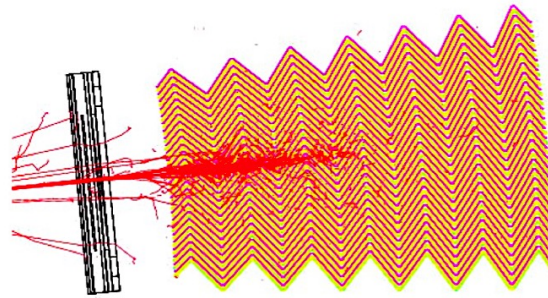


FIGURE 6.1 – Simulation of the shower shape development of a 10 GeV electron inside the ECAL performed with Geant4.

The discrepancies due to the different particle-type and  $p_T$  range must be quantified using alternative methods, in order to validate the calibration chain before applying it in physics analyses. This is what I was involved in during my first year of PhD. In particular, I tested the extrapolation of the systematic uncertainties for low energy electrons, deriving the energy calibration with a complementary and lower mass standard model candle ( $J/\psi$ ). The results are in good agreement with the  $Z \rightarrow ee$  extrapolation, with discrepancies of less than 1.5% in the whole pseudorapidity range. This study has not been directly applied to the VH,  $H \rightarrow bb$  analysis, which makes

use of higher  $p_T$  electrons. But it has been important for other Higgs boson precision measurements, such as the first Run-2 measurement of the Higgs boson mass in the four lepton channel [170], which makes use of electrons with a  $p_T$  threshold as low as 5 GeV [171].

This Chapter is an overview of the techniques used in ATLAS to perform the electron and photon energy calibration in Run-2. The calibration with low energy electrons is presented in more details in the second part of the Chapter.

## 6.1 Overview of the calibration procedure

The final reconstructed energy, as well as the energy resolution of electrons and photons, can suffer from inaccuracies due to several effects [172]:

- Energy loss due to material in front of the ECAL (i.e. cryogenic system, the inner tracker, the solenoid).
- Energy loss due to inactive material inside the ECAL (i.e. cables and LAr system).
- Lateral energy leakages outside the reconstructed cluster, due to the finite number of cells used to reconstruct the cluster.
- Longitudinal energy leakages behind the electromagnetic calorimeter for energetic particles not fully absorbed by the ECAL.

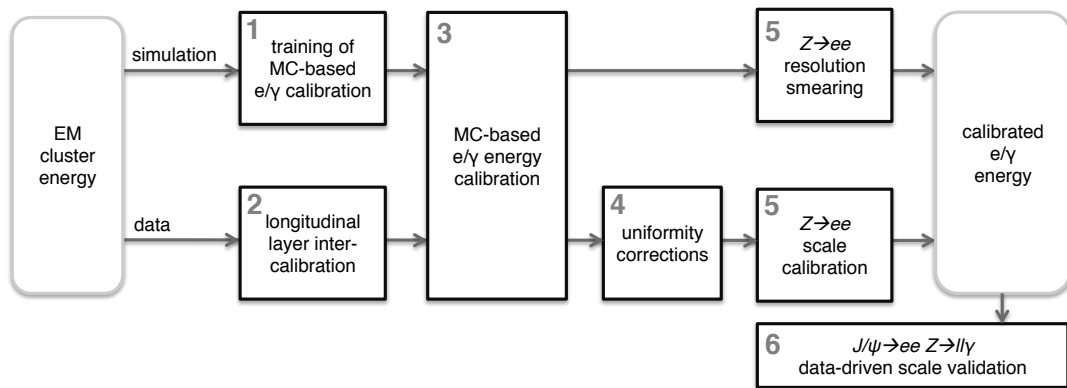


FIGURE 6.2 – Schematic overview of the procedure used to calibrate the energy response of electrons and photons in ATLAS [99].

The simple sum of the energy deposits in the calorimeter is referred to as the raw energy  $E_{raw}$  of the cluster<sup>1</sup>.

The goal of the calibration is to quantify the total energy loss using measurable quantities and recover the bias between  $E_{raw}$  and the true energy of the particle. The different steps of the procedure are shown in Figure 6.2, and they can be summarized as follows:

- The properties of the electromagnetic shower are combined in a multivariate algorithm based on a Boosted Decision Tree and the raw energy of the cluster is calibrated to the original (truth) energy in simulated MC samples. This correction is applied both to data and simulated samples and it represents the core of the calibration procedure.

1. The  $E_{raw}$  energy is obtained converting the electric signal induced in the LAr gaps. The signal is amplified, shaped and sampled (at a rate of 40 MHz). The sampled signal is digitized by ADC converters and the digitized samples are then converted in energy deposits using a hardware calibration, periodically updated to follow the data taking conditions. More details are given in Ref. [173].

- The ECAL has a multiple layers design as described in Section 3.2.4. In order to ensure a uniform response, the relative energy scales of the different layers must be adjusted in data. This is valid also for local non-uniformity corrections, such as non-nominal HV settings, geometric effects or biases associated with the LAr calorimeter electronic calibration.
- An in-situ calibration based on  $Z \rightarrow ee$  events is used to correct for remaining discrepancies between data and MC after the previous two calibration steps. In data, the energy scale is corrected such that the position of the di-electron invariant mass peak is equal to the expectations from MC. Then, corrections to match the energy resolution in data and MC are derived and applied to the simulation.
- The calibrated energy scales are validated with two cross-checks: at lower energies using electrons from  $J/\psi \rightarrow ee$  decays and with photons from radiative  $Z \rightarrow ll\gamma$  events ( $l = \mu, e$ ).

More details about each step of the calibration procedure are given in the following Sections.

## 6.2 Simulation based energy calibration

The simulation based calibration [174] is the first step and it aims at recovering the energy loss outside the cluster and the loss due to passive material. A set of variables sensitive to the energy response is used to train a BDT-based regression on simulated single electrons and photons. The list of variables used for the 2015-2016 training campaign is presented in Table 6.1. One prerequisite for these variables is a good data/simulation agreement of the distributions, to avoid overcorrections or distortions. The BDT optimisation is performed separately for electrons, converted and unconverted photons and the resulting multivariate calibration is then applied to data as well as simulation.

The output of the regression BDT is the correction  $E_{true}/E_{acc}$ , which applied back to  $E_{acc}$  should give a calibrated value ( $E_{calib}$ ) close to  $E_{true}$ . Multivariate regression algorithms generally aim at minimising the root mean square (RMS) between observed and predicted values [175]. This leads to an optimisation in which the mean value of the output energy  $E_{calib}$  is close to  $E_{true}$ , but not necessarily equal to it. This is true especially for low  $E_T$  electrons, for which the energy response is not completely Gaussian, but exhibits tails mostly due to bremsstrahlung in the material upstream the calorimeter. Figure 6.3(a) shows the  $E_{calib}/E_{true}$  distribution for electrons with  $E_T$  between 50 and 100 GeV and  $|\eta|$  in the 1.4-1.6 region. The distribution is peaked at 1, with a standard deviation  $\sigma$  of  $\sim 3\%$  evaluated with a Gaussian fit. Figure 6.3(b) shows the related relative effective energy resolution ( $\sigma/E$ ) as a function of  $|\eta_{cluster}|$  for different true transverse energies. The values are varying between 1% and 8% depending on the electron energy, with a peak of  $\sim 10\%$  in the transition region for  $5 < E_T < 10$  GeV electrons.

## 6.3 Layer intercalibrations

To ensure a uniform response in  $p_T$  (linearity), the relative energy scales of the different layers must be adjusted in data before estimating the energy of the electron or photon. This step is performed using muon energy deposits in the calorimeter. Being charged minimum ionizing particles (MIP), muons are essentially insensitive to the amount of material upstream the EM calorimeter, their energy deposit is a

Variable	Description
$E_{acc}$	$E_{acc} = E_{s1}^{raw} + E_{s2}^{raw} + E_{s3}^{raw}$ total raw cluster energy, defined as the sum of the uncalibrated <sup>2</sup> energies of the various layers (strips, middle and back).
$E_{s0}^{raw} / E_{acc}$	Ratio of the energy in the presampler to the total raw cluster energy, used only for clusters in the acceptance of the presampler ( $ \eta  < 1.8$ ).
$E_{s1}^{raw} / E_{s2}^{raw}$	Ratio of the energy in the first accordion layer to the second one.
$\eta_{cluster}$	Pseudorapidity in the ATLAS frame (i.e. taking into account the misalignment of the detector).
$\eta_{calo} / \Delta\eta$	Cell index: an integer identifying a cell in the middle layer, with $\eta_{calo}$ the pseudorapidity of the cluster in the calorimeter frame and $\Delta\eta = 0.025$ is the size of one cell in the middle layer.
$\eta_{edge}$	It is defined as $\eta_{calo} \bmod$ the width of one cell of the middle layer ( $\Delta\eta = 0.025$ ). It corrects for variations in the lateral energy leakage, which are larger when the particle hits close to the cell edge.
$\phi_{abs}$	$\phi_{calo}$ with respect to the lead absorbers, with a periodicity of the lead sheets in the calorimeter of $2\pi/1024$ ( $2\pi/768$ ) in the barrel (end-cap). It corrects for variations in the sampling fraction as a function of $\phi$ . It is defined as $\phi_{calo} \bmod 2\pi/1024$ ( $2\pi/768$ ).
$E_4$	Energy deposited in the "crack" scintillator cells (part of the Tile calorimeter in $1.4 <  \eta  < 1.6$ , with $\Delta\eta \times \Delta\phi = 0.1 \times 0.1$ ).
$\Delta\phi = \phi_{cluster} - \phi_{E_4}$	Difference between the cluster position and the centre of the $E_4$ cell.

TABLE 6.1 – Discriminating variables used in the BDT to match  $E_{raw}$  to  $E_{true}$ . Additional variables are used for converted photons and summarized in Ref. [174].



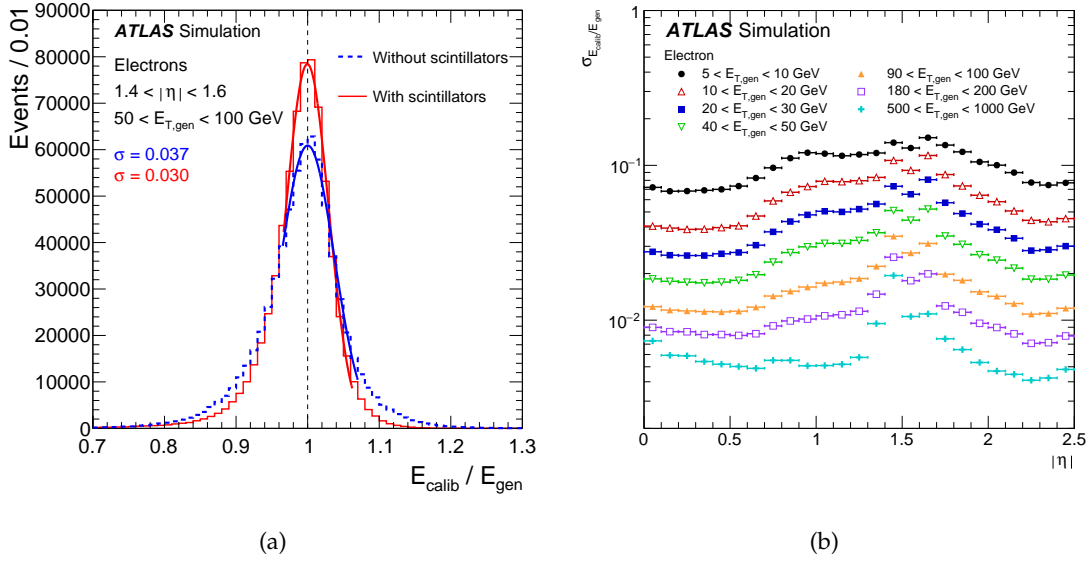


FIGURE 6.3 – (a) Distribution of the calibrated energy  $E_{calib}$ , divided by the generated energy  $E_{true}$ , for electrons with  $1.4 < |\eta| < 1.6$  and  $50 < E_{T,true} < 100$  GeV. The dashed (solid) histogram shows the results based on the energy calibration without (with) the scintillator information, while the curves represent Gaussian fits to the cores of the distributions. (b) Relative  $\sigma/E$  resolution as a function of  $|\eta|$  for electrons at different energies [173].

direct measurement of the total active material (LAr) the traversed. This energy can, however, be incorrectly reconstructed due to cross-talk or electronics effects. The purpose of this calibration is to correct for those non-linearities and restore good energy response in the EM calorimeter disentangling pure calibration from material effects. The measured muon energy is typically 60 MeV in the strips and about 210 MeV in the middle layer, with a signal to noise ratio of about three [176]. Furthermore, muon energy deposits are quite localised, most of the energy being reconstructed in one or two cells.

A correction factor  $\alpha_{1/2}$  is extracted as a double ratio of the energy deposits in the first and second calorimeter layer in data and simulation:

$$\alpha_{1/2} = \frac{\langle E_{1/2}^{\text{data}} \rangle}{\langle E_{1/2}^{\text{MC}} \rangle}, \quad (6.1)$$

where  $\langle E_{1/2} \rangle = E_1/E_2$  is the ratio of the most probable values (MPV) of the energy deposited by a particle in the first and the second layer of the EM calorimeter.

The observed muon energy distribution in each layer is given by the convolution of a Landau distribution describing the energy deposit, and a noise distribution to account for electronic and pile-up noise. The MPV of the deposited energy is extracted in different  $\eta$  bins using either an analytic fit or a truncated mean (TM) method. In the first method, the MPV is extracted from a fit of the convolution function to the observed muon energy distribution. The noise distribution is determined from templates computed separately in data and simulation and for each  $\eta$  bin. The templates in data are determined from events triggered on random LHC bunch crossing, with a trigger rate proportional to the instantaneous luminosity ("zero-bias events"). Such events are not available in simulation, so the MC templates are built looking at the energy in cells far from the particles, using dedicated single-particle samples.

The second method tries to estimate the mean energy of the distribution, but as the energy loss resembles a Landau distribution, with a long tail on the high values side, the mean cannot be analytically defined. The location of the Landau peak is then evaluated by computing the mean on a truncated range of this distribution. The nominal scale factors are obtained by averaging the results calculated with the two methods, and half of their difference is taken as an uncertainty in the result.

Due to a possible mismodelling in the simulation, pileup effects do not cancel in the double ratio, leading to remaining differences in the scales as a function of  $\mu$ . To correct for this effect, each  $\eta$  category is split in pileup bins of  $\Delta\mu = 1$  and the results are linearly extrapolated to a 0-pileup-like region. Zero pileup MC samples are used to validate the procedure. The final scale factors are presented in Figure

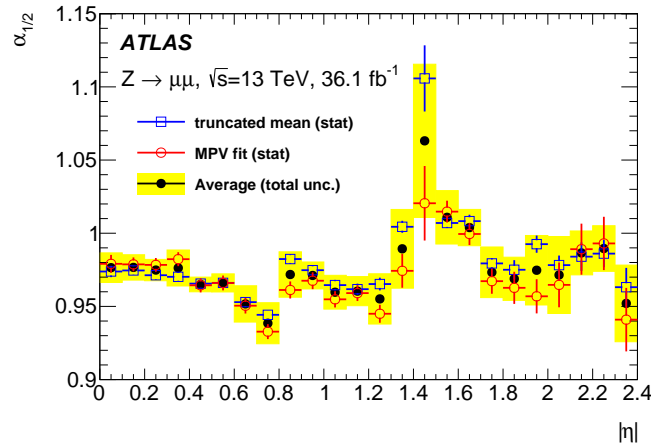


FIGURE 6.4 – The  $\alpha_{1/2}(\eta)$  corrections obtained from the study of the muon energy deposits in the first two layers of the calorimeter. The results from the two methods are shown with their statistical uncertainties. The final average measurement is shown with its total uncertainty including the statistical and systematic uncertainties [173].

6.4 as a function of the muon pseudorapidity. The main sources of systematic uncertainty affecting the measurement are: the modeling of the energy loss outside the cells (uncertainty between 0.5% to 1%), the accuracy of the pile-up extrapolation in MC (uncertainty between 0.2% and 1.5%), the choice of the cell in  $\phi$  ( $\sim 0.2\%$  uncertainty), change the range for the calculation of the truncated mean ( $\sim 0.5\%$  uncertainty) and, as said before, half of the difference between the MPV and the truncated-mean methods (uncertainty between 0.5% and 1%) [177].

When performing the E1/E2 calibration, the "true" energy loss by the muon in the active area of the calorimeter is assumed to be perfectly simulated in the Monte-Carlo. Additional systematic uncertainties on the amount of cross talk in the cells and other effects changing the true energy loss are taken as systematic uncertainties on the scales. Furthermore, the layer scales must be extrapolated to electrons and photons before being applied, and this process can be impacted by geometry. The total uncertainty on this extrapolation is visible in Figure 6.8, under the label  $\alpha_{1/2}(\mu \rightarrow e)$ . The single sources contributing to this uncertainty were defined in Run-1 and they have not changed for the Run-2 measurement [178]. The main sources are: the uncertainty on the effective geometry of the area between the two layers (active area, location of the transition), the uncertainty on the cross-talk between L1 and L2 and within the cells of the same layer, the difference on the lateral shower profile in data and MC for electrons (and photons) and the uncertainty on the effective charge collection in

LAr. Finally, the scales are applied to the data as an  $|\eta|$ -dependent correction to the energy measured in the middle layer ( $E_{corr} = E_2 \times \alpha_{1/2}$ ).

For most EM showers, the bulk of the particle energy is deposited into the second calorimeter layer, while the third layer usually does not absorb a significant fraction of the energy and serves mostly to quantify the amount of energy "leaking" out into the hadron calorimeter. Its impact on the electron and photon calibration is negligible, therefore no dedicated intercalibration of the back layer has been carried out.

A thin presampler (PS) layer is installed in front of the accordion calorimeter in the pseudorapidity interval  $|\eta| < 1.8$ , as described in Section 3.2.4. This layer is used to correct for the energy loss upstream the calorimeter. The PS energy scale  $\alpha_{PS}$  is defined as the ratio of the PS energy ( $E_0$ ) in data and MC simulation and is estimated using electrons from Z boson decays. Prior to the measurement, the effects on  $E_0$  of the mismodellings in the amount of passive material upstream the PS (i.e. read-out cables, cooling systems, support infrastructures) must be taken into account, since they would result in an apparent PS energy scale bias.

The longitudinal profile of electromagnetic showers can be used to quantify the relative abundance of material in a specific region of the detector. In particular, the relative amount of energy deposited into the first and second accordion layers depends significantly on where the shower is initiated. Higher values of  $E_{1/2}$  in data than in simulation indicate an earlier shower development, and hence a local excess of material in comparison with the simulation. Conversely, relatively late shower development, and so lower values of  $E_{1/2}$ , would imply that the region has lower amounts of material than in simulation.

The measured PS energy scale  $\alpha_{PS}$  is thus:

$$\alpha_{PS}(\eta) = \frac{E_0^{\text{data}}(\eta)}{E_0^{\text{corr}}(\eta)}, \quad (6.2)$$

where  $E_0^{\text{corr}}$  is the PS energy in the simulation after applying the various material corrections. Since the amount of passive material upstream the calorimeter leading to energy loss and to miscalibrations of the electron energy scales varies in pseudorapidity, the energy scale corrections  $\alpha_{PS}$  are computed as a function of  $\eta$ .

Taking into account the correlation between the ratio  $E_{1/2}$  and the PS energy at a given  $\eta$ ,  $E_0^{\text{corr}}$  can be parameterized as follows:

$$\frac{E_0^{\text{corr}}(\eta)}{E_0^{\text{MC}}(\eta)} = 1 + A(\eta) \left( \frac{E_{1/2}^{\text{data}}(\eta)}{E_{1/2}^{\text{MC}}(\eta) b_{1/2}(\eta)} - 1 \right), \quad (6.3)$$

where  $A(\eta)$  is the correlation factor, estimated from simulations with various amounts of additional material upstream the PS and  $b_{1/2}(\eta)$  is the correction for the passive material between the PS and L1, estimated in data from unconverted photons with low PS activity.  $E_{1/2}(\eta)$  is the ratio of the energy in the first and second layer of the ECAL as described above. In data the  $E_2(\eta)$  in the  $E_{1/2}(\eta)$  ratio has been corrected by the scale factors derived with muons as described in the previous paragraph. The PS energy corrections  $\alpha_{PS}$  are extracted averaging  $E_0^{\text{data}}(\eta)/E_0^{\text{corr}}(\eta)$  over pseudorapidity intervals corresponding to the presampler module size (i.e.  $\Delta\eta = 0.2$  in the barrel and  $\Delta\eta = 0.3$  in the end-caps). As shown in Figure 6.5, the corrected measurement are uniform at the 2-3% level, depending on  $\eta$ .

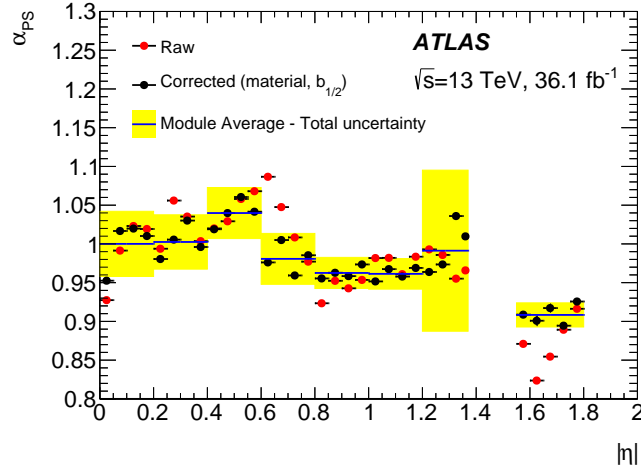


FIGURE 6.5 – Ratio of the average PS energies,  $E_0^{\text{data}}/E_0^{\text{MC}}$ , for electrons in data and simulation as a function of  $|\eta|$ , before and after corrections for  $b_{1/2}$  and material upstream of the PS. The full lines with shaded bands represent the PS energy scale as a function of  $|\eta|$ ,  $\alpha_{PS}(\eta)$ , and its uncertainty [173]. The peak at 0.7 for the uncorrected values is due to a change in the amount of TRT material as shown in Figure 3.6.

## 6.4 Uniformity corrections

Additional corrections are needed in data to counterbalance inhomogeneities in the high-voltage and energy loss in the inter-module spaces between the barrel ECAL modules not present in the simulation. For example, the liquid argon gaps in-between the 16 barrel modules are slightly larger than the gaps within the modules, causing an underestimation of the measured energy in these regions. The gaps are further altered in  $\phi$  due to gravity distortions, which causes the gaps to be smaller at the bottom and larger at the top. The correction is obtained using the ratio  $E/p$  of the calorimeter energy to the track momentum as a function of  $\phi$  and it is observed to be up to 2% [179].

Some specific sectors ( $\Delta\eta \times \Delta\phi = 0.2 \times 0.2$ ) use non-nominal HV settings for the readout of the electromagnetic calorimeter. This effect is, in principle, already corrected at reconstruction level. However, residual effects can still arise, for example in case of large currents. An empirical correction is extracted from the  $E/p$  profiles in data computed for these regions, to restore a uniform response in the whole  $\eta - \phi$  plane. The correction factors are between 1% and 7% and they are applied to 2% of the calorimeter acceptance (considering only  $|\eta| < 2.5$ ). These corrections are validated using  $Z \rightarrow ee$  events.

## 6.5 In-situ energy scale and resolution corrections

After the previous corrections have been applied, the remaining discrepancies between data and simulation are quantified using in-situ calibration techniques. The origin of these discrepancies is not precisely known (e.g. temperature can be one factor); the in-situ calibration corrects the effects based on a data to MC comparison of  $Z \rightarrow ee$  events. In data, the energy scale is corrected such that the position of the Z mass peak matches the expectations from the simulation. Energy scale factors are derived in bins of  $\eta$  and applied on the energy of electron and photon candidate objects. At the same time, corrections to match the energy resolution in data and

MC are derived and applied to the simulation. Additional systematic uncertainties are derived to account for the electron-to-photon extrapolation.

The energy miscalibration  $\alpha(\eta)$  is quantified as the relative difference in response between data and simulation and is parameterized as:

$$E_{\text{reco}}^{\text{Data}}(\eta) = E_{\text{reco}}^{\text{MC}}(\eta)(1 + \alpha(\eta)) \quad (6.4)$$

where  $E_{\text{reco}}^{\text{Data}}$  is the reconstructed electron energy in data and  $E_{\text{reco}}^{\text{MC}}$  is the reconstructed electron energy in the simulation.

The invariant mass of a reconstructed  $Z \rightarrow ee$  candidate can be written as:

$$m_{ee}^2 = 2E_i E_j (1 - \cos \theta_{ij}), \quad (6.5)$$

where  $E_i$  and  $E_j$  are the energies of the two electrons corrected by all the factors described so far and  $\theta_{ij}$  is the angle between the electrons measured by the inner detector. The  $\theta_{ij}$  angle for electrons at 40 GeV is known with a resolution of  $\sim 10^{-4}$  rad according to [180] (Figure 3.6). Thus, the impact of the  $\theta_{ij}$  resolution on the final di-electron mass can be neglected. The effect of the electron energy miscalibration on the di-electron invariant mass is:

$$m_{ee}^{\text{Data}} \simeq m_{ee}^{\text{MC}} \left( 1 + \frac{\alpha_i + \alpha_j}{2} \right), \quad (6.6)$$

where  $m_{ee}^{\text{Data}}$  ( $m_{ee}^{\text{MC}}$ ) is the reconstructed di-electron mass in data (MC), and second-order terms in the  $\alpha_i$ 's have been neglected due to the smallness of such factors. The "reco" label is omitted for simplicity and the  $\frac{\alpha_i + \alpha_j}{2}$  term can be referred to as  $\alpha_{ij}$ . Additionally, since the relative resolution of the ECAL can be written as in Equation 3.9 in Section 3.2.4, and that  $c$  is one of the dominant terms for  $Z \rightarrow ee$  electrons<sup>3</sup>, the corrections to match the MC resolution to the one in data can be parameterized as an additional constant term  $c_i$  in the resolution formula:

$$\left( \frac{\sigma}{E} \right)_{\text{Data}} = \left( \frac{\sigma}{E} \right)_{\text{MC}} \oplus c'_i \quad (6.7)$$

Similarly to the energy scales, the smearing of the single-electron energy from Equation 6.7 propagates to the invariant mass of two electrons falling in  $\eta_{\text{calo}}$  bins  $i$  and  $j$  in the following way:

$$\left( \frac{\sigma(m_{ij})}{m_{ij}} \right)_{\text{Data}}^2 \simeq \frac{1}{4} \left( \left( \frac{\sigma(E_i)}{E_i} \right)_{\text{data}}^2 + \left( \frac{\sigma(E_j)}{E_j} \right)_{\text{data}}^2 \right) \quad (6.8)$$

$$= \frac{1}{4} \left( \left( \frac{\sigma(E_i)}{E_i} \right)_{\text{MC}}^2 + c_i'^2 + \left( \frac{\sigma(E_j)}{E_j} \right)_{\text{MC}}^2 + c_j'^2 \right) \quad (6.9)$$

$$= \left( \frac{\sigma(m_{ij})}{m_{ij}} \right)_{\text{MC}}^2 + \frac{c_i'^2 + c_j'^2}{4}, \quad (6.10)$$

Considering the effective correction  $c'_{ij}$  to apply on both electrons, the additional constant term in the MC energy resolution has an effect on the mass resolution such

3. And assuming the  $a$  and  $b$  terms well known from external measurements.

that:

$$\left( \frac{\sigma(m_{ij})}{m_{ij}} \right)_{\text{Data}}^2 = \left( \frac{\sigma(m_{ij})}{m_{ij}} \right)_{\text{MC}}^2 + \frac{c_i'^2 + c_j'^2}{4} = \left( \frac{\sigma(m_{ij})}{m_{ij}} \right)_{\text{MC}}^2 + \frac{c_{ij}^{\prime 2}}{2} \quad (6.11)$$

leading to:

$$c_{ij}^{\prime 2} = \frac{c_i'^2 + c_j'^2}{2} = \frac{c_i' \oplus c_j'}{2} \quad (6.12)$$

The quantities  $\alpha_{ij}$  and  $c_{ij}'$  are evaluated independently for each  $(\eta_i, \eta_j)$  configuration of the two electrons. The corrections are extracted using the so-called "template fit method". Another method, referred to as the "lineshape method", has been used as cross-check and the differences have been taken into account in the evaluation of the systematic uncertainties. Since this cross-check relies on the same procedure used for the  $J/\psi \rightarrow ee$  study, a detailed description will be given directly in Section 6.8.

In the template method, a set of template histograms of the invariant mass are created from the simulation, with extra values of energy scale  $\alpha_{ij}$  and resolution smearing  $c_{ij}'$  added to the nominal distribution as described before, in a range covering the expected uncertainty in narrow steps. The templates are built separately for the various electron pseudorapidity configurations  $(\eta_i, \eta_j)$ . Analog distributions are built in data for each  $(\eta_i, \eta_j)$  category. The templates are then compared to the data distribution fixing one of the two parameters at a time ( $\alpha_{ij}$  first and then  $c_{ij}'$ ).

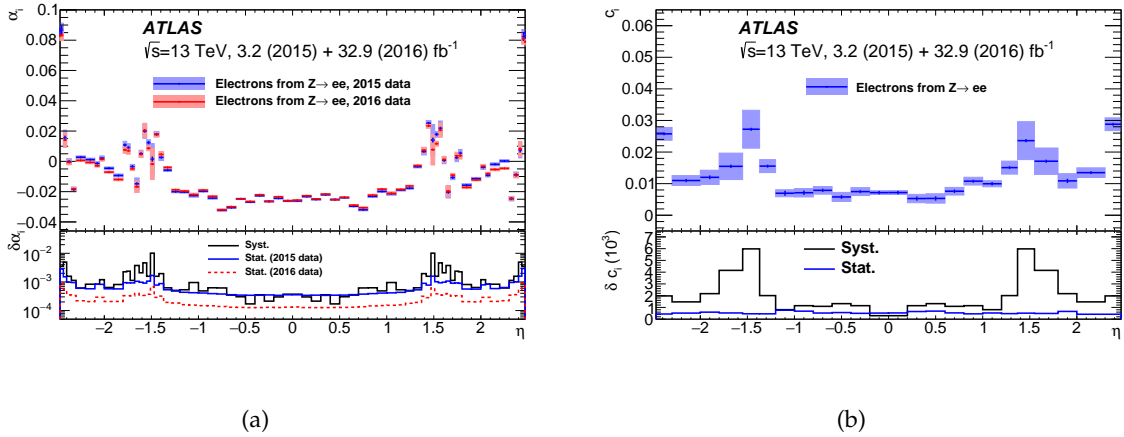


FIGURE 6.6 – Results of the data-to-MC calibration from  $Z \rightarrow ee$  events for (a) the energy scale corrections ( $\alpha_i$ ) and (b) the energy resolution corrections ( $c_i$ ) as a function of  $\eta$ . The systematic and statistical uncertainties are shown separately in the bottom panels [173].

The results are shown in Figure 6.6. The energy scale correction factors are typically of the order of 1-2%, with uncertainty around  $\sim 0.05\%$ , rising to 0.1% in particular regions of the acceptance affected by large amounts of material upstream of the calorimeter. The additional constant term varies between 0.7% and  $\sim 2\%$  for  $|\eta| < 2.4$ , with 0.4% as highest uncertainty. The energy scale factors and the additional constant terms are applied on data and MC respectively. The calibrated  $Z \rightarrow ee$  mass distribution is shown in Figure 6.7. Data and simulation are now compatible within the systematic uncertainties. A combination of multiple residual effects creates the non-linear shape of the data/MC ratio shown in the Figure, for example,

the slope at low values comes mainly from a residual QCD contamination passing the event selection, while the difference at higher values is mainly due to material effects. In both cases, the difference is covered by systematic uncertainties.

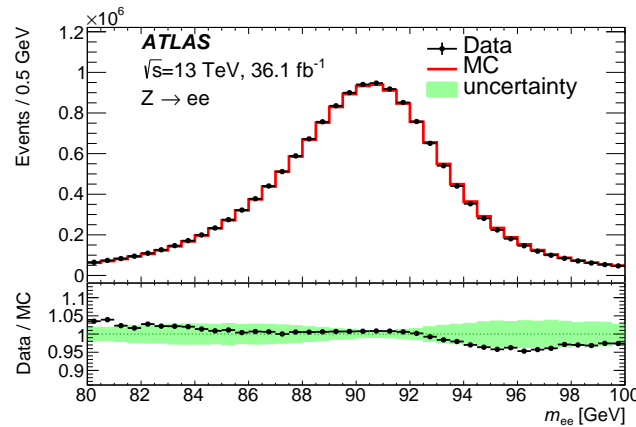


FIGURE 6.7 –  $Z \rightarrow ee$  mass distribution around the Z-mass peak for data (black) and MC (red) after applying the in-situ calibration. The calibrated data distribution is shown without applying any background subtraction and the simulation is normalised to data. The green band in the bottom panel corresponds to the total scale factors systematic uncertainty [173].

## 6.6 Systematic uncertainties

The full model of the energy scale uncertainties consists of 64 independent nuisance parameters (see Section 7.4.2), while the full model of the energy resolution uncertainties consists of 9 independent nuisance parameters. The total systematic uncertainty is the sum in quadrature of all the single independent uncertainty sources. Figure 6.8 shows the main sources of uncertainty on both energy scale and energy resolution for electrons with  $|\eta| < 0.3$  and energy  $5 \text{ GeV} < E_T < 200 - 500 \text{ GeV}$ . The uncertainties are also listed below.

- *Layer intercalibration*: The impact of PS and L1/L2 layer intercalibrations are taken into account with 5 dedicated uncertainties, varying in  $\eta$ . Two for the  $\alpha_{1/2}$  measurement and three for the PS calibration. An additional uncertainty is added for the calibration of the gap scintillators ( $1.4 < |\eta| < 1.6$ ).
- *Cell energy non-linearity*: The uncertainty on the gain intercalibration is taken into account separately for Layer 1 and 2. These uncertainties are determined from  $Z \rightarrow ee$  events in normal running conditions and special run data. No segmentation in  $\eta$  is assumed. The typical gain uncertainties are  $\sim 0.10 - 0.15\%$  in the barrel and  $\sim 0.3 - 0.5\%$  in the end-caps for unconverted photons with  $E_T = 60 \text{ GeV}$ .
- *Material*: The impact of the material upstream the calorimeter is covered by 11 uncertainties. Among them, 3 account for the uncertainty in the inner detector material, taken from detector construction reports, while the others correspond to the uncertainty in the material between the inner detector and the calorimeter. Different values of the systematic uncertainties are applied in regions with and without the presampler.
- *Lateral shower shape modelling*: The electron energy response as a function of the shower width (in the  $\eta$  direction) can differ in data and simulation. Their



difference is taken as systematic uncertainty for the calibration. Furthermore, an imperfect modelling of the lateral shower development in the simulation can lead to a wrong lateral leakage description in simulation. Dependence on shower  $\eta$  width. The in-situ energy calibration absorbs this MC-data discrepancy only for electrons, while for photons there are two dedicated uncertainties accounting for the lateral leakage in converted and unconverted photons.

- *Z  $\rightarrow ee$  calibration:* The total systematic uncertainty on the in-situ calibration is extracted as the sum of different sources of uncertainty, like the mass window variation, the event and electron selection, trigger, identification and reconstruction efficiencies, bremsstrahlung electrons, pile-up, background impact and closure of the method. An accurate description of the different systematic uncertainties is given in Ref. [111].
- *Photon-specific uncertainties:* Three types of uncertainty are specifically added in case of converted and unconverted photons. The first one covers the imperfect descriptions of the conversion efficiency, while the second accounts for the different conversion fake rate in data and simulation. The third covers the uncertainty on the radius chosen for the track-cluster association. In fact, larger radii increase the probability for pileup induced tracks or fake tracks to be associated with an EM energy cluster.

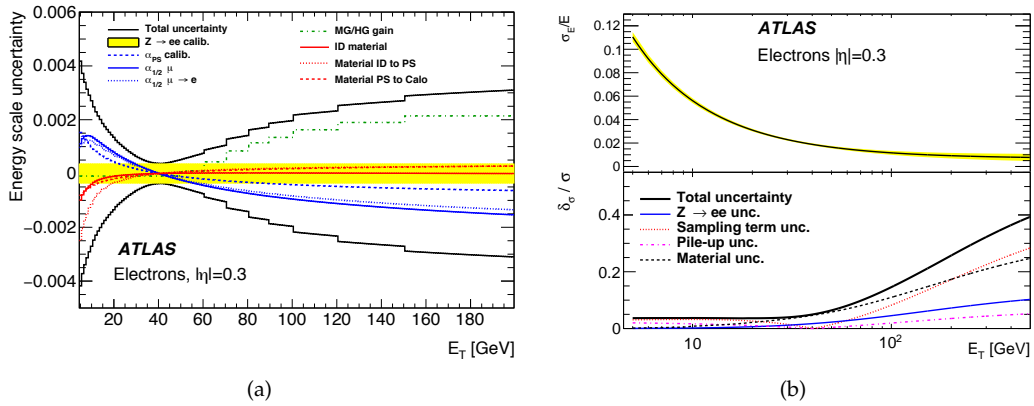


FIGURE 6.8 – Fractional energy scale calibration uncertainty for (a) electrons as a function of  $E_T$  for  $|\eta|=0.3$ . The total uncertainty is shown as well as the main contributions, which are represented by the signed impact of a one-sided variation of the corresponding uncertainty. Relative energy resolution,  $\sigma(E)/E$ , as a function of  $E_T$  for electrons at  $|\eta| = 0.3$ . The yellow band in the top panel shows the total uncertainty in the resolution. The breakdown of the relative uncertainty in the energy resolution,  $\delta\sigma/\sigma$  is shown in the bottom panel. [173].

The systematic uncertainties for electrons from  $Z \rightarrow ee$  events are entirely obtained from the  $Z \rightarrow ee$  calibration described above. Since the  $Z \rightarrow ee$  events give access mainly to electrons at  $\langle E_T^{e(Z \rightarrow ee)} \rangle \sim 40$  GeV, the effect of these uncertainties needs to be extrapolated at different energies (and particle-types) as follows:

$$\delta E_i^{e,\gamma}(E_T, \eta) = \Delta E_i^{e,\gamma}(E_T, \eta) - \Delta E_i^e(\langle E_T^{e(Z \rightarrow ee)} \rangle, \eta). \quad (6.13)$$

where  $\Delta E_i(E_T, \eta)$  is the total change in energy induced by the source  $i$  as a function of  $E_T$  and  $\eta$ . This effect is partially absorbed by the Z-based effective calibration for electrons of  $E_T \sim \langle E_T^{e(Z \rightarrow ee)} \rangle$ , with a net change in energy of  $\delta E_i^{e,\gamma}$ . The effect on the

energy can be positive or negative with a possible change of sign near  $\langle E_T^{e(Z \rightarrow ee)} \rangle$ . In case of electrons with  $E_T$  around 40 GeV the total uncertainty on the scales is 0.02% in the barrel and 0.1% in the end-caps. For electrons of 10 GeV the total uncertainty varies up to 0.5% in the barrel and 0.8% in the end-caps.

## 6.7 Photon calibration with $Z \rightarrow ll\gamma$ events

The scale factors extracted from  $Z \rightarrow ee$  events are assumed to be valid also for photons, within the uncertainties estimated as explained in the previous paragraph. This assumption is validated using photons from radiative  $Z \rightarrow ll\gamma$  events, with  $l$  being  $\mu$  or  $e$ . Photon energy scales are computed for the muon and electron channels separately and as a function of different photon properties, such as conversion status, energy and pseudo-rapidity. The photon energy scales (PES) can be parameterized with a standard correction to the individual photon energy as:

$$E_T^{\gamma, \text{Data}} = E_T^{\gamma, \text{MC}} (1 + \alpha_\gamma), \quad (6.14)$$

where  $E_T^\gamma$  is the energy after the full standard calibration, and  $\alpha_\gamma$  is the scaling factor term applied to the photon energy. To reduce as much as possible the impact of the lepton energy and momentum scales, the measured three-body invariant mass is divided by the measured two-body decay mass, leading to the following double ratio:

$$R(\alpha) = \frac{\langle m(ll\gamma(\alpha))_{\text{data}} \rangle / \langle m(ll)_{\text{data}} \rangle}{\langle m(ll\gamma)_{\text{MC}} \rangle / \langle m(ll)_{\text{MC}} \rangle} \quad (6.15)$$

where  $\langle m_{ll\gamma} \rangle$  and  $\langle m_{ll} \rangle$  are the measured MPV of the three-body and two-body invariant mass. A sample of  $Z$  bosons decaying into two leptons, with no photon requirement, is used to extract the  $\langle m_{ee} \rangle$  and  $\langle m_{\mu\mu} \rangle$  two-body mass measurement. The central value of  $\alpha_i$  in a specific bin is determined from the condition  $R(\alpha) = 1$ . As shown in Figure 6.9 the discrepancies with the  $Z \rightarrow ee$  based calibration are less than 0.4% throughout the entire ECAL pseudo-rapidity region and covered by the uncertainty of the calibration procedure.

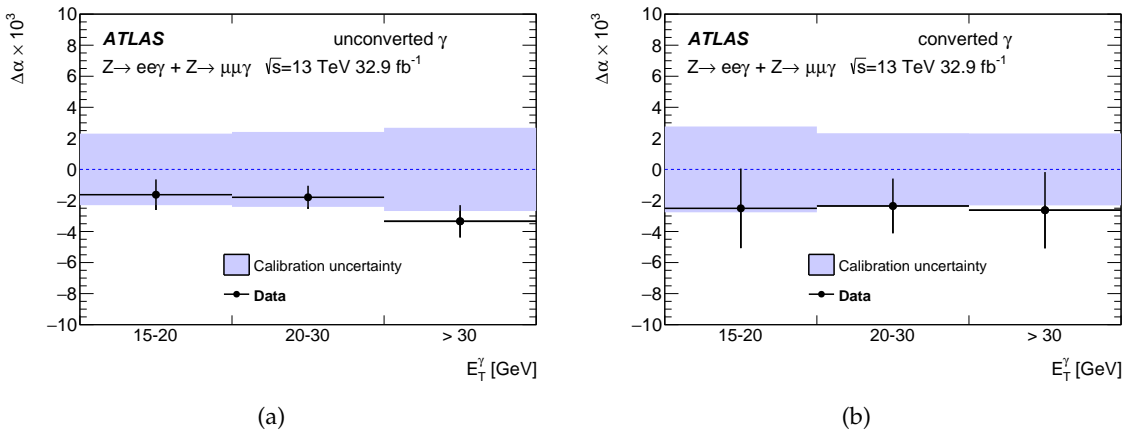


FIGURE 6.9 – Energy scale factor,  $\Delta\alpha$ , for (a) unconverted and (b) converted photons with their uncertainties. The points show the measurement with its total uncertainty. The superimposed band represents the full energy calibration uncertainty for photons from  $Z \rightarrow ll\gamma$  decays. [173].

## 6.8 Low-momentum electron energy calibration

The average energy of electrons coming from  $J/\psi \rightarrow ee$  decays varies between 12 GeV in the barrel and 28 GeV in the end-caps. Thus, this alternative SM "candle" represents a perfect probe to test the calibration at energies much lower than the Z peak. Prior to the measurement, the nominal corrections obtained from  $Z \rightarrow ee$  events are applied, so the measure focuses only on the miscalibrations due to the change in the electron energy.

The method used to extract the energy scale corrections follows closely the one used in Run-1 [181] and is briefly summarised here. Any miscalibration of the electron energy can be parameterized as in Equation 6.4 and its impact on the di-electron invariant mass follows the calculation explicited for the  $Z \rightarrow ee$  case, leading to equation 6.6, reported here for completeness:

$$m_{ee}^{\text{Data}} \simeq m_{ee}^{\text{MC}} \left( 1 + \frac{\alpha_i + \alpha_j}{2} \right),$$

where  $m_{ee}^{\text{Data}}$  ( $m_{ee}^{\text{MC}}$ ) is the reconstructed di-electron mass in data (MC) from  $J/\psi \rightarrow ee$  events, and second-order terms in the  $\alpha_i$ 's have been neglected due to the smallness of such factors.

Thus, the reconstructed distribution of the dielectron  $J/\psi$  peak in data ( $m_{ee}^{\text{Data}}$ ) and in the simulation ( $m_{ee}^{\text{MC}}$ ) are compared in an interval around the  $J/\psi$  mass. This allows for a measurement of the energy scale correction  $\alpha$  in intervals of the electron pseudorapidity. Such corrections are determined by minimising an unbinned log-likelihood:

$$-\ln L_{\text{tot}} = \sum_{k=1}^{N_{\text{events}}} -\ln L_{ij} \left( \frac{m_{ee}^{(k)}}{1 + \frac{\alpha_i(k) + \alpha_j(k)}{2}} \right), \quad (6.16)$$

with  $0 < i, j < N_{\text{regions}}$ ,  $i$  and  $j$  being the pseudorapidity regions (or categories) with the leading electron in the  $i^{\text{th}}$  pseudorapidity bin and the other electron in the  $j^{\text{th}}$  pseudorapidity bin.  $N_{\text{events}}$  is the total number of selected events and each event is related to just one  $ij$  category.  $L_{ij}(m_{ee} | \alpha_i \alpha_j)$  is the probability density function (PDF) describing the  $m_{ee}$  distribution in MC for the  $ij$  category: the number of categories have been reduced assuming  $L_{ij} = L_{ji}$ . The PDFs ( $L_{ij}(m_{ee})$ ) are produced separately for each configuration ( $\eta_i, \eta_j$ ) using the following binning:

$$[\pm 0, \pm 0.4, \pm 0.8, \pm 1.10, \pm 1.37, \pm 1.52, \pm 2.40] \quad (6.17)$$

The statistics collected in Run-2 is much smaller than in Run-1 [111], due to a heavier prescaling of the  $J/\psi \rightarrow ee$  triggers. This binning was chosen to maintain the statistical uncertainties below  $10^{-3}$  in the barrel region.

The fit on the two electrons invariant mass has been also extended to the resolution variables, in order to measure the energy resolution of low  $E_T$  electrons. This directly probed some of the parameters used to describe the energy resolution of the ATLAS electromagnetic calorimeter described in Section 3.2.4. In particular,  $J/\psi \rightarrow ee$  electrons are good probes for the measurement of the sampling term of the energy resolution formula. In fact, at their typical energies, the effect of the sampling term is expected to be significantly larger than the one of the constant term, and larger or comparable in size to the noise term. Assuming the constant term and the noise term well known from  $Z \rightarrow ee$  and zero-bias (pile-up only) events respectively, as described in Section 3.2.4, then the resolution corrections can be parameterized

as:

$$\left(\frac{\sigma}{E}\right)_{\text{Data}} = \left(\frac{\sigma}{E}\right)_{\text{MC}} \oplus \frac{\Delta a}{\sqrt{E}} \quad (6.18)$$

with  $\Delta a/\sqrt{E}$  an extra sampling term. A detailed description of the procedure to extract both energy scales and energy resolution factors is given in the next Sections.

### 6.8.1 Data and simulated samples

#### Data samples

The analysis is performed on  $\sqrt{s} = 13$  TeV  $pp$  collision data collected in 2015 and 2016. The data have been collected using an OR of the following  $J/\psi \rightarrow ee$  triggers:

- HLT\_e5\_lhtight\_nod0\_e4\_etcut\_Jpsiee
- HLT\_e9\_lhtight\_nod0\_e4\_etcut\_Jpsiee
- HLT\_e14\_lhtight\_nod0\_e4\_etcut\_Jpsiee

which are selecting di-leptonic events with  $E_T$  of the subleading electrons above 4 GeV and leading electrons with increasing thresholds in  $E_T$  of 5 GeV, 9 GeV and 14 GeV respectively. A tight identification requirement is asked for the leading- $E_T$  electron as described in Section 4.2.1.

Due to the large background rate, such triggers are highly prescaled as can be inferred from the collected luminosities in the second column of Table 6.2. Events are required to pass standard data quality requirements ("AllGood" good run lists, ignoring the toroid status). After the trigger and data quality requirements, the integrated luminosity of the selected data sample is  $0.71 \text{ fb}^{-1}$ . The integrated luminosity collected by each  $J/\psi$  trigger separately is listed in Table 6.2.

#### Monte Carlo samples

The  $J/\psi$  candidates produced in  $pp$  collisions at the LHC can be either:

- **prompt**, when they come as a direct product of the proton-proton collision.
- **non-prompt**, when they originate from the decay of a b-hadron.

In the ATLAS 2016 Monte Carlo simulation campaign, samples of  $J/\psi$  particles decaying to dielectrons have been produced separately for prompt and non-prompt  $J/\psi$ , and with varying lower thresholds on the leading electron transverse momentum, increasing from 3 GeV to 8 GeV and then to 13 GeV. Both prompt and non-prompt samples are generated with PYTHIA 8 and processed through a full ATLAS detector simulation based on Geant4. This separation between prompt and non-prompt component has no particular advantage for calibration purposes, but the same simulated events have been shared with the  $J/\psi \rightarrow ee$  Tag and Probe analysis measuring the isolation SFs, which needs such separation. In this work, the two components have been merged by carefully choosing a correct normalization fraction (see next Section). An additional complication is given by the fact that the samples have been produced in  $E_T$  slices, which must be orthogonalized across each other before merging.

In practice, the samples are orthogonalized and merged with a method relating energy and trigger selection. Each simulated sample is related to just one of the triggers listed in the previous paragraph, depending on the transverse energy of the leading electron as shown in Table 6.2. For each simulated sample, the event is selected only if it passes the related trigger and if the transverse energy of the leading electron is in the selected range. In this way, an orthogonalization of the

simulated samples is performed and topologically identical events coming from different samples are treated consistently. Four slices in  $E_T$  have been created after this orthogonalization. The luminosity profiles are expected to differ, due to the different prescaling of the various triggers. Thus, the average interaction per bunch crossing distributions in data are derived separately for each particular trigger and the simulations are reweighted accordingly for each  $E_T$  slice.

The expected fraction of prompt and non-prompt events changes as a function of  $E_T$  [182]. Thus, the normalization factors used to merge the prompt and non-prompt components in each slice have been extracted directly from data, with a fit to the pseudo proper time distribution of  $J/\psi \rightarrow ee$  events. A more detailed description of the method is given in Section 6.8.2. The normalization of the two components has been performed first pre-normalizing both prompt and non-prompt simulated samples in each slice to the number of data events in that slice, and then rescaling each component for the corresponding fraction, as summarized in the last column of Table 6.2.

Trigger	int. Lumi [fb <sup>-1</sup> ]	Leading $E_T$ [GeV]	MC sample	$f_p$ [%]
HLT_e5_lhtight_nod0_e4_etcut_Jpsiee	0.004	[5,7]	e3e3	$0.83^{+0.09}_{-0.09}^{+0.08}_{-0.11}$
		[7,9]	e3e3	$0.76^{+0.04}_{-0.04}^{+0.10}_{-0.06}$
HLT_e9_lhtight_nod0_e4_etcut_Jpsiee	0.070	[9,14]	e3e8	$0.68^{+0.03}_{-0.03}^{+0.02}_{-0.05}$
HLT_e14_lhtight_nod0_e4_etcut_Jpsiee	0.636	[14,30]	e3e13	$0.68^{+0.01}_{-0.01}^{+0.01}_{-0.04}$

TABLE 6.2 – Summary of the relation between triggers, transverse energy range of the leading electron and MC samples. The MC samples have been generated in slices of leading electron transverse energy and labelled as shown in the "MC sample" column (i.e. e3: above 3 GeV electron, e8: above 8 GeV electron). The MC orthogonalization has been performed applying a requirement in  $E_T$  as shown in the "Leading  $E_T$ " column, and requiring the events to pass just the related trigger ("Trigger" column). The "int. Lumi" column is the integrated luminosity collected for each trigger, while the last column shows the fractions of prompt events extracted from the fit on the pseudo-proper time for each slice in  $E_T$ . The error on  $f_p$  shows both statistical and systematic uncertainties.

## 6.8.2 Event selection

A more stringent selection on top of the trigger requirements described above is applied to data and simulation to isolate  $J/\psi \rightarrow ee$  events. Both data and MC events are required to contain two electrons with the following properties:

- opposite charge,
- leading electron transverse energy  $5 < E_T < 30$  GeV,
- subleading electron transverse energy  $5 < E_T < 15$  GeV,
- electron pseudorapidity within  $|\eta| < 2.47$ , to exploit the information from the tracker system.
- fixed cut loose isolation (see Section 4.2.2),
- likelihood-based tight identification, to suppress fake electron candidates from misidentified hadronic jets, defined as described in Section 4.2.1,
- invariant mass of the di-lepton system in the range [2.1, 4.1] GeV. In this way, the  $\psi(2s)$  peak is also reconstructed, thus contributing to the determination of the energy scale corrections. This large  $ee$  invariant mass sidebands allow also for a better constraint of the background yield and shape,

- In case of multiple  $J/\psi$  candidates in the event, only the one with highest  $E_T$  is selected.

The upper limits on the leading and subleading electron  $E_T$  have been added to suppress the background contamination in the high part of the spectrum, probably coming from Drell-Yan processes, noticed looking at the higher tail of the  $J/\psi$  invariant mass distribution.

All the corrections from the nominal calibrations have been applied while producing the samples: scale corrections, layer corrections, smearing of the MC, pile-up reweighting, isolation, reconstruction and identification efficiency scale factors and  $Z \rightarrow ee$  in-situ calibration scale factors.

Around 60 000 events were collected, using the full 13 TeV  $pp$  data collected in 2015 and 2016 ( $3.2 + 33.9 \text{ fb}^{-1}$ ), instead of the 118 000 collected in Run-1 ( $20.3 \text{ fb}^{-1}$  at 8 TeV in 2012), due to the much tighter prescaling of the  $J/\psi$  dedicated triggers.

A summary of the number of dielectron candidates collected per  $\eta$  bin is shown in Figure 6.10. The binning has been chosen as a compromise between the number of dielectron candidates in each bin, necessary to make the fit converge, and the pseudorapidity granularity of the electron energy scale measurement.

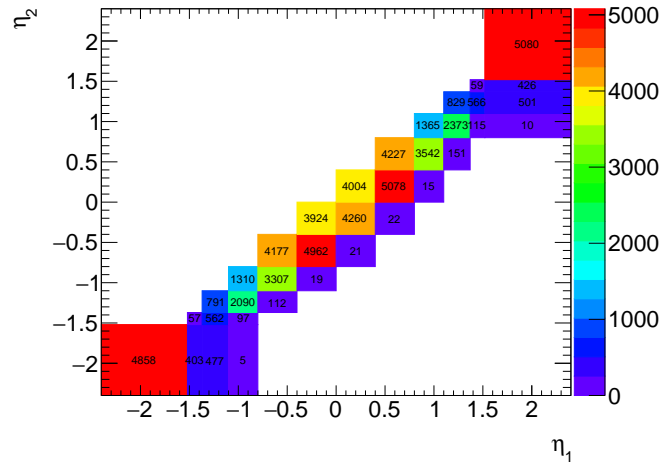


FIGURE 6.10 – 2D pseudorapidity distribution of the dielectron candidates selected in data.  $\eta_1$  refers to the electron with higher pseudorapidity and  $\eta_2$  is the other one.

### Pseudo-proper time fit

An effective way to quantify the fraction of prompt and non-prompt  $J/\psi$  candidates in data is to study their pseudo proper time ( $\tau$ ) distribution. The pseudo proper time is related to the decay length in the transverse plane by:

$$\tau = \frac{L_{xy} m^{J/\psi}}{p_T^{J/\psi}}, \quad (6.19)$$

where  $L_{xy}$  is the decay length in the  $xy$  plane, defined as  $L_{xy} = \mathbf{L} \cdot \mathbf{p}_T^{J/\psi} / p_T^{J/\psi}$ ,  $\mathbf{L}$  the vector from the primary vertex to the  $J/\psi$  decay vertex,  $m^{J/\psi}$  the world-average mass of the  $J/\psi$  meson [20],  $p_T^{J/\psi}$  the transverse momentum of the  $J/\psi$  and  $p_T^{J/\psi} = |\mathbf{p}_T^{J/\psi}|$  its magnitude.



Promptly produced  $J/\psi$  mesons are expected to have small pseudo proper times because they come directly from the hard interaction primary vertex. On the contrary, many of the  $J/\psi$  mesons produced in b-hadron decays will have a measurably displaced decay point, due to the long lifetime of the b-hadron parent. An unbinned maximum likelihood fit on this quantity has been used to distinguish the two contributions and extract the prompt fraction directly from data.

The PDF used in the fit to the  $\tau$  distribution consists of two terms, the first describing the prompt  $J/\psi$  ( $P_P$ ) and the second describing non-prompt  $J/\psi$  coming from b-hadrons ( $P_B$ ), weighted for the fraction of the prompt component  $f_P$ . The pseudo proper time distribution of promptly produced particles can be modelled as a Dirac's delta function peaked at zero, convoluted with a resolution function which accounts for the detector resolution. The decay probability for a b-hadron is an exponential distribution  $E(\tau)$ , so the PDF for non-promptly produced  $J/\psi$  will be an exponential decay convoluted with the same detector resolution function of the prompt candidates. Let  $R(\tau' - \tau, \mu_\tau, \sigma_\tau)$  be the resolution function represented as the sum of three Gaussians. Here  $(\tau' - \tau)$  defines the mean of the resolution Gaussians, with  $\tau$  the measured pseudo proper time and  $\tau'$  the unbiased pseudo proper time, while  $\mu_\tau$  is a parameter defining if the mean is left free to vary in the fit or fixed to zero and  $\sigma_\tau$  is the width of the resolution Gaussian. The total PDF can be written as:

$$f(\tau) = f_P \cdot P_P(\tau) + (1 - f_P)P_B(\tau) \quad (6.20)$$

$$= f_P(R \otimes \delta)(\tau) + (1 - f_P)(R \otimes E)(\tau) \quad (6.21)$$

For every fit, the same resolution for prompt and non-prompt Gaussians was assumed. Regarding the means, all possible combinations of fixed/free parameters were investigated to account for any possible small bias  $(\tau' - \tau)$  different from zero. The resolution Gaussians can be written as

$$R(\tau' - \tau, \mu_\tau, \sigma_\tau) = \begin{cases} R(\tau' - \tau, \mu_P, \sigma_P) & \text{with } \sigma_P = \sigma_{NP} \\ R(\tau' - \tau, \mu_{NP}, \sigma_{NP}) & \text{and } \mu_P = 0, \mu_{NP} = \text{Free} \end{cases} \quad (6.22)$$

with  $\sigma_P$  and  $\sigma_{NP}$  the width for the prompt and non-prompt resolution Gaussians and  $\mu_P$  and  $\mu_{NP}$  the choices for the prompt and non-prompt  $\mu_\tau$  parameters. The values indicated in the Equation represent the best choice from MC toys (see later).

The fit range was optimized by varying the range boundaries in steps of 0.1 ps in the interval [-1.3] ps. The range [-1.1, 2.9] ps was giving the best  $\chi^2$ , thus it was chosen as nominal. The ranges differing by  $\pm 0.1$  ps were used to quantify the systematic uncertainties. The results of the fit for the bin with leading electron  $E_T$  between 9 and 14 GeV are shown in Figure 6.11(a)-(d). The combination ensuring the best fit stability in the largest range has been chosen using simulated pseudo-data (see more details while discussing the closure test). It is found to be with the prompt mean fixed to zero and the non-prompt mean free 6.11(c). A cross-check has been done using directly the  $\tau$  distributions from the MC samples as template PDFs, as shown in Figure 6.11(e). All these methods will be used as input to evaluate the systematic uncertainties on the energy scales as described in Section 6.8.5.

All possible combinations (see Table 6.3) were investigated and the difference between the default and the maximum and minimum variation has been taken as a systematic uncertainty. The results of the fit for each slice of the leading electron  $E_T$  are summarized in Table 6.2. The results are quite different from those used in Run-1, where the fractions were assumed to vary between 0.62 for  $e3e3$  and 0.44 for



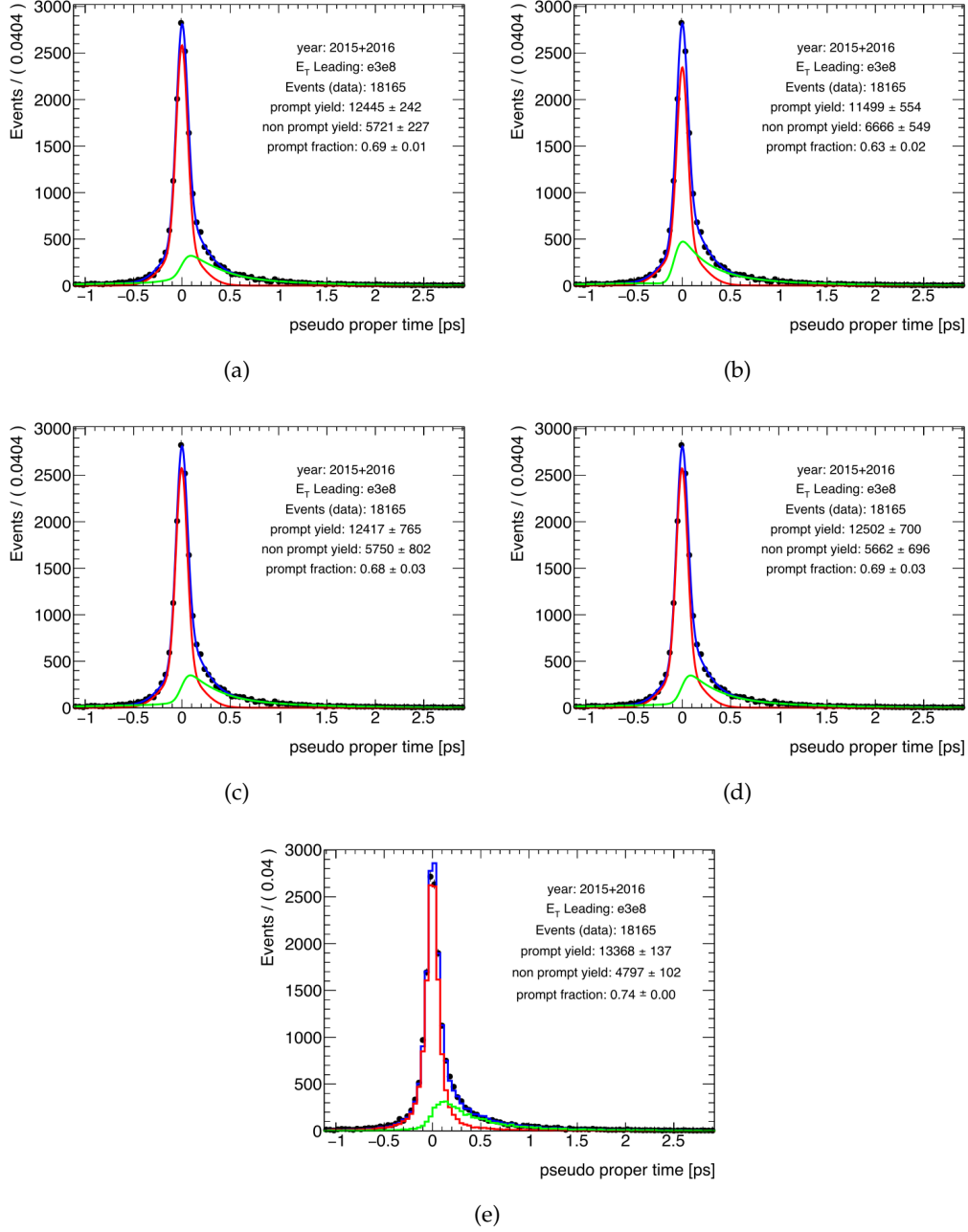


FIGURE 6.11 – Pseudo proper time fit in data used to extract the fraction of prompt events using the unbinned fit and a model PDF. The mean of the Gaussians in the resolution functions are kept: (a) both free for prompt and non-prompt, (b) free for the prompt and fixed to zero for the non-prompt, (c) fixed for the prompt and free for the non-prompt (nominal case), (d) both fixed. (e) Cross-check with a binned fit using prompt and non-prompt MC as template PDF.

Option	Prompt		Non-Prompt	
	mean	$\sigma$	mean	$\sigma$
Both Free	free	free	free	= prompt
PromptFree - NonPromptFix	free	free	fix(0)	= prompt
PromptFix - NonPromptFree	fix(0)	free	free	= prompt
BothFix	fix(0)	free	fix(0)	= prompt

TABLE 6.3 – Table summarizing the options for  $\sigma$  and mean of the resolution Gaussians of prompt and non-prompt PDFs used in the fit to the pseudo proper time. "= prompt" means that the resolution is assumed to be the same for prompt and non-prompt electrons, this is implemented using the same  $\sigma$  parameters in both PDFs.

$e3e13$ . Run-1 assumptions and almost all the measurements found in literature are based on  $J/\psi \rightarrow \mu\mu$  events [182] [183], obtained with a different kinematic selection that might not suppress as much as in our case (due to the tight identification and electron isolation requirement) the non-prompt component in which the electrons are produced together with nearby hadrons.

The fit has been validated performing a closure test on simulation. Prompt and non-prompt MC samples were merged using a specific fraction defined a priori and then the resulting dataset was used as input for the pseudo proper time fit. The results of the closure test for injected fractions equal to 0.4 and 0.85 are shown in Figure 6.12 (a) and (b). Good agreement between the fitted values and the injected ones is observed. As said before, the parametrization of the mean for prompt and non-prompt resolution Gaussians has been optimised using this closure test on MC. The default settings for the resolution Gaussians have been chosen as the combination of prompt mean fixed to zero and non-prompt mean free because this ensures good fit stability in the largest range of fractions (0.30-0.85). For lower fractions (below 0.3) the option "both fixed" gives better results, while for higher fractions (above 0.8) the best estimation comes from the "both free" option. The closure test has been also used to adjust the fit range.

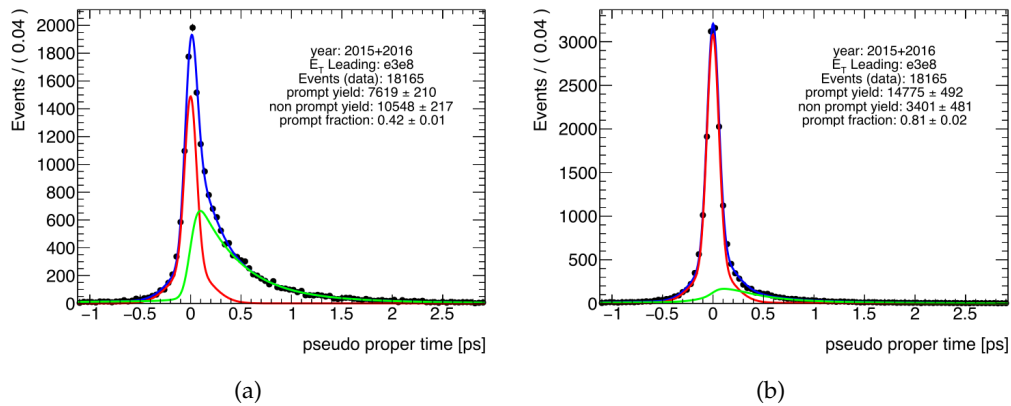


FIGURE 6.12 – Closure test for the pseudo proper time fit. The default fit settings have been used. (a) injected prompt fraction 0.4, (b) injected prompt fraction 0.85.

### 6.8.3 Kinematic distributions

The prompt/non-prompt merging procedure is validated comparing the kinematic distributions in data and in simulation. Some examples are reported in Figure 6.13. As shown in Figure 6.13 (a)-(b), the pseudorapidity distributions of leading and subleading electrons show good agreement in the barrel region, but the agreement degrades in the end-caps where non closures up to  $\sim 20\%$  are observed, probably due to mis-modellings in simulation. An  $\eta_1 \times \eta_2$  reweighting has been applied to simulation to recover a good data/MC agreement in the full pseudorapidity range. This extra MC weight has been evaluated as the data/MC ratio of the 2-D  $(\eta_1, \eta_2)$  distribution. The weights have been obtained separately for each region of Table 6.2 dividing the 2015+2016 data for the corresponding MC distribution previously normalized as described in Section 6.8.1. As presented in Figure 6.14, the extra weights are generally close to 1 with peaks for the bins with low statistics. In case of bins with zero MC entries a weight equal to 1 is assigned by default. The  $\eta$  distributions after the reweighting are shown in Figure 6.13 (c)-(d). The  $E_T$  distributions, presented in Figure 6.13 (e)-(f), being already well described are not significantly improved by this correction. More kinematic distributions are available in Appendix A.

### 6.8.4 Energy scale measurement

The energy scale corrections  $\alpha_i$  are extracted through a simultaneous maximum likelihood fit to the dielectron invariant mass distributions of all the pseudorapidity categories, implemented using the RooFit package [184]. The measurement is performed in two steps: first with a fit to simulated  $J/\psi \rightarrow ee$  events to obtain the  $m_{\text{reco}}^{\text{MC}}$  distribution in Equation 6.5, and then with a simultaneous fit on data of all the categories.

#### Signal and background modeling

The PDF used for the fit in each category is a *signal + background* PDF evaluated in multiple steps. The  $J/\psi$  signal peak is modelled using a Double Sided Crystal Ball (DSCB) PDF, defined as a Gaussian core with power law tails on both sides, parameterized as:

$$f(x; \beta_1, \beta_2, n_1, n_2, \bar{x}, \sigma) = \begin{cases} A_1 \cdot (B_1 - \frac{x-\bar{x}}{\sigma})^{-n_1}, & \text{for } \frac{x-\bar{x}}{\sigma} < -\beta_1 \\ e^{(-\frac{1}{2} \frac{(x-\bar{x})^2}{\sigma^2})}, & \text{for } \beta_1 < \frac{x-\bar{x}}{\sigma} < \beta_2 \\ A_2 \cdot (B_2 - \frac{x-\bar{x}}{\sigma})^{-n_2}, & \text{for } \frac{x-\bar{x}}{\sigma} > \beta_2 \end{cases} \quad (6.23)$$

The right  $n$  parameter is fixed to  $n_1 = 10$  and the other tail is left free to fluctuate in the range  $n_2 \in [0.5, 15]$ . Both the other two tail parameters  $\beta_1$  and  $\beta_2$  are free to vary in the range  $[0, 10]$ . The mean can vary in the range  $2.9 - 3.2$  GeV, while  $\sigma$  is constrained between 0.0 and 0.5 GeV. The background includes two contributions: the small peak coming from the  $\psi(2s)$  resonance, expected at 3.686 GeV, and the continuous irreducible background coming from Drell-Yan processes or misidentified electrons.

The shape of the  $\psi(2s)$  peak is evaluated rescaling the parameters<sup>4</sup> of the  $J/\psi$  DSCB of a factor  $m_{\psi 2s}^{\text{PDG}} / m_{J\psi}^{\text{PDG}} = 3.686 / 3.096$  [20], while the continuous background is modelled by a second-order Chebychev polynomial. The final PDF is thus the sum

4. The rescaled parameters are: mean (floating),  $\sigma$  (then kept fixed) and the two  $\beta$  ( $\beta_1$  and  $\beta_2$ , fixed parameters). The DSCB tail parameters  $n_1$  and  $n_2$  are fixed to the  $J/\psi$  estimation with no rescaling.

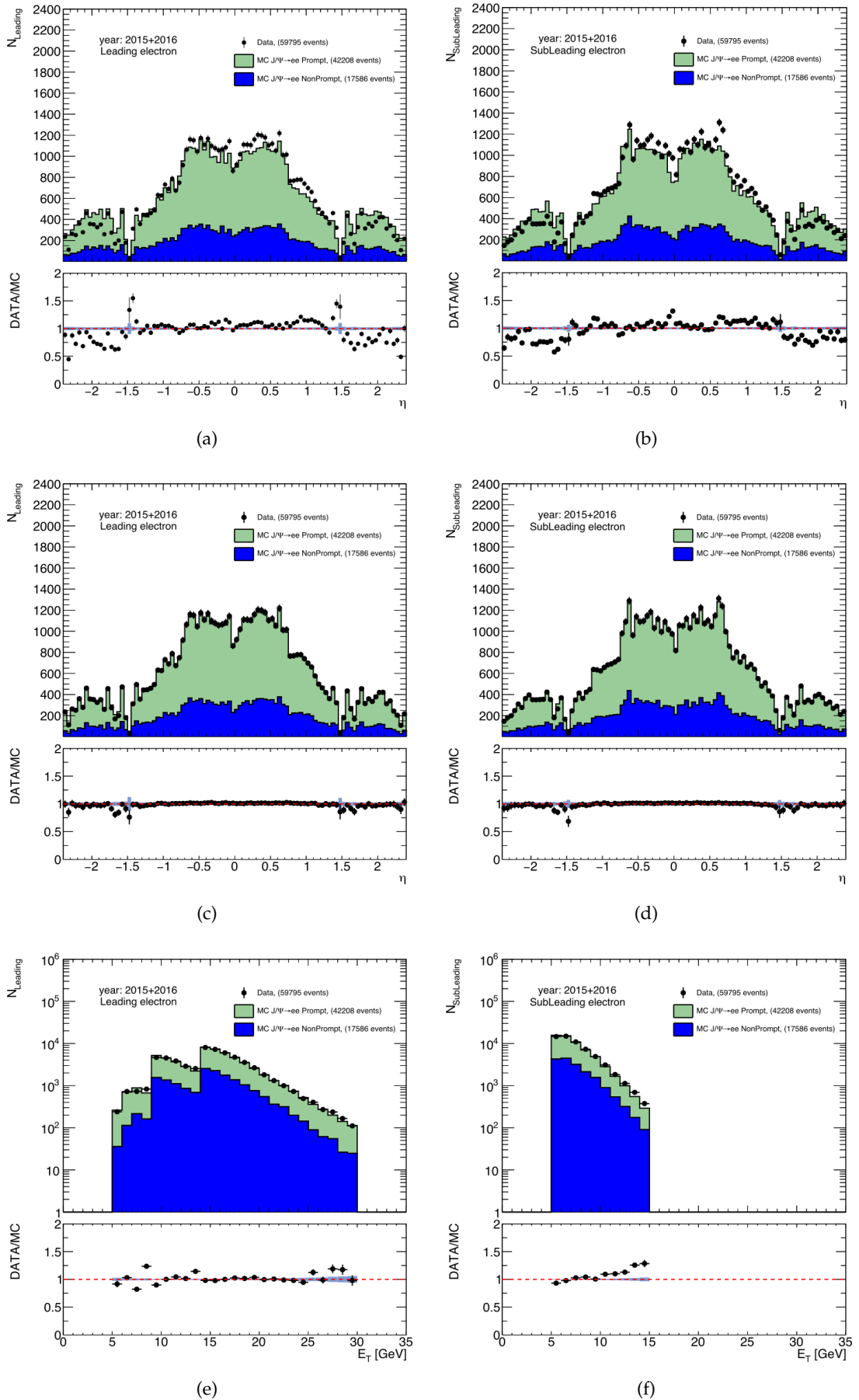


FIGURE 6.13 – (a)-(b) show the leading and subleading  $\eta$  distributions before the 2D reweighting, while (c)-(d) show the corresponding pseudorapidity distributions after the 2D reweighting. In addition, (e)-(f) are the leading and subleading electron  $E_T$  distributions after the  $\eta$  reweighting. Further distributions are shown in Appendix A.

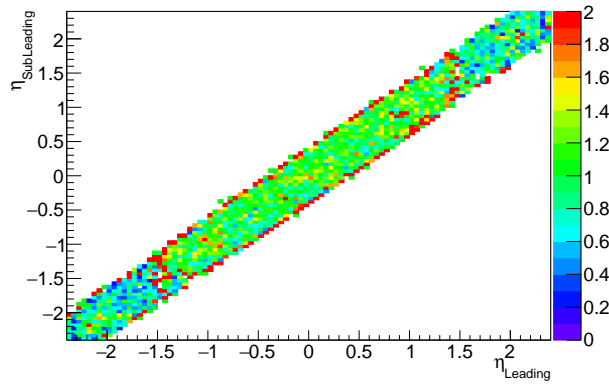


FIGURE 6.14 – Extra MC weights applied to correct for the data/MC disagreement in the electron pseudorapidity distribution. The weights are evaluated as the data/MC ratio of the 2D  $\eta$  distribution of leading and subleading electrons. Zoom along the z-axis in the range of weights [0-2].

of three contributions:

$$f(m_{ee}^{\text{reco}}) = \text{DSCB}(J/\psi) + \text{DSCB}(\psi(2s)) + \text{ChebPol}(2), \quad (6.24)$$

two double sided Crystal Ball PDFs describing the  $J/\psi$  and  $\psi(2s)$  candidates and the Chebychev polynomial [185] for the continuous background. When performing the final fit, many of the shape parameters are fixed to the MC shape (see next paragraph for more details), while the means of  $J/\psi$  and  $\psi(2s)$  DSCBs, expressed as a function of  $\alpha_i$  and  $\alpha_j$ , are floating. In total there are 7 free parameters for each  $\eta_i, \eta_j$  category:

- 3 yields ( $J/\psi$ ,  $\psi(2s)$  and background).
- 2  $\alpha_i$ , because the mean value of the  $J/\psi$  peak is parameterized as described in Equation 6.6, and the scale correction parameters of the  $\psi(2s)$  distribution are required to be the same as those of the  $J/\psi$ .
- 2 parameters to model the background shape.

### Energy scale measurement

The procedure to measure the energy scales can be summarized in the following steps:

- The samples is divided into  $ij$  categories depending on the pseudorapidity of the two electrons (no distinction between leading and subleading has been done, so category  $ij = ji$ ).
- For each category a binned fit to the dielectron mass distribution in the signal MC is performed using the DSCB PDF described in the previous section. This step is necessary to fix the  $J/\psi$  peak shape. Some examples of these fits are shown in Figure 6.15 (a)-(b).
- Once the  $J/\psi$  MC signal shapes are defined for all the  $ij$  categories, the  $J/\psi$  and  $\psi(2s)$  shapes for the fit on data are defined by fixing the tails and the  $\sigma$  to the MC ones. The only parameter left free to vary is the mean, which is expressed as a function of  $\alpha_i$  and  $\alpha_j$  as in Equation 6.6. A quadratic Chebychev polynomial is finally added independently for each category, to complete the PDF for the simultaneous fit on data.

- The parameters of the continuous background polynomials are initialized with the results of a first fit performed independently for each category. This helps the final simultaneous fit to converge faster.
- Finally all the categories are fitted simultaneously. In order to speed up the computation, and to obtain results with small statistical uncertainties, only categories with at least 600 events are considered for the simultaneous fit. The result of the simultaneous fit for some categories, both for diagonal ( $i = j$ ) and non-diagonal ( $i \neq j$ ) bins, are shown in Figure 6.15(c)-(d).

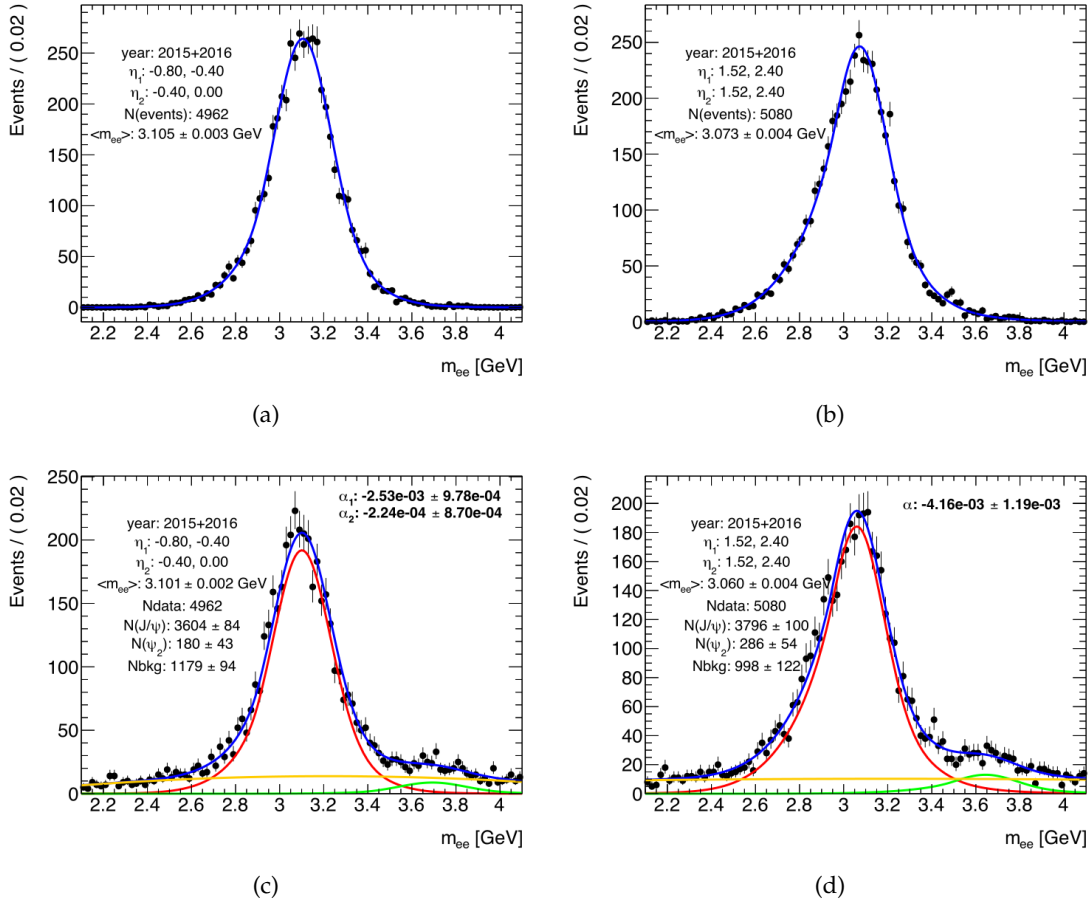


FIGURE 6.15 – Some examples of fit to the dielectron invariant mass distribution in the simulation (a) in the barrel and (b) in the end-caps. (c) and (d) are the related results of the simultaneous fit on data for the same (a) and (b)  $\eta$  categories respectively. The blue line represents the total fitted PDF while the red line corresponds to the  $J/\psi$  contribution, the green line to the  $\psi(2s)$  contribution, and the yellow line to the continuous background. The (a)-(c) plots refer to an off-diagonal bin with  $\alpha_i \neq \alpha_j$ , while (b) and (d) refer to a diagonal bin in which  $\alpha_i = \alpha_j$ , thus only a single  $\alpha$  is indicated. More distributions are in Appendix A.

### 6.8.5 Systematic uncertainties

To assess the systematic uncertainties on the measured energy scale corrections, the fit has been repeated several times after varying different inputs or settings of the fit. The envelope of the resulting energy scale corrections has been used: taking the difference between the nominal  $\alpha_i$  and the maximum (or minimum) variation on

$\alpha_i$  as systematic uncertainty<sup>5</sup>.

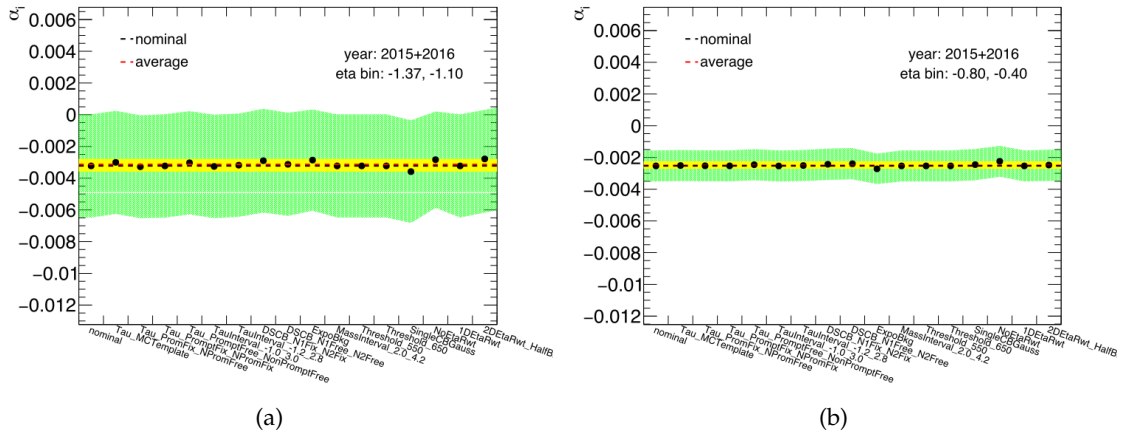


FIGURE 6.16 – Examples of scale variations for two different  $\eta$  bins. The difference between the nominal value and the maximum and minimum variation is taken as systematic uncertainty on the energy scale corrections  $\alpha_i$ . The green band represents the statistical uncertainties from the simultaneous fit, which are assumed to be correlated across the measurements. The yellow band represents the asymmetric systematic uncertainty, the black line highlights the nominal  $\alpha$  value, while the red line refers to the arithmetic mean of all the  $\alpha$ .

Some examples of energy scales measured for each variation are shown in Figure 6.16. The variations giving  $\chi^2$  probabilities above 5% are the following:

- The shape of the signal PDF has been varied from a DSCB function to the sum of a single Crystal Ball function and a Gaussian function ("SingleCBGauss"). Other signal models have been tried, such as the single CB or the double Gaussian, but they all gave  $\chi^2$  probability below 5% so they were not included in the variations.
- The  $n$  parameters of the tails of the DSCB function have been varied from one fixed and one free to both free ("DSCB\_N1Free\_N2Free") or both fixed ("DSCB\_N1Fix\_N2Fix").
- The second order polynomial used to model the continuous background has been replaced by an exponential function ("ExpoBkg").
- The threshold on the minimum number of events per category has been varied between 550 and 650 ("Threshold550" and "Threshold650").
- The nominal range boundaries of the pseudo-proper time fit have been varied by  $\pm 0.1$ . The results of the fit have been used to merge again the prompt/non-prompt components. ("TauInterval\_-1.2\_2.8" and "TauInterval\_-1.0\_3.0").
- The mean of the Gaussians used for the pseudo proper time fit, usually kept fixed for the prompt and free for the non-prompt PDF, have been varied considering all possible cases ("Tau\_PromptFree\_NonPromptFix", "PromFix\_NPromFree", ..).
- The MC template method to perform the pseudo proper-time fit described in Section 6.8.2 has also been considered ("Tau\_MCTemplate").
- The mass window for the fit has been enlarged to [2.0,4.2] GeV ("MassInterval\_2.0\_4.2").

5. Note that the variations are not fully decorrelated.



- The scales with a 1D  $\eta$  reweighting and no  $\eta$  reweighting have been considered in the variations ("1DEtaRwt" and "NoEtaRwt"), together with a variation of the number of pseudorapidity bins for the 2D- $\eta$  reweighting ("2DEtaRwt\_HalfB").

### 6.8.6 Results

The resulting energy scales are shown in Figure 6.17(a). The plot shows both the contributions of systematic and statistical uncertainties. The scales are found to be close to zero in the central barrel, positive in the outer barrel region ( $\sim +1\%$ ) and negative in the end-caps ( $\sim -0.5\%$ ). No measurement has been performed in the so-called crack transition region  $1.37 < |\eta| < 1.52$ , which is not used in offline analyses.

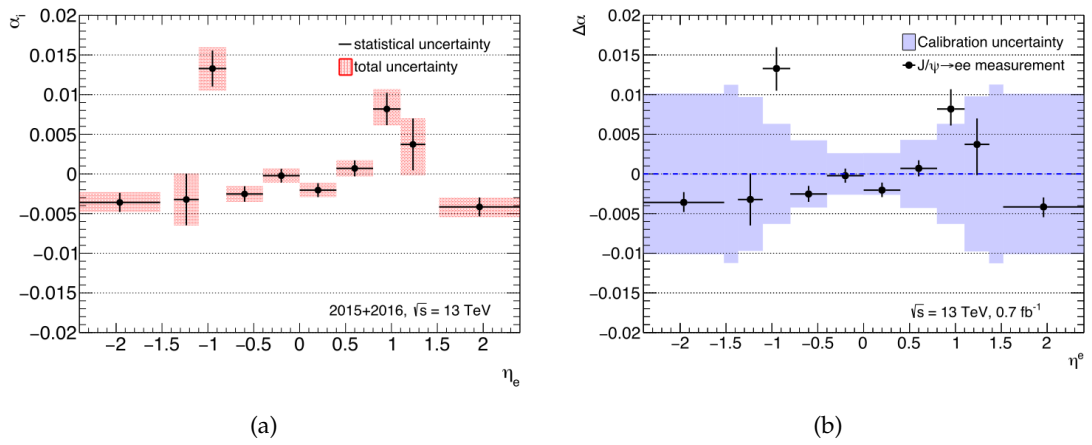


FIGURE 6.17 – (a) Energy scale corrections extracted from  $J/\psi$  events. Statistical and systematic uncertainties are shown separately. (b) Comparison between the energy scale corrections from  $J/\psi \rightarrow ee$  events and the systematic uncertainty extrapolated from the  $Z \rightarrow ee$  calibration. The error bars on the data points represent the total uncertainty specific to the  $J/\psi \rightarrow ee$  analysis.

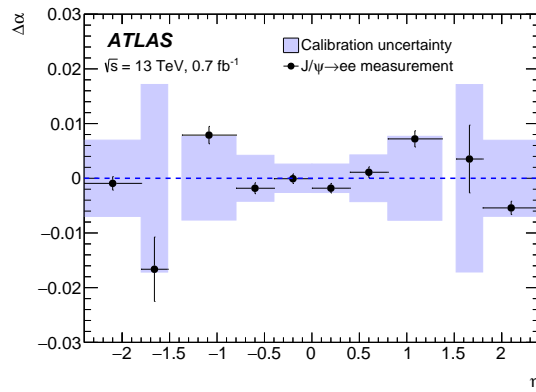


FIGURE 6.18 – Energy scales from  $J/\psi \rightarrow ee$  with a different  $\eta$  binning, to investigate the behaviour in the end-caps (black dots) compared with the extrapolated uncertainties from  $Z \rightarrow ee$  events (violet band). The error bars on the  $J/\psi$  scales contain both statistical and systematic uncertainties [173].

Figure 6.17(b) shows the comparison between the energy scale corrections extracted from  $J/\psi \rightarrow ee$  and the systematic uncertainties extrapolated from the full model (with  $Z \rightarrow ee$  corrections) for an  $\eta$ - $p_T$  spectrum expected from  $J/\psi$  decays, as described in Equation 6.13. The energy scales at low transverse momentum are compatible with the systematic uncertainties computed from  $Z \rightarrow ee$ . In order to further investigate the behavior in the end-caps, where there is more material upstream the calorimeter, the binning was changed as shown in Figure 6.18 adding the  $[\pm 1.52, \pm 1.80]$  bin and merging the  $[0.8-1.1]$  and  $[1.1, 1.37]$  regions to increase the stability of the fit.

The difference with respect to the full model in this region increases up to  $-1.8\%$ , but as for the other bins, the miscalibration remains within the extrapolated systematic uncertainty from the full model using the  $Z \rightarrow ee$  in-situ corrections. In general, the  $J/\psi$  energy scales are symmetric in  $\eta$ . The largest asymmetry, at the level of  $\sim 1.5\sigma$ , is found in the  $1.1-1.37$   $|\eta|$  bin. This asymmetry can be due to small miscalibrations of the gap scintillators (used in  $1.0 < |\eta| < 1.6$ ), which can induce some energy non linearity (i. e. differences between electrons from  $J/\psi$  and  $Z$  boson decays). Further studies, like the pile-up dependence of the energy scales and a comparison with Run-1 results, are presented in Appendix A. To summarize, no significant dependence of the  $J/\psi \rightarrow ee$  energy scales has been observed as a function of pile-up and the pseudo-rapidity dependence has been found in good agreement with the Run-1 measurement, with an overall negative shift of the  $J/\psi \rightarrow ee$  energy scale corrections by approximately  $\sim -0.3\%$ . A possible explanation of this small discrepancy is discussed in the dedicated Section in Appendix A.

Two closure tests have been performed to validate the procedure, both with positive results as shown in Figure 6.19. The first one consists in the re-evaluation of the energy scale corrections after having further corrected the data with the extracted ones, while in the second test the data have been substituted with MC samples as inputs for the second step of the mass fit procedure. For this second method, the background component in each category has been generated using Monte Carlo toys. A successful closure (better than one per-mil) is observed.

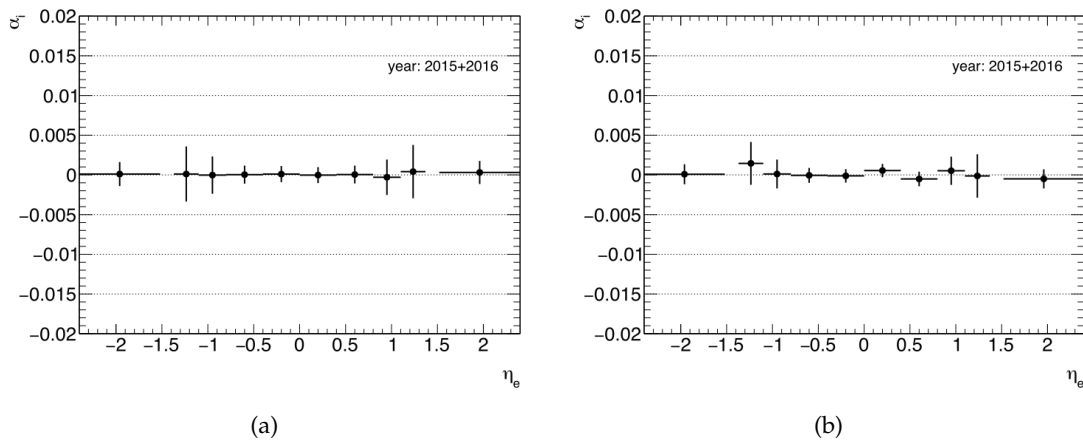


FIGURE 6.19 – (a) data-based closure test, performed re-running the fit after applying the residual (from Figure 6.17) scales to data. (b) MC-based closure test, performed substituting the data with MC samples in the second step of the invariant mass fit.

### Transverse energy dependence

The dependence of the energy scales on the electron transverse energy has been studied splitting the sample in  $E_T$  bins integrated in  $\eta$  and applying the same procedure described in Section 6.8.4. The results of this study are presented in Figure 6.20. The errors include both statistical and systematic uncertainties. The systematic uncertainties have been evaluated using the same variations of Section 6.8.5, excluding the signal variations "SingleCBGauss" and "CB" because they are not giving acceptable  $\chi^2$ s. The  $J/\psi \rightarrow ee$  scale corrections remain within 0.5% in the whole investigated  $E_T$  range. A direct comparison shows that these miscalibrations are generally compatible with the systematic uncertainties extrapolated from the full model (with  $Z \rightarrow ee$  corrections) for an  $\eta$ - $p_T$  spectrum expected from  $J/\psi$  decays (blue bands in Figure 6.20). The discrepancy in the last bin can be due to the combination of different aspects. For example, it can be due to a statistical fluctuation (included in the error bar). Also, the contributions from Drell-Yan/ $Z \rightarrow ee$  starts to have a non negligible impact. These contributions have not been taken into account with dedicated simulations, but their effect on the data/MC agreement (generating a disagreement for  $p_T > 30$  GeV) was controlled with a dedicated upper bound on the electron  $p_T$ , as mentioned in Section 6.8.2.

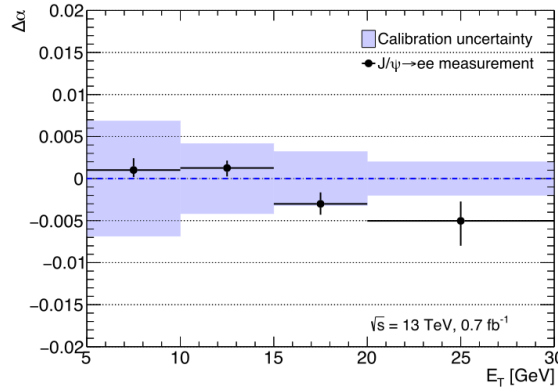


FIGURE 6.20 – Energy scales as a function of the electron transverse energy extracted from  $J/\psi$  events (black dots) compared to the systematic uncertainties extrapolated from the  $Z \rightarrow ee$  calibration. The error bars on the data points represent the total uncertainty specific to the  $J/\psi \rightarrow ee$  analysis and include both statistical and systematic errors.

### 6.8.7 Resolution corrections

The resolution corrections for  $J/\psi \rightarrow ee$  electrons can be parameterized in terms of an extra sampling term  $\Delta a/\sqrt{E}$ , as described by equation 6.18. The procedure to extract  $\Delta a$  is similar to the one used to measure  $c$  with  $Z \rightarrow ee$  events, and it is basically an extension of the invariant mass fit described in the previous paragraphs.

### Methodology

The PDF used for the fit on data is still a *signal + background* type PDF taking into account  $J/\psi$  and  $\psi(2s)$  resonances and the continuous background. The  $J/\psi$  signal is modelled by a Breit-Wigner analytically convoluted with the sum of two Gaussian functions. The width of the Breit-Wigner has been fixed to the PDG value

(92.9 keV). The two Gaussians have the same mean parameter, but different  $\sigma$ s; depending on the fit configuration (two-steps or one-step, as described later) they can be fixed to the MC value or left free to vary. The  $\psi(2s)$  signal PDF remains a Double Sided Crystal Ball with all the parameters taken from a fit to simulated  $J/\psi$  events scaled by 3.686/3.096 and fixed, since it does not provide, with the current statistics, sensitivity to the electron energy resolution. Also the background PDF is unchanged and it is modelled by a second order Chebychev polynomial. The total PDF used for the fit on data is the sum of these three contributions:

$$f(m_{\text{reco}}^{\text{Data}}) = BW \otimes 2\text{Gauss}(J/\psi) + DSCB(\psi(2s)) + \text{ChebPol}(2) \quad (6.25)$$

In order to simplify the fit implementation, the energy dependence of the sampling term is neglected, and the average energy of the electrons in a certain  $\eta$  bin is used instead of each electron energy in the  $a/\sqrt{E}$  term. Figure 6.21 shows the distribution of  $\langle E \rangle_j$  along  $\eta$ . The main advantage of this averaging is that now the fit is based on simple constant terms, as it is done for the  $Z \rightarrow ee$ , so the same parametrization as  $Z \rightarrow ee$  can be used.

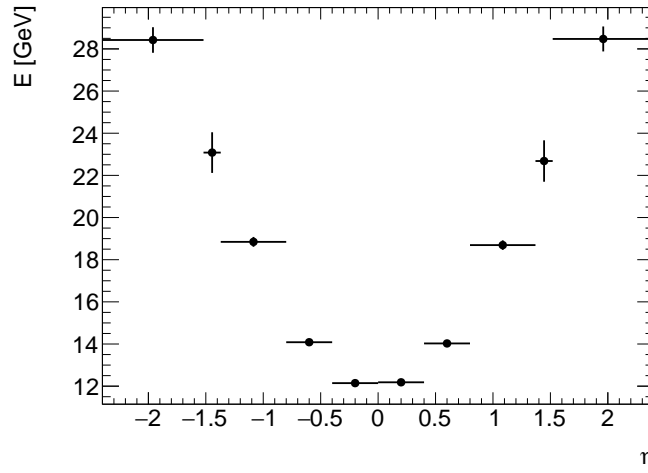


FIGURE 6.21 – Average energy distribution per pseudorapidity interval.

Assuming the electron direction resolution from the inner detector small enough to contribute negligibly to the invariant mass resolution  $\sigma_m$ , the relation between  $\sigma_m$  and the electron energy resolution can be derived from Equation 6.5:

$$\left(\frac{\sigma_m}{m}\right)_{\text{reco}} = \frac{1}{2} \left[ \left(\frac{\sigma_i}{E_i}\right)_{\text{reco}} \oplus \left(\frac{\sigma_j}{E_j}\right)_{\text{reco}} \right] \quad (6.26)$$

Introducing in this equation the relation between the resolution in data and MC (Equation 6.18), and replacing  $\frac{a}{\sqrt{E}}$  with  $\frac{a}{\sqrt{\langle E \rangle}}$ , the result is:

$$\left(\frac{\sigma_m}{m}\right)_{\text{reco}}^{\text{Data}} = \left(\frac{\sigma_m}{m}\right)_{\text{reco}}^{\text{MC}} \oplus \frac{\frac{\Delta a_i}{\sqrt{\langle E_i \rangle}} \oplus \frac{\Delta a_j}{\sqrt{\langle E_j \rangle}}}{2} \quad (6.27)$$

The relations between the position of the peak of the  $J/\psi$  Breit-Wigner in data and MC, and between the widths of the Gaussian resolution functions in data and MC,

are thus:

$$m_{ee}^{\text{Data}} = m_{ee}^{\text{MC}} \left( 1 + \frac{\alpha_i + \alpha_j}{2} \right), \quad (6.28)$$

$$\sigma_{m_{ee}^{\text{Data}}} = \left( 1 + \frac{\alpha_i + \alpha_j}{2} \right) \sqrt{\sigma_{m_{ee}^{\text{MC}}}^2 + \frac{(m_{ee}^{\text{MC}})^2}{4} \left( \frac{\Delta a_i^2}{\langle E_i \rangle} + \frac{\Delta a_j^2}{\langle E_j \rangle} \right)}, \quad (6.29)$$

where the label "reco" is dropped for simplicity. To obtain the  $\Delta a_i$  terms, the following "Two-Step" procedure is performed. The first step consists in extracting the  $\alpha_j$ :

- Fit to the  $J/\psi$  MC invariant mass distributions with the  $J/\psi$  signal PDF (Breit-Wigner convoluted with two Gaussians) to extract the  $m_{ee}^{\text{MC}}$  and  $\sigma_{\text{MC}}$  parameters.
- Fit to the data with the total PDF of equation 6.25 fixing the  $\Delta a_i$  terms to zero, in order to extract the scales  $\alpha_j$ .

The second step consists in extracting the resolution corrections:

- Apply the extracted  $\alpha_j$  scales to data.
- Do again the fit to MC and the fit to Data described above, but fixing the scales  $\alpha_i$  to zero, and floating  $\Delta a_i$ , in order to extract the resolution corrections.

In order to simplify the procedure, the  $\alpha_j$  and the  $\Delta a_i$  can be determined at the same time in one single fit ("One-Step" method). To make the fit converge in a reasonable time the binning is decreased to 10 bins:

$$\{\pm 0, \pm 0.4, \pm 0.8, \pm 1.37, \pm 1.52, \pm 2.40\} \quad (6.30)$$

Examples of fits on MC (step 1) and on data (step 2) using the Two-Step method can be found in Figure 6.22 and in Appendix A.

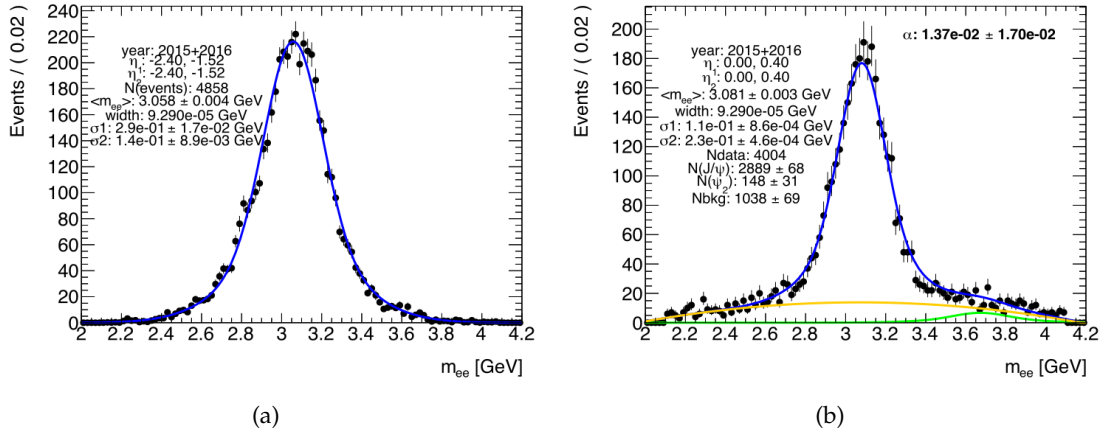


FIGURE 6.22 – Some examples of fit to the dielectron invariant mass distribution both in simulation (a) and data (b) for the "Two-step" method. Here all the parameters of the  $\psi(2s)$  peak have been scaled and fixed to MC, using a second fit with a DSCB as PDF. This simplification reduces the accuracy of the final PDF with respect to the one in equation 6.24 (see Figure 6.15), but due to the small yield of this signal, this effect is negligible. More post-fit distributions are shown in Appendix A.

## Results

The results of the Two-Step fit applied to 2015+2016 data are shown in Figure 6.23. The extracted energy scales, are compatible with the measure presented in Section 6.8.6 (Figure 6.18). Note the change of binning between the plot of Figure 6.23 and 6.18. The extra sampling terms are consistent with zero, with uncertainties varying between 2% and 4% depending on the  $\eta$  bin. An important remark is that due to the quadratic dependence of  $\sigma_{m_{ee}^{\text{Data}}}$  on  $\Delta a$ , presented in equation 6.29, this study is sensitive only to positive values of the resolution term. Thus, a value of  $\Delta a$  compatible with zero means that the MC resolution is equal or larger than the resolution in data. In this second case a direct measurement of this difference is not accessible with this method. This study is however sensitive to possible underestimations of the resolution smearing applied to MC when going to low energies, that would translate in positive values of  $\Delta a$ , which are directly measurable.

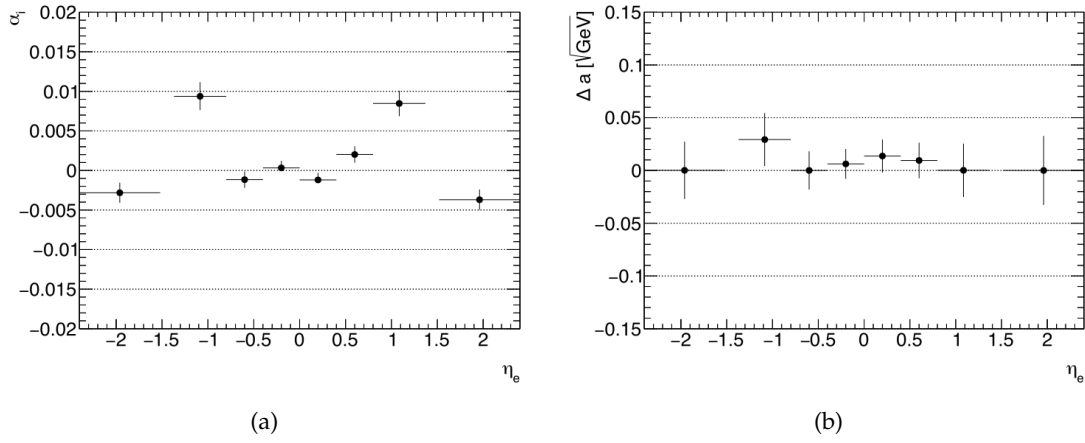


FIGURE 6.23 – Results of the Two-Step method applied to  $J/\psi$  events: (a) Energy scale corrections and (b) sampling term  $\Delta a$ . In both cases the uncertainties are only statistical.

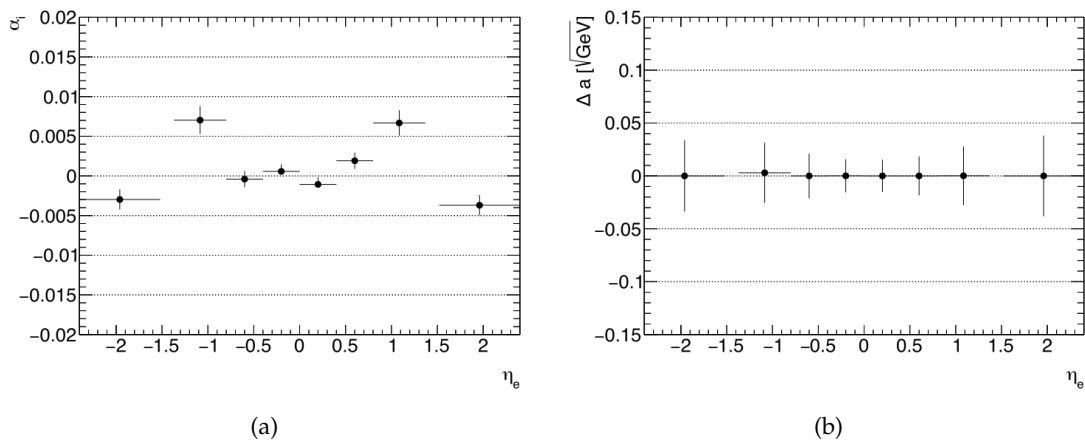


FIGURE 6.24 – Results of the One-Step method applied to  $J/\psi$  events: (a) Energy scale corrections and (b) sampling term  $\Delta a$  as a function of  $\eta$ . In both cases the uncertainties are only statistical.

Figure 6.24 shows energy scales and resolution corrections extracted simultaneously with a single fit ("One-Step"). Good agreement has been observed within the two methods, both for scales and resolution corrections.

Up to now the noise term and the constant term were considered as perfectly modelled by the MC simulation, but in practice, the measured value of  $b$  has an uncertainty estimated to be  $100\text{MeV}/E_T$  ( $200\text{MeV}/E_T$  for  $\eta$  between 1.4 and 1.8). This uncertainty translates directly into an uncertainty on the measured sampling term of around 3% in the barrel and 4% in the end-caps<sup>6</sup>. The uncertainty raises up to 8% in the region  $1.4 < |\eta| < 1.8$ . These extra uncertainties should be summed in quadrature with the errors computed from the  $J/\psi \rightarrow ee$  resolution to get the total uncertainty.

Translating the uncertainties on  $\Delta a$  (Figure 6.23) in terms of relative change on the sampling term  $a$ , would allow to roughly compare the precision of this measurement with respect to the official uncertainty on the sampling term. A 2% (4% in the end-caps) deviation in  $\Delta a$  would translate in a 2% (8%) relative change on the sampling term<sup>7</sup>. Adding the noise term uncertainties, the total uncertainty on the sampling term rises to 4% (5.5%) in the barrel (end-caps), which translates in an 8% (14%) possible relative change on  $a$ . So, with the current statistics, the precision of the measurement is roughly compatible with the default uncertainty used for the sampling term ( $\pm 0.01$ ). In conclusion, this method probed with direct measurements the central value of the sampling term, which has been determined from test beams before the commissioning of the detector years ago [112]. No significant difference from the official values has been observed, so the sampling term parameters can be conservatively kept to  $0.1 \pm 0.01$ .

### Closure Test

The method used to determine the electron energy scale and resolution corrections has been validated with a closure test using pseudo-data. The MC samples have been normalized and merged as described in Section 6.8.1 and used to build signal templates for the "Two-Step" fit. The  $\psi(2s)$  contribution has been ignored, while the continuous background has been generated specifically for each category using the background PDFs resulting from a previous fit on data. The number of background events generated for this test was equal to the background yields found by the fit. These events have been added to the MC signal to create the final pseudo-data categories. The resulting scales and resolution corrections are shown in Figure 6.25. Good closure for both the energy scales and the resolutions is observed. For the outer barrel and the end-caps bins the fit is less accurate, even if the agreement with the injected values remain generally within the errors.

## 6.9 Summary

This chapter summarized the procedure to extract the electron and photon energy calibration in ATLAS using 2015 and 2016 data of LHC proton-proton collisions at  $\sqrt{s} = 13$  TeV. The core of the calibration is the MC-based regression BDT, which corrects the raw energy reconstructed from the clusters to be as close as possible to the true energy of the particle.

The imperfections of the calorimeter are corrected in data with specific  $\eta$  dependent corrections. The intercalibration of the different layers of the ECAL has been

6. This is evaluated assuming the uncertainty on  $a$  as coming entirely from the  $b$  term.  $\frac{\Delta a}{a} = \frac{\Delta b}{E_T}$ , so  $d\Delta a = \frac{100 \text{ MeV}}{E_T} \sqrt{E}$ . This leads, for  $E_T \sim 12$  (14) GeV and  $E \sim 12$  (28) GeV in the barrel (end-caps), to an uncertainty of 2.9% (3.8%).

7. This assuming  $a = 0.1(\pm 0.01)$ . In fact the relative change is calculated as:  $\Delta = \frac{\sqrt{d\Delta a^2 + a^2}}{a} - 1 = 1.9\%$  in the barrel and  $7.7\%$  in the end-caps.



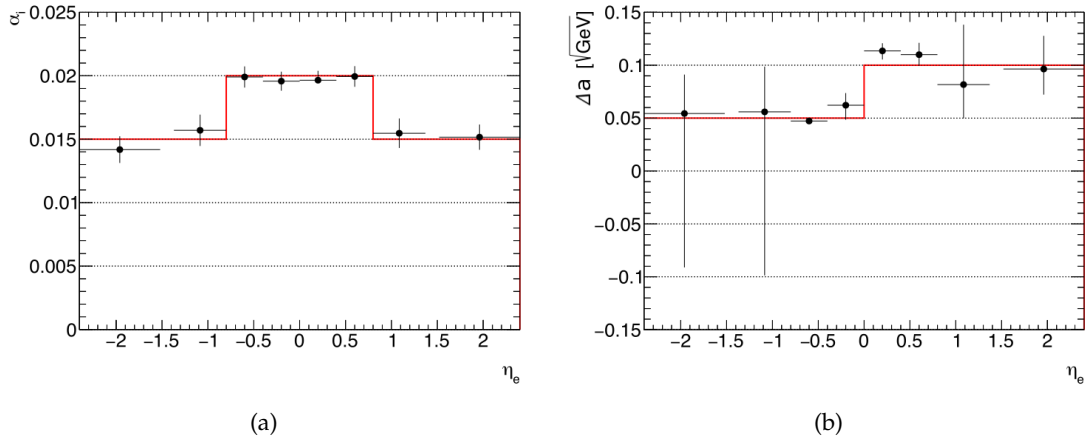


FIGURE 6.25 – Closure test on MC, performed normalizing the samples to the number of events in data. The red line shows the injected values, while the black dots are the extracted measurements. The threshold on the minimum number of events per category has been fixed to 700.

achieved using muons ( $\alpha_{1/2}$ ) and electrons and photon showers ( $\alpha_{PS}$ ). The measured  $\alpha_{1/2}$  have an accuracy of  $\sim 0.7\%$  to  $2.5\%$  depending on the  $\eta$  region, while the accuracy on the presampler scales varies between  $1.5\%$  and  $3\%$ .

The overall energy scale and resolution are measured after having applied all the previous corrections, with an in-situ data-driven method exploiting  $Z \rightarrow ee$  events. The accuracy of the energy scale measurement varies between  $0.03\%$  and  $0.2\%$ , while the extra constant term in the energy resolution is less than  $1\%$  in the barrel and typically  $1\text{--}2\%$  in the end-caps.

Accuracy and linearity of this calibration are probed with low-energy electrons from  $J/\psi \rightarrow ee$  events and with photons from radiative Z boson decays. In both cases, the calibration differences remain within the uncertainties. The measurement of the energy scale corrections for low energy electrons using  $J/\psi \rightarrow ee$  decays has been explained in more details in the last part of the Chapter. The measured dependence of the energy scale corrections as a function of  $\eta$  was found compatible with zero, with the highest disagreement ( $\sim +1.3\%$ ) in the outer barrel ( $\eta$  in  $[0.8, 1.10]$ ) and in the end-caps ( $\sim -0.4\%$ ). The extracted energy scale corrections are compatible with the systematic uncertainties. The measured sampling term corrections ( $\Delta a$ ) are found to be compatible with zero in the whole  $\eta$  region, with uncertainties varying between  $2\%$  and  $4\%$ , confirming that no significant degradation (for example due to ageing), of the default value of the sampling term occurred in these years of data taking.



## 7 | Observation of the Higgs boson decay to $b\bar{b}$ quarks

As described in Chapter 2, the mechanism of quark mass generation is one of the fundamental open questions in particle physics. The Run-1 of LHC allowed for the discovery of the Higgs boson in the so-called "golden" channels, providing a first direct proof of the Brout-Englert-Higgs theory. However, still much to explore is left in the quark sector, where no significant measurement has been performed in Run-1.

In the SM Yukawa mechanism, the coupling strength of the Higgs boson to quarks is predicted to be proportional to the quark mass, thus the highest couplings are expected to be with the third quark generation,  $b$  and  $t$ . The top quark is too heavy to allow for a decay of the Higgs boson into a pair of top quarks, and therefore its coupling strength can be probed only via the production modes, such as  $t\bar{t}H$  or  $tH$ , and indirectly via  $ggH$ .

On the contrary, the  $H \rightarrow b\bar{b}$  decay is allowed in the Standard Model, with the highest BR predicted among the Higgs boson decay channels, representing more than a half of the total Higgs boson width ( $\text{BR} \sim 58\%$ ). This decay channel is the most direct way to probe the coupling of the Higgs boson with down-type quarks. In addition, having a direct measurement of this decay rate would strongly constrain the possibility of new physics phenomena in the Higgs sector.

The main Higgs production mode at the LHC is gluon-gluon fusion. The signature of gluon fusion events in which a Higgs boson decays to  $b\bar{b}$  is given by two b-jets plus potentially extra jets from initial or final state radiation. However, the cross section of inclusive  $b\bar{b}$  production from QCD is approximately  $10^7$  times larger than the expected gluon-gluon fusion Higgs production cross section, making the signal completely overwhelmed by the QCD background.

A possible solution to this problem consists in focusing on alternative production modes. These production modes suffer from lower cross sections, but in return they ensure higher signal to background ratios due to clearer signatures in the detector, based on the presence of additional particles in the final state. Both the vector boson fusion (VBF) and the associated production with a vector boson (VH) channels have been studied at LHC. The VBF mode still leads to a fully hadronic final state, therefore trigger and background modelling remain challenging<sup>1</sup>. On the contrary, in the VH production mode, with the vector boson decaying leptonically, the additional leptonic signature can be exploited for triggering and to highly suppress the QCD background. Since the Tevatron searches [186], this has been the most sensitive and thus preferred channel for  $H \rightarrow b\bar{b}$  searches in hadron colliders.

The  $VH, H \rightarrow b\bar{b}$  signature is categorized by the decays of the vector bosons (Z or W) into:  $ZH \rightarrow \nu\nu b\bar{b}$ ,  $WH \rightarrow \ell\nu b\bar{b}$  and  $ZH \rightarrow \ell\ell b\bar{b}$ . Depending on the number

---

1. Except for VBF+ $\gamma$  which however suffers from very low statistics.

of leptons in the final state, the events are referred to as 0-, 1- and 2-lepton channels in the following. The tree-level Feynman diagrams of the three different production channels are shown in Figure 7.1.

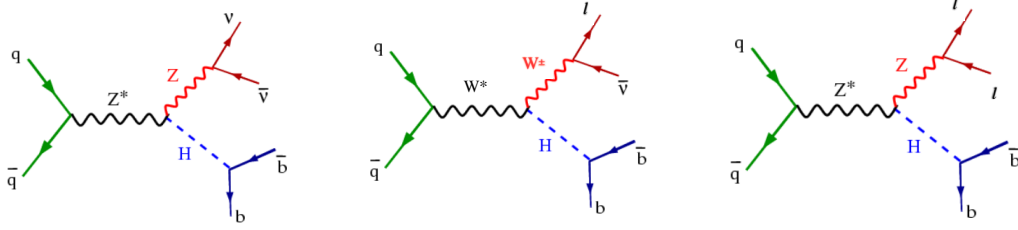


FIGURE 7.1 – Examples of Feynman diagrams of the  $VH \rightarrow b\bar{b}$  leptonic decay channels.

Whilst the QCD background is greatly reduced thanks to the additional leptonic signature, several SM backgrounds still remain. In large part, these backgrounds are common to all channels but contribute in different proportions across them. The main backgrounds are  $t\bar{t}$ ,  $V$ +jets and single top-quark production. The  $V$ +jets can be  $Z$ +jets or  $W$ +jets, sometimes the  $V$ + $b\bar{b}$  ( $x = b, c$  or  $l$ ) contribution is separated from the other contributions and referred to as  $V$ +HF (Heavy Flavour). Some Feynman diagrams of the main background processes are shown in Figure 7.2.

The first evidence of the for  $H \rightarrow b\bar{b}$  decay has been provided in 2012 at the Tevatron, by the combination of  $10 \text{ fb}^{-1}$  of CDF and  $D\bar{O}$   $p\bar{p}$  data, with a global significance of  $3.1\sigma$  ( $2.6\sigma$  expected for  $m_H = 125 \text{ GeV}$ ) [54]. In 2014, the ATLAS and CMS Run-1 combination yielded an observed signal significance of  $2.6\sigma$  ( $3.7\sigma$  expected) [9]. In Run-2, both ATLAS and CMS claimed evidence for the  $VH, H \rightarrow b\bar{b}$  process, with observed (expected) significances of  $3.5\sigma$  ( $3.0\sigma$ ) for ATLAS [187] and  $3.8\sigma$  ( $3.8\sigma$ ) for CMS [188]. This Chapter is an overview of the Run-2 analysis with  $80 \text{ fb}^{-1}$  of  $\sqrt{s} = 13 \text{ TeV}$  ATLAS data. The nominal analysis is based on multivariate (MVA) techniques used to enhance the overall discriminating power of the analysis. The final result is extracted in terms of inclusive signal strength, with a binned simultaneous likelihood fit to the final MVA discriminant, combining different channels and analysis regions. Two independent cross-checks are also presented: the *di-jet mass analysis* and the *diboson analysis*, both used to check the robustness of the main  $VH, H \rightarrow b\bar{b}$  strategy. Both analyses keep the same structure as the nominal one. In the di-jet mass analysis the fit to the MVA discriminant distribution is replaced by a fit to the invariant mass of the di-jet system, which allows for an independent check of the likelihood fit structure. The diboson analysis aims at checking the robustness of the MVA approach, so  $VZ, Z \rightarrow b\bar{b}$  events are used to retrain the MVA classifier and perform a measurement of the SM  $VZ$  signal strength, which is a well known SM process. The observations of the  $VH$  production and  $H \rightarrow b\bar{b}$  decay processes have been obtained via the combination with other production or decay modes, as presented in the last part of the Chapter.

## 7.1 Data and simulated samples

The data used in this analysis were collected by the ATLAS detector during the 2015, 2016 and 2017 proton-proton runs of the LHC, and correspond to  $79.8 \text{ fb}^{-1}$  at  $\sqrt{s} = 13 \text{ TeV}$ . Data are required to pass good quality requirements, ensuring that all components of the detector are operating as expected.

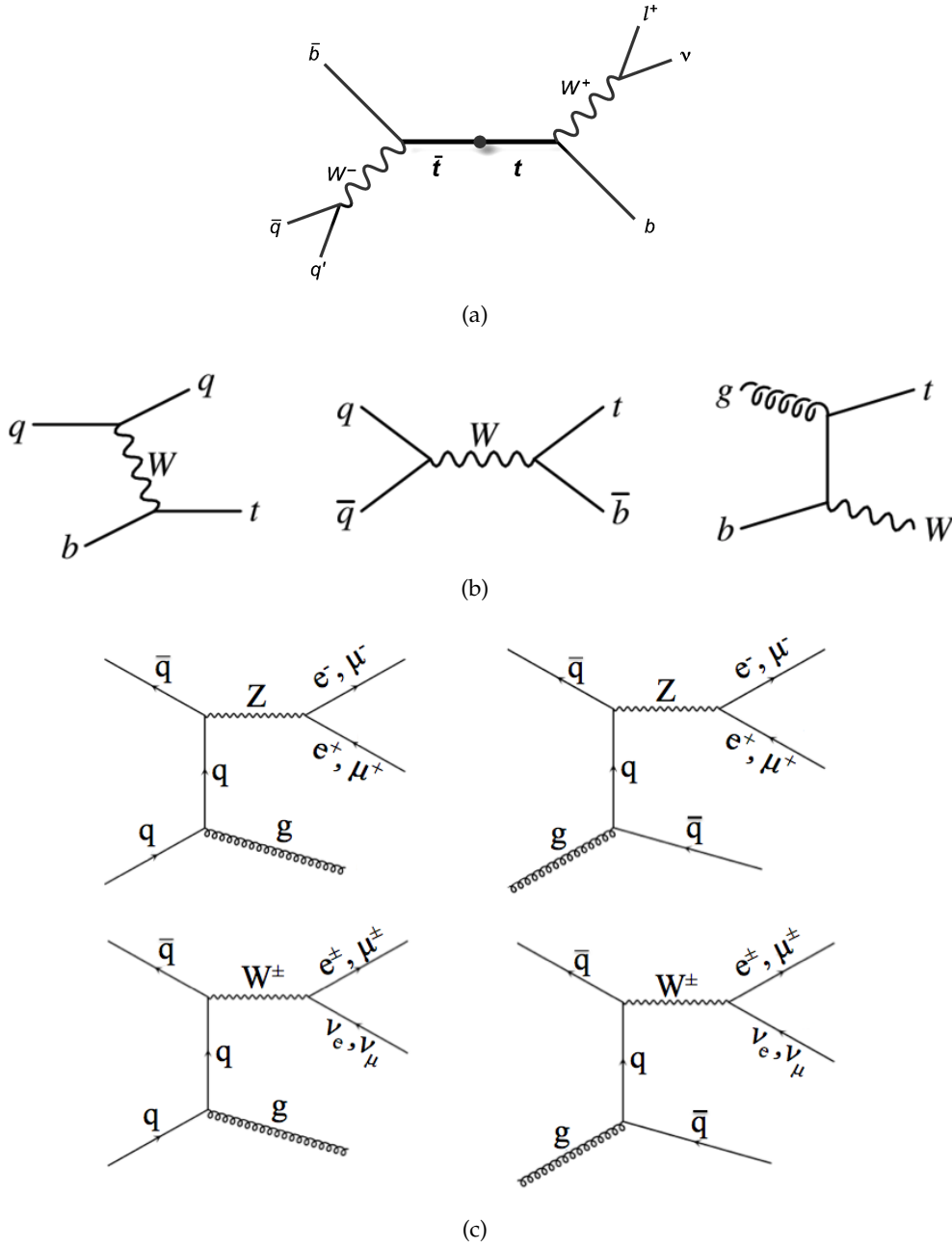


FIGURE 7.2 – Lowest order Feynman diagrams for (a)  $t\bar{t}$ , (b) single-top in the  $t$ ,  $s$  and  $Wt$  channels respectively and (c) the quark induced and gluon induced  $Z$ +jet and  $W$ +jet backgrounds.

Most of the signal and background processes are simulated using Monte Carlo (MC) generators, except for the multi-jet background in the 1-lepton channel, which is estimated using a data-driven technique, as described in Section 7.1.3. Both signal and background simulated processes are passed through the ATLAS detector simulation program [72], based on a detailed simulation of the ATLAS detector with Geant4 [189], and reconstructed with the ATLAS reconstruction software. Table 7.1 lists the matrix element generators, parton showers, Parton Distribution Function (PDF) and corresponding cross-sections for each process. An overview of the principles behind these generators and a brief description of their differences are presented in Section 2.7. All samples are normalised to the best theoretical prediction of the cross section for the different processes. The signal cross sections are obtained from the LHC Higgs Cross Section Working Group prescriptions for a Higgs boson mass of  $m_H = 125$  GeV [48]. The top related cross sections are computed assuming a top quark mass of 172.5 GeV [20]. The simulated samples, except those generated with SHERPA, exploit the EVTGEN 1.2.0 program [190] to describe properties of the bottom and charm hadron decays. More details about the signal and background processes are given in the next two Sections.

As discussed in Chapter 4, a series of corrections are applied to data and simulation during the event reconstruction process. First, the events undergo the overlap removal procedure described in Section 4.5. In addition, the pileup profile of the Monte Carlo is re-weighted to match the measured profile of  $\langle\mu\rangle$  in data. The single objects are corrected as described in Chapter 4. Therefore electrons, muons,  $E_T^{\text{miss}}$  soft terms calibrations or Jet Energy Scale (JES) and Jet Mass Resolution (JMR) corrections or additional reweightings such as trigger or flavour tagging scale factors are applied to the objects involved in the event.

Process	Matrix Element	PDF Set	Parton Shower	$\sigma$ order	$\sigma \times \text{Br}$ [pb]
$q\bar{q} \rightarrow ZH \rightarrow \nu\nu b\bar{b}$	PowHeg-Box v2 + GoSam + MinLo	NNPDF3.0NLO	Pythia-8.212	NNLO(QCD)+ NLO(EW)	$8.91 \times 10^{-2}$
$q\bar{q} \rightarrow WH \rightarrow \ell\nu b\bar{b}$	PowHeg-Box v2 + GoSam + MinLo	NNPDF3.0NLO	Pythia-8.212	NNLO(QCD)+ NLO(EW)	$2.69 \times 10^{-1}$
$q\bar{q} \rightarrow ZH \rightarrow \ell\ell b\bar{b}$	PowHeg-Box v2 + GoSam + MinLo	NNPDF3.0NLO	Pythia-8.212	NNLO (QCD)+NLO(EW)	$2.99 \times 10^{-2}$
$g\bar{g} \rightarrow ZH \rightarrow \nu\nu b\bar{b}$	PowHeg-Box v2	NNPDF3.0NLO	Pythia-8.212	NLO+NLL	$1.43 \times 10^{-2}$
$g\bar{g} \rightarrow ZH \rightarrow \ell\ell b\bar{b}$	PowHeg-Box v2	NNPDF3.0NLO	Pythia-8.212	NLO+NLL	$4.80 \times 10^{-3}$
$Z \rightarrow \nu\nu + \text{jets}$	Sherpa 2.2.1	NNPDF3.0NNLO	Sherpa 2.2.1	NNLO	10700
$W \rightarrow \ell\nu + \text{jets}$	Sherpa 2.2.1	NNPDF3.0NNLO	Sherpa 2.2.1	NNLO	60200
$Z \rightarrow \ell\ell + \text{jets}$	Sherpa 2.2.1	NNPDF3.0NNLO	Sherpa 2.2.1	NNLO	6300
$t\bar{t}$	Powheg-Box v2	NNPDF3.0NLO	Pythia-8.230	NNLO+NNLL	832
single-top (s)	Powheg-Box v2	NNPDF3.0NLO	Pythia-8.230	NLO	3.35
single-top (t)	Powheg-Box v2	NNPDF3.0NLO	Pythia-8.230	NLO	70.4
single-top (Wt)	Powheg-Box v2	NNPDF3.0NLO	Pythia-8.230	Approx. NNLO	71.7
$q\bar{q} \rightarrow WW$	Sherpa 2.2.1	NNPDF3.0NNLO	Sherpa 2.2.1	NLO	45.7
$q\bar{q} \rightarrow WZ$	Sherpa 2.2.1	NNPDF3.0NNLO	Sherpa 2.2.1	NLO	21.7
$q\bar{q} \rightarrow ZZ$	Sherpa 2.2.1	NNPDF3.0NNLO	Sherpa 2.2.1	NLO	6.53
$g\bar{g} \rightarrow VV$	Sherpa 2.2.2	NNPDF3.0NNLO	Sherpa 2.2.2	NLO	3.09

TABLE 7.1 – The nominal Monte Carlo samples used in  $VH, H \rightarrow b\bar{b}$  analysis, and the corresponding process cross-sections at  $\sqrt{s} = 13$  TeV.

### 7.1.1 Signal processes

All  $q\bar{q}$ -initiated production processes are simulated using the POWHEG generator with the MiNLO (Multiscale Improved NLO) procedure applied [82], interfaced to the PYTHIA 8.212 [78] MC generator for the modelling of parton shower (PS), underlying event (UE) and multiple parton interactions (MPI), applying the AZNLO tune [191] with the NNPDF3.0NLO PDF [192] for the matrix-element (ME). The  $g\bar{g}$ -initiated ZH contribution relies on the POWHEG prediction interfaced with PYTHIA 8. The cross sections for WH and ZH are calculated at NNLO in QCD [193] and

NLO in EW [194]. The computation of the one-loop amplitudes is performed with the GoSam automated software [195]. The signal modelling has been cross-checked using POWHEG + MiNLO+ HERWIG 7 samples, generated using the same setup of POWHEG as for the nominal POWHEG + PYTHIA 8 sample, while parton shower (PS), hadronisation, underlying event and multiple parton interactions are simulated with HERWIG 7.0 [138]. Additional electroweak corrections at NLO are applied to the  $qq \rightarrow VH$  processes as a function of the transverse momentum of the vector boson. These corrections are applied as reweightings of the VH differential cross-section and they are computed with Hawk [196] [197].

### 7.1.2 Background processes

The main background processes are simulated using the following MC generators:

**V+jets:** the production of V ( $V = W$  or  $Z$ ) bosons in association with jets is one of the main backgrounds for all the channels considered in this analysis. The V+jet processes are simulated with SHERPA 2.2.1 [80] with the NNPDF3.0NNLO PDF set [192] for both the matrix element calculation and the parton shower tuning. In order to generate enough statistics in the high  $p_T^V$  region, the V+jets samples are split according to the  $p_T$  of the vector boson and the transverse energy of the event, introducing a cut at generation level, and producing samples for different slices in  $\max(H_T, p_T^V)$ , where  $H_T$  is the scalar  $p_T$  sum of all parton-level jets with  $p_T > 20$  GeV. Furthermore, to ensure sufficient statistics for events having heavy-flavours in the final state, the V+jets samples are generated applying different filters to select the flavour composition of the jets produced in association with the V boson: *b-filter* samples have at least 1 b-hadron present, *c-filter + b-veto* samples have at least 1 c-hadron present and a veto on the events passing the b-filter, while *c-veto + b-veto* are vetoing the events which pass the b-filter and c-filter. Alternative samples are considered for the V+jets modelling studies, generated using MADGRAPH 5 [83] interfaced to PYTHIA 8 for the modelling of the parton shower and the underlying event.

**Top-pair production:** the default MC sample for the  $t\bar{t}$  process is generated with the POWHEG generator using an NLO calculation for the matrix element [198] [199] and interfaced to PYTHIA 8.230 [200] with NNPDF3.0NLO PDFs and the A14 set [79] of parameters for the parton shower, hadronization and underlying event description. A filtering at generator level is applied using truth information. Samples defined as *non-all-had* are required to have at least one W boson decaying leptonically, while the *dilepton  $t\bar{t}$*  samples are required to have both W bosons decaying leptonically. Several alternative  $t\bar{t}$  samples have been produced for modelling studies: a POWHEG + HERWIG 7 sample generated using the same setup for POWHEG as for the nominal sample, while parton shower, hadronisation and underlying event are simulated with HERWIG 7.0 [138] with the H7UE tune [81]; a MADGRAPH 5\_aMC@NLO + PYTHIA 8.2 sample produced using MADGRAPH 5\_aMC@NLO [83] for the hard scattering generation at NLO precision and PYTHIA 8.2 for the PS, hadronisation and UE simulation. Also, alternative POWHEG + PYTHIA 8 samples with different tunings of the initial and final state radiations have been used. The cross sections are calculated with top++2.0 [201] at next-to-next-to-leading order (NNLO) in QCD, including resummation of next-to-next-to-leading logarithmic (NNLL) soft gluon terms.



**Single-top:** single-top processes are generated separately for the different channels (s-channel, t-channel, Wt-channel) using the POWHEG MC generator for the hard scattering prediction with NNPDF3.0NLO PDFs, interfaced with PYTHIA 8.230 for the simulation of parton shower, underlying event and multiple parton interactions with A14. The cross sections are calculated (for a top quark mass of 172.5 GeV) at next-to-leading order (NLO) in QCD with Hathor v2.1 [202] [203].

**Diboson:** the diboson background consists of final states arising from WW, WZ, and ZZ events. The nominal simulation of these processes relies on the SHERPA 2.2.1 MC generator, with the NNPDF3.0NNLO PDF sets for both the ME calculation and the parton shower. The  $q\bar{q}$ -initiated and the gg-initiated processes are simulated separately. The generator used for the nominal samples provides the NLO calculation for the diboson cross-sections. The alternative samples for this process include a POWHEG + PYTHIA8 sample, which uses the POWHEG v2 generator interfaced to the PYTHIA 8 parton shower model and a POWHEG + HERWIG ++ sample generated using the same setup for POWHEG as for the POWHEG + PYTHIA 8 sample, while parton shower, hadronisation, underlying event and multiple parton interactions are simulated with HERWIG ++ (version 2.7.1) with the UE-EE-5 [204] tune.

### 7.1.3 Multi-jet estimation

Studies have shown that the multi-jet (MJ) contamination is negligible in the 0- and 2-lepton channels if adding a series of angular cuts as described in Ref. [187]. However, in the 1-lepton channel the contribution is expected to be of the order of few per cent and therefore not completely negligible for a good background modelling. The dominant contribution to this background comes from real muons or electrons from heavy-flavour hadrons decaying semileptonically or from misreconstructed converted photons ( $\gamma \rightarrow ee$ ) in neutral pion decays, which trigger the event. Those leptons are not expected to be isolated, but a small (non-negligible) fraction passes the lepton isolation requirements.

Using Monte Carlo technologies to achieve good modelling is very difficult, mostly because the fraction of events that passes the selection criteria is very limited, and the available simulations do not ensure enough statistics in this phase space. Thus, a data-driven template method is used to extract the multi-jet shape and normalization for each 1-lepton region separately. A multi-jet-enriched control region is defined inverting the strict lepton isolation requirements, described in Section 7.2. The electrons in the inverted isolation control region are still required to pass the loosest lepton isolation working point, to reduce the contamination from fake electrons. In this way, the selected events are kinematically close to the corresponding signal region but not overlapping with it. The assumption is that the multi-jet shape does not change when loosening the isolation cuts since in any case the main source of MJ background entering in this region is still due to semileptonic heavy flavour decays (and not for example from misreconstructed gluon jet events which might bias the kinematic). Despite the nominal analysis requires exactly two b-tagged jets in the event selection, the criteria is here loosened to allow also the 1-tag events - since the kinematic properties are expected to be similar in the background region - so to increase the size of the control sample.

The background enriched control region is created to provide the template for the multi-jet shape of any variable, once the *electroweak component* (top, single-top, diboson, V+jet) is subtracted from the data. The normalisation factors of the multi-jet and the single electroweak (EW) components are extracted in the signal region, with

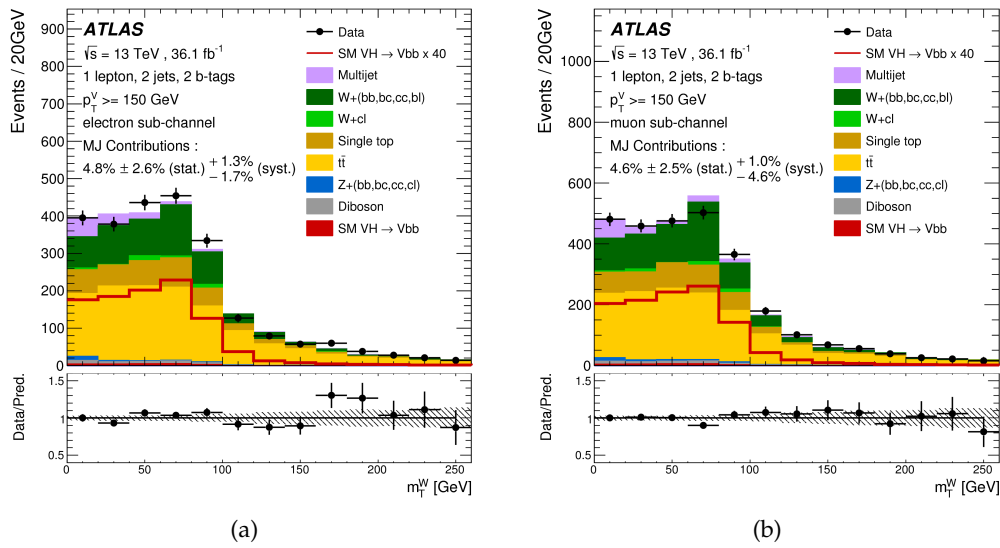


FIGURE 7.3 – Multi-jet estimate in the 1-lepton channel. The plots show the result of the multi-jet template fit in terms of  $m_T^W$  distribution separately in the electron (a) and muon (b) sub-channels in the signal region. The respective estimates are reported in the plots together with the associated statistical and systematic uncertainties. The Higgs boson signal ( $m_H = 125$  GeV) is shown as a filled red histogram, its shape is enhanced and shown as an unstacked open histogram, scaled by the factor indicated in the legend. These plots refer to the 2015+2016 estimation only [187]. The estimation for the full 2015+2016+2017 dataset has been performed with the same method.

a simultaneous fit to the transverse W-candidate mass ( $m_T^W$ ) distribution in data. This variable has been found to provide the best discrimination between the MJ and EW backgrounds, and thus the best control on the normalisation factors. Separate templates for the multi-jet contributions are obtained depending on lepton flavour ( $e/\mu$ ), jet multiplicity (2/3-jet regions) and  $p_T^V$  region. In order to improve the statistical precision in the determination of the W + jet and top quark background normalisation factors, the multi-jet template fit is performed simultaneously in the electron and muon sub-channels. A simultaneous fit to the two sub-channels is performed with common W + jet and top quark background normalisation factors. Once the normalisation factor of the MJ and electroweak components are measured from the  $m_T^W$  fit, they can be used in the background enriched control region to extract the shape template of any other variable, in particular the MVA discriminant. These shape templates are then used in the signal region.

Figure 7.3 presents the results of the multi-jet estimation in the 1-lepton 2-jet electron and muon sub-channels (in the signal region) for the  $m_T^W$  distribution using 2015+2016 data. When adding also 2017 data, the total fake electron (muon) contamination in the 2-jet channel is estimated to be 1.9% (2.8%) of the total background contribution in the electron (muon) sub-channel, while in the 3-jet category it is found to be 0.2% (0.4%).

## 7.2 Object and Event selection

The description of the objects (leptons, jets,  $E_{\text{miss}}^T$ ) and the reconstruction and identification techniques used for this analysis closely follow the definitions of Chapter 3. Since the background composition is very different in the various channels, the

object selection is optimised separately for 0-, 1- and 2- leptons. The following event selection is applied to reduce as much as possible the background contamination in the various channels:

- **Triggers:** Events in the 1-lepton electron sub-channel and in the 2-lepton channel are selected using the lowest unprescaled single lepton triggers, having  $p_T$  thresholds at 24 (26) GeV for the 2015+2016 (2017) periods. These triggers are 80-90% efficient already at 30 GeV, and they become fully efficient (above 97%) around 50 GeV (80 GeV for electrons). In the 0-lepton channel the analysis uses missing transverse energy ( $E_T^{\text{miss}}$ ) triggers with lower thresholds at 70 GeV for 2015, 90 GeV or 110 GeV in 2016 and 110 GeV in 2017. The  $E_T^{\text{miss}}$  trigger efficiency is 85-90% for  $p_T^V = 150$  GeV and reaches  $\sim 100\%$  around 180 GeV.

In the 1-lepton muon sub-channel, the single muon triggers have an efficiency of around  $\sim 80\%$ . This is mainly due to the reduced acceptance of the fast muon chambers, covering only the region  $|\eta| < 2.4$  (plus gaps at  $|\eta| < 0.1$ ). In order to recover a high level of efficiency also for the muon-sub channel, the single muon triggers are complemented with  $E_T^{\text{miss}}$  triggers. The  $E_T^{\text{miss}}$  triggers exploit the presence of the neutrino and the fact that muons are MIP. In fact these triggers are relying only on calorimeter informations, thus they can fire also in case of high  $p_T$  muons, which have very minimal energy losses at calorimeter level. The efficiency of the  $E_T^{\text{miss}}$  triggers have been found to be around 98% for the signal in the  $p_T^V$  region above 150 GeV.

- **Leptons:** Two different lepton selections, identified as *VH-loose* and *VH-signal*, are applied. Due to the higher contamination from non-isolated fake leptons in the 1-lepton channel (from multi-jet background), the *VH-signal* criteria are further split in *ZH-signal* and *WH-signal* and optimised separately. A summary of the electron and muon requirements is given in Table 7.2 and Table 7.3 respectively.

The *VH-loose* criteria require an electron (muon) passing loose identification and at least  $p_T > 7$  GeV,  $|\eta| < 2.47$  (2.7), impact parameter significance  $|\sigma_{d_0}/d_0| < 5$  (3) and  $|\Delta z_0 \sin \theta| < 0.5$  mm to reject tracks from pile-up (and cosmics). The *ZH-signal* criteria require  $p_T > 27$  GeV in addition to the *VH-loose* criteria. In both cases a loose isolation based only on track information is required. More details about the *Loose-Track* isolation working points for electrons and muons are given in Section 4.2.2 and 4.3.2 respectively. In 1-lepton, the presence of isolated leptons is crucial to reduce the fake-lepton background (i.e. QCD multi-jets), therefore a tighter selection is applied: the *WH-signal* requires  $p_T > 27$  GeV as well as medium identification (tight ID for electrons) and *tighter* HighPt-calorimeter isolation, based only on the calorimeter information, for electrons and HighPt-track isolation, based on track information, for muons. More details about the *HighPt* isolation working points for electrons and muons are given in Section 4.2.2 and 4.3.2 respectively.

At last, in the 2-lepton channel the invariant mass of the two leptons,  $m_{\ell\ell}$ , is required to be consistent with the mass of the Z boson:  $81 < m_{\ell\ell} < 101$  GeV.

- $E_T^{\text{miss}}$ : In the 0-lepton channel the  $p_T^V$  of the vector boson is reconstructed as the  $E_T^{\text{miss}}$ , therefore a requirement  $E_T^{\text{miss}} > 150$  GeV is applied to select the high  $p_T^V$  region. In the 1-lepton electron sub-channel a selection of  $E_T^{\text{miss}} > 30$  GeV is applied to reduce the background from multi-jet production.

Category	$p_T$	$\eta$	ID	$d_0^{\text{sig}}$	$ \Delta z_0 \sin \theta $	Isolation
VH-loose	$> 7 \text{ GeV}$	$ \eta  < 2.47$	Loose-LH	$< 5$	$< 0.5 \text{ mm}$	Loose-track
ZH-signal	$> 27 \text{ GeV}$	$ \eta  < 2.47$	Loose-LH	$< 5$	$< 0.5 \text{ mm}$	Loose-track
WH-signal	$> 27 \text{ GeV}$	$ \eta  < 2.47$	Tight-LH	$< 5$	$< 0.5 \text{ mm}$	HighPt-calo

TABLE 7.2 – Electron selection requirements.

Category	$p_T$	$\eta$	ID	$d_0^{\text{sig}}$	$ \Delta z_0 \sin \theta $	Isolation
VH-loose	$> 7 \text{ GeV}$	$ \eta  < 2.7$	Loose-ID	$< 3$	$< 0.5 \text{ mm}$	Loose-track
ZH-signal	$> 27 \text{ GeV}$	$ \eta  < 2.5$	Loose-ID	$< 3$	$< 0.5 \text{ mm}$	Loose-track
WH-signal	$> 25 \text{ GeV}$	$ \eta  < 2.5$	Medium-ID	$< 3$	$< 0.5 \text{ mm}$	HighPt-track

TABLE 7.3 – Muon selection requirements.

- **Jets:** The jets are divided into signal jets and forward jets, a summary of their selection requirements is given in Table 7.4. Signal jets are the ones used for b-tagging, and they are required to have  $p_T > 20 \text{ GeV}$  and  $|\eta| < 2.5$ . Jets with  $20 \leq p_T < 60 \text{ GeV}$  and  $|\eta| < 2.4$  have to pass a certain quality threshold (JVT  $> 0.59$ , with JVT defined in Section 4.4.2). Events are required to have at least 2 signal jets, with the highest- $p_T$  (leading) b-tagged jet with  $p_T > 45 \text{ GeV}$ . The 0-lepton and 1-lepton channels only consider events with at most 3-jets, with at least two signal jets and the third jet allowed to be in the forward region ( $|\eta| < 4$ ). Since the 2-lepton channel kinematics is more constrained, this channel exploits also events with more than three jets to gain in sensitivity.

Category	Selection requirement
Signal Jets	$p_T > 20 \text{ GeV}$
	$ \eta  < 2.5$
	JVT $\geq 0.59$ (if $p_T < 60 \text{ GeV}$ and $ \eta  < 2.4$ )
Forward Jets	$p_T > 30 \text{ GeV}, 2.5 \leq  \eta  < 4.5$

TABLE 7.4 – Jet selection requirements.

- **b-tagging:** All the signal jets are considered for b-tagging. Among them, exactly two signal jets are required to be b-tagged at the 70% efficiency working point using the MV2c10 tagger. In case of three jets, a veto on the b-tagging of the third jet is applied (meaning that the third jet is required not to pass the 70% working point). Truth tagging is applied to the V+jets samples with b-veto, so not containing b-hadrons (described in Section 7.1), and to WW. More details are given in Section 7.6.2. The two b-tagged jets are used to construct the  $H \rightarrow b\bar{b}$  candidate.
- **Vector boson:** In 1-lepton the  $p_T^V$  of the vector boson is the vectorial sum of the  $E_T^{\text{miss}}$  and the  $p_T$  of the lepton, in 2-leptons it is the vectorial sum of the two lepton  $p_T$  and in 0-lepton it is the  $E_T^{\text{miss}}$  as described before. In the 0-lepton and 1-lepton channel the reconstructed vector boson is required to have a minimum transverse momentum of 150 GeV, due to the slow turn on of the  $E_T^{\text{miss}}$  triggers and to the huge multi-jet contamination at lower values. In 2-leptons the minimum  $p_T^V$  requirement is lowered to 75 GeV, keeping the separation at 150 GeV to disentangle medium and high  $p_T^V$  regions.

Table 7.5 summarises the event selection criteria described above, while Table 7.6 summarizes the acceptance for the three channels after the full event selection, as well as the predicted cross-sections times branching fractions separately for the each signal process.

### 7.2.1 Improvements on $m_{bb}$ resolution

The di-jet mass variable is the most discriminating variable to disentangle the  $VH, H \rightarrow b\bar{b}$  signal from the background. Its resolution is however deteriorated by inaccuracies in the b-jet energy measurement, which reduce the overall discriminating power by broadening the resonant peak. Different corrections are applied to recover for these effects. Improvements up to  $\sim 40\%$  in the  $m_{bb}$  resolution can be achieved depending on the channel, as shown in Figure 7.4. The applied corrections are briefly described below:

- **Muon in Jet:** as described in Section 5.1.5 the leptonic+semi-leptonic b-quark BR is  $\sim 42\%$ , including electron and muon contributions. Therefore, b-jets are expected to contain a muon  $\sim 20\%$  of the times. The total energy of the jet is calculated starting from calorimeter information, but the muon energy is often lost in this calculation since it deposits just a small amount of energy in the calorimeters (typical value  $\sim 3$  GeV). To correct for this effect, if a muon with at least medium quality criteria and  $p_T$  larger than 5 GeV is found within a jet ( $\Delta R(\text{jet}, \text{muon}) < 0.4$ ), its momentum is added to the total momentum of the jet.
- **PtReco correction:** this correction is applied after the muon in jet correction, to compensate for biases in the jet response due to residual effects beyond the semi-leptonic decays, out-of-cone energy losses and undetectable neutrinos. The correction is obtained from  $ZH \rightarrow \ell\ell b\bar{b}$  events from simulation by comparing the calibrated energy of the jet with its true energy. The ratio is taken as a correction scale factor.
- **Kinematic Fit (2-lepton only):** in the 2-lepton channel no significant  $E_T^{\text{miss}}$  is present, therefore the full kinematic of the event can be reconstructed. Since the lepton resolution is much better than the b-jet resolution, the transverse energy of the di-jet system is corrected to perfectly balance the one of the di-lepton system. This is achieved with a kinematic likelihood fit (KF). The dilepton invariant mass is fitted with a Breit-Wigner distribution with Z boson mass as its mean and the Z decay width as its width, while the transverse momentum of the total  $\ell\ell b\bar{b}$  system is described by a Gaussian smearing function, with mean value fixed at 0 (complete balance) and width fixed to 9 GeV, determined by measurements in simulated ZH events based on truth level information. The transverse momenta of each object in the fit ( $\ell, \ell, b, b$ ) are smeared by a Gaussian resolution function separately. The correction outcoming from the fit leads to an improvement of  $\sim 20\%$  in the di-jet mass resolution. The kinematic fit is applied in combination with the muon in jet correction and no PtReco correction is applied, since it is already taken into account by the fit.

Selection	0-lepton	1-lepton		2-lepton
Trigger	$E_T^{\text{miss}}$	$e$ sub-channel	$\mu$ sub-channel	
Leptons		Single lepton	$E_T^{\text{miss}}$	Single lepton
$E_T^{\text{miss}}$	0 <i>loose</i> leptons with $p_T > 7$ GeV	1 <i>tight</i> electron $p_T > 27$ GeV	1 <i>tight</i> muon $p_T > 25$ GeV	2 <i>loose</i> leptons with $p_T > 7$ GeV $\geq 1$ lepton with $p_T > 27$ GeV
$m_{\ell\ell}$	$> 150$ GeV	$> 30$ GeV	–	–
Jets	–	–	–	$81 \text{ GeV} < m_{\ell\ell} < 101 \text{ GeV}$
Jet $p_T$	Exactly 2 / Exactly 3 jets	Exactly 3 jets	–	Exactly 2 / $\geq 3$ jets
$b$ -jets	$> 20$ GeV for $ \eta  < 2.5$ and $> 30$ GeV for $2.5 <  \eta  < 4.5$	–	–	–
Leading $b$ -tagged jet $p_T$	–	Exactly 2 $b$ -tagged jets	–	–
$H_T$	$> 120$ (2 jets), $> 150$ GeV (3 jets)	$> 45$ GeV	–	–
$\min[\Delta\phi(\vec{E}_T^{\text{miss}}, \vec{\text{jets}})]$	$> 20^\circ$ (2 jets), $> 30^\circ$ (3 jets)	–	–	–
$\Delta\phi(\vec{E}_T^{\text{miss}}, \vec{bb})$	$> 120^\circ$	–	–	–
$\Delta\phi(\vec{b}_1, \vec{b}_2)$	$< 140^\circ$	–	–	–
$\Delta\phi(\vec{E}_T^{\text{miss}}, \vec{E}_{T,\text{trk}}^{\text{miss}})$	$< 90^\circ$	–	–	–
$p_T^V$ regions	$> 150$ GeV	–	–	$75 \text{ GeV} < p_T^V < 150 \text{ GeV}, > 150 \text{ GeV}$
Signal regions	–	$m_{bb} \geq 75 \text{ GeV}$ or $m_{\text{top}} \leq 225 \text{ GeV}$	–	Same-flavour leptons Opposite-sign charges ( $\mu\mu$ sub-channel)
Control regions	–	$m_{bb} < 75 \text{ GeV}$ and $m_{\text{top}} > 225 \text{ GeV}$	–	Different-flavour leptons Opposite-sign charges

TABLE 7.5 – Summary of the event selection in the 0-, 1- and 2-lepton channels of the  $VH, H \rightarrow bb$  analysis, where  $b_1$  and  $b_2$  are the two  $b$ -tagged jets forming the Higgs boson candidate di-jet system,  $H_T$  is the scalar sum of the  $p_T$  of the jets in an event and  $E_T^{\text{miss}}$  is the missing transverse momentum [205].



Process	$\sigma \times \mathcal{B}$ [fb]	Acceptance [%]		
		0-lepton	1-lepton	2-lepton
$qq \rightarrow ZH \rightarrow \ell\ell b\bar{b}$	29.9	<0.1	0.1	6.0
$gg \rightarrow ZH \rightarrow \ell\ell b\bar{b}$	4.8	<0.1	0.2	13.5
$qq \rightarrow WH \rightarrow \ell\nu b\bar{b}$	269.0	0.2	1.0	–
$qq \rightarrow ZH \rightarrow \nu\nu b\bar{b}$	89.1	1.9	–	–
$gg \rightarrow ZH \rightarrow \nu\nu b\bar{b}$	14.3	3.5	–	–

TABLE 7.6 – The cross-section ( $\sigma$ ) times branching ratio ( $\mathcal{B}$ ) and acceptance for the three channels at  $\sqrt{s} = 13$  TeV. The qq- and gg-initiated  $ZH$  processes are shown separately. The branching ratios are calculated considering only decays to muons and electrons for  $Z \rightarrow \ell\ell$ , decays to all three lepton flavours for  $W \rightarrow \ell\nu$  and decays to all neutrino flavours for  $Z \rightarrow \nu\nu$ . The acceptance is calculated as the fraction of events remaining in the combined signal and control regions after the full event selection [205].

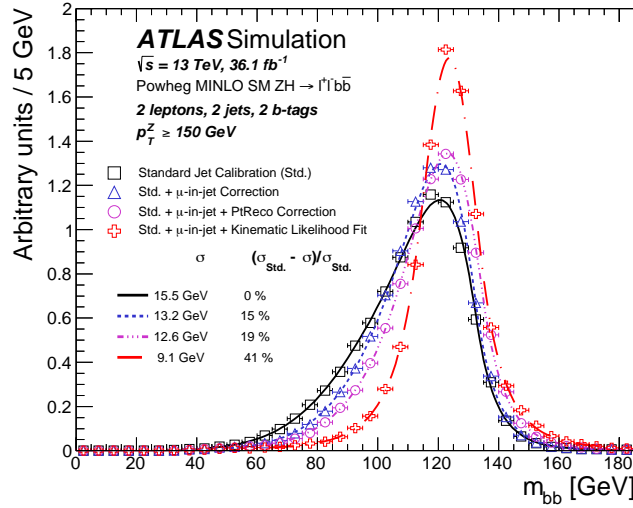


FIGURE 7.4 – Comparison of the  $m_{b\bar{b}}$  distributions as additional corrections are applied to the jet energy scale, shown for simulated events in the 2-lepton channel in the 2-jet and  $p_T^Z > 150$  GeV region. A fit to a Bukin function [206] is superimposed on each distribution, and the resolution values and improvements are reported in the legend [187].



### 7.2.2 Di-jet mass analysis additional selection

As described in the introduction, the nominal analysis is cross-checked with a second analysis: the di-jet mass analysis, which substitutes the fit to the MVA distribution with a fit on the di-jet invariant mass. Since this analysis relies on a fit to a single variable, rather than a fit on a combined MVA classifier, specific requirements must be applied at selection level to reduce the background under the di-jet mass ( $m_{bb}$ ) peak in the signal region. The additional selection criteria are summarized in Table 7.7 and briefly described below:

- The fitting regions are further separated into two  $p_T^V$  regions:  $150 < p_T^V < 200$  GeV and above 200 GeV.
- The angular separation of the two jets,  $|\Delta R(b_1, b_2)|$ , is required to be smaller than certain thresholds, separately optimised in each  $p_T^V$  region. In fact, the angular separation decreases when the Higgs boson candidate momentum, and therefore  $p_T^V$  increases. At first approximation this relation can be written as:

$$\Delta R(b, b) \sim \frac{2m_{bb}}{p_T^{bb}} \quad (7.1)$$

with  $m_{bb}$  the di-jet invariant mass and  $p_T^{bb}$  the transverse momentum of the di-jet system.

- In 1-lepton the  $t\bar{t}$  background is further suppressed requiring  $m_T^W$  to be below 120 GeV (as can be seen in Figure 7.3), with  $m_T^W$  defined as:

$$m_T^W = \sqrt{2p_T^\ell E_T^{\text{miss}}(1 - \cos(\phi^\ell - \phi^{\text{miss}}))} \quad (7.2)$$

- In 2-lepton the  $t\bar{t}$  background is suppressed requiring  $E_T^{\text{miss}}/\sqrt{S_T}$  to be below  $3.5\sqrt{\text{GeV}}$ , with  $S_T$  being the scalar sum of the transverse momentum of the two leptons and all the reconstructed jets in the event.

Channel			
Selection	0-lepton	1-lepton	2-lepton
$m_T^W$	-	< 120 GeV	-
$E_T^{\text{miss}}/\sqrt{S_T}$	-	-	< $3.5\sqrt{\text{GeV}}$
$p_T^V$ regions			
$p_T^V$	(75, 150] GeV (2-lepton only)	(150, 200] GeV	> 200 GeV
$\Delta R(\vec{b}_1, \vec{b}_2)$	< 3.0	< 1.8	< 1.2

TABLE 7.7 – Summary of the signal event selection in the 0-, 1- and 2-lepton channels of the cut-based di-jet mass  $VH \rightarrow bb$  analysis.

### 7.2.3 Analysis regions

The events passing the outlined selection criteria are further split into different categories. In total eight signal regions (SR) and six control regions (CR) are defined. The categorisation is performed per lepton channel by counting the number of reconstructed leptons (0-,1-,2-leptons), jet multiplicity, and momentum of the vector

boson. Since the background contamination is reduced at high  $p_T$  of the Higgs boson candidate (or equivalently of the vector boson), events are categorised according to the reconstructed transverse momentum of the vector boson  $p_T^V$ , to increase the overall S/B ratio. In the 0-lepton and 1-lepton cases just one  $p_T^V$  region is defined requiring  $p_T^V > 150$  GeV, while in the 2-lepton case two regions  $75 < p_T^V < 150$  GeV and  $p_T^V > 150$  GeV are retained as described in the previous Section.

Events are further categorised depending on the jet multiplicity: in the 0- and 1-lepton case the events are divided into exactly two jets (2-jets) or exactly three jet (3-jet) categories to reduce the  $t\bar{t}$  contamination, while in the 2-lepton channel the three jet category is modified to contain events with *at least* three jets (3p-jet).

To reduce the dependence on the Monte Carlo simulation and the effect of systematic uncertainties, the shapes and/or normalizations of some of the main backgrounds are determined directly on data, by defining specific control regions (CR) enriched in one particular background process. Additional criteria are applied to select these regions, on top of those described in the previous Sections. These requirements are designed to make the control regions orthogonal to the signal regions, with a negligible amount of signal contamination. Two main control regions are defined: the W+HF control region in the 1-lepton channel and the top  $e\mu$  control region in the 2-lepton channel. More details are given in the next Sections. In the di-jet mass analysis, the regions are modified to enhance the overall sensitivity as described in Section 7.2.2, and in the 1-lepton channel the W+HF CR is merged into the signal region.

### W+HF control region

This control region aims at constraining the normalisation of the W+HF background directly from data, considerably reducing the related normalisation uncertainty in the fit. This goal is achieved selecting a region of the 1-lepton channel phase space with high W+HF purity, both in the 2-jet and 3-jet categories. The selection cuts are applied to disentangle the W+HF process from the semi-leptonically decaying  $t\bar{t}$  process, which is the dominant background contribution in the 1-lepton channel. Exploiting the kinematics of the event, the mass of the top quark decaying to  $Wb \rightarrow \ell\nu b$  can be reconstructed and the majority of the  $t\bar{t}$  events can be separated from the W+HF background.

The first step in the calculation of the top mass variable consists in the estimation of the longitudinal momentum of the neutrino. Assuming the lepton-neutrino pair to be produced in a W boson decay, and the  $E_T^{\text{miss}}$  to entirely arise from the neutrino, the longitudinal momentum of the neutrino can be achieved imposing the conservation of energy and requiring the invariant mass of the lepton-neutrino system to be equal to the W boson mass. The solution of the conservation of energy equation are

$$p_z^\nu = \frac{1}{2(p_T^\ell)^2} (p_z^\ell X \pm E_\ell \sqrt{X^2 - 4(p_T^\ell)^2 (E_T^{\text{miss}})^2}), \quad (7.3)$$

with  $X$  defined as:

$$X = m_W^2 + 2p_x^\ell E_x^{\text{miss}} + 2p_y^\ell E_y^{\text{miss}} \quad (7.4)$$

with  $p_x^\ell, p_y^\ell, p_z^\ell$  the  $x, y$  and  $z$  components of the lepton four-momentum,  $p_T^\ell$  the lepton transverse momentum and  $E_{x,y}^{\text{miss}}$  the  $x$  and  $y$  components of the  $E_T^{\text{miss}}$  in the transverse plane. Of the two possible solutions, the smallest one is considered. Sometimes, the transverse mass of the reconstructed lepton-neutrino system can be larger than the mass of the mother particle (W), leading to imaginary values of the square

root. This is assumed to be entirely due to resolution effects and corrected by setting the discriminant<sup>2</sup> equal to zero. In these cases only one real solution to the equation is available. The final  $M_{top}$  variable is then reconstructed by selecting the jet from the two b-tagged jets minimising  $M_{top}$ . For true  $t\bar{t}$  events the  $M_{top}$  distribution is peaked at  $M_{top} \sim 172.5$  GeV, while for W+HF no peak is expected; cutting on this variable therefore allows to remove a large fraction of this background from the control region. The cut  $M_{top} > 225$  GeV was found to be a good compromise between a high  $t\bar{t}$  suppression and enough W + HF statistics in the CR.

In order to ensure the minimal signal contamination for this control region, an additional selection is applied to the di-jet mass, requiring  $m_{bb} < 75$  GeV. The combination of these cuts allows having a W+HF purity in the control region of  $\sim 80\%$  (75%) in the 2-jet (3-jet) region. Due to limited statistics, a single bin is defined both in 2-jet and in 3-jet categories, meaning that this W+HF CR is only used to constrain the normalization of the W+HF background in the SR, but not the modelling uncertainties related to its differential distributions (see Section 7.5.2).

### Top $e\mu$ control region

The second most important background normalization uncertainty in the analysis is the  $t\bar{t}$  normalization. As for the W+HF case, having a dedicated control region to constrain the  $t\bar{t}$  background parameters directly from data highly reduces this uncertainty in the final fit. Therefore, a dedicated  $t\bar{t}$  and  $Wt$  enriched region is defined starting from the 2-lepton channel selection, requiring the two leptons to have different lepton flavours, i.e.  $e\mu$ . This is orthogonal to the 2-lepton channel signal region selection, where the two leptons must have the same flavour (to fulfill the lepton flavour conservation in the Z decay).

This region is called top  $e\mu$  CR and it is 99% pure in  $t\bar{t}$  and  $Wt$ . The kinematics of  $t\bar{t}$  events in this region is similar to that observed in the signal region, thus it can be exploited to constrain both normalization and modelling (of the  $m_{bb}$  component) in the 2-lepton channel. Examples of the  $m_{bb}$  distributions from the 3-jet top  $e\mu$  CR are presented in Figure 7.5.

## 7.3 Multivariate analysis

A multivariate analysis (MVA) making use of boosted decision trees [207] is implemented, to separate the Higgs boson signal from the large V+jets and top backgrounds, as well as from subdominant ones, such as the diboson production. Multivariate discriminants are constructed, trained and evaluated in each lepton channel and signal region separately. The input variables used for the BDTs are chosen to maximise the separation power. The MVA approach is expected to bring an improvement of  $\sim 15\%$  in sensitivity with respect to the di-jet cut-based analysis [208]. Additional BDTs are trained for the diboson cross-check analysis, using the same input variables as the  $VH, H \rightarrow b\bar{b}$  case, but using the diboson contribution as signal and the VH as part of the background in the training. In order to distinguish the two BDTs, the label  $BDT_{VZ}$  is added in case of the diboson BDT.

The general idea of any multivariate classification method is to combine a set of chosen variables  $x_{i,\dots,n}$  able to discriminate between signal and background - or multiple hypotheses when speaking of multi classifiers - into a single variable  $y$  which overall will have an enhanced separation power. The relation between the input

2. The expression under the square root as in Equation 7.3.

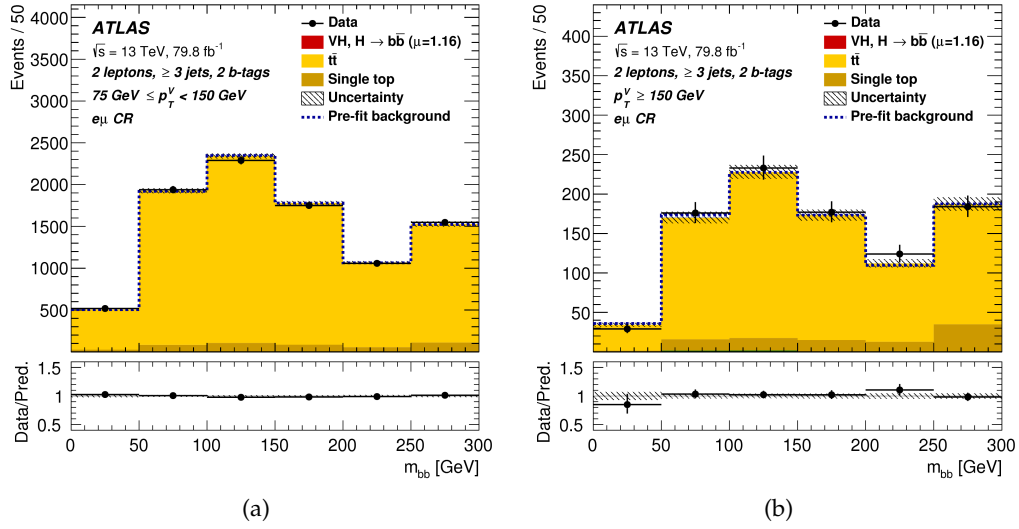


FIGURE 7.5 – The  $m_{bb}$  distributions in the  $e\mu$  control regions for the  $VH, H \rightarrow b\bar{b}$  analysis for (a) the 3-jets  $75 < p_T^V < 150$  GeV category and (b) the 3-jets  $p_T^V > 150$  GeV category. The dashed histogram shows the total pre-fit background. The entries in overflow are included in the last bin. The ratio of the data to the sum of the signal and fitted background is shown in the lower panel [205].

variables and the final classifier is

$$y = f(x_1, \dots, x_n) \quad (7.5)$$

with  $f$  a function to be determined starting from the input variables  $x_{i, \dots, n}$ . The best  $f(x_1, \dots, x_n)$  functions for signal and background are built starting from large sets of events pre-labelled as signal or background (see later for more details on the building process). This procedure is also called *training*. If the number of events is not enough, the MVA can be sensitive to the so-called *overtraining*, meaning the specialisation of the  $f$  function to the particular set of data used for the training, which makes the algorithm fail to predict observations reliably on an alternative dataset. For the  $VH, H \rightarrow b\bar{b}$  analysis the Boosted Decision Tree algorithm was chosen as the best compromise between training-tuning time and robustness, following from studies discussed in Ref. [208].

### 7.3.1 Boosted Decision Trees

Boosted Decision Trees (BDTs) are combinations of Decision Trees (DT). A Decision Tree can be intuitively seen as the optimization of a cut-and-count approach in a multi-dimensional phase space. A decision tree takes a set of variables as inputs and splits the events recursively based on those features. The final result is a tree with decision nodes and leaf nodes. A decision node has two or more branches, while a leaf node represents a classification or a decision. Each node carries a cut qualification so that a tested candidate advances from this node either to the left or right daughter nodes depending whether it fails or not the cut. Consequently, any event that fails a certain cut will not be thrown away immediately as background, but continue to be analyzed.

The decision tree training uses a set of known signal and background training events, each with event weight  $w_i$ , to build a tree structure of cuts node by node. The event

weights  $w_i$  can be set to unity or to event-by-event values. In the  $VH, H \rightarrow b\bar{b}$  analysis the initial weights are set to the Monte Carlo event weight, which contains all the corrections described in Section 7.1 and the normalization of the samples to the correct cross-sections. The function used to optimise the decision cuts in the tree relies on the *Gini* index:

$$Gini(c_i) = 2p(c_i)(1 - p(c_i)) \quad (7.6)$$

where  $c_i$  represents the cut threshold of the variable  $i$  and  $p(c_i)$  is the purity:

$$p = \frac{S}{S+B} = \frac{\sum_s w_s}{\sum_s w_s + \sum_b w_b} \quad (7.7)$$

and  $S(B)$  is the weighted total number of signal (background) events which arrived on the node during training. Therefore, the *Gini* index is 0 when the node is either only pure signal or pure background (1 or 0) and maximized when the purity is 0.5. The maximum separation is defined as the maximum change in the *Gini* index between the mother node and the two daughter nodes, defined as:

$$\Delta Gini = Gini_{Mother} - f_L \cdot Gini_L - f_R Gini_R \quad (7.8)$$

with  $L$  and  $R$  the left and right daughter nodes and  $f_{L(R)}$  the weighted fraction of events in the daughter node. The cut corresponding to the highest  $\Delta Gini$  is chosen and the process continues for the daughter nodes with the remaining cuts, growing the tree until the split in each node results in less than a minimum number of events in the daughter node. This node is then defined as *leaf*, with a certain purity assigned. Depending on its purity, a leaf can be a signal or a background leaf, meaning that events falling in that leaf will be classified as signal or background events accordingly. A schematic view of the structure of a Decision Tree is given in Figure 7.6. A test event will go through the cut conditions until it falls in a decision leaf.

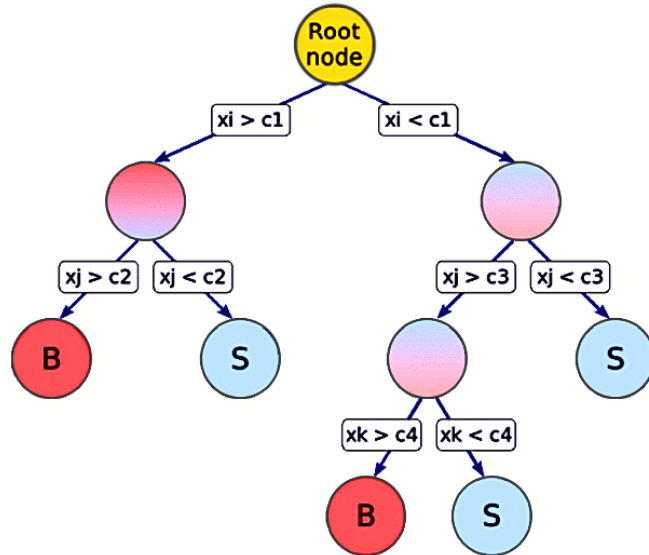


FIGURE 7.6 – Scheme of a decision tree with nodes (intermediate steps) and leaves (decision nodes). The blue indicates a signal-like leaf, while the red indicates a background-like leaf [209].

### Boosting

While a single decision tree already improves upon a simple cut-based analysis, boosting significantly increases the performance of the algorithm. The idea behind boosting is to combine many Decision Trees consecutively, as described in this Section. The trees are trained consecutively with new weights calculated after each iteration. A stronger weight, determined as explained below, is assigned to the candidates misclassified by the previous tree, to increase their importance during the next training. The change of weights at each step makes the overall algorithm less influenced by the statistical fluctuations of the training sample. This ensures more stability and robustness against *overtraining*, which occurs when the classifier specializes the  $f(x_1, \dots, x_n)$  function on features of the training sample. Several methods to quantify the overtraining are available, as described in the next Section. The misclassification rate of the  $m^{\text{th}}$  tree can be defined as the weighted fraction of misclassified events:

$$err_m = \frac{\sum_j w_{m,j} \cdot M_m(j)}{\sum_j w_{m,j}} \quad (7.9)$$

with a loop over the  $j$  events in the training sample with a weight  $w_{m,j}$  and using the value  $M_m(j) = 1$  for misclassified candidates and 0 otherwise. The boost weight  $\alpha_m$  assigned to a specific Decision Tree is defined as:

$$\alpha_m = \ln \left( \frac{1 - err_m}{err_m} \right). \quad (7.10)$$

In the next  $m + 1$  training, the final weight of the  $i$  event is defined as:

$$w_{m+1,i} = w_{m,i} \cdot e^{\alpha_m \cdot M_m(i)} \quad (7.11)$$

Thus, the weights of correctly classified candidates are not changed. The Decision Tree scores are combined to determine the BDT score  $y$  of the event, being:

$$y = \frac{1}{N_{\text{collection}}} \sum_n^{N_{\text{collection}}} \alpha_n \cdot h_n(x_1, \dots, x_n) \quad (7.12)$$

with  $N_{\text{collection}}$  the number of classifiers in the collection,  $\alpha_n$  the weight of the event in the  $n$ -th classifier and  $h_n(x_1, \dots, x_n)$  the result of an individual classifier, given the variables  $x_1, \dots, x_n$ , which can be -1 for a background-like or +1 for a signal-like decision.

The output  $y$  is a number between -1 and 1, which can be intuitively seen as the likelihood for an event to be classified as signal or background. Signal events are expected to be closer to 1, while background events are distributed at lower BDT values. There are many different boosting techniques: [210]: AdaBoost [211], GradientBoosting [212], XGBoost [213]. For historical reasons, the algorithm used for the  $VH, H \rightarrow b\bar{b}$  analysis is AdaBoost<sup>3</sup>. The formalism corresponds to the one reported in this Section, with a small modification in the definition of the  $\alpha$  parameter:

$$\alpha_m = \ln \left( \beta \cdot \frac{1 - err_m}{err_m} \right) \quad (7.13)$$

with  $\beta$  a specific parameter called *learning rate*, which is set by the user.

<sup>3</sup>. Alternative methods were tested in Run-1, resulting in similar performance compared to AdaBoost



### 7.3.2 The MVA training setup

Only events that passed the event selection described in Section 7.2, are considered in the multivariate analysis. Since each channel has its specific background composition, the input variables are chosen independently for each channel, to maximize the individual signal and background separation.

Variable	0-lepton	1-lepton	2-lepton
$p_T^V$	$\equiv E_T^{\text{miss}}$	×	×
$E_T^{\text{miss}}$	×	×	×
$p_T^{b_1}$	×	×	×
$p_T^{b_2}$	×	×	×
$m_{bb}$	×	×	×
$\Delta R(\vec{b}_1, \vec{b}_2)$	×	×	×
$ \Delta\eta(\vec{b}_1, \vec{b}_2) $	×		
$\Delta\phi(\vec{V}, \vec{bb})$	×	×	×
$ \Delta\eta(\vec{V}, \vec{bb}) $			×
$m_{\text{eff}}$	×		
$\min[\Delta\phi(\vec{\ell}, \vec{b})]$		×	
$m_T^W$		×	
$m_{\ell\ell}$			×
$m_{\text{top}}$		×	
$ \Delta Y(\vec{V}, \vec{bb}) $		×	
Only in 3-jet events			
$p_T^{\text{jet}_3}$	×	×	×
$m_{bbj}$	×	×	×

TABLE 7.8 – Variables used for the multivariate discriminant in each channel [205].

The choice of variables for the BDT has been made in Run-1 [208] as an iterative process. Starting from  $m_{bb}$ , additional variables are added looking at the sensitivity gain of the BDT after the new training. Only the variables with the highest separation power are kept<sup>4</sup>, until no further improvement is observed. Good modelling is required for the input variables to ensure no bias in the implementation of the BDT. A summary of all the variables used in the 0-, 1- and 2-lepton BDTs is presented in Table 7.8. The best separation power is given by the  $m_{bb}$  and  $\Delta R(bb)$  variables, which exploit the correlation of the two b-jets and the constraints on their kinematics given by the Higgs boson decay. These correlations do not exist in the background processes since the b-jets do not originate from the decay of a resonance, except for the diboson process, which represents a sub-dominant contribution compared to the overall background. The 1-lepton and 2-lepton channels include also variables to specifically increase the separation power with respect to  $t\bar{t}$  events, such as  $M_{\text{top}}$  in the 1-lepton channel,  $m_{\ell\ell}$  and  $E_T^{\text{miss}}$  in the 2-lepton channel.

The BDT parameters (also referred to as *hyper-parameters*) have been tuned performing a scan of the various combinations. The settings were chosen in the previous round of the analysis and not changed in the 2018 iteration, due to the limited

4. The variables were found to be optimal also in the 2017 round of the analysis (with  $36 \text{ fb}^{-1}$  of Run-2 data at  $\sqrt{s} = 13 \text{ TeV}$ ), and they have been kept unchanged for the  $80 \text{ fb}^{-1}$  publication.



amount of time. Table 7.9 summarises the settings of the BDT used in the three channels.

Configuration	Value	Definition
BoostType	AdaBoost	Boosting procedure
AdaBoostBeta	0.15	Learning rate
SeparationType	GiniIndex	Node separation gain
NTrees	200	Number of trees
MaxDepth	4	Maximum tree depth
NCuts	100	Number of equally spaced cuts tested per variable per node
NEventsMin	5%	Minimum number of events in a node w.r.t. total

TABLE 7.9 – Nominal BDT<sub>VH</sub> and BDT<sub>VZ</sub> configuration parameters implemented for the  $VH, H \rightarrow b\bar{b}$  analysis.

In order to control the impact of the limited Monte Carlo statistics on the BDT performance, the available dataset is split into two sub-sets based on the event number, even and odd. These sub-sets are named *folds* and no difference is expected between them. The two folds are reciprocally used for training and testing several BDTs, meaning that first the BDT is trained on one fold and tested on the other and a second training is performed reverting the two sub-sets. The BDT outputs are expected to be insensitive to this change, because there is no physical difference between even and odd events, therefore the BDT shapes should coincide in training and evaluation. If the BDT outputs are different, it means that the BDT has been optimised on statistical fluctuations of the training dataset, and therefore there is *overtraining*. Figure 7.7 shows the comparison of the BDT output in the training and evaluation datasets for signal and background superimposed for the 1-lepton channel. The training and evaluation distributions are almost perfectly overlapping, for both signal and background, meaning that no overtraining is present.

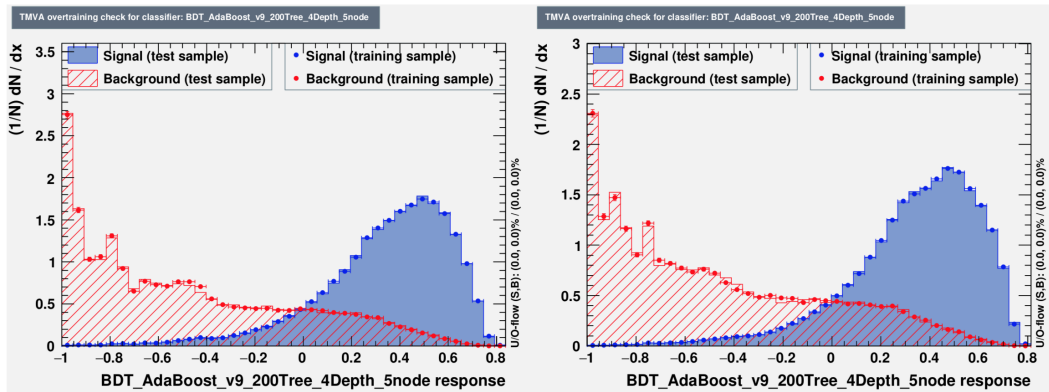


FIGURE 7.7 – The BDT distributions of the signal (blue) and sum of all background (red) processes in the 1-lepton 2 jet region obtained with training (dots) and testing (histogram) samples. Both folds of the training are shown: (left) even and (right) odd event numbers in the training.

To enhance the number of events in the training sample and therefore reduce the risk of overtraining, truth tagging is applied to all the events. As described in Section 5.4, truth tagging is a statistical reweighting based on  $\eta$  and  $p_T$  efficiency maps, which however does not take into account other important variables of the process, such as the angular separation  $\Delta R_{bb}$  between the two b-jet candidates. Therefore, changes in the shapes of the BDT variables can be observed, and the resulting BDT

can be slightly sub-optimal. A 5% decrease in performance was observed in the 0-lepton BDT when moving to truth tagging with respect to direct tagging, according to a study performed in 2016 [214].

### 7.3.3 BDT transformation

The output of the BDT is stored in histograms with 1000 bins. A variable-size re-binning has been developed to optimise the sensitivity, while improving the stability of the final fit. For each bin, the fit needs to handle the specific signal and background uncertainties (bin-dependent) and the correlations across the bins for all the considered regions, therefore the complexity of the fit grows very quickly.

A numerical optimization algorithm is defined to search for the optimal binning. The optimisation has been done for the analysis of  $36 \text{ fb}^{-1}$  of Run 2 data, maximising the expected statistical significance from the Likelihood fit for a given number of bins in the output histogram and not changed for the  $80 \text{ fb}^{-1}$  analysis due to the limited amount of time. The transformation function  $Z$  is defined as:

$$Z = z_s \frac{n_s}{N_s} + z_b \frac{n_b}{N_b} \quad (7.14)$$

with  $N_s$  and  $N_b$  the total number of fine bins for signal and background,  $z_s$  and  $z_b$  are the free transformation parameters to be optimised and  $n_{s,b}$  are the numbers of signal (background) events in the interval containing a certain number of bins. Starting from the highest bin (i.e. the right-most bin), the algorithm starts grouping the bins one by one re-computing the  $Z$  function at each step, updating the value of  $n_s$  and  $n_b$ , until the condition  $Z > 1$  is fulfilled. These bins are then merged in one single bin and the procedure is repeated iteratively until all the bins are considered.

With this algorithm the number of bins in the output histogram,  $N_{bin}$ , is directly connected to the free  $z$  parameters:  $N_{bin} = z_s + z_b$ . The BDT shape is impacted by this rebinning, but the underlying physics is not affected since its shape is not directly related to a physical interpretation. To visualize the impact of the  $z_s$  and  $z_b$  tuning on the BDT shape, one can look at two extreme cases: for  $z_s = 0$ ,  $z_b > 0$  the background would be equally distributed among the bins, with  $N_{bin} = z_b$ . On the contrary, for  $z_s > 0$ ,  $z_b = 0$  the output would be a flat signal distribution. The tuning allows to adjust the shape of the output distribution by interpolating between these cases. The goal is to obtain a smoother distribution for the background and a finer binning for the bins with the largest signal contribution, while keeping the statistical uncertainty of the simulated events under a certain threshold for each bin. The BDT transformation parameters have been optimised for the  $36 \text{ fb}^{-1}$  analysis to be:  $z_s = 10$  and  $z_b = 5$ , leading to a total of 15 bins after the reweighting. These values have been chosen to maintain the statistical uncertainty of the simulated events (especially in the most sensitive regions) below 20% in each bin.

## 7.4 Statistical Treatment

The analysis regions described in Section 7.2.3 are combined in a simultaneous fit to extract the  $VH, H \rightarrow b\bar{b}$  signal strength, defined in Chapter 2 as:

$$\mu = \frac{\sigma \cdot BR}{\sigma_{SM} \cdot BR_{SM}}. \quad (7.15)$$

The fit is based on the so-called profile likelihood formalism, which is explained in more detail in the next Sections.

### 7.4.1 Hypothesis Testing

The hypothesis testing is the statistical procedure used to verify or exclude a certain hypothesis, with a pre-defined level of confidence. Usually, two statistical datasets are compared: one obtained from experimental observations and one generated from theoretical predictions. Various hypotheses can be proposed on the relationship between these two datasets. The null hypothesis ( $H_0$ ) is referred to as the *background only* hypothesis, while the alternative hypothesis ( $H_1$ ) can have different formulations, for the purpose of this thesis work the alternative hypothesis is formulated as the *expected signal+background hypothesis* ( $H_1 = S + B$ ). The hypothesis test aims at verifying the null hypothesis comparing experimental and simulated datasets. If the null hypothesis fails with at least a predefined probability the test is defined statistically significant and the null hypothesis can be discarded.

The test is usually performed on a specific quantity calculated from the data sample, called test statistic, which estimates how probable the observed result is with respect to the null hypothesis. The test statistic is defined in such a way to attribute the null hypothesis to the SM “background only” hypothesis and the alternative hypothesis to the signal+background. For this type of analyses the test statistic is usually defined as the Likelihood Ratio (see next Section). The  $p$  – *value* variable quantifies the probability to have a value of test statistic larger than the observed one, assuming the null hypothesis as true (see Figure 7.8). The smaller is the p-value, the worse the background-only hypothesis describes the data sample. In other words, the p-value quantifies the probability of observing random excesses which can fake a signal+background hypothesis, in case the background only hypothesis is true.

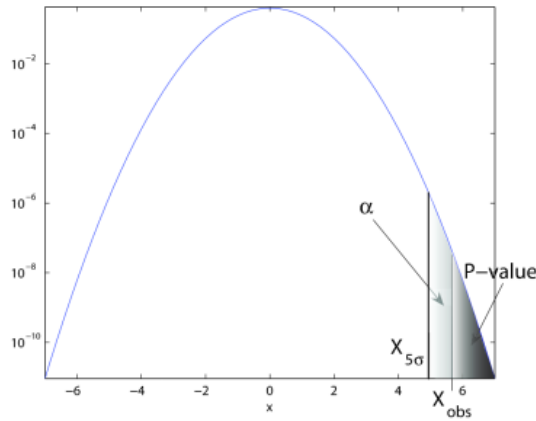


FIGURE 7.8 – Illustration showing the control area  $\alpha$  and the p-value of a Gaussian distribution.  $X_{obs}$  corresponds to the observation, while  $x = X_{5\sigma}$  corresponds to the  $x$  value at  $5\sigma$  from the null hypothesis, having a probability of  $2.87/10^7$  to be associated with the null hypothesis.

If this p-value is smaller than a certain threshold, explaining the observed data with a background-only hypothesis becomes more and more unrealistic and the  $H_0$  hypothesis can be rejected. The p-value is usually converted into the so-called significance  $Z$ , defined in terms of standard deviations of a standard Gaussian distribution:

$$Z = \Phi^{-1}(1 - p_0) \quad (7.16)$$

where  $\Phi^{-1}$  is the inverse of the cumulative distribution of the standard Gaussian. Conventionally, the test is said to be statistically significant and the null hypothesis is rejected in favour of the alternative one (signal+background) when  $Z=5$ . This  $5\sigma$  significance needed to claim a discovery is equivalent to a p-value of  $2.87/10^7$ , which means a probability of less than  $\sim 3$  over 10 million that the observation is due to a background fluctuation.

### 7.4.2 Likelihood Ratio

The hypotheses considered in the hypothesis testing can be expressed as  $\mu s + b$ , where  $\mu$  is the signal strength. The background only hypothesis corresponds to  $\mu = 0$  while  $\mu = 1$  corresponds to the signal+background hypothesis for a SM Higgs boson decay.

Given a set  $X$  of  $n$  observed signal events, denoted by the measurements of the variable - or vector of variables -  $x$ , with  $X = [x_1, \dots, x_n]$ , and a simulated probability density  $g(x|\mu)$ , where  $\mu$  is defined as the parameter of interest (free parameter), the probability to have the sample  $X$  is given by the product of the probabilities of the single  $i$  measurements to be in the interval  $[x_i, x_i + dx_i]$ :

$$P = \prod_{i=1}^n P(x_i) = \prod_{i=1}^n g(x_i|\mu) dx_i = \mathcal{L}(X|\mu) \prod_{i=1}^n dx_i, \quad (7.17)$$

where  $P(x_i)$  is the probability to find a measurement ( $x_i$ ) in an infinitesimal interval  $[x_i, x_i + dx_i]$ . The quantity  $\mathcal{L}(X|\mu)$ , which defines the convolution of probability density functions, is the so-called *likelihood* function.

The  $VH, H \rightarrow b\bar{b}$  statistical analysis uses a binned version of the likelihood function, where the observed  $x_i$  are substituted by the histogram bins ( $N_{bins}$ ) after the BDT transformation described in Section 7.3.3. In addition, the cross section of interesting events is usually really small, therefore the signal is considered as Poisson distributed. Under these assumptions the binned likelihood function can be expressed as:

$$\mathcal{L}(\mu) = \prod_{i=1}^{N_{bins}} \frac{(\mu s_i + b_i)^{n_i}}{n_i!} e^{-(\mu s_i + b_i)} \quad (7.18)$$

with  $\mu$  the measured signal strength of Equation 7.15,  $s_i$  and  $b_i$  the expected number of signal and background events in the bin  $i$  and  $n_i$  the number of observed data events in the bin  $i$ .

The effect of systematic uncertainties is incorporated in the likelihood definition through additional so-called *nuisance parameters* (NP). They allow for an increase of the flexibility of the model and its capability to better agree with the data. The NP are estimated from data or external measurements, which provide both central value and uncertainties. Each independent source of systematic uncertainty corresponds to a specific nuisance parameter  $\theta$ , therefore calling  $\theta$  the vector of nuisance parameters, the likelihood function becomes:

$$\mathcal{L}(\mu, \theta) = \prod_{i=1}^{N_{bins}} \frac{(\mu s_i(\theta) + b_i(\theta))^{n_i}}{n_i!} e^{-(\mu s_i(\theta) + b_i(\theta))} \times \mathcal{L}_{aux}(\theta) \quad (7.19)$$

with  $\mathcal{L}_{aux}(\theta)$  the auxiliary likelihood function constraining the distribution of the systematic uncertainties around their central value. In most cases this distribution can be parametrised by a Gaussian function, therefore the auxiliary likelihood for a

number of systematic uncertainties  $N_{syst}$  appears as<sup>5</sup>:

$$\mathcal{L}_{aux}(\boldsymbol{\theta}) = \prod_j^{N_{syst}} \frac{1}{\sqrt{2\pi}\sigma_j} \cdot e^{-\frac{(\bar{\theta}_j - \theta_j)^2}{2\sigma_j^2}}, \quad (7.20)$$

where  $\bar{\theta}_j$  is the central value of the Gaussian, which by convention is set to  $\bar{\theta} = 1$  for the normalization NPs and to  $\bar{\theta} = 0$  for the other NPs, shifting the nominal central value of the prediction;  $\theta_j$  is a generic value for the NP and  $\sigma_j$  is the prior uncertainty of  $\theta_j$ . This additional term acts as penalty term, penalising large deviations from the value set a priori  $\bar{\theta}_j$  in the likelihood.

Some nuisance parameters, called *freely floating parameters*, are completely determined from the fit and no prior or penalty is set for them. Usually this applies to the NP related to signal and background normalisations. The maximisation of the likelihood thus produces a joint measurement of the parameter of interest  $\mu$  and the nuisance parameters  $\theta$ . The fit can shift ("pull") a nuisance parameter to better accommodate the data/MC description or/and, at the same time, constrain the error on the initial value of the NP. The latter happens if the size of the prior uncertainty is too large with respect to the statistical power of data, which can be higher than the independent dataset used to determine the NP priors in the first place. The opposite case, when some NP can appear more weakly constrained than the initial priors (i.e. the post-fit uncertainties are larger than the priors), requires additional investigations since it generally indicates problems in the fit, for example, if the fit did not converge or in case of errors in the normalization, or in the definition of the parameters.

Finally, the statistical uncertainties of the Monte Carlo simulations are also incorporated in the likelihood definition. Following a simplified version of the approach used by Barlow and Beeston [215], a single nuisance parameter is introduced for each bin of the fitted distributions allowing the total MC prediction in that bin to vary within its statistical uncertainty.

The likelihood is used to build the test statistics for the background only  $\mu_0 = 0$  hypothesis described above in the following way:

$$q_0(X) = \begin{cases} -2\ln\lambda(0) = -2\ln \frac{\mathcal{L}(0, \hat{\hat{\theta}}(0))}{\mathcal{L}(\hat{\mu}, \hat{\theta})} & \hat{\mu} \geq 0 \\ 0 & \hat{\mu} < 0 \end{cases} \quad (7.21)$$

The denominator is the likelihood evaluated at the maximum likelihood point, i.e. with  $\mu = \hat{\mu}$  and  $\boldsymbol{\theta} = \hat{\boldsymbol{\theta}}$  the values maximizing the likelihood function, while the numerator is the likelihood obtained fixing  $\mu$  to the constant value  $\mu = \mu_0$  and fitting only the nuisance parameters  $\boldsymbol{\theta}$ , with  $\hat{\hat{\boldsymbol{\theta}}}$  the values maximizing  $\mathcal{L}(\mu_0, \boldsymbol{\theta})$ . The fact that the test statistic is defined to be non zero only for  $\hat{\mu} \geq 0$  implies that the limits on the signal strength are only one-sided, in particular only upward signal strength fluctuations are considered. Finding values of  $\hat{\mu}$  much below zero may indicate an error in the prediction of the background hypothesis or some other systematic error, more than an evidence against the background-only model.

In case of  $\hat{\mu} > 0$ , the test statistics becomes larger, indicating higher incompatibility between the data and the background-only hypothesis. This incompatibility can be

5. Equation 7.20 is valid under the assumption that all systematic uncertainties are considered uncorrelated.

quantified by calculating the *p-value*, also named  $p_0$  in these cases, defined as:

$$p_{0,obs} = \int_{q_{0,obs}}^{\infty} f(q_0|\mu = 0)dq_0 \quad (7.22)$$

where  $q_{0,obs}$  is the value of the test statistic measured from the observed data, and  $f(q_0|\mu = 0)$  the probability distribution function of the test statistic  $q_0$  under the background only hypothesis ( $\mu = 0$ ).

In many realistic cases, finding the correct distribution of  $f(q_0|\mu = 0)$  is not easy, and approximate solutions are adopted. The Wilk's theorem [216] ensures that, if  $H_0$  is true, the quantity:

$$\lambda(\mu_0) = \frac{\mathcal{L}(\mu_0, \hat{\theta}(\mu_0))}{\mathcal{L}(\hat{\mu}, \hat{\theta})} \quad (7.23)$$

is asymptotically distributed as a  $\chi^2$  with a number of degrees of freedom equal to the difference between the dimensionality of numerator and denominator. Thus, in this particular case with  $\mu = \mu_0$ , the Wilk's theorem ensures that  $\lambda(\mu_0)$  is distributed as a  $\chi^2$  distribution with *one* degree of freedom.

Thus, following Equation 7.16, the p-value is related to the significance Z. Following the demonstration described in Ref. [217] and combining the results with Equation 7.16, the significance of the  $\mu = 0$  hypothesis can be defined as:

$$Z_0 = \Phi^{-1}(1 - p_0) = \sqrt{q_0}. \quad (7.24)$$

### 7.4.3 Asimov dataset

The sensitivity of an experiment to a potential discovery can be determined from the simulation by quantifying the expected (median) significance with which a non-zero value of  $\mu$  can be rejected (specifically the nominal  $\mu = 1$ ). This value should be obtained repeating the fit using a large quantity of MC toys and looking at the median significance obtained from these measurements, which is very expensive in terms of computational time and complexity. An alternative method is to calculate directly the median significance, using approximated formulas holding in the limit of large samples, using an extension of the Wilk's theorem carried by Wald [218]. Generalising Equation 7.22, the expected p-value is defined as:

$$p_0 = \int_{q_{0,exp}}^{\infty} f(q_0|0)dq_0, \quad (7.25)$$

the key ingredients to calculate the  $p_{0,exp}$  are therefore  $f(q_0|0)$ , defined as the probability density function of the log likelihood test statistics, and  $q_{0,exp}$  defined as:

$$q_{0,exp} = med[f(q_0|\mu = \mu')] \quad (7.26)$$

which is the median of the probability density function for a value of  $\mu = \mu'$ , with  $\mu' \neq 0$ . The Wald theorem generalizes the form of the  $f(q_0|\mu = \mu')$  distribution for non zero  $\mu$  hypotheses ( $\mu = \mu'$ ) for a large number of data:

$$q_\mu = -2 \log \lambda(\mu) = -2 \left( \log(L(\mu, \hat{\theta})) - \log L(\hat{\mu}, \hat{\theta}) \right) \approx \left( \frac{\mu - \hat{\mu}}{\sigma_\mu} \right)^2 \quad (7.27)$$



with  $\hat{\mu}$  distributed as a Gaussian with mean  $\mu'$  and standard deviation  $\sigma_\mu$ . If  $\hat{\mu}$  follows this Gaussian distribution and neglecting the  $\mathcal{O}(1/\sqrt{N})$  terms, then  $q_\mu$  is represented by a non central  $\chi^2$  distribution with *one* degree of freedom. An artificial 'representative' dataset can be created, such that when it is used to evaluate the likelihood, it returns exactly the true values of the parameters. This dataset is defined as the 'Asimov' dataset [217] and it is found by imposing the derivatives of  $\ln(L)$  (evaluated for a specific  $\mu$ ) with respect to each parameter equal to zero. This holds if the parameters are equal to their hypothesized values. Furthermore, the  $\sigma_\mu$  parameter can not be analytically obtained since it depends on the nuisance parameters. One way to overcome this problem is to set the average  $\sigma_\mu$  of the toy dataset to a value that recovers the known properties of  $\lambda(\mu)$ . This is achieved inverting Equation 7.27 and imposing the variance of the dataset  $\sigma$  to be:

$$\sigma_A^2 = \frac{(\mu - \mu')^2}{q_{\mu,A}}, \quad (7.28)$$

where the label  $A$  is added to distinguish this dataset from the nominal dataset obtained from the measurements. This dataset is therefore the most representative dataset among all the possible pseudo-experiments since it perfectly follows the probability distribution function for a specific  $\mu = \mu'$  without statistical fluctuations. In particular, when computing the test statistic, it gives the median of the distribution by construction. In case of discovery, where the  $\mu$  hypothesis under test is  $\mu = 0$ , Equation 7.28 reduces to:

$$\sigma_A^2 = \frac{\mu'^2}{q_{0,A}}. \quad (7.29)$$

The median significance is then obtained evaluating  $Z$  as a function of the median test statistic. Combining Equation 7.16 and Equation 7.25, one can show that the significance  $Z$  is a monotonic function of  $q_\mu$ . Thus, the median  $Z$  can be estimated directly from the median of  $q_\mu$ .

Following from Equation 7.24, the median  $Z$  for a  $\mu' \neq 0$  is:

$$\text{med}[Z_0|\mu'] = \sqrt{q_{0,A}} \quad (7.30)$$

#### 7.4.4 Correlations

The nuisance parameters are sometimes correlated among each other, meaning that when one is changed in the fit, the other one is also changing. The correlation matrix helps to understand the reason for pulled or constrained parameters.

In the limit of large samples, the likelihood tend to a zero variance function, meaning that the biases on the estimators tend to zero. Thus, the correlation matrix can be extracted from the observed Fisher information as the Hessian matrix  $H$ <sup>6</sup>:

$$H = \begin{bmatrix} \frac{\partial^2 \mathcal{L}}{\partial \theta_1 \partial \theta_1} & \frac{\partial^2 \mathcal{L}}{\partial \theta_1 \partial \theta_2} & \cdots & \frac{\partial^2 \mathcal{L}}{\partial \theta_1 \partial \theta_n} \\ \vdots & \vdots & \ddots & \vdots \\ \frac{\partial^2 \mathcal{L}}{\partial \theta_n \partial \theta_1} & \frac{\partial^2 \mathcal{L}}{\partial \theta_n \partial \theta_2} & \cdots & \frac{\partial^2 \mathcal{L}}{\partial \theta_n \partial \theta_n} \end{bmatrix} \quad (7.31)$$

The value of a correlation coefficient can vary from minus one to plus one. If there is no relationship between the two variables, their correlation is zero. An important choice in the parameterization of the NPs is the correlation among regions. Some

6. Here  $\mathcal{L}$  is equal to  $\mathcal{L} = -\ln L$ , with  $L$  the likelihood.



uncertainties, such as experimental effects, have one specific source and should be correlated among all regions. More details about the correlation scheme across the various NPs are given in the following Section.

## 7.5 Systematic uncertainties

The systematic uncertainties affecting the  $VH, H \rightarrow b\bar{b}$  analysis can be divided into two main categories: experimental, and modelling uncertainties. The modelling uncertainties are divided into normalization/acceptance uncertainties and shape modelling uncertainties. In the following Sections these categories will be described in more details.

### 7.5.1 Experimental systematic uncertainties

These uncertainties group together the uncertainties affecting the single objects involved in the event, such as calibrations, reconstruction or identification efficiencies and the experimental setup, i.e. luminosity or pile-up uncertainties. These uncertainties are mainly provided by external measurements. The control samples and the methodologies used to extract these measurements have been briefly described in Chapter 4. Overall, the experimental systematic uncertainties can be summarized per object-type as follows:

**Leptons:** The lepton related uncertainties consider the calibration, both for energy scales and resolution, as well as the identification, reconstruction and isolation efficiency as sources of systematic uncertainties. For muons, they are extracted as described in Ref. [219]. For electrons, the calibration uncertainties are extracted as described in Chapter 6, while the efficiency related variations are described in Ref. [127]. The impact of lepton systematic uncertainties in the analysis is about 1% on the signal strength.

**Jets:** The systematic uncertainties affecting the jet energy calibration are divided into Jet energy Scale (JES) and Jet Energy Resolution (JER) uncertainties. A reduced set of 23 decorrelated uncertainties is chosen for the JES, accounting for different effects such as eta intercalibration, high- $p_T$  jets, pile-up, flavour composition, and punch-through jets. The reduced set combines the variations in such a way as to preserve correlations among the jet-kinematic regions. On the contrary, the JER is expressed by one single NP. These uncertainties are extracted as described in Section 4.4.1 and they represent the second source of experimental systematic uncertainty after b-tagging, with an overall impact on the signal strength of 2-3%.

**b-tagging:** the uncertainties related to flavour tagging are applied as variations to the "nominal" efficiency and inefficiency scale factors. A total of  $\sim 160$  variations should be counted. This number is drastically reduced thanks to the principal component analysis described in Section 5.3.1. The actual number of NP used in the fit is about 15, considering b-,c and light-flavours. The approximate size of the uncertainty on the tagging efficiency is 2% for b-jets, 10% for c-jets and 30% for light-jets. Overall the b-tagging uncertainties have a  $\sim 10\%$  impact on the signal strength.

**$E_T^{\text{miss}}$ :** The uncertainties on the energy calibration (8%) and resolution (2.5%) of the so-called soft-terms described in Section 4.7 are considered as source of systematic uncertainty. Furthermore, the uncertainties on the lepton and jet energy scales

are propagated in the  $E_T^{\text{miss}}$  calculation.

**Trigger:** the trigger efficiency uncertainties affect both the single lepton triggers and the  $E_T^{\text{miss}}$  triggers. There are proper trigger scale factors and systematics for the OR of the lepton triggers used in the analysis. These trigger SFs are evaluated as described in Ref. [220] for electrons and Ref. [221] for muons. The  $E_T^{\text{miss}}$  trigger variations are derived inside the  $VH, H \rightarrow b\bar{b}$  group using  $W(\mu, \nu)$ +jets. The uncertainty is smaller than 1% for high- $E_T^{\text{miss}}$  and  $\sim 3\%$  for low- $E_T^{\text{miss}}$  events.

**Luminosity:** the uncertainty on the integrated luminosity for the 2015-2017 period is 2.0%. The procedure to derive this uncertainty is detailed in Ref. [120].

**Pile-up:** the nominal  $\mu_{\text{data}}$  distribution is normally scaled by 1.0/1.03 during the pile-up reweighting correction. The uncertainty on this procedure is computed changing the scaling by 1.0/1.00 or 1.0/1.18 to get the up and down variations respectively. This follows the indications of the pile-up-reweighting working group, described in Ref. [222].

## 7.5.2 Introduction to modelling uncertainties

Many Monte Carlo generators are currently available, with remarkable differences in terms of parton shower, hadronisation and decay models. Differences in the final result can therefore arise just by changing the choice of MC generator. The modelling uncertainties aim at quantifying these differences in terms of shape and normalisation in the different regions, for the signal and each background process separately. The modelling uncertainties are divided into normalisation/acceptance uncertainties and shape uncertainties.

### Normalisation uncertainties

The normalisation uncertainties are calculated as an overall uncertainty on the yield of the process, which affects all the considered regions. These uncertainties are calculated in the region of highest purity, which might be a control region, and extrapolated to the other regions. Additional uncertainties are added to account for this extrapolation.

### Acceptance uncertainties

The acceptance uncertainties account for the possible change in the distribution of events inside the phase space of the analysis, due to the choice of the generator. This would result in a possible migration of events from one region to another, or more in general, in a change in the ratio between the number of events across the regions. In this case, to better preserve correlations, the priors on the Gaussian constraints applied to the NP are calculated as double-ratios:

$$\frac{\text{Acceptance}[\text{Cat.}^A(\text{nominal}_{\text{MC}})]}{\text{Acceptance}[\text{Cat.}^B(\text{nominal}_{\text{MC}})]} \bigg/ \frac{\text{Acceptance}[\text{Cat.}^A(\text{alternative}_{\text{MC}})]}{\text{Acceptance}[\text{Cat.}^B(\text{alternative}_{\text{MC}})]} \quad (7.32)$$

where category A ( $\text{Cat.}^A$ ) is the region with highest purity and B is the other region under test. To extract the acceptance uncertainties, the samples are normalised to the same cross section since these uncertainties are already accounted for by the normalisation uncertainties.

### Shape uncertainties

The shape systematic uncertainties are calculated by evaluating the possible effects on the shape of the most important variables of the analysis when comparing alternative MC samples. In particular, these uncertainties are computed at truth level for the most discriminating variables ( $m_{bb}$  and  $p_T^V$ ) of the BDT input variables, across many alternative generators, including the one used as default. The choice of using just  $m_{bb}$  and  $p_T^V$  has been made in Run-1 since the uncertainties on these two variables are sufficiently large to cover the shape uncertainties of the other BDT input variables. In order to reduce the impact of statistical fluctuations, the maximum difference between the nominal and alternative generator is fitted with a particular function, which can vary across the channels and jet regions, and the fitted shape is taken as uncertainty in the fit. In some specific cases, where no suitable fit function can be found, the difference between the smoothed histograms is taken as uncertainty. Before computing the fit, the distributions are normalised to the same area since the acceptance uncertainties are already considered separately. Examples of the  $m_{bb}$  and  $p_T^V$  shape uncertainties evaluation for  $W$ +jets events in the 1 lepton channel are presented in Figure 7.9.

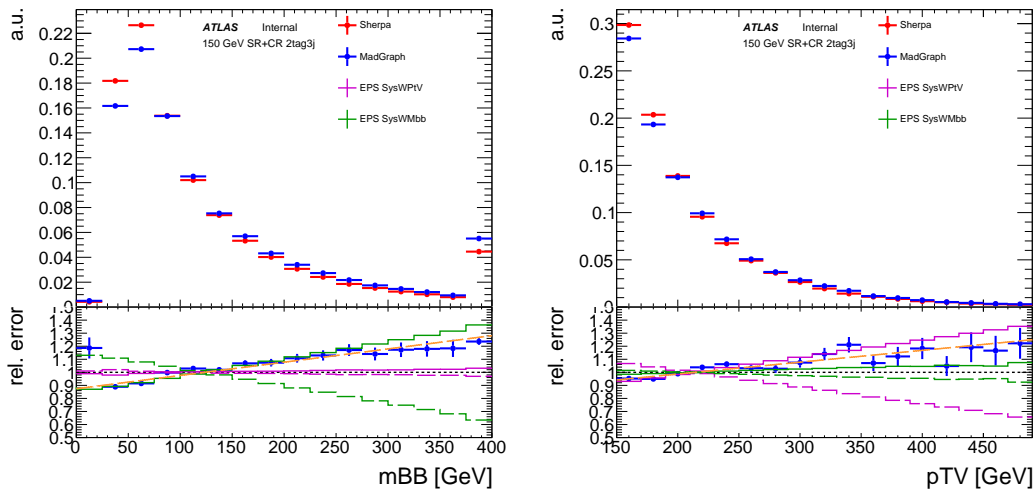


FIGURE 7.9 – The  $m_{bb}$  shape variation for  $W$ +jets events in 1 lepton channel 3-jet SR+CRs a) and the transverse momentum of the  $W$   $p_T^W$  for the 1 lepton channel 3-jet SR+CR b). The blue dots in the lower panel represent the ratio of MADGRAPH to SHERPA and the orange line corresponds to a linear fit of this ratio. The  $m_{bb}$  and  $p_T^V$  shape variations derived for the 2017 round of the analysis with  $36 \text{ fb}^{-1}$  are overlaid on the ratio. They were found to be compatible to the new linear fit and therefore kept unchanged for the 2018 analysis.

### 7.5.3 Signal uncertainties

The  $VH, H \rightarrow b\bar{b}$  processes are mainly affected by uncertainties on the  $H \rightarrow b\bar{b}$  branching ratio, the NNLO(QCD)+NLO(EW) cross section calculation, or by acceptance and shape differences coming from different MC modellings. Their specific implementation in the fit is defined as follows:

**cross section uncertainties:** they account for the uncertainty on the predicted  $VH$  production cross section and the  $H \rightarrow b\bar{b}$  BR, as well as for higher order electroweak effects not considered in the NLO(EW) calculation. They are implemented as overall normalisation uncertainties, following the recommendations of the LHC Higgs working group [48] [223]. One single uncertainty is defined for the  $H \rightarrow b\bar{b}$  BR (ATLAS\_BR\_bb), while for the production cross section, QCD and PDF+ $\alpha_s$  scale uncertainties are considered separately, distinguishing between  $qq \rightarrow VH$  and  $gg \rightarrow ZH$  processes (ATLAS\_QCDscale\_VH, ATLAS\_QCDscale\_ggZH, ATLAS\_pdf\_Higgs\_VH and ATLAS\_pdf\_Higgs\_ggZH).

**PS and UE variations:** The parton shower and underlying event modelling can be considerably different across the different generators. To quantify these differences the nominal generator (POWHEG + PYTHIA 8) is compared to the alternative generators described in Section 7.1.1. The UE variations are computed from the difference between a MADGRAPH 5\_aMC@NLO+PYTHIA 8 sample produced with the A14 tune, and alternative samples produced with the nominal generator but different settings of the A14 tune. The PS uncertainty is obtained comparing the nominal generator with the POWHEG + HERWIG 7 alternative sample. Acceptance and shape uncertainties are considered separately.

The acceptance variations have been evaluated for 2-jet (ATLAS\_UEPS\_VH\_hbb) and propagated to the 3-jet category with a double ratio technique as described above (ATLAS\_UEPS\_VH\_hbb\_32JR). The final PS/UE uncertainty is calculated taking the envelope between the UE and PS uncertainties. The UE uncertainty is obtained summing in quadrature the uncertainties of all the considered UE tunes, taking the absolute maximum variation (up or down) for each tune. These uncertainties are used for all the  $VH$  processes, both  $gg$  and  $qq$  initiated, fully correlating them across the  $VH$  processes.

The shape variations for the A14 tune are obtained comparing the baseline MADGRAPH 5\_aMC@NLO+PYTHIA 8 with each tune variation and fitting the ratio with a linear function for  $p_T^V$  and a second order polynomial for  $m_{bb}$ . For  $p_T^V$  the PS shape differences were found smaller than the UE ones (obtained varying the A14 tunes), therefore no  $p_T^V$  PS shape uncertainty is assigned. On the contrary, for  $m_{bb}$  the highest deviation comes from the PS model comparison. No fit has been performed, but smoothed histograms have been used to quantify these differences. The largest deviation was used as the  $m_{bb}$  PS shape uncertainty (ATLAS\_UEPS\_VH\_hbb\_MBB). The  $p_T^V$  and  $m_{bb}$  shape uncertainties are considered as correlated among the  $VH$  processes.

**Scale variations:** These uncertainties account for the  $\mu_R$  (renormalisation scale) and  $\mu_F$  (factorisation scale) variations described in Section 2.4.1.

The nominal POWHEG + PYTHIA 8 sample is compared to alternative samples generated with varied factorisation and renormalisation scales. As in the previous case, acceptance and shape effects are considered separately. The acceptance systematics are evaluated taking the envelope of all scale choices separately for each jet category and channel (QCDscale\_VH\_ANA\_hbb\_J2, QCDscale\_VH\_ANA\_hbb\_J3). The final uncertainty is determined using the Stewart-Tackmann correlation scheme [224], with an additional uncertainty added to the 0- and 1-lepton channels to account for the fact that the events with more than three jets are vetoed (QCDscale\_VH\_ANA\_hbb\_JVeto). The shape uncertainties are calculated in  $p_T^V$  and  $m_{bb}$  (QCDscale\_VH\_ANA\_hbb\_VPT and QCDscale\_VH\_ANA\_hbb\_MBB) fitting the ratio of the baseline prediction and each scale variation with a linear fit and a second order polynomial respectively. The  $p_T^V$  shapes are very similar across all regions, therefore only the largest variation was

Signal	
Cross section (scale)	0.7% ( $qq$ ), 27% ( $gg$ )
Cross section (PDF)	1.9% ( $qq \rightarrow WH$ ), 1.6% ( $qq \rightarrow ZH$ ), 5% ( $gg$ )
$H \rightarrow b\bar{b}$ branching ratio	1.7 %
Acceptance from scale variations (var.)	2.5 – 8.8%
Acceptance from PS/UE var. for 2 or more jets	2.9 – 6.2% (depending on lepton channel)
Acceptance from PS/UE var. for 3 jets	1.8 – 11%
Acceptance from PDF+ $\alpha_s$ var.	0.5 – 1.3%
$m_{bb}, p_T^V$ , from scale var.	S
$m_{bb}, p_T^V$ , from PS/UE var.	S
$m_{bb}, p_T^V$ , from PDF+ $\alpha_s$ var.	S
$p_T^V$ from NLO EW correction	S

TABLE 7.10 – Summary of the systematic uncertainties in the modelling for the  $VH \rightarrow b\bar{b}$  signal. An ‘S’ symbol is used when only a shape uncertainty is assessed. The processes for which the normalisations float independently are listed in brackets. Where the size of an acceptance systematic uncertainty varies between regions, a range is displayed [205].

considered and correlated across all channels.

**PDF +  $\alpha_s$  uncertainties:** changes in shape and acceptance are expected when varying the parton distribution function or the QCD coupling strength  $\alpha_s$  value. The PDF dependence is evaluated by comparing the nominal samples with alternative samples generated with variations from the PDF4LHC15\_30 PDF set [225]. The total PDF component of the acceptance uncertainty was derived taking the sum in quadrature of all the considered variations with altered PDF uncertainties. Only one uncertainty to 2-jet and 3-jet channels is considered. On the contrary, the  $\alpha_s$  component was taken as the *average* of the variations coming from samples with altered  $\alpha_s$ . The total acceptance uncertainty (pdf\_HIGGS\_VH\_ANA\_hbb) is obtained adding these two components in quadrature.

The shape uncertainties are obtained as for the other shape uncertainties, fitting the deviation between the nominal and the alternative generators in  $p_T^V$  and  $m_{bb}$  with a linear fit and a second order polynomial respectively. Both PDF and  $\alpha_s$  variations have a negligible effect on  $m_{bb}$ , so no  $m_{bb}$  shape uncertainty is assigned. In  $p_T^V$  the shapes have been evaluated separately in the 2-jet and 3-jet categories (pdf\_HIGGS\_VH\_ANA\_hbb\_PTV). One single variation is used for all the channels, defined as the largest variation across them.

A summary of the systematic uncertainties affecting the  $VH$  signal is presented in Table 7.10.

### 7.5.4 Background uncertainties

The modelling uncertainties are studied independently for each background process. A summary of the diboson-related uncertainties is presented in Table 7.13, while the values adopted for the main backgrounds  $t\bar{t}$ , W+jets and single-top are summarised in Table 7.14. The methods used to obtain these uncertainties are briefly summarised here:

**W+jet:** the W+HF is the dominant background in the 1-lepton channel. A separate floating normalisation is adopted for 2-jet (norm\_Wbb\_J2) and 3-jet (norm\_Wbb\_J3) regions, heavily constrained by the dedicated 1-lepton W+HF control region. A common uncertainty (SysWbbNorm\_DWhfCR\_L1) of 10% on the relative yields in SR and CR

is assigned to both the 2 and 3-jet signal regions in 1-lepton. The W+HF normalisation is obtained in the 1-lepton channel and extrapolated to the 0-lepton channel. An additional common uncertainty of 5% on the ratio of the 0-lepton and 1-lepton yields is assigned to the 2-jet and 3-jet 0-lepton regions (SysWbbNorm\_L0) to account for this extrapolation. A flavour composition uncertainty, implemented as ratio between the bc (SysWbcWbbRatio), bl (SysWblWbbRatio) and cc (SysWccWbbRatio) yields relative to the bb component, is added to account for the uncertainty on the W+jet composition. The W+l and W+cl backgrounds are strongly suppressed and they represent less than 1% of the total background. Thus, single normalisations uncertainties are applied (SysWlNorm and SysWclNorm respectively) individually correlated across all regions.

The  $m_{bb}$  and  $p_T^V$  shape uncertainties have been determined comparing the different generators described in Section 7.1.2 and fitting their difference with a straight line. For both  $p_T^V$  and  $m_{bb}$  the highest effect is between the MADGRAPH and SHERPA 2.2.1 predictions. The systematic uncertainties have the same direction and order of magnitude in all channels and categories, therefore the highest uncertainty was chosen and used in all channels/regions fully correlated. For  $p_T^V$  the highest value is in the 1-lepton 3-jet region (SysWPtV), while for  $m_{bb}$  the one in the 1-lepton 2-jet region has been adopted as default uncertainty (SysWMbb).

**Z+jet:** the Z+HF background is the dominant contribution in 0- and 2-lepton channels. A floating normalisation is adopted for the Z+HF process, separately for the 2-jet and 3-jet regions (norm\_Zbb\_J2, norm\_Zbb\_J3). This parameter is constrained in the 2-lepton channel SR, which has the highest Z+HF purity and extrapolated to the 0-lepton channel. An additional NP in the 0-lepton region is introduced to cover this extrapolation using a 0-to-2-lepton region ratio of the yields as additional uncertainty (SysZbbNorm\_0L). The uncertainty has been computed looking at the  $p_T^V > 150$  GeV region only. Additional uncertainties on the flavour composition (bb, bc, bl and cc) of the Z+HF background are implemented as normalisation uncertainties, relative to the bb component (SysZbcZbbRatio, SysZblZbbRatio and SysZccZbbRatio). A single normalisation uncertainty is applied to the Z+l and Z+cl backgrounds (SysZlNorm and SysZclNorm) for the 2-jet and 3-jet regions since their contribution is less than 1% of the total background.

The Z+jets shape uncertainties are studied only in the 2 lepton channel. A control region enriched in Z+jets is defined in data. A MET significance cut lower than 3.5 is applied to disentangle Z+jets from the  $t\bar{t}$  background. The assumption is that in this control region the observed data MC differences are only due to modelling uncertainties in the Z+jets samples. The residual background is then subtracted in data and the Z+jet background is scaled to data. The estimation has been performed in the 2-tag category, restricted to the  $110 \text{ GeV} < m_{bb} < 140 \text{ GeV}$  region. Both  $p_T^Z$  (ZPtV) and  $m_{bb}$  (ZMbb) shape uncertainties are derived by fitting the data/MC difference in this Z+jet enriched region with particular functions: for  $p_T^Z$  it is  $\pm 0.2 \log_{10}(p_T^Z/50 \text{ GeV})$ , while for  $m_{jj}$  it is  $\pm 0.0005 \times (m_{jj} - 100 \text{ GeV})$ . These functions have been defined in Run-1 and tested in the Run-2 analysis to confirm that they still provide a reasonable estimate. These uncertainties are applied also to the 0 lepton channel, fully correlated with the 2-lepton uncertainty.

**Top pair production:** the  $t\bar{t}$  background contaminates all the three channels. The overall normalisation of the  $t\bar{t}$  background is a free floating parameter of the fit, with no priors. The alternative generators used to simulate  $t\bar{t}$  events and their role in the evaluation of the systematic uncertainties are summarized in Table 7.11.



As described in Section 7.5.2, the acceptance uncertainties are calculated using double ratios between analysis regions. In the 0-lepton and 1-lepton channels, the 3-to-2 jet uncertainty (SysttbarNorm\_J2) is defined as the ratio of the 3 jet region of the 0+1-lepton channel and the 2-jet region of the 0+1 lepton channel. A common uncertainty is assigned for the 3-to-2 jet variations in 0- and 1-lepton channel since it demonstrated a similar behaviour and order of magnitude in both channels. Furthermore, a 1-to-0-lepton uncertainty (SysttbarNorm\_L0) is defined as the ratio of the 2+3-jet regions in 1-lepton channel and the 2+3-jet regions in the 0-lepton channel. Finally, in the 1-lepton channel a SR-to-CR uncertainty (SysttbarNorm\_DWhfCR\_L1) is determined by the ratio of the SR and the 1-lepton W+HF CR yields, with the SR acting as the purer region in  $t\bar{t}$ . In the 2-lepton channel, floating normalisation factors have been implemented in the 2j (norm\_ttbar\_J2\_L2) and the 3-jet regions (norm\_ttbar\_J3\_L2) regions, exploiting the dedicated top  $e\mu$  CR.

Generator	Setup Details	Systematic Effect
POWHEG +PYTHIA 8	A14 tune NNPDF30NLO & NNPDF23LO hdamp = $1.5 \cdot m_{top}$ nonallhad filter	nominal sample
POWHEG +PYTHIA 8	nominal setup scale variations low ( $\mu_R = \mu_F = 2$ ) hdamp = $1.5 \cdot m_{top}$ Up variation of A14 tune (Var3c) nonallhad filter	low variation for additional radiation
POWHEG +PYTHIA 8	nominal setup scale variations high ( $\mu_R = \mu_F = 0.5$ ) hdamp = $3.0 \cdot m_{top}$ Down variation of A14 tune (Var3c) nonallhad filter	high variation for additional radiation
POWHEG +HERWIG 7	H7UE tune CT10 & MMHT2014lo68cl hdamp=175.2GeV nonallhad filter	fragmentation/hadronisation model
MADGRAPH 5_aMC@NLO+PYTHIA 8	A14 tune NNPDF30NLO & NNPDF23LO nonallhad filter	hard scatter generation and matching

TABLE 7.11 –  $t\bar{t}$  MC samples generated for the estimate of systematic uncertainties.

In the 2-lepton channel the shape differences in  $m_{bb}$  and  $p_T^V$  are fitted with a linear slope (TTbarMBB\_L2 and TTbarPTV\_L2) and the difference with the nominal is propagated to the analysis through a reweighting procedure. The same procedure has been applied to the 0-lepton and 1-lepton channels. In this case the  $m_{bb}$  shape differences (TTbarMBB) have been fitted with an exponential function, while a linear shape has been used for  $p_T^V$  (TTbarPTV). The 1-lepton uncertainties have been used for the 0-lepton channel as well, due to the limited  $t\bar{t}$  statistics passing the 0-lepton channel selection. Both magnitude and sign of the shape variations are very consistent between the 2 and 3-jet regions, therefore the NPs are fully correlated across these regions.

**Single-top:** the single-top normalisation uncertainties are derived following the recommendations given by the LHC top working group for each of the single-top processes. These normalisation uncertainties are obtained summing in quadrature the scale variations due to renormalisation and factorisation, the uncertainties on  $\alpha_S$  and the PDF uncertainties. An overall normalisation uncertainty of 4.4%, 4.6% and 6.2% is obtained for the t- (stoptNorm), s- (stopsNorm) and Wt-channel (stopWtNorm) respectively.



The single-top modelling uncertainties are estimated comparing the alternative samples described in Section 7.1.2, with a procedure similar to what used for the  $t\bar{t}$  modelling uncertainties. A summary of the single-top MC samples and their relation with the estimate of the systematic uncertainties is presented in Table 7.12. The single-top production has a negligible contribution in the 0- and 2-lepton channels, therefore both acceptance and shape systematic uncertainties are derived only in the 1-lepton channel, and only for the  $t$  and  $Wt$  processes, and applied to the other channels fully correlating them.

Generator	Setup Details	Systematic Effect
POWHEG +PYTHIA 6	nominal setup scale variations low ( $\mu_R = \mu_F = 2$ ) low radiation PERUGIA2012 tune variation	<i>low variation</i> for additional radiation
POWHEG +PYTHIA 6	nominal setup scale variations high ( $\mu_R = \mu_F = 0.5$ ) high radiation PERUGIA2012 tune variation	<i>high variation</i> for additional radiation
POWHEG +PYTHIA 6	$Wt$ -channel nominal setup 'diagram subtraction' scheme setup in the POWHEG ME calculation	alternative ME calculation scheme
POWHEG +HERWIG ++	nominal setup parton showering with HERWIG ++ CTEQ6L1-UE-EE-5 tune for PS	alternative PS
MADGRAPH 5_aMC@NLO+HERWIG ++	alternative setup ME with MADGRAPH 5_aMC@NLO CT10f4 PDF in ME	alternative ME

TABLE 7.12 – Single-top MC samples generated for the estimate of systematic uncertainties.

For the acceptance, separate normalisation uncertainties for the 2-jet and 3-jet regions in the  $Wt$  (stopWtbbAcc, stopWtothAcc) and  $t$ -channel (stoptAcc) are calculated. These two uncertainties are fully correlated in the fit since they vary in the same direction for each of the different alternative samples in both the 2-jet and 3-jet regions.

The shape uncertainties for the stop- $t$  (StoptPTV and StoptMBB) and stop- $Wt$  channels (StopWtPTV and StopWtMBB) are derived by fitting a linear slope through the largest variation of the  $p_T^V$  and  $m_{bb}$  distributions, and symmetrising the result.

**Diboson:** The definition of the modelling systematic uncertainties follows the scheme of the  $VH$  signal uncertainties described in the previous Section. Three cross section uncertainties (SysWWNorm, SysWZNorm, SysZZNorm) are obtained considering the effect of scale variations in the SHERPA simulated samples and the difference between SHERPA and POWHEG. In fact, for the  $pp \rightarrow Z(\rightarrow qq) + Z(\rightarrow \ell\ell)$  process POWHEG generates event including the non-resonant  $ZZ$  diagrams, while SHERPA does not include them. This results in a remarkable difference between the two generators above 100 GeV, as seen in Figure 7.10.

The acceptance uncertainties are computed separately for scale variations and PS/UE sources. The total PS/UE variations (SysVZ\_UEPS\_Acc) are computed as in the  $VH$  signal case, by summing in quadrature the maximum of each PS tune variation and taking the envelope of this sum and the parton shower model variations as total uncertainty. The effect is calculated in the 2-jet region and an additional variable is added (SysVZ\_UEPS\_32JR) to account for the uncertainty on the ratio of the yields between the two regions. The residual effect of the uncertainties on the normalisation across different analysis regions are taken into account as double ratios: a first for  $WZ$  (SysWZNorm\_L0) accounting for the uncertainties in the 0-lepton versus 1-lepton events, while the second for the  $ZZ$  process (SysZZNorm\_L0) to account for

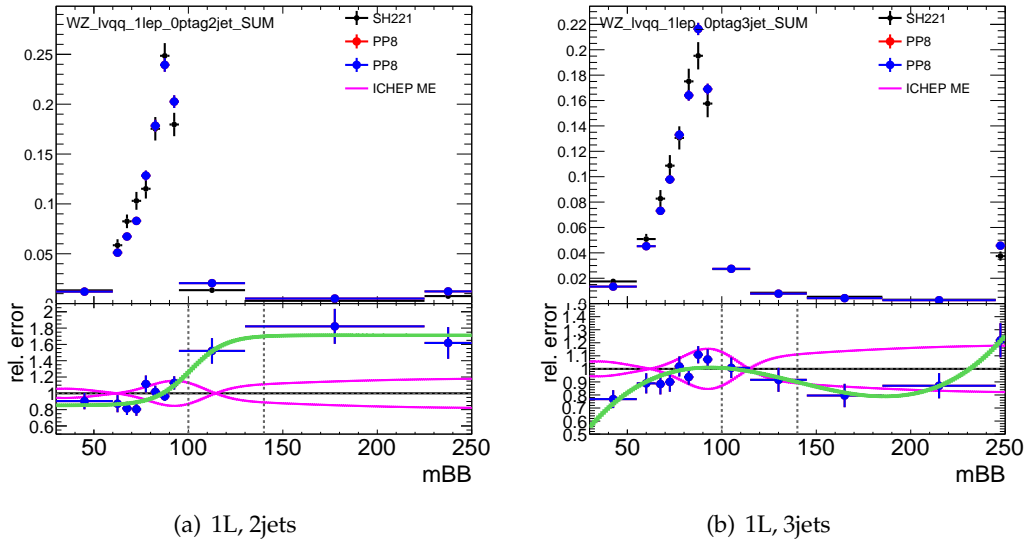


FIGURE 7.10 – Example shape variations from SHERPA versus POWHEG in the  $m_{bb}$  variable, shown for the 1-lepton 2-jet (left) and 3-jet (right) selections, approximated by tanh and capped 3rd-degree polynomial functions respectively. The ‘ICHEP’ fit corresponds to the fit derived for this round of the analysis with  $80 \text{ fb}^{-1}$ .

the difference between 0-lepton and 2-lepton events.

The UE/PS shape uncertainties are obtained comparing the  $p_T^V$  (SysVZ\_UEPS\_VPT) and  $m_{bb}$  (SysVZ\_UEPS\_MBB) distributions of the nominal SHERPA sample with the alternative samples described in Section 7.1.2, separately for scale variations, PS/UE and PDF/ $\alpha_s$  variations. No  $p_T^V$  distribution from the PS/UE variations was assigned, while the  $m_{bb}$  PS/UE distribution was taken from a binned smoothed histogram comparing PYTHIA 8 and HERWIG ++. No shape variations are considered for the WW process, due to its small contribution to the overall background yield ( $<1\%$ ). A summary of the aforementioned VZ uncertainties is presented in Table 7.13.

The renormalisation and factorisation scale uncertainties are computed reweighting the SHERPA 2.2.1 doubling and halving the renormalisation scale ( $2\mu_R$  and  $0.5\mu_R$ ) and doubling and halving the factorisation scale ( $2\mu_F$  and  $0.5\mu_F$ ). The acceptance uncertainties arising from the changes in  $\mu_R$  and  $\mu_F$  are computed using the Stewart-Tackman method. This method leads to three independent nuisance parameters: one for the overall acceptance (SysVZ\_QCDscale\_J2) calculated in the 2-jet region, one for the relative migration between 2 and 3 jets (SysVZ\_QCDscale\_J3) and the third due to the veto of events with more than 3-jet in the 0-lepton and 1-lepton channels (SysVZ\_QCDscale\_JVeto).

For the  $\mu_R$  and  $\mu_F$  effects on the shape variations, in  $p_T^V$  (SysVZ\_QCDscale\_VPT) the variations are compatible with the MC statistical uncertainties of the nominal samples, as well as for the  $m_{bb}$  distribution (SysVZ\_QCDscale\_MBB) in the 2-jet channel. Therefore no additional NPs are added in these regions.

Finally, a shape-only NP is added to account for the very different modelling of the extra jet radiation between SHERPA and Powheg. No significant difference was found in  $p_T^V$ . For  $m_{bb}$  this difference has been assessed fitting the 2-jet and 3-jet regions with a hyperbolic tangent and a third degree polynomial respectively. No additional variations are added for the PDF and  $\alpha_s$  uncertainties since they were found to be negligible.

$ZZ$	
Normalisation	20%
0-to-2 lepton ratio	6%
Acceptance from scale variations (var.)	10 – 18%
Acceptance from PS/UE var. for 2 or more jets	6%
Acceptance from PS/UE var. for 3 jets	7% (0-lepton), 3% (2-lepton)
$m_{bb}, p_T^V$ , from scale var.	S (correlated with $WZ$ uncertainties)
$m_{bb}, p_T^V$ , from PS/UE var.	S (correlated with $WZ$ uncertainties)
$m_{bb}$ , from matrix-element var.	S (correlated with $WZ$ uncertainties)
$WZ$	
Normalisation	26%
0-to-1 lepton ratio	11%
Acceptance from scale var.	13 – 21%
Acceptance from PS/UE var. for 2 or more jets	4%
Acceptance from PS/UE var. for 3 jets	11%
$m_{bb}, p_T^V$ , from scale var.	S (correlated with $ZZ$ uncertainties)
$m_{bb}, p_T^V$ , from PS/UE var.	S (correlated with $ZZ$ uncertainties)
$m_{bb}$ , from matrix-element var.	S (correlated with $ZZ$ uncertainties)
$WW$	
Normalisation	25%

TABLE 7.13 – Summary of the systematic uncertainties in the background modelling for the VZ processes. An ‘S’ symbol is used when only a shape uncertainty is assessed. The regions for which the normalisations float independently are listed in brackets. Where the size of an acceptance systematic uncertainty varies between regions, a range is displayed.

**Multi-jet:** The contribution of this background has a negligible impact in the 0- and 2-lepton channels, therefore dedicated systematic uncertainties are added only in the 1-lepton case. Many sources of systematic uncertainties are considered (separately for 2-jet and 3-jet categories and for electron and muon sub-channels) as possibly impacting the final multi-jet BDT distribution, both in terms of normalisation and shape. The uncertainties are obtained considering the following variations:

- Use the lowest  $p_T$  lepton trigger, instead of the combination mentioned in Section 7.2, to quantify the impact of the trigger choice.
- The impact of the extrapolation from the inverted isolation region is evaluated by tightening the isolation requirement to define a reduced inverted-isolation region. This reduced inverted-isolation region targets events close to the signal region, thus with a lower extrapolation uncertainty. The shape difference in the total inverted-isolation region and this reduced-region is taken as uncertainty.
- The impact of the electroweak backgrounds normalisation factors is taken into account by calculating the MJ template shape with and without these normalisation factors and quoting the difference as a systematic uncertainty.

The shape uncertainties are obtained normalising the template distributions to the nominal MJ yield. These uncertainties are considered uncorrelated between the electron and muon sub-channels and are evaluated directly on the  $BDT_{VH}$  shape.

The normalisation uncertainties are obtained looking directly at the changes in the  $m_T^W$  template distributions and extrapolated using the relative yield in the signal and W+HF control regions. A single normalisation uncertainty is obtained for each sub-channel and jet category summing in quadrature the above-mentioned contributions and including two more variations: a template fit without the  $E_T^{\text{miss}}$  cut in the electron mode and two fits using alternative distributions instead of  $m_T^W$  ( $\Delta\phi(\ell, bb)$  in 2-jet and  $\Delta\phi(\ell, bbj)$  in 3-jet). The normalisation uncertainties are uncorrelated

between the two sub-channels and for the 2-jet and 3-jet regions.

### 7.5.5 Smoothing of the systematic uncertainties

Statistical fluctuations can lead to artificially large and irregular shape variations that could easily produce over constraints in the fit. To prevent this, a smoothing procedure has been adopted. The relative effect of the systematic uncertainty is iteratively 're-binned' until the statistical uncertainty in each of the merged bins, calculated in the nominal template, is smaller than 5%. The new value of the uncertainty is then used as the associated uncertainty for all the nominal bins in the set.

### 7.5.6 Pruning of the systematic uncertainties

Several uncertainties described in this Section have a negligible impact on the distributions entering in the fit. In order to ease the convergence of the fit and reduce the computation time, a "pruning" procedure is applied:

- Systematic uncertainties inducing a normalisation effect smaller than 0.5%, or with both up and down variations having the same sign are neglected.
- Shape uncertainties are neglected if none of the bins in the distribution has a deviation over 0.5% after the overall normalisation or if only the up or the down variation is non-zero and passed the previous pruning steps.
- In case of very small background processes, both the shape and normalisation uncertainties are neglected in different ways depending if the region is a sensitive region (where the signal is more than 2% of the total) or not. In the sensitive regions the uncertainties are pruned only if the sample yield is less than 2% of the *signal*, while for non-sensitive regions the uncertainties are pruned if they have an impact lower than 0.5% of the *total background*.

The pruning is applied independently for each systematic uncertainty, for each template process and in each analysis region. The procedure has been largely tested in Run-1 and cross-checked for the  $80 \text{ fb}^{-1}$  publication. The effect introduced by the pruning procedure has been quantified to be below 1%.

## 7.6 BTagging studies

Several studies related to the implementation of the b-tagging algorithms in the  $VH, H \rightarrow b\bar{b}$  analysis have been carried for the  $80 \text{ fb}^{-1}$  publication. For time reasons, some of them have not been adopted in the final analysis strategy, and they are shown here as preliminary. These studies have been optimised later, towards the full Run-2 publication with  $140 \text{ fb}^{-1}$  of data. A detailed description of the improvements is presented in the next Chapter.

### 7.6.1 MV2c10 vs DL1 studies

As described in Section 5.2.3, there are several high level taggers available in Run-2. The DL1 tagger is expected to have better performance in terms of c- and light-jet rejection compared to MV2c10, and the IP RNN based taggers are expected to have better performance with respect to the IPxD based variants. All these taggers have been tested in the analysis to select the one to use by default. The tagger has been chosen as the one maximising the expected significance based on a fit to the Asimov dataset. The study has been performed only in the 0-lepton and 1-lepton channel for simplicity and considering full truth tagged samples. Since this was a

$Z + \text{jets}$	
$Z + ll$ normalisation	18%
$Z + cl$ normalisation	23%
$Z + \text{HF}$ normalisation	Floating (2-jet, 3-jet)
$Z + bc\text{-to-}Z + bb$ ratio	30 – 40%
$Z + cc\text{-to-}Z + bb$ ratio	13 – 15%
$Z + bl\text{-to-}Z + bb$ ratio	20 – 25%
0-to-2 lepton ratio	7%
$m_{bb}^V, p_T^V$	S
$W + \text{jets}$	
$W + ll$ normalisation	32%
$W + cl$ normalisation	37%
$W + \text{HF}$ normalisation	Floating (2-jet, 3-jet)
$W + bl\text{-to-}W + bb$ ratio	26% (0-lepton) and 23% (1-lepton)
$W + bc\text{-to-}W + bb$ ratio	15% (0-lepton) and 30% (1-lepton)
$W + cc\text{-to-}W + bb$ ratio	10% (0-lepton) and 30% (1-lepton)
0-to-1 lepton ratio	5%
$W + \text{HF}$ CR to SR ratio	10% (1-lepton)
$m_{bb}^V, p_T^V$	S
$t\bar{t}$ (all are uncorrelated between the 0+1- and 2-lepton channels)	
$t\bar{t}$ normalisation	Floating (0+1-lepton, 2-lepton 2-jet, 2-lepton 3-jet)
0-to-1 lepton ratio	8%
2-to-3-jet ratio	9% (0+1-lepton only)
$W + \text{HF}$ CR to SR ratio	25%
$m_{bb}^V, p_T^V$	S
Single top-quark	
Cross-section	4.6% ( $s$ -channel), 4.4% ( $t$ -channel), 6.2% ( $Wt$ )
Acceptance 2-jet	17% ( $t$ -channel), 55% ( $Wt(bb)$ ), 24% ( $Wt(\text{other})$ )
Acceptance 3-jet	20% ( $t$ -channel), 51% ( $Wt(bb)$ ), 21% ( $Wt(\text{other})$ )
$m_{bb}^V, p_T^V$	S ( $t$ -channel, $Wt(bb)$ , $Wt(\text{other})$ )
Multi-jet (1-lepton)	
Normalisation	60 – 100% (2-jet), 90 – 140% (3-jet)
BDT template	S

TABLE 7.14 – Summary of the systematic uncertainties in the background modelling for  $Z$ +jets,  $W$ +jets,  $t\bar{t}$ , single top-quark and multi-jet production. An ‘S’ symbol is used when only a shape uncertainty is assessed. The regions for which the normalisations float independently are listed in brackets. Where the size of an acceptance systematic uncertainty varies between regions, a range is displayed.

preliminary study, it has been performed on  $36 \text{ fb}^{-1}$  only. Furthermore, the maps used for truth tagging were not the ones used in the final 2018 publication, but the difference is expected to be small. No b-tagging scale factors for DL1 were available at the time when this study was performed, so they have been ignored for both tagger families.

The full analysis chain is repeated for each b-tagger and working point: the final BDT discriminant is retrained, to avoid biases in the results in favour of the MV2c10 70% scenario, the usual overtraining checks are performed, and the new BDT is used to build the histograms for the final fit. Finally, the expected 0-lepton and 1-lepton channel significances are computed separately. The BDT settings are kept as described in Section 7.3.2. The 0-lepton channel results for a fit on Asimov with only the statistical uncertainties are shown in Table 7.15: the 60% and 85% operating points are disfavoured, because of the small signal acceptance (60% WP) or the higher contamination from c- and light-jet entering in the signal region (85% WP), despite improved rejection thanks to the use of the SMT and RNNIP algorithms. The 70% and 77% operating points have similar significances, perhaps a bit better for 77%, which profits of a small gain in signal acceptance without the high level of c- and light-jet background contamination observed for the 85% WP. The best result can be achieved with the DL1rnn at 77% WP, with an overall  $\sim 3\%$  gain with respect to the nominal MV2c10 at 70% WP.

tagger	60% WP	70% WP	77% WP	85% WP
MV2c10	2.54	2.80	2.79	2.47
MV2c10mu	2.53	2.76	2.77	2.55
MV2c10rnn	2.53	2.81	2.86	2.61
DL1	2.61	2.84	2.84	2.52
DL1mu	2.61	2.84	2.88	2.57
DL1rnn	2.61	2.87	2.89	2.60

TABLE 7.15 – Significance of the 0-lepton channel fits to Asimov for different taggers and working points using  $36.1 \text{ fb}^{-1}$  of data. Only statistical uncertainties are included in the fit. Caveats: full truth tagging is used for all the sample and no b-tagging scale factors are applied. The *rnn* version also includes the SMT.

The same procedure has been applied to the 1-lepton channel and the results are shown in Table 7.16. The same considerations as the 0-lepton channel case can be drawn for the 60% and 85% operating points. The 70% operating point is slightly favored with respect to the 77%, because the increase in signal acceptance is hidden by the higher level of W+HF background contamination entering in the signal regions. An overall 4% gain in significance can be observed when passing from MV2c10 to DL1rnn at 70% operating point.

In general, the IP RNN variants provide the best significance when comparing the same operating point, but the gain is limited to a few per cent. Furthermore, DL1 is marginally better than MV2c10 for the same WP, but again with small improvements ( $\sim 2\%$ ) in both channels. This preliminary study showed a marginal gain when testing the newly available tagger variations. Since the majority of the modelling systematic uncertainties have been evaluated using the nominal MV2c10 at 70% efficiency and the b-tagging efficiency scale factors were not available for the alternative (XX\_rnn) taggers, additional work would have been necessary to re-evaluate these uncertainties with the new tagger choice. Therefore it was decided to conservatively keep the nominal MV2c10 at 70% operating point as default.



tagger	60% WP	70% WP	77% WP	85% WP
MV2c10	2.51	2.58	2.49	2.15
MV2c10mu	2.54	2.57	2.48	2.22
MV2c10rnn	2.51	2.62	2.59	2.30
DL1	2.58	2.63	2.54	2.19
DL1mu	2.62	2.64	2.60	2.24
DL1rnn	2.60	2.68	2.61	2.7

TABLE 7.16 – Significance of the 1-lepton channel fits to Asimov for different taggers and working points using  $36.1 \text{ fb}^{-1}$  of data. Only statistical uncertainties are included in the fit. Caveats: full truth tagging is used for all the sample and no b-tagging scale factors are applied.

## 7.6.2 Statistical tagging

As described in Section 5.4, some samples can profit from an alternative method to perform b-tagging, based on statistical reweighting. This alternative b-tagging strategy significantly increases the statistical precision of the MC templates, since no MC event is discarded. This is highly beneficial to the  $VH, H \rightarrow b\bar{b}$  analysis when considering that the largest uncertainty of the last published result was the MC statistics [187]. This reduction in the MC statistical error can be seen in Figure 7.11, where  $Wl$ ,  $Wcl$  and  $Wcc$  processes in the 1-lepton 2-tag 2-jet signal region are compared for direct tagging (black) and statistical tagging (red), also referred to as "truth" tagging.

For the  $Vbb$ ,  $Vbc$ ,  $Vbl$  and  $t\bar{t}$  samples a non closure between the direct and truth tagged distributions is observed, with statistically significant differences in both normalisation and shape, as shown in Figure 7.12. This difference is not completely understood, but it is partially due to the efficiency maps, which have been found to be sub-optimal for the  $VH, H \rightarrow b\bar{b}$  analysis, as discussed in Chapter 5. Given this non-closure, all MC samples are direct tagged, except for the c-hadron and light-jet filtered V+jet samples and WW samples, where the large statistical error of the direct tagged distributions makes the two approaches to be within the statistical uncertainties of each other.

The V+jet samples with no b-hadrons in the final state are approximately 12% (13%) of the total W+jets background in the 1-lepton 2-tag 2-jet (3-jet) region, therefore any systematic bias introduced by this non-closure on the analysis is highly suppressed. Furthermore, as described in Section 7.5, a large modelling uncertainty is assigned to the  $Vcc$ ,  $Vcl$  and  $Vl$  backgrounds in the likelihood fit. More specifically, the normalisation nuisance parameter priors are 37% for  $\sigma(V + cl)$  and 32% for  $\sigma(V + l)$ , so any additional non-closure effect is absorbed by these NP. Overall, the use of truth tagging - even if limited to the  $Vl$ ,  $Vcl$  and  $Vcc$  samples - allowed for a reduction between 1.5 and 2.3 times the MC statistical error on W+jet and Z+jet in the 2-jet region depending on the channel. Table 7.17 summarizes yields and statistical errors for the V+jet contributions that have been direct tagged in the  $80 \text{ fb}^{-1}$  analysis. Table 7.18 shows the V+jet which have been truth tagged, with the gain in terms of MC statistical error compared to the direct tagging case.

## 7.6.3 Hybrid tagging

For the reasons explained above, the truth tagging is currently applied only to  $V + cc$ ,  $V + cl$  and  $V + l$  samples, even if also other samples contain a large fraction



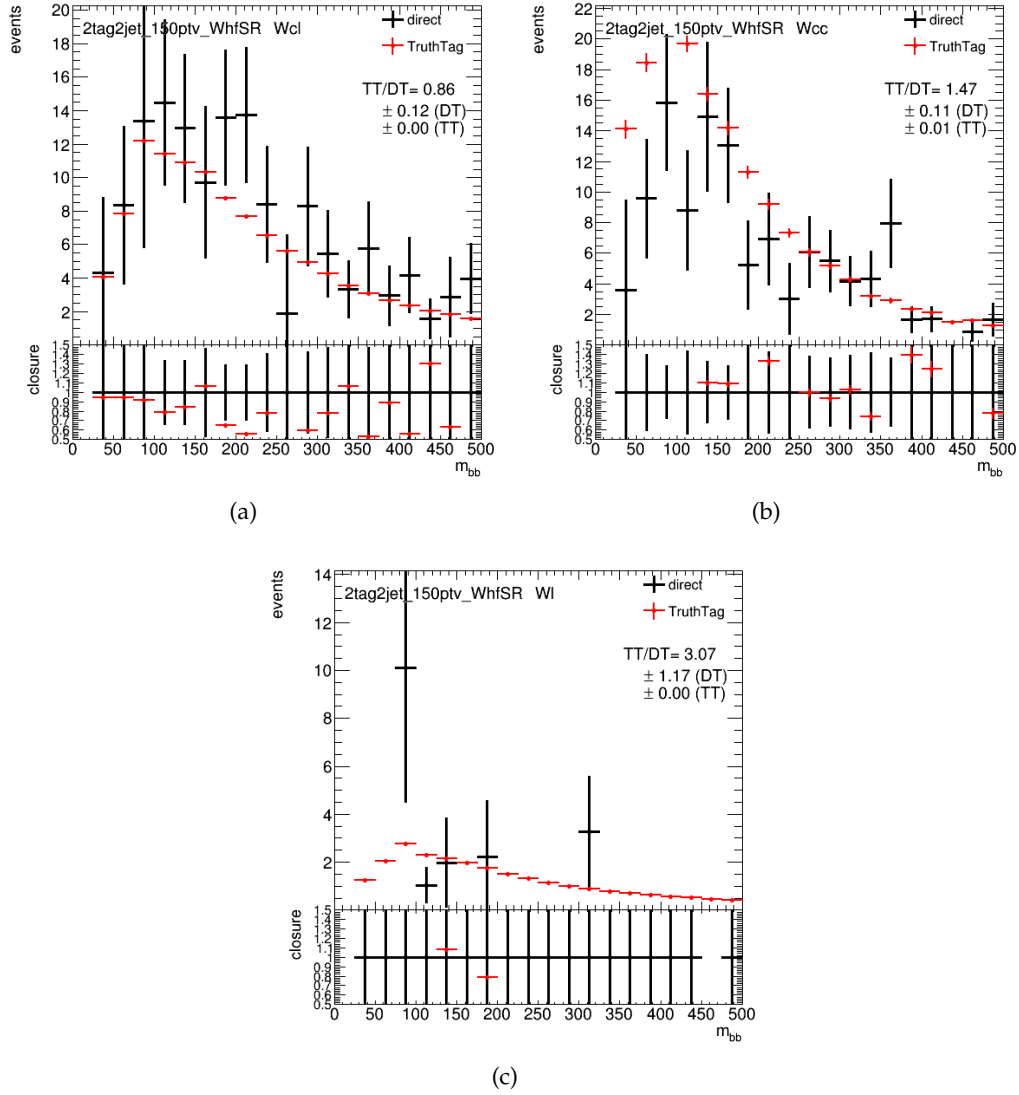


FIGURE 7.11 – (a)  $Wcl$ , (b)  $Wcc$  and (c)  $Wl$  distributions using direct (black) and truth (red) tagging strategies.

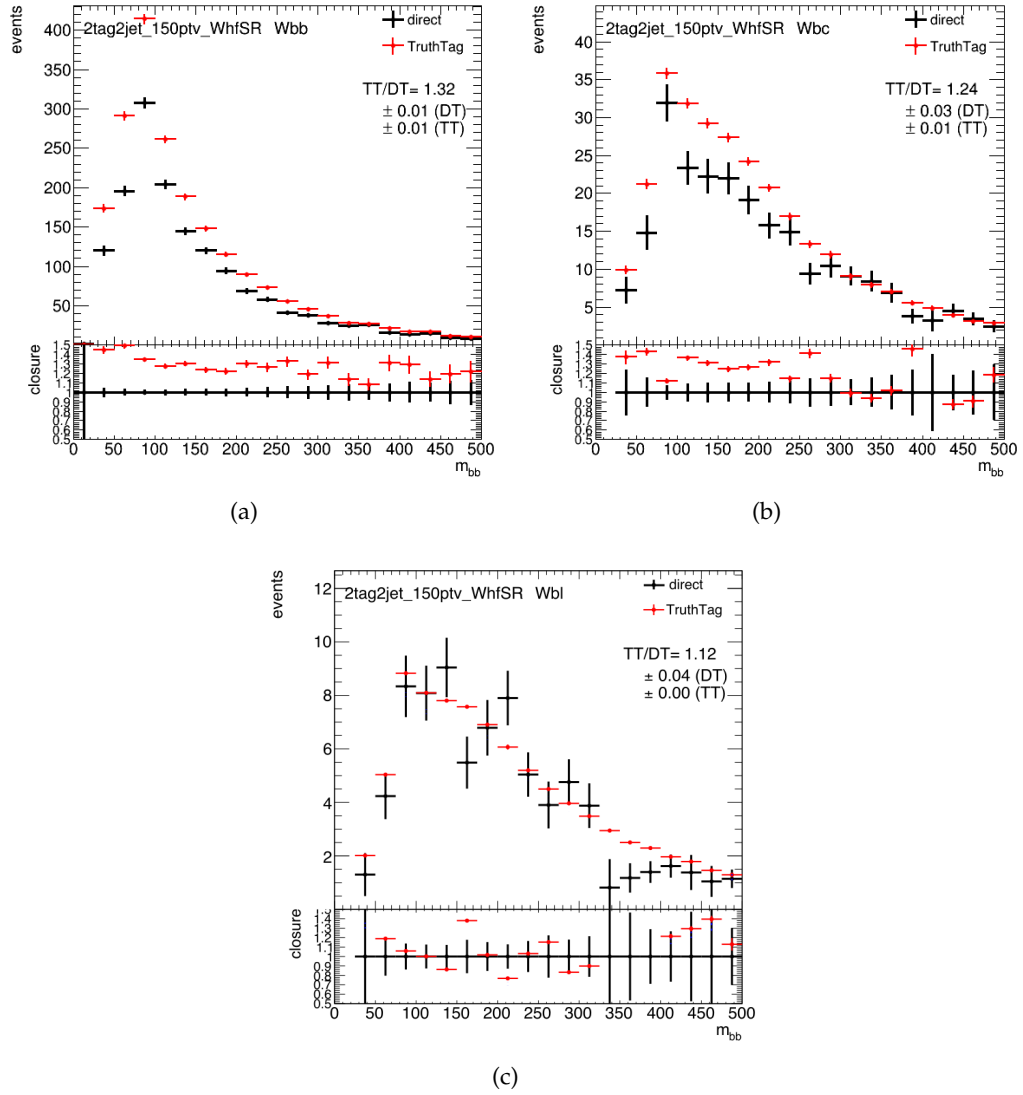


FIGURE 7.12 – (a)  $Wbb$ , (b)  $Wbc$  and (c)  $Wbl$  distributions using direct (black) and truth (red) tagging strategies.

Process	Direct tagging	
	yield	error
0-lepton		
Zbb	2949.96	23.04
Zbc	161.73	6.21
Zbl	134.39	6.43
1-lepton		
Wbb	1586.52	15.82
Wbc	247.86	7.28
Wbl	128.02	5.86
2-lepton		
Zbb	974.39	6.88
Zbc	50.96	2.04
Zbl	38.94	1.97

TABLE 7.17 – Yields and associated statistical uncertainties of the V+jet direct tagged processes in the analysis in 0-, 1- and 2-lepton channels.

Process	Direct tagging		Truth tagging	
	yield	error	yield	error
0-lepton				
Zcc	100.11	8.94	132.03	0.93
Zcl	48.88	7.70	41.78	0.12
Zl	19.77	6.64	15.34	0.03
1-lepton				
Wcc	117.89	13.24	173.45	1.55
Wcl	146.7	16.94	125.78	0.30
Wl	9.65	11.33	29.62	0.04
2-lepton				
Zcc	37.01	3.98	34.78	0.36
Zcl	9.78	2.92	10.64	0.04
Zl	5.94	4.25	3.64	0.01

TABLE 7.18 – Yields and associated statistical uncertainties of the V+jet truth tagged processes in 0-, 1- and 2-lepton channels. The left column contains the yields in case of direct tagging, while the right column contains the final yields with truth tagging.

of c- and light-jets. A new "hybrid" tagging strategy, which optimizes the use of direct tagging and statistical tagging in the analysis, has been developed and tested with preliminary results for the  $80 \text{ fb}^{-1}$  analysis. In the hybrid approach the choice of truth tagged and direct tagged jets is done on an event basis, in this way also  $bc$  and  $bl$  events can profit of the advantages of the statistical reweighting, even if they contain b-jets. In practice, the hybrid tagging strategy can be summarised in the following steps:

- Divide the jets of each event in two groups, depending on the truth tag flavour: a group with only true b-jets and the other with non b-jets.
- All b-jets in the first group are direct tagged.
- The remaining group of c- and light-jets is truth tagged imposing a number of tagged jets proportional to the difference between the number of required jets in the signal region and the number of true b-jets in the first group passing the b-tag requirement.

The new strategy can be better explained with an example:

jet index	flavour type	b-tagging scores
1	b	0.99
2	b	0.74
3	c	0.24
4	c	0.16
5	light	0.07

This is a 5-jet event, with 2-b jets with b-tagging scores above and below the 70% working point threshold (0.8244 according to Table 5.5), and 3 c- or light-flavour jets. Just the first b-jet passes the b-tagging requirement when applying direct tagging to the b-jet group. Therefore, one extra jet is needed to make the event enter the signal region (2-tag). This extra jet is taken by applying truth tagging to the non-b-tagged group and configuring the truth tagging to have exactly one truth tagged jet. In the example, the 3rd jet has the highest probability to be chosen as the truth tagged jet. Thus, the event will be identified as a  $bc$  event entering in the signal region with a b-tagging event weight calculated as the product of the b-jet flavour tagging SFs and the truth-tagging weight (described in Section 5.4).

By construction, perfect closure is expected between hybrid and direct tagging in case of 2-jet  $bb$  events, while improvements in the MC statistics are foreseen for  $bc$  and  $bl$  events. No change is expected for the "historically" truth tagged samples  $Vcl$ ,  $Vcc$  and  $Vl$ , which do not contain b-jets and therefore only truth tagging is applied. Figure 7.13 shows a comparison between hybrid (blue), truth (red) and direct (black) tagging strategies in  $bb$ ,  $bc$  and  $bl$  samples. A reduction of 9.9% and 7.7% in the relative MC statistical uncertainty is observed in the 2-jet and 3-jet signal regions respectively. Due to non closure problems in the efficiency maps, mentioned in the previous Section, biases in the  $bc$  and  $bl$  yields of the V+jets (i.e. 12% in  $Wbc$  and 25% in  $Zbc$  in the 1-lepton channel) arise comparing hybrid and direct tagging. Thus, the method has not been used for the official publication. New improvements, ensuring better closure between the two methods will be discussed in the next Chapter.

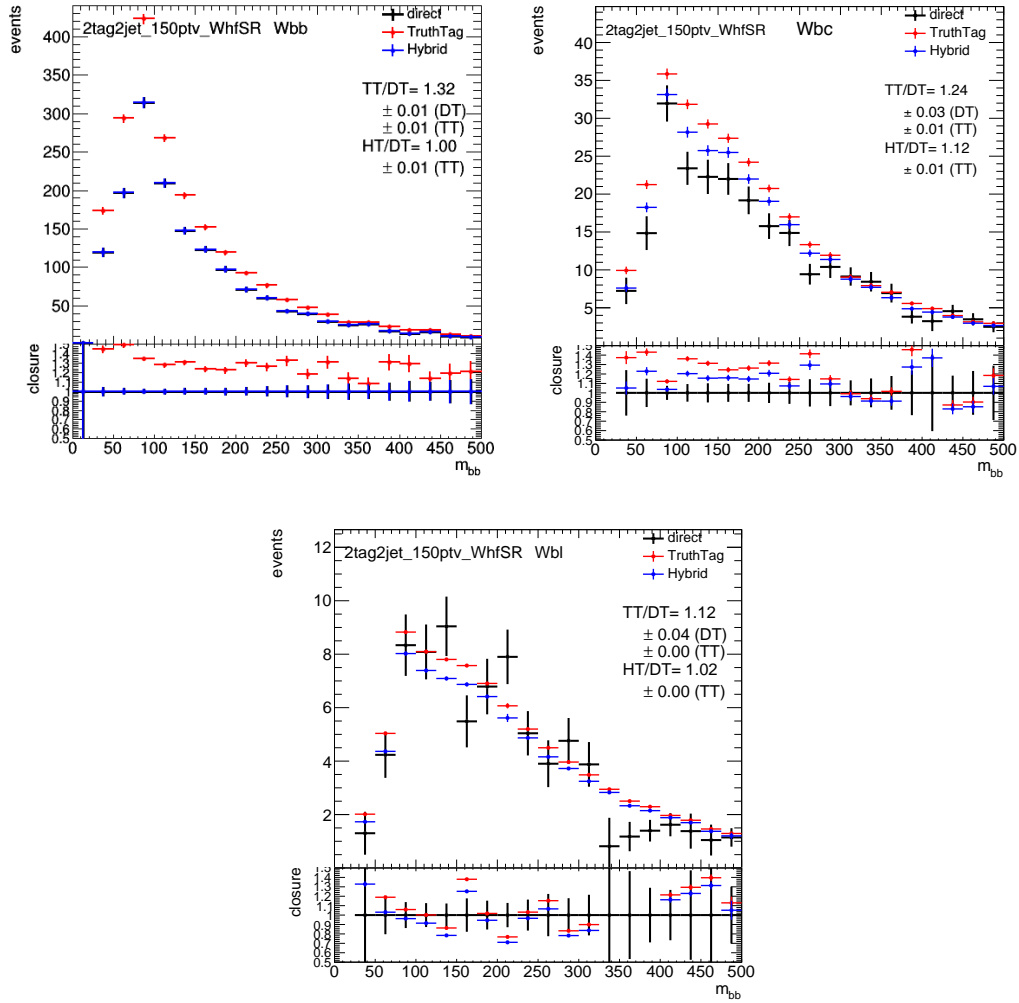


FIGURE 7.13 – (a)  $Wbb$ , (b)  $Wbc$  and (c)  $Wbl$  distributions using Direct (black), Truth (red) and Hybrid (blue) tagging strategies.

## 7.7 Fit Results

The following Section focuses on the results of the official  $VH, H \rightarrow b\bar{b}$  analysis with  $80 \text{ fb}^{-1}$  of ATLAS data [205].

### 7.7.1 Post-fit plots

After the event selection described in Section 7.2, around 130 Higgs candidates are expected for both the 0- and 1-lepton channels in the 2-tag 2-jet regions, while the expected number of background events varies between 8 000 in the 0-lepton channel to 12 000 in the 1-lepton channel. In the 2-lepton channel the signal to background ratio is much smaller, due to both  $Z$ -jet and  $t\bar{t}$ , a total of 1 600 (10 000) background events are expected in the 2-jet region with  $p_T^V > 150 \text{ GeV}$  ( $75 < p_T^V < 150 \text{ GeV}$ ), compared to  $\sim 30$  (50) signal events expected. The signal to background ratio is smaller in the 3-jet categories. Table 7.19 summarises the contribution of each background to the total expected yield in simulation, compared to the total number of selected data events.

Figure 7.14, 7.15 and 7.16 show the distribution of the BDT output in data and simulation for the different lepton channels and analysis categories, when applying the normalisation factors extracted from the simultaneous fit. The  $t\bar{t}$  CR are shown in Figure 7.5. No mismodelling is observed, and the prediction from MC simulation is well in agreement with the data. The post-fit distributions of other kinematic variables across the different channels are shown in Figure 7.17.

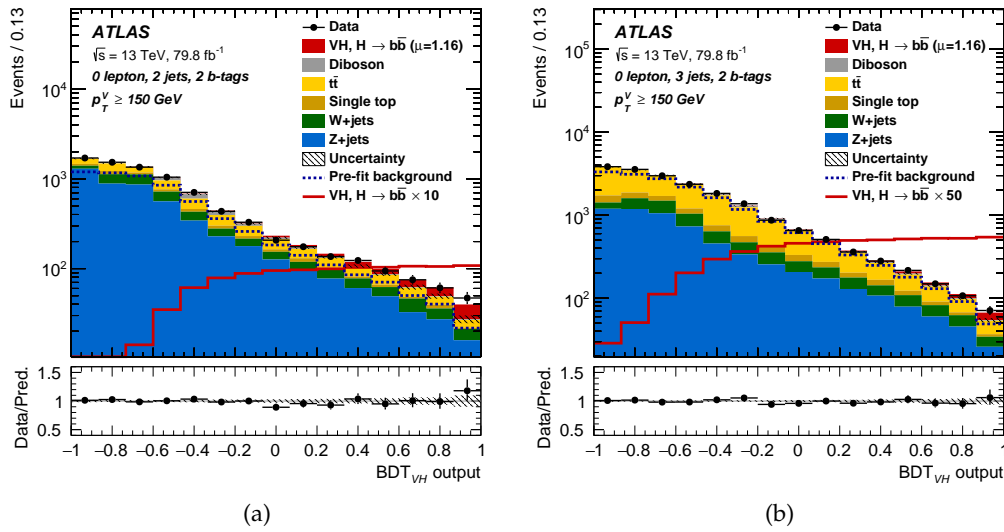


FIGURE 7.14 – The  $BDT_{VH}$  output post-fit distributions in the 0-lepton channel for 2-b-tag events, in the 2-jet (a) and exactly 3-jet (b) categories. The background contributions after the global likelihood fit are shown as filled histograms. The Higgs boson signal ( $m_H = 125 \text{ GeV}$ ) is shown as a filled histogram on top of the fitted backgrounds normalised to the signal yield extracted from data ( $\mu = 1.16$ ), and unstacked as an open histogram, scaled by the factor indicated in the legend. The dashed histogram shows the total pre-fit background. The size of the combined statistical and systematic uncertainty for the sum of the fitted signal and background is indicated by the hatched band. The ratio of the data to the sum of the fitted signal ( $\mu = 1.16$ ) and background is shown in the lower panel. The  $BDT_{VH}$  output distributions are shown with the binning used in the global likelihood fit [205].

Process	0-lepton			1-lepton			2-lepton		
	$p_T^V > 150 \text{ GeV}, 2-b\text{-tag}$	2-jet	3-jet	$p_T^V > 150 \text{ GeV}, 2-b\text{-tag}$	2-jet	3-jet	$75 \text{ GeV} < p_T^V < 150 \text{ GeV}, 2-b\text{-tag}$	2-jet	$p_T^V > 150 \text{ GeV}, 2-b\text{-tag}$
$Z + ll$	$17 \pm 11$	$27 \pm 18$		$2 \pm 1$	$3 \pm 2$		$14 \pm 9$	$4 \pm 3$	$30 \pm 19$
$Z + cl$	$45 \pm 18$	$76 \pm 30$		$3 \pm 1$	$7 \pm 3$		$43 \pm 17$	$12 \pm 5$	$88 \pm 35$
$Z + \text{HF}$	$4770 \pm 140$	$5940 \pm 300$		$180 \pm 9$	$348 \pm 21$		$7400 \pm 120$	$1421 \pm 34$	$5370 \pm 100$
$W + ll$	$20 \pm 13$	$32 \pm 22$		$31 \pm 23$	$65 \pm 48$		$< 1$	$< 1$	$< 1$
$W + cl$	$43 \pm 20$	$83 \pm 38$		$139 \pm 67$	$250 \pm 120$		$< 1$	$< 1$	$< 1$
$W + \text{HF}$	$1000 \pm 87$	$1990 \pm 200$		$2660 \pm 270$	$5400 \pm 670$		$2 \pm 0$	$1 \pm 0$	$4 \pm 1$
Single top quark	$368 \pm 53$	$1410 \pm 210$		$2080 \pm 290$	$9400 \pm 1400$		$188 \pm 89$	$23 \pm 7$	$93 \pm 26$
$t\bar{t}$	$1333 \pm 82$	$9150 \pm 400$		$6600 \pm 320$	$50200 \pm 1400$		$3170 \pm 100$	$104 \pm 6$	$839 \pm 40$
Diboson	$254 \pm 49$	$318 \pm 90$		$178 \pm 47$	$330 \pm 110$		$152 \pm 32$	$52 \pm 11$	$196 \pm 35$
Multi-jet $e$ sub-ch.	—	—		$100 \pm 100$	$41 \pm 35$		—	—	—
Multi-jet $\mu$ sub-ch.	—	—		$138 \pm 92$	$260 \pm 270$		—	—	—
Total bkg.	$7850 \pm 90$	$19020 \pm 140$		$12110 \pm 120$	$66230 \pm 270$		$10960 \pm 100$	$1620 \pm 30$	$6620 \pm 80$
Signal (post-fit)	$128 \pm 28$	$128 \pm 29$		$131 \pm 30$	$125 \pm 30$		$51 \pm 11$	$28 \pm 6$	$67 \pm 17$
Data	8003	19143		12242	66348		11014	1626	6686

TABLE 7.19 – The Higgs boson signal, background and data yields for each signal region category in each channel after the full selection of the multivariate analysis. The signal and background yields are normalised to the results of the global likelihood fit. All systematic uncertainties are included in the quoted uncertainties. An entry of "—" indicates that a specific background component is negligible in a certain region, or that no simulated events are left after the analysis selection.



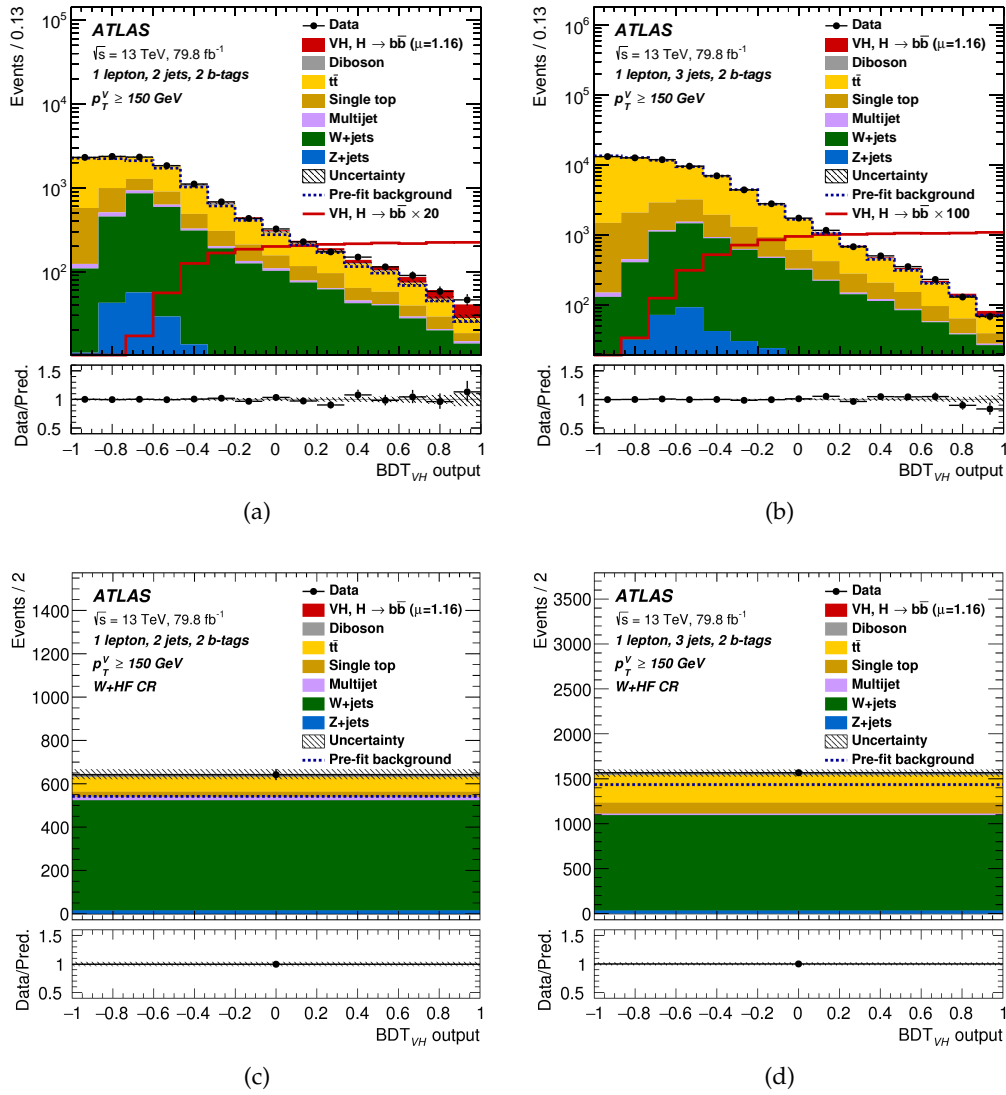
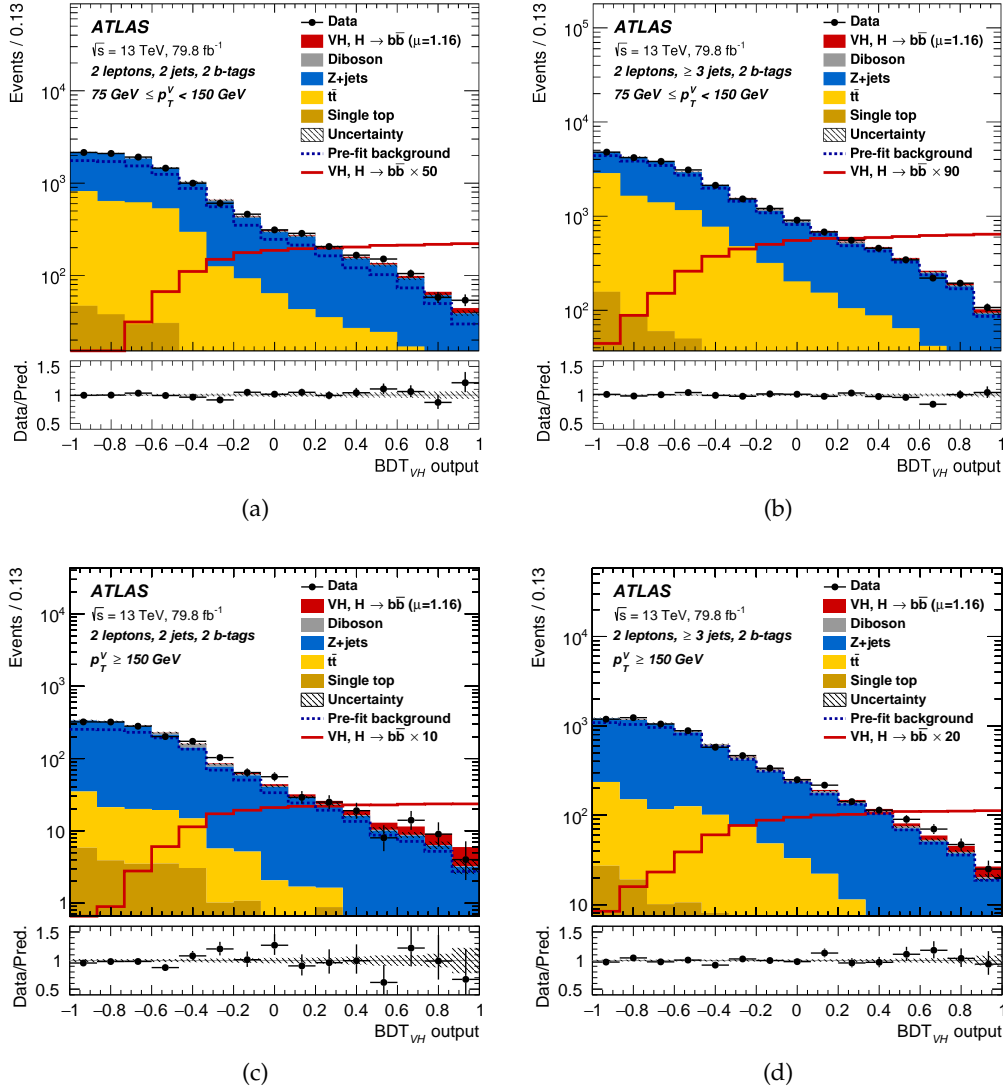


FIGURE 7.15 – The  $BDT_{VH}$  output post-fit distributions in the 1-lepton channel for 2-b-tag events, in the 2-jet (a) and exactly 3-jet (b) signal regions and (c) and (d) in the corresponding control regions. The background contributions after the global likelihood fit are shown as filled histograms. The Higgs boson signal ( $m_H = 125$  GeV) is shown as a filled histogram on top of the fitted backgrounds normalised to the signal yield extracted from data ( $\mu = 1.16$ ), and unstacked as an open histogram, scaled by the factor indicated in the legend. The dashed histogram shows the total pre-fit background. The size of the combined statistical and systematic uncertainty for the sum of the fitted signal and background is indicated by the hatched band. The ratio of the data to the sum of the fitted signal ( $\mu = 1.16$ ) and background is shown in the lower panel. The  $BDT_{VH}$  output distributions are shown with the binning used in the global likelihood fit [205].



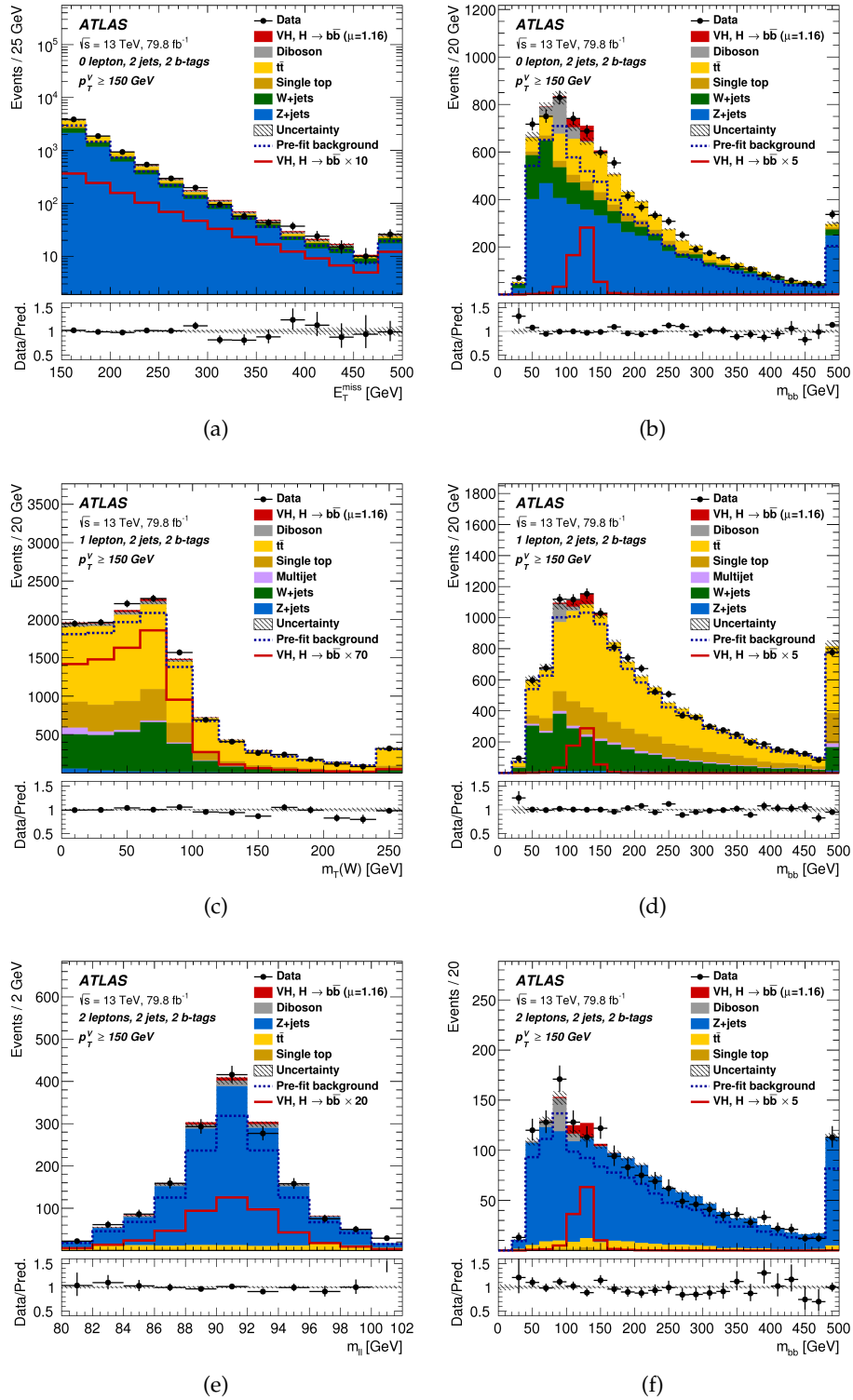


FIGURE 7.17 – The post-fit distributions for  $E_T^{miss}$  (a), and  $m_{bb}$  (b) in the 0-lepton channel, (c)  $m_T^W$  and (d)  $m_{bb}$  in the 1-lepton channel and (e)  $m_{\ell\ell}$  and (f)  $m_{bb}$  in the 2-lepton channel for 2-jet, 2-b-tag events in the high  $p_T^V$  region. The background contributions after the global likelihood fit are shown as filled histograms. The Higgs boson signal ( $m_H = 125$  GeV) is shown as a filled histogram on top of the fitted backgrounds normalised to the signal yield extracted from data ( $\mu = 1.16$ ), and unstaked as an open histogram, scaled by the factor indicated in the legend. The entries in overflow are included in the last bin. The dashed histogram shows the total pre-fit background. The hatched band combines statistical and systematic uncertainty for the sum of the fitted signal and background. The ratio of the data to the sum of the fitted signal and background is shown in the lower panel [205].

### 7.7.2 Significances and signal strength

The expected and observed significances for the combined fit with all channels are presented in Table 7.20. The observed significance for the fit with one  $\mu$  value for all channels is  $4.9\sigma$ , extracted from an unconditional fit to data, where all the NP are free to vary and the signal strength is initialized to a value of  $\mu = 1$ . The expected significance is extracted from a fit to an Asimov dataset, generated using the result of a conditional  $\mu = 1$  fit to data<sup>7</sup> for a more realistic description of the nuisance parameters, especially the normalization factors. The expected significance is equal to  $4.3\sigma$ . The measured signal strength for the  $VH, H \rightarrow b\bar{b}$  process is:

$$\mu = 1.16^{+0.16}_{-0.16}(\text{stat.})^{+0.21}_{-0.19}(\text{syst.}) \quad (7.33)$$

where the total systematic uncertainty is calculated starting from the sources described in Section 7.5.

The compatibility among the channels is measured by repeating the simultaneous fit assigning to each channel an independent free-floating signal strength parameter. The results of the fit are shown in Figure 7.18(a) for the entries with the label MVA, compared to the results from the di-jet analysis (DMA), which will be discussed in the next Section. The associated p-values are summarized in the first rows of Table 7.20. The compatibility of the measured  $\mu$  in the three lepton channels is 80.2%. This number is extracted comparing the maximum likelihood values of the multiple  $\mu$  fit with the single  $\mu$  one. In the asymptotic regime defined in Section 7.4.2 the compatibility between the maximum likelihood fits differing only in the number of parameters of interest follows a  $\chi^2$  distribution with a number of degrees of freedom equal to this difference. The two hypotheses can be thus compared to a  $\chi^2$  with *two* degrees of freedom to extract the aforementioned probability.

Signal strength	Signal strength	$p_0$		Significance	
		Exp.	Obs.	Exp.	Obs.
0-lepton	$1.04^{+0.34}_{-0.32}$	$9.5 \cdot 10^{-4}$	$5.1 \cdot 10^{-4}$	3.1	3.3
1-lepton	$1.09^{+0.46}_{-0.42}$	$8.7 \cdot 10^{-3}$	$4.9 \cdot 10^{-3}$	2.4	2.6
2-lepton	$1.38^{+0.46}_{-0.42}$	$4.0 \cdot 10^{-3}$	$3.3 \cdot 10^{-4}$	2.6	3.4
$VH, H \rightarrow b\bar{b}$ combination	$1.16^{+0.27}_{-0.25}$	$7.3 \cdot 10^{-6}$	$5.3 \cdot 10^{-7}$	4.3	4.9

TABLE 7.20 – Measured signal strengths with their combined statistical and systematic uncertainties, expected and observed  $p_0$  and significance values (in standard deviations) from the combined fit with a single signal strength, and from a combined fit where each of the lepton channels has its own signal strength, using  $80 \text{ fb}^{-1}$  of  $\sqrt{s} = 13$  TeV data.

The compatibility between the WH and ZH production modes is also checked, by repeating the simultaneous fit with independent signal strength parameters for the two production modes ( $\mu_{WH}$  and  $\mu_{ZH}$ ). The level of compatibility between the two individual signal strengths is 84%, with both measured  $\mu_{WH}$  and  $\mu_{ZH}$  compatible with the  $\mu = 1$  hypothesis within the uncertainties, as shown in Figure 7.18(b).

Figure 7.19 shows the data and simulation comparison of the BDT output bins combined into bins of  $\log_{10}(S/B)$ , S and B are the fitted signal and background yields in each bin, with the signal contribution scaled by the VH signal strength

7. This fit is obtained fixing the  $\mu$  parameter to 1 and leaving all the other NP free to vary.

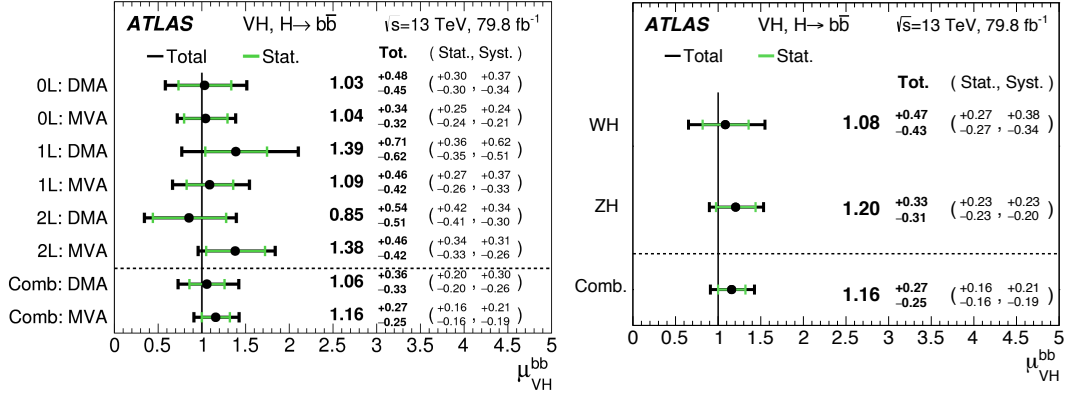


FIGURE 7.18 – The fitted values of the Higgs boson signal strength  $\mu_{VH}^{bb}$  for  $m_H = 125$  GeV for a simultaneous fit with (a) the signal strength for each channel floating independently and (b) the signal strength for the WH and ZH processes floating independently. In (a) the results are shown both for the nominal multivariate analysis (MVA) and for the di-jet mass analysis (DMA) [205].

$\mu = 1.16$ . In the bottom panel, a clear deviation from the background only hypothesis (dashed line) is visible. As described by the solid red line, this excess is compatible with the expectations, built in simulation as the ratio of the sum of the fitted SM signal+background distribution over the fitted background.

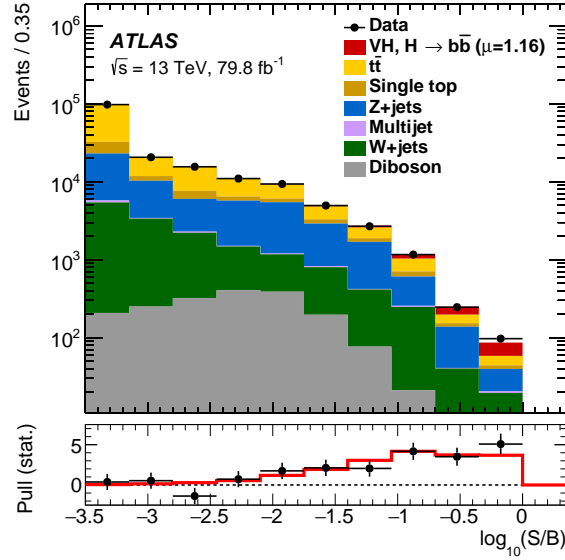


FIGURE 7.19 – Event yields as a function of  $\log_{10}(S/B)$  for data, background and a Higgs boson signal with  $m_H = 125$  GeV. Final-discriminant bins in all regions are combined into bins of  $\log_{10}(S/B)$ , with S being the fitted signal and B the fitted background yields. The Higgs boson signal contribution is shown after rescaling the SM cross-section according to the value of the signal strength extracted from data ( $\mu = 1.16$ ). In the lower panel, the pull of the data relative to the background (the statistical significance of the difference between data and fitted background) is shown with statistical uncertainties only. The full line indicates the pull expected from the sum of the fitted signal and background relative to the fitted background. The dashed line represents the expectations for the background only hypothesis [205].

### 7.7.3 Ranking of the systematic uncertainties

The systematic uncertainties can be ranked depending on their impact on the signal strength variation. This ranking is calculated iteratively considering all the nuisance parameters  $\theta$  described in Section 7.5. The simultaneous fit is repeated fixing the NP under test to its best fit value  $\hat{\theta}$  modified upwards or downwards by its fitted uncertainty, and leaving all the other parameters free to vary to account for correlations. The higher the difference between the nominal  $\hat{\mu}$  and the new  $\mu$  value, the higher the impact of the considered nuisance parameter on the signal strength, and therefore its position in the ranking. Figure 7.20 shows the impact of the first 15 nuisance parameters on  $\mu_{VH}$  for the 0-, 1-, 2-channel combined fit. The highest con-

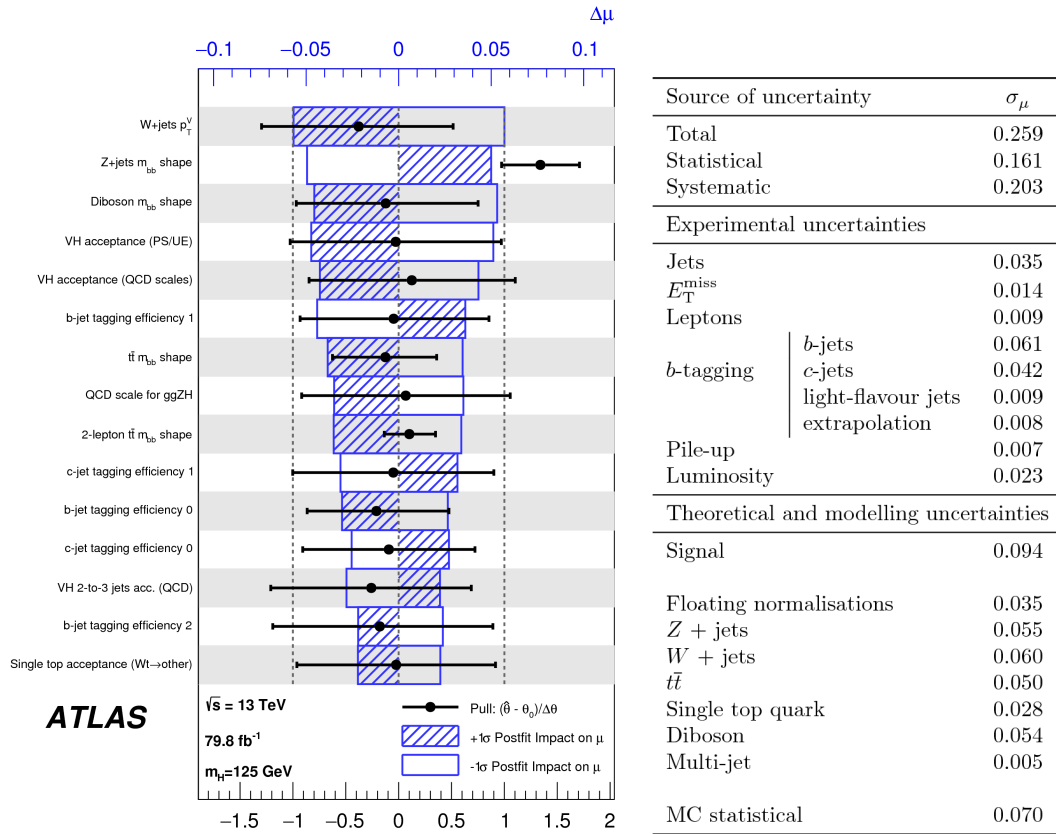


FIGURE 7.20 – (a) Impact of systematic uncertainties for the fitted Higgs boson signal strength  $\mu$  for the nominal MVA analysis applied to the 13 TeV data. The systematic uncertainties are listed in decreasing order of their impact on  $\mu$ . The boxes show the variations of  $\mu$ , referring to the top x-axis. The hatched and open areas correspond to the upwards and downwards variations, respectively. The filled circles, referring to the bottom x-axis, show the deviations of the fitted nuisance parameters  $\hat{\theta}$  from their nominal values, expressed in terms of standard deviations with respect to their nominal uncertainties  $\Delta\theta$ . The associated error bars show the fitted uncertainties of the nuisance parameters, relative to their nominal uncertainties. (b) Breakdown of the contributions to the uncertainty in  $\mu$ . The sum in quadrature of the systematic uncertainties related to the categories differs from the total systematic uncertainty due to correlations [205].

tributions come from the modelling of the  $p_T^V$  and  $m_{bb}$  shapes of  $V$ +jets and diboson. The uncertainties can be grouped depending on the origin - i.e. modelling, signal, experimental and so on - in a single breakdown table as presented in Figure 7.20. Each entry of the breakdown is calculated as the difference in quadrature between

the error on the signal strength  $\sigma_\mu^{\text{all}}$  calculated from a fit with *all* the NP free to vary and the same fit performed fixing the NP of interest to their best values  $\sigma_\mu^{\text{all-NP}_{\text{int}}}$ .

The final result is given as  $\sqrt{(\sigma_\mu^{\text{all}})^2 - (\sigma_\mu^{\text{all-NP}_{\text{int}}})^2}$ .

The highest experimental contribution comes from the b-tagging uncertainties, while the signal and V+jets uncertainties are the highest modelling-related uncertainties. Also, the statistical uncertainty on the number of simulated events has a non-negligible impact (0.07).

#### 7.7.4 Focus on the one-lepton channel

The results for the 1-lepton channel standalone analysis are presented here as a baseline for the improvements described in the next Chapter. The measured signal strength for a fit in the 1-lepton channel is:

$$\mu = 1.02_{-0.26}^{+0.27}(\text{stat.})_{-0.33}^{+0.37}(\text{syst.}). \quad (7.34)$$

The excess has an observed significance of 2.36 standard deviations, compared to an expected significance of 2.32 standard deviations, obtained as explained above from a fit to a "realistic Asimov" dataset, based on a conditional fit to data with  $\mu = 1$ . Figure 7.21 shows a detailed view of the different contributions, both in terms of breakdown and ranking.

As expected, the highest ranked NP is the one related to the W+jets  $p_T^V$  modelling, which is also the highest contribution to the combined fit in Figure 7.20. Immediately after, there are the contributions from the NPs related to the uncertainty on the number of simulated events. In total, five of these NPs are observed among the first 15 highly ranked NPs<sup>8</sup>. Also the b- and c-tagging related uncertainties are highly ranked in the fit, with three contributions among the first 15 NPs.

### 7.8 Cross-check analyses

As mentioned in the introduction, the MVA analysis is cross-checked with two alternative analyses. The BDT approach is validated with  $VZ, Z \rightarrow b\bar{b}$  events. The same MVA is retrained specifically for this process, while the fit structure has been validated by fitting directly the di-jet mass distribution, as briefly discussed below.

#### 7.8.1 The di-jet analysis

The di-jet analysis is based on a cut-based approach where the BDT fit is replaced with the  $m_{bb}$  fit. The general structure of the analysis is unchanged, apart for some optimizations in the event selection described in Section 7.2.2. This allows for a completely independent cross-check of the architecture of the simultaneous fit. The fitted value of the signal strength parameter for the simultaneous fit to the di-jet mass with all the channels combined is

$$\mu = 1.06_{-0.20}^{+0.20}(\text{stat.})_{-0.26}^{+0.30}(\text{syst.}) \quad (7.35)$$

in good agreement with the result of the multivariate analysis. The observed significance is 3.6 standard deviations, in comparison to an expectation of 3.5 standard deviations. The quoted excess in data is clearly visible in Figure 7.22, compared to the sum of SM Higgs and diboson expectations taken from simulations. The back-

8. Among them, the bins 12,13,14 are among the right-most bins where the S/B ratio is higher.



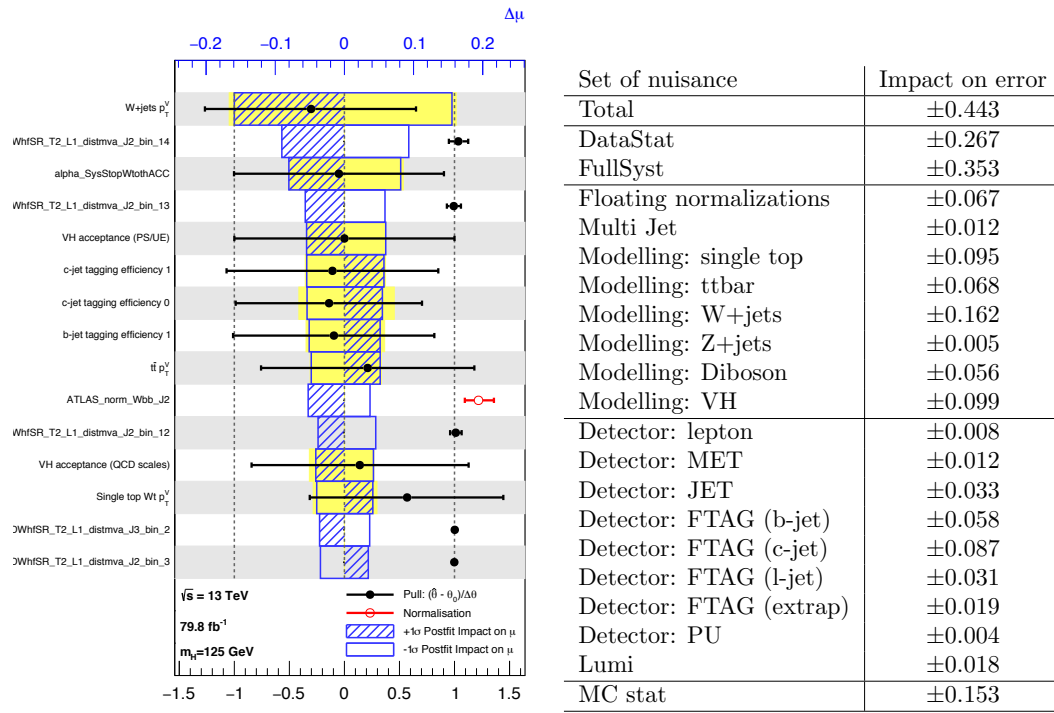


FIGURE 7.21 – (a) Impact of systematic uncertainties for the fitted Higgs boson signal strength  $\mu$  in the 1-lepton channel, based on an unconditional fit to data at  $80 \text{ fb}^{-1}$ . The systematic uncertainties are listed in decreasing order of their impact on  $\mu$ . The color conventions are the same as Figure 7.20(a). The yellow bands correspond to the so-called prefit impact of the nuisance parameters, which is evaluated by changing the values of the nuisance parameters by 1 (which is the prefit uncertainty on the NP). (b) Breakdown of the contributions to the uncertainty of  $\mu$  for the fit to the 1-lepton channel. The sum in quadrature of the systematic uncertainties related to the categories differs from the total systematic uncertainty due to correlations.

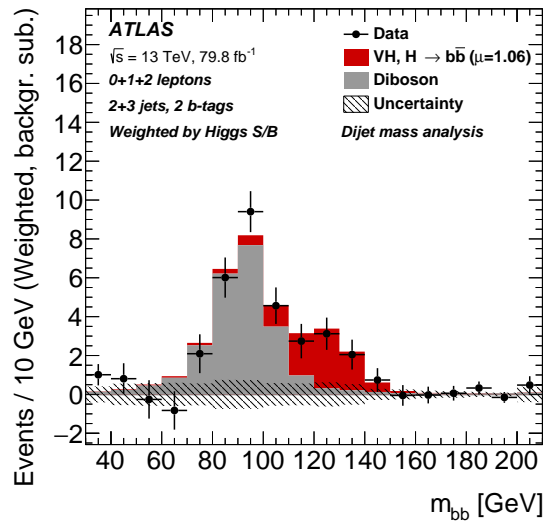


FIGURE 7.22 – The distribution of  $m_{bb}$  in data after subtraction of all backgrounds except for the WZ and ZZ processes in the dijet-mass analysis. The contributions from all the categories are summed and weighted by their respective S/B, with S being the total fitted signal and B the total fitted background in each region. The expected contribution of the associated WH and ZH production of a SM Higgs boson with  $m_H = 125$  GeV is shown scaled by the measured signal strength ( $\mu = 1.06$ ). The hatched band shows the combined statistical and systematic uncertainty for the background [205].

ground yields, have been subtracted in data and each region is added weighting each bin by the ratio of the fitted signal yield to background yield, S/B.

The post-fit plots of the  $m_{bb}$  distribution in all the three channels are shown in Figure 7.23, 7.24 and 7.25. As for the MVA analysis, good agreement between data and simulation is observed. As shown in Figure 7.18 (DMA labels), a high compatibility between the signal strengths in the various channels and between the di-jet mass and MVA analyses is also observed, being a further validation of the robustness of the fit design. Overall, the di-jet analysis is 27% (19% for the expectation) less sensitive than the MVA one.

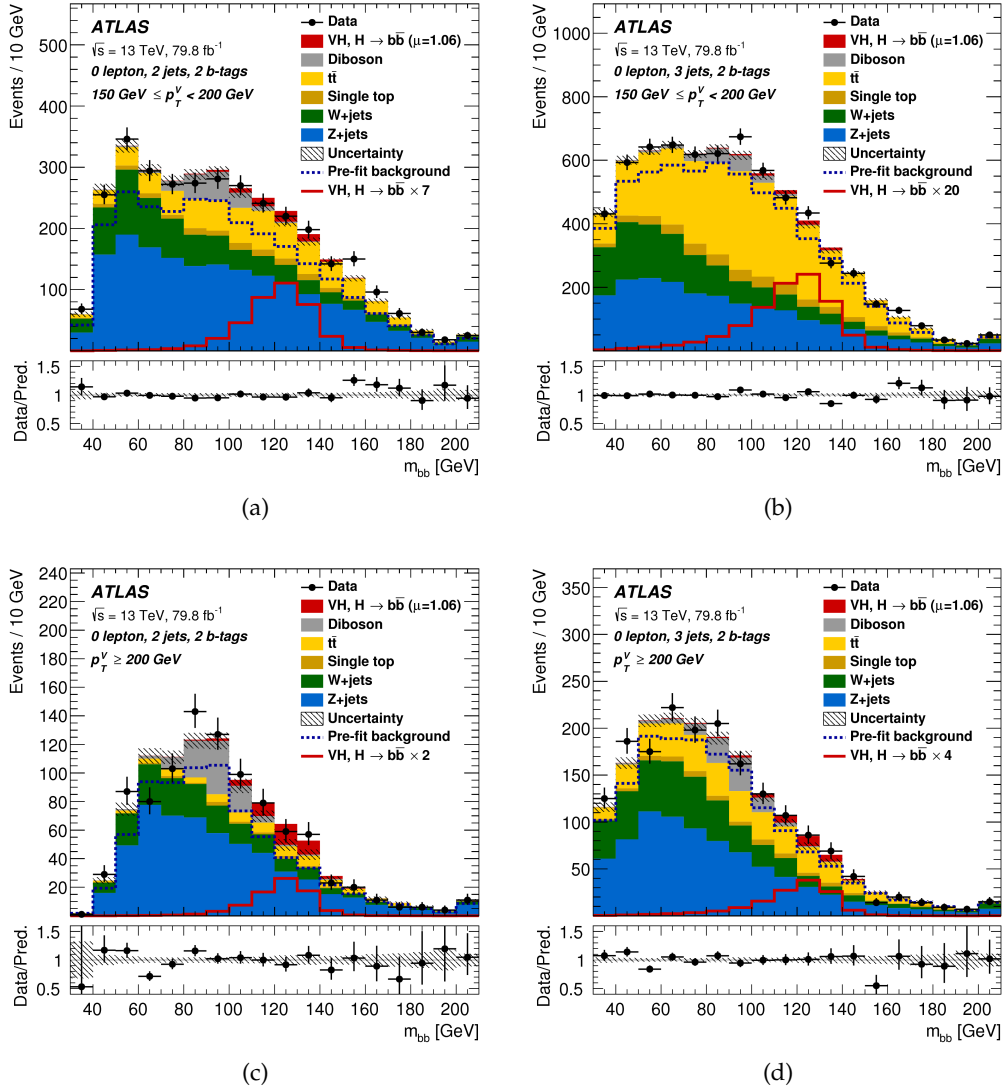


FIGURE 7.23 – Distributions of  $m_{bb}$  used as input to the global likelihood fit of the di-jet mass analysis. The distributions refer to the signal regions of the 0-lepton channel. The data are shown as points with error bars, while the background contributions after the global likelihood fit are shown as filled histograms. The Higgs boson signal ( $m_H = 125$  GeV) is shown as a filled histogram on top of the fitted backgrounds normalised to the signal yield extracted from data ( $\mu = 1.06$ ), and unstacked as an open histogram, scaled by the factor indicated in the legend. The color convention is the same as described in Figure 7.14 [205].

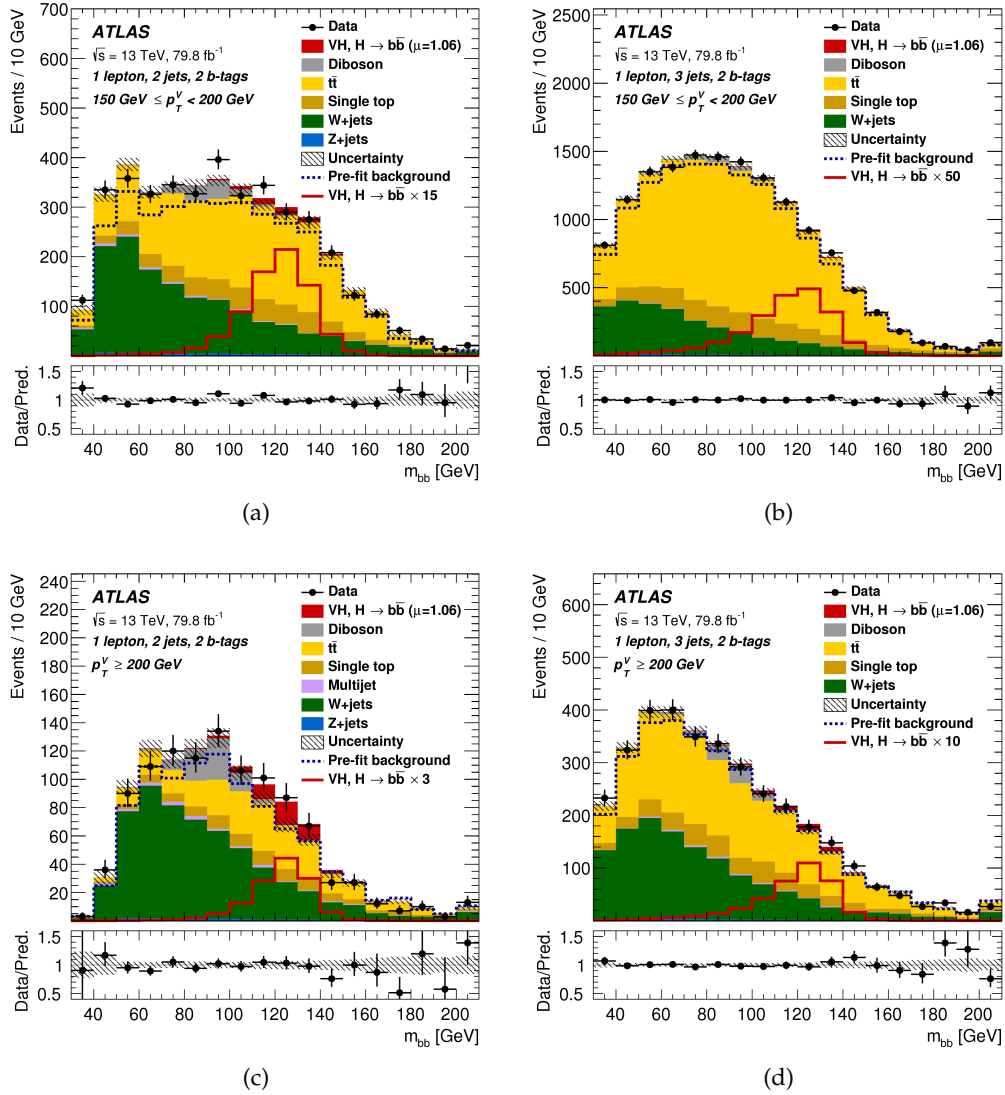


FIGURE 7.24 – Distributions of  $m_{bb}$  used as input to the global likelihood fit of the di-jet mass analysis. The distributions refer to the signal regions of the 1-lepton channel. The data are shown as points with error bars, while the background contributions after the global likelihood fit are shown as filled histograms. The Higgs boson signal ( $m_H = 125$  GeV) is shown as a filled histogram on top of the fitted backgrounds normalised to the signal yield extracted from data ( $\mu = 1.06$ ), and unstacked as an open histogram, scaled by the factor indicated in the legend. The color convention is the same as described in Figure 7.15 [205].

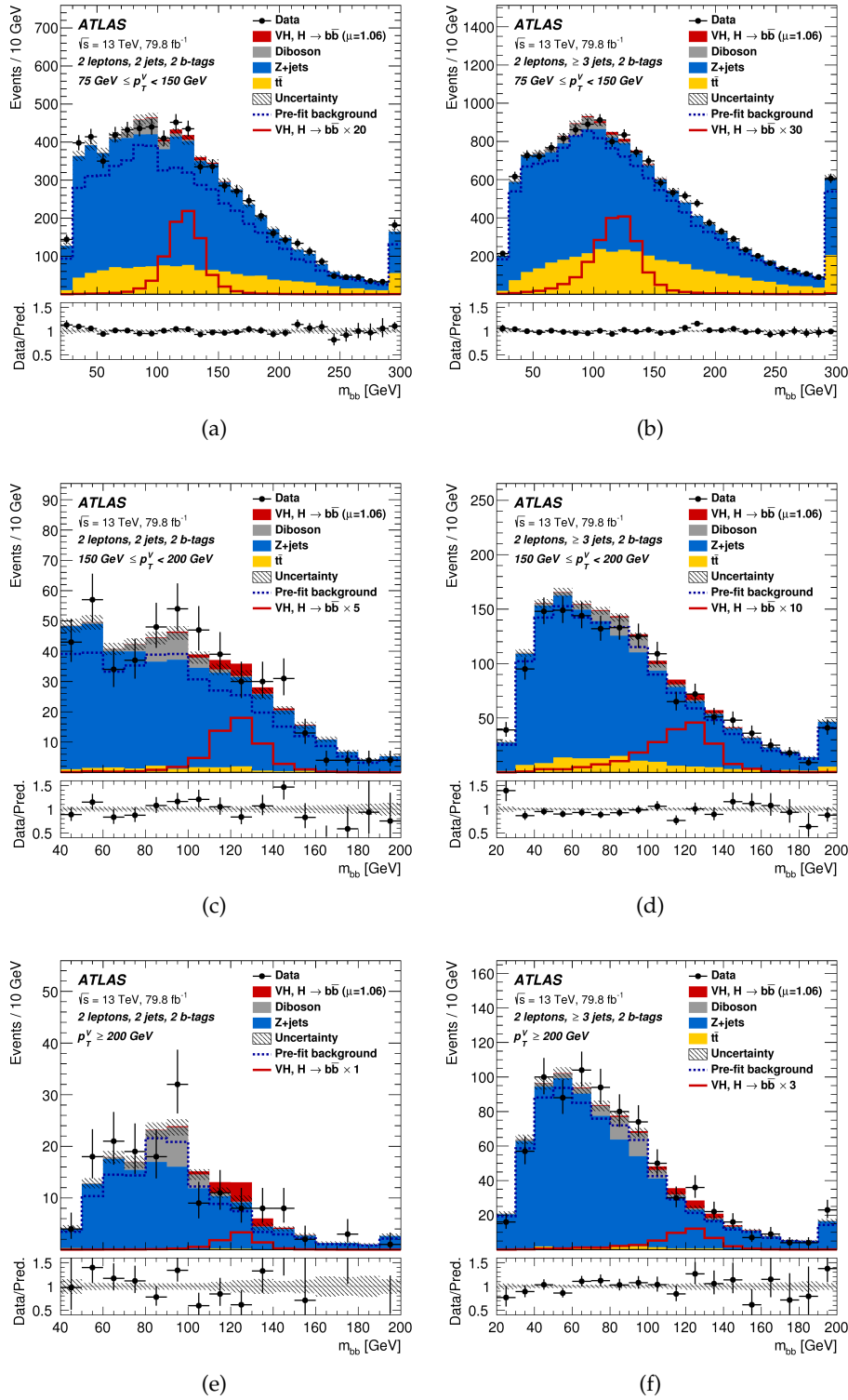


FIGURE 7.25 – Distributions of  $m_{bb}$  used as input to the global likelihood fit of the di-jet mass analysis. The distributions refer to the signal regions of the 2-lepton channel. The data are shown as points with error bars, while the background contributions after the global likelihood fit are shown as filled histograms. The Higgs boson signal ( $m_H = 125$  GeV) is shown as a filled histogram on top of the fitted backgrounds normalised to the signal yield extracted from data ( $\mu = 1.06$ ), and unstacked as an open histogram, scaled by the factor indicated in the legend. The color convention is the same as described in Figure 7.16 [205].

## 7.8.2 The diboson analysis

The diboson production processes  $VZ, Z \rightarrow b\bar{b}$  are used to probe the robustness of the MVA approach. Their signature is similar to the  $VH, H \rightarrow b\bar{b}$  signal, thus a second BDT is trained using the same variables of the VH analysis, but replacing the VH signal with the diboson VZ one. A measurement of the diboson signal strength is then performed using this new BDT as input to the fit. The infrastructure of the fit is identical to the one described in Section 7.2.3 with minor adaptations. Due to the smaller number of events in the diboson simulated samples, the granularity of the BDT transformation has been reoptimised and lowered from 15 to 10 bins. Furthermore, the VH signal is included in the fit as additional background, with a NP on its normalization constrained to the SM prediction with a conservative uncertainty of 50%. The post-fit plots for the  $BDT_{VZ}$  distributions in the 0-,1-,2-leptons channels are presented in Figure 7.26, 7.27 and 7.28. The CR were used as described for the nominal VH analysis, but they are not shown here.

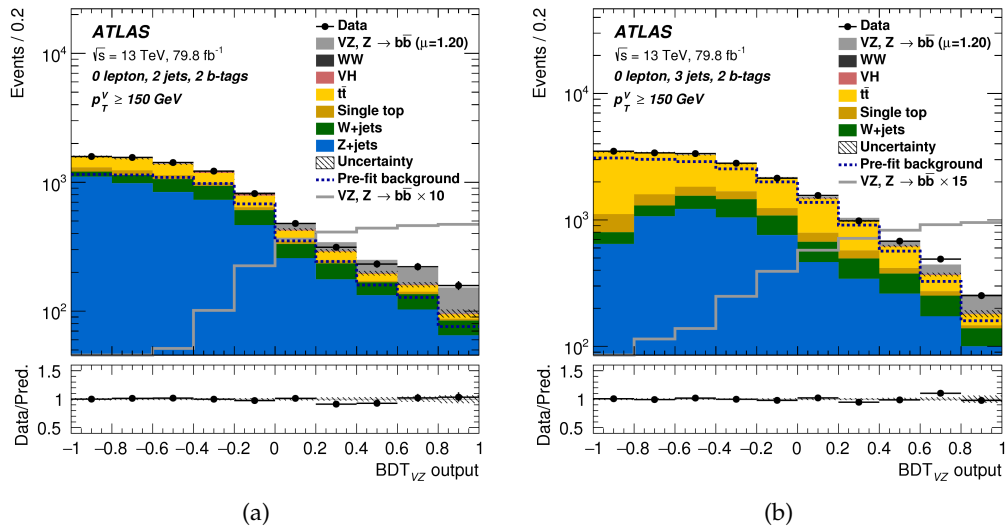


FIGURE 7.26 – The  $BDT_{VZ}$  output post-fit distributions in the 0-lepton channel for 2 b-tag events in 2-jet (a) and 3-jet (b) regions. The background contributions after the global likelihood fit are shown as filled histograms. The VZ diboson signal is shown as a filled histogram on top of the fitted backgrounds normalised to the signal yield extracted from data ( $\mu = 1.20$ ), and unstacked as an open histogram, scaled by the factor indicated in the legend. The dashed histogram shows the total pre-fit background. The size of the combined statistical and systematic uncertainty for the sum of the fitted signal and background is indicated by the hatched band. The ratio of the data to the sum of the fitted signal and background is shown in the lower panel.

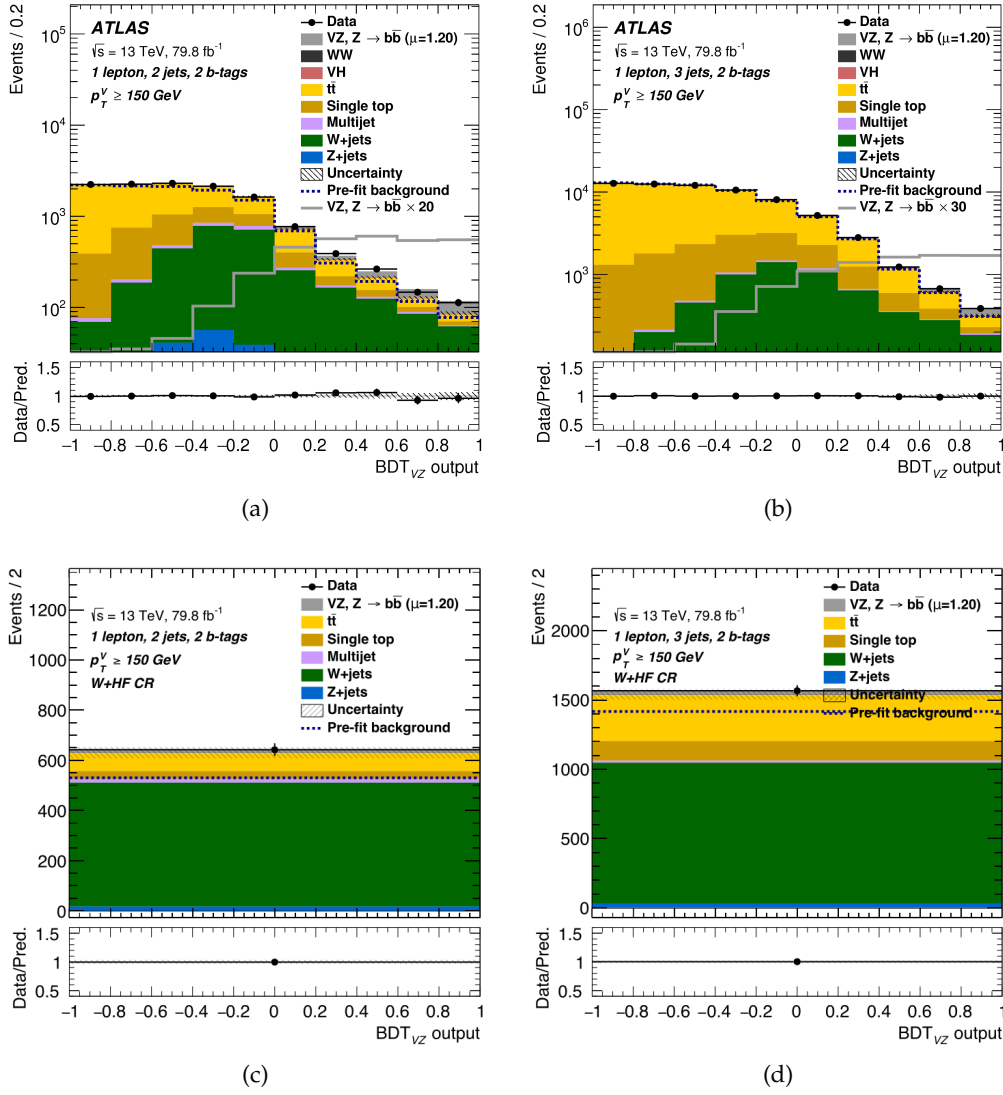


FIGURE 7.27 – The  $BDT_{VZ}$  output post-fit distributions in the 1-lepton channel for 2 b-tag events in 2-jet (a)-(c) and 3-jet (b)-(d) regions. The background contributions after the global likelihood fit are shown as filled histograms. The  $VZ$  diboson signal is shown as a filled histogram on top of the fitted backgrounds normalised to the signal yield extracted from data ( $\mu = 1.20$ ), and unstacked as an open histogram, scaled by the factor indicated in the legend. The dashed histogram shows the total pre-fit background. The size of the combined statistical and systematic uncertainty for the sum of the fitted signal and background is indicated by the hatched band. The ratio of the data to the sum of the fitted signal and background is shown in the lower panel.



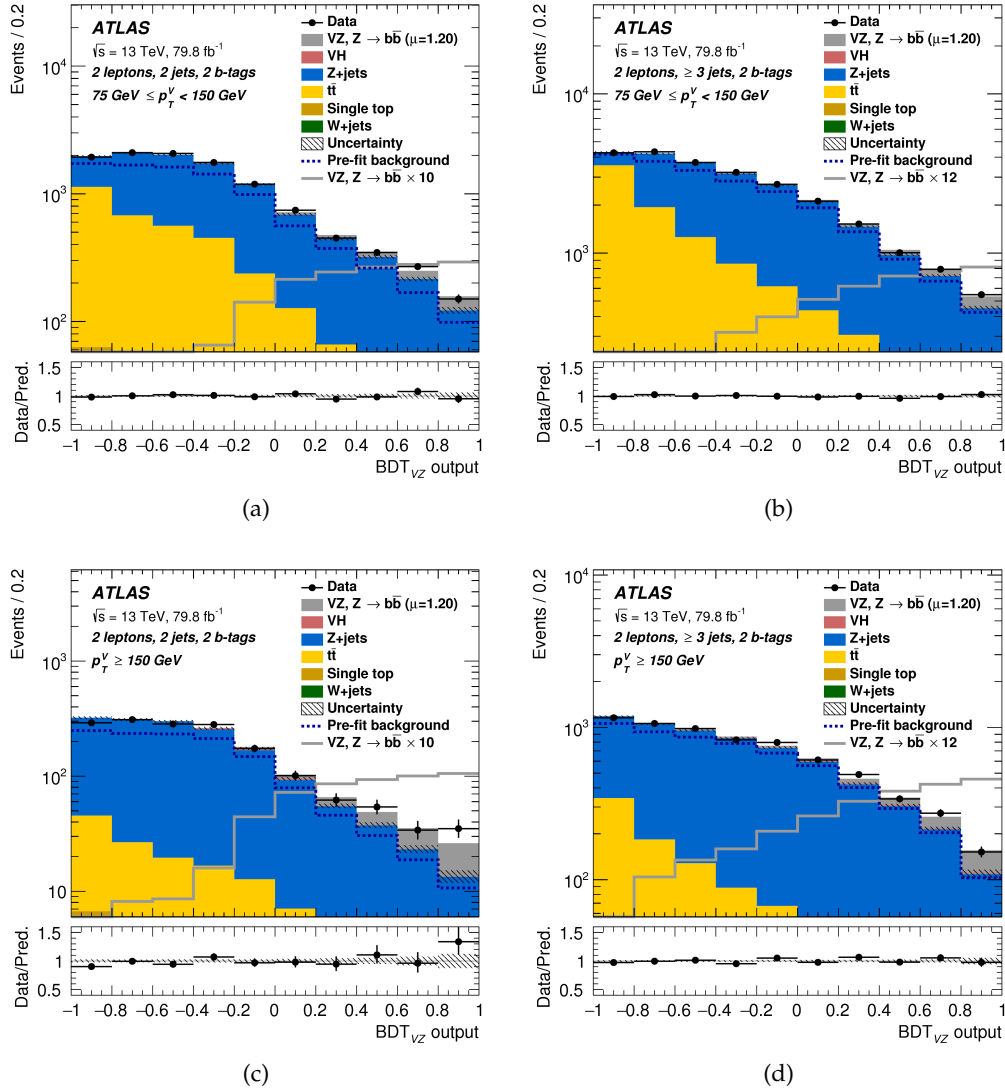


FIGURE 7.28 – The  $BDT_{VZ}$  output post-fit distributions in the 1-lepton channel for 2 b-tag events in 2-jet (a)-(c) and 3-jet (b)-(d) regions, with (a)-(b) the high  $p_T^V$  region and (c)-(d) the medium  $p_T^V$  region. The background contributions after the global likelihood fit are shown as filled histograms. The  $VZ$  diboson signal is shown as a filled histogram on top of the fitted backgrounds normalised to the signal yield extracted from data ( $\mu = 1.20$ ), and unstacked as an open histogram, scaled by the factor indicated in the legend. The dashed histogram shows the total pre-fit background. The size of the combined statistical and systematic uncertainty for the sum of the fitted signal and background is indicated by the hatched band. The ratio of the data to the sum of the fitted signal and background is shown in the lower panel.

### 7.8.3 Signal strength

The process has been observed with a  $\sim 10\sigma$  significance. The resulting best-fit value is:

$$\mu = 1.20^{+0.08}_{-0.08}(\text{stat.})^{+0.19}_{-0.16}(\text{syst.}), \quad (7.36)$$

in good agreement with the SM expectation within uncertainties. As in the VH analysis, the robustness of the fit has been probed looking at the compatibility among the three channels with a simultaneous fit with multiple  $\mu$  parameters. The results are shown in Figure 7.29(a). The compatibility between the signal strengths is 64%.

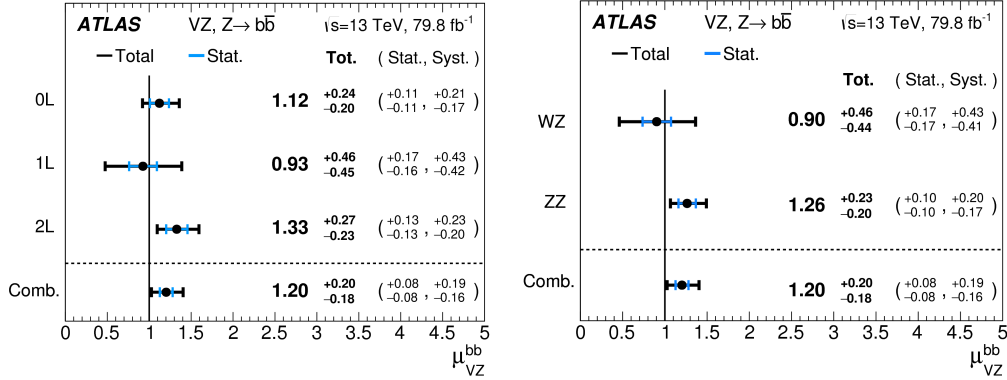


FIGURE 7.29 – (a) The fitted values of the VZ signal strength  $\mu_{VZ}$  for the 0-, 1- and 2-lepton channels and their combination. The individual  $\mu_{VZ}$  values for the lepton channels are obtained from a simultaneous fit with the signal strengths for each of the lepton channels floating independently. (b) The fitted values of the VZ signal strength  $\mu_{VZ}$  for the WZ and ZZ processes and their combination. The individual  $\mu_{VZ}$  values for the (W/Z)Z processes are obtained from a simultaneous fit with the signal strengths for each of the WZ and ZZ processes floating independently.

The higher uncertainty in the 1-lepton channel, and thus its lower significance, is due to the high contamination of  $W + HF$  background. The compatibility between the WZ and ZZ processes has been probed with a multiple  $\mu$  fit and presented in Figure 7.29(b). The WZ signal strength is constrained only by the 1-lepton channel, thus its uncertainty is higher than the ZZ process. The probability of compatibility of the individual signal strengths is 47%.

An alternative way to visualize the diboson signal is to compare data and simulation in bins of  $\log_{10}(S/B)$ . This is obtained analogously to the VH analysis, by combining the final discriminant  $BDT_{VZ}$  in all regions into bins of  $\log_{10}(S/B)$ , with S the fitted signal and B the fitted background yields, rescaling the SM cross section by the extracted SM value ( $\mu = 1.20$ ). The results are shown in Figure 7.30.

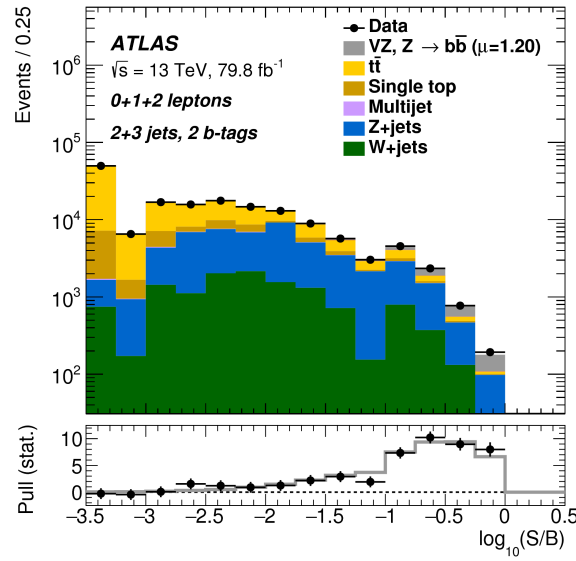


FIGURE 7.30 – Event yields as a function of  $\log_{10}(S/B)$  for data, background and a diboson signal (VZ). Final-discriminant bins in all regions are combined into bins of  $\log_{10}(S/B)$ , with S being the fitted signal and B the fitted background yields. The diboson signal contribution is shown after rescaling the SM cross section according to the value of the signal strength extracted from data ( $\mu = 1.20$ ). In the lower panel, the pull of the data with respect to the background (the statistical significance of the difference between data and fitted background) is shown with statistical uncertainties only. The full line indicates the pull expected from the sum of the fitted signal and background with respect to the fitted background.

## 7.9 Combinations

The results presented in Section 7.7 are combined with Run-1 results [208] to increase the expected significance of the measurement. In addition, two combinations with similar analyses targeting the same production or the same decay mode have been performed separately. These two combinations have been instrumental to have a first significant measurement of the VH production mode and of the  $H \rightarrow b\bar{b}$  decay mode. More details about these combinations are given in the next Sections.

### 7.9.1 Combination with the Run-1 $VH, H \rightarrow b\bar{b}$ search

The Run-1  $VH, H \rightarrow b\bar{b}$  analysis [208] has been performed with  $4.7 \text{ fb}^{-1}$  of  $pp$  collisions at  $\sqrt{s} = 7 \text{ TeV}$  and  $20.3 \text{ fb}^{-1}$  at  $\sqrt{s} = 8 \text{ GeV}$ . The observed signal strength is  $\mu = 0.52 \pm 0.32(\text{stat.})^{+0.24}_{-0.24}(\text{syst.})$ , corresponding to an observed (expected) significance of 1.4 (2.6) standard deviations. The measurement has been combined with the  $79.8 \text{ fb}^{-1}$  analysis for a total dataset of  $\sim 105 \text{ fb}^{-1}$ .

Significant differences are observed in the way systematic uncertainties were computed in Run-1 and Run-2, therefore the choice in most cases was not to correlate the systematic uncertainties across the two analyses. The impact of correlating experimental and modelling nuisance parameters was checked and found to have a negligible impact on the fit results, validating this choice. Among the experimental systematic uncertainties, only the b-jet energy scales were found to have a non-negligible impact on the combined fit result when correlated. Regarding the signal, only the theory-related uncertainties (QCD, PDF, branching ratio, and  $p_T^V$ -dependent NLO EW corrections) have been correlated between the two periods. The value of

the signal strength is:

$$\mu_{VH}^{bb} = 0.98^{+0.22}_{-0.21} = 0.98 \pm 0.14(\text{stat.})^{+0.17}_{-0.16}(\text{syst.}). \quad (7.37)$$

The observed significance is  $4.9\sigma$  (corresponding to a  $p_0$  value of  $5.5 \cdot 10^{-7}$ ) compared to an expected significance of  $5.1\sigma$ . Furthermore, a fit with multiple  $\mu$  floated independently for the WH and ZH production processes has been performed and the results are shown in Figure 7.31. The compatibility between the signal strengths for the WH and ZH production processes is 72%.

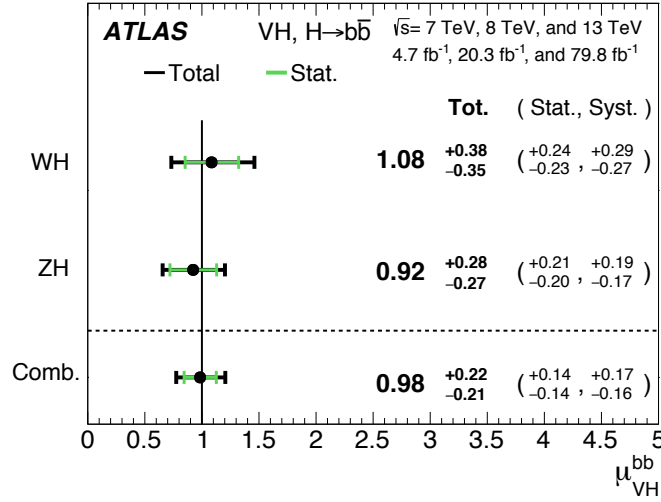


FIGURE 7.31 – The fitted values of the Higgs boson signal strength  $\mu_{VH}^{bb}$  for  $m_H = 125$  GeV for the WH and ZH processes and their combination, using the 7 TeV, 8 TeV and 13 TeV data. The individual  $\mu_{VH}^{bb}$  values for the (W/Z)H processes are obtained from a simultaneous fit with the signal strengths for each of the WH and ZH processes floating independently [205].

### 7.9.2 VH combination

The Run-2  $VH, H \rightarrow b\bar{b}$  results have been combined with the following other analyses sensitive to the  $VH$  production mode:

**$H \rightarrow \gamma\gamma$**  : The analysis uses  $79.8 \text{ fb}^{-1}$  of data at  $\sqrt{s} = 13 \text{ TeV}$ , more details about the Run-2 strategy can be found in Ref. [226]. Several categories are defined, targeting at different decay processes: five categories for the leptonic decays of the vector boson, two categories for the hadronic decays of the vector boson and separate categories designed to constrain the contamination from the  $t\bar{t}H$ , VBF, and ggF production modes. The signal yield is extracted in each category using a fit to the diphoton invariant mass distribution in the range 105–160 GeV.

**$H \rightarrow 4\ell$**  : This analysis targets the  $VH$  production in the four-lepton final state, with  $\ell = e$  or  $\mu$ . The details can be found in Ref. [227] for an analysis with  $79.8 \text{ fb}^{-1}$  of Run-2 data. In total the analysis contains three  $VH$  categories targeting: the hadronic decays of the vector boson, the charged leptonic decays of the vector boson and the decays of the vector boson containing one or more neutrinos.

Assuming the relative branching fractions of the three decay modes as predicted by the SM, the observed significance for the VH production mode is 5.3 standard deviations, with an expected significance of 4.8 standard deviations. The fitted value of the VH signal strength is:

$$\mu_{VH} = 1.13^{+0.24}_{-0.23} = 1.13 \pm 0.15(\text{stat.})^{+0.18}_{-0.17}(\text{syst.}). \quad (7.38)$$

The robustness of the fit has been cross-checked with a fit with the signal strengths of each decay mode floating independently. The results of this multiple  $\mu_{VH}$  fit are shown in Figure 7.32. A 96% level of compatibility among the signal strengths have been found for this fit.

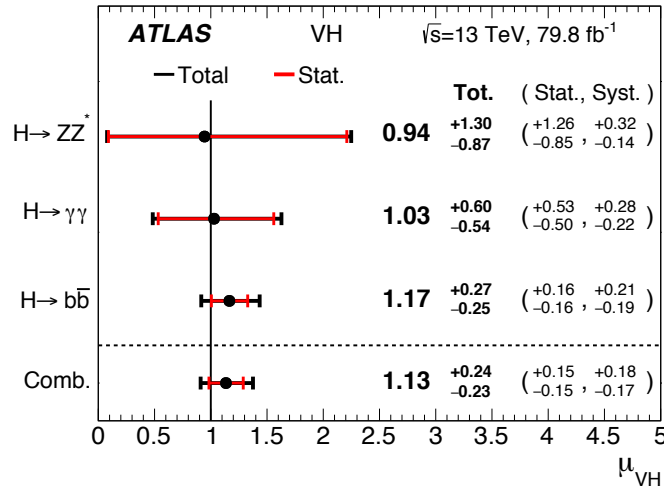


FIGURE 7.32 – The fitted values of the Higgs boson signal strength  $\mu_{VH}$  for  $m_H = 125$  GeV separately for the  $H \rightarrow b\bar{b}$ ,  $H \rightarrow \gamma\gamma$  and  $H \rightarrow ZZ^* \rightarrow 4\ell$  decay modes, along with their combination. The individual  $\mu_{VH}$  values for the different decay modes are obtained from a simultaneous fit with the signal strengths for each of the processes floating independently [205].

### 7.9.3 $H \rightarrow b\bar{b}$ combination

A third combination is performed combining a total of six Run-1 and Run-2 analyses looking at the  $H \rightarrow b\bar{b}$  decay mode:

**VH  $\rightarrow b\bar{b}$  (Run-1 and Run-2):** The Run-2 analysis is the one described in this Chapter, while the  $VH \rightarrow b\bar{b}$  Run-1 analysis has been briefly introduced in Section 7.9.1 and more details can be found in Ref. [208].

**VBF (Run-1 and Run-2):** these analyses target the Vector Boson Fusion Higgs production mode, selecting the  $H \rightarrow b\bar{b}$  decay channel. The Run-1 analysis [228] is performed with  $20.2 \text{ fb}^{-1}$  of data at  $\sqrt{s} = 8 \text{ TeV}$  and the presence of dedicated gluon fusion categories in the selection makes it sensitive to the  $H \rightarrow b\bar{b}$  produced by VBF and gluon gluon fusion. The observed signal strength for the  $H \rightarrow b\bar{b}$  decay is  $\mu = -0.8 \pm 1.3(\text{stat.})^{+1.8}_{-1.9}(\text{syst.})$ . The Run-2 analysis [229] relies on the same strategy, repeated for  $30.6 \text{ fb}^{-1}$  of data at  $\sqrt{s} = 13 \text{ GeV}$ . The observed signal strength is  $\mu = 2.5 \pm 1.3(\text{stat.})^{+0.4}_{-0.4}(\text{syst.})$ , with an observed (expected) significance of 1.9 (0.8) standard deviations.

**$t\bar{t}H$  (Run-1 and Run-2):** these analyses are primarily sensitive to the  $t\bar{t}H(\rightarrow b\bar{b})$  channel, but they also have a smaller contribution from the  $tH(\rightarrow b\bar{b})$  process. Both Run-1 and Run-2 analyses have been performed only in the lepton+jets and dileptonic channels. The Run-1 analysis [230] [231] has been performed on  $20.2 \text{ fb}^{-1}$  of data at  $\sqrt{s} = 8 \text{ GeV}$ , leading to a measured signal strength of  $\mu = 1.5 \pm 0.7(\text{stat.}) \pm 0.8(\text{syst.})$ , with an observed (expected) signal significance of 1.4 (1.1) standard deviations. The Run-2 result [232] was obtained with  $36.1 \text{ fb}^{-1}$  of  $\sqrt{s} = 13 \text{ GeV}$  data, leading to an observed signal strength of  $\mu = 0.84 \pm 0.29(\text{stat.})^{+0.57}_{-0.54}(\text{syst.})$ , with a  $1.4\sigma$  level of significance, for a  $1.6\sigma$  expected significance.

The scheme used to correlate the systematic uncertainties across the analyses was optimised case by case, correlating only when the impact of such correlation was clearly understood and the variation on the fit was observed to be non-negligible. The only NP correlated across all the six analyses is the  $H \rightarrow b\bar{b}$  branching ratio. Furthermore, few other parameters have been correlated: the three Run-1 analyses have been correlated only for branching ratio and luminosity uncertainties, following the studies presented in Ref. [9]. Across the Run-2 analyses,  $t\bar{t}H(\rightarrow b\bar{b})$  and VBF were correlated for the luminosity, branching ratio, JES, JVT, JER and pile-up, as described in Ref. [64], while for the  $t\bar{t}H(\rightarrow b\bar{b})$  dilepton and  $t\bar{t}H(\rightarrow b\bar{b})$  lepton+jets all NPs have been correlated following the scheme of the  $t\bar{t}H$  observation paper in Ref. [10]. The correlations between Run-1 and Run-2 analyses tend to follow the scheme described in Section 7.9.1, correlating only signal theory and b-jet energy scales.

The cross-sections of the production modes are constrained to their SM prediction to have a direct measurement of the  $\mu_{H \rightarrow b\bar{b}}$ , defined as the ratio of the observed  $BR(H \rightarrow b\bar{b})$  over the SM prediction. The measured value is:

$$\mu_{H \rightarrow b\bar{b}} = 1.01 \pm 0.2 = 1.01 \pm 0.12(\text{stat.})^{+0.16}_{-0.15}(\text{syst.}) \quad (7.39)$$

The observed (expected) significance of the measurement is 5.4 (5.5) standard deviations, providing direct observation of the Higgs boson decay into b-quarks. Figure 7.33 shows the signal strengths obtained from a fit with multiple  $\mu$ , fitted simultaneously for the three production modes. The compatibility among the individual signal strengths is 83%.

## 7.10 Summary

This Chapter focused on the results of the Run-2 analysis with  $80 \text{ fb}^{-1}$  of data collected at  $\sqrt{s} = 13 \text{ TeV}$  between 2015 and 2017. The analysis makes use of Boosted Decision Trees combining different kinematic variables, to increase the overall sensitivity. The final results are obtained with a simultaneous binned likelihood fit to the BDT output of all the analysis regions combined. The best fit value of the signal strength ( $\sigma \cdot BR / \sigma_{SM} \cdot BR_{SM}$ ) of the  $VH \rightarrow b\bar{b}$  process is:

$$\mu = 1.16^{+0.16}_{-0.16}(\text{stat.})^{+0.21}_{-0.19}(\text{syst.}).$$

The  $VH \rightarrow b\bar{b}$  process is measured with an observed significance of  $4.9\sigma$  and an expected significance of  $4.3\sigma$ . Good agreement between the three analysis channels and between the WH and ZH production modes is observed, providing a robust validation of the fit implementation.

The results have been validated also with two independent cross-checks: the dijet analysis and the diboson analysis. In both cases the results are compatible with

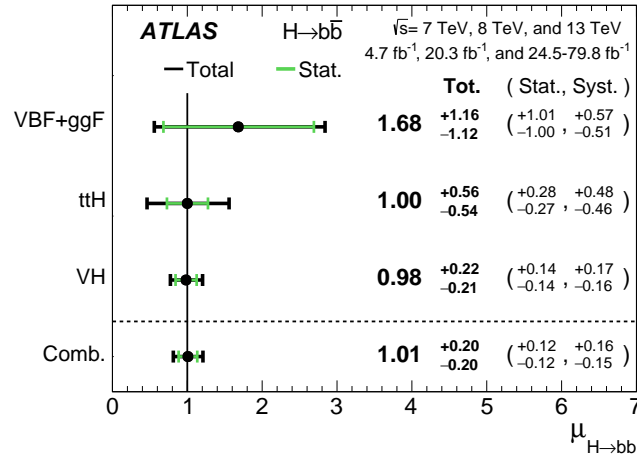


FIGURE 7.33 – The fitted values of the Higgs boson signal strength  $\mu_{H \rightarrow b\bar{b}}$  for  $m_H = 125$  GeV separately for the VH, ttH and VBF+ggF analyses along with their combination, using the 7 TeV, 8 TeV and 13 TeV data. The individual  $\mu_{H \rightarrow b\bar{b}}$  values for the different production modes are obtained from a simultaneous fit with the signal strengths for each of the processes floating independently [205].

the SM expectations, giving an independent validation of the fitting procedure and the BDT performance.

Three combinations have been carried out to increase the overall sensitivity of the measurement. The first combination is with Run-1 ATLAS data. A signal strength of  $\mu_{VH}^{bb} = 0.98^{+0.22}_{-0.21} = 0.98 \pm 0.14(\text{stat.})^{+0.17}_{-0.16}(\text{syst.})$  is measured, for a total observed (expected) significance of 4.9 (5.1) standard deviations.

The second combination has been carried out with other ATLAS analyses targeting the VH production mode, such as  $VH, H \rightarrow \gamma\gamma$  and  $VH, H \rightarrow 4\ell$ . An overall signal strength of  $\mu_{VH} = 1.13^{+0.24}_{-0.23} = 1.13 \pm 0.15(\text{stat.})^{+0.18}_{-0.17}(\text{syst.})$  for the VH production cross section is measured, obtained by fixing the branching ratios to their SM values. The measurement has a significance of 5.3 standard deviations - compared to an expectation of 4.8 standard deviations - thus above the  $5\sigma$  threshold to claim the observation of the VH production mode.

The last combination has been performed across ATLAS analyses sensitive to the  $H \rightarrow b\bar{b}$  decay (i.e.  $VH, H \rightarrow b\bar{b}$ ,  $ttH, H \rightarrow b\bar{b}$  and  $VBF, H \rightarrow b\bar{b}$ ). The signal strength of the  $H \rightarrow b\bar{b}$  decay, obtained fixing the production modes to their SM predictions, is  $\mu_{H \rightarrow b\bar{b}} = 1.01 \pm 0.2 = 1.01 \pm 0.12(\text{stat.})^{+0.16}_{-0.15}(\text{syst.})$ , with an expected (observed) significance of 5.4 (5.5) standard deviations. As for the VH production mode, the significance of the  $H \rightarrow b\bar{b}$  decay measurement is above the threshold to claim the observation, with excellent agreement with the SM predictions. This means that the results are consistent with the predicted value of the Yukawa coupling to bottom quarks in the Standard Model. In particular, this combination is the first measurement to successfully probe the Yukawa mechanism for down-type quarks with a sufficient level of precision to exclude the background-only hypothesis.



## 8 | Further improvements towards the full Run-2 analysis

The results described in the previous Chapter represent a remarkable achievement in our understanding of the Higgs boson properties. However, this is just a small step if compared to the final goal of a complete understanding of the Higgs sector in the Standard Model. In fact, from what was described in Chapter 2, there are motivations to believe that the SM might be just the low energy realisation of a more fundamental theory. Concerning the Higgs sector, these hints of new physics could be seen, for example, as anomalous behaviours of the Higgs kinematic distributions of the different production and decay modes, or as deviations from the expected values of the reaction rates.

Such tensions with the SM predictions could be revealed by increasing the precision of the analysis. In fact, if the uncertainties are reduced to a fraction of the anomaly, then the disagreement between observed and expected results can reach several standard deviations and make the non-SM behaviour significant. Up to now, no significant deviations from the SM predictions have been observed in the Higgs sector, but the  $H \rightarrow b\bar{b}$  channel, thanks to its high branching ratio, could represent an excellent candidate to search for such anomalies. The first attempts are reported in Ref. [233], where the  $VH, H \rightarrow b\bar{b}$  production cross section has been measured as a function of the vector-boson transverse momentum.

In the future, the  $VH, H \rightarrow b\bar{b}$  analysis will evolve from a single inclusive signal search into a precision differential measurement. The statistics of the dataset will be improved by adding the  $58.5 \text{ fb}^{-1}$  of data delivered by LHC in 2018 - which were not included in the analysis presented in the previous Chapter - for a total of  $\sim 140 \text{ fb}^{-1}$ . Several improvements in different aspects of the analysis will be implemented to increase the sensitivity and reduce the impact of systematic uncertainties. Among them, non-negligible improvements can be obtained by optimizing the use of the b-tagging information. The first part of the Chapter will summarize the latest developments to solve the non-closure problems of the statistical tagging, highlighting the improvements given by its extended use in the analysis, while the second part will focus on the inclusion of the b-tagging information in the final BDT discriminant to enhance the overall sensitivity of the analysis.

### 8.1 Statistical tagging in $VH, H \rightarrow b\bar{b}$

The statistical tagging - as described in Section 7.6.2 - represents a powerful tool to reduce the uncertainty on the number of simulated events. However, due to the

non-closure problems highlighted in the previous Chapter, it has always been used only to estimate the expected yields from sub-dominant processes. Dedicated studies showed that these effects are mainly related to the quality of the efficiency maps. In particular, the non closure was found to be related to the combination of multiple effects:

- The event selection used to derive the maps, summarized in Section 5.4, was not the same as the one used in the analysis, especially in terms of jet isolation requirements ( $\Delta R > 0.8$ ).
- The maps have been derived on  $t\bar{t}$  samples, whilst they have been applied also to  $V + \text{jet}$  samples.
- The maps have been derived without the event level MC corrections (pile-up reweighting, SFs etc..).
- The binning chosen for the official maps was sometimes too coarse, especially in  $\eta$ , to resolve significant variations within bins.

These effects have been solved producing new dedicated efficiency maps optimised for the  $VH, H \rightarrow b\bar{b}$  analysis phase space. In particular, to reduce as much as possible the aforementioned effects, and suppress all the residual non closures coming from differences in the phase space and in the event topology (for example  $\Delta R(\text{jet}, \text{jet})$ ), the new efficiency maps have been derived using exactly the same event selection of the MVA analysis, summarized in Table 7.5, apart for the requirement on the number of jets. Furthermore, the sample dependence discussed in the second bullet has been solved deriving the  $V+\text{jet}$  maps directly on the same  $V+\text{jet}$  samples used in the analysis.

The maps have been derived on the full simulated sample of events available, corresponding to the 2015-2018 data taking period<sup>1</sup>, and for the 1-lepton and 2-lepton channels. The 0-lepton channel was not included because not all 2018 MC samples were ready at that time, and the statistics was already sufficient to keep the statistical error on the efficiencies between  $10^{-3}$  for b-jets and  $10^{-5}$  for light-jets.

The new efficiency maps have been derived separately for the two nominal generators involved in the analysis: POWHEG +PYTHIA 8 using  $t\bar{t}$  events and SHERPA 2.2.1 using  $V+\text{jet}$  events. In this second case, the  $V+\text{jet}$  sample is intended to be the sum of  $W+\text{jet}$  in the 1-lepton channel and  $Z+\text{jet}$  in the 2-lepton channel. The maps have been derived for the nominal  $VH, H \rightarrow b\bar{b}$  b-tagging working point (70%). Furthermore, the binning effects have been reduced (in some cases up to 30%) optimising the  $\eta - p_T$  granularity. In particular, for both generators the  $\eta$  granularity has been increased by 50% (apart for light- and  $\tau$ -jets at high  $\eta$ , due to the lack of statistics). In  $p_T$ , the granularity has been adapted separately for each flavour and generator, in order to be more granular in the transition regions - regions of fast changes in the efficiency values - with 5 GeV steps, and less granular when allowed, to reduce the uncertainty on the final efficiency. Furthermore, the fine granularity of the maps has been extended at least to 250-300 GeV in  $p_T$ .

---

1. Each reweighted by its specific pile-up profile and with all the simulation correction applied (except the b-tagging corrections).

### 8.1.1 Efficiency maps

The four efficiency maps produced from POWHEG +PYTHIA 8  $t\bar{t}$  events are shown in Figure 8.1, while the efficiency maps produced using SHERPA 2.2.1  $V$ +jet samples are presented in Figure 8.2.

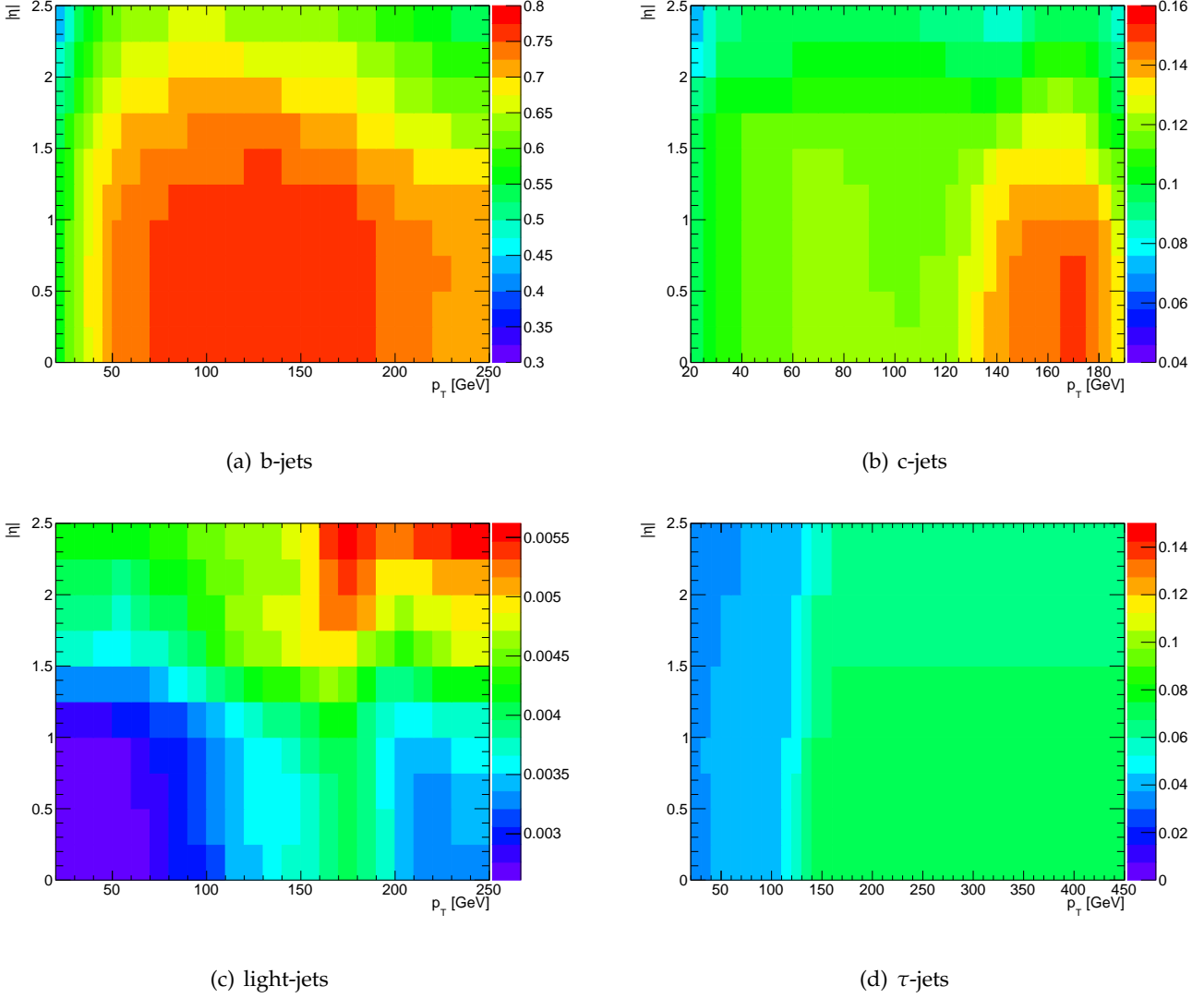


FIGURE 8.1 – Efficiency maps for b-, c-, light- and  $\tau$ - jets as a function of jet  $p_T$  and  $|\eta|$  for MV2c10 at 70% working point computed using  $t\bar{t}$  events generated with POWHEG +PYTHIA 8 and passing the full  $VH, H \rightarrow b\bar{b}$  selection (but the 2 b-tagged jets requirements).

In addition, a total of 48 control maps was produced to cross-check the whole procedure and justify the merging. One map for each combination of channels (1-lepton, 2-lepton), flavours (b,c,light, $\tau$ ), data taking periods (2015-16, 2017, 2018) and generators (POWHEG +PYTHIA 8 and SHERPA 2.2.1).

Compatibility checks have been performed across all these control maps, to verify the good closure across the different channels and periods. These checks were performed computing the ratio of different combinations of control maps, as shown in Figure 8.3 and 8.4. The Figures show the compatibility between the final combined maps presented above and the efficiency maps obtained using the 2015-2016 and the

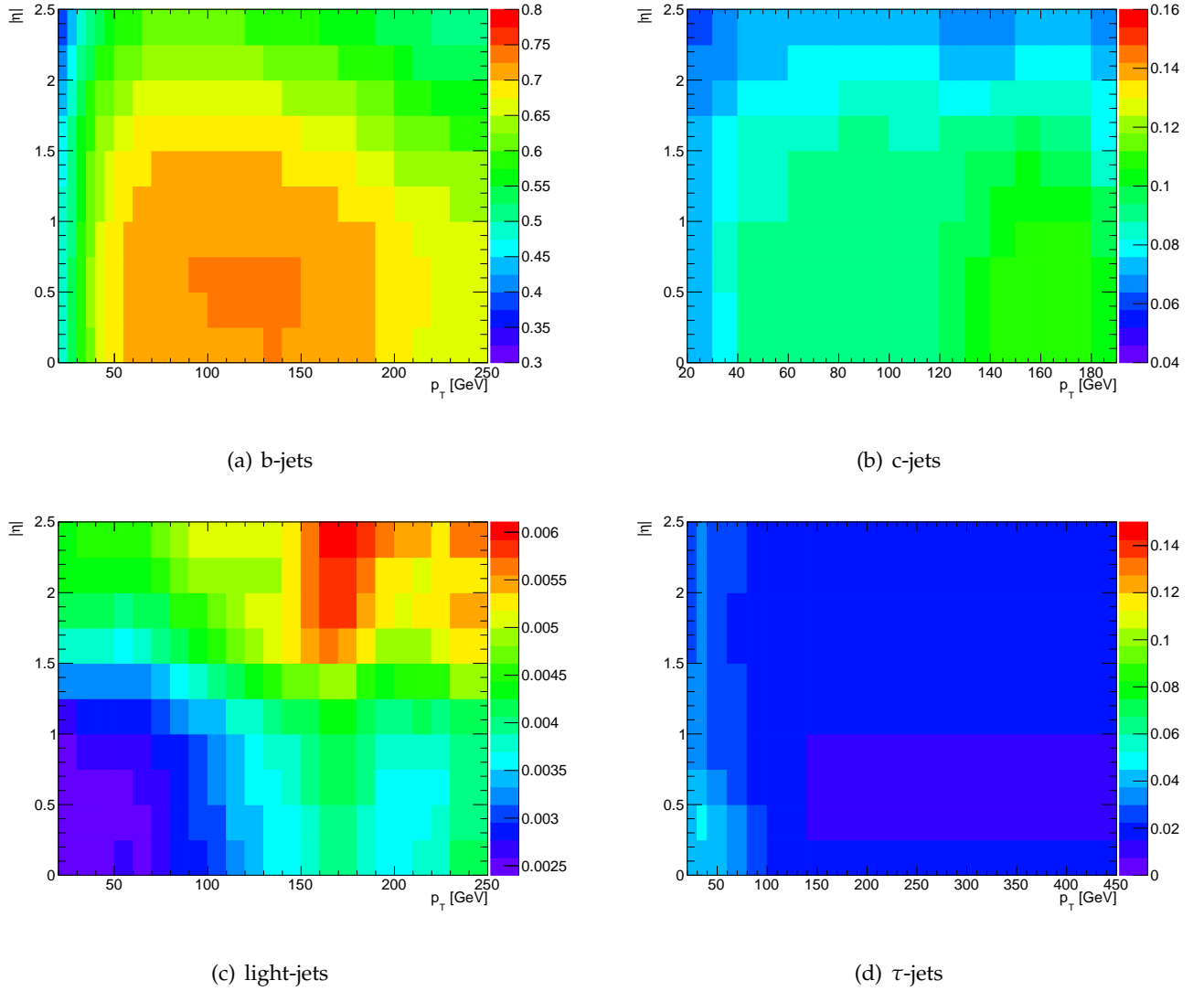


FIGURE 8.2 – Efficiency maps for b-, c-, light- and  $\tau$ - jets as a function of jet  $p_T$  and  $|\eta|$  for MV2c10 at 70% working point computed using W+jet events in 1-lepton and Z+jet events in 2-lepton, generated with Sherpa2.2.1 and passing the full  $VH, H \rightarrow b\bar{b}$  selection.

2018 datasets separately, for both POWHEG + PYTHIA 8 and SHERPA 2.2.1. Additional checks on the compatibility between 1-lepton and 2-lepton channels are presented in Appendix B. The ratios are very close to 1, showing overall good compatibility across data taking periods and channels, with maximum variations for  $b$ - and  $c$ -jets of the order of  $\sim 3\%$  (the larger variations at high  $\eta$  visible in the  $b$ - and  $c$ -jet ratio maps are in bins with very low statistics, far from the bulk of the distributions). Light- and  $\tau$ -jets suffer from higher statistical fluctuations and therefore the maximum variations when considering separate data taking periods are slightly higher ( $\mathcal{O}(10\%)$ ). In any case, by construction, these incompatibilities average out when considering the full 2015-2018 dataset.

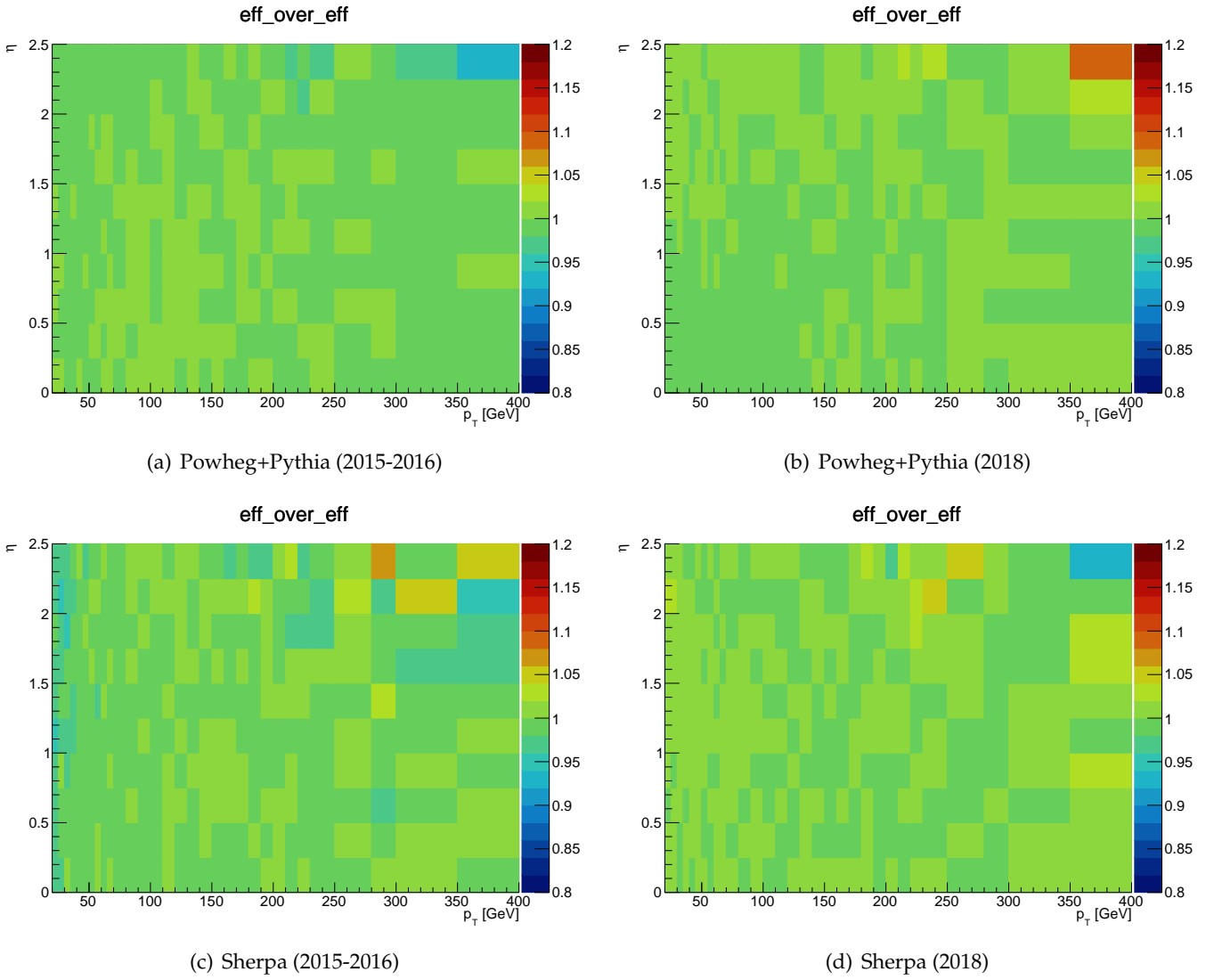


FIGURE 8.3 – Ratio between the combined map and the control maps computed using only (a)-(c) the 2015-2016 datasets and (b)-(d) the 2018 dataset for  $b$ -jets. The (a)-(b) maps refer to POWHEG + PYTHIA while (c)-(d) maps are for SHERPA.

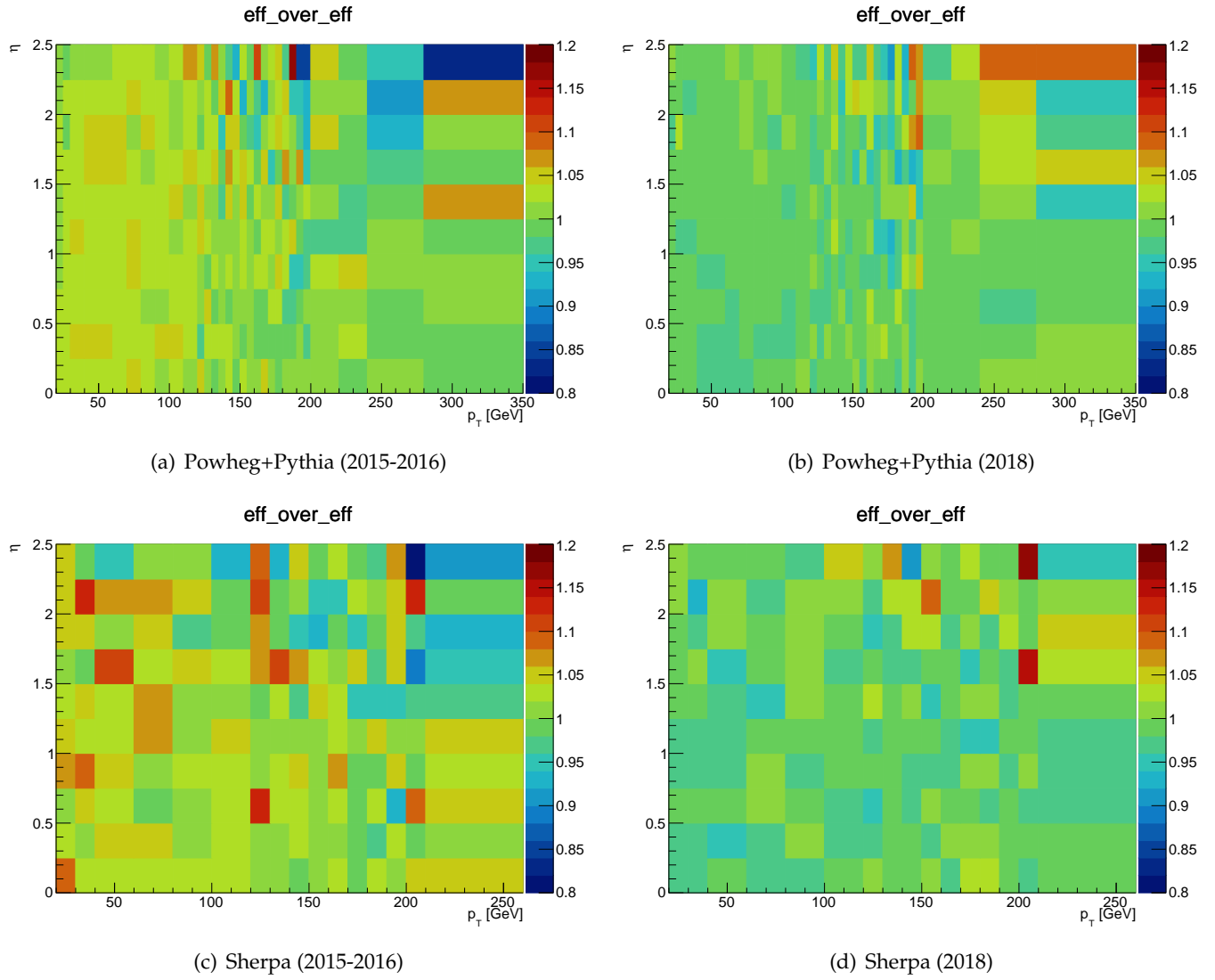


FIGURE 8.4 – Ratio between the combined map and the control maps computed using only (a)-(c) the 2015-2016 datasets and (b)-(d) the 2018 dataset for  $c$ -jets. The (a)-(b) maps refer to POWHEG + PYTHIA while the (c)-(d) maps are for SHERPA.

### 8.1.2 Results

The validation of these efficiency maps has been performed using 2017 samples only since the compatibility across the data-taking periods has been validated using the map-ratio methods described in the previous Section. The closure test has been done comparing the main kinematic variables of  $t\bar{t}$  and V+jet samples processed using truth tagging and direct tagging. The flavour tagging scale factors and their uncertainties remained unchanged since they have been calculated using direct tagging, which is not impacted by the change of efficiency maps. In any case, the validation has been done without the flavour tagging scale factors, to isolate the non closure effects of the efficiency maps from those potentially introduced by the correction factors.

Some examples of such closure tests are presented in Figure 8.5, for different kinematic variables of  $t\bar{t}$  samples passing the 1-lepton channel selection. The  $t\bar{t}$  events have been studied as  $t\bar{t}(b\bar{b})$ ,  $t\bar{t}(bc)$  or  $t\bar{t}(bl)$  based on the true flavour of the selected jets and studied separately to probe the behaviour of b-, c- and light-jets. The coarse binning effects of the official maps, discussed in the previous Section, are clearly visible in Figure 8.5(b), where the non closure at high  $\eta$  is the result of the unique large bin between 1.5 and 2.5 of Figure 5.18, which averages out the gradual changes in the efficiency. This effect is much reduced for the new finely binned efficiency maps thanks to the increased granularity. A residual topological effect in  $\Delta R(\text{jet}, \text{jet})$  - not completely covered by the  $(\eta - p_T)$  maps - is still visible, even if it has been partially corrected by the use of the same isolation requirement as in the analysis. In general, both  $t\bar{t}(bc)$  and  $t\bar{t}(bl)$  events show good closure, at least within the statistical uncertainties of the direct tagging.

The validation of the new SHERPA efficiency maps has been done with W+jet samples in the 1-lepton channel. The results are shown in Figure 8.6. A residual non-closure for  $W+b\bar{b}$  is visible, but well under control as explained in the next Section. The other two main W+jet processes,  $W+bc$  and  $W+bl$ , show good closure both in shapes and yields.

### 8.1.3 Hybrid tagging and impact on the analysis

To summarize, the use of the new customized maps considerably increased the level of closure between direct and truth tagged samples. Excellent agreement in both shapes and yields was found for  $t\bar{t}(bc)$  and  $W+bl$  events. A sufficient level of closure, meaning that the shape variations remain within the statistical uncertainty of the direct tagged samples was found for  $t\bar{t}(bl)$ ,  $W+bc$ ,  $W+cl$ ,  $W+ll$  and  $W+cc$ .

However, the residual non closures observed for the main backgrounds -  $W+b\bar{b}$  and  $t\bar{t}(b\bar{b})$  - do not allow the  $VH, H \rightarrow b\bar{b}$  analysis to switch to a full truth tagging approach. So, as discussed in Chapter 7, the best compromise in this case is to adopt a *hybrid* approach at *event* level. As explained in Section 7.6.3, the hybrid approach consists in applying direct tagging to b-jets and truth tagging to non-b jets, separately for each event. Thus, the  $b\bar{b}$  samples will be direct tagged, while the  $bc$  and  $bl$  ones will profit from the truth tagging of the non-b jets in the event to increase the statistics in the signal regions. Some examples comparing direct, truth and hybrid tagging with the new customized efficiency maps in 1-lepton are shown in Figure 8.7.

The validation checks on the yields are presented in Table 8.1 for the main V+jet samples of each channel. There is an overall good closure between the direct tagged and the hybrid tagged samples in all channels, with discrepancies of the order of  $\mathcal{O}(3\%)$  for the *inclusive* V+jet. The non closure in the 1-lepton channel for  $W+bc$



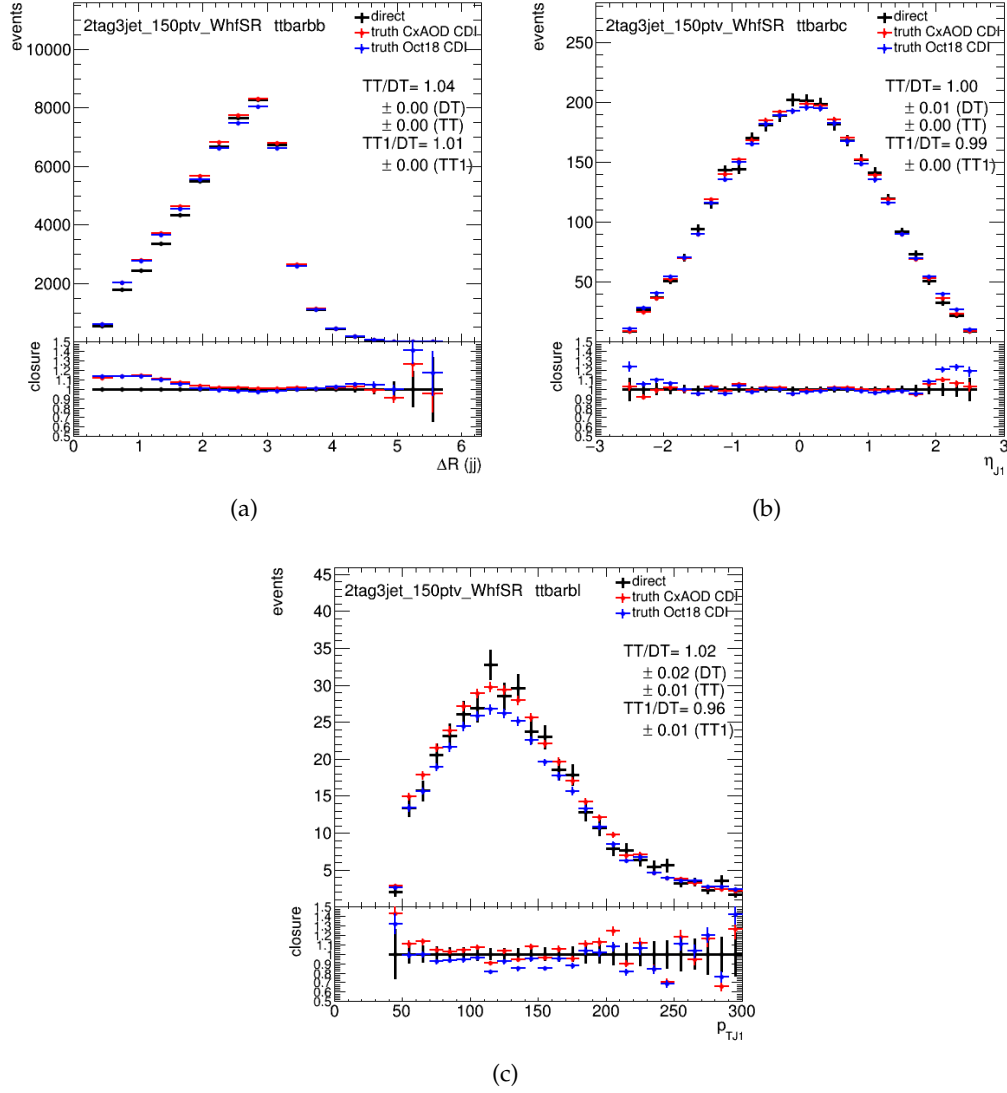


FIGURE 8.5 – (a)  $\Delta R(\text{jet}, \text{jet})$  distribution in  $t\bar{t}(b\bar{b})$  events, (b)  $\eta$  distribution in  $t\bar{t}(b\bar{c})$  events and (c)  $p_T$  distribution of the leading jet in  $t\bar{t}(b\bar{l})$  events, using (black) DT: direct tagging and (red) TT: truth tagging with the new customized maps, compared to (blue) TT1: the truth tagging computed with the official efficiency maps. The numbers on the right represent the ratio of the yields with respect to direct tagging.

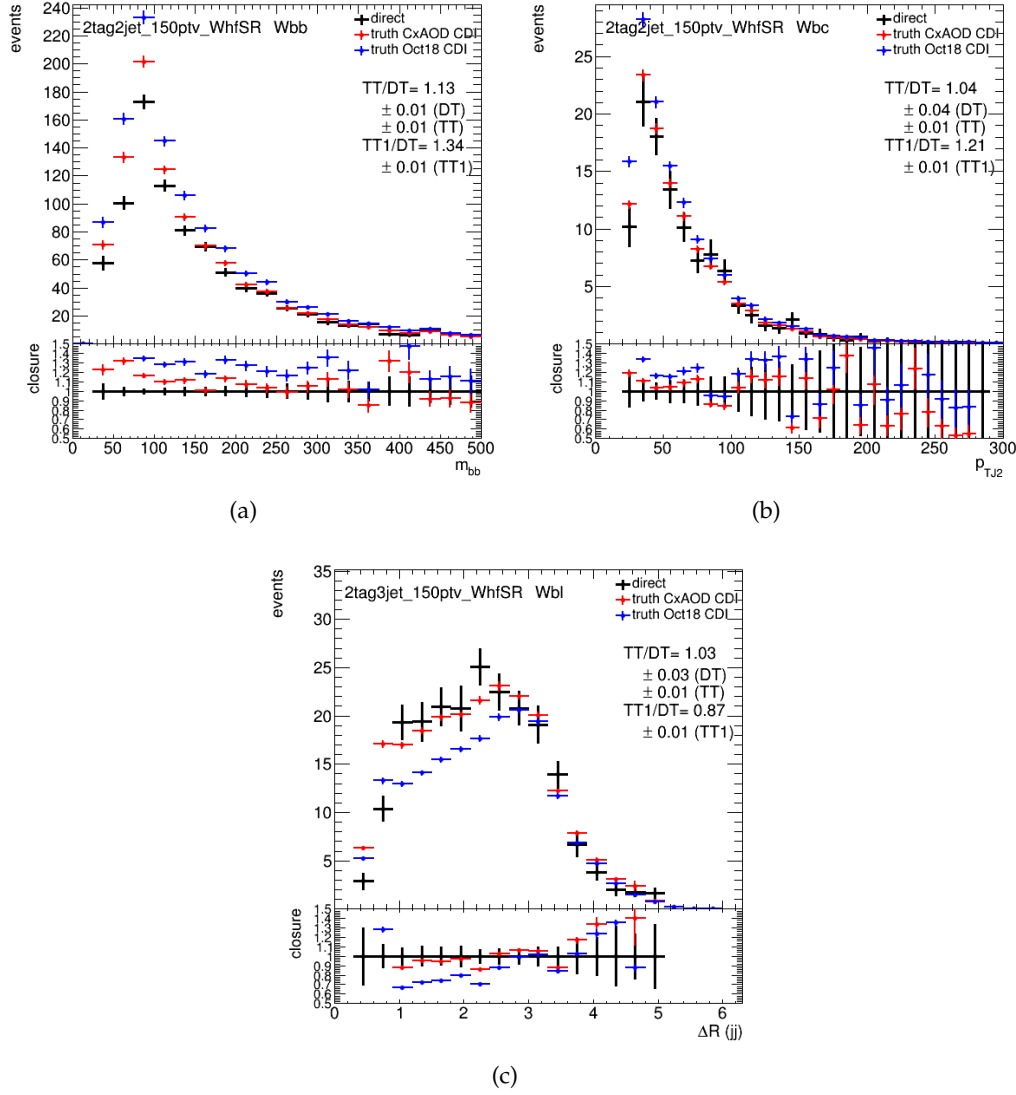


FIGURE 8.6 – (a)  $m_{bb}$  distribution in  $W+bb$  events, (b)  $p_T$  of the sub-leading jet for  $W+bc$  events and (c)  $dR(\text{jet}, \text{jet})$  distribution for  $W+bl$  events using (black) DT: direct tagging and (red) TT: truth tagging with the new customized maps, compared to (blue) TT1: the truth tagging computed with the official efficiency maps. The numbers on the right represent the ratio of the yields with respect to direct tagging.

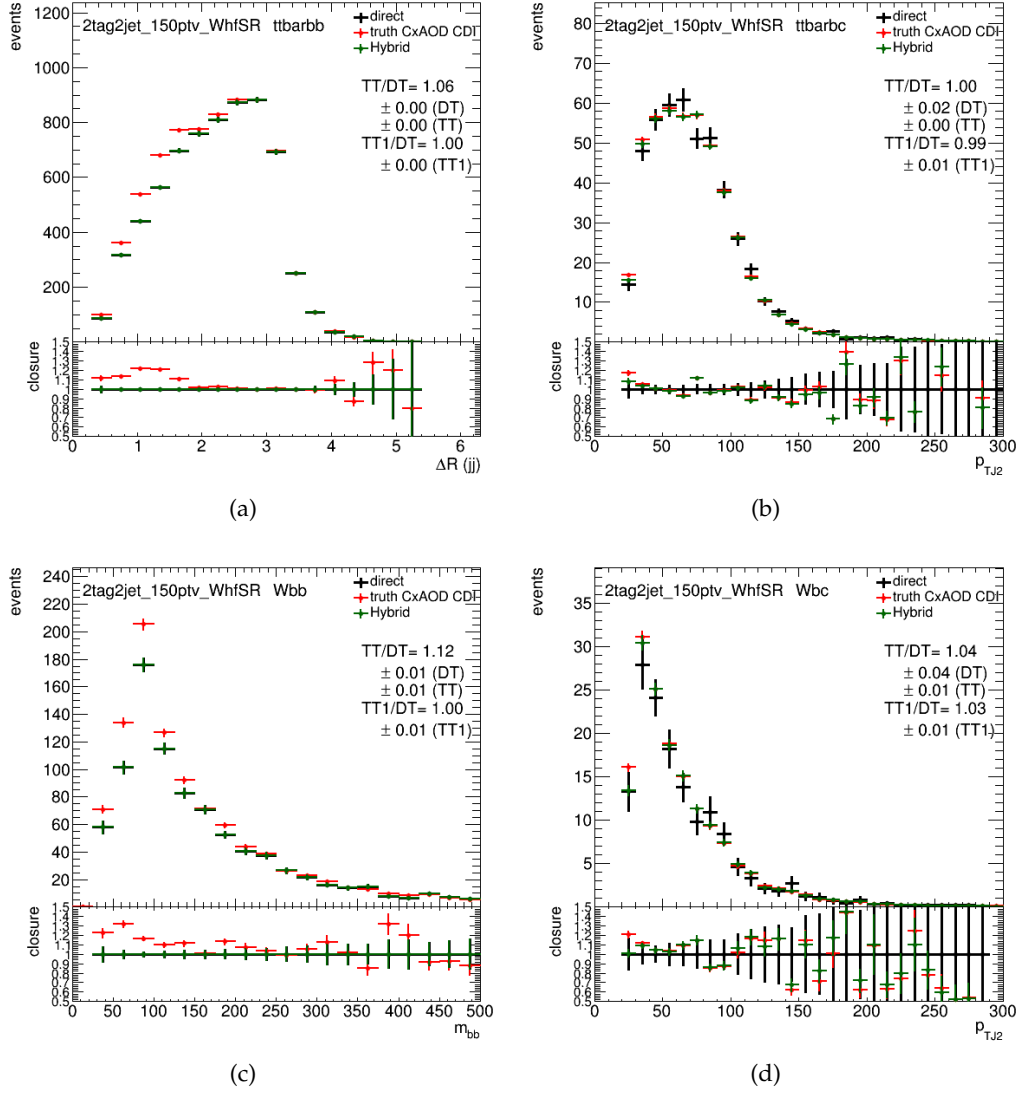


FIGURE 8.7 – (a)  $\Delta R(\text{jet}, \text{jet})$  distribution of  $t\bar{t}(bb)$  events, (b)  $p_T$  distribution of the sub-leading jet in  $t\bar{t}(bc)$  events, (c)  $m_{bb}$  distribution on  $W+bb$  events and (d)  $p_T$  distribution of the sub-leading jet in  $W+bc$  events, using (black) DT: direct tagging, (red) TT: truth tagging and (green) TT1 (HT): hybrid tagging with the new customized maps. The numbers on the right represent the ratio of the yields with respect to direct tagging.

quoted in the previous chapter was 12%, while now it has been reduced to 2-3% with the difference fully covered by the statistical uncertainty of the direct tagging. The discrepancy in  $Z+bl$  is slightly higher for the 0-lepton channel, probably because it has not been directly used to compute the efficiency maps. However, looking at the distributions in Appendix B, it is clear that there are no main problems in the shapes and that the difference is just due to negative fluctuations of the direct-tagged sample, which have been smoothed away by the hybrid approach.

The improvements related to the use of hybrid tagging can be summarized as:

- Reduction by a factor 3-4 of the statistical uncertainty related to the number of simulated events with respect to direct tagging.
- Reduction by  $\sim 60\%$  ( $\sim 3 \rightarrow \sim 1$ ) of the statistical uncertainty related to the number of simulated events on  $V+bc$ .
- Reduction by almost a factor 10 ( $\sim 3 \rightarrow \sim 0.3$ ) of the statistical uncertainty related to the number of simulated events on  $V+bl$ .

Process	Direct tagging		Truth tagging		Difference
	yield	error	yield	error	
0-lepton					
Zbb	788.96	9.35	788.96	9.35	0.0%
Zbc	47.32	2.63	50.37	0.81	6.4%
Zbl	36.17	2.78	44.00	0.20	21.6%
Zcc	57.94	8.11	75.77	0.81	30.8%
Zcl	27.20	7.45	30.09	0.14	10.6%
Zl	20.47	7.52	14.19	0.04	-30.7%
Z+jet	978.06	37.84	1003.38	11.35	+2.59%
1-lepton					
Wbb	894.56	12.57	894.56	12.57	0.0%
Wbc	148.55	6.04	152.39	1.81	2.6%
Wbl	81.11	5.01	82.11	0.38	1.2%
Wcc	87.61	11.21	104.64	1.10	19.4%
Wcl	80.34	13.78	88.41	0.26	10.0%
Wl	16.05	10.56	24.42	0.06	52.1%
W+jet	1308.22	59.17	1346.53	16.18	+2.59%
2-lepton					
Zbb	483.819	5.07	483.81	5.07	0.0%
Zbc	25.30	1.92	28.11	0.42	11.1%
Zbl	24.84	1.48	22.72	0.09	-8.5%
Zcc	21.60	2.96	18.07	0.28	-16.3%
Zcl	12.71	2.67	6.90	0.04	-45.5%
Zl	1.59	5.74	1.95	0.01	22.6%
Z+jet	567.67	19.84	561.56	5.91	-1.08%

TABLE 8.1 – Yields and associated statistical uncertainties of the main  $V+jet$  errors across the three channels for the 2017 dataset period in the 2-jet signal region. The left column contains the yields in case of direct tagging, while the right column contains the final yields in *hybrid* tagging.

In the 1-lepton channel, the effects have been studied in more details also for the other samples. The yield tables for all the processes involved in the analysis are presented in Appendix B. An 8% reduction on the statistical error of the inclusive  $t\bar{t}$ , a

$\sim 20\%$  reduction on the MC statistical uncertainty of the single-top(Wt) and a  $\sim 10\%$  on the WZ statistical uncertainties are observed, in addition to the improvements on V+jets. The signal is mostly made of true b-jets, so it remains basically unchanged when moving to the hybrid tagging.

The impact of this change in the final fit has been quantified using a fit to an Asimov dataset ( $\mu = 1$ ), in the 1-lepton channel only. The study has been performed without the addition of the 2018 dataset to better compare with the results presented in the previous Chapter. The systematic uncertainties are described in Section 7.5, apart for some experimental uncertainties which have been updated. For example, a new scheme for JES and JER uncertainties has been introduced for this round of the analysis, with 7 JER uncertainties instead of a single one. The multijet uncertainties have not been included in this study. Table 8.2 shows the comparison between the breakdown table of the nominal version of the analysis - with truth tagging applied only to the small samples ("ICHEP-style" tagging) - and the same table for a dataset produced with full hybrid tagging. The new customized maps have been used in both cases.

(a)		(b)	
Set of nuisance	Impact on error	Set of nuisance	Impact on error
Total	$\pm 0.431$	Total	$\pm 0.427$
DataStat	$\pm 0.275$	DataStat	$\pm 0.272$
FullSyst	$\pm 0.333$	FullSyst	$\pm 0.329$
Data stat only	$\pm 0.260$	Data stat only	$\pm 0.258$
Floating normalizations	$\pm 0.068$	Floating normalizations	$\pm 0.081$
Modelling: VH	$\pm 0.122$	Modelling: VH	$\pm 0.125$
Modelling: Background	$\pm 0.245$	Modelling: Background	$\pm 0.228$
Multi Jet	$\pm 0.000$	Multi Jet	$\pm 0.000$
Modelling: single top	$\pm 0.096$	Modelling: single top	$\pm 0.103$
Modelling: ttbar	$\pm 0.089$	Modelling: ttbar	$\pm 0.075$
Modelling: W+jets	$\pm 0.154$	Modelling: W+jets	$\pm 0.154$
Modelling: Z+jets	$\pm 0.009$	Modelling: Z+jets	$\pm 0.013$
Modelling: Diboson	$\pm 0.049$	Modelling: Diboson	$\pm 0.052$
MC stat	$\pm 0.112$	MC stat	$\pm 0.083$
Experimental Syst	$\pm 0.148$	Experimental Syst	$\pm 0.156$
Detector: Lepton	$\pm 0.030$	Detector: Lepton	$\pm 0.027$
Detector: MET	$\pm 0.041$	Detector: MET	$\pm 0.048$
Detector: JET	$\pm 0.080$	Detector: JET	$\pm 0.094$
Detector: FTAG (b-jet)	$\pm 0.053$	Detector: FTAG (b-jet)	$\pm 0.044$
Detector: FTAG (c-jet)	$\pm 0.088$	Detector: FTAG (c-jet)	$\pm 0.084$
Detector: FTAG (l-jet)	$\pm 0.031$	Detector: FTAG (l-jet)	$\pm 0.015$
Detector: FTAG (extrap)	$\pm 0.006$	Detector: FTAG (extrap)	$\pm 0.003$
Detector: PU	$\pm 0.012$	Detector: PU	$\pm 0.016$
Lumi	$\pm 0.019$	Lumi	$\pm 0.021$

TABLE 8.2 – Breakdown of the systematic uncertainties for a fit to an Asimov dataset with  $\mu = 1$  in the 1-lepton channel with  $80 \text{ fb}^{-1}$ . a) "ICHEP style" truth tagging configuration, b) full *hybrid* tagging. A description of the various systematic uncertainties can be found in Section 7.5. The sum does not match the sum in quadrature of the different entries due to correlations.

A reduction of 27% on the uncertainty associated with the MC statistics is observed when switching to the full hybrid tagging regime. The modelling and the statistical uncertainty on data remain compatible, as expected since the change in shapes and yields are minimal. The observed differences might be due to underlying correlations across the NP. The experimental systematic uncertainties (lepton and jet-related mainly) are slightly different. Investigations are currently on-going to understand

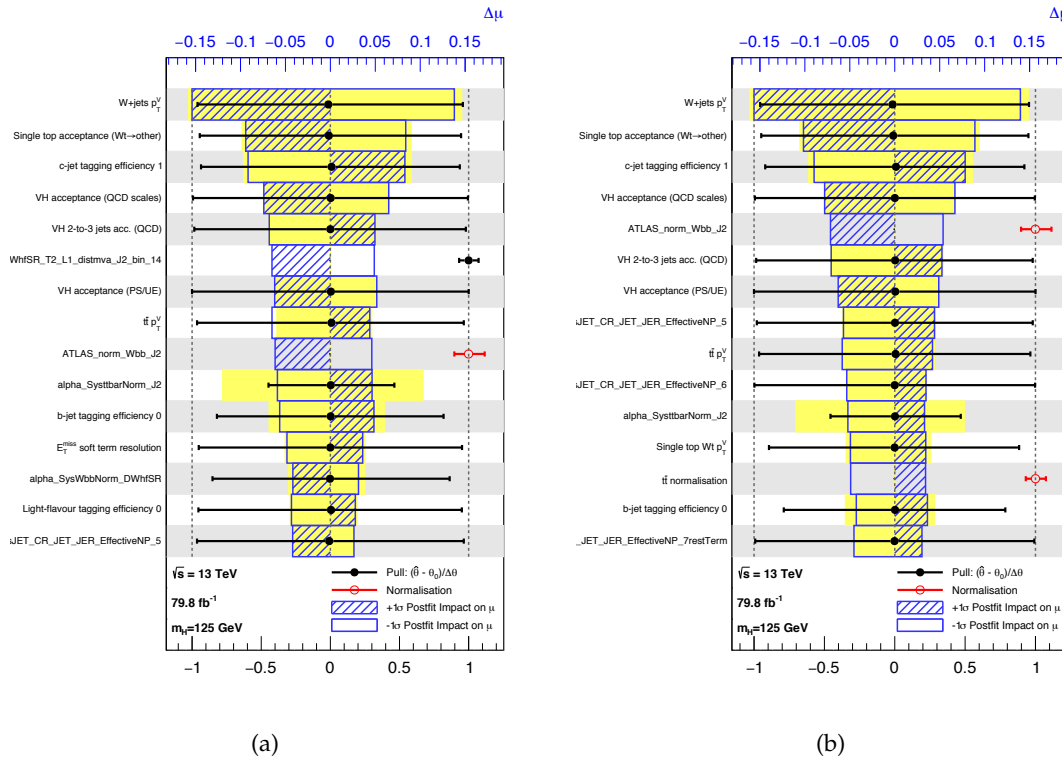


FIGURE 8.8 – Ranking of the systematic uncertainties for a fit to an Asimov dataset with  $\mu = 1$  in the 1-lepton channel with  $80 \text{ fb}^{-1}$ . The plotting scheme is described in Figure 7.21. a) "ICHEP style" truth tagging configuration, b) full *hybrid* tagging. A description of the various systematic uncertainties can be found in Section 7.5. WhfSR\_T2\_L1\_distmva\_J2\_bin\_14 refers to the MC statistical uncertainty of bin 14 of the transformed BDT output.

the reason for such behaviour. From preliminary results it seems that the increased impact might be related to the different pruning pattern<sup>2</sup>, which has not been fully validated for the new JER systematic uncertainties yet, or to underlying correlations with other NP such as the floating normalizations.

The ranking plots comparing the impact of the main systematic uncertainties using the "ICHEP style" tagging and the full hybrid tagging are presented in Figure 8.8. The MC statistical uncertainty entered as 6th in the ranking for the ICHEP style tagging, while in hybrid tagging the impact of this uncertainty is lowered and ranked as 22th (not plotted). A net improvement with respect to the ranking presented in the previous Chapter<sup>3</sup> is achieved, in fact 5 out of the 15 highly ranked uncertainties were related to the MC statistics.

## 8.2 Inclusion of the b-tagging score in the final classifier

The output of a b-tagging algorithm has, by construction, the best discriminating power to disentangle b-jets against c- or light-jets, which makes it a very good discriminating variable for the  $VH, H \rightarrow b\bar{b}$  analysis. In Run-1, this discriminating

2. As explained in Section 7.5.6, the small uncertainties are pruned with different criteria depending on the distribution in each bin. Even small differences in the shapes might induce different pruning schemes.

3. Also thanks to some  $t\bar{t}$  di-leptonic and single-top(Wt) extensions recently added to the analysis

power has been exploited to increase the overall signal to background ratio (S/B). Tight-Tight, Loose-Tight and Loose-Loose categories were defined so to distinguish between signal-like events having two tight b-tagged jets at 50% working point (Tight-Tight), from less signal like events with jets having lower b-tagging scores. Furthermore, the b-tagging information of the two tagged jets was used as a discriminating variable in the MVA and as additional distribution in the final likelihood fit (the latter just for the 1-tag categories). This categorisation was implemented to maximise the significance in case of a much lower statistics sample of  $20.3 \text{ fb}^{-1}$ . A +15% improvement in significance for the 1-lepton, 7% for the 0-lepton and 9% for the 2-lepton channel [208] has been achieved with respect to the un-categorised analysis. The main drawback of this analysis strategy was the complexity since many more regions had to be simultaneously considered in the final fit.

This categorisation has been dropped for simplicity for the published analyses of Run-2 [187] [205]. The b-tagging information is currently used only in the event selection and just in a binary way to disentangle tagged jets above threshold from the non-tagged jets, completely neglecting the additional discriminating power of the full b-tagging distribution.

A new approach, partially following the Run-1 strategy, has been studied to recover the power of the b-tagging information in the analysis. The idea is to maintain the simple structure of the current analysis, but with two main modifications:

- Two additional variables corresponding to the binned MV2c10 score of the two tagged jets are added to the training of the  $BDT_{VH}$ , both in the 2-jet and 3-jet categories.
- Each bin of the pseudo-continuous b-tagging distribution needs to be corrected with its own efficiency scale factor. It is therefore mandatory to move to the "pseudo-continuous" working point described in Section 5.2.4.

The pseudo-continuous distribution of the MV2c10 score is defined as the binned calibrated version of the continuous MV2c10 output, and it is presented in Figure 5.15 in Section 5.2.4.

No modifications to the event selection are proposed in this approach, so a fixed-cut requirement on the b-tagging score is still needed to select the 2-tag events entering in the signal regions. Motivated by the studies presented in Section 7.6.1, the 70% WP was kept as default b-tagging requirement in the event selection. As described in Section 5.4, for the truth tagged samples the binned MV2c10 score has been generated a posteriori, accordingly to the tagging choice.

The truth tagging had to be modified, to cope with an event selection based on a fixed cut working point, but "pseudo-continuous" efficiency scale factors. Furthermore, dedicated pruning criteria had to be defined to reduce the number of b-tagging variations associated with the continuous working point. More details will be given in the next Sections. The performance of this new setup has been tested also in the final fit, as discussed in the last part of the Section.

## 8.2.1 Truth tagging in pseudo-continuous working point

The first challenge towards the implementation of the new proposed approach was to extend the current version of the statistical tagging to the pseudo-continuous working point. In statistical tagging, the tagged and non-tagged jets are chosen a priori, and the assigned weight reflects the probability for the jets to be above the tagging threshold. However, by definition, in pseudo-continuous working point there is no a priori tagging threshold. This (in this case the 70% WP), is specified as an additional parameter introduced ad hoc for the pseudo-continuous case.



Furthermore, there is a fundamental difference between the definition of flavour-tagging efficiency in the cumulative and pseudo-continuous working points. In the first case the efficiency defines the probability for a jet to have a value *above* the b-tagging requirement, which is exactly what is needed in statistical tagging, while in the second case the efficiency quantifies the probability for a jet to fall *in one specific* bin of the pseudo-continuous distribution:

$$[100 - 85]\%, [85 - 77]\%, [77 - 70]\%, [70 - 60]\% \text{ or } [60 - 0]\%.$$

Thus, an additional step is needed to convert this definition of efficiency in probability to *pass* a cumulative tagging requirement.

The efficiency maps are provided as 3-D maps in  $(p_T, \eta, \text{weight})$ , where *weight* is the b-tagging information divided in 5 bins. The probability for a jet to fall in a particular b-tagging bin ( $i_{op}$ ) is

$$\text{Eff}_{\text{bin}}^{i_{op}} = \text{MCeff}_{\text{bin}}^{i_{op}} \cdot \text{SF}_{\text{bin}}^{i_{op}} \quad (8.1)$$

with  $\text{MCeff}_{\text{bin}}^{i_{op}}$  the MC efficiency of that particular bin, taken from the efficiency maps, and  $\text{SF}_{\text{bin}}^{i_{op}}$  the flavour tagging scale factor associated with the bin. In order to recover the same definition of efficiency as the cumulative working point, the bins from 1 to  $i_{op}$  needs to be summed together:

$$\text{Eff}_{\text{cut}}^{i_{op}} = \sum_1^{i_{op}} \text{Eff}_{\text{bin}}^{i_{op}} \quad (8.2)$$

For example, the probability for a jet to pass the 70% operating point will be given by the sum of the efficiencies in the [70,60]% and [60-0]% bins, each of them corrected for the SF of that particular bin taken from the pseudo-continuous working point.

Another thing to be noticed is that the scale factors are defined differently with respect to the cumulative working point. In practice, they are a non-trivial extension of the efficiency and inefficiency scale factors used for the regular calibrations, modified so that the tag weight fractions (both in data and in MC) sum up to unity for each given kinematic bin. All the scale factors are provided by the flavour-tagging working group as described in Section 5.3.

### Customized efficiency maps

The customized efficiency maps for the pseudo-continuous WP have been derived from the same dataset described in Section 8.1.1, thus combining 1L, 2L and all the MC samples available for the 2015-2018 period, both for  $t\bar{t}$  and V+jet, to produce PYTHIA and SHERPA maps respectively. The pseudo-continuous efficiency maps are computed:

- subtracting bin-by-bin the cumulative WP maps, previously produced for all the working points (85%, 77%, 70%, 60%).
- Imposing that the sum of the efficiencies of the 5 tag-bins is 1 in each kinematic bin.

The 2-D projections of the PYTHIA efficiency maps are shown in Figure 8.9 for all the four flavours. As expected, the highest fraction of b-jets is concentrated in the [60-0]% bin, while c- and light-jets are most probably in the lowest bins. For light-jets, 90% of the efficiency is in the [100-85]% bin.

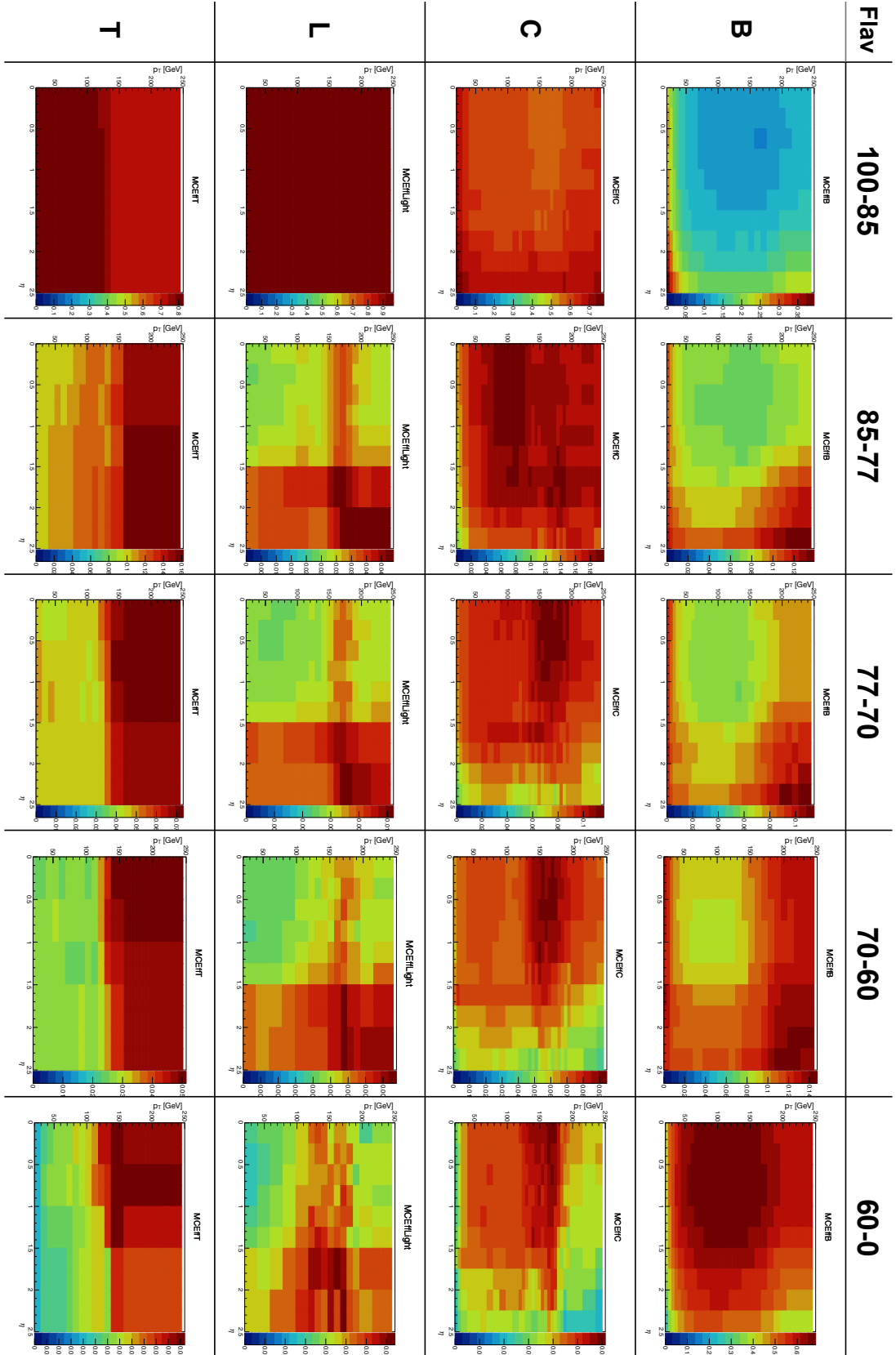


FIGURE 8.9 – 2-D projections in  $p_T$  and  $\eta$  of the new customized efficiency maps in pseudo-continuous working point, calculated from POWHEG + PYTHIA  $t\bar{t}$  events passing the full  $VH, H \rightarrow b\bar{b}$  selection, for the various flavour-types and tag-weight bins.

The efficiency maps in pseudo-continuous WP have been validated comparing the direct and truth tagging distributions of  $t\bar{t}$  and  $V+jet$  samples, with respect to the 70% cumulative working point shown in Section 8.1.2. The two results should be compatible at least within the uncertainties since they are expected to pass the same selection at 70% working point and differ just for the scale factors. Figure 8.10 shows some examples for both  $W+jet$  and  $t\bar{t}$ . The small differences observed are due to the different SFs, but overall there is a good agreement between cumulative and continuous WP both in truth and direct tagging, meaning that no biases, especially in terms of normalization, are introduced in the pseudo-continuous WP when summing the corrected efficiencies bin-by-bin.

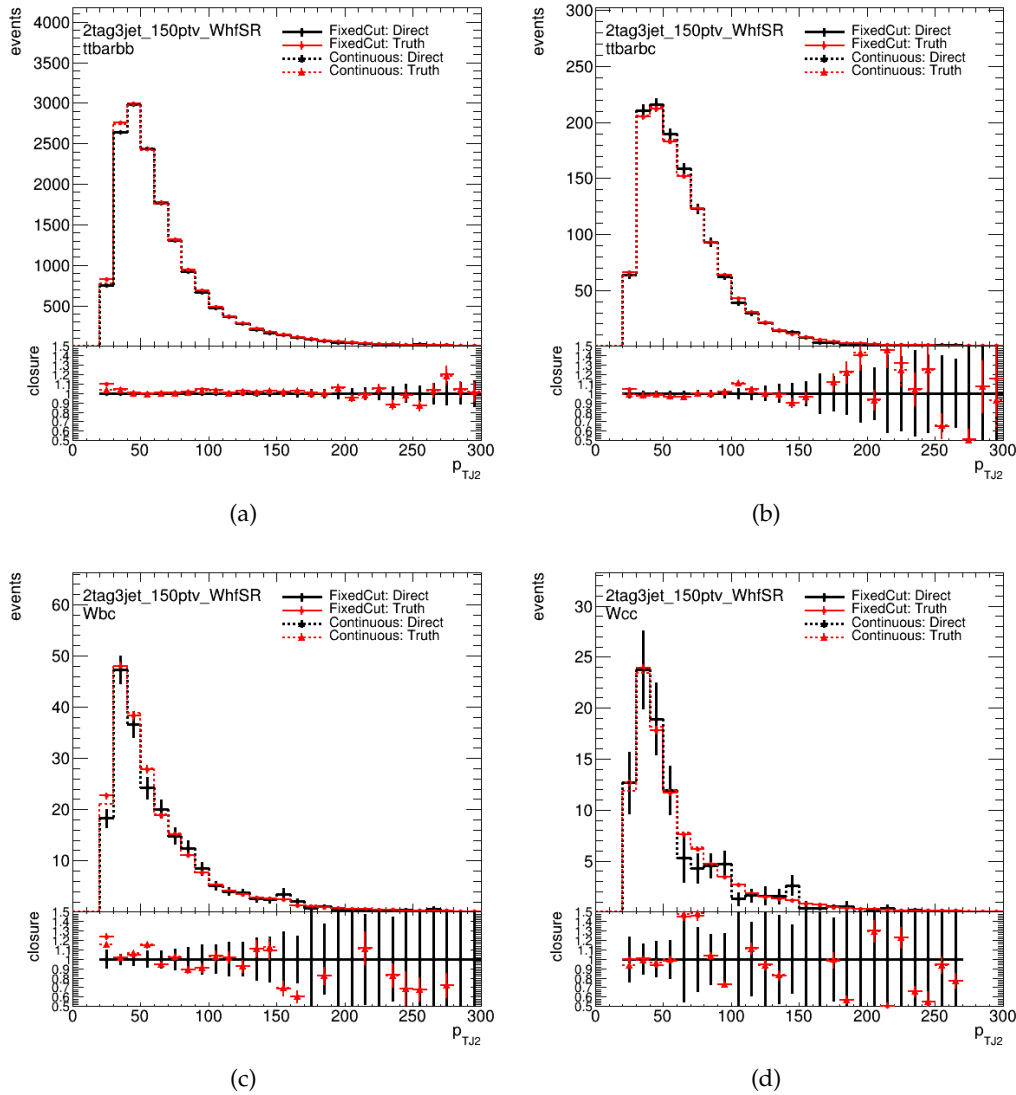


FIGURE 8.10 – Distribution of the sub-leading jet  $p_T$  in (a)  $t\bar{t}(bb)$ , (b)  $t\bar{t}(bc)$ , (c)  $W(bc)$  and (d)  $W(cc)$ , comparing the 70% cumulative working point (points and solid lines) and the pseudo continuous WP (dashed lines). For both WP, the black lines represent direct tagging, while red lines are for truth tagging. In both cases the new customized efficiency maps have been used.

## 8.2.2 Training of the $BDT_{VH}$

The BDT trainings have been performed using the full 2015-2018 available MC statistics and with the same parameter settings described in Table 7.9. The training dataset has been produced using hybrid tagging and the pseudo-continuous WP with the new customized efficiency maps. As said in the introduction, two new variables have been added:

- binned MV2c10 score of the leading *tagged* jet.
- binned MV2c10 score of the sub-leading *tagged* jet.

The jets need to pass the 70% WP requirement to be used in the training so, in the end, only 2 bins of the pseudo-continuous distribution are exploited: the [70,60]% bin and the [60,0]% bin. The signal and background distributions of the two new variables are shown in Figure 8.11 for the 2-jet and 3-jet categories. A certain discrimination power is visible between signal and background even if just two bins are exploited. The overtraining checks of the new retrained BDT are presented in Figure 8.12. Good agreement between the training and test sample is observed, both in terms of ROC curves and BDT outputs, meaning that no evident sign of overtraining is visible.

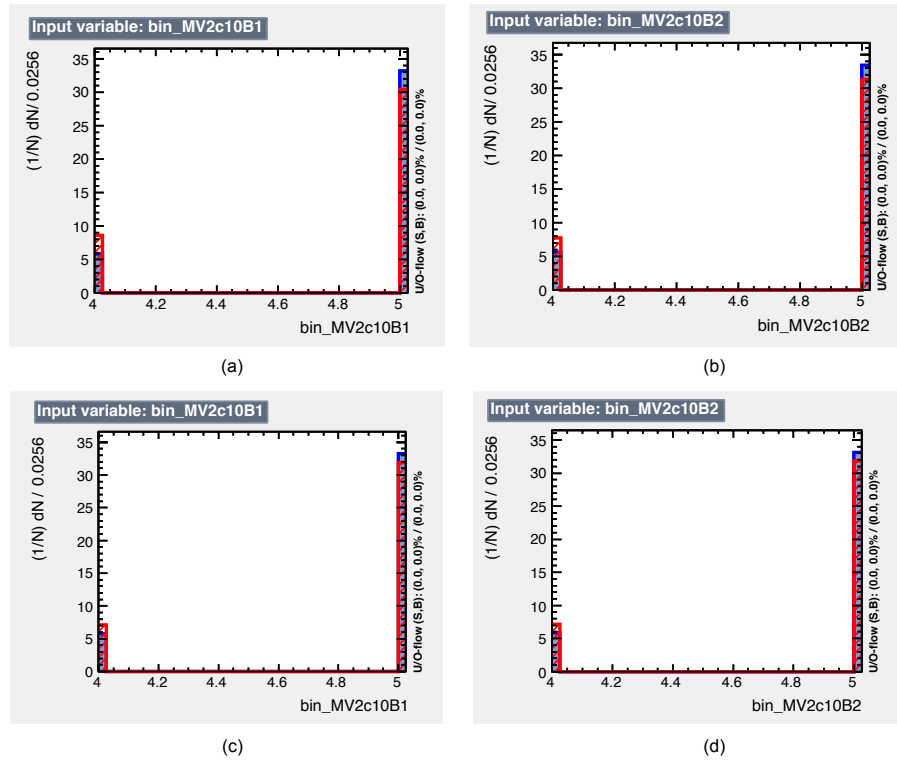


FIGURE 8.11 – The normalized signal and background distributions of the quantiles for (a) the leading and (b) the sub-leading jet in the 2-jet category, while (c) is the leading and (d) is the sub-leading jet in the 3-jet category. The quantiles are the bins of the pseudo-continuous distribution, in this case 4 (70-60%) and 5 (60-0%).

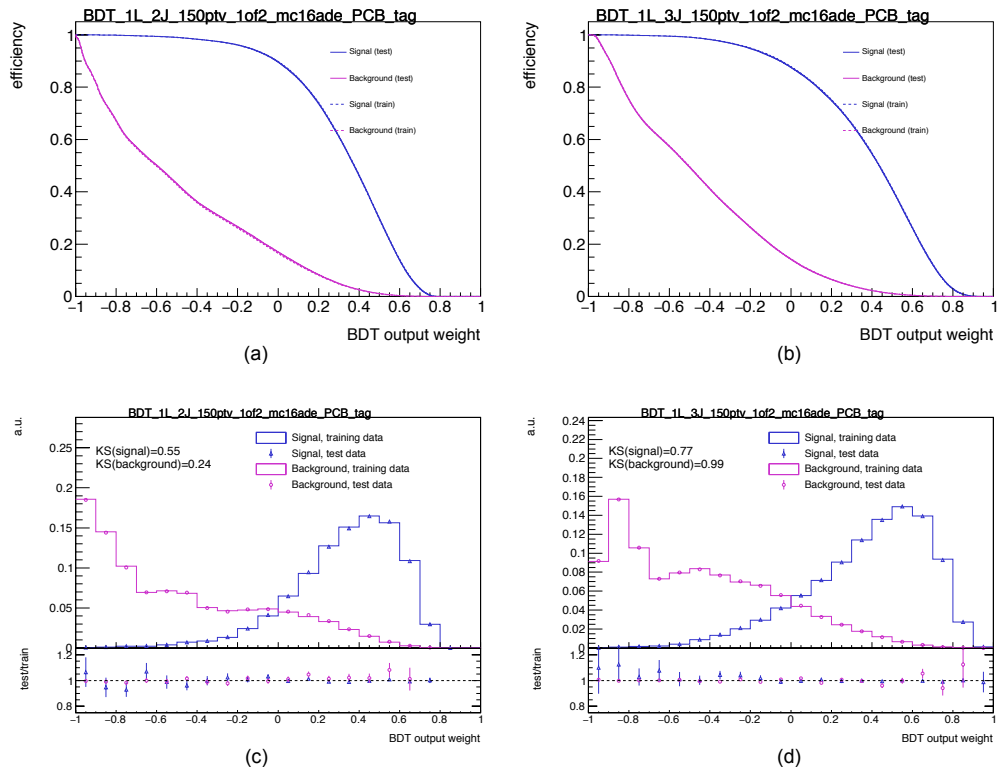


FIGURE 8.12 – Over-training checks for the new 1-lepton BDT trained with the addition of the b-tagging information of the two tagged jets. (a) and (b) efficiency vs cut on the BDT output for signal and background in 2-jet and 3-jet respectively, (c) and (d) BDT output distribution of signal and background in the 2-jet and 3-jet trainings respectively.

### 8.2.3 Pruning of the systematic uncertainties

The pseudo-continuous operating point has an additional intrinsic complication, given by the large number of independent nuisance parameters needed to account for flavour-tagging related uncertainties. A total of 85 NP, 45 for b-jets, 20 for c-jets and 20 for light-jets are provided for the pseudo-continuous WP as described in Section 5.3. This number is quite critical in terms of computing time and manageability of the fit model. Thus, a dedicated pruning procedure has been developed to reduce the total number of flavour-tagging related NP.

As described in Section 5.3, the b-tagging variations of the pseudo-continuous working point are computed as a function of  $p_T$  and b-tagging weight and then converted in a set of independent nuisance parameters to be used by the analyses, always expressed as a function of  $p_T$  and MV2c10 variable, also later generalized as "b-tagging weight". The b-tagging weight bins are determined by the values in Table 5.5 (column "Selection"), and they identify a specific interval in b-tagging efficiency:

- b-tag weight bin  $\in [-1, 0.11]$  corresponds to the [100, 85]% b-tag efficiency interval,
- b-tag weight bin  $\in [0.11, 0.64]$  corresponds to the [85, 77]% b-tag efficiency interval,
- ...
- b-tag weight bin  $\in [0.94, 1]$  corresponds to the [60, 0]% b-tag efficiency interval.

To facilitate the representation of these 2D uncertainties, each nuisance parameter is decomposed in five 1-D projections along  $p_T$ , one for each bin of the b-tagging weight. As example, the projections for one b-jet flavour-tagging NP are shown in Figure 8.13, compared to the total b-jet flavour-tagging uncertainty of each bin. These five histograms represent the building blocks of a b-tagging nuisance param-

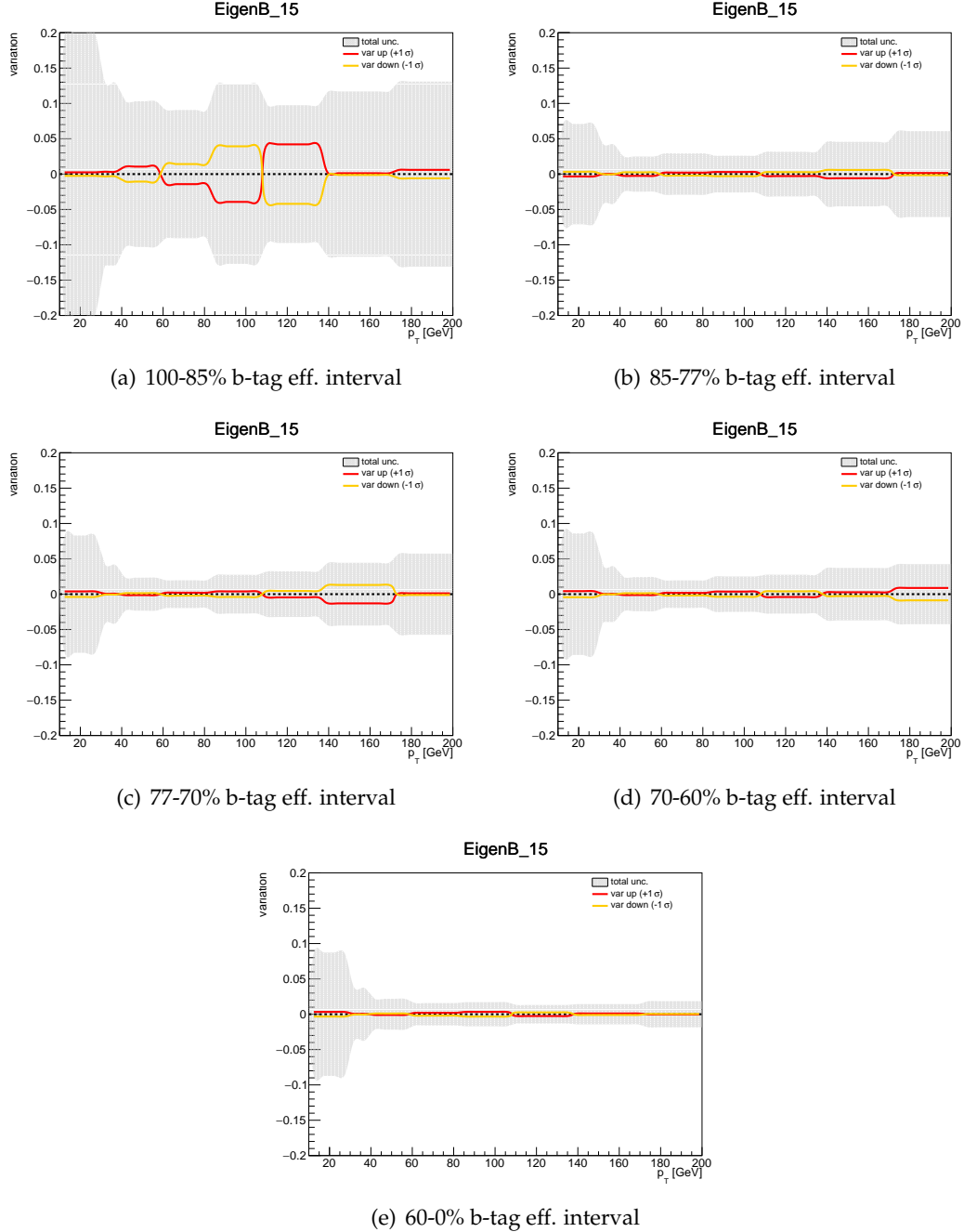


FIGURE 8.13 – 1-D projections along  $p_T$  of one b-tagging nuisance parameter for b-jet. The grey band is the total uncertainty, while the red and yellow lines are the up (+1 $\sigma$ ) and down (-1 $\sigma$ ) variations for this NP.

eter, and they have been largely used to establish the pruning criteria. As a first attempt, one can impose that a NP is pruned if *all* the  $p_T$  and tag-weight bins (so all the five 1-D projections at the same time, in all the  $p_T$  bins) have absolute

variations smaller than a certain threshold. However, this requirement is not very effective in terms of actual reduction of the total number of uncertainties, for multiple reasons. First, the projections have very different shapes, thus finding a suitable threshold valid in all bins at the same time is quite challenging, and second the considerable number of projections to look at ( $45 \times 5$  for b-jets,  $20 \times 5$  for c- and light-jets for a total of 425 histograms) makes the tuning procedure even more complex.

For these reasons, the requirement has been loosened adopting a simplified approach, which focuses on the *real* impact of the b-tagging bins in the analysis. Exploiting the fact that the analysis requires the jets to pass the 70% working point and that the MVA only makes use of *tagged* jets, the BDT is actually sensitive to only 2 out of 5 b-tagging bins. The other three bins [100-85]%, [85-77]% and [77-70]% are actually not resolved by the BDT, and can thus be merged in one single bin from 100% to 70%. This implies a net reduction of 40% in the number of 1-D projections to consider. In the limit of high statistics, the shape of the variation in the merged [100-70]% bin can be inferred from the shapes of the projections in the single bins. Intuitively, the highest contributions to the final shape should come from the regions of the phase space with the highest efficiency<sup>4</sup>. The merging has been performed bin-by-bin, averaging the three projections in the [100-70]% range using a *weighted average*. The weights have been taken from  $\eta$ -inclusive MC efficiency maps, computed in the same way as the ones shown in Figure 8.9:

$$var_{\text{tot}}(p_T) = \frac{\sum_i (var_i(p_T) \cdot \text{MCEff}_i^{\text{bin}}(p_T))}{\sum_i \text{MCEff}_i^{\text{bin}}(p_T)} \quad (8.3)$$

with  $i$  the index running over the three b-tag weight bins, MCEff the MC efficiency as a function of  $p_T$  for each b-tagging bin. The three  $\eta$ -inclusive MC efficiency maps for the [100-85]%, [85-77]% and [77-70]% b-tag weight bins computed for b-jets are shown in Figure 8.14.

The result of this merging procedure for the current b-jet example is shown in Figure 8.15. Partial compensations between the single contributions are observed, and in the end, even if the initial projections are individually large, the final variation is smaller. This compensation can happen by chance, as in this case, or because one of the three bins has much larger weight (due to the higher efficiency), as described with some examples involving c- and light-jets in Appendix B. With this merging procedure, the number of 1-D projections for each b-tagging nuisance parameter is reduced to three. Keeping the same b-jet NP example as reference, the three projections to be considered now are the [100-70]% merged bin (Figure 8.15) and the two bins above the 70% WP threshold: the [70-60]% bin (Figure 8.13d) and the [60-0]% bin (Figure 8.13-e), which were left un-changed by the merging procedure.

Different sets of pruning requirements have been tested. The criteria ensuring the best trade-off between a good number of pruned variations and a sufficient description of the total b-tagging uncertainty are:

- The variation is below 1% in all the  $p_T$  bins for all the 3 projections.
- The variation is above 1% in some bins, but in these bins its contribution is below 10% of the total uncertainty in that bin.

The criteria have been applied to all the nuisance parameters and flavours. Overall, a total of 57 nuisance parameters (corresponding to 114 variations) has been kept, compared to an initial number of 85 NP (45 for b-jets, 20 for light- and 20 for c-jets). This corresponds to a 30% reduction with respect to the initial number of NP.

4. The higher the probability for a jet to fall in a specific ( $p_T$ , b-tag weight) bin, the higher the impact of that bin on the final shape.



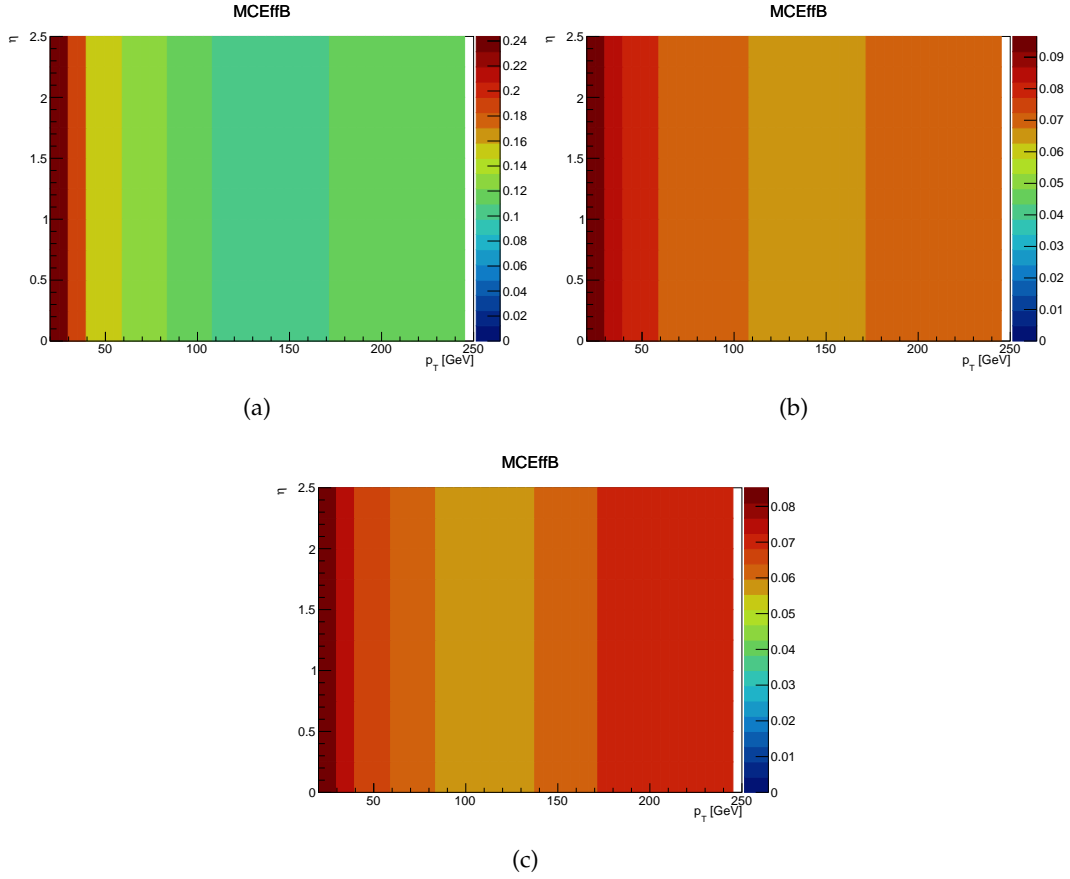


FIGURE 8.14 – The Powheg+Pythia  $\eta$ -inclusive MC efficiency maps for b-jets computed from  $VH, H \rightarrow b\bar{b}$  samples as described in Section 8.1.1. (a) Efficiency map for the b-tagging bin [100-85]%, (b) Efficiency map for the b-tagging bin [85-77]% and (c) Efficiency map for the b-tagging bin [77-70]%.

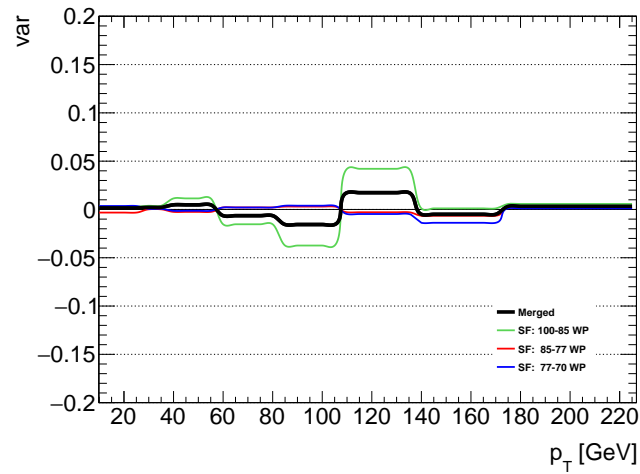


FIGURE 8.15 – The 1D projection of a b-jet NP in the [100-70]% tag-weight bin, after the merging procedure has been applied. The results are calculated as in Equation 8.3. The black solid line represents the final shape of the variation in the [100-70]% tag-weight bin, while the other thinner lines are the variations in the three single b-tag weight bins.

flavour	Total	After pruning	Keeping only $+1\sigma$
B	90	58	29
C	40	36	18
Light	40	20	10
Total	170	114	57

TABLE 8.3 – Number of variations in pseudo-continuous WP for each flavour before and after the pruning procedure.

In addition, the treatment of the systematic uncertainties has been further optimized exploiting the fact that  $+1\sigma$  and  $-1\sigma$  b-tagging variations are currently given as *symmetric* multiplicative weights. Since no asymmetric variations are expected from symmetric multiplicative weights, an immediate 50% reduction has been achieved by storing just the  $+1\sigma$  variations and symmetrizing the uncertainties directly in the fit.

Overall, a total of 170 flavour-tagging related variations<sup>5</sup> should have been considered by default, while after the optimizations described in this Section only 57 are retained, with a net reduction by  $\sim 2/3$ , as shown in Table 8.3.

This represents a preliminary attempt and further checks on the actual impact of the pruning procedure on the final fit are still on-going. The criteria will require a more accurate fine-tuning before declaring the procedure fully validated.

#### 8.2.4 Impact on the analysis

The performance of the new trained BDT has been evaluated using the same luminosity used in Chapter 7 -  $80 \text{ fb}^{-1}$  of Run-2 data at 13 TeV - to isolate the gain of the new approach from the effect of the additional statistics, and in the 1-lepton channel only. The tests have been done comparing two different classifiers:

- The "nominal"  $BDT_{VH}$ , trained with all the Run-2 available MC statistics.
- The "new"  $BDT_{VH}$ , retrained with all the Run-2 available MC statistics, with the addition of the b-tagging information.

The two datasets have been produced using pseudo-continuous b-tagging scale factors, the 70% WP requirement and with the hybrid tagging. The robustness of the fit model has been tested comparing fits to an Asimov dataset and conditional fits to data<sup>6</sup>, both with  $\mu$  fixed to 1. The fits have been performed first considering only the statistical uncertainties and then including all the systematic uncertainties discussed in Section 7.5. All the uncertainties have been kept unchanged with respect to the analysis described in the previous Chapter, apart for the experimental uncertainties, which have been updated as described in Section 8.1.2.

Table 8.4 shows the gain in significance for the new MVA with respect to the nominal BDT approach. As shown in Figure 8.16, and discussed in Section 8.2.2, the inclusion of the new variables increases the expected separation power of the final  $BDT_{VH}$  against the main backgrounds:  $t\bar{t}$ , especially  $t\bar{t}(bc)$ , single-top and W+HF. For example, there is a 40% increase in the S/B ratio in the region of interest (above 0.6) between the signal and  $t\bar{t}$  in 2-jet. A similar behaviour is observed in the ratio of the signal to single-top. Furthermore, an increase of 30% in the ratio between W+bb and the other W+jet events is observed in the region of interest, suggesting

5. 85 "up" variations ( $+1\sigma$ ) and 85 "down" variations ( $-1\sigma$ ).

6. A conditional fit to data means that the normalizations are extracted directly from data (while in a "pure" Asimov fit the normalizations come from MC), so they are more realistic. The signal strength is kept to a fixed value, usually  $\mu = 1$ , to maintain the analysis blinded.

that the new  $BDT_{VH}$  has a better separation power between the  $bb$  component and the  $bc/bl$  ones. This leads to an overall gain of 6.5% in statistical significance - con-

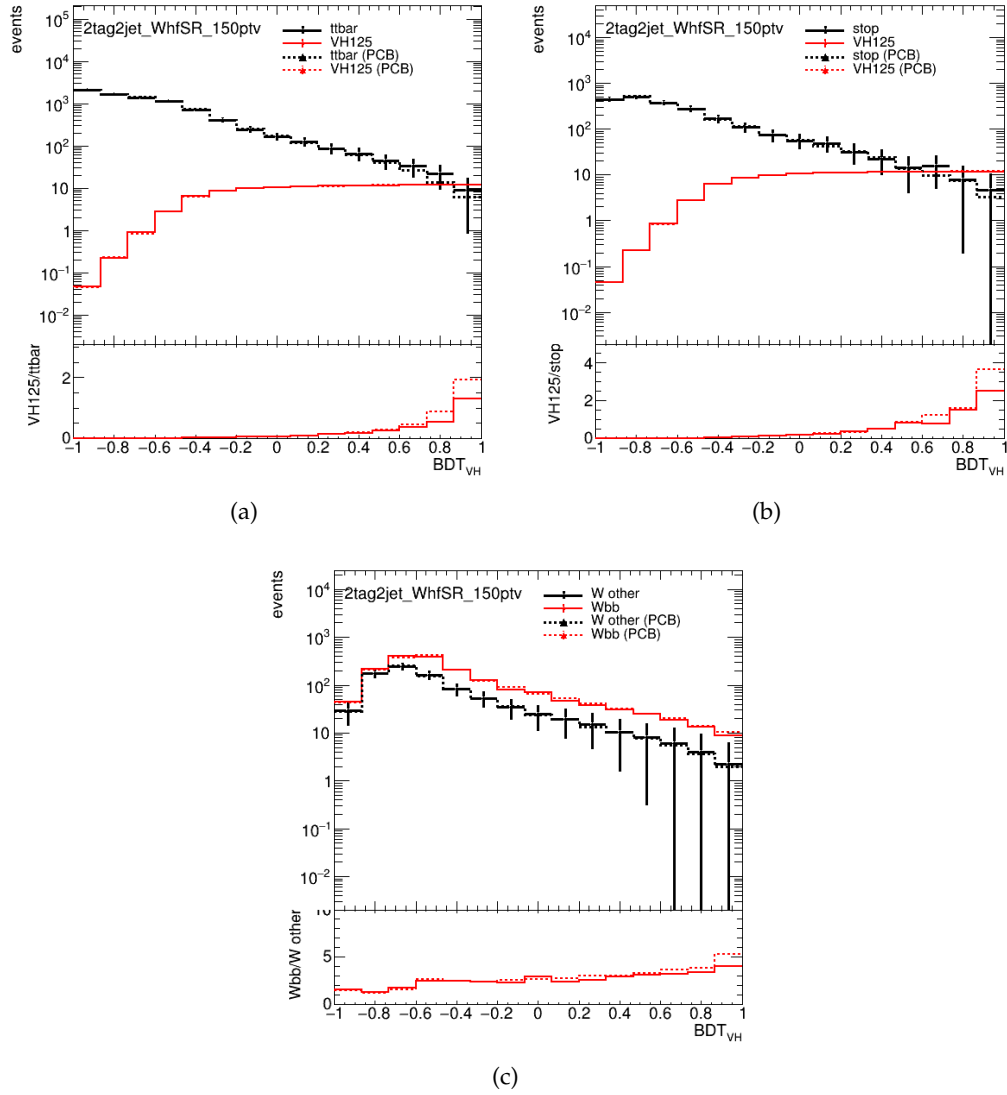


FIGURE 8.16 – Comparison between the  $BDT_{VH}$  outputs of (a) the signal and  $t\bar{t}(bc)$  (b) the signal and single-top and (c) W+bb and W+others in the 2-tag 2-jet region. The rebinning has been performed as discussed in Section 7.3.3. In case the denominator has zero entries in a bin, the ratio is set to zero by default. The first two plots show an increase in the S/B ratio for the new approach, while the third shows that the non-bb component of W+jet is 30% less in the region of interest (right-most bins), thanks to the addition of the new variables. Legend: the dashed lines are for the new set-up, while the solid lines are for the nominal  $BDT_{VH}$ . Red: signal in a) and b). Black: a specific background (see legend). For the third plot, the red is the W+(non-bb) component and the black is W+bb.

sidering only the statistical uncertainties - for both a fit to an Asimov dataset and a conditional fit to data<sup>7</sup>.

7. The calculation of the expected significance for the conditional fit to data is performed in two steps, to reduce the impact of the statistical fluctuations on the quoted value. First, a fit to data with  $\mu$  fixed to 1 is performed to extract the normalization values. Then, these values are used to build a "realistic" Asimov dataset based on the post-fit MC, which is finally used to extract the significance.

Fit	Strategy	nominal	nominal + b-tag	%
Asimov	Stat. only	4.15	4.33	6.5%
	Syst.	2.57	2.73	10.6%
Data ( $\mu = 1$ )	Stat. only	4.15	4.32	6.4%
	Syst.	2.54	2.72	14.4 %

TABLE 8.4 – Significances for (top) a fit to an Asimov dataset and (b) a conditional fit to data with  $\mu = 1$  in the 1-lepton channel using  $80 \text{ fb}^{-1}$  of data. The fit has been performed including only the statistical uncertainties on data (Stat. only) or all the systematic uncertainties (Syst.). Both fits do not include the multijet background estimation.

When including the systematic uncertainties, the gain increases to +10% for a fit on Asimov dataset and up to +14% for the conditional fit to data. Understanding the way the fit handles the NP, especially those related to the modelling uncertainties, is not straightforward. Further checks have been performed to exclude possible biases in the fit and confirm the robustness of the quoted results.

A first qualitative check consists in looking at the data-MC post-fit distributions. Any serious problem in the fit can in fact manifest itself as a poor agreement between data and post-fit MC. This possibility is excluded by the excellent agreement of the data-MC post-fit distributions shown in Figure 8.17. The results are shown for the conditional fit to data with systematic uncertainties. Furthermore, Figure 8.18 shows the binned MV2c10 scores in the two signal regions. Again, the excellent data-MC agreement is a hint of the robustness of the fit.

A more quantitative check consists in looking directly at the best fit values of the nuisance parameters, and their errors. As explained in Section 7.4.2, parameters showing post-fit uncertainties higher than the initial priors are a clear indication of underlying problems. On the contrary, pulled or constrained values reveal a certain sensitivity of the dataset to measure the corresponding nuisance parameter, which is tolerable as soon as it does not contradict the initial looser prior. If not, it might indicate some underlying correlations which are not visible from the estimated uncertainties on the individual nuisance parameters or some tensions in the definition of the likelihood parametrization. Figure 8.19 shows the NP comparison between the nominal and the new approach for a fit to an Asimov dataset. No weakly constrained parameters are present (i.e. NP with uncertainties larger than 1) and only a few parameters are constrained, mainly those related to the  $t\bar{t}$  and single-top uncertainties. Good compatibility is observed between the nominal and the new approach, meaning that such constraints are not introduced by the addition of the  $b$ -tagging information in the BDT. Some  $b$ -tagging related variations are not present in the new fit because of the different pruning pattern. The effect on the final fit was negligible.

Figure 8.20 shows the same comparison, but for the conditional fit to data. Overall, the two fits look compatible, with no major problems apart from two suspiciously pulled parameters related to the single-top modelling. The problem seems to be reduced in the new approach.

The correlation matrices, shown in Figure 8.21, revealed that the problem comes from the high correlation between the  $p_T^V$  modelling and the acceptance uncertainties of single-top(Wt)  $bb$  events. The  $p_T^V$  modelling uncertainty is in fact dominated by the  $bb$  channel, due to the interference between the NLO single-top Wt and the LO  $t\bar{t}$  process, as described in Ref. [234]. This translates in large  $p_T^V$  and  $m_{BB}$  modelling

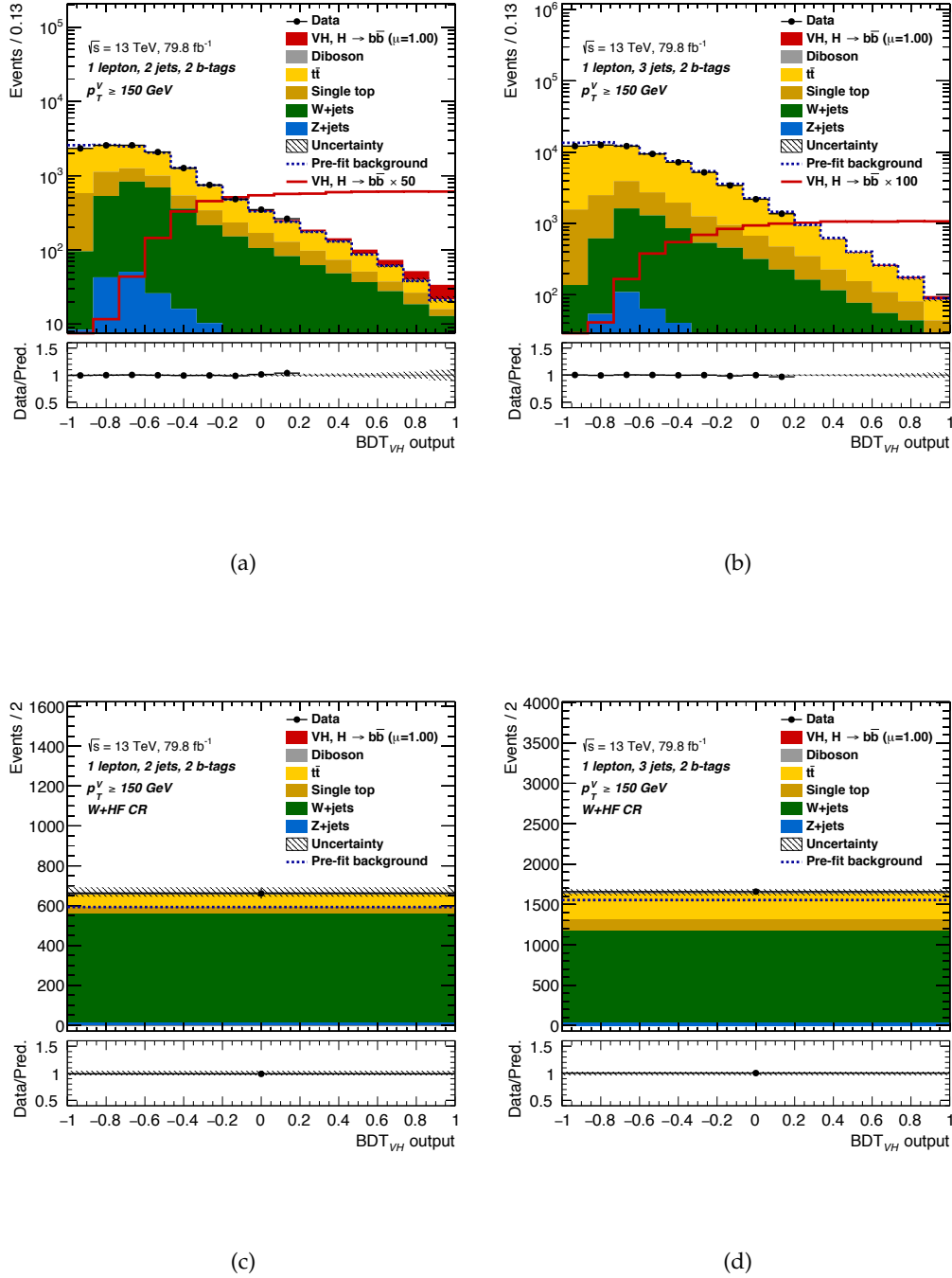


FIGURE 8.17 – Post-fit distributions of the new final classifier for a conditional fit to data ( $\mu = 1$ ) with the systematic uncertainties, (a)-(b) signal regions, (c)-(d) control regions. The fit was performed with  $80 \text{ fb}^{-1}$  and in the 1-lepton channel only. The black-dots represent the data, while the filled histograms are the different simulations normalized to their post-fit normalization factors. The solid red line represents the signal expectation, normalized to a certain factor explicated in the plot. The ratio between the data and MC distributions is shown in the bottom pads. The most sensitive bins with a  $S/B > 0.05$  are blinded.

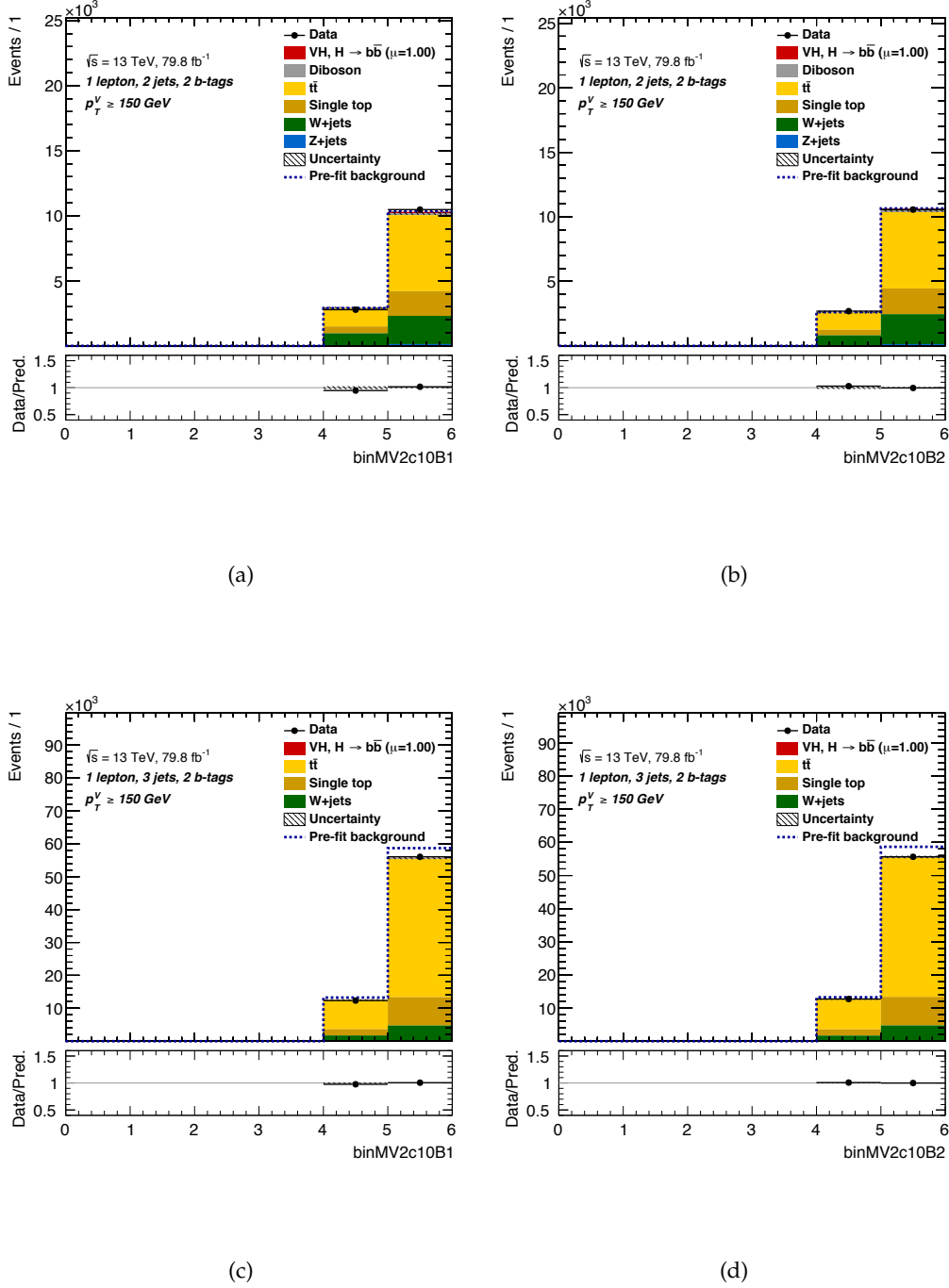


FIGURE 8.18 – Post-fit distribution of the binned MV2c10 distribution for (a)-(b) the 2-tag 2-jet signal region and (c)-(d) the 2-tag 3-jet signal region, reweighted for the results of a conditional fit to data ( $\mu = 1$ ) in the 1-lepton channel. (a) and (c) quantile of the leading jet in  $p_T$  and (b) and (d) quantile of the sub-leading jet in  $p_T$ . The plotting scheme is the same as Figure 8.17.

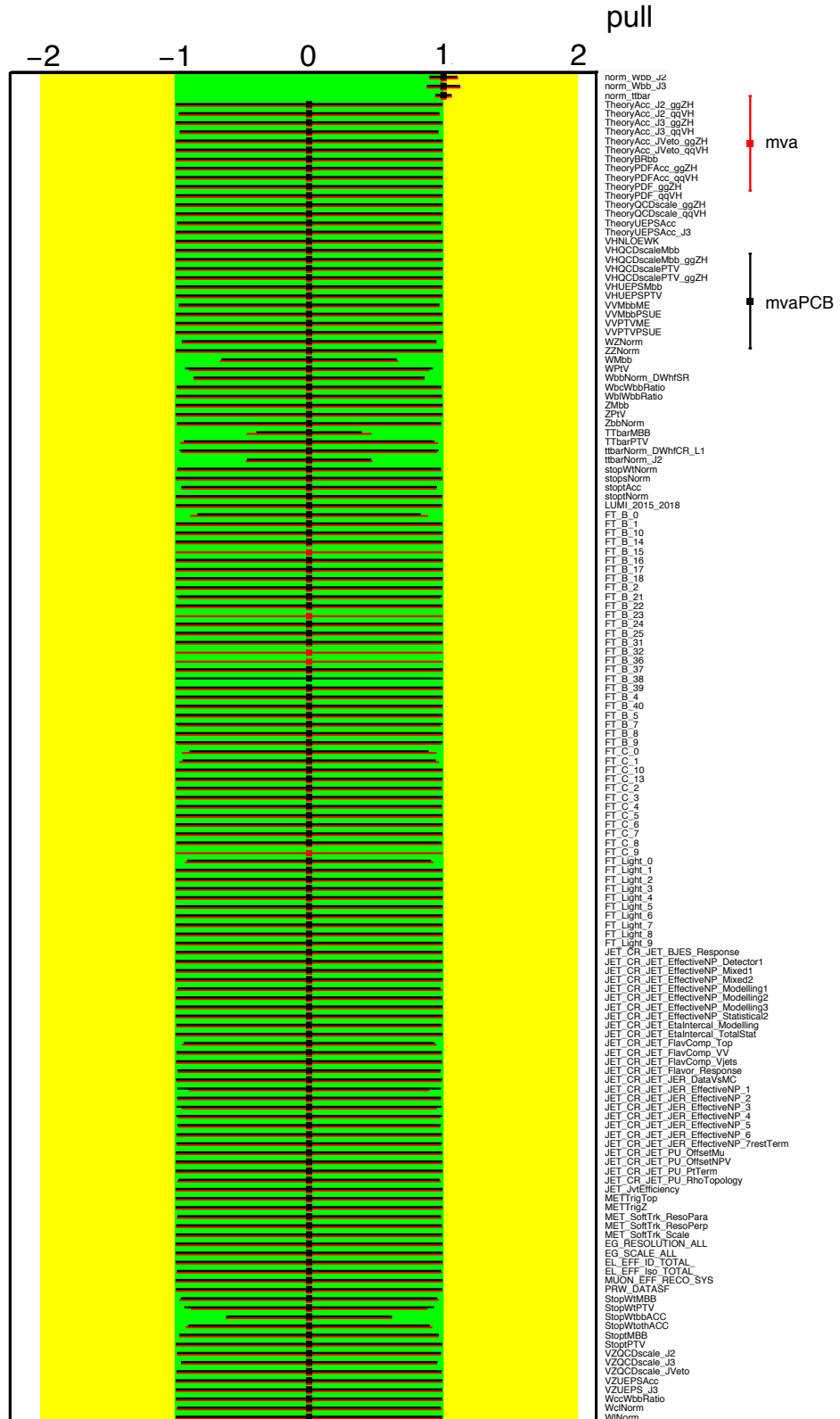


FIGURE 8.19 – Post-fit systematic uncertainties from the fit to an Asimov dataset with  $\mu = 1$ . The red dots represent the nominal MVA, while the black dots represent the new configuration. The green band shows the  $1\sigma$  deviation from the initial value, while the yellow band is the  $2\sigma$  deviation. The  $1\sigma$  and  $2\sigma$  convention is not valid for the NP related to the normalization since they are initialized to 1.



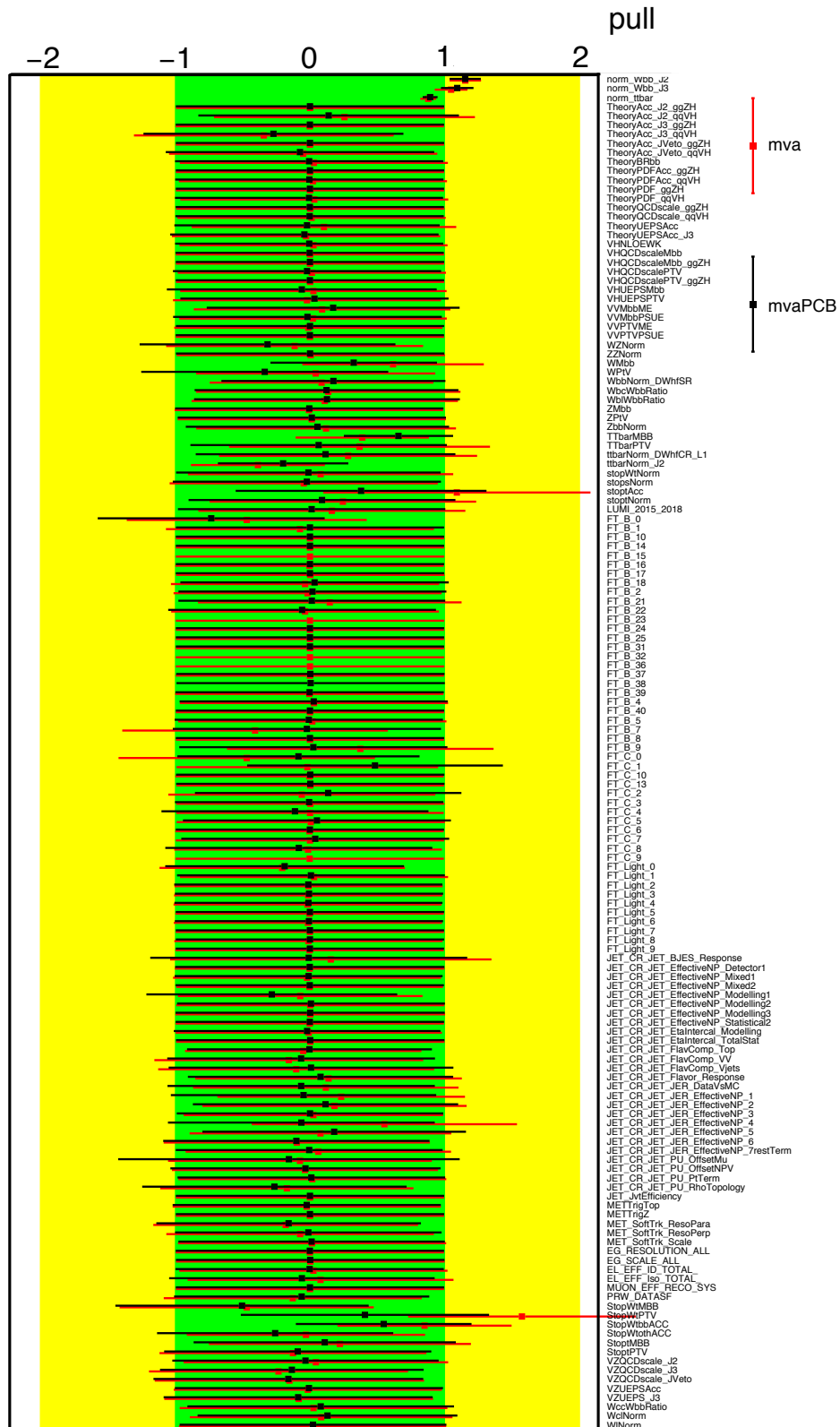


FIGURE 8.20 – Post-fit systematic uncertainties after a conditional fit to data with  $\mu$  fixed to 1. The red dots represent the nominal MVA, while the black dots represent the new configuration. The green band shows the  $1\sigma$  deviation from the initial value, while the yellow band is the  $2\sigma$  deviation. The  $1\sigma$  and  $2\sigma$  convention is not valid for the NP related to the normalization since they are initialized to 1.



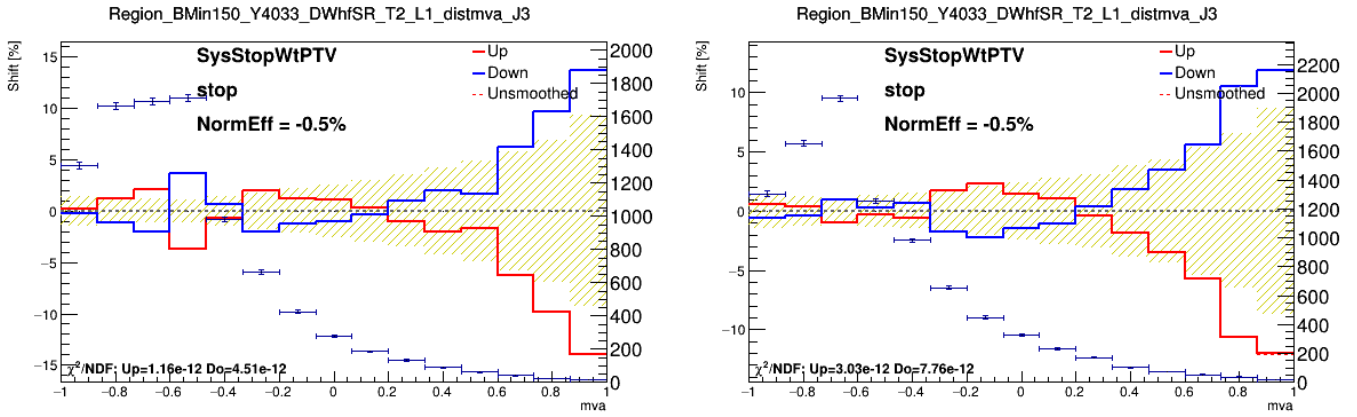


FIGURE 8.22 – Comparison between the effect of the single-top  $Wt$   $p_T^V$  modelling uncertainty on the  $BDT_{VH}$  of the 3-jet signal region. In yellow the statistical uncertainty, in solid red the up variation and in solid blue the down variation, related to the y-axis on the left. The blue dots show the distribution of the single-top  $BDT_{VH}$ , referring to the y-axis on the right. The "NormEff" indicates the impact of this uncertainty on the normalization.

the pruning scheme or to the underlying correlation with the normalization uncertainties (up to 60%), which are also increasing as discussed above. Finally, a non-negligible increase in the impact of the c-tagging uncertainties could be explained by the fact that the  $BDT_{VH}$  is now able to better separate the  $bb$  and  $bc$  components, so the c-jet uncertainties have a higher impact. Further checks on the correlation scheme would be needed to verify the aforementioned hypotheses.

### 8.3 Summary

This Chapter focused on two possible improvements to be implemented in the analysis towards the full Run-2  $VH, H \rightarrow b\bar{b}$  publication. The first is the so-called *hybrid* tagging, which combines the use of direct and statistical tagging to maximize the available MC statistics for c- and light-jets. New efficiency maps have been produced for the  $VH, H \rightarrow b\bar{b}$  analysis to ensure good closure between the two tagging regimes. Tests showed a reduction of 60% in the pre-fit uncertainties on V+bc and of a factor 10 for V+bl in all the three channels. In the fit, the hybrid tagging allows for a reduction of  $\sim 40\%$  of the total MC statistical error.

The second proposed improvement involves the inclusion of the b-tagging information in the final BDT discriminant. The idea has been developed in Run-1 and here it has been proposed in an alternative and simpler way to better adapt to the current structure of the analysis. The final classifier shows an increased separation power between the signal and the other main backgrounds, especially in 3-jets. This translates in an increase of 14.4% (10.6%) in significance for a conditional fit to data (Asimov) with  $\mu = 1$  and a  $-5\%$  reduction on the total uncertainty on  $\mu$  for a fit to an Asimov dataset. The pulls do not show evident underlying problems in the fit, but further checks would be necessary to better understand the correlation pattern and the impact of the single uncertainties. More studies to confirm the validity of the pruning and smoothing schemes for the current implementation of the uncertainties are also needed before including this last improvement in the analysis.

(a)		(b)	
Set of nuisance	Impact on error	Set of nuisance	Impact on error
Total	$\pm 0.417$	Total	$\pm 0.412$
DataStat	$\pm 0.270$	DataStat	$\pm 0.261$
FullSyst	$\pm 0.318$	FullSyst	$\pm 0.318$
Data stat only	$\pm 0.256$	Data stat only	$\pm 0.248$
Floating normalizations	$\pm 0.084$	Floating normalizations	$\pm 0.103$
Modelling: VH	$\pm 0.123$	Modelling: VH	$\pm 0.136$
Modelling: Background	$\pm 0.236$	Modelling: Background	$\pm 0.228$
Multi Jet	$\pm 0.000$	Multi Jet	$\pm 0.000$
Modelling: single top	$\pm 0.110$	Modelling: single top	$\pm 0.090$
Modelling: ttbar	$\pm 0.076$	Modelling: ttbar	$\pm 0.065$
Modelling: W+jets	$\pm 0.158$	Modelling: W+jets	$\pm 0.157$
Modelling: Z+jets	$\pm 0.010$	Modelling: Z+jets	$\pm 0.005$
Modelling: Diboson	$\pm 0.050$	Modelling: Diboson	$\pm 0.044$
MC stat	$\pm 0.080$	MC stat	$\pm 0.082$
Experimental Syst	$\pm 0.133$	Experimental Syst	$\pm 0.159$
Detector: Lepton	$\pm 0.025$	Detector: Lepton	$\pm 0.032$
Detector: MET	$\pm 0.031$	Detector: MET	$\pm 0.025$
Detector: JET	$\pm 0.086$	Detector: JET	$\pm 0.108$
Detector: FTAG (b-jet)	$\pm 0.059$	Detector: FTAG (b-jet)	$\pm 0.053$
Detector: FTAG (c-jet)	$\pm 0.053$	Detector: FTAG (c-jet)	$\pm 0.089$
Detector: FTAG (l-jet)	$\pm 0.022$	Detector: FTAG (l-jet)	$\pm 0.013$
Detector: FTAG (extrap)	$\pm 0.000$	Detector: FTAG (extrap)	$\pm 0.000$
Detector: PU	$\pm 0.013$	Detector: PU	$\pm 0.022$
Lumi	$\pm 0.019$	Lumi	$\pm 0.022$

TABLE 8.5 – Breakdown of the systematic uncertainties for a conditional fit to data fixing  $\mu = 1$  in the 1-lepton channel with  $80 \text{ fb}^{-1}$ . (a) "nominal" configuration. (b) the configuration with the additional MV2c10 score included in the BDT. A description of the various systematic uncertainties can be find in Section 7.5. The sum does not match the sum in quadrature of the different entries due to correlations.

## 9 | Conclusions

This manuscript described the work done during my three years of PhD, between October 2016 and July 2019. Three main areas of interest have been studied: the measurement of the energy scale and resolution corrections of low energy electrons with  $J/\psi \rightarrow ee$  events, the Higgs sector and the  $VH, H \rightarrow b\bar{b}$  analysis, and the developments in b-tagging. The results obtained in these three topics are briefly summarized below.

The offline energy calibration chain of electrons and photons in ATLAS has been briefly presented in Chapter 6. The Standard Model candle used to perform the nominal data-driven calibration is  $Z \rightarrow ee$ , which gives access to electrons at transverse energies peaking at  $\sim 40$  GeV. The scale factors extracted with this data-driven method are then applied to all the electrons and photons in ATLAS, independently from their energy, with additional uncertainties related to the extrapolation at different energies and particle type than electrons from  $Z$  decays. The work of my qualification task consisted in checking the linearity of this calibration, using an independent SM candle:  $J/\psi \rightarrow ee$ . The low mass of the  $J/\psi$ , allows to investigate the low part of the spectrum, in the region from 5 GeV to 30 GeV, which is almost orthogonal to the measurement performed with  $Z \rightarrow ee$ .

The energy scales and resolution of such electrons have been measured using  $J/\psi \rightarrow ee$  events selected from ATLAS data at  $\sqrt{s} = 13$  TeV, recorded during 2015 and 2016. The measurement has been obtained using a simultaneous fit to the invariant mass peak of the  $ee$  system. A fit to the pseudo-proper time of the  $J/\psi$  has been implemented to quantify the fraction of prompt and non-prompt events directly from data. The measured scales are in good agreement with the nominal values extracted using  $Z \rightarrow ee$  events, with maximum disagreements of  $\sim +1.3\%$  in the outer barrel ( $\eta$  in  $[0.8, 1.10]$ ) and of  $\sim -0.4\%$  in the endcaps, and accuracies varying between 0.03% and 0.2% depending on the  $\eta$  bin. These residual scales were found to be compatible with the systematic uncertainties, meaning that the overall linearity of the calibration chain is validated within uncertainties.

The  $J/\psi \rightarrow ee$  events have been used to limit the residual sampling term corrections ( $\Delta a$ ) of the electromagnetic calorimeter. The values are compatible with zero in the whole  $\eta$  region, with uncertainties varying between 2% and 4%. This confirmed, for the first time with a direct measurement (and not from test beams), that the value used for the sampling term still holds. Even if it is still in a preliminary stage, this method represents a promising way to measure the sampling term with better accuracy than the currently quoted value.

Most of the work of my thesis has been dedicated to the  $VH, H \rightarrow b\bar{b}$  analysis. Here I presented the results of the Run-2 analysis with  $80 \text{ fb}^{-1}$  of Run-2 ATLAS data at  $\sqrt{s} = 13$  TeV, which have been of great importance to claim the observation of two

SM processes: the  $VH$  production mode and the  $H \rightarrow b\bar{b}$  decay. The analysis is based on MVA techniques, and in particular Boosted Decision Trees, separately optimized in each signal region to enhance the overall signal to background ratio. The final results are obtained with a simultaneous binned likelihood fit to the BDT output distributions. The best fit value of the signal strength ( $\sigma \cdot BR / \sigma_{SM} \cdot BR_{SM}$ ) of the  $VH, H \rightarrow b\bar{b}$  process is  $\mu = 1.16^{+0.16}_{-0.16}(\text{stat.})^{+0.21}_{-0.19}(\text{syst.})$ , measured with an observed significance of  $4.9\sigma$  and an expected significance of  $4.3\sigma$ . Two cross-checks have been used to validate the result: the di-jet mass analysis and the diboson analysis, searching for the  $VZ, Z \rightarrow b\bar{b}$  SM process.

Three combinations have been performed: the first with the Run-1  $VH, H \rightarrow b\bar{b}$  analysis performed with  $20 \text{ fb}^{-1}$  of ATLAS data at 8 TeV. A signal strength of  $\mu_{VH}^{bb} = 0.98^{+0.22}_{-0.21} = 0.98 \pm 0.14(\text{stat.})^{+0.17}_{-0.16}(\text{syst.})$  has been measured, for an observed (expected) significance of 4.9 (5.1) standard deviations.

The second combination targeted the  $VH$  production mode. The other Higgs boson analyses sensitive to the  $VH$  production mode, such as  $VH, H \rightarrow \gamma\gamma$  and  $VH, H \rightarrow 4\ell$ , have been combined with  $VH, H \rightarrow b\bar{b}$  to enhance the sensitivity to the  $VH$  production. Fixing the branching ratios of each analysis to its SM value, the overall signal strength of the  $VH$  process is  $\mu_{VH} = 1.13^{+0.24}_{-0.23} = 1.13 \pm 0.15(\text{stat.})^{+0.18}_{-0.17}(\text{syst.})$ , with an observed significance of 5.3 standard deviations, and an expected significance of 4.8 standard deviations. This is the first observation of the  $VH$  production mode.

The last combination targeted the  $H \rightarrow b\bar{b}$  decay. The combined analyses were  $VH, H \rightarrow b\bar{b}$ ,  $ttH, H \rightarrow b\bar{b}$  and  $VBF, H \rightarrow b\bar{b}$  from Run-1 and Run-2. The signal strength of the  $H \rightarrow b\bar{b}$  decay has been obtained fixing the production modes to their SM predictions. The combined value is  $\mu_{H \rightarrow b\bar{b}} = 1.01 \pm 0.2 = 1.01 \pm 0.12(\text{stat.})^{+0.16}_{-0.15}(\text{syst.})$ , with an expected (observed) significance of 5.4 (5.5) standard deviations. This is the first observation of the  $H \rightarrow b\bar{b}$  decay mode and the first significant measurement probing the Yukawa mechanism for down-type quarks. In both cases, the  $VH, H \rightarrow b\bar{b}$  analysis has been the leading channel in sensitivity for the observation.

The last part of this work focused on future developments not yet public. Two improvements related to the implementation of b-tagging in the analysis have been developed towards the next result. The first is *hybrid* tagging, which optimizes the use of direct and statistical tagging in the analysis. A reduction of 40% in the MC statistical error is observed when moving to a full hybrid tagging regime in the analysis. The main improvement is visible on V+jet, with a reduction of 60% on the MC statistical error of V+bc and a reduction of a factor 10 for V+bl in all the three channels. New efficiency maps have been produced and validated to solve the problems with statistical tagging observed in the previous rounds of the analysis.

The last improvement proposes a change in the analysis structure to better exploit the discriminating power of the b-tagging information (i.e. the MV2c10 output), which could enhance the S/B ratio as proved in Run-1. In the current structure, the b-tagging information is just used in a binary way to disentangle tagged and non tagged jets. The proposed approach preserves the current analysis structure and includes this information as an additional variable in the  $BDT_{VH}$ . The new  $BDT_{VH}$  shows an increased separation power between the signal and the other main backgrounds, especially in 3-jets. An increase of +14.4% in significance has been observed for a conditional fit to data with  $\mu = 1$ , consistent with the +10.6% observed for a fit to an Asimov dataset. The result seems solid but further checks are needed before including this last improvement in the analysis.

# A | Additional material for the $J/\psi \rightarrow ee$ calibration

Further material is collected in this appendix for the low energy electron calibration study with  $J/\psi \rightarrow ee$  events. Figure A.1 shows some kinematic distributions of the electrons passing the event selection, before applying the 2-dimensional  $\eta$  reweighting. Regarding the fit part, more MC templates are shown in Figure A.2, corresponding to both diagonal and off-diagonal bins. The related fits on data are shown in Figure A.3.

## A.0.1 Comparison with Run-1

A comparison with the Run-1 result can be found in Figure A.4. The dependence of the energy scales on the electron pseudorapidity is similar in the two data taking periods, but for Run-2 there is an overall shift of the energy scale corrections to negative values by approximately  $\sim 0.3\%$ . This effect is more pronounced in the endcaps, where a  $\sim 0.6\%$  negative shift is visible. The discrepancy might be due to the sum of different contributions: in Run-1 there was no automated correction for pileup and pedestal shift systematics, so the Run-1 scales are expected to be more systematically biased to higher values ( $+1\sigma$ ), even if this bias was fully covered by the pedestal systematic uncertainty of  $10\text{MeV}/E_T$ . The second contribution can come by the amount of material upstream the calorimeter, which in Run-2 is different than in Run-1, especially for  $|\eta| > 2$ . Some extra effects, possibly related to  $E_1/E_2$  values or to differences in the  $J/\psi$  and Z luminosity profiles<sup>1</sup> might also contribute to this difference in the energy scales.

## A.0.2 Pile-up dependence

The pile-up dependence of the residual energy scale factors has been studied splitting the sample into three regions of increasing  $\mu$  values: 0-13, 13-18 and above 18. The values have been selected to have regions with  $\sim 20\text{k}$  events each. Due to the low statistics available, the study has been performed using only two pseudorapidity categories:  $|\eta_e| < 1.37$  (barrel) and  $1.52 < |\eta_e| < 2.47$  (endcap). The results of this study are presented in Figure A.5. No significant differences between the residual energy scale factors of the three  $\mu$  subsamples are visible in the barrel. In the endcaps the scales vary by  $\sim -0.4\%$  for the two lowest  $\mu$  intervals, while for  $\mu > 18$  the variation is  $\sim -0.8 \pm 0.2\%$ . This might be the hint of a pile-up dependence of the scales in the high  $\eta$  region, but more data would be necessary to confirm this trend.

1. We are currently assuming that the luminosity profile of  $J/\psi$  is similar enough to the one of Z so that luminosity related effects on the energy scales in the endcaps cancel in the Z to  $J/\psi$  extrapolation for Run-2.



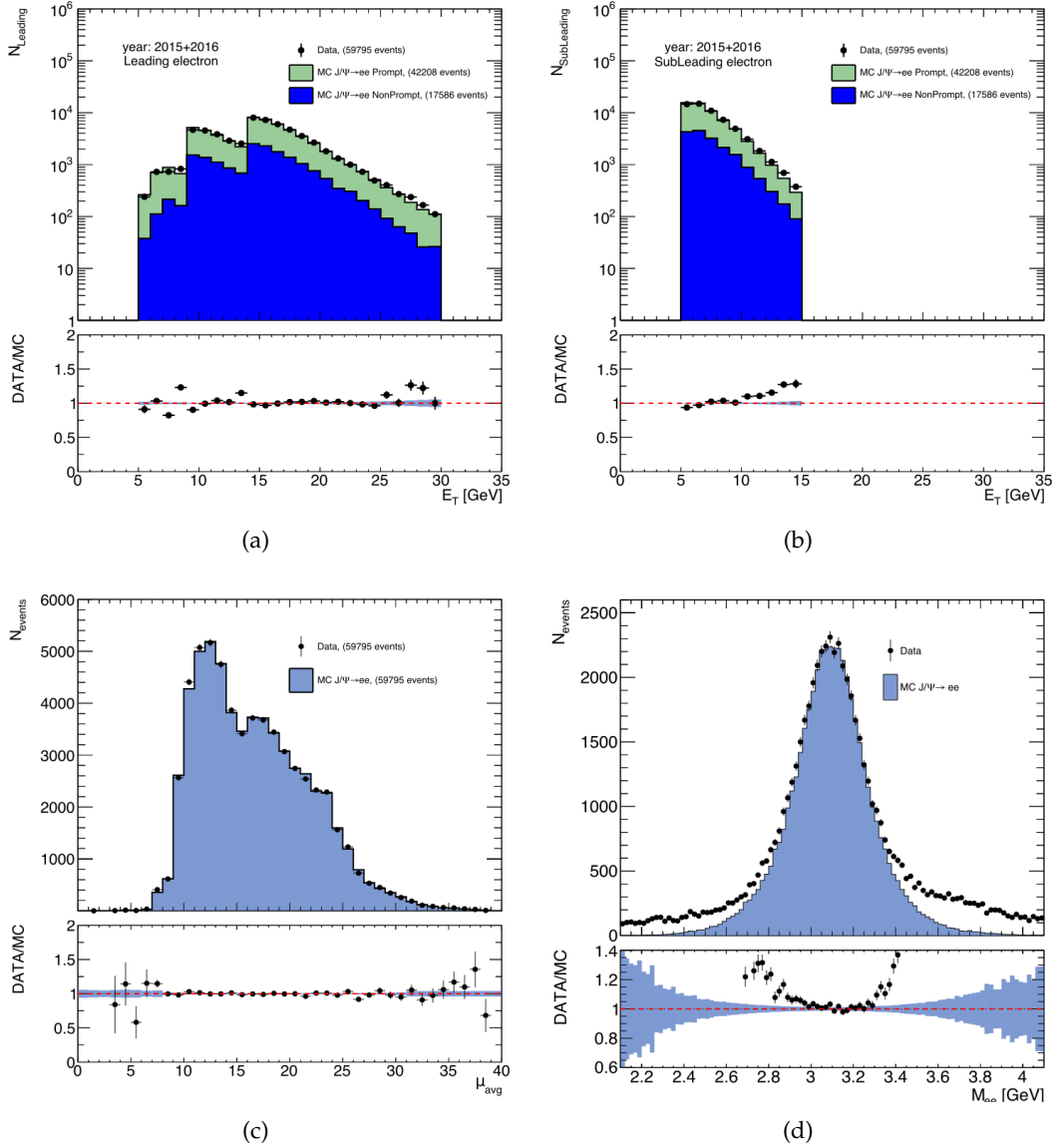


FIGURE A.1 – Kinematic distributions for leading and subleading electrons in data and simulation. (a) Leading and (b) subleading electron  $E_T$  distributions showing prompt and non prompt contributions to the simulation, before the  $(\eta_1, \eta_2)$  reweighting procedure is applied. (c) Pile-up distribution in data and simulation after the pile-up reweighting. (d) Inclusive invariant mass peak in data and simulation. Note: for (d) the MC is normalized to match the data in peak height and not the number of events. This is done to show residual scale and resolution effects. The large disagreement on the tails is due to the continuous background for which no MC is provided.

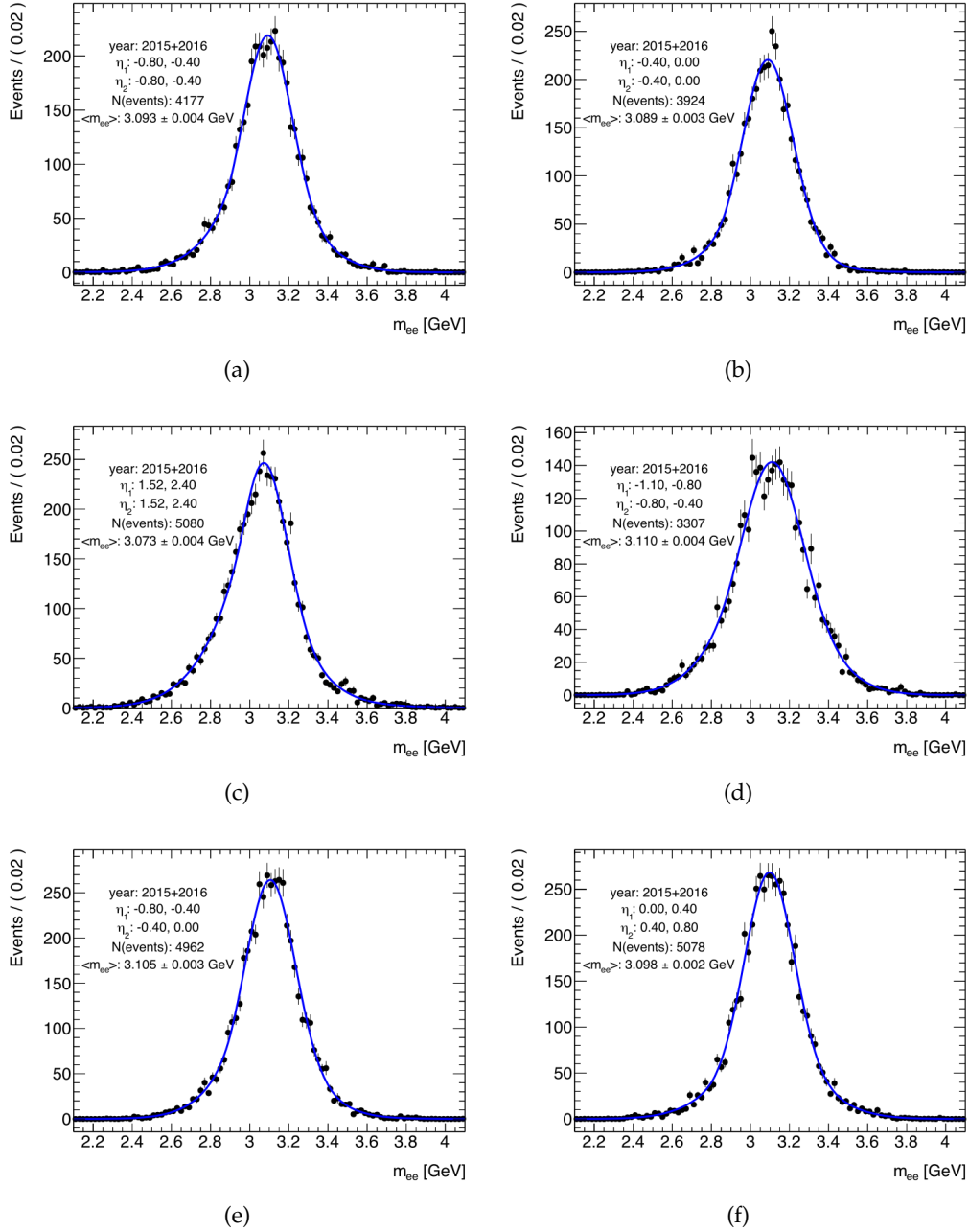


FIGURE A.2 – Some examples of fit to the dielectron invariant mass distribution in the simulation. The first three, (a)–(c), refer to diagonal bins, while the last three, (d)–(f), refer to non-diagonal bins.

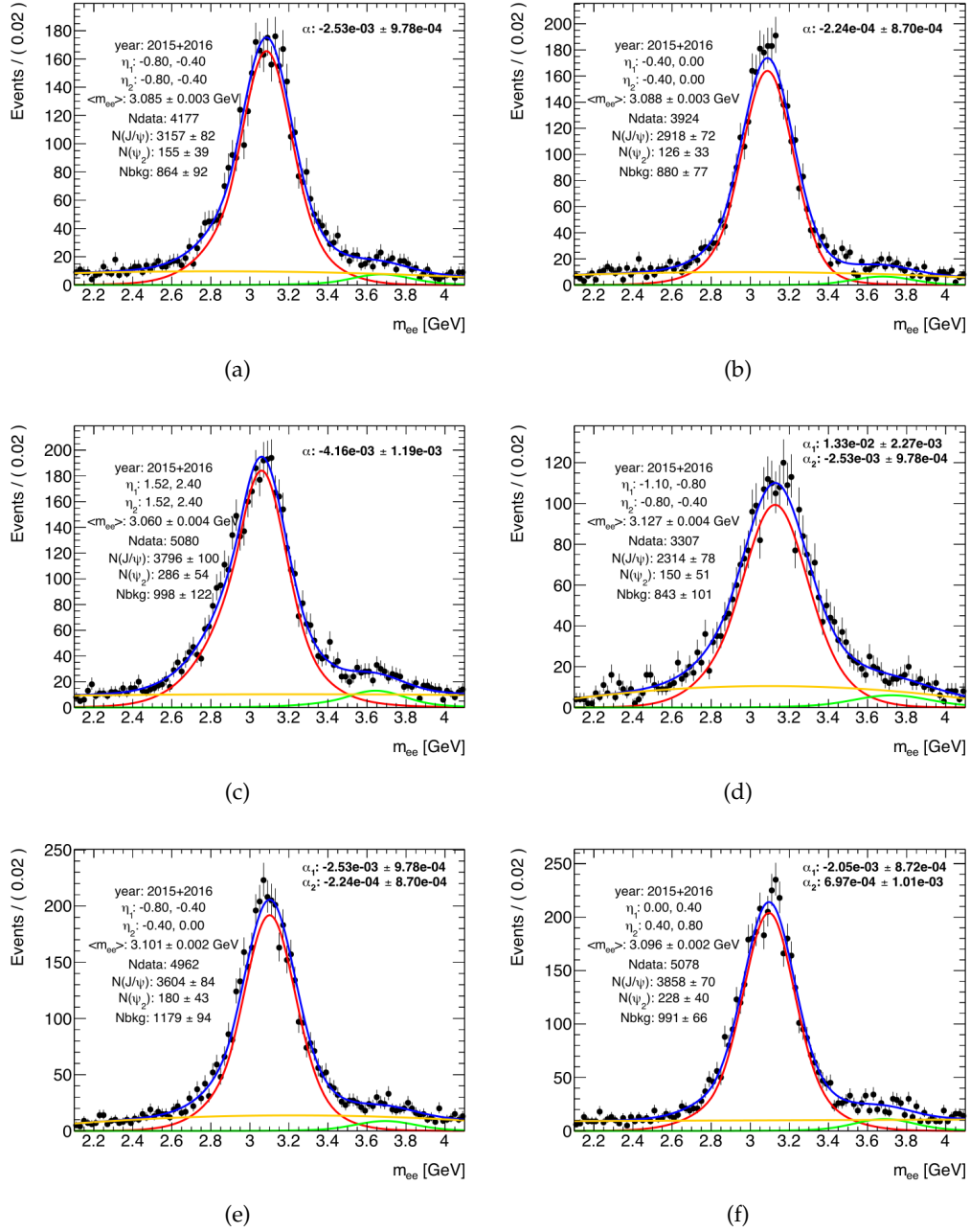


FIGURE A.3 – Result of the simultaneous fit on data, presented for the same categories showed in the previous figure. The blue line represents the total fitted PDF while the red line corresponds to the  $J/\psi$  contribution, the green line to the  $\psi(2s)$  contribution, and the yellow line to the continuous background.

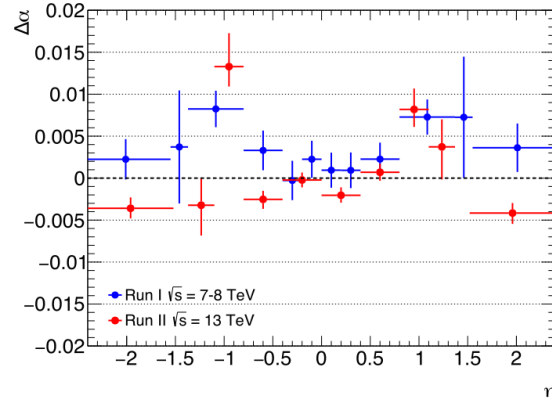


FIGURE A.4 – Comparison between Run-1 and Run-2  $J/\psi \rightarrow ee$  scales. The errors include both systematics and statistical uncertainties. Note:  $\eta$  in Run-1 refers to the track-based eta, while in Run-2 it refers to the  $\eta$  of the calorimeter.

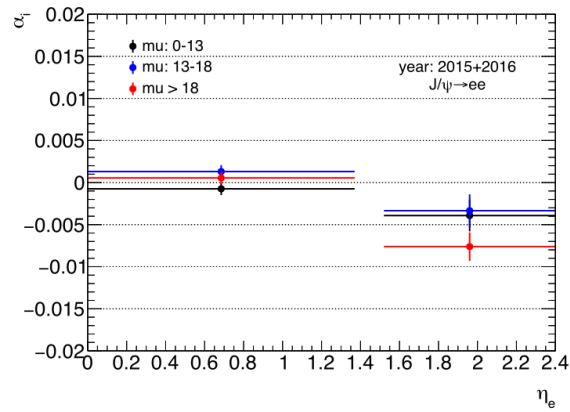


FIGURE A.5 – Study of the  $\mu$  dependence of the residual energy scale factors performed dividing the sample (2015+2016) in three categories with increasing  $\mu$  values. The study has been performed assuming no difference between regions of positive and negative pseudorapidities and keeping only the distinction between barrel and endcaps.

### A.0.3 Resolution fit

Figure A.6 shows additional distributions for the step 1 (fit to MC) and step 2 (fit to data) of the "Two-step method" used to extract the resolution terms.

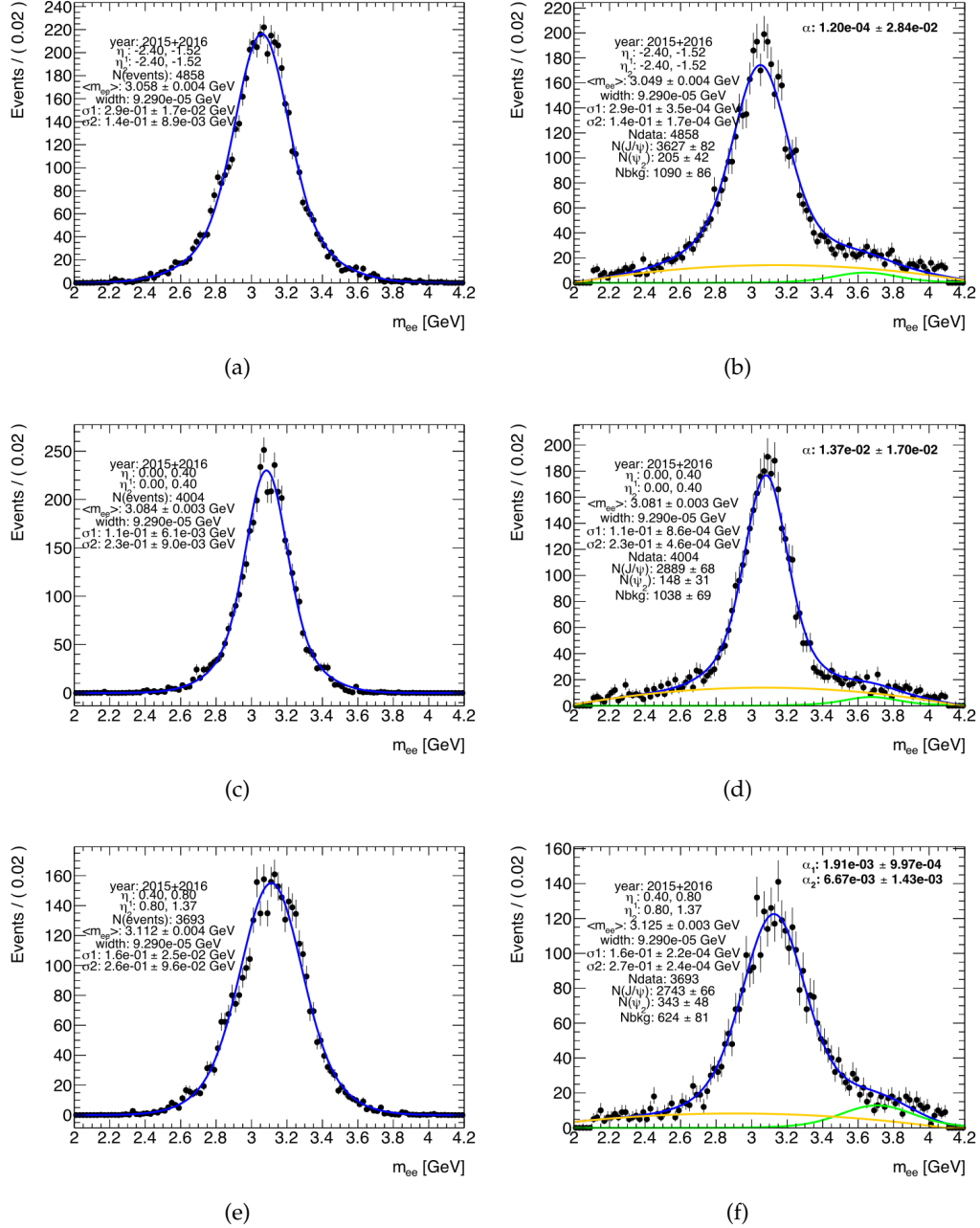


FIGURE A.6 – Some examples of fit to the dielectron invariant mass distribution both in MC (left) and data (right), corresponding to step 1) and 2) respectively. Here all the parameters of the  $\psi(2s)$  peak have been scaled and fixed to MC, using a second fit with a DSCB as PDF. This simplification reduces the accuracy of the final PDF with respect to the one in equation 6.24 (see Figure 6.15), but due to the small yield of this background, this effect is negligible.

## B | Additional material for the full Run-2 $VH, H \rightarrow b\bar{b}$ analysis

This Appendix collects additional material related to Chapter 8. The three macro-arguments treated in the following Sections are the compatibility checks for the new customized efficiency maps, the yield tables in 2-jet and 3-jet of all the samples in 1-lepton compared for "ICHEPStyle" tagging and "Hybrid tagging" and the validation in the 0-lepton channel. And a last, some further examples of pruning of the systematic uncertainties for the pseudo-continuous working point.

### B.1 Compatibility cross-checks for the new customized maps

Figure B.1 shows the bin-by-bin ratio between the official customized maps, produced merging 1-lepton and 2-lepton channels and the 2015-2018 data taking periods, and the maps produced with the 1-lepton and 2-lepton dataset separately. Both b-jets and c-jets are shown.

Furthermore, Figure B.2 shows the ratios of the official customized maps of light-jets and the maps obtained with 2015-2016 (left) or 2018 (right) datasets separately. Fluctuations are expected due to the small statistics available.

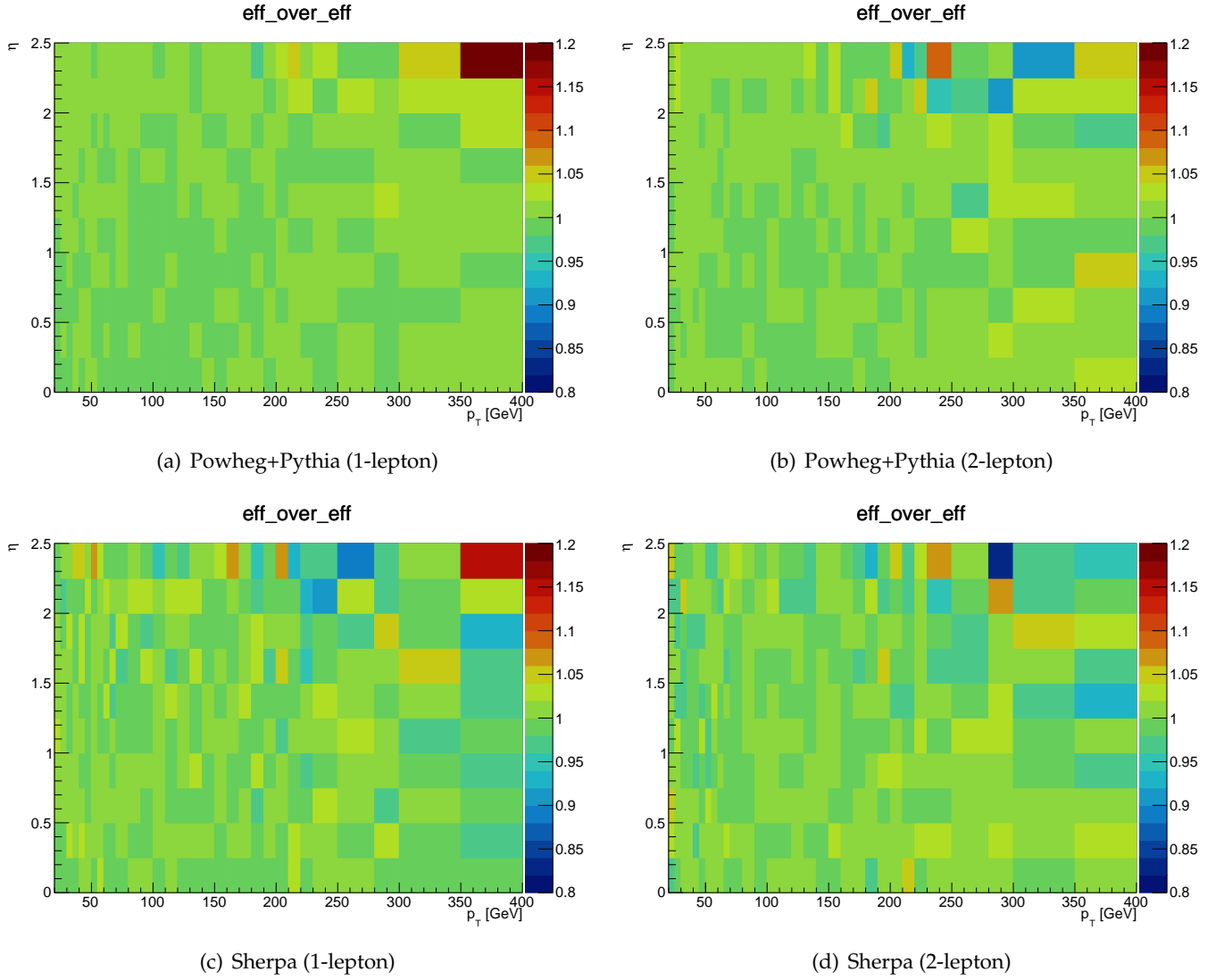
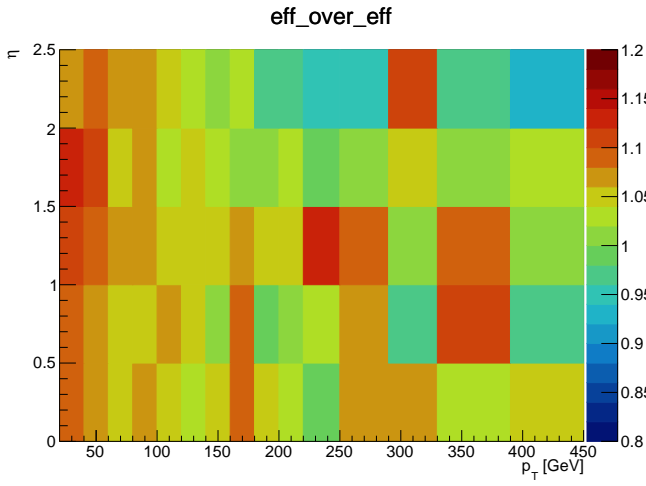
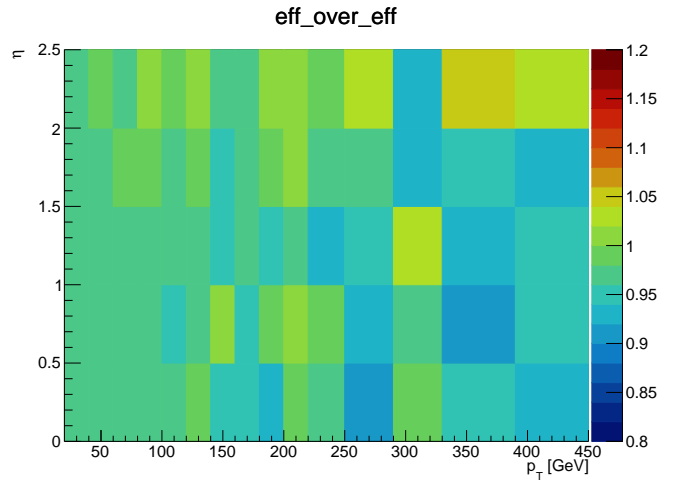


FIGURE B.1 – Ratio between the combined map and the control maps computed for  $b$ -jets in (a - c) the 1-lepton channel and (b - d) the 2-lepton channel. The top maps refer to Powheg+Pythia while the bottom maps are for Sherpa.

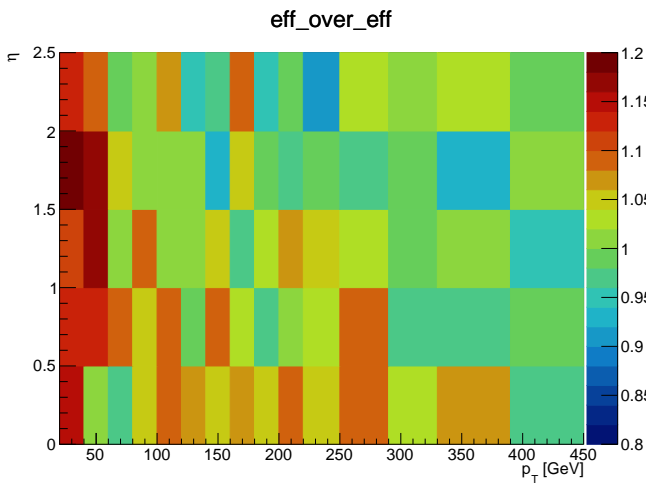




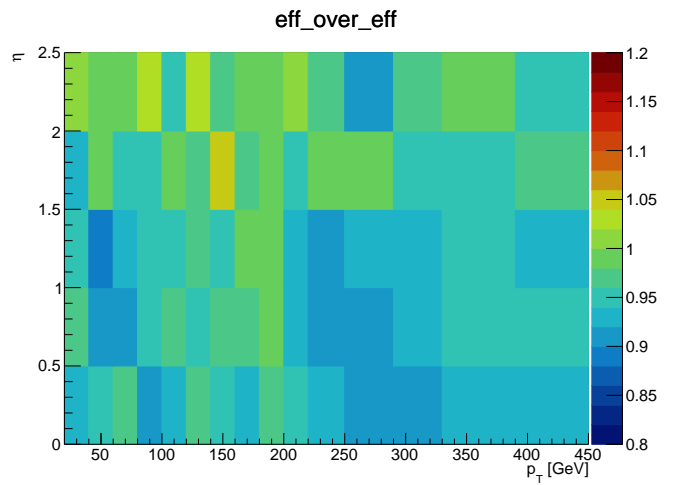
(a) Powheg+Pythia (2015-2016)



(b) Powheg+Pythia (2018)



(c) Sherpa (2015-2016)



(d) Sherpa (2018)

FIGURE B.2 – Ratio between the combined map and the control maps computed using only the 2015-2016 datasets (left) and the 2018 dataset (right) for *light-jets*. The top maps refer to Powheg+Pythia while the bottom maps are for Sherpa.

## B.2 Zero-lepton validation plots

Some examples of validation plots for the Z+jet samples in the 0-lepton channels, showing the comparison between direct and truth tagged events in some key kinematic variables are shown in Figure B.3. The difference in yields is non-negligible, but looking at the plots is visible that this difference comes from non-negligible fluctuations in the direct-tagged sample, which are smoothed away when using a full hybrid tagging approach.

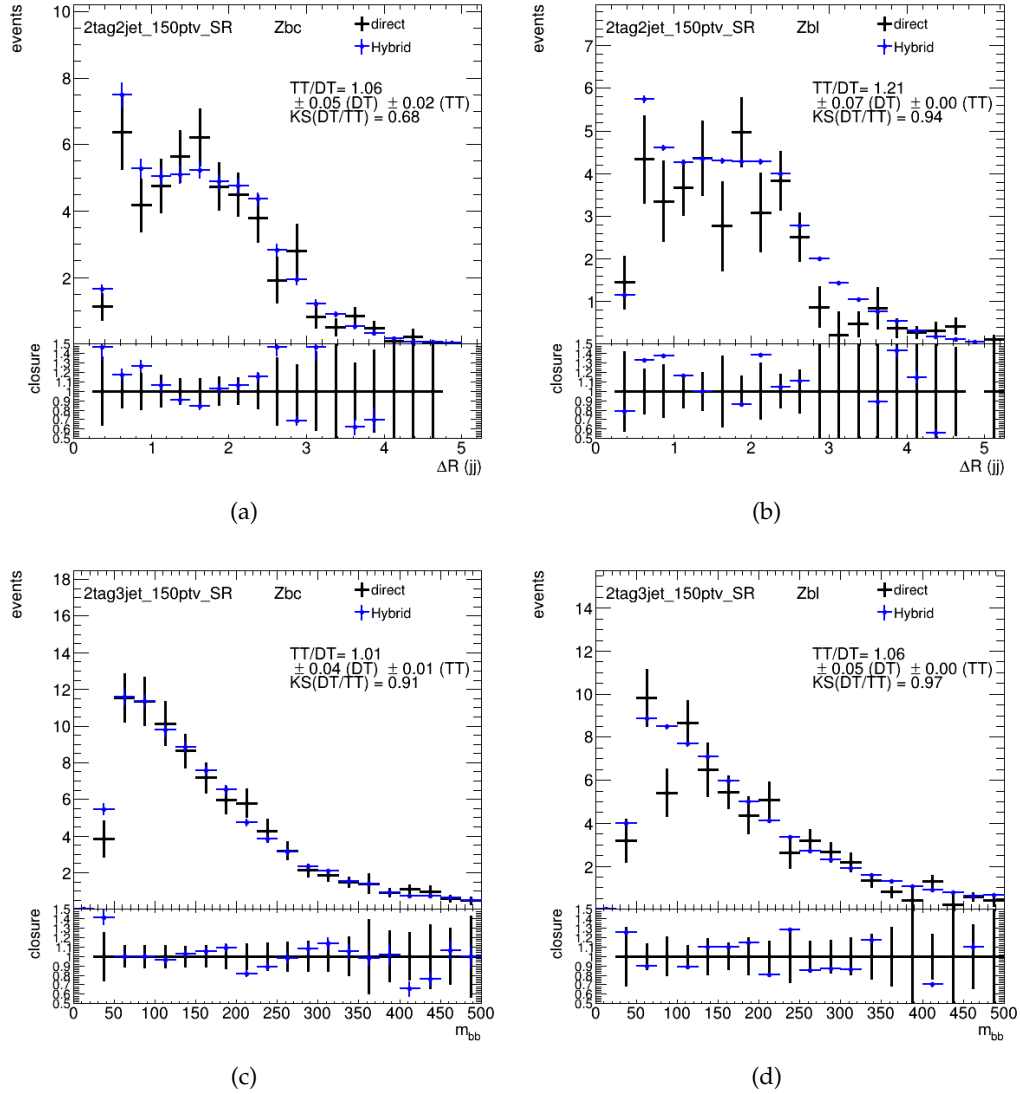


FIGURE B.3 – (a)  $\Delta R(\text{jet}, \text{jet})$  distribution in 2-tag 2-jet SR Z + bc events, (b)  $\Delta R(\text{jet}, \text{jet})$  distribution in 2-tag 2-jet SR Z + bl events, (c)  $m_{bb}$  distribution in 2-tag 3-jet SR Z + bc events and (d)  $m_{bb}$  distribution in 2-tag 3-jet SR Z + bl events using (black) direct tagging compared to (blue) the hybrid tagging computed with the new customized efficiency maps.

### B.3 Yield tables for different tagging regimes

This Section shows a more detailed comparison of the yields and their related errors in the two tagging regimes: the "ICHEP-Style" tagging, where the statistical tagging is used only for V+cc, V+cl and V+l samples, and the "Hybrid" tagging in which the statistical tagging is used for all the c- and light-jets in the event. The differences in the yields is given by a reduction of the statistical fluctuations and in most cases is covered by the statistical uncertainties of direct tagging. The yields in the two singal regions 2-tag 2-jet and 2-tag 3-jet are showed in Figure B.1 and B.2 respectively.

sample	ICHEPStyle		Hybrid tag	
	yields	error	yields	error
data	13254.0000	$\pm 115.1260$	13254.0000	$\pm 115.126$
ggZllH125	0.3709	$\pm 0.0122$	0.8042	$\pm 0.2332$
qqZvvH125	0.0041	$\pm 0.0030$	0.0044	$\pm 0.0030$
qqZllH125	1.9454	$\pm 0.0190$	1.9474	$\pm 0.0188$
qqWlvH125	115.9121	$\pm 0.2388$	115.9361	$\pm 0.2379$
ggZvvH125	0.0000	$\pm 0.0000$	0.0001	$\pm 0.0001$
WW	12.5579	$\pm 3.4871$	8.7364	$\pm 0.3386$
ZZ	8.5995	$\pm 0.3078$	8.7286	$\pm 0.2745$
WZ	173.5595	$\pm 2.4720$	173.3796	$\pm 2.2171$
Wl	44.6802	$\pm 1.4069$	45.3436	$\pm 0.0732$
Wcl	166.6967	$\pm 2.5569$	166.7397	$\pm 0.3548$
Wbb	1728.5203	$\pm 16.9439$	1728.0953	$\pm 16.943$
Wcc	198.8104	$\pm 2.5223$	199.6272	$\pm 1.5061$
Wbl	153.3839	$\pm 6.4058$	157.7349	$\pm 0.4997$
Wbc	278.6052	$\pm 7.9744$	297.2878	$\pm 2.4629$
Zl	2.5351	$\pm 0.1414$	2.4255	$\pm 0.0197$
Zcc	7.0323	$\pm 0.2574$	6.6288	$\pm 0.2042$
Zbl	11.6557	$\pm 1.7913$	11.0889	$\pm 0.3048$
Zbb	136.8253	$\pm 3.3241$	136.8253	$\pm 3.3241$
Zcl	4.9915	$\pm 0.4721$	4.1121	$\pm 0.0759$
Zbc	8.7381	$\pm 0.9770$	8.8920	$\pm 0.3181$
ttbar	8148.8335	$\pm 26.9484$	8242.9580	$\pm 25.1407$
stopWt	862.9928	$\pm 13.5861$	853.9300	$\pm 10.7041$
stopt	975.7306	$\pm 18.6347$	970.8962	$\pm 17.7270$
stops	327.5535	$\pm 3.2449$	327.7739	$\pm 3.2334$
Total Bkgd	13252.7529	$\pm 0.3119$	13352.1670	$\pm 0.2786$

TABLE B.1 – Yield and Statistical errors comparison of the 2-tag 2-jet signal region in the 1-lepton channel using the 2015-2017 dataset at  $80 \text{ fb}^{-1}$ . The left columns are extracted from the "ICHEP Style" tagging, while the two right-most colimns are taken from a full hybrid dataset.

### B.4 Pruned uncertainties in the pseudo-continuous WP

To better handle the systematic variations in the final fit when moving to pseudo-continuous b-tagging, an ad-hoc pruning has been implemented. The criteria are applied to three tag-weight bins: [100-70]%, [70-60]% and [60-0]%. Figure B.4 show

sample	ICHEPStyle		Hybrid tag	
	yields	error	yields	error
data	68362.0000	$\pm 261.4613$	0.8042	$\pm 0.2332$
ggZllH125	0.7794	$\pm 0.0176$	0.0044	$\pm 0.0030$
qqZvvH125	0.0018	$\pm 0.0008$	1.9474	$\pm 0.0188$
qqZllH125	2.7217	$\pm 0.0231$	115.9361	$\pm 0.2379$
qqWlvH125	108.4877	$\pm 0.2375$	0.0001	$\pm 0.0001$
WW	33.5761	$\pm 3.7166$	8.7364	$\pm 0.3386$
ggZZ	0.8544	$\pm 0.1728$	0.9621	$\pm 0.1716$
ZZ	12.0668	$\pm 0.4177$	8.7286	$\pm 0.2745$
WZ	287.3037	$\pm 3.2966$	173.3796	$\pm 2.2171$
Wl	87.7770	$\pm 2.1481$	45.3436	$\pm 0.0732$
Wcl	308.7161	$\pm 3.4464$	166.7397	$\pm 0.3548$
Wbb	3720.0876	$\pm 25.8556$	1728.0953	$\pm 16.9438$
Wcc	387.4063	$\pm 3.7075$	199.6272	$\pm 1.5061$
Wbl	317.6732	$\pm 9.6608$	157.7349	$\pm 0.4997$
Wbc	575.8297	$\pm 12.0540$	297.2878	$\pm 2.4629$
Zl	5.6938	$\pm 0.3547$	2.4255	$\pm 0.0197$
Zcc	15.2022	$\pm 0.4598$	6.6288	$\pm 0.2042$
Zbl	26.2434	$\pm 1.8006$	11.0889	$\pm 0.3048$
Zbb	303.7503	$\pm 4.8905$	136.8253	$\pm 3.3241$
Zcl	10.9314	$\pm 0.3994$	4.1121	$\pm 0.0759$
Zbc	20.5199	$\pm 1.3009$	8.8920	$\pm 0.3181$
ttbar	56180.4306	$\pm 75.6459$	8242.9580	$\pm 25.1407$
stopWt	4139.0257	$\pm 31.4622$	853.9300	$\pm 10.7041$
stopt	4684.2314	$\pm 38.8028$	970.8962	$\pm 17.7270$
stops	448.3102	$\pm 3.7752$	327.7739	$\pm 3.2334$
Total Bkgd	71565.6250	$\pm 0.1342$	13352.167	$\pm 0.2786$

TABLE B.2 – Yield and Statistical errors comparison of the 2-tag 3-jet signal region in the 1-lepton channel using the 2015-2017 dataset at  $80 \text{ fb}^{-1}$ . The left columns are extracted from the "ICHEP Style" tagging, while the two right-most columns are taken from a full hybrid dataset.

further examples for b-, c- and light- variations which fulfill the requirement of 1% everywhere, and so have been pruned. Figure B.5 shows the efficiency maps which have been used to do the reweighting. They have been calculated inclusively in  $\eta$  and with the same binning as the flavour tagging calibrations for each flavour.

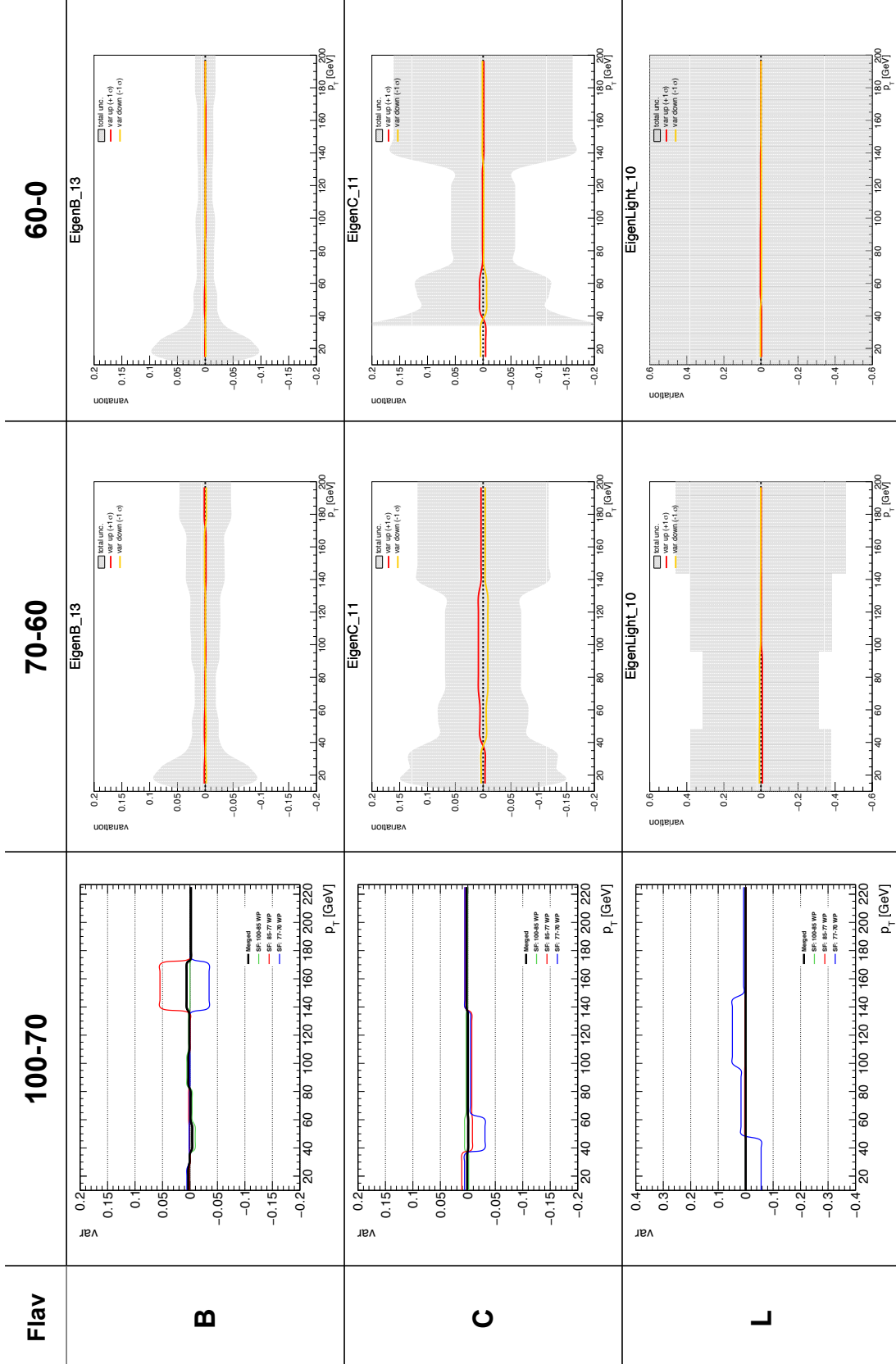


FIGURE B.4 – Examples of pruned variations for b- (top), c- (middle) and light-jets (bottom). The 2-D projection in the three tag-weight bins of interest is explicated, with decreasing efficiency from left to right. The variations have been picked randomly among the pruned ones.

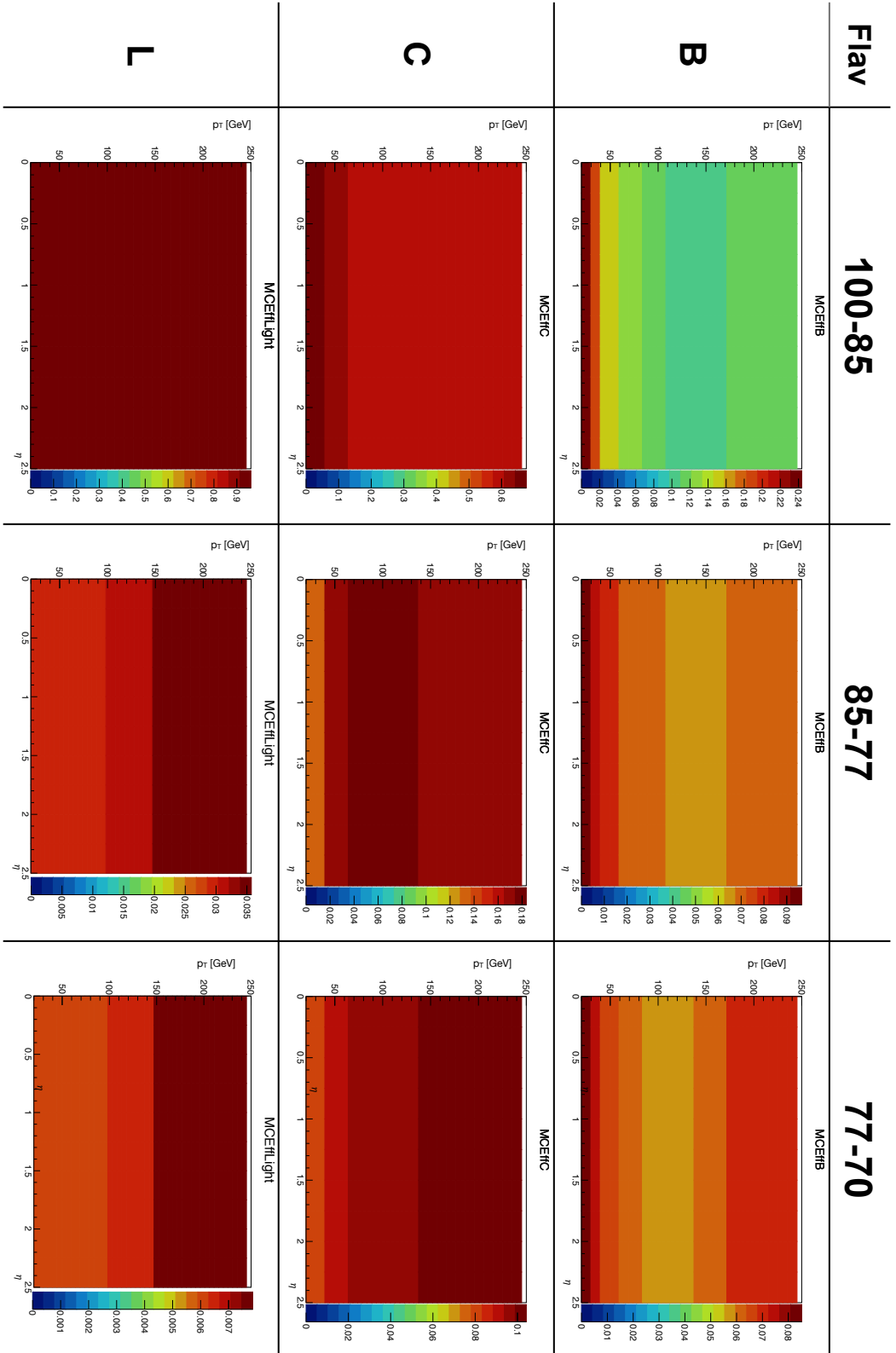


FIGURE B.5 – Efficiency maps used to implement the weighted average of the eigenvalues in the [100-70]% bin. The maps have been computed inclusively in  $\eta$  and with the same  $p_T$  binning of the flavour tagging calibration for each flavour.

# Bibliography

- [1] J.J. Thomson. “Cathode Rays”. In: *Philosophical Magazine Letters* 87.5 (2007), pp. 303–326. DOI: [10.1080/09500830701306165](https://doi.org/10.1080/09500830701306165). eprint: <https://doi.org/10.1080/09500830701306165>.
- [2] E. Rutherford. “The scattering of  $\alpha$  and  $\beta$  particles by matter and the structure of the atom”. In: *The London, Edinburgh, and Dublin Philosophical Magazine and Journal of Science* 21.125 (1911), pp. 669–688. DOI: [10.1080/14786440508637080](https://doi.org/10.1080/14786440508637080). eprint: <https://doi.org/10.1080/14786440508637080>. URL: <https://doi.org/10.1080/14786440508637080>.
- [3] J. D. Cockcroft and E. T. S. Walton. “Experiments with High Velocity Positive Ions. (I) Further Developments in the Method of Obtaining High Velocity Positive Ions”. In: *Proceedings of the Royal Society of London Series A* 136 (June 1932), pp. 619–630. DOI: [10.1098/rspa.1932.0107](https://doi.org/10.1098/rspa.1932.0107).
- [4] W. Gerlach and O. Stern. *Das magnetische Moment des Silberatoms*. Ed. by Hans-Reinhard Bachmann and Helmut Rechenberg. Berlin, Heidelberg: Springer Berlin Heidelberg, 1989, pp. 30–32. ISBN: 978-3-642-74813-4. DOI: [10.1007/978-3-642-74813-4\\_5](https://doi.org/10.1007/978-3-642-74813-4_5). URL: [https://doi.org/10.1007/978-3-642-74813-4\\_5](https://doi.org/10.1007/978-3-642-74813-4_5).
- [5] G. Aad et al. “Measurements of Higgs boson production and couplings in diboson final states with the ATLAS detector at the LHC”. In: *Phys. Lett. B* 726 (2013). [Erratum: *Phys. Lett. B* 734, 406 (2014)], pp. 88–119. DOI: [10.1016/j.physletb.2014.05.011](https://doi.org/10.1016/j.physletb.2014.05.011), [10.1016/j.physletb.2013.08.010](https://doi.org/10.1016/j.physletb.2013.08.010). arXiv: [1307.1427](https://arxiv.org/abs/1307.1427) [hep-ex].
- [6] S. Chatrchyan et al. “Observation of a new boson at a mass of 125 GeV with the CMS experiment at the LHC”. In: *Phys. Lett. B* 716 (2012), pp. 30–61. DOI: [10.1016/j.physletb.2012.08.021](https://doi.org/10.1016/j.physletb.2012.08.021). arXiv: [1207.7235](https://arxiv.org/abs/1207.7235) [hep-ex].
- [7] F. Englert and R. Brout. “Broken Symmetry and the Mass of Gauge Vector Mesons”. In: *Phys. Rev. Lett.* 13 (1964), pp. 321–323. DOI: [10.1103/PhysRevLett.13.321](https://doi.org/10.1103/PhysRevLett.13.321).
- [8] P. W. Higgs. “Broken Symmetries and the Masses of Gauge Bosons”. In: *Phys. Rev. Lett.* 13 (1964), pp. 508–509. DOI: [10.1103/PhysRevLett.13.508](https://doi.org/10.1103/PhysRevLett.13.508).
- [9] G. Aad et al. “Measurements of the Higgs boson production and decay rates and constraints on its couplings from a combined ATLAS and CMS analysis of the LHC pp collision data at  $\sqrt{s} = 7$  and 8 TeV”. In: *JHEP* 08 (2016), p. 045. DOI: [10.1007/JHEP08\(2016\)045](https://doi.org/10.1007/JHEP08(2016)045). arXiv: [1606.02266](https://arxiv.org/abs/1606.02266) [hep-ex].
- [10] M. Aaboud et al. “Observation of Higgs boson production in association with a top quark pair at the LHC with the ATLAS detector”. In: *Phys. Lett. B* 784 (2018), pp. 173–191. DOI: [10.1016/j.physletb.2018.07.035](https://doi.org/10.1016/j.physletb.2018.07.035). arXiv: [1806.00425](https://arxiv.org/abs/1806.00425) [hep-ex].



- [11] A. M. Sirunyan et al. "Observation of  $t\bar{t}H$  production". In: *Phys. Rev. Lett.* 120.23 (2018), p. 231801. DOI: [10.1103/PhysRevLett.120.231801](https://doi.org/10.1103/PhysRevLett.120.231801). arXiv: [1804.02610](https://arxiv.org/abs/1804.02610) [hep-ex].
- [12] Frank Tackmann et al. "Simplified template cross sections". In: (Mar. 2016). URL: <https://cds.cern.ch/record/2138079>.
- [13] G. Arnison et al. "Experimental Observation of Isolated Large Transverse Energy Electrons with Associated Missing Energy at  $s^{1/2} = 540\text{-GeV}$ ". In: *Phys. Lett.* B122 (1983). [611(1983)], pp. 103–116. DOI: [10.1016/0370-2693\(83\)91177-2](https://doi.org/10.1016/0370-2693(83)91177-2).
- [14] G. Arnison et al. "Experimental Observation of Lepton Pairs of Invariant Mass Around  $95\text{-GeV}/c^2$  at the CERN SPS Collider". In: *Phys. Lett.* B126 (1983). [7.55(1983)], pp. 398–410. DOI: [10.1016/0370-2693\(83\)90188-0](https://doi.org/10.1016/0370-2693(83)90188-0).
- [15] P. Bagnaia et al. "Evidence for  $Z \rightarrow e^+e^-$  at the CERN anti-p p Collider". In: *Phys. Lett.* B129 (1983). [7.69(1983)], pp. 130–140. DOI: [10.1016/0370-2693\(83\)90744-X](https://doi.org/10.1016/0370-2693(83)90744-X).
- [16] F. Abe et al. "Observation of top quark production in  $\bar{p}p$  collisions". In: *Phys. Rev. Lett.* 74 (1995), pp. 2626–2631. DOI: [10.1103/PhysRevLett.74.2626](https://doi.org/10.1103/PhysRevLett.74.2626). arXiv: [hep-ex/9503002](https://arxiv.org/abs/hep-ex/9503002) [hep-ex].
- [17] S. Abachi et al. "Observation of the top quark". In: *Phys. Rev. Lett.* 74 (1995), pp. 2632–2637. DOI: [10.1103/PhysRevLett.74.2632](https://doi.org/10.1103/PhysRevLett.74.2632). arXiv: [hep-ex/9503003](https://arxiv.org/abs/hep-ex/9503003) [hep-ex].
- [18] F. Halzen and Alan D. Martin. *Quarks and Leptons: An introductory course in Modern Particle Physics*. 1984.
- [19] Philip G. Ratcliffe. *An Introduction to Elementary Particle Phenomenology*. 2053-2563. IOP Publishing, 2014. DOI: [10.1088/978-0-7503-1072-7](https://doi.org/10.1088/978-0-7503-1072-7). URL: <http://dx.doi.org/10.1088/978-0-7503-1072-7>.
- [20] C. Patrignani et al. "Review of Particle Physics". In: *Chin. Phys.* C40.10 (2016), p. 100001. DOI: [10.1088/1674-1137/40/10/100001](https://doi.org/10.1088/1674-1137/40/10/100001).
- [21] J. C. Maxwell. "A dynamical theory of the electromagnetic field". In: *Philosophical Transactions of the Royal Society of London* 155 (1865), pp. 459–513.
- [22] S. Mandelstam. "Feynman rules for electromagnetic and Yang-Mills fields from the gauge independent field theoretic formalism". In: *Phys. Rev.* 175 (1968), pp. 1580–1623. DOI: [10.1103/PhysRev.175.1580](https://doi.org/10.1103/PhysRev.175.1580).
- [23] R. P. Feynman. *Quantum Electrodynamics*. Ed. by "Avalon Publishing". "1998", p. 208. DOI: [081334638X](https://doi.org/081334638X), [9780813346380](https://doi.org/9780813346380).
- [24] G. Sardanashvily. *Noether's theorems: applications in mechanics and field theory*. Atlantis studies in variational geometry. Paris: Springer, 2016. DOI: [10.2991/978-94-6239-171-0](https://doi.org/10.2991/978-94-6239-171-0). URL: <https://cds.cern.ch/record/2143630>.
- [25] N. Cabibbo. "Unitary Symmetry and Leptonic Decays". In: *Physical Review Letters* 10 (June 1963), pp. 531–533. DOI: [10.1103/PhysRevLett.10.531](https://doi.org/10.1103/PhysRevLett.10.531).
- [26] Makoto Kobayashi and Toshihide Maskawa. "CP Violation in the Renormalizable Theory of Weak Interaction". In: *Prog. Theor. Phys.* 49 (1973), pp. 652–657. DOI: [10.1143/PTP.49.652](https://doi.org/10.1143/PTP.49.652).
- [27] Y. Fukuda et al. "Evidence for oscillation of atmospheric neutrinos". In: *Phys. Rev. Lett.* 81 (1998), pp. 1562–1567. DOI: [10.1103/PhysRevLett.81.1562](https://doi.org/10.1103/PhysRevLett.81.1562). arXiv: [hep-ex/9807003](https://arxiv.org/abs/hep-ex/9807003) [hep-ex].

- [28] V.M. Lobashev. “The search for the neutrino mass by direct method in the tritium beta-decay and perspectives of study it in the project KATRIN”. In: *Nuclear Physics A* 719 (2003), pp. C153–C160. ISSN: 0375-9474. DOI: [https://doi.org/10.1016/S0375-9474\(03\)00985-0](https://doi.org/10.1016/S0375-9474(03)00985-0). URL: <http://www.sciencedirect.com/science/article/pii/S0375947403009850>.
- [29] B. Pontecorvo. “Inverse beta processes and nonconservation of lepton charge”. In: *Sov. Phys. JETP* 7 (1958), pp. 172–173.
- [30] Z. Maki, M. Nakagawa, and S. Sakata. “Remarks on the unified model of elementary particles”. In: *Prog. Theor. Phys.* 28 (1962), pp. 870–880. DOI: [10.1143/PTP.28.870](https://doi.org/10.1143/PTP.28.870).
- [31] S. L. Glashow. “Partial Symmetries of Weak Interactions”. In: *Nucl. Phys.* 22 (1961), pp. 579–588. DOI: [10.1016/0029-5582\(61\)90469-2](https://doi.org/10.1016/0029-5582(61)90469-2).
- [32] S. Weinberg. “A Model of Leptons”. In: *Phys. Rev. Lett.* 19 (1967), pp. 1264–1266. DOI: [10.1103/PhysRevLett.19.1264](https://doi.org/10.1103/PhysRevLett.19.1264).
- [33] A. Salam. “Weak and Electromagnetic Interactions”. In: *Conf. Proc.* C680519 (1968), pp. 367–377.
- [34] E. Fermi. “Tentativo di una Teoria Dei Raggi  $\beta$ ”. In: *Il Nuovo Cimento* 11 (Jan. 1934), pp. 1–19. DOI: [10.1007/BF02959820](https://doi.org/10.1007/BF02959820).
- [35] Young K. et al. “Theory and Applications of the Poincaré Group”. In: (Jan. 1986). DOI: [10.1007/978-94-009-4558-6](https://doi.org/10.1007/978-94-009-4558-6).
- [36] R. Turra. “Energy calibration and observation of the Higgs boson in the diphoton decay with the ATLAS experiment”. In: 2 (A.Y. 2011/2012).
- [37] Dirac P. and Bohr N. “The quantum theory of the emission and absorption of radiation”. In: *Proceedings of the Royal Society of London. Series A* 114.767 (1927), pp. 243–265. DOI: [10.1098/rspa.1927.0039](https://doi.org/10.1098/rspa.1927.0039).
- [38] J. Orear and E. Fermi. *Nuclear Physics: A Course Given by Enrico Fermi at the University of Chicago*. University of Chicago Press, 1950. URL: <https://books.google.fr/books?id=B9gmAAAAAAAJ>.
- [39] Y. L. Dokshitzer. “Calculation of the Structure Functions for Deep Inelastic Scattering and  $e^+e^-$  Annihilation by Perturbation Theory in Quantum Chromodynamics.” In: *Sov. Phys. JETP* 46 (1977), pp. 641–653.
- [40] V. N. Gribov and L. N. Lipatov. “Deep inelastic  $e p$  scattering in perturbation theory”. In: *Sov. J. Nucl. Phys.* 15 (1972), pp. 438–450.
- [41] G. Altarelli and G. Parisi. “Asymptotic Freedom in Parton Language”. In: *Nucl. Phys.* B126 (1977), pp. 298–318. DOI: [10.1016/0550-3213\(77\)90384-4](https://doi.org/10.1016/0550-3213(77)90384-4).
- [42] Hung-Liang Lai et al. “New parton distributions for collider physics”. In: *Phys. Rev. D* 82 (2010), p. 074024. DOI: [10.1103/PhysRevD.82.074024](https://doi.org/10.1103/PhysRevD.82.074024). arXiv: [1007.2241](https://arxiv.org/abs/1007.2241) [hep-ph].
- [43] Martin Goebel. “Tests of the electroweak standard model and measurement of the weak mixing angle with the ATLAS detector”. Presented 19 Sep 2011. 2011. URL: <https://cds.cern.ch/record/1399668>.
- [44] S. Schael et al. “Precision electroweak measurements on the Z resonance”. In: *Phys. Rept.* 427 (2006), pp. 257–454. DOI: [10.1016/j.physrep.2005.12.006](https://doi.org/10.1016/j.physrep.2005.12.006). arXiv: [hep-ex/0509008](https://arxiv.org/abs/hep-ex/0509008) [hep-ex].

- [45] M. Peskin and D. Schroeder. *An Introduction to quantum field theory*. Reading, USA: Addison-Wesley, 1995. URL: <http://www.slac.stanford.edu/~mpeskin/QFT.html>.
- [46] D. Griffiths. *Introduction to elementary particles*. 2008. ISBN: 9783527406012.
- [47] LEP Collaborations. “A Combination of preliminary electroweak measurements and constraints on the standard model”. In: (2001). arXiv: [hep-ex/0103048](#) [[hep-ex](#)].
- [48] Heinemeyer et al. *Handbook of LHC Higgs Cross Sections: 3. Higgs Properties: Report of the LHC Higgs Cross Section Working Group*. Ed. by S Heinemeyer. CERN Yellow Reports: Monographs. July 2013. URL: <https://cds.cern.ch/record/1559921>.
- [49] D. de Florian et al. “Handbook of LHC Higgs Cross Sections: 4. Deciphering the Nature of the Higgs Sector”. In: (2016). DOI: [10.23731/CYRM-2017-002](#). arXiv: [1610.07922](#) [[hep-ph](#)].
- [50] M. Awramik et al. “Precise prediction for the W boson mass in the standard model”. In: *Phys. Rev. D* 69 (2004), p. 053006. DOI: [10.1103/PhysRevD.69.053006](#). arXiv: [hep-ph/0311148](#) [[hep-ph](#)].
- [51] LEP Electroweak Working Group. “Precision Electroweak Measurements and Constraints on the Standard Model”. In: (2010). arXiv: [1012.2367](#) [[hep-ex](#)].
- [52] The LEP Electroweak Working Group. (visited Sept. 2019). URL: <http://lepewwg.web.cern.ch/LEPEWWG/>.
- [53] “Search for the Standard Model Higgs boson at LEP”. In: *Physics Letters B* 565 (2003), pp. 61–75. ISSN: 0370-2693. DOI: [https://doi.org/10.1016/S0370-2693\(03\)00614-2](https://doi.org/10.1016/S0370-2693(03)00614-2). URL: <http://www.sciencedirect.com/science/article/pii/S0370269303006142>.
- [54] CDF Collaboration and D0 Collaboration. “Evidence for a Particle Produced in Association with Weak Bosons and Decaying to a  $b\bar{b}$  Quark Pair in Higgs Boson Searches at the Tevatron”. In: vol. 109. American Physical Society, Aug. 2012, p. 071804. DOI: [10.1103/PhysRevLett.109.071804](#). URL: <https://link.aps.org/doi/10.1103/PhysRevLett.109.071804>.
- [55] A. M. Sirunyan et al. “Measurements of properties of the Higgs boson decaying into the four-lepton final state in pp collisions at  $\sqrt{s} = 13$  TeV”. In: *JHEP* 11 (2017), p. 047. DOI: [10.1007/JHEP11\(2017\)047](#). arXiv: [1706.09936](#) [[hep-ex](#)].
- [56] M. Aaboud et al. “Measurement of the Higgs boson mass in the  $H \rightarrow ZZ^* \rightarrow 4\ell$  and  $H \rightarrow \gamma\gamma$  channels with  $\sqrt{s} = 13$  TeV pp collisions using the ATLAS detector”. In: *Phys. Lett. B* 784 (2018), pp. 345–366. DOI: [10.1016/j.physletb.2018.07.050](#). arXiv: [1806.00242](#) [[hep-ex](#)].
- [57] G. Aad et al. “Study of the spin and parity of the Higgs boson in diboson decays with the ATLAS detector”. In: *Eur. Phys. J. C* 75.10 (2015), p. 476. DOI: [10.1140/epjc/s10052-015-3685-1](#), [10.1140/epjc/s10052-016-3934-y](#). arXiv: [1506.05669](#) [[hep-ex](#)].
- [58] A. M. Sirunyan et al. “Observation of the Higgs boson decay to a pair of  $\tau$  leptons with the CMS detector”. In: *Phys. Lett. B* 779 (2018), pp. 283–316. DOI: [10.1016/j.physletb.2018.02.004](#). arXiv: [1708.00373](#) [[hep-ex](#)].

- [59] M. Aaboud et al. “Cross-section measurements of the Higgs boson decaying into a pair of  $\tau$ -leptons in proton-proton collisions at  $\sqrt{s} = 13$  TeV with the ATLAS detector”. In: *Phys. Rev. D* 99 (2019), p. 072001. DOI: [10.1103/PhysRevD.99.072001](https://doi.org/10.1103/PhysRevD.99.072001). arXiv: [1811.08856](https://arxiv.org/abs/1811.08856) [hep-ex].
- [60] A. M. Sirunyan et al. “Search for the Higgs boson decaying to two muons in proton-proton collisions at  $\sqrt{s} = 13$  TeV”. In: *Phys. Rev. Lett.* 122.2 (2019), p. 021801. DOI: [10.1103/PhysRevLett.122.021801](https://doi.org/10.1103/PhysRevLett.122.021801). arXiv: [1807.06325](https://arxiv.org/abs/1807.06325) [hep-ex].
- [61] ATLAS Collaboration. *A search for the decay of the Standard Model Higgs boson to dimuons in pp collisions at  $\sqrt{s} = 13$  TeV with the ATLAS Detector*. Tech. rep. ATL-COM-PHYS-2019-690. Geneva: CERN, June 2019. URL: <https://cds.cern.ch/record/2678539>.
- [62] M. Aaboud et al. “Search for the Decay of the Higgs Boson to Charm Quarks with the ATLAS Experiment”. In: *Phys. Rev. Lett.* 120.21 (2018), p. 211802. DOI: [10.1103/PhysRevLett.120.211802](https://doi.org/10.1103/PhysRevLett.120.211802). arXiv: [1802.04329](https://arxiv.org/abs/1802.04329) [hep-ex].
- [63] *Search for the standard model Higgs boson decaying to charm quarks*. Tech. rep. CMS-PAS-HIG-18-031. Geneva: CERN, 2019. URL: <https://cds.cern.ch/record/2682638>.
- [64] The ATLAS collaboration. *Combined measurements of Higgs boson production and decay using up to  $80\text{ fb}^{-1}$  of proton-proton collision data at  $\sqrt{s} = 13$  TeV collected with the ATLAS experiment*. Tech. rep. ATLAS-CONF-2019-005. Geneva: CERN, Mar. 2019. URL: <https://cds.cern.ch/record/2668375>.
- [65] J. D. Wells. “Higgs naturalness and the scalar boson proliferation instability problem”. In: *Synthese* 194.2 (2017), pp. 477–490. DOI: [10.1007/s11229-014-0618-8](https://doi.org/10.1007/s11229-014-0618-8). arXiv: [1603.06131](https://arxiv.org/abs/1603.06131) [hep-ph].
- [66] E. Komatsu, K. M. Smith, et al. “Seven-year Wilkinson Microwave Anisotropy Probe (WMAP) Observations: Cosmological Interpretation”. In: *The Astrophysical Journal Supplement Series* 192.2 (Jan. 2011), p. 18. DOI: [10.1088/0067-0049/192/2/18](https://doi.org/10.1088/0067-0049/192/2/18). URL: <https://doi.org/10.1088/0067-0049/192/2/18>.
- [67] L. Canetti, M. Drewes, and M. Shaposhnikov. “Matter and Antimatter in the Universe”. In: *New J. Phys.* 14 (2012), p. 095012. DOI: [10.1088/1367-2630/14/9/095012](https://doi.org/10.1088/1367-2630/14/9/095012). arXiv: [1204.4186](https://arxiv.org/abs/1204.4186) [hep-ph].
- [68] Keith A. Olive, Gary Steigman, and Terry P. Walker. “Primordial nucleosynthesis: Theory and observations”. In: *Phys. Rept.* 333 (2000), pp. 389–407. DOI: [10.1016/S0370-1573\(00\)00031-4](https://doi.org/10.1016/S0370-1573(00)00031-4). arXiv: [astro-ph/9905320](https://arxiv.org/abs/astro-ph/9905320) [astro-ph].
- [69] A. D. Sakharov. “Violation of CP Invariance, C asymmetry, and baryon asymmetry of the universe”. In: *Pisma Zh. Eksp. Teor. Fiz.* 5 (1967), pp. 32–35. DOI: [10.1070/PU1991v034n05ABEH002497](https://doi.org/10.1070/PU1991v034n05ABEH002497).
- [70] G. Abbas. “Solving the fermionic mass hierarchy of the standard model”. In: (2017). arXiv: [1712.08052](https://arxiv.org/abs/1712.08052) [hep-ph].
- [71] P. Ramond. “Fermion masses and multiplicity”. In: *Comments Nucl. Part. Phys.* 16.1 (1986), pp. 1–21.
- [72] ATLAS Collaboration. “The ATLAS Simulation Infrastructure”. In: *Eur. Phys. J. C* 70.3 (2010), p. 823874. DOI: [10.1140/epjc/s10052-010-1429-9](https://doi.org/10.1140/epjc/s10052-010-1429-9).

- [73] S. Alioli et al. “Monte Carlo event generators for high energy particle physics event simulation”. In: (2019). Ed. by Andy Buckley et al. arXiv: [1902.01674 \[hep-ph\]](#).
- [74] J. C. Collins. “Sudakov form-factors”. In: *Adv. Ser. Direct. High Energy Phys.* 5 (1989), pp. 573–614. DOI: [10.1142/9789814503266\\_0006](#). arXiv: [hep-ph/0312336 \[hep-ph\]](#).
- [75] T. Sjostrand. “Monte Carlo Generators”. In: *High-energy physics. Proceedings, European School, Aronsborg, Sweden, June 18–July 1, 2006*. 2006, pp. 51–74. arXiv: [hep-ph/0611247 \[hep-ph\]](#). URL: <http://weblib.cern.ch/abstract?CERN-LCGAPP-2006-06>.
- [76] P. Skands. “Introduction to QCD”. In: *Proceedings, AEP SHEP 2014: Puri, India, November 04–17, 2014*. 2013, pp. 341–420. DOI: [10.1142/9789814525220\\_0008](#), [10.23730/CYRSP-2017-002.63](#). arXiv: [1207.2389 \[hep-ph\]](#).
- [77] A. amd Butterworth J. Buckley et al. “General-purpose event generators for LHC physics”. In: *Physics Reports* 504.5 (2011), pp. 145–233. ISSN: 0370-1573. DOI: <https://doi.org/10.1016/j.physrep.2011.03.005>. URL: <http://www.sciencedirect.com/science/article/pii/S0370157311000846>.
- [78] T. Sjöstrand, S. Mrenna, and P. Skands. “A brief introduction to PYTHIA 8.1”. In: *Computer Physics Communications* 178.11 (2008), pp. 852–867. ISSN: 0010-4655. DOI: <https://doi.org/10.1016/j.cpc.2008.01.036>. URL: <http://www.sciencedirect.com/science/article/pii/S0010465508000441>.
- [79] *ATLAS Run 1 Pythia8 tunes*. Tech. rep. ATL-PHYS-PUB-2014-021. Geneva: CERN, Nov. 2014. URL: <https://cds.cern.ch/record/1966419>.
- [80] T. Gleisberg, Shöche, et al. “Event generation with SHERPA 1.1”. In: *Journal of High Energy Physics* 2009.02 (Feb. 2009), pp. 007–007. DOI: [10.1088/1126-6708/2009/02/007](#). URL: <https://doi.org/10.1088%2F1126-6708%2F2009%2F02%2F007>.
- [81] J. Bellm et al. “Herwig 7.0/Herwig++ 3.0 release note”. In: *Eur. Phys. J. C* 76.4 (2016), p. 196. DOI: [10.1140/epjc/s10052-016-4018-8](#). arXiv: [1512.01178 \[hep-ph\]](#).
- [82] Nason P. Luisoni G. et al. “HW  $\pm$ /HZ + 0 and 1 jet at NLO with the POWHEG BOX interfaced to GoSam and their merging within MiNLO”. In: *J. High Energ. Phys.* 2013: 83 (2013.). DOI: [https://doi.org/10.1007/JHEP10\(2013\)083](https://doi.org/10.1007/JHEP10(2013)083). URL: <https://link.springer.com/article/10.1007%2FJHEP10%282013%29083>.
- [83] J. Alwall, R. Frederix, et al. “The automated computation of tree-level and next-to-leading order differential cross sections, and their matching to parton shower simulations”. In: *JHEP* 07 (2014), p. 079. DOI: [10.1007/JHEP07\(2014\)079](#). arXiv: [1405.0301 \[hep-ph\]](#).
- [84] L. V. de Broglie and P. Raymond. “Recherches sur la théorie des quanta”. In: *Annals Phys.* 2 (1925), pp. 22–128.
- [85] T. Aushev et al. “Physics at Super B Factory”. In: (2010). arXiv: [1002.5012 \[hep-ex\]](#).



- [86] A. Einstein. "Ist die Trägheit eines Körpers von seinem Energieinhalt abhängig?" In: *Annalen der Physik* 323.13 (1905), pp. 639–641. DOI: [10.1002/andp.19053231314](https://doi.org/10.1002/andp.19053231314). eprint: <https://onlinelibrary.wiley.com/doi/pdf/10.1002/andp.19053231314>. URL: <https://onlinelibrary.wiley.com/doi/abs/10.1002/andp.19053231314>.
- [87] L. Evans and P. Bryant. "LHC Machine". In: *Journal of Instrumentation* 3.08 (Aug. 2008), S08001–S08001. DOI: [10.1088/1748-0221/3/08/s08001](https://doi.org/10.1088/1748-0221/3/08/s08001). URL: <https://doi.org/10.1088/1748-0221/3/08/s08001>.
- [88] S. Holmes, R. Moore, and V. Shiltsev. "Overview of the Tevatron collider complex: goals, operations and performance". In: *Journal of Instrumentation* 6.08 (Aug. 2011), T08001–T08001. DOI: [10.1088/1748-0221/6/08/t08001](https://doi.org/10.1088/1748-0221/6/08/t08001). URL: <https://doi.org/10.1088/1748-0221/6/08/t08001>.
- [89] S Fartoukh et al. "Experimental validation of the Achromatic Telescopic Squeezing (ATS) scheme at the LHC". In: *J. Phys. : Conf. Ser.* 874.CERN-ACC-2017-328. 1 (2017), 012010. 7 p. DOI: [10.1088/1742-6596/874/1/012010](https://doi.org/10.1088/1742-6596/874/1/012010). URL: <https://cds.cern.ch/record/2275964>.
- [90] L Rossi. "The LHC Main Dipoles and Quadrupoles toward Series Production". In: *IEEE Trans. Appl. Supercond.* 13.CERN-LHC-Project-Report-623 (Dec. 2002), 1221–1228. 9 p. URL: <https://cds.cern.ch/record/599389>.
- [91] Rende Steerenberg. "Batch Compression Merging and Splitting (BCMS). Batch Compression Merging and Splitting (BCMS)". In: (Apr. 2017). General Photo. URL: <http://cds.cern.ch/record/2259071>.
- [92] K. Aamodt et al. "The ALICE experiment at the CERN LHC". In: *JINST* 3 (2008), S08002. DOI: [10.1088/1748-0221/3/08/S08002](https://doi.org/10.1088/1748-0221/3/08/S08002).
- [93] G. Aad et al. "The ATLAS Experiment at the CERN Large Hadron Collider". In: *JINST* 3 (2008), S08003. DOI: [10.1088/1748-0221/3/08/S08003](https://doi.org/10.1088/1748-0221/3/08/S08003).
- [94] S. Chatrchyan et al. "The CMS Experiment at the CERN LHC". In: *JINST* 3 (2008), S08004. DOI: [10.1088/1748-0221/3/08/S08004](https://doi.org/10.1088/1748-0221/3/08/S08004).
- [95] The LHCb Collaboration. "The LHCb Detector at the LHC". In: *Journal of Instrumentation* 3.08 (Aug. 2008), S08005–S08005. DOI: [10.1088/1748-0221/3/08/s08005](https://doi.org/10.1088/1748-0221/3/08/s08005). URL: <https://doi.org/10.1088/1748-0221/3/08/s08005>.
- [96] "ATLAS magnet system: Technical design report". In: (1997).
- [97] R. Wigmans. "Calorimetry: Energy measurement in particle physics". In: *Int. Ser. Monogr. Phys.* 107 (2000), pp. 1–726.
- [98] *ATLAS inner detector: Technical Design Report, 1*. Technical Design Report ATLAS. Geneva: CERN, 1997. URL: <https://cds.cern.ch/record/331063>.
- [99] G. Aad et al. "Electron and photon energy calibration with the ATLAS detector using LHC Run 1 data". In: *Eur. Phys. J. C* 74.10 (2014), p. 3071. DOI: [10.1140/epjc/s10052-014-3071-4](https://doi.org/10.1140/epjc/s10052-014-3071-4). arXiv: [1407.5063](https://arxiv.org/abs/1407.5063) [hep-ex].
- [100] G.Aad et al. "ATLAS pixel detector electronics and sensors". In: *Journal of Instrumentation* 3.07 (July 2008), P07007–P07007. DOI: [10.1088/1748-0221/3/07/p07007](https://doi.org/10.1088/1748-0221/3/07/p07007). URL: <https://doi.org/10.1088/1748-0221/3/07/p07007>.
- [101] M Capeans, G. Darbo, et al. *ATLAS Insertable B-Layer Technical Design Report*. Tech. rep. CERN-LHCC-2010-013. ATLAS-TDR-19. Sept. 2010. URL: <https://cds.cern.ch/record/1291633>.

- [102] C. Da Via, Boscardin M., et al. “3D silicon sensors: Design, large area production and quality assurance for the ATLAS IBL pixel detector upgrade”. In: *Nuclear Instruments and Methods, Section A* 694 (2012), pp. 321–330. ISSN: 0168-9002. DOI: <https://doi.org/10.1016/j.nima.2012.07.058>. URL: <http://www.sciencedirect.com/science/article/pii/S0168900212008509>.
- [103] *IBL Efficiency and Single Point Resolution in Collision Events*. Tech. rep. ATL-INDET-PUB-2016-001. Geneva: CERN, Aug. 2016. URL: <https://cds.cern.ch/record/2203893>.
- [104] Troncon C. “Radiation hardness performance of ATLAS pixel tracker”. In: *Nuclear Instruments and Methods, Section A* 530.1 (2004). Proceeding, pp. 65–70. ISSN: 0168-9002. DOI: <https://doi.org/10.1016/j.nima.2004.05.049>. URL: <http://www.sciencedirect.com/science/article/pii/S0168900204010356>.
- [105] M. Aaboud et al. “Modelling radiation damage to pixel sensors in the ATLAS detector”. In: *Submitted to: JINST* (2019). arXiv: [1905.03739](https://arxiv.org/abs/1905.03739) [[physics.ins-det](https://arxiv.org/archive/physics)].
- [106] The ATLAS collaboration. “Operation and performance of the ATLAS semiconductor tracker”. In: *Journal of Instrumentation* 9.08 (Aug. 2014), P08009–P08009. DOI: [10.1088/1748-0221/9/08/p08009](https://doi.org/10.1088/1748-0221/9/08/p08009). URL: <https://doi.org/10.1088/1748-0221/9/08/p08009>.
- [107] A Vogel. *ATLAS Transition Radiation Tracker (TRT): Straw Tube Gaseous Detectors at High Rates*. Tech. rep. ATL-INDET-PROC-2013-005. Geneva: CERN, Apr. 2013. URL: <https://cds.cern.ch/record/1537991>.
- [108] A. Airapetian et al. “ATLAS calorimeter performance Technical Design Report”. In: (1996).
- [109] G. Unal et al. “Electron and Photon energy resolutions and their uncertainties for the Run I calibration”. In: *ATL-COM-PHYS-2013-1651* (2013). URL: <https://cds.cern.ch/record/1637528>.
- [110] The ATLAS Collaboration. “Readiness of the ATLAS Tile Calorimeter for LHC collisions. Readiness of the ATLAS Tile Calorimeter for LHC collisions”. In: *Eur. Phys. J. C* 70. arXiv:1007.5423. CERN-PH-EP-2010-024 (July 2010), 1193–1236. 64 p. DOI: [10.1140/epjc/s10052-010-1508-y](https://cds.cern.ch/record/1282535). URL: <https://cds.cern.ch/record/1282535>.
- [111] ATLAS Collaboration. “Electron and photon energy calibration with the ATLAS detector using data collected in 2015 at  $\sqrt{s} = 13$  TeV”. In: *ATL-PHYS-PUB-2016-015* (Aug. 2016). URL: <https://cds.cern.ch/record/2203514>.
- [112] M. Aharrouché et al. “Energy linearity and resolution of the ATLAS electromagnetic barrel calorimeter in an electron test-beam”. In: *Nuclear Instruments and Methods in Physics Research A* 568 (Dec. 2006), pp. 601–623. DOI: [10.1016/j.nima.2006.07.053](https://doi.org/10.1016/j.nima.2006.07.053). eprint: [physics/0608012](https://arxiv.org/abs/hep-ex/0608012).
- [113] “ATLAS tile calorimeter: Technical design report”. In: (1996).
- [114] T. Barillari. “The ATLAS liquid argon hadronic end-cap calorimeter: construction and selected beam test results”. In: *Nuclear Physics B - Proceedings Supplements* 150 (2006). Proceeding, pp. 102–105. ISSN: 0920-5632. DOI: <https://doi.org/10.1016/j.nuclphysbps.2004.10.087>. URL: <http://www.sciencedirect.com/science/article/pii/S0920563205008194>.
- [115] *ATLAS muon spectrometer: Technical Design Report*. Technical Design Report ATLAS. Geneva: CERN, 1997. URL: <https://cds.cern.ch/record/331068>.



- [116] *Technical Design Report for the Phase-I Upgrade of the ATLAS TDAQ System*. CERN-LHCC-2013-018. ATLAS-TDR-023. Sept. 2013. URL: <https://cds.cern.ch/record/1602235>.
- [117] *ATLAS level-1 trigger: Technical Design Report*. Technical Design Report ATLAS. Geneva: CERN, 1998. URL: <https://cds.cern.ch/record/381429>.
- [118] Collaboration ATLAS. *ATLAS High-Level Trigger, Data Acquisition and Controls Technical Design Report*. eng. Vol. ATLAS TDR-016. ATLAS Technical Design Reports. 2003, p. 369.
- [119] V. Cindro et al. "The ATLAS Beam Conditions Monitor". In: *Journal of Instrumentation* 3.02 (Feb. 2008), P02004–P02004. DOI: 10.1088/1748-0221/3/02/p02004. URL: <https://doi.org/10.1088/1748-0221/3/02/p02004>.
- [120] M. Aaboud et al. "Luminosity determination in pp collisions at  $\sqrt{s} = 8$  TeV using the ATLAS detector at the LHC". In: *Eur. Phys. J. C* 76.12 (2016), p. 653. DOI: 10.1140/epjc/s10052-016-4466-1. arXiv: 1608.03953 [hep-ex].
- [121] M. Aaboud et al. "Performance of the ATLAS track reconstruction algorithms in dense environments in LHC Run 2". In: *The European Physical Journal C* 77.10 (Oct. 2017), p. 673. ISSN: 1434-6052. DOI: 10.1140/epjc/s10052-017-5225-7. URL: <https://doi.org/10.1140/epjc/s10052-017-5225-7>.
- [122] P. Zarchan and H. Musoff. *Fundamentals of Kalman Filtering: A Practical Approach*. Fundamentals of Kalman filtering: a practical approach v. 190. American Institute of Aeronautics and Astronautics, Incorporated, 2000. URL: <https://books.google.co.uk/books?id=AQxRAAAAMAAJ>.
- [123] Garcia-Sciveres M. and N. Wermes. "A review of advances in pixel detectors for experiments with high rate and radiation". In: *Reports on Progress in Physics* 81.6 (May 2018), p. 066101. DOI: 10.1088/1361-6633/aab064. URL: <https://doi.org/10.1088/1361-6633/aab064>.
- [124] *Track Reconstruction Performance of the ATLAS Inner Detector at  $\sqrt{s} = 13$  TeV*. Tech. rep. ATL-PHYS-PUB-2015-018. Geneva: CERN, July 2015. URL: <https://cds.cern.ch/record/2037683>.
- [125] D. Stampfer, M Regler, and R. Fruhwirth. "Track fitting with energy loss". In: *Computer Physics Communications* 79.2 (1994), pp. 157–164. ISSN: 0010-4655. DOI: [https://doi.org/10.1016/0010-4655\(94\)90064-7](https://doi.org/10.1016/0010-4655(94)90064-7). URL: <http://www.sciencedirect.com/science/article/pii/0010465594900647>.
- [126] G. Borissov, D. Casper, et al. "ATLAS strategy for primary vertex reconstruction during Run-2 of the LHC". In: *Journal of Physics: Conference Series* 664.7 (Dec. 2015), p. 072041. DOI: 10.1088/1742-6596/664/7/072041. URL: <https://doi.org/10.1088/1742-6596/664/7/072041>.
- [127] M. Aaboud et al. "Electron reconstruction and identification in the ATLAS experiment using the 2015 and 2016 LHC proton-proton collision data at  $\sqrt{s} = 13$  TeV". In: *Submitted to: Eur. Phys. J.* (Feb. 2019). arXiv: 1902.04655 [physics.ins-det]. URL: <https://cds.cern.ch/record/2657964>.
- [128] *Electron and photon reconstruction and performance in ATLAS using a dynamical, topological cell clustering-based approach*. Tech. rep. ATL-PHYS-PUB-2017-022. Geneva: CERN, Dec. 2017. URL: <https://cds.cern.ch/record/2298955>.

- [129] ATLAS Collaboration. “Electron performance of the ATLAS detector using the  $J/\psi \rightarrow e^+e^-$  decays”. In: ATL-COM-PHYS-2010-518 (2010). URL: <https://atlas.web.cern.ch/Atlas/GROUPS/PHYSICS/EGAMMA/PublicPlots/20100721/ATL-COM-PHYS-2010-518/>.
- [130] *Performance of the ATLAS electromagnetic calorimeter for  $\pi^0 \rightarrow \gamma\gamma$  and  $\eta \rightarrow \gamma\gamma$  events*. Tech. rep. ATLAS-CONF-2010-006. Geneva: CERN, June 2010. URL: <https://cds.cern.ch/record/1273999>.
- [131] M. Aaboud et al. “Electron efficiency measurements with the ATLAS detector using 2012 LHC proton-proton collision data”. In: *Eur. Phys. J. C* 77.3 (2017), p. 195. DOI: [10.1140/epjc/s10052-017-4756-2](https://doi.org/10.1140/epjc/s10052-017-4756-2). arXiv: [1612.01456](https://arxiv.org/abs/1612.01456) [hep-ex].
- [132] M. Cacciari, G. P. Salam, and G. Soyez. “The anti- $k_t$  jet clustering algorithm”. In: *JHEP* 04 (2008), p. 063. DOI: [10.1088/1126-6708/2008/04/063](https://doi.org/10.1088/1126-6708/2008/04/063). arXiv: [0802.1189](https://arxiv.org/abs/0802.1189) [hep-ph].
- [133] G. Aad et al. “Muon reconstruction performance of the ATLAS detector in proton-proton collision data at  $\sqrt{s}=13$  TeV”. In: *Eur. Phys. J. C* 76.5 (2016), p. 292. DOI: [10.1140/epjc/s10052-016-4120-y](https://doi.org/10.1140/epjc/s10052-016-4120-y). arXiv: [1603.05598](https://arxiv.org/abs/1603.05598) [hep-ex].
- [134] G. Barone et al. *Muon performance results with 2018 dataset: efficiencies, scales, and resolutions*. Tech. rep. ATL-COM-PHYS-2018-661. Geneva: CERN, May 2018. URL: <https://cds.cern.ch/record/2320120>.
- [135] J. Jungeburth and N. Koehler. *Muon reconstruction efficiency on full 2018 pp data set evaluated using  $Z \rightarrow \mu\mu$  events*. Tech. rep. ATL-COM-PHYS-2018-1624. Geneva: CERN, Nov. 2018. URL: <https://cds.cern.ch/record/2648573>.
- [136] G. Aad et al. “Topological cell clustering in the ATLAS calorimeters and its performance in LHC Run 1”. In: *Eur. Phys. J. C* 77 (2017), p. 490. DOI: [10.1140/epjc/s10052-017-5004-5](https://doi.org/10.1140/epjc/s10052-017-5004-5). arXiv: [1603.02934](https://arxiv.org/abs/1603.02934) [hep-ex].
- [137] S. Zenz. “Understanding Jet Structure and Constituents: Track Jets and Jet Shapes at ATLAS”. In: 2010. URL: <http://cdsweb.cern.ch/record/1310336/files/ATL-PHYS-PROC-2010-126.pdf>.
- [138] M. Bahr et al. “Herwig++ Physics and Manual”. In: *Eur. Phys. J. C* 58 (2008), pp. 639–707. DOI: [10.1140/epjc/s10052-008-0798-9](https://doi.org/10.1140/epjc/s10052-008-0798-9). arXiv: [0803.0883](https://arxiv.org/abs/0803.0883) [hep-ph].
- [139] M. Aaboud et al. “Jet energy scale measurements and their systematic uncertainties in proton-proton collisions at  $\sqrt{s}=13$  TeV with the ATLAS detector”. In: *Phys. Rev. D* 96.7 (2017), p. 072002. DOI: [10.1103/PhysRevD.96.072002](https://doi.org/10.1103/PhysRevD.96.072002). arXiv: [1703.09665](https://arxiv.org/abs/1703.09665) [hep-ex].
- [140] G. Aad et al. “Jet energy resolution in proton-proton collisions at  $\sqrt{s}=7$  TeV recorded in 2010 with the ATLAS detector”. In: *Eur. Phys. J. C* 73.3 (2013), p. 2306. DOI: [10.1140/epjc/s10052-013-2306-0](https://doi.org/10.1140/epjc/s10052-013-2306-0). arXiv: [1210.6210](https://arxiv.org/abs/1210.6210) [hep-ex].
- [141] *Jet Calibration and Systematic Uncertainties for Jets Reconstructed in the ATLAS Detector at  $\sqrt{s}=13$  TeV*. Tech. rep. ATL-PHYS-PUB-2015-015. Geneva: CERN, July 2015. URL: <https://cds.cern.ch/record/2037613>.
- [142] The ATLAS Collaboration. “Jet energy resolution in 2017 data and simulation”. Geneva, Sept. 2018. URL: <https://atlas.web.cern.ch/Atlas/GROUPS/PHYSICS/PLOTS/JETM-2018-005/>.

- [143] The ATLAS Collaboration. “Jet energy scale and uncertainties in 2015-2017 data and simulation”. Geneva, Nov. 2018. URL: <https://atlas.web.cern.ch/Atlas/GROUPS/PHYSICS/PLOTS/JETM-2018-006/>.
- [144] *Tagging and suppression of pileup jets with the ATLAS detector*. Tech. rep. ATLAS-CONF-2014-018. Geneva: CERN, May 2014. URL: <https://cds.cern.ch/record/1700870>.
- [145] The ATLAS Collaboration. *Recommendations of the Physics Objects and Analysis Harmonisation Study Groups 2014*. Tech. rep. ATL-COM-PHYS-2014-451. Geneva: CERN, May 2014. URL: <https://cds.cern.ch/record/1700874>.
- [146] *Reconstruction, Energy Calibration, and Identification of Hadronically Decaying Tau Leptons in the ATLAS Experiment for Run-2 of the LHC*. Tech. rep. ATL-PHYS-PUB-2015-045. Geneva: CERN, Nov. 2015. URL: <https://cds.cern.ch/record/2064383>.
- [147] *Expected performance of missing transverse momentum reconstruction for the ATLAS detector at  $\sqrt{s} = 13$  TeV*. Tech. rep. ATL-PHYS-PUB-2015-023. Geneva: CERN, July 2015. URL: <https://cds.cern.ch/record/2037700>.
- [148]  $E_T^{\text{miss}}$  performance in the ATLAS detector using 2015-2016 LHC  $p$ - $p$  collisions. Tech. rep. ATLAS-CONF-2018-023. Geneva: CERN, June 2018. URL: <https://cds.cern.ch/record/2625233>.
- [149] *Performance of missing transverse momentum reconstruction for the ATLAS detector in the first proton-proton collisions at  $\sqrt{s} = 13$  TeV*. Tech. rep. ATL-PHYS-PUB-2015-027. Geneva: CERN, July 2015. URL: <https://cds.cern.ch/record/2037904>.
- [150]  $E_T^{\text{miss}}$  performance in the ATLAS detector using 2015-2016 LHC  $p$ - $p$  collisions. Tech. rep. ATLAS-CONF-2018-023. Geneva: CERN, June 2018. URL: <http://cds.cern.ch/record/2625233>.
- [151] Morad Aaboud et al. “Study of the material of the ATLAS inner detector for Run 2 of the LHC”. In: *JINST* 12.12 (2017), P12009. DOI: [10.1088/1748-0221/12/12/P12009](https://doi.org/10.1088/1748-0221/12/12/P12009). arXiv: [1707.02826](https://arxiv.org/abs/1707.02826) [hep-ex].
- [152] *Expected performance of the ATLAS  $b$ -tagging algorithms in Run-2*. Tech. rep. ATL-PHYS-PUB-2015-022. Geneva: CERN, July 2015. URL: <https://cds.cern.ch/record/2037697>.
- [153] *Identification of Jets Containing  $b$ -Hadrons with Recurrent Neural Networks at the ATLAS Experiment*. Tech. rep. ATL-PHYS-PUB-2017-003. Geneva: CERN, Mar. 2017. URL: <http://cds.cern.ch/record/2255226>.
- [154] Nicola Giacinto Piacquadio. “Identification of  $b$ -jets and investigation of the discovery potential of a Higgs boson in the  $WH \rightarrow l\nu b\bar{b}$  channel with the ATLAS experiment”. In: (Jan. 2010).
- [155] *Optimisation of the ATLAS  $b$ -tagging performance for the 2016 LHC Run*. Tech. rep. ATL-PHYS-PUB-2016-012. Geneva: CERN, June 2016. URL: <http://cds.cern.ch/record/2160731>.
- [156] A. Graves. *Supervised Sequence Labelling with Recurrent Neural Networks*. Studies in Computational Intelligence. Springer, 2012. ISBN: 978-3-642-24796-5. DOI: [10.1007/978-3-642-24797-2](https://doi.org/10.1007/978-3-642-24797-2). URL: <https://doi.org/10.1007/978-3-642-24797-2>.

- [157] *Commissioning of the ATLAS high-performance b-tagging algorithms in the 7 TeV collision data*. Tech. rep. ATLAS-CONF-2011-102. Geneva: CERN, July 2011. URL: <https://cds.cern.ch/record/1369219>.
- [158] B. Heinemann et al. *Performance of the SV0 Tagger in 900 GeV Collision Data*. Tech. rep. ATL-COM-PHYS-2010-084. Geneva: CERN, Feb. 2010. URL: <https://cds.cern.ch/record/1240853>.
- [159] Giacinto Nicola Piacquadio and Christian Weiser. “A new inclusive secondary vertex algorithm for b-jet tagging in ATLAS”. In: 2008. DOI: [10.1088/1742-6596/119/3/032032](https://doi.org/10.1088/1742-6596/119/3/032032).
- [160] P. Zarchan and H. H. Musoff. *Fundamentals of Kalman Filtering: A Practical Approach*. Vol. 190. American Institute of Aeronautics and Astronautics. 2000. URL: <https://books.google.co.uk/books?id=AQxRAAAAMAAJ>.
- [161] *Optimisation and performance studies of the ATLAS b-tagging algorithms for the 2017-18 LHC run*. Tech. rep. ATL-PHYS-PUB-2017-013. Geneva: CERN, July 2017. URL: <https://cds.cern.ch/record/2273281>.
- [162] A. Sciandra. *Development of a new Soft Muon Tagger for the identification of b-jets in ATLAS*. Tech. rep. ATL-PHYS-PROC-2017-190. Geneva: CERN, Oct. 2017. URL: <https://cds.cern.ch/record/2287545>.
- [163] G. Aad et al. “ATLAS b-jet identification performance and efficiency measurement with  $t\bar{t}$  events in  $pp$  collisions at  $\sqrt{s} = 13$  TeV”. In: (2019). arXiv: [1907.05120](https://arxiv.org/abs/1907.05120) [hep-ex].
- [164] Guth M. *Performance Plots of a Hyper Parameter Scan with the Deep Learning Heavy Flavour Tagger (DL1)*. Tech. rep. ATL-COM-PHYS-2019-091. Geneva: CERN, Feb. 2019. URL: <https://cds.cern.ch/record/2657971>.
- [165] I. Goodfellow, J. Pouget-Abadie, et al. “Generative Adversarial Nets”. In: *Advances in Neural Information Processing Systems 27*. Ed. by Z. Ghahramani et al. Curran Associates, Inc., 2014, pp. 2672–2680. URL: <http://papers.nips.cc/paper/5423-generative-adversarial-nets.pdf>.
- [166] *Calibration of the performance of b-tagging for c and light-flavour jets in the 2012 ATLAS data*. Tech. rep. ATLAS-CONF-2014-046. Geneva: CERN, July 2014. URL: <https://cds.cern.ch/record/1741020>.
- [167] *Measurement of b-tagging Efficiency of c-jets in  $t\bar{t}$  Events Using a Likelihood Approach with the ATLAS Detector*. Tech. rep. ATLAS-CONF-2018-001. Geneva: CERN, Mar. 2018. URL: <https://cds.cern.ch/record/2306649>.
- [168] *Calibration of light-flavour jet b-tagging rates on ATLAS proton-proton collision data at  $\sqrt{s} = 13$  TeV*. Tech. rep. ATLAS-CONF-2018-006. Geneva: CERN, Apr. 2018. URL: <https://cds.cern.ch/record/2314418>.
- [169] The ATLAS collaboration. “Measurements of b-jet tagging efficiency with the ATLAS detector using  $t\bar{t}$  events at  $\sqrt{s} = 13$  TeV”. In: *Journal of High Energy Physics* 2018.8 (Aug. 2018), p. 89. ISSN: 1029-8479. DOI: [10.1007/JHEP08\(2018\)089](https://doi.org/10.1007/JHEP08(2018)089). URL: [https://doi.org/10.1007/JHEP08\(2018\)089](https://doi.org/10.1007/JHEP08(2018)089).
- [170] *Measurement of the Higgs boson mass in the  $H \rightarrow ZZ^* \rightarrow 4\ell$  and  $H \rightarrow \gamma\gamma$  channels with  $\sqrt{s}=13\text{TeV}$   $pp$  collisions using the ATLAS detector*. Tech. rep. ATLAS-CONF-2017-046. Geneva: CERN, July 2017. URL: <https://cds.cern.ch/record/2273853>.

- [171]  $ZZ \rightarrow \ell^+ \ell^- \ell'^+ \ell'^-$  cross-section measurements and aTGC search in 13 TeV  $pp$  collisions with the ATLAS detector. Tech. rep. ATLAS-CONF-2017-031. Geneva: CERN, May 2017. URL: <https://cds.cern.ch/record/2263045>.
- [172] S. Manzoni, L. Carminati, and G. Marchiori. “Physics with photons with the ATLAS Run 2 data: calibration and identification, measurement of the Higgs boson mass and search for supersymmetry in di-photon final state.” Oct. 2017. URL: <https://cds.cern.ch/record/2303078>.
- [173] M. Aaboud et al. “Electron and photon energy calibration with the ATLAS detector using 2015-2016 LHC proton-proton collision data”. In: *Journal of Instrumentation* 14.03 (Mar. 2019), P03017–P03017. DOI: 10.1088/1748-0221/14/03/p03017. URL: <https://doi.org/10.1088%5C%2F1748-0221%5C%2F14%5C%2F03%5C%2Fp03017>.
- [174] B. Lenzi and R. Turra. *Monte Carlo calibration update for electrons and photons using multivariate techniques*. Tech. rep. ATL-COM-PHYS-2013-1426. Geneva: CERN, Oct. 2013. URL: <https://cds.cern.ch/record/1609589>.
- [175] L. Breiman, J. Friedman, et al. “Classification and Regression Trees”. In: (1984).
- [176] The ATLAS Collaboration. “Readiness of the ATLAS liquid argon calorimeter for LHC collisions”. In: *The European Physical Journal C* 70.3 (Dec. 2010), pp. 723–753. ISSN: 1434-6052. DOI: 10.1140/epjc/s10052-010-1354-y. URL: <https://doi.org/10.1140/epjc/s10052-010-1354-y>.
- [177] A. Laudrain, L. Iconomidou-Fayard, et al. *Electromagnetic calorimeter layers energy scale determination*. Tech. rep. ATL-COM-PHYS-2017-760. Geneva: CERN, June 2017. URL: <https://cds.cern.ch/record/2268812>.
- [178] M. Boonekamp et al. *Electromagnetic calorimeter layers energy scales determination*. Tech. rep. ATL-COM-PHYS-2013-1423. Geneva: CERN, Oct. 2013. URL: <https://cds.cern.ch/record/1609068>.
- [179] M. Aleksa, N. Andari, et al. *Calibration stability, uniformity and linearity measurements of electrons and photons*. Tech. rep. ATL-COM-PHYS-2017-758. CERN, June 2017. URL: <https://cds.cern.ch/record/2268802>.
- [180] ATLAS Collaboration. *Technical Design Report for the ATLAS Inner Tracker Pixel Detector*. Tech. rep. CERN-LHCC-2017-021. ATLAS-TDR-030. Geneva: CERN, Sept. 2017. URL: <https://cds.cern.ch/record/2285585>.
- [181] J-B. Blanchard, J-B. de Vivie, and P. Mastrandrea. “In-situ scales and smearings from  $Z$  and  $J/\psi$  events”. In: ATL-COM-PHYS-2013-1653 (Dec. 2013). URL: <https://cds.cern.ch/record/1637533>.
- [182] ATLAS Collaboration. “Measurement of the differential non-prompt  $J/\psi$  production fraction in  $\sqrt{s} = 13$  TeV  $pp$  collisions at the ATLAS experiment”. In: ATLAS-CONF-2015-030 (July 2015). URL: <https://cds.cern.ch/record/2037967>.
- [183] ATLAS Collaboration. “A first measurement of the differential cross section for the  $J/\psi \rightarrow \mu\mu$  resonance and the non-prompt to prompt  $J/\psi$  cross-section ratio with  $pp$  collisions at  $\sqrt{s}=7$  TeV in ATLAS”. In: ATLAS-CONF-2010-062 (July 2010). URL: <http://cds.cern.ch/record/1281335>.
- [184] W. Verkerke and D. P. Kirkby. “The RooFit toolkit for data modeling”. In: *eConf C0303241* (2003), MOLT007. arXiv: [physics/0306116](https://arxiv.org/abs/physics/0306116) [physics].



- [185] P. L. Tchebychev. *Théorie des mécanismes connus sous le nom de parallélogrammes*. Imprimerie de l'Académie impériale des sciences, 1853. URL: [https://books.google.fr/books?id=eUP%5C\\_nAEACAAJ](https://books.google.fr/books?id=eUP%5C_nAEACAAJ).
- [186] T. Aaltonen et al. "Evidence for a particle produced in association with weak bosons and decaying to a bottom-antibottom quark pair in Higgs boson searches at the Tevatron". In: *Phys. Rev. Lett.* 109 (2012), p. 071804. DOI: [10.1103/PhysRevLett.109.071804](https://doi.org/10.1103/PhysRevLett.109.071804). arXiv: [1207.6436](https://arxiv.org/abs/1207.6436) [hep-ex].
- [187] M. Aaboud et al. "Observation of  $H \rightarrow b\bar{b}$  decays and  $VH$  production with the ATLAS detector". In: *Phys. Lett. B* 786 (2018), pp. 59–86. DOI: [10.1016/j.physletb.2018.09.013](https://doi.org/10.1016/j.physletb.2018.09.013). arXiv: [1808.08238](https://arxiv.org/abs/1808.08238) [hep-ex].
- [188] A. Sirunyan et al. "Evidence for the Higgs boson decay to a bottom quark-antiquark pair". In: *Phys. Lett. B* 780 (2018), pp. 501–532. DOI: [10.1016/j.physletb.2018.02.050](https://doi.org/10.1016/j.physletb.2018.02.050). arXiv: [1709.07497](https://arxiv.org/abs/1709.07497) [hep-ex].
- [189] S. Agostinelli et al. "Geant4 a simulation toolkit". In: *Nuclear Instruments and Methods in Physics Research Section A: Accelerators, Spectrometers, Detectors and Associated Equipment* 506.3 (2003), pp. 250–303. ISSN: 0168-9002. DOI: [https://doi.org/10.1016/S0168-9002\(03\)01368-8](https://doi.org/10.1016/S0168-9002(03)01368-8). URL: <http://www.sciencedirect.com/science/article/pii/S0168900203013688>.
- [190] D. Lange. "The EvtGen particle decay simulation package". In: *Nuclear Instruments and Methods in Physics Research Section A: Accelerators, Spectrometers, Detectors and Associated Equipment* 462.1 (2001). BEAUTY2000, Proceedings, pp. 152–155. ISSN: 0168-9002. DOI: [https://doi.org/10.1016/S0168-9002\(01\)00089-4](https://doi.org/10.1016/S0168-9002(01)00089-4). URL: <http://www.sciencedirect.com/science/article/pii/S0168900201000894>.
- [191] G. Aad et al. "Measurement of the  $Z/\gamma^*$  boson transverse momentum distribution in  $pp$  collisions at  $\sqrt{s} = 7$  TeV with the ATLAS detector". In: *JHEP* 09 (2014), p. 145. DOI: [10.1007/JHEP09\(2014\)145](https://doi.org/10.1007/JHEP09(2014)145). arXiv: [1406.3660](https://arxiv.org/abs/1406.3660) [hep-ex].
- [192] R. D. Ball et al. "Parton distributions for the LHC Run II". In: *JHEP* 04 (2015), p. 040. DOI: [10.1007/JHEP04\(2015\)040](https://doi.org/10.1007/JHEP04(2015)040). arXiv: [1410.8849](https://arxiv.org/abs/1410.8849) [hep-ph].
- [193] O. Brein, A. Djouadi, and R. Harlander. "NNLO QCD corrections to the Higgs-strahlung processes at hadron colliders". In: *Physics Letters B* 579.1 (2004), pp. 149–156. ISSN: 0370-2693. DOI: <https://doi.org/10.1016/j.physletb.2003.10.112>. URL: <http://www.sciencedirect.com/science/article/pii/S0370269303017234>.
- [194] R. Ball et al. "Parton Distribution Benchmarking with LHC Data". In: *JHEP* 04 (2013), p. 125. DOI: [10.1007/JHEP04\(2013\)125](https://doi.org/10.1007/JHEP04(2013)125). arXiv: [1211.5142](https://arxiv.org/abs/1211.5142) [hep-ph].
- [195] Gavin Cullen et al. "Automated One-Loop Calculations with GoSam". In: *Eur. Phys. J. C* 72 (2012), p. 1889. DOI: [10.1140/epjc/s10052-012-1889-1](https://doi.org/10.1140/epjc/s10052-012-1889-1). arXiv: [1111.2034](https://arxiv.org/abs/1111.2034) [hep-ph].
- [196] A. Denner et al. "Electroweak corrections to Higgs-strahlung off  $W/Z$  bosons at the Tevatron and the LHC with HAWK". In: *JHEP* 03 (2012), p. 075. DOI: [10.1007/JHEP03\(2012\)075](https://doi.org/10.1007/JHEP03(2012)075). arXiv: [1112.5142](https://arxiv.org/abs/1112.5142) [hep-ph].
- [197] A. Denner et al. "HAWK 2.0: A Monte Carlo program for Higgs production in vector-boson fusion and Higgs strahlung at hadron colliders". In: *Comput. Phys. Commun.* 195 (2015), pp. 161–171. DOI: [10.1016/j.cpc.2015.04.021](https://doi.org/10.1016/j.cpc.2015.04.021). arXiv: [1412.5390](https://arxiv.org/abs/1412.5390) [hep-ph].

- [198] S. Frixione, P. Nason, and G. Ridolfi. “A Positive-weight next-to-leading-order Monte Carlo for heavy flavour hadroproduction”. In: *JHEP* 09 (2007), p. 126. DOI: [10.1088/1126-6708/2007/09/126](https://doi.org/10.1088/1126-6708/2007/09/126). arXiv: [0707.3088 \[hep-ph\]](https://arxiv.org/abs/hep-ph/0707.3088).
- [199] P. Nason. “A New method for combining NLO QCD with shower Monte Carlo algorithms”. In: *JHEP* 11 (2004), p. 040. DOI: [10.1088/1126-6708/2004/11/040](https://doi.org/10.1088/1126-6708/2004/11/040). arXiv: [hep-ph/0409146 \[hep-ph\]](https://arxiv.org/abs/hep-ph/0409146).
- [200] T. Sjöstrand, S. Ask, J. Christiansen, et al. “An Introduction to PYTHIA 8.2”. In: *Comput. Phys. Commun.* 191 (2015), pp. 159–177. DOI: [10.1016/j.cpc.2015.01.024](https://doi.org/10.1016/j.cpc.2015.01.024). arXiv: [1410.3012 \[hep-ph\]](https://arxiv.org/abs/1410.3012).
- [201] M. Czakon and A. Mitov. “Top++: A Program for the Calculation of the Top-Pair Cross-Section at Hadron Colliders”. In: *Comput. Phys. Commun.* 185 (2014), p. 2930. DOI: [10.1016/j.cpc.2014.06.021](https://doi.org/10.1016/j.cpc.2014.06.021). arXiv: [1112.5675 \[hep-ph\]](https://arxiv.org/abs/1112.5675).
- [202] M. Aliev, H. Lacker, et al. “HATHOR HAdronic Top and Heavy quarks crOss section calculatoR”. In: *Computer Physics Communications* 182.4 (2011). ISSN: 0010-4655. DOI: <https://doi.org/10.1016/j.cpc.2010.12.040>. URL: <http://www.sciencedirect.com/science/article/pii/S0010465510005333>.
- [203] P. Kant, O.M. Kind, et al. “HatHor for single top-quark production: Updated predictions and uncertainty estimates for single top-quark production in hadronic collisions”. In: *Computer Physics Communications* 191 (2015), pp. 74–89. ISSN: 0010-4655. DOI: <https://doi.org/10.1016/j.cpc.2015.02.001>. URL: <http://www.sciencedirect.com/science/article/pii/S0010465515000454>.
- [204] M. H. Seymour and A. Siodmok. “Constraining MPI models using  $\sigma_{eff}$  and recent Tevatron and LHC Underlying Event data”. In: *JHEP* 10 (2013), p. 113. DOI: [10.1007/JHEP10\(2013\)113](https://doi.org/10.1007/JHEP10(2013)113). arXiv: [1307.5015 \[hep-ph\]](https://arxiv.org/abs/1307.5015).
- [205] M. Aaboud et al. “Observation of  $H \rightarrow b\bar{b}$  decays and  $VH$  production with the ATLAS detector”. In: *Phys. Lett. B* 786 (2018), pp. 59–86. DOI: [10.1016/j.physletb.2018.09.013](https://doi.org/10.1016/j.physletb.2018.09.013). arXiv: [1808.08238 \[hep-ex\]](https://arxiv.org/abs/1808.08238).
- [206] A. D. Bukin. *Fitting function for asymmetric peaks*. 2007. arXiv: [0711.4449 \[physics.data-an\]](https://arxiv.org/abs/0711.4449).
- [207] Yann Coadou. “Boosted Decision Trees and Applications”. In: *EPJ Web Conf.* 55 (2013), p. 02004. DOI: [10.1051/epjconf/20135502004](https://doi.org/10.1051/epjconf/20135502004).
- [208] G. Aad et al. “Search for the  $b\bar{b}$  decay of the Standard Model Higgs boson in associated  $(W/Z)H$  production with the ATLAS detector”. In: *JHEP* 01 (2015), p. 069. DOI: [10.1007/JHEP01\(2015\)069](https://doi.org/10.1007/JHEP01(2015)069). arXiv: [1409.6212 \[hep-ex\]](https://arxiv.org/abs/1409.6212).
- [209] A. Hocker et al. *TMVA - Toolkit for Multivariate Data Analysis with ROOT: Users guide*. *TMVA - Toolkit for Multivariate Data Analysis*. Tech. rep. physics/0703039. TMVA-v4 Users Guide: 135 pages, 19 figures, numerous code examples and references. Geneva: CERN, Mar. 2007. URL: <https://cds.cern.ch/record/1019880>.
- [210] Jerome Friedman, Trevor Hastie, and Robert Tibshirani. “Additive Logistic Regression: a Statistical View of Boosting”. In: *Annals of Statistics* 28 (1998), p. 2000.
- [211] Y. Freund and R. E. Schapire. *Experiments with a New Boosting Algorithm*. 1996.
- [212] J. H. Friedman. “Stochastic Gradient Boosting”. In: *Comput. Stat. Data Anal.* 38.4 (Feb. 2002), pp. 367–378. ISSN: 0167-9473. DOI: [10.1016/S0167-9473\(01\)00065-2](https://doi.org/10.1016/S0167-9473(01)00065-2). URL: [http://dx.doi.org/10.1016/S0167-9473\(01\)00065-2](http://dx.doi.org/10.1016/S0167-9473(01)00065-2).



- [213] T. Chen and C. Guestrin. “XGBoost: A Scalable Tree Boosting System”. In: *CoRR* abs/1603.02754 (2016). arXiv: 1603.02754. URL: <http://arxiv.org/abs/1603.02754>.
- [214] C. Delporte. “Study of the Higgs boson decay into b-quarks with the ATLAS experiment - run 2”. In: CERN-THESIS (2018).
- [215] R. J. Barlow and C. Beeston. “Fitting using finite Monte Carlo samples”. In: *Comput. Phys. Commun.* 77 (1993), pp. 219–228. DOI: 10.1016/0010-4655(93)90005-W.
- [216] S. S. Wilks. “The Large-Sample Distribution of the Likelihood Ratio for Testing Composite Hypotheses”. In: *Annals Math. Statist.* 9.1 (1938), pp. 60–62. DOI: 10.1214/aoms/1177732360.
- [217] G. Cowan et al. “Asymptotic formulae for likelihood-based tests of new physics”. In: *Eur. Phys. J. C* 71 (2011). [*Eur. Phys. J.* C73,2501(2013)], p. 1554. DOI: 10.1140/epjc/s10052-011-1554-0, 10.1140/epjc/s10052-013-2501-z. arXiv: 1007.1727 [physics.data-an].
- [218] A. Wald. “Tests of Statistical Hypotheses Concerning Several Parameters When the Number of Observations is Large”. In: *Transactions of the American Mathematical Society* 54.3 (1943), pp. 426–482. ISSN: 00029947. URL: <http://www.jstor.org/stable/1990256>.
- [219] G. Aad et al. “Muon reconstruction performance of the ATLAS detector in proton-proton collision data at  $\sqrt{s}=13$  TeV”. In: *Eur. Phys. J. C* 76.5 (2016), p. 292. DOI: 10.1140/epjc/s10052-016-4120-y. arXiv: 1603.05598 [hep-ex].
- [220] ATLAS Collaboration. “Electron Efficiencies for Run2 (scale factors and uncertainties)”. 2016. URL: <https://twiki.cern.ch/twiki/bin/viewauth/AtlasProtected/ElectronEfficiencyRun2>.
- [221] The ATLAS Collaboration. “MCP Guidelines”. 2016. URL: <https://twiki.cern.ch/twiki/bin/view/AtlasProtected/MCPAnalysisGuidelinesMC15>.
- [222] M. Aaboud et al. “Measurement of the Inelastic Proton-Proton Cross Section at  $\sqrt{s}=13$  TeV with the ATLAS Detector at the LHC”. In: *Phys. Rev. Lett.* 117.18 (2016), p. 182002. DOI: 10.1103/PhysRevLett.117.182002. arXiv: 1606.02625 [hep-ex].
- [223] B. Mellado Garcia et al. “CERN Report 4: Part I Standard Model Predictions”. In: (May 2016). URL: <https://cds.cern.ch/record/2150771>.
- [224] I. W. Stewart and F. J. Tackmann. “Theory uncertainties for Higgs mass and other searches using jet bins”. In: *Phys. Rev. D* 85 (3 Feb. 2012), p. 034011. DOI: 10.1103/PhysRevD.85.034011. URL: <https://link.aps.org/doi/10.1103/PhysRevD.85.034011>.
- [225] J. Butterworth et al. “PDF4LHC recommendations for LHC Run II”. In: *J. Phys. G* 43 (2016), p. 023001. DOI: 10.1088/0954-3899/43/2/023001. arXiv: 1510.03865 [hep-ph].
- [226] M. Aaboud et al. “Measurements of Higgs boson properties in the diphoton decay channel with  $36\text{ fb}^{-1}$  of  $pp$  collision data at  $\sqrt{s}=13$  TeV with the ATLAS detector”. In: *Phys. Rev. D* 98 (2018), p. 052005. DOI: 10.1103/PhysRevD.98.052005. arXiv: 1802.04146 [hep-ex].

- [227] M. Aaboud et al. “Measurement of the Higgs boson coupling properties in the  $H \rightarrow ZZ^* \rightarrow 4\ell$  decay channel at  $\sqrt{s} = 13$  TeV with the ATLAS detector”. In: *JHEP* 03 (2018), p. 095. DOI: [10.1007/JHEP03\(2018\)095](https://doi.org/10.1007/JHEP03(2018)095). arXiv: [1712.02304](https://arxiv.org/abs/1712.02304) [hep-ex].
- [228] M. Aaboud et al. “Search for the Standard Model Higgs boson produced by vector-boson fusion and decaying to bottom quarks in  $\sqrt{s} = 8$  TeV pp collisions with the ATLAS detector”. In: *JHEP* 11 (2016), p. 112. DOI: [10.1007/JHEP11\(2016\)112](https://doi.org/10.1007/JHEP11(2016)112). arXiv: [1606.02181](https://arxiv.org/abs/1606.02181) [hep-ex].
- [229] M. Aaboud et al. “Search for Higgs bosons produced via vector-boson fusion and decaying into bottom quark pairs in  $\sqrt{s} = 13$  TeV  $pp$  collisions with the ATLAS detector”. In: *Phys. Rev. D* 98.5 (2018), p. 052003. DOI: [10.1103/PhysRevD.98.052003](https://doi.org/10.1103/PhysRevD.98.052003). arXiv: [1807.08639](https://arxiv.org/abs/1807.08639) [hep-ex].
- [230] G. Aad et al. “Search for the Standard Model Higgs boson produced in association with top quarks and decaying into  $b\bar{b}$  in pp collisions at  $\sqrt{s} = 8$  TeV with the ATLAS detector”. In: *Eur. Phys. J. C* 75.7 (2015), p. 349. DOI: [10.1140/epjc/s10052-015-3543-1](https://doi.org/10.1140/epjc/s10052-015-3543-1). arXiv: [1503.05066](https://arxiv.org/abs/1503.05066) [hep-ex].
- [231] G. Aad et al. “Search for the Standard Model Higgs boson decaying into  $b\bar{b}$  produced in association with top quarks decaying hadronically in pp collisions at  $\sqrt{s} = 8$  TeV with the ATLAS detector”. In: *JHEP* 05 (2016), p. 160. DOI: [10.1007/JHEP05\(2016\)160](https://doi.org/10.1007/JHEP05(2016)160). arXiv: [1604.03812](https://arxiv.org/abs/1604.03812) [hep-ex].
- [232] M. Aaboud et al. “Search for the standard model Higgs boson produced in association with top quarks and decaying into a  $b\bar{b}$  pair in  $pp$  collisions at  $\sqrt{s} = 13$  TeV with the ATLAS detector”. In: *Phys. Rev. D* 97.7 (2018), p. 072016. DOI: [10.1103/PhysRevD.97.072016](https://doi.org/10.1103/PhysRevD.97.072016). arXiv: [1712.08895](https://arxiv.org/abs/1712.08895) [hep-ex].
- [233] M. Aaboud et al. “Measurement of  $VH, H \rightarrow b\bar{b}$  production as a function of the vector-boson transverse momentum in 13 TeV pp collisions with the ATLAS detector”. In: *JHEP* 05 (2019), p. 141. DOI: [10.1007/JHEP05\(2019\)141](https://doi.org/10.1007/JHEP05(2019)141). arXiv: [1903.04618](https://arxiv.org/abs/1903.04618) [hep-ex].
- [234] M. Aaboud, G. Aad, et al. “Probing the Quantum Interference between Singly and Doubly Resonant Top-Quark Production in  $pp$  Collisions at  $\sqrt{s} = 13$  TeV with the ATLAS Detector”. In: *Phys. Rev. Lett.* 121 (15 Oct. 2018), p. 152002. DOI: [10.1103/PhysRevLett.121.152002](https://doi.org/10.1103/PhysRevLett.121.152002). URL: <https://link.aps.org/doi/10.1103/PhysRevLett.121.152002>.